DTIC FILE COPY

2

THE
GEORGE
WASHINGTON
UNIVERSITY

School of Engineering and Applied Science / Washington, D.C. 20052

Department of Civil, Mechani
and Environmental Engineering
(202) 994-6749

AD-A196 831

Dr. Yapa Rajapakse
Office Of Naval Research
Department of the Navy
800 North Quincy Street
Code 1132SM
Arlington, VA 22217-5000

DTIC
ELECTE
JUN 2 2 1988
S D
CD

May 26, 1988

Dear Dr. Rajapakse:

Enclosed please find the final technical report for ONR Contract #N00014-84-K-0027, "Creep and Fracture Characteristics of Materials and Structures at Elevated Temperatures". This report is also being sent to the ONR distribution list dated 11/1/1986.

If you require further information, please do not hesitate to contact me.

Sincerely,

E. Thomas Moyer Jr.
Assoc. Prof. of Engineering and Applied Science

Enclosure.

cc:
Mr. Gary Henman, ONR (1 copy)
Director, NRL (1 copy)
Defense Technical Information Center (12 copies)

DISTRIBUTION STATEMENT A
Approved for public release
Distribution Unlimited

88 6 1 151

FINAL REPORT - ONR CONTRACT #N00014-84-K-0027

CREEP AND FRACTURE CHARACTERISTICS OF MATERIALS AND STRUCTURES AT ELEVATED TEMPERATURES

Principal Investigator: Harold Liebowitz
Dean of the School of Engineering
and Applied Science

Technical Director: E. Thomas Moyer Jr.
Associate Professor of Engineering
and Applied Science

The George Washington University

May, 1988

Accesion For
NTIS CRA&I ✓
DTIC TAB ☐
Unannounced ☐
Justification
By per ltr
Distribution /
Availability Codes
Dist
A-1

FINAL REPORT - ONR CONTRACT #N00014-84-K-0027

CREEP AND FRACTURE CHARACTERISTICS OF MATERIALS AND STRUCTURES AT ELEVATED TEMPERATURES

PRINCIPAL INVESTIGATOR - DEAN HAROLD LIEBOWITZ
TECHNICAL DIRECTOR - ASSOC. PROF. E. THOMAS MOYER JR.

Significant research was performed under ONR Contract #N00014-84-K-0027 during the period of the contract. As listed in Appendix A, this work resulted in eight refereed publications and four invited presentations at International Conferences. The work also resulted in four student theses listed in Appendix B. In addition, experimental progress was made in creep fracture testing. As outlined below, this work was has not been completed due to the lack of continuation of the contract.

The work under this contract was concentrated in three major areas: the effect of mixed mode loading on fracture characteristics, the nature of crack tip stress, strain and energy fields in ductile materials and the nature of crack tip stress strain and energy fields in materials undergoing rate dependent viscoplastic deformation. In each of these areas, new insight was obtained and better understanding of the fundamental physical processes gained.

Early work on this contract focused on mixed mode fracture characteristics. Experimental studies and finite element modeling determined specimen characteristics and design modifications for a mode two fracture specimen. This specimen has the unique capability of testing from pure mode one to pure mode two without significant crack face rotation. This work is documented in two student thesis (students were successful candidates for the Diplome degree through a joint, cooperative program between the University of Stuttgart and the George Washington University). In addition, further work developed a computational procedure based on the nodal force approach for the determination of stress intensity factor distributions along arbitrary crack fronts in three dimensions. This work was presented at an ASTM conference and will appear in ASTM STP #969. This work is also documented in a student masters thesis (all student theses are listed in Appendix B).

Work on ductile fracture was carried out for three dimensional, mode one crack geometries. The effect of specimen thickness and material hardening characteristics was studied. In addition to useful understanding, the thickness range where plane strain and plane stress are valid assumptions were discovered. Depending on the ductility of the material, the plane strain thickness did not correspond to the ASTM requirement due to the assumptions of elasticity employed. A modified approach for determination of plane strain thickness was proposed. In addition to the three dimensional studies involving a stationary mode one crack, further research was performed in the areas of mixed mode ductile fracture and ductile crack growth. The mixed mode ductile fracture studies demonstrated the crack opening characteristics as a function of mode ratio. It was demonstrated that for dominant mode one, a distinct notch effect is observed. This notch opening removes the HRR singularity and produces a ductile zone which is characterized by a weaker energy singularity than was previously known. In addition, as mode two becomes more dominant, the deformed crack remains sharper and the local HRR characteristics return. In addition, the significant rotation occurs at the crack tip altering the amplitude of the local field. Mode one crack growth studies were performed. This work demonstrated a computational approach for accurately modeling stable crack growth with a commercial finite element code. The physical results demonstrate the disappearance of the HRR zone due to notch opening and the appearance of a significant transition zone which dominates the local fracture zone. This zone is characterized by an energy singularity which is weaker than 1/r. This is a new result which is under further investigation. The two dimensional studies are documented in student theses listed in Appendix B. To date, work is continuing on this problem and the results are not yet available in the open literature. The student theses, therefore, are included as Appendices D and E.

Studies on creep fracture characteristics were the focus of significant study under this contract. Experimental work focused on crack growth studies on IN 718 at 650 degrees C. At this temperature, significant constituitive data was available. These results demonstrated that the C^* integral was not employable as a crack driving force measure. In addition, it was determined that experimental scatter was due to crack front curvature effects which could be minimized through careful experimental technique. The final results demonstrated a two stage growth regime which was numerically fit to explicit time functions for crack growth simulation. This work was part of an ONR progress report and is included as Appendix E. Finite element studies of creep crack growth were performed and the results are part of a recent publication included as Appendix F. This study demonstrated the influence of finite strains in the crack region and the inability of local asymptotic solutions to characterize the stress fields near stationary and growing cracks. In addition, convergence and accuracy of the numerical approach was studied extensively. New understanding of convergence characteristics was obtained.

Experiments were initiated at 550 degrees C to determine if the results at 650 degrees were characteristic of creep crack growth in general or were a qualitative function of temperature. Unfortunately, insufficient constituitive data was available at 550 degrees and the data was not able to be analyzed. Constituitive tests were initiated, however, the contract resources were not sufficient to complete the work. If future funding is available for this work, the tests will be completed and the results will be forwarded to ONR.

The appendices of this work document the significant research contribution that was made under ONR contract #N00014-84-K-0027. All publications cited in the appendices were forwarded to ONR at publication and were included in the quarterly progress reports. In addition, all publications have been sent to the ONR distribution list at the time of publication.

APPENDIX A - PUBLICATIONS FROM ONR CONTRACT #N00014-84-K-0027

1] "Creep Crack Growth Modeling and Near Tip Stress Fields" E. Thomas Moyer Jr. and Harold Liebowitz, Engineering Fracture Mechanics, Vol. 28, pp. 601, 1987.

2] "Finite Element Methods in Fracture Mechanics" Harold Liebowitz and E. Thomas Moyer Jr., Proc. 5th International Conference in Australia in Fracture Mechanics, University of Melbourne, Australia, 1987.

3] "Finite Element Modeling for Elastic-Plastic Fracture Problems in Three Dimensions", International Journal for Numerical Methods in Engineering, Vol. 22, pp. 289, 1986.

4] "Prediction of Plasticity Characteristics for Three-Dimensional Fracture Specimens: Comparison with Experiment" E.T. Moyer Jr., H. Liebowitz and P.K. Poulose, Engineering Fracture Mechanics, Vol. 24, pp. 677, 1986.

5] "Accurate Modeling of Ductile and Creep Fracture Specimens and Processes", E. Thomas Moyer Jr., Proc. of the ASM Conference on Fatigue, Corrosion Cracking, Fracture Mechanics and Failure Analysis, ASM publications, 1985.

6] "Methodology for Mixed Mode Stress Intensity Factor Calculations" E. Thomas Moyer Jr., ASTM STP #969, to appear, July 1988.

7] "An Overview of the Finite Element Method for the Analysis of Engineering Metals", E. Thomas Moyer Jr., in Computer Simulation in Materials Science, ASM International, 1988.

8] "Effect of Specimen Thickness on Crack Front Plasticity Characteristics in Three Dimensions", E. Thomas Moyer Jr., Proc. 6th Intl. Congress on Fracture, New Delhi, 1984.

9] "Biaxial Load Effects in the Mechanics of Fracture" E. Thomas Moyer Jr. and Harold Liebowitz, Journal of the Aeronautical Society of India, Vol. 36, pp. 17, 1984.

APPENDIX B - STUDENT THESES UNDER ONR CONTRACT #N00014-84-K-0027

1] Determination of Two Dimensional Stress Intensity
By: Peter Bauerle, 1985, Diplome Thesis.

2] Fracture Under Mixed Mode Loading
By: Roland Gerstner, 1985, Diplome Thesis.

3] The Nodal Force Approach for Mixed Mode Stress Intensity Factor Calculations in Three Dimensions
By: Kornelius Hengle, 1987, Master of Science Thesis.

4] Ductile Crack Growth Simulation - Local Deformation and Field Variable Analysis
By: Kurt Kunze, 1987, Master of Science Thesis.

5] Local Crack Tip Field Quantities with Ductile Material Behavior for General Mixed Mode Problems
By: Martin Haegele, 1988, Master of Science Thesis.

APPENDIX C: FRACTURE TESTS ON IN 718 - INSIGHT INTO CREEP FRACTURE BEHAVIOR

FRACTURE TESTS ON IN 718 -
INSIGHT INTO CREEP FRACTURE PHENOMENA

E. T. Moyer, Jr. and H. Liebowitz
The George Washington University

ABSTRACT

Fracture tests on IN 718 superalloy demonstrate that the C^* fracture parameter is not a sufficient quantity for the quantitative description of creep crack growth. The results contained in this communication show that the crack velocity is not uniquely predicted by C^* but is also a function of test load. In addition, the results indicate that the crack velocity would also be affected by geometry changes (e.g., specimen size).

The results presented in this communication also demonstrate that crack growth initiates extremely early in the test history. No unique initiation time was identifiable. Also evident is a two stage growth process with stage 1 (characterized by constant crack velocity) contributing significantly to the total useful life even at relatively high initial crack velocities (on the order of 0.001 inches/minute).

Investigation was made into the widely observed scatter in creep fracture data reported in the literature. This scatter is often suggested to be due to crack tunneling, material

variability, etc. The results presented in this work show that initial crack front curvature, irregular geometries, forming inconsistencies (e.g., rolling irregularities) cause extreme scatter in experimental results. These irregularities, however, are observable continuum phenomena which are inconsistent with the assumptions inherent in the analysis of the test data. When specimens exhibiting these irregularities are removed from the data base, scatter is reduced to acceptable levels (e.g., less than 10% in measured quantities). The fracture surfaces also indicate that tunneling does not occur for the geometry, loading, temperature and material conditions studied.

FRACTURE TESTS ON IN 718 - INSIGHT INTO CREEP FRACTURE PHENOMENA

E. T. Moyer, Jr. and H. Liebowitz
The George Washington University

A series of constant load creep fracture tests were performed on IN 718 specimens at 650°C. The specimen geometry was standard compact tension with dimensions ($a = 1.0$ in., $W = 2.0$ in., $B = 0.4$ in.). Tests were run for load levels between 1000-1500 lb. Mouth opening displacement and crack length were monitored continuously during the test. To establish a sharp initial crack, the specimens were fatigue precracked at room temperature at 15 Ksi - $\sqrt{in}$. Crack length is measured optically to a precision of 0.0015 in.

The first Figure is a plot of the crack length vs time at five different load levels. All the data indicates a two stage crack growth process. The first stage is characterized by essentially constant crack velocity (the linear portion of the crack length vs time curve) and the second stage is characterized by continuous acceleration. For the growth range studied, stage 1 crack growth accounts for a significant portion of the growth history (at 1000 lb., stage 1 accounts for approximately 65% of the time required to increase the crack length 40%; at 1500 lb., stage 1 accounts for approximately 40% of this time history). At the load levels tested, crack growth was observed very early in the history. A unique "initiation" time was not identifiable.

The crack length vs time curves clearly indicate that stage 1 growth is evident even when initial crack velocities are of a "average" magnitude. Previous studies have indicated that stage 1 is present only for very slowly growing cracks [1]. In the data presented here, initial crack velocities varied by almost an order of magnitude and all tests exhibit stage 1 behavior for significant portions of the growth history.

The second Figure is a plot of crack velocity (da/dt) vs C^*. The formulation of Kumar and Shih (K-S) is used for the calculation of C^* [2]. This formulation is to be preferred to the Harper and Ellison (H-E) formulation for two reasons: first, the assumptions made in the derivation are less restrictive (e.g., zone size requirements in the H-E formulation, proportioning of deformation due to crack growth and creep, etc.) and second, because the K-S formulation requires only a knowledge of the geometry and loading and not the load line displacement rate (which is measured less accurately). Indeed, for reasonable crack velocities, the H-E formulation can be shown to be a measure of da/dt and not C^* [3].

The da/dt vs C^* plot demonstrates that the C^* is not a sufficient parameter to describe crack growth. It has been postulated in the literature that da/dt can be uniquely related to C^*, independent of loading and geometry (see, for example, [4,5]). The results presented by the authors demonstrate that da/dt is a function of the test loading in addition to the parameters involved in calculating C^*. This is understandable as during stage 1 growth, C^* is steadily increasing while da/dt remains constant. In addition, convergence toward a unique da/dt vs C^* relationship is not evident until the crack velocity and length have grown appreciably. At the larger da/dt values, many of the assumptions required for the application of the K-S formula become dubious. In the region in which the K-S assumptions are valid, the results demonstrate that C^* is not a sufficient correlating parameter.

For the range of geometry and loading presented in this work, K is not a viable fracture parameter. At 1000 lb. loading, the stress intensity factor calculated from the mouth opening displacement reached a value of 27 Ksi - $\sqrt{\text{in}}$. prior to crack growth where the linear elastic K value was 17 Ksi - $\sqrt{\text{in}}$. corresponding to the load. It was evident, therefore, that the creep deformation exceeded the K controlled region from the start of the test. K, therefore is not a viable fracture parameter for this data.

Creep fracture studies often exhibit much experimental scatter. Many reasons are proposed including environmental effects, deformation transitions, tunneling, mechanism transitions, etc. Data which exhibits large scatter cannot be used to establish or reject the validity of any theoretical model as the error in the data can be on the order of the phenomena being described. To minimize scatter in our results, data was only taken in the range where oxidation effects are small. Oxidation influences are a function of the test duration and the local strain state near the crack [6]. The presence of oxidation can be seen on the fracture surface as a change in color from the standard metallic color to a blue color. Only data obtained before the color change became appreciable was used in the analysis.

In addition to avoiding oxidation driven growth data, closer examination of the fracture specimens revealed observable causes for the scatter observed. Several specimens which exhibited data far from the mean had extensively curved crack fronts after fatigue precracking. These specimens tended to exhibit much slower crack growth than those with relatively straight crack fronts. If extreme curvature was exhibited in the fatigue crack (greater than approximately 1/16 in.) the data was rejected.

Photo 1 and Photo 2 show fracture specimens whose data were excepted (number 1 was loaded at 1000 lb. and number 2 was loaded at 1500 lb.). Both exhibit typical fatigue cracks which produced consistent data. Photo 3 shows a specimen which was loaded at 1000 lb. The data from that test exhibit twice the lifetime of the mean at that load. The geometric discontinuity introduced by a machining error (the kink in the notch) caused the crack to grow in a uneven manner prolonging life.

Other scatter occurred due to discontinuities in the material. Photo 4 shows a specimen which was loaded at

1500 lb. The fracture surface discontinuity again prolonged the life of the specimen. This discontinuity is believed to be caused by imprecision in the rolling process during forming. None of the sources of scatter described could have been predicted without examination of the fracture surface. These phenomena, however, are not due to material variability or microstructure. All the observations are continuum irregularities which are inconsistent with the analytical assumptions of continuum crack growth.

After discarding the specimens with continuum discontinuities, the data exhibited very little scatter from test to test. The data presented in this work is the average of that obtained from multiple tests. The test to test differences in crack length was less than 5% and the difference in crack velocities was less than 10%. Mouth opening displacements were contained within a scatter band of approximately 3% with deviations in opening rate of approximately 7%. It is felt that these numbers accurately represent the "scatter" which is due to testing configuration, material variability (which should be small since all specimens are from a single batch of material, were heat treated identically and were cut in the same direction relative to the rolling) and microstructure.

The data presented demonstrate the inability of either C^* or K to be a valid constitutive parameter for creep crack growth in IN 718 at 650°C. In addition, these results viewed with other investigators' work (for various materials, e.g., [1,3,6]), demonstrate that a valid fracture parameter characterizing creep crack growth behavior for a realistic range of geometry and loading has yet to be found. In addition, new insight into the "Sources of Scatter" have been identified. This testing sequence suggests that continuum reasons for observed scatter can often be identified which violate the continuity assumptions inherent in the test procedure and analysis.

REFERENCES

1] E. Maas and A. Pineau. International Journal of Engineering Fracture Mechanics, Vol. 22, pp. 307, 1985.

2] V. Kumar and C. F. Shih. Fracture Mechanics, Twelfth Conference, ASTM STP #700, pp. 406, Philadelphia, Pennsylvania.

3] P. L. Bensussan, D. A. Jablonski and R. M. Pelloux. Metallurgical Transactions A, 1984, Vol. 154, pp. 107.

4] C. E. Jaske. The Mechanism of Fracture, pp. 577, 1986, American Society for Metals.

5] M. P. Harper and E. G. Ellison. Journal of Strain Analysis, Vol. 12, pp. 167, 1977.

6] K. Sadananda and P. Shahinian. International Journal of Engineering Fracture Mechanics, Vol. 15, pp. 327, 1981.

7] P. Bensussan, G. Cailletaud, A. Pineau and R. Pelloux. The Mechanism of Fracture, pp. 587, 1986, American Society for Metals.

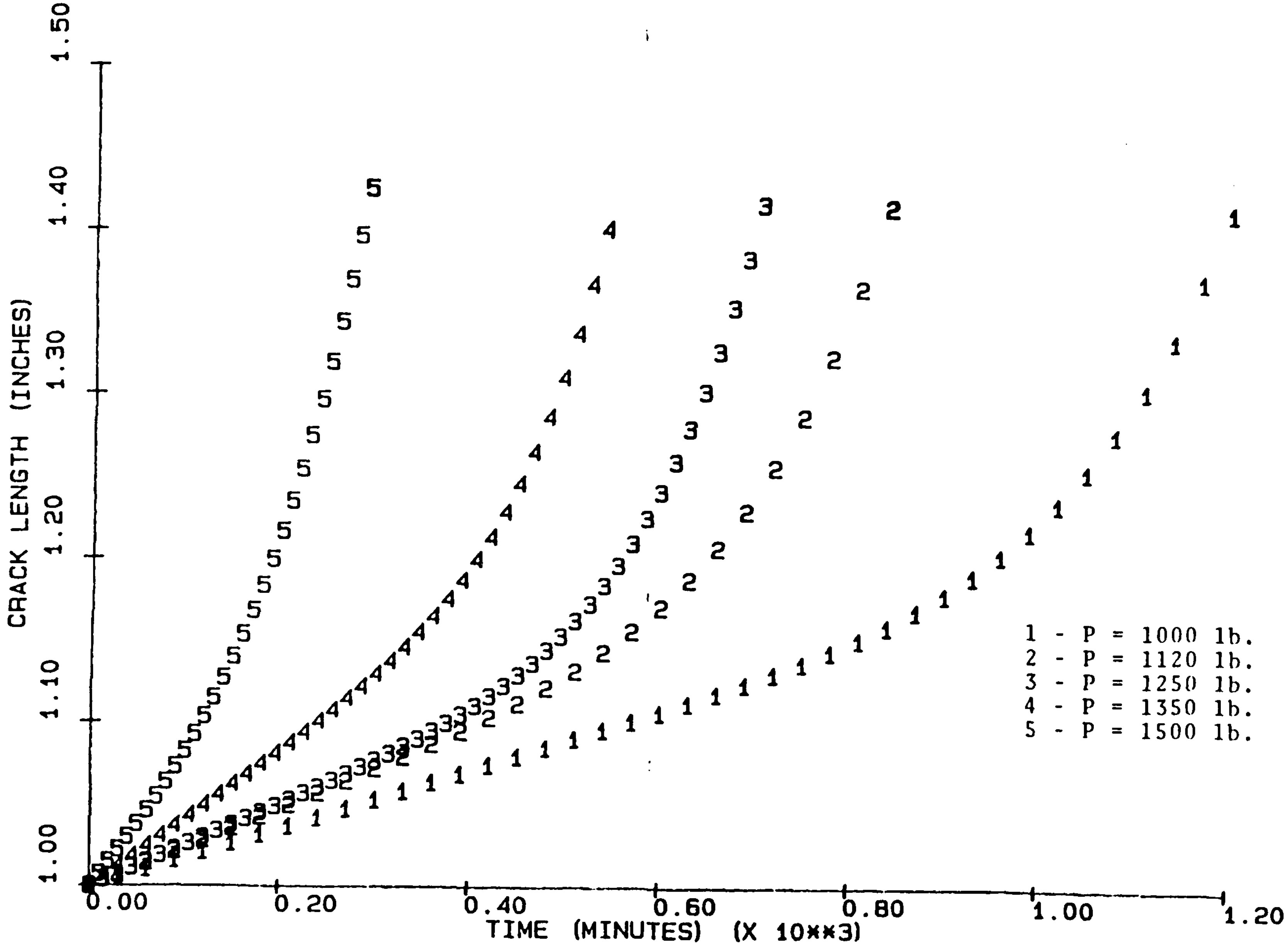

CRACK LENGTH VS. TIME FOR IN 718

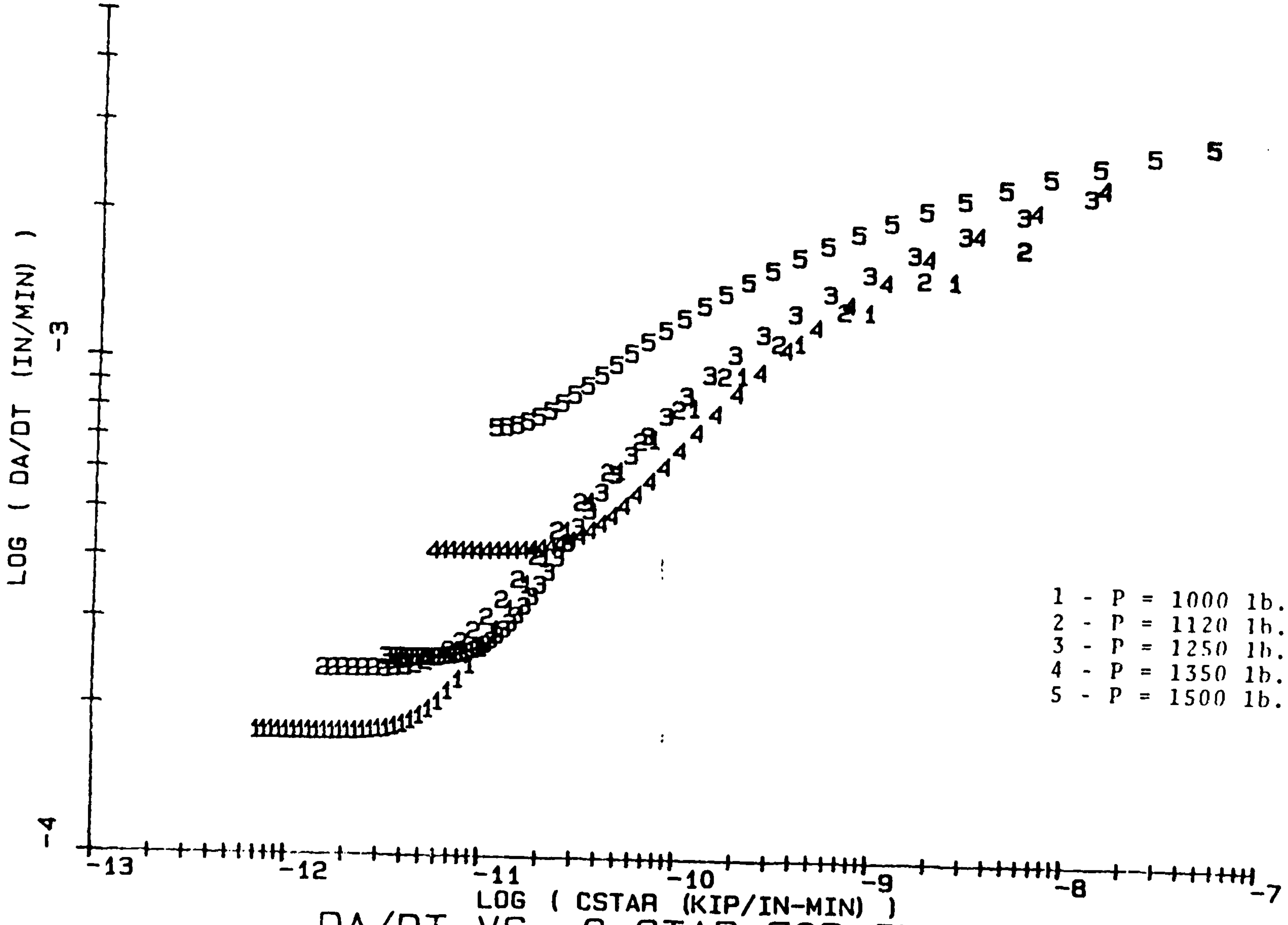

DA/DT VS. C-STAR FOR IN 718

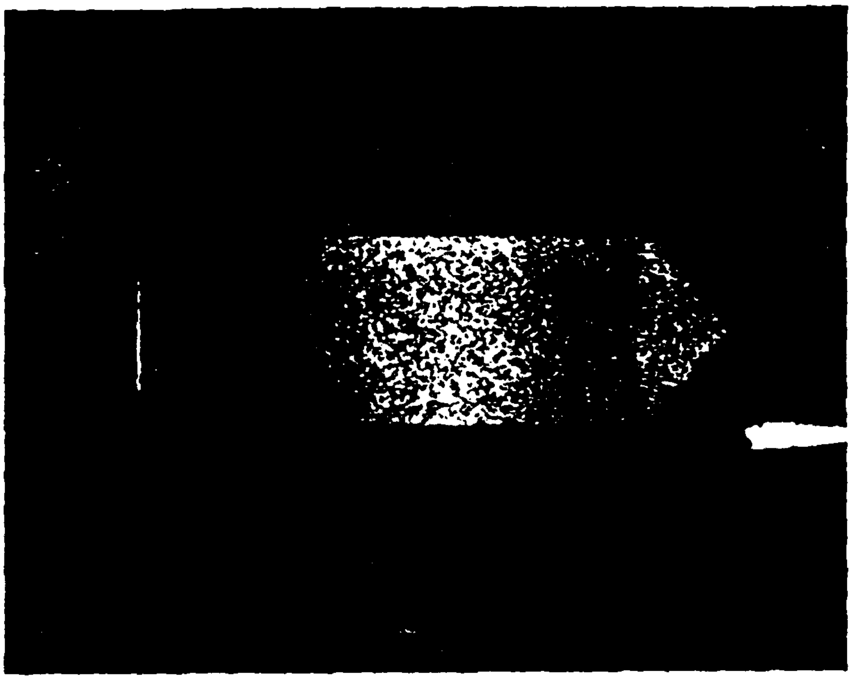

Photo #1.

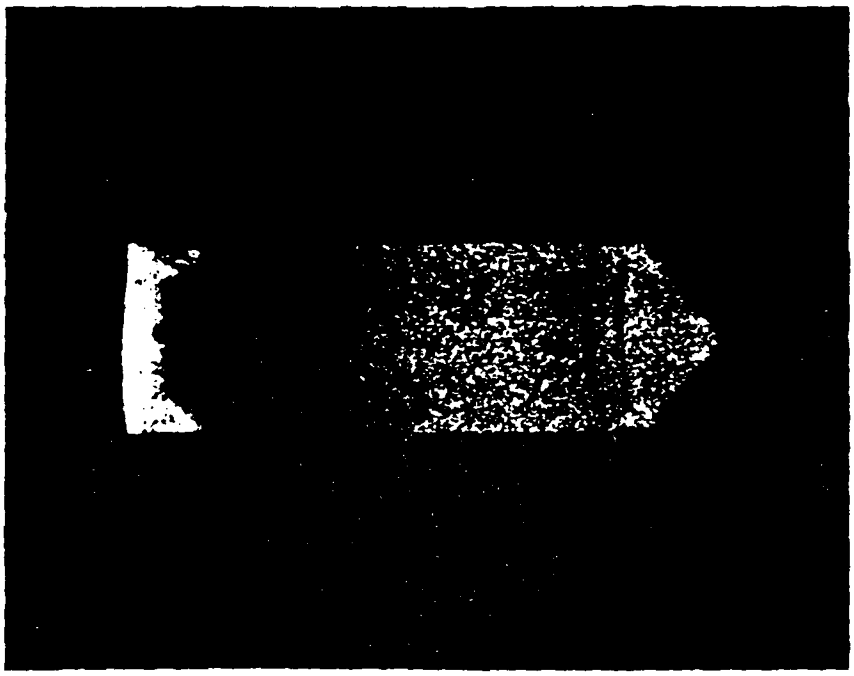

Original color photos have been sent to Dr. Rajapakse

Photo #2.

TYPICAL FRACTURE SURFACES

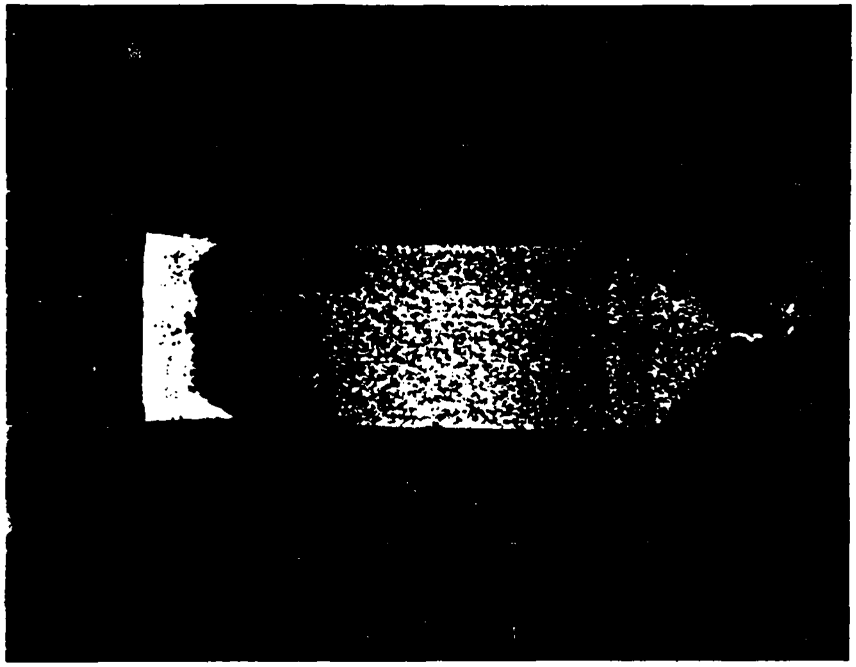

Photo #3.

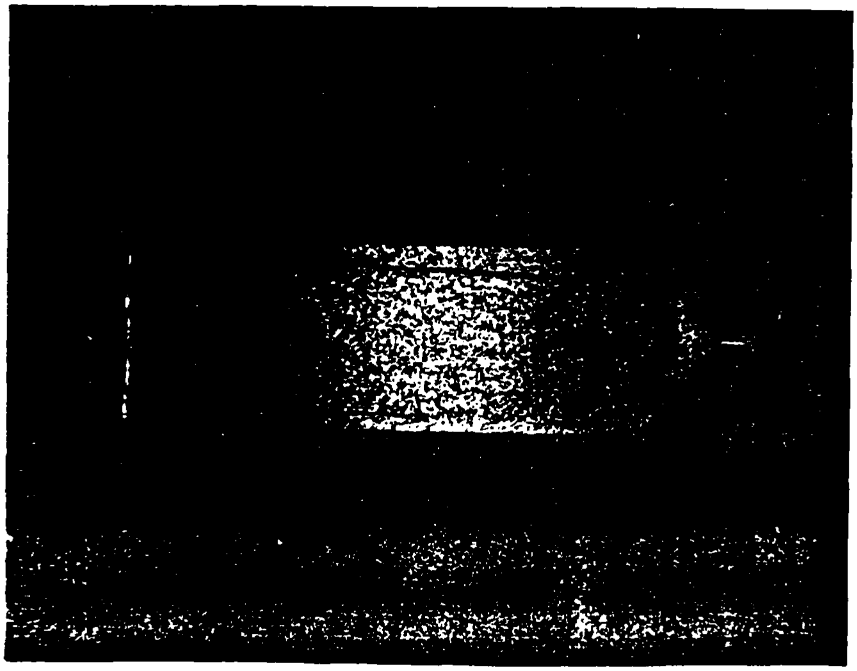

Photo #4.

TYPICAL FRACTURE SURFACES

APPENDIX D: LOCAL CRACK TIP FIELD QUANTITIES WITH DUCTILE MATERIAL BEHAVIOR FOR GENERAL MIXED MODE PROBLEMS

LOCAL CRACK TIP FIELD QUANTITIES WITH DUCTILE MATERIAL BEHAVIOR FOR GENERAL MIXED MODE PROBLEMS.

By

Martin Haegele

Vordiplom September 1984, Universität Stuttgart

A Thesis submitted to

The Faculty of
The School of Engineering and Applied Science
of The George Washington University
in partial satisfaction of the requirements for the
degree of Master of Science in Engineering

January 1988

Thesis directed by
Erwin Thomas Moyer, Jr., Ph.D.
Associate Professor of Engineering and Applied Science

ACKNOWLEDGMENTS

I would like to express my deep appreciation and thanks to my thesis advisor, Professor E. Thomas Moyer Jr., for his guidance, support and patience during the progress of this thesis. Numerous dicussions with him helped me to develop an understanding for the fields of fracture mechanics and the finite element method.

This thesis research was carried out as a part of the exchange program between The George Washington University and the Universität Stuttgart. I wish to express my thanks to Professor Kussmaul, Professor Dietman and Professor Liebowitz who made this exchange program possible.

I would also like to thank the Deutsche Akadmische Austausch Dienst (DAAD) who sponsored my studies in the United States of America.

This research was carried out on an IBM 4341 computer provided to The George Washington University as part of the CAD-CAM initiative grant program by IBM. This grant also included the CAEDS software package written by Structural Dynamics Research Corporation. Hibbitt, Karlsson and Sorensen, Inc. made the use of the finite element package, ABAQUS, available to The George Washington University. I am indebted to all companies for providing the resources for this work.

Finally, I am greatful to all those who made the sucessful completion of this thesis research possible.

ABSTRACT

In the present work, local crack-tip field quantities under ductile material behavior were studied for mixed-mode loading ranging from pure mode I to pure mode II under the assumption of plane strain. In order to become independent of a specific specimen, the local crack-tip region was modeled as a disk with the crack tip at its center. Based on the assumption of small scale yielding, displacements evaluated from the linear elastic solution were applied on the model boundary. For ten comparable cases of mixed-mode loading the body response was calculated using the J_2 flow theory of incremental plasticity employing small strain theory. The finite element mesh employed consisted of 1178 eight node plane strain elements and 3643 nodes.

In the evalution of the results emphasis was placed on :

i) The investigation of field quantities in terms of their exposed singular behavior, magnitude and distribution inside the plastic zone

ii) The examination of the influence of mixed-mode loading on the singular behavior of the field quantities and the validity of the HRR singular field for mixed modes

iii) The discussion of the strain energy density as a criterion predicting onset and direction of crack growth for mixed mode loading with ductile material behavior and

iv) The determination of the stress functions from the finite element results and their comparison with the numerical calculation of an asymptotic solution.

TABLE OF CONTENTS

ACKNOWLEDGMENTS

ABSTRACT

TABLE OF CONTENTS

LIST OF FIGURES

LIST OF TABLES

NOMENCLATURE

1. INTRODUCTION 1

2. STRESS AND DISPLACEMENT FIELDS IN LINEAR ELASTIC FRACTURE MECHANICS 5

3. MIXED-MODE FRACTURE CRITERIA 8

   3.1 THE STRAIN ENERGY DENSITY CONCEPT AS A FRACTURE CRITERION 9

4. INCREMENTAL PLASTICITY 12

5. THE FINITE ELEMENT METHOD 17

   5.1 THE FINITE ELEMENT FORMULATION FOR LINEAR MATERIAL BEHAVIOR 22

   5.2 THE FINITE ELEMENT FORMULATION FOR NONLINEAR MATERIAL BEHAVIOR 24

6. MODEL CREATION AND SOLUTION 26

6.1 CREATION OF THE FINITE ELEMENT MESH OF THE EMPLOYED SPECIMEN 26

6.2 MATERIAL 27

6.3 USING THE FINITE ELEMENT SOLVER 'ABAQUS' 28

7. THE J-INTEGRAL 31

7.1 DEFINITION AND PROPERTIES 31

7.2 CALCULATION OF THE J-INTEGRAL VALUE 34

7.3 RESULTS OF THE J_1- AND J_2-INTEGRAL CALCULATIONS 36

8. FIELD QUANTITIES 38

8.1 THE FAR TIP FIELD 38

8.2 THE NEAR TIP FIELD 39

8.3 THE INTERMEDIATE ZONE 42

9. DISCUSSION OF THE FIELD VARIABLES 43

9.1 THE STRESS FIELDS 43

9.2 STRESS AND STRAIN DISTRIBUTION, PLASTIC ZONE AND CRACK BLUNTING 45

9.3 THE STRAIN ENERGY DENSITY 46

10. RESOLVING THE STRESS FUNCTIONS FROM FINITE ELEMENT RESULTS 49

11. CONCLUSIONS AND RECOMMENDATIONS FOR FURTHER RESEARCH 52

REFERENCES
FIGURES
TABLES

LIST OF FIGURES

Figure 1 : Definition of the three modes of fracture.

Figure 2 : Definition of the crack-tip stresses, showing rectangular and polar coordinate components.

Figure 3 : Definition of crack angle and fracture angle in the center cracked panel with slanted crack under uniaxial tensile stress.

Figure 4 : K_I - K_{II} curve according to the fracture criterion due to Sih [29].

Figure 5 : Idealized constitutive material behavior of (i) incrementally elastic-plastic material conforming to incremental theory of plasticity, (ii) incrementally elastic-plastic material conforming to deformation theory of plasticity.

Figure 6 : Mapping of the eight-node prabolic element from spatial coordinates (x, y) to local coordiantes (ξ, η). Definition of the node and integration point numbering.

Figure 7 : Contour Plots of the von Mises yield stress for selected cases of mixed-mode loading.

Figure 8 : Generation of the eight-node collapsed element: (i) rectangular eight - node element, (ii) degenerated triangular eight-node element.

Figure 9 : Configuration of the degenerated crack-tip elements.

Figure 10 : Main fan of the finite element model of the specimen, inner radius : 1mm, outer radius : 10 mm.

Figure 11 : Boundary of the finite element mesh of the specimen, inner radius : 5mm, outer radius : 100 mm.

Figure 12 : Stress - strain curve of the steel A304.

Figure 13 : A contour Γ around the crack tip and parameters defining the J-integral.

Figure 14 : J_1- and J_2-integral values for all mixed-mode cases considered.

Figure 15 : Illustration of the crack tip region under small scale yielding condition.

Figure 16 : Effective von Mises stresses along line $\theta = 0°$ for all mixed-modes cases considered.

Figure 17 : Effective von Mises stresses around crack tip. Radius $r = 0.4$ mm for selected mixed-mode cases.

Figure 18 : Full logarithmic representation of effective von Mises stresses along line $\theta = 0°$ for all mixed-mode cases considered.

Figure 19 : σ_{yy} - stresses along line $\theta = 0°$ for selected mixed-mode cases.

Figure 20 : Equivalent von Mises stress around crack tip. Radius $r = 1$ mm. Stress intensity factor ratio : $K_I/K_{II} = 2230/0$.

Figure 21 : Equivalent von Mises stress around crack tip. Radius $r = 1$ mm. Stress intensity factor ratio : $K_I/K_{II} = 1927/987$.

Figure 22 : Equivalent von Mises stress around crack tip. Radius $r = 1$ mm. Stress intensity factor ratio : $K_I/K_{II} = 1683/1252$.

Figure 23 : Equivalent von Mises stress around crack tip. Radius $r = 1$ mm. Stress intensity factor ratio : $K_I/K_{II} = 1405/1462$.

Figure 24 : Equivalent von Mises stress around crack tip. Radius $r = 1$ mm. Stress intensity factor ratio : $K_I/K_{II} = 772/1774$.

Figure 25 : Equivalent von Mises stress around crack tip. Radius $r = 1$ mm. Stress intensity factor ratio : $K_I/K_{II} = 396/1903$.

Figure 26 : Equivalent von Mises stress around crack tip. Radius $r = 1$ mm. Stress intensity factor ratio : $K_I/K_{II} = 0/2018$

Figure 27 : Equivalent von Mises stress around crack tip. Inner radius 1 mm, outer radius 10 mm. Stress intensity factor ratio : $K_I/K_{II} = 2230/0$.

Figure 28 : Equivalent von Mises stress around crack tip. Inner radius 1 mm, outer radius 10 mm. Stress intensity factor ratio : $K_I/K_{II} = 1927/987$.

Figure 29 : Equivalent von Mises stress around crack tip. Inner radius 1 mm, outer radius 10 mm. Stress intensity factor ratio : $K_I/K_{II} = 1683/1252$.

Figure 30 : Equivalent von Mises stress around crack tip. Inner radius 1 mm, outer radius 10 mm. Stress intensity factor ratio : $K_I/K_{II} = 1098/1633$.

Figure 31 : Equivalent von Mises stress around crack tip. Inner radius 1 mm, outer radius 10 mm. Stress intensity factor ratio : $K_I/K_{II} = 772/1774$.

Figure 32 : Equivalent von Mises stress around crack tip. Inner radius 1 mm, outer radius 20 mm. Stress intensity factor ratio : K_I/K_{II} = 396/1903.

Figure 33 : Equivalent von Mises stress around crack tip. Inner radius 1 mm, outer radius 20 mm. Stress intensity factor ratio : K_I/K_{II} = 0/2018.

Figure 34 : Equivalent plastic strain around crack tip. Radius r= 1 mm. Stress intensity factor ratio : K_I/K_{II} = 2230/0.

Figure 35 : Equivalent plastic strain around crack tip. Radius r= 1 mm. Stress intensity factor ratio : K_I/K_{II} = 1927/987.

Figure 36 : Equivalent plastic strain around crack tip. Radius r= 1 mm. Stress intensity factor ratio : K_I/K_{II} = 1098/1633.

Figure 37 : Equivalent plastic strain around crack tip. Radius r= 1 mm. Stress intensity factor ratio : K_I/K_{II} = 0/2018.

Figure 38 : Equivalent plastic strain around crack tip. Inner radius 1 mm, outer radius 10 mm. Stress intensity factor ratio : K_I/K_{II} = 2230/0.

Figure 39 : Equivalent plastic strain around crack tip. Inner radius 1 mm, outer radius 10 mm. Stress intensity factor ratio : K_I/K_{II} = 1927/987.

Figure 40 : Equivalent plastic strain around crack tip. Inner radius 1 mm, outer radius 10 mm. Stress intensity factor ratio : K_I/K_{II} = 1405/1462.

Figure 41 : Equivalent plastic strain around crack tip. Inner radius 1 mm, outer radius 10 mm. Stress intensity factor ratio : K_I/K_{II} = 772/1774.

Figure 42 : Equivalent plastic strain around crack tip. Inner radius 1 mm, outer radius 20 mm. Stress intensity factor ratio : K_I/K_{II} = 396/1903.

Figure 43 : Equivalent plastic strain around crack tip. Inner radius 1 mm, outer radius 20 mm. Stress intensity factor ratio : K_I/K_{II} = 0/2018.

Figure 44 : Deformed Mesh, outer radius r= 1mm. Stress intensity factor ratio : K_I/K_{II} = 2230/0.

Figure 45 : Deformed Mesh, outer radius r= 1mm. Stress intensity factor ratio : K_I/K_{II} = 1927/987.

Figure 46 : Deformed Mesh, outer radius r= 1mm. Stress intensity factor ratio : K_I/K_{II} = 1405/1462.

Figure 47 : Deformed Mesh, outer radius r= 1mm.
Stress intensity factor ratio : K_I/K_{II} = 1098/1633.

Figure 48 : Deformed Mesh, outer radius r= 1mm.
Stress intensity factor ratio : K_I/K_{II} = 0/2018.

Figure 49 : Crack deformation. Plotted crack length 10 mm.
Stress intensity factor ratio : K_I/K_{II} = 2230/0.

Figure 50 : Crack deformation. Plotted crack length 10 mm.
Stress intensity factor ratio : K_I/K_{II} = 1927/987.

Figure 51 : Crack deformation. Plotted crack length 10 mm.
Stress intensity factor ratio : K_I/K_{II} = 1098/1633.

Figure 52 : Crack deformation. Plotted crack length 10 mm.
Stress intensity factor ratio : K_I/K_{II} = 0/2018.

Figure 53 : Deformed and undeformed meshes. Inner radius 1 mm, outer radius 10 mm.
Stress intensity factor ratio : K_I/K_{II} = 2230/0.

Figure 54 : Deformed and undeformed meshes. Inner radius 1 mm, outer radius 10 mm.
Stress intensity factor ratio : K_I/K_{II} = 1683/1252.

Figure 55 : Deformed and undeformed meshes. Inner radius 1 mm, outer radius 10mm.
Stress intensity factor ratio : K_I/K_{II} = 1098/1633.

Figure 56 : Deformed and undeformed meshes. Inner radius 1 mm, outer radius 10mm.
Stress intensity factor ratio : K_I/K_{II} = 0/2018.

Figure 57 : Strain energy density along a circular path around the crack tip for selected cases of mixed-mode loading. Radius r= 1 mm from crack tip.

Figure 58 : Full logarithmic representation of the strain energy density along the line $\theta = 0°$ for selected mixed-mode cases .

Figure 59 : Graphical illustration of the interval halving method.

Figure 60 : Angular variation of the stress functions $\tilde{\sigma}_{rr}$,$\tilde{\sigma}_{\theta\theta}$,$\tilde{\sigma}_{\theta}$ and $\tilde{\sigma}_{r\theta}$.
Stress intensity factor ratio : K_I/K_{II} = 2230/0.

Figure 61 : Angular variation of the stress functions $\tilde{\sigma}_{rr}$,$\tilde{\sigma}_{\theta\theta}$,$\tilde{\sigma}_{\theta}$ and $\tilde{\sigma}_{r\theta}$.
Stress intensity factor ratio : K_I/K_{II} = 2222/175.

Figure 62 : Angular variation of the stress functions $\tilde{\sigma}_{rr}$,$\tilde{\sigma}_{\theta\theta}$,$\tilde{\sigma}_{e}$ and $\tilde{\sigma}_{r\theta}$.
Stress intensity factor ratio : K_I/K_{II} = 2107/670.

Figure 63 : Angular variation of the stress functions $\tilde{\sigma}_{rr}$,$\tilde{\sigma}_{\theta\theta}$,$\tilde{\sigma}_{e}$ and $\tilde{\sigma}_{r\theta}$.
Stress intensity factor ratio : K_I/K_{II} = 1927/987.

Figure 64 : Angular variation of the stress functions $\tilde{\sigma}_{rr}$,$\tilde{\sigma}_{\theta\theta}$,$\tilde{\sigma}_{e}$ and $\tilde{\sigma}_{r\theta}$.
Stress intensity factor ratio : K_I/K_{II} = 1683/1252.

Figure 65 : Angular variation of the stress functions $\tilde{\sigma}_{rr}$,$\tilde{\sigma}_{\theta\theta}$,$\tilde{\sigma}_{e}$ and $\tilde{\sigma}_{r\theta}$.
Stress intensity factor ratio : K_I/K_{II} = 1405/1462.

Figure 66 : Angular variation of the stress functions $\tilde{\sigma}_{rr}$,$\tilde{\sigma}_{\theta\theta}$,$\tilde{\sigma}_{e}$ and $\tilde{\sigma}_{r\theta}$.
Stress intensity factor ratio : K_I/K_{II} = 1098/1633.

Figure 67 : Angular variation of the stress functions $\tilde{\sigma}_{rr}$,$\tilde{\sigma}_{\theta\theta}$,$\tilde{\sigma}_{e}$ and $\tilde{\sigma}_{r\theta}$.
Stress intensity factor ratio : K_I/K_{II} = 772/1774.

Figure 68 : Angular variation of the stress functions $\tilde{\sigma}_{rr}$,$\tilde{\sigma}_{\theta\theta}$,$\tilde{\sigma}_{e}$ and $\tilde{\sigma}_{r\theta}$.
Stress intensity factor ratio : K_I/K_{II} = 396/1903.

Figure 69 : Angular variation of the stress functions $\tilde{\sigma}_{rr}$,$\tilde{\sigma}_{\theta\theta}$,$\tilde{\sigma}_{e}$ and $\tilde{\sigma}_{r\theta}$.
Stress intensity factor ratio : K_I/K_{II} = 0/2018.

Figure 70 : Ratio of $\sigma_{\theta\theta}/\sigma_{r\theta}$ along the line θ =0° for selected mixed-mode cases.

Figure 71 : I_n versus plastic mixity parameter M^{pl} for all mixed-mode cases considered. Comparison with the values of I_n obtained by Shih [27].

LIST OF TABLES

Table 1 : K_I - K_{II} -values according to the fracture criterion by Sih.

Table 2 : Shape functions of the eight node isoparametric plane strain element.

Table 3 : Chemical composition and material data of the stainless steel A304.

Table 4 : Comparison of J-integral values obtained by the virtual crack extension method and the direct integration method.

Table 5 : Powers characterizing singular behavior of the effective von Mises stress along the line $\theta = 0°$ ahead of the crack tip.

Table 6 : Fracture angle θ and corresponding strain energy density 0.4 mm from the crack tip for all cases of mixed-mode cases considered.

Table 7 : Powers of the singularity of the strain energy density in the vicinity of the crack tip along the line $\theta=0°$ from least square approximation.

NOMENCLATURE

a	crack length
$\underline{a}^*$	flow vector
$\underline{a}$	nodal displacement vector
A	slope of the uniaxial stress-strain curve
$\underline{b}$	vector of body forces
$\underline{B}$	strain-displacement matrix
$\underline{C}$	element mapping matrix
C	constant term
D	radius of the HRR field
$\underline{D}$	linear elastic constitutive matrix
$\underline{D}_{ep}$	elastic-plastic constitutive matrix
E	Young's modulus
f_{ij}^{I}, f_{ij}^{II}	stress functions for linear elastic material behavior
f	*yield criterion*
$\underline{f}$	nodal force vector
$\underline{f}_b$	nodal force vector caused by body forces
$\underline{f}_s$	nodal force vector caused by surface tractions
F	function
g_i^{I}, g_i^{II}	displacement functions for linear elastic material behavior
G	global energy release rate
G_I, G_{II}	energy release rate in x - and y -direction
I_n	constant
J_1, J_2	J-integral refering to crack extentions in x - and y -direction
J_k	J-integral vector
J_{res}	resultant J-integral value of the J-integral vector
$\underline{J}$	Jacobian matrix

k_1, k_2	stress intensity factor refering to mode I and mode II
$K_I = k_1\sqrt{\pi}$	stress intensity factor, mode I
$K_{II} = k_2\sqrt{\pi}$	stress intensity factor, mode II
$\underset{\sim}{K}$	element stiffness matrix
$\underset{\sim}{K}_T$	tangential stiffness matrix
l	length
n	strain hardening index
N_i	shape fanctions for element nodes
$\underset{\sim}{N}$	shape function matrix
r	radius
r_0	inner radius of the HRR field
s	distance
$\underset{\sim}{s}$	vector of surface forces
S	quadric strain energy density functional
$\underset{\sim}{T}$	vector of surface tractions
u, v	displacement components in x - and y -direction
$\underset{\sim}{u}$	displacement vector
u	displacement function
S	quadric strain energy density functional
V	volume
W	strain energy density (general)
W_e	external work
W_i	internal strain energy density
x, y, z	cartesian coordiantes
α	material constant
$\underset{\sim}{\alpha}$	vector of polynoial coefficients
β	angle of crack inclination
γ	exponent

Γ	boundary
Φ	interpolation polynomial
δ	vector of u_i displacements of an element
ϵ	strain
$\underline{\epsilon}$	vector of strain components
θ	angle (general)
θ_0	angle of crack extention
κ	hardening parameter
μ	shear modulus
$\underline{\Psi}$	residual force vector
σ	stress
$\underline{\sigma}$	vector of stress components
σ	stress functions
τ	shear stress
υ	Poisson's ratio
ξ , η	intrinsic coordinates

Subscripts

i, j	components referring to cartesian or polar coordinate system
cr	critical
e	elastic
pl	plastic
min, max	maximum, minimum
y	yield

Superscripts

T	transpose

1. INTRODUCTION

Historically, conventional stress analysis was based on the assumption of flawless material behavior. Since the existence of crack-like flaws cannot be precluded in any engineering material, fracture theories had to be developed which account for local stress concentrations.

The significance of intense and localized concentration of stresses around sharp notches was first emphasized by Inglis [1]. He realized through considerations of the stress concentration around an elliptical hole that the stress becomes infinitely large at the tip of a sharp crack. Based on the ultimate stress concept, this would indicate that a cracked component cannot sustain any loading.

Griffith [2,3] applied energy conservation principles to the problem of a cracked glass plate. This work set the theoretical foundation for the field of continuum fracture mechanics. Irwin [4] and Orowan [5] subsequently modified the original Griffith theory so that it could be applied to metals by adding a term involving the plastic energy dissipation rate in the plastically deformed region near the crack tip. Due to difficulties in the practical application of the energy balance concept, new approaches had to be found to characterize the material behavior under the influence of a sharp crack. Irwin [6] was able to utilize the cracked body solutions of Westergaard [7] to establish a relation between the strain energy release rate G, (a global parameter) and the stress intensity factor K (a local crack tip parameter). These stress intensity factors can be related to three independent local movements as shown in Figure 1. These are categorized as :

- Mode I, or opening mode
- Mode II, or sliding mode
- Mode III, or tearing mode.

Any crack deformation in the case of linear elastic material behavior can be idealized by the appropriate superposition of theses cases. Unlike the brittle glass considered by Griffith, most metals exhibit the phenomenon of ductility. Crack tips are, therefore, engulfed by plastic yield zones with finite stresses.

Early attempts to model the plastic deformation surrounding the crack tip were based upon extensions of the linear elastic fracture mechanics (LEFM). Irwin [8] broadened the applicability of LEFM by introducing a modified stress intensity factor K_p. At the same time Wells [9] established the crack opening displacement (COD) as a parameter governing crack extension even beyond general yielding. Dugdale [10] extended the COD approach and established a relation between a plastic zone estimate around the crack tip and the crack opening displacement in thin sheets.

A significant contribution to the field of elastic-plastic fracture mechanics (EPFM) was the introduction of the path independent J-integral. This integral (originally derived by Eshelby [11] and Cherepanov [12]) was introduced into the field of fracture mechanics by Rice [13]. Begley and Landes [14] showed its applicability as a parameter describing the stress concentration at the crack tip and suggested the use of a critical J-integral value J_{IC} to predict the onset of stable crack growth.

Several attempts have been made in recent years to arrive at a more general definition of the J-integral which would minimize the assumption of elastic material behavior and the absence of body forces while still retaining its desirable features. Some of the proposed formulations extend the definition of J to axisymmetric three dimensional problems, others consider more general loading conditions [15-20].

Hutchinson [21] and Rice and Rosengren [22] independently determined the characteristic singular behavior of stresses and strains inside the plastic zone (using deformation theory of plasticity) where elastic strains are negligible compared to plastic strains. This zone is commonly referred to as the HRR singular field due to its distinct singular character in terms of stresses and strains. In their analysis, which took full advantage of the path independence of the J-integral, they showed that stress, strain and displacement components can be related to dimensionless functions. These functions are only dependent on the hardening characteristics of the material and whether the material is in a state of plane stress or plane strain. Stress, strain and displacement components inside the HRR field are, therefore, determined by an appropriate stress, strain or displacement function and a singular term involving the J-integral value which characterizes the amplitudes of these fields. The validity of expressing crack-tip quantities in terms of the HRR singular solution has been shown by a number of scientists [23-26]. Shih [24] established (through considerations of the displacement function of the HRR-theory) a relationship between the J-integral and the COD-concept and proved the similarity of both concepts. This analysis assumes that the HRR field dominate the region around the crack tip having a size of at least ten times larger the crack-tip opening displacement.

Shih [27,28] applied the HRR singular field solution to the case of a body under mixed-mode loading. The stress, strain and displacement functions in this case depend on the relative composition of mode I and mode II directly ahead of the crack. The J-integral, in combination with a parameter sensitive to the composition of mode I and mode II, governs the amplitude of the singular field.

Though many cracks in structures may be initially under mixed-mode conditions, most research in the field of fracture mechanics is focused on the study of fracture behavior under pure mode I conditions. The major reason for this is the general observation that a crack subjected to mixed-mode loading tends to grow toward a mode I condition. The main interest in mixed-mode fracture mechanics, therefore, is focused on determining criteria which predict the onset of crack growth and the angle of crack extension in relation to the existing crack. In contrast to pure mode I where the critical value J_{IC} has been employed to predict the onset of crack growth, this quantity is no longer valid for mixed-mode conditions since the crack usually does not extend in its own plane. The most promising concepts of mixed-mode fracture criteria are therefore based on energy principles, i.e. the maxima or minima of either the total strain energy density or of its components [29-32]. Both the concept of the strain energy criterion, introduced by Sih [29] and the T-criterion suggested by Theocaris [33] have been extended for use in the elastic-plastic regime. Since these criteria are of local nature, they depend on the local stress and strain response of the material.

In the analysis of cracked bodies, the finite element method has become the major numerical technique for the solution of fracture problems (both linear and nonlinear). The theory of incremental plasticity, which is usually incorporated in modern finite element programs, relates increments of stress to increments of strain. The formulation of the incremental theory of plasticity accounts for elastic unloading effects and has been very successful in simulating ductile material behavior.

In the present investigation local crack-tip field quantities were examined for mixed-mode loading ranging from pure mode I to pure mode II. A ductile material was modeled and the commercial finite element package ABAQUS was employed to perform the calculation. All considerations were based on the assumption of small scale yielding which requires the plastic zone to be small relative to other dimensions (i.e. crack length or specimen size).

Although a variety of mixed-mode fracture specimens have been suggested in the past [34,35], there is still no universally accepted standard mixed-mode specimen. In this work, therefore, the local crack-tip region is modeled without employing a mixed mode fracture specimen. Displacements on the boundary are calculated by assuming elastic stress intensity factors for both mode I and mode II a priori. These displacements are applied to the boundary of the local crack-tip region.

Ten loading combinations which span the range from pure mode I to pure mode II were investigated. The J-integral values were calculated to measure the strength of the field singularities. Stresses, strains and both total and elastic strain energies were examined with respect to their singular behavior and angular variation within the plastic zone. Details of plastic zone sizes and shapes as well as the crack blunting under varying mixed mode I and II contributions were investigated. The stress functions for all investigated cases were determined as well as parameters describing the amplitude of the plastic near-tip field.

2. STRESS AND DISPLACEMENT FIELDS IN LINEAR ELASTIC FRACTURE MECHANICS

The stress and displacement fields around a crack in a linear elastic material have been investigated by a number of scientists. Although a basic solution was worked out by Muskhelishvili [36], Westergaard [7], Williams [37], Irwin [6] and Sih [38] solved the same problem using different approaches. A decisive step in linear elastic fracture mechanics (LEFM) was the introduction of the stress intensity factor K by Irwin [6]. His work employed using Westergaard's solution for the near-tip stress field of a cracked body. If the elastic solution for a cracked body is available, the stress intensity factors, K_I and K_{II}, can be defined as :

$$K_I = \lim_{r \to 0} \sigma_{yy}(r,\theta=0)(2\pi r)^{1/2}$$

$$K_{II} = \lim_{r \to 0} \sigma_{xy}(r,\theta=0)(2\pi r)^{1/2}. \qquad (2.1)$$

Both stress and displacement fields are based on the linear theory of elasticity and may, therefore, be superimposed. The stresses and displacements under combined mode I and mode II can be written as for the coordinate system (given in Figure 2) :

$$\begin{bmatrix} \sigma_{xx} \\ \sigma_{yy} \\ \sigma_{xy} \end{bmatrix} = \frac{K_I}{\sqrt{2\pi r}} \cos\frac{\theta}{2} \begin{bmatrix} 1 - \sin\frac{\theta}{2} \sin\frac{3\theta}{2} \\ 1 + \sin\frac{\theta}{2} \sin\frac{3\theta}{2} \\ \sin\frac{\theta}{2} \sin\frac{3\theta}{2} \end{bmatrix} + \frac{K_{II}}{\sqrt{2\pi r}} \begin{bmatrix} -\sin\frac{\theta}{2} [\, 2 + \cos\frac{\theta}{2} \cos\frac{3\theta}{2} \,] \\ \sin\frac{\theta}{2} \cos\frac{\theta}{2} \cos\frac{3\theta}{2} \\ \cos\frac{\theta}{2} [\, 1 - \sin\frac{\theta}{2} \sin\frac{3\theta}{2} \,] \end{bmatrix} \qquad (2.2)$$

$$\begin{bmatrix} u \\ v \end{bmatrix} = \frac{K_I}{2E} \sqrt{\frac{r}{2\pi}} \begin{bmatrix} (1+\upsilon)\, [\, (2\kappa - 1) \cos\frac{\theta}{2} - \cos\frac{3\theta}{2} \,] \\ (1+\upsilon) [\, (2\kappa + 1) \sin\frac{\theta}{2} - \sin\frac{3\theta}{2} \,] \end{bmatrix} + \frac{K_{II}}{2E} \sqrt{\frac{r}{2\pi}} \begin{bmatrix} (1+\upsilon)\, [\, (2\kappa + 3) \sin\frac{\theta}{2} + \sin\frac{3\theta}{2} \,] \\ -(1+\upsilon) [\, (2\kappa - 3) \cos\frac{\theta}{2} + \cos\frac{3\theta}{2} \,] \end{bmatrix}$$

where E is Young's modulus,

υ is Poisson's ratio and

κ is given for the case of plane strain as $\kappa = 3\text{-}4\upsilon$.

By expressing equation (2.2) in the form :

$$\begin{aligned} \sigma_{ij} &= \frac{K_I}{\sqrt{2\pi r}} f_{ij}^{I}(\theta) + \frac{K_{II}}{\sqrt{2\pi r}} f_{ij}^{II}(\theta) \\ u_i &= \frac{K_I}{2E}\sqrt{\frac{r}{2\pi}}\, g_i^{I}(\theta) + \frac{K_{II}}{2E}\sqrt{\frac{r}{2\pi}}\, g_i^{II}(\theta) \end{aligned} \qquad (2.3)$$

several characteristics of these solutions can be observed. The stress intensity factors depend only on the applied loading and consequently determine the intensity of the local field. The remaining terms depend on the spatial coordinates around the crack tip and determine the distribution of the field. These subdivide into a singular $1/\sqrt{r}$ component and an angular component expressed by the geometric functions f_{ij}^{I}, f_{ij}^{II}, g_i^{I} and g_i^{II}.

Higher order terms of the actual series solution have been neglected. More higher ordered terms need to be included if the field had to match outer boundary conditions. Eftis et al. [39,40], in revisiting the stress and displacement fields of the one parameter representation given in equation (2.2), proved the inaccuracy of these relations for the case of biaxial loading. This stems from the arbitrary omission of the second term of the series expansion for the stress components which contain a term independent of the distance from the crack but dependent of tne angular position around the crack tip. Eftis improved the singular solution for the inclined crack under biaxial tensile load by including this term which finally affects only the x-component of the stress field. Theocaris et al. [41] developed a closed form solution solution of stresses and displacements of a slant crack under biaxial tensile loading for arbitrary radius (r) away from the crack tip.

Irwin [42] derived the relationship between the stress intensity factors and the energy release rate (G) for cracks extending in their original plane. For pure mode I and pure mode II (under plane strain conditions) these relations are given as :

$$G_I = \frac{K_I}{E}(1 - u^2) \qquad G_{II} = \frac{K_{II}}{E}(1 - u^2) \tag{2.4}$$

Energy release rates can be added for a crack remaining in its plane according to :

$$G = G_I + G_{II} \tag{2.5}$$

For a linear elastic material subjected to pure mode I loading conditions the energy available to create a unit surface is G_I . The critical strength parameter governing failure, therefore, can be expressed as G_{IC}. This parameter can be related to the critical stress intensity factor K_{IC} by equation (2.4).

3. MIXED MODE FRACTURE CRITERIA

In order to assure a comparison of field quantities for arbitrary ratios of stress intensity factors, a criterion had to be applied which relates K_{II}-values to a given K_I-value. In contrast to a pure mode I Griffith crack, a mixed mode crack does not necessarily extend in its own plane. Since the direction of crack extent is not known a priori it would be incorrect to obtain the mixed mode energy release rate by adding G_I and G_{II}. In contrast to pure mode I fracture analysis where the fracture criterion is founded on a given K_{IC}-value, there is sill no well established criterion for the case of mixed-mode fracture. The most widely used mixed mode fracture criteria are [33,43-45] :

- criterion of maximal tangential stress
- various criteria based on the energy release rate
- various criteria based on the energy density
- criterion according to DiLeonardo
- principal strain criterion
- J-integral criterion
- modified T-criterion and
- various empirical criteria based on experimental K_I-K_{II} failure curves.

The energy density criterion introduced by Sih [29] was chosen for two reasons:

- it is generally in good agreement with experimental results [29,47] and
- it provides a concise relationship between the critical energy density factor and the stress intensity factors for mode I and II.

3.1 THE STRAIN ENERGY DENSITY CONCEPT AS A FRACTURE CRITERION

Sih [29] proposed a criterion based on the strain energy density in the vicinity of a crack tip. For an elastic material the strain energy density is given in its general form as :

$$\left(\frac{dW}{dV}\right) = \frac{1}{2E}(\sigma_x{}^2+\sigma_y{}^2+\sigma_z{}^2) - \frac{\upsilon}{E}(\sigma_x\sigma_y+\sigma_y\sigma_z+\sigma_z\sigma_x) + \frac{1}{2\mu}(\tau_{xy}{}^2+\tau_{xy}{}^2+\tau_{yz}{}^2) \qquad (3.1)$$

where E is Young's modulus,

υ is Poisson's ratio and

μ is the shear modulus.

Substituting the stress components from the asymptotic linear elastic two dimensional stress solutions given in equation (2.2), the strain energy density can be obtained as:

$$\left(\frac{dW}{dV}\right) = \frac{S}{r} = \frac{1}{r}(a_{11}k_1{}^2 + 2a_{12}k_1k_2 + a_{22}k_2{}^2) \qquad (3.2)$$

The coefficients a_{ij} are given as:

$$a_{11} = \frac{1}{16\mu}[(3\text{-}4\upsilon-\cos\theta)\ (1+\cos\theta)]$$

$$a_{12} = \frac{1}{8\mu}\sin\theta\ [\cos\theta-(1-2\upsilon)]$$

$$a_{22} = \frac{1}{16\mu}[4\ (1-\upsilon)\ (1-\cos\theta) + (1+\cos\theta)\ (3\cos\theta-1)] .$$

It can be seen that the strain energy density is characterized by a 1/r singular term where r is the distance from the crack. The quadric term, S, in equation (3.2) can be considered as a material constant [29] and varies only in the angle θ around the crack tip, Figure 2.

Determination of pairs of K_I- K_{II} - values with respect to an assumed maximum value of

Determination of pairs of K_I- K_{II} - values with respect to an assumed maximum value of K_{IC} is based on taking advantage of two hypothesis formulated by Sih [29]:

1. A crack will extend in the direction of maximal potential energy.
2. The critical intensity S_{cr} of this potential field governs the onset of crack propagation

The potential energy per unit volume, P, is defined as:

$$P = -\frac{S}{r} \tag{3.3}$$

Therefore, P assumes a maximum if the following relations hold:

$$\frac{\partial P}{\partial \theta} = 0 \quad ; \quad \frac{\partial^2 P}{\partial \theta^2} < 0 \qquad \text{at } \theta = \theta_0 . \tag{3.4}$$

The formulation of the stress intensity factors k_1 and k_2 for a crack inclined by an angle β, and of length 2a under tensile stress σ (see Figure 3) is given as:

$$\begin{aligned} k_1 &= \sigma \sqrt{a} \sin^2 \beta \\ k_2 &= \sigma \sqrt{a} \sin \beta \cos \beta . \end{aligned} \tag{3.5}$$

Substituting these expressions into equation (3.2) yields an expression for S :

$$S = k_1{}^2 (a_{11} \sin \beta + 2 a_{12} \sin \beta \cos \beta + a_{22} \cos^2 \beta) \sin \beta . \tag{3.6}$$

Again, according to the first hypothesis and equation (3.3), S has to be a minimum if P shows a maximum. Differentiating equation (3.6) with respect to θ and setting the result to

$$2\,(1-2\upsilon)\,\sin\,(\theta_0 - \beta) - 2\,\sin\,[2\,(\theta_0 - \beta)] - \sin\,2\theta_0 = 0\,. \qquad (3.7)$$

The critical values of K_I and K_{II} lie on a curve in the K_I-K_{II} plane determined from equations (3.5) and (3.7).

A FORTRAN program has been written to perform the outlined procedure to find pairs of K_I-K_{II} values for a given pure mode stress intensity factor K_I. The material data are presented in chapter 6.2. For values of β ranging from 0 to $\pi/2$ equation (3.7) was solved numerically using the Newton-Raphson Method. Figure 4 shows the plot of K_{II} values over K_I for an assumed pure mode I value of $K_I = 2230\ N/\sqrt{mm^{3/2}}$.

Ten pairs of stress intensity factors which span the range from pure mode I to pure mode II are given in Table 1 and will be referred to in all further considerations. These pairs of stress intensity factors represent points on the K_I-K_{II} curve which are the endpoints of equal length curve segments.

4. INCREMENTAL PLASTICITY

A characteristic of plastically deformable materials is that a particular material can undergo different histories of response prior to the body reaching its end state. Reversibility, therefore, cannot be guaranteed after load removal. The final strain is found to be dependent on the history of loading, in addition to the beginning and final loading. This means that plastic behavior is a path function and requires the use of an incremental theory where strains are integrated over the strain path whenever the total induced strain is to be determined. A common approach (employed in this work) is the incremental theory of plasticity.

The deformation theory of plasticity is based on an assumed nonlinear elastic material response. Plastic strains depend only on the current state of stress and are independent of the path leading to this state. This theory (though contrary to the observed nature of plastic behavior) is computationally far less expensive than the incremental theory and is therefore widely used. Figure 5 depicts the basic difference between these two basic approaches in elastic-plastic modeling.

The incremental stress-strain relationship of an isotropic strain hardening material can be derived on the basis of the following relations :

- a yield criterion
- a yield function
- a flow rule
- the assumption of strain rate decomposition and
- the linear-elastic constitutive relation.

i) Yield Criterion :

Various criteria have been suggested in the past to predict the onset of yielding in a material subjected to loading. The Von Mises yield criterion, which is widely used, is based on the assumption that yielding occurs when the second invariant, J_2, of the deviatoric-stress tensor reaches a critical value, $J_2 = 2/3\ \sigma_y^2$. With the deviatoric stress tensor s_{ij} defined as :

$$s_{ij} = \sigma_{ij} - \frac{1}{3}\delta_{ij}\sigma_{kk} \tag{4.1}$$

The critical value of J_2 is given as :

$$s_{ij}\,s_{ij} = \frac{2}{3}\,\sigma_y^2 \tag{4.2}$$

The effective stress may be written as :

$$\sigma = \sqrt{\frac{1}{2}[(\sigma_x-\sigma_y)^2+(\sigma_y-\sigma_z)^2+(\sigma_z-\sigma_y)^2+6\tau_{xy}^2+6\tau_{xz}^2+6\tau_{xz}^2]}\ . \tag{4.3}$$

ii) The Yield Function :

The amount of hardening of an isotropic strain hardening material can be expressed by the amount of plastic work which is :

$$W_p = \int \sigma_{ij}\,(d\epsilon_{ij})_p = \kappa \tag{4.4}$$

where $(d\epsilon_{ij})_p$ is the plastic components of the strain differential and

κ is the strain hardening parameter.

The integral is path (history) dependent. Like the equivalent von Mises stress given by equation (4.3), the equivalent plastic strain increment $(d\epsilon)_p$ can also be obtained from the second invariant of its incremental strain tensor $(d\epsilon_{ij})p$ as :

$$(d\epsilon)_p = \sqrt{\frac{2}{3}\{ (d\epsilon_{ij}')_p \, (d\epsilon_{ij}')_p \}_p} \, . \qquad (4.5)$$

iii) The Flow Rule :

The flow rule governs the plastic flow after yielding and can be derived from various yield criteria by using the concept of a plastic potential (f). This method proposes that the incremental strains resulting from a stress tensor σ_{ij} are found by using :

$$(d\epsilon_{ij})_p = \lambda \frac{\partial f}{\partial \sigma_{ij}} \qquad (4.6)$$

where f is termed the yield function and
λ is a constant.

The strain history and its current magnitude can be determined by the yield function (f). If the J_2 flow rule is used , (see equation (4.3)) the yield function can be expressed as :

$$f(\sigma_{ij}) = (s_{ij}\, s_{ij}) = \text{const} \qquad (4.7)$$

and

$$df = \frac{\partial f}{\partial \sigma_{ij}} d\sigma_{ij} \qquad (4.8)$$

Three cases of (df) are possible :

df < 0 : elastic unloading of an elastic plastic material occurs df = 0 : neutral loading of an elstic-plastic material and

df > 0 : plastic loading of an elastic-plastic material.

For the case where (f) is taken as the Mises criterion, given in equation (4.2), taking the derivative yields :

$$\frac{\partial f}{\partial \sigma_{ij}} = \frac{\partial J_2}{\partial \sigma_{ij}} = s_{ij} \qquad (4.9)$$

and equation (4.6) simplifies to :

$$(d\epsilon_{ij})_p = \lambda \ s_{ij} \qquad (4.10)$$

Equations (4.9) and (4.10) are referred to as the Prantl-Reuss equations.

iv) The Strain Rate Decomposition :

During an stress increment the resulting strain increments can be split into their elastic and plastic part :

$$d\underline{\epsilon} = d\underline{\epsilon}_e + d\underline{\epsilon}_p \qquad (4.11)$$

v) Elasticity :

The elastic strains can be related to the deviatoric and hydrostatic stress components by the relations :

$$(\epsilon_{ij})_e = \frac{1+\upsilon}{E} \ s_{ij} + \frac{1-2\upsilon}{3E} \sigma_{kk}\delta_{ij} \qquad (4.12)$$

Elastic and plastic parts can be added and the complete incremental relationship between stress and strain for elastic-plastic deformation can be obtained as :

$$(d\epsilon_{ij})_e = \frac{ds_{ij}}{2\mu} + \frac{1-2\upsilon}{E} d\delta_{ij} d\sigma_{kk} + \lambda s_{ij} \qquad (4.13)$$

It can be shown that the complete incremental elastic-plastic stress-strain relation can be written as derived in [48,49] :

$$d\underline{\sigma} = \underline{D}_{ep} d\underline{\epsilon} \qquad (4.14)$$

The elastic-plastic matrix D_{ep} is given as :

$$\underline{D}_{ep} = \underline{D} - \frac{\underline{d}_D \underline{d}_D^T}{A + \underline{d}^T \underline{a}^*} \quad ; \quad \underline{d}_D = \underline{D}\,\underline{a} \qquad (4.15)$$

where A is the local slope of the uniaxial stress-strain curve and can be gained from the stress- strain curve of the given material,

$\underline{a}$ is the flow vector which is a partial differential of the yield criterion with respect to its components and is given in equation (4.9).

$\underline{D}$ is the elasticity matrix having the form for the case of plane strain :

$$\underline{D} = \frac{E}{(1-2\upsilon)(1+2\upsilon)} \begin{vmatrix} 1-\upsilon & \upsilon & 0 \\ \upsilon & 1-\upsilon & 0 \\ 0 & 0 & \frac{1-2\upsilon}{2} \end{vmatrix}$$

5. THE FINITE ELEMENT METHOD

5.1 THE FINITE ELEMENT FORMULATION FOR LINEAR MATERIAL BEHAVIOR

Today the finite element method is firmly established as a standard numerical procedure for the solution of engineering problems. Its versatility is based on the following characteristics:

- irregular geometries can be modeled
- any kind of boundary condition can easily be formulated and
- it provides sufficient accuracy for many engineering purposes.

Especially in the field of fracture mechanics, the finite element method has been proven to be an efficient numerical method to model the response of a body under the influence of a sharp crack.

The basic idea behind the finite element method is to divide a given structure, body or region into a number of elements. The elements can be two or three dimensional. A discrete number of nodes situated on the element boundaries connect the elements. In structural problems, the finite element method solves the response of a model which is subjected to a given load by determining the nodal displacements. A set of interpolation functions (which are referred to as shape functions) uniquely define the displacement state within each element. The formulation of the shape function depends on:

- the number of nodes in each element (order of element) and
- the number of independent degrees of freedom in the problem considered.

The finite element formulation for a continuum can be obtained by taking advantage of the formulation of the principle of virtual displacement (which is a special case of the principle of virtual work) or of the principle of minimum potential energy (which assumes elastic body behavior).

In the following very brief introduction of the basic finite element formulation, only the two dimensional case will be considered.

The principle of virtual displacement states that equilibrium is obtained if the work done by external forces W_e on an arbitrary virtual displacement field equals the increase in strain energy (W_i) of the system [48]. This relation can be expressed in a variational form:

$$\delta W_i = \delta W_e \,. \qquad (5.1)$$

The principle of virtual work can be formulated as the volume integrals of the variations in strain energy density and the sum of variations of external energies resulting from body forces, surface tractions and point loads. Employing matrix notation, the variation in internal strain energy density is given as:

$$\delta W_i = \int (\delta \underline{\epsilon})^T \underline{\sigma} \, dV \qquad (5.2)$$

where $\delta \underline{\epsilon}^T$ represents the variation of the strain vector $\epsilon = [\, \epsilon_x, \ \epsilon_y, \ \gamma_{xy} \,]^T$ and

σ is the stress vector $\sigma = [\, \sigma_x, \ \sigma_y, \ \tau_{xy} \,]^T$.

The variation of the external work can be expressed as:

$$\delta W_e = \int (\delta \underline{u})^T \underline{b} \, dv + \int (\delta \underline{u})^T \underline{s} \, d\Gamma + \Sigma \ (\delta \underline{u})^T f_p \qquad (5.3)$$

where $\delta \underline{u}$ is the variation of the displacement vector $\underline{u} = [\, u_1, u_2 \,]^T$,

$\underline{b}$ is the vector of body forces $\underline{b} = [\, b_1, b_2 \,]^T$,

$\underline{s}$ is the vector of surface tractions $\underline{s} = [\, s_1, s_2 \,]^T$,

Γ is the boundary where surface tractions are applied and

f_p are nodal forces.

The finite element approach is based on the assumption that displacements within an element are adequately described by a polynomial. The second order rectangle has eight nodes and its interpolation polynomial approximation to the displacement field is assumed in the form :

$$\Phi = \alpha_1 + \alpha_2 x + \alpha_3 y + \alpha_4 x^2 + \alpha_5 xy + \alpha_6 y^2 + \alpha_7 xy^2 + \alpha_8 x^2 y \qquad (5.4)$$

In order to assure interelement compatibility, equation (5.4) must be complete in terms of a specific power. The eight constants, α_i, can be evaluated by solving a set of eight simultaneous equations if the nodal coordinate are inserted into equation (5.4) and the displacements equated to the appropriate nodal displacements. Performing this operation, equation (5.4) becomes :

$$u_i = [1,\ x_i,\ y_i,\ x_i^2,\ x_i y_i,\ y_i^2,\ x_i y_i^2,\ x_i^2 y_i] \begin{bmatrix} \alpha_1 \\ \cdot \\ \cdot \\ \alpha_8 \end{bmatrix} \qquad (5.5)$$

or :

$$\underline{\delta} = \underline{C}\,\underline{\alpha} \qquad (5.6)$$

where δ is the vector of u displacements of an element $\underline{\delta} = [\,u_1, u_2\ , u_3, \ldots, u_8\,]^T$.

Solving equation (5.6) the vector of constants α can be obtained in terms of nodal displacements by :

$$\underline{\alpha} = \underline{C}^{-1}\,\underline{\delta}\,. \qquad (5.7)$$

The vector $\underline{\alpha}$ can be substituted back into equation (5.6) and :

$$\underline{u} = \underline{C}\,\underline{C}^{-1}\underline{\delta} \qquad (5.8)$$

is obtained. From this relation, the shape function matrix $\underline{N}$ can be obtained as :

$$\underline{u} = \underline{N}\,\delta \qquad (5.9)$$

where $\underline{N}$ is the shape function matrix $\underline{N} = [N_1, N_2, \ldots, N_7, N_8]^T$.

Similarly, equation (5.9) holds for the v component of the displacement vector. Equation (5.9) can easily be generalized for the displacement vector $\underline{u}$ by writing :

$$\underline{u} = \underline{N}\,\underline{a} \qquad (5.10)$$

where $\underline{a}$ is the nodal displacement vector $\underline{a} = [u_1, v_1; u_2, v_2; \cdots; u_7, v_7; u_8, v_8]^T$

and

$\underline{N}$ is the shape function matrix $\underline{N} = [\,\underline{I}\,N_1, \underline{I}\,N_2, \ldots, \underline{I}\,N_7, \underline{I}\,N_8]^T$.

The isoparametric finite element formulation has proven very effective in structural analysis. Isoparametric elements are characterized by the transformation of the element geometry, into a square in 2 - D problems, using a local coordinate system defined by its $\xi - \eta$ coordinate axes, see Figure 6 . Axes ξ and η pass through mid points of opposite sides, so that the edges are defined by $\xi = \pm 1$ and $\eta = \pm 1$. If the shape functions used to describe the geometry and displacements of an element are the same then this element is called isoparametric. The shape function of the employed isoparametric eight node parabolic element are given in Table 2.

The displacement components of any point within the element are defined in terms of nodal displacements. In equation (5.2) the matrix equation for the strain becomes :

$$\underline{\epsilon} = \underline{B}\,\underline{a} \qquad (5.11)$$

The matrix $\underline{B}$ is defined as :

$$\underline{B} = \begin{bmatrix} \frac{\partial N_i}{\partial x} & 0 \\ 0 & \frac{\partial N_i}{\partial y} \\ \frac{\partial N_i}{\partial y} & \frac{\partial N_i}{\partial x} \end{bmatrix} \qquad (5.12)$$

Assuming linear elastic behavior, the stress-strain relation is defined through the generalized Hook's Law :

$$\underline{\sigma} = \underline{D}\,\underline{\varepsilon} = \underline{D}\,\underline{B}\,\underline{a} \qquad (5.13)$$

where $\underline{D}$ is the linear elasticity matrix given in equation (4.15).

In the isoparametric finite element representation the shape functions N_i, given in local coordinates ξ, η, have to be differenciated with respect to global coordinates. The chain rule must be applied to differentiate :

$$\frac{\partial N}{\partial x} = \frac{\partial N}{\partial \xi}\frac{\partial \xi}{\partial x} + \frac{\partial N}{\partial \eta}\frac{\partial \eta}{\partial x} \qquad (5.14a)$$

and

$$\frac{\partial N}{\partial y} = \frac{\partial N}{\partial \xi}\frac{\partial \xi}{\partial y} + \frac{\partial N}{\partial \eta}\frac{\partial \eta}{\partial y} \qquad (5.14b)$$

The derivative $(\partial\xi/\partial x)$ etc. can be evaluated from the inverse of the Jacobian matrix, $\underline{J}^{-1}$. Using the Jacobian matrix the volume integral (when setting $dz=1$ for the case of plane strain) becomes :

$$dxdy = (\det J)\,d\xi\, d\eta \qquad (5.15)$$

Equation (5.15) can be substituted into equation (5.2). Employing the stress-strain relation of equation (5.13) and employing equations (5.10) and (5.11) the finite element formulation (5.2),(5.3) can be given as :

$$\{ \iint \underline{B}^T \underline{D} \underline{B} (\det \underline{J}) \, d\xi \, d\eta \} \; \underline{a} = f_b + f_s \qquad (5.16)$$

where f_b is the volume integral of the body forces, $f_b = \iint \underline{N}^T \underline{b} \det \underline{J} \, d\xi \, d\eta$ and

f_s is the integral of the surface tractions, $f_s = \iint \underline{N}^T \underline{s} \det \underline{J} \, d\xi \, d\eta$.

The first term in (5.16) is referred to as the element stiffness matrix $\underline{K}$. Equation (5.16) can be numerically integrated using the Gauss-Legendre quadrature formula where nine integration points are defined for the isoparametric plane-strain rectangle, see Figure 5. The integration is performed in the ξ, η space where the coordinates of the element side range from -1 to 1.

5.2 THE FINITE ELEMENT FORMULATION FOR NONLINEAR MATERIAL BEHAVIOR

The described finite element method for linear elastic material behavior can be extended to materials showing nonlinear behavior. For most problems in material plasticity an incremental algorithm is used. It is based on the incremental theory of plasticity where the plastic action is followed as it develops, and, therefore, accounts for the path dependence of plasticity.

The initial step of an elastic-plastic finite element calculation assumes linear elastic behavior. If yielding occurs at one or more nodes a system of residual forces $\underline{\psi}$ will exist, such that:

$$\underline{\Psi} = \int \underline{B}\, \underline{\sigma}\, dv - (\underline{f} + \int \underline{N}^T \underline{b}\, dv) \neq 0 \qquad (5.17)$$

where $\underline{f}$ is the vector of applied external forces. If the effective stress at one or more nodes exceeds the yield stress, the material stiffness matrix is continually varied. Then increments of strains are related to increments of stresses according to equation (4.14) :

$$d\underline{\varepsilon} = \underline{D}_{ep}\, d\underline{\sigma} \qquad (5.18)$$

where $\underline{D}_{ep}$ is the elastic-plastic matrix given by equation (4.15). Equation (5.18) can be substituted into (5.17) and a relation between an incremental load $\Delta\underline{u}$ and the increments of the residual vector $\Delta\underline{\Psi}$ (which is usually not zero) is obtained as :

$$\Delta \underline{\Psi} = \underline{K}_T\, \Delta\underline{u} - (\Delta\underline{f} + \int \underline{N}^T \Delta\underline{b}\, dv) \neq 0 \qquad (5.19)$$

where $\underline{K}_t$ is the tangential element stiffness matrix in the elastic-plastic range and is given as :

$$\underline{K}_t = \int \underline{B}^T \underline{D}_{ep}\, \underline{B}\, dv \,.$$

Equation (5.19) can only be solved iteratively according to the following steps :

1. Employing incremental displacements $\Delta\underline{u}$ in each iteration step r, an iterative correction $(\delta\underline{u})^r$ is calculated using the Newton Raphson Method :

$$(\delta\underline{u})^r = [\, \underline{K}_T{}^r \,]^{-1}\, \Delta\underline{\Psi}^r \qquad (5.20)$$

2. At the end of each iteration the improved displacement estimate is:

$$\Delta \underline{u}^{r+1} = \Delta \underline{u}^{r} + (\delta \underline{u})^{r} \tag{5.21}$$

This value $\Delta \underline{u}^{r+1}$ is substituted in (5.19) to evaluate the residual force vector $\Delta \underline{\Psi}$ which is used in (5.21) to calculate the correction of the displacement.

This algorithm is repeated until the maximum of the residual force vector is smaller than a user defined number. ABAQUS uses the modified Newton Raphson method where the stiffness matrix $\underline{K}_t$ calculated after each convergent solution instead of being modified after each iteration. This results in a significant decrease in computing time.

5.3 GENERATION OF THE FINITE ELEMENT MESH

A central aspect of the application of the finite element method is the generation of an appropriate mesh. The quality of the finite element mesh affects:

- the accuracy of the solution
- the amount of required computing time and
- the convenience of postprocessing the results.

Today, most finite element meshes are generated with the help of a finite element modeling program. For the present investigation the mesh of the mixed mode fracture model was created on an IBM 5080 workstation using the CAEDS software package [49]. CAEDS is a computer aided design tool which provides the ability to model and analyze the behavior of mechanical structures. CAEDS divides this task into three consecutive steps:

1. Geometry definition:
   The model geometry is defined by points and their connecting lines. Subareas have to be defined in the model which help control pattern and density of the finite element mesh to be generated.

2. Mesh Generation:

   The mesh generation accesses the geometry of the model through defined subareas. Concentration and configuration of the finite element mesh can be influenced by defining nodes or a node concentration on the boundary of the subarea. Thus the finite element mesh for every subarea is generated automatically in an exactly predictable manner.

3. Model Checking:

   This module assures the correctness of the created mesh. Internal free edges, node and element coincidence and element distortion can easily be detected and corrected. Furthermore, the bandwidth and the profile of the stored matrix can be optimized and the nodes of the model renumbered accordingly (which shortens the computing time significantly).

6. MODEL CREATION AND SOLUTION

6.1 CREATION OF THE FINITE ELEMENT MESH OF THE EMPLOYED SPECIMEN

For the present investigation, a disk shaped fracture model with a sharp crack was modeled. The dimensions of the specimen were mainly determined by the definition of small scale yielding which limits the plastic zone size to approximately 20 percent of the specimen size [27]. Therefore, for the given sets of K_I and K_{II} values, the plastic zone size was estimated using approximation formulas. Employing the plastic zone size estimation formula by Irwin [8] yielded a maximum plastic zone size radius of $r_p = 3.75$ mm in the case of pure mode I (under plane strain conditions). The yield stress contour which is given in Figure 7 for a selection of mixed modes indicates in the case of pure mode II loading a plastic zone size radius of approximately $r_p = 24$ mm. The specimen radius was therefore chosen to be 100 mm. The crack width was modeled as small as possible to produce a sharp crack.

Conventional elements cannot simulate the singularities in the strain fields which exist near sharp cracks in the case of elastic and elastic-plastic material behavior. Various authors, therefore, have suggested finite elements which account for these singularities without using large numbers of elements.

Henshell and Shaw [50] and Barsoum [51] proposed the use of isoparametric eight node quadrilateral elements with midsize nodes displaced by a quarter of the edge length towards the crack tip. This collapsed quarter point element produces a $1/\sqrt{r}$ singularity in the elastic strains. Barsoum [51] proposed that, in the case of crack-tip plasticity, eight isoparametric eight node elements can be degenerated into triangular shape elements by collapsing the element at their crack-tip nodes without shifting the midsize node, Figure 8. All collapsed nodes at the crack tip remain unconstrained and have independent degrees of freedom. It has been shown [52-54] that this causes three effects :

- *a singularity of the order of 1/r is simulated in the approximation of the strain* components. This coincides very well with perfectly plastic material behavior in the near-tip field
- the ability to reproduce large strain gradients is retained and
- spurious numerical unloading often encountered with the collapsed quarterpoint element is eliminated.

Comparison with analytical results performed by Shih [52] showed that this element simulates the material response at the crack tip reasonably well. Barsoum [51], however has shown that this type of element possesses theoretically unbounded terms in the stiffness matrix but which are usually suppressed by the smoothing character of the Gauss-Legendre quadrature.

Figure 9 shows the finite element mesh of the modeled specimen in the vicinity of the crack tip. A fan of 24 degenerated elements with a side length of 0.04 mm defines the crack tip. The crack-tip width was modeled as 0.004 mm. Adjacent to this fan is an intermediate zone which connects the crack-tip fan to the main fan consisting of 23 circumferential layers of 32 element segments, see Figure 10. Three circumferential element layers are needed to model the boundary element layer of 16 elements, (Figure 11), where the displacement components act on the outer nodes. The finite element model of the specimen consists of 1178 elements and 3643 nodes. In order to investigate the accuracy of the finite element model, the elastic stress intensity factors were calculated. These agreed with the input values to within 0.1 percent.

6.2 MATERIAL

The material properties of the stainless steel A304 [55] were used as the material data input in the finite element calculation. This steel finds its main application in pressure containments in the high temperature range due to its ability to sustain high plastic deformation beyond the yield stress. Table 3 lists the material data of the steel A304 and its chemical composition given by Newman [56]. The stress-strain behavior of the employed material was modelled using the Ramberg-Osgood relation. In the case of the power hardening simulation of the material response, the uniaxial stress-strain relation is given as :

$$\begin{aligned} \epsilon &= \frac{\sigma}{E} && \text{for } \sigma < \sigma_y \\ \frac{\epsilon}{\epsilon_y} &= \frac{\sigma}{\sigma_y} + \alpha\left(\frac{\sigma}{\sigma_y}\right)^n && \text{for } \sigma > \sigma_y \end{aligned} \qquad (6.1)$$

where σ is the uniaxial tensile stress,

ϵ_y is the yield strain,

σ_y is the yield stress,

α is a material constant which is given as 0.75 for the steel A304 and

n is the hardening index which is given as 6 for the present material.

Figure 12 shows the modeled stress-strain behavior of the employed steel A304.

6.3 USING THE FINITE ELEMENT SOLVER 'ABAQUS'

The commercially available finite element package ABAQUS [57] was used for model solution. Nodal coordinates and element connectivity generated by CAEDS can be accessed through a universal file. A FORTRAN program has been written to both reformat the universal file for the correct ABAQUS input and to correct the node numbering direction since CAEDS does not employ a consistent node numbering direction within an element. The applied boundary displacements for all cases of mixed modes considered were calculated according to equation (2.2). The element type CPE8 (eight node parabolic plane strain isoparametric element) was employed in this model.

Based on the modeled stress strain curve of the employed material, discrete values of stresses and plastic strains had to be specified in the ABAQUS input. Element sets for both data output and graphic display of deformed meshes and contours of specified variables were defined.

For all cases considered, the model response for the elastic-plastic material behavior was calculated using small strain theory. ABAQUS generates increment sizes automatically and assumes a maximum number of six iterations per increment. This usually assures good convergence at relatively short computing time.

While good convergence was obtained for cases of mixed modes with either predominant mode I and mode II contributions, the following four cases of mixed modes had to be subdivided into separate steps of increasing pairs of K_I - K_{II} values to obtain a convergent solution :

- $K_I / K_{II} = 2107/670$
- $K_I / K_{II} = 1927/987$
- $K_I / K_{II} = 1683/1252$
- $K_I / K_{II} = 1405/1462$

Four increasing pairs of combinations of K_I and K_{II} values (of equal ratio) were assumed which resulted in good convergence for each step. J-integral values, however, cannot be obtained by ABAQUS if a calculation is subdivided into separate steps [57].

In order to permit an efficient postprocessing of ABAQUS data, a FORTRAN program has been written which reads any variable from the data output file :

- along a line having a specified angle to the x - axis

- in a circular segment and
- along a circular path.

7. THE J - INTEGRAL

7.1 DEFINITION AND PROPERTIES

The J-integral, which was originally established by Eshelby [11], was introduced by Rice [13] into the field of fracture mechanics. Rice showed that the potential energy release rate for a two dimensional crack extending in its plane in a homogeneous linear or non-linear elastic material was equal to a path independent integral. Its definition is given in cartesian coordinates as, (see Figure 13) :

$$J = \int_{\Gamma} W dx_2 - T_i \frac{\partial u_i}{\partial x_1} ds \qquad (7.1)$$

where W is the energy density, defined as $W = \int \sigma_{ij} d\epsilon_{ij}$,

Γ is an arbitrary path around the crack ,

T_i is the traction vector defined according to the outward normal n along Γ and is given as $T_i = \sigma_{ij} n_i$.

The J-integral is well established as a parameter which describes the magnitude of near-tip stress and strain fields. Knowles and Sternberg [58] subsequently generalized the J-integral to be a vector, J_k , corresponding to the potential energy release rate in any coordinate direction of the crack extension. J_k is defined as:

$$J_k = \int_{\Gamma} W n_k - \sigma_{ij} n_j \frac{\partial u_i}{\partial n_k} ds \qquad (7.2)$$

where n_k denotes the unit outward normal to Γ, lying in the same plane of the crack.

For the two dimensional combined mode I and mode II fracture, only the J_1- and J_2-integral definitions need to be considered. Both integrals have the following important properties:

i) Path Independence :

A proof of the path independence of the J-integral can be found in [59]. Finite element investigations of J-integral values obtained for paths very close to the crack tip, however, (assuming elastic-plastic material behavior) showed significant path dependence where J-integral values approach zero very rapidly. McMeeking [60,61] investigated this behavior systematically and showed that it can be related to the large deformations around the blunting crack. The J-integral values calculated along paths more than 5 to 10 times the crack opening away from the crack tip can be considered as path independent. Their role as parameter characterizing the crack-tip field quantities is probably retained.

ii) Compatibility with Linear Elastic Fracture Mechanics :

For linear elastic behavior J_1 and J_2 are equivalent to the energy release rate G in x_1 and x_2 direction, respectively. Hellen et al. [62] and Blackburn [63] related J_1- and J_2-integral values to stress intensity factors for a two dimensional crack. The relations are given for the case of plane strain as :

(7.3)

iii) Application in Elastic Plastic Fracture Mechanics:

The J-integral value for two dimensional crack problems has been used by many authors to predict the onset of crack growth initiation in cracked bodies both for linear elastic and elastic plastic material behavior. This concept was introduced by Begley and Landes [14], [64]. A critical value of J_{IC} in pure mode I for plane strain conditions can be determined by a standard test method if the conditions of quasistatic loading, negligible body forces, monotonic loading and stationary crack are met. Kishimoto et al. [15], in their interpretation of J_1 an J_2 as vector quantities of the strain energy release rate for crack extension in the two dimensional case, defined a resultant vector J_{res}. Its magnitude is given as :

$$J_{res} = \sqrt{J_1{}^2 + J_2{}^2} \qquad (7.4)$$

They proposed that failure in mixed mode occurs if the resultant J-integral equals the critical energy release rate:

$$J_{res} \geq G_{cr} \qquad (7.5)$$

According to Bakker [65] this criterion has found little experimental verification for the case of mixed mode fracture.

7.2 CALCULATION OF THE J - INTEGRAL VALUE

Various procedures have been developed in the past to calculate the J-integral value. A survey of different methods can be found in [66]. In the present investigation the virtual crack extension method and the direct integration method were employed.

i) The Virtual Crack Extension Method :

This method originally described by Parks [67] as the stiffness derivative method is an implemented feature in most commercial finite element programs like ABAQUS. In this method, the potential energy release rate is evaluated directly in a single finite element analysis by advancing the crack tip or crack front by a small amount . This small advance changes the stiffness of some of the elements in the mesh and the change in potential energy can be calculated. Even for coarse meshes this method yields very accurate results [53]. According to Nagtegaal [66], the method of virtual crack extension is particularly accurate if collapsed elements at the crack tip are used.

ii) The Direct Integration Method :

A direct way of calculating both J_1- and J_2-integral values is the numerical integration of equation (7.1) using discrete data points (e.g. from a finite element analysis). The circumferentially arranged elements in the present mesh suggested the use of circular paths around the tip. The definition of J_1 and J_2 had to be expressed in polar coordinates. The transformation of x and y into polar coordinates is given as:

$$x = r\cos\theta, \qquad y = r\sin\theta \tag{7.6}$$

The path increment ds can be expressed as :

$$ds = r\,d\theta \qquad (7.7)$$

The displacement derivatives with respect to x_1 and x_2 assume the following form, respectively :

$$\begin{aligned}\frac{\partial u_i}{\partial x} &= \cos\theta\,\frac{\partial u_i}{\partial r} - \frac{1}{r}\sin\theta\,\frac{\partial u_i}{\partial \theta}\\ \frac{\partial u_i}{\partial y} &= \sin\theta\,\frac{\partial u_i}{\partial r} + \frac{1}{r}\cos\theta\,\frac{\partial u_i}{\partial \theta}\end{aligned} \qquad (7.8)$$

The traction vector can be expressed along a circular path as :

$$\begin{bmatrix} T_1 \\ T_2 \end{bmatrix} = \begin{bmatrix} \sigma_{xx} & \sigma_{xy} \\ \sigma_{xy} & \sigma_{yy} \end{bmatrix} \begin{bmatrix} \cos\theta \\ \sin\theta \end{bmatrix} \qquad (7.9)$$

J_1 and J_2, calculated along a circular path can now be given as :

$$\begin{aligned}J_1 &= r\int_{-\pi}^{\pi}[W\cos\theta - T_i\,(\cos\theta\,\frac{\partial u_i}{\partial r} - \frac{1}{r}\sin\theta\,\frac{\partial u_i}{\partial \theta})]\,d\theta\\ J_2 &= r\int_{-\pi}^{\pi}[W\sin\theta - T_i\,(\sin\theta\,\frac{\partial u_i}{\partial r} + \frac{1}{r}\cos\theta\,\frac{\partial u_i}{\partial \theta})]\,d\theta\end{aligned} \qquad (7.11)$$

Here, *For the case of elastic-plastic material* behavior, the strain energy density is the sum of its elastic and plastic (dissipative) part :

$$W = W_e + W_{pl} \tag{7.10}$$

A FORTRAN program has been written to perform the numerical calculation. Stress components, elastic energy density as well as plastic dissipation and displacements were read from the ABAQUS output file along a defined path by a data post processing program. All quantities related to an integration point, (e.g. stress components, linear energy density and plastic dissipation) were interpolated linearly for the adjacent element node. The derivatives of the displacement components were computed using a sixth order finite difference formula. The integration along a path, defined by 65 equally spaced element nodes, was performed numerically using the Simpson's second order integration rule.

For all mixed mode cases considered both J_1- and J_2-integral values were calculated for radii ranging from 0.6 to 8.3 mm from the crack tip.

7.3 RESULTS OF THE J_1 AND J_2 INTEGRAL CALCULATIONS

Figure 14 depicts the variations of the J_1- and J_2-integral values for all mixed modes considered over the radial distance r from the crack tip. J_1-integral values range between 9.8 N/mm for the case of pure mode II to 21.2 N/mm for the case of mixed modes given as K_I/K_{II}= 2222/172. J_2 values are generally negative and range between $J_2 = 0$ for the cases of both pure modes I and II and -14.9 for the case of K_I/K_{II} =1405/1462.

Good path independence was obtained for all cases considered. For increasing mode II contribution, however, greater variations in the J_1-integral values can be observed. The maximum deviation reaches 9.3 percent for pure mode II loading in comparison to a deviation of 1.12 percent in the case of pure mode I.

J_2-integral values are generally less accurate and therefore show more path dependence in their results. Hellen et al [62] pointed out that due to higher overall displacement gradients in the x_2 -direction, the associated numerical errors are large. This can be seen from the deviations of J_2 - integral values which range between 9 percent (for the case of $K_I/K_{II} = 2222/175$) and 17 percent (for the case of $K_I/K_{II} = 1405/1463$).

Both J_1- and J_2- integral values show little variation for outer paths between 4.1 and 8.6 mm and, therefore, these values may be viewed as more accurate.

Table 5 lists the J_1-integral values for the outermost path from both the direct integration and the virtual crack extension performed by ABAQUS. As pointed out in chapter 6.2, the J_1-integral calculations of four cases of mixed modes could not be calculated by ABAQUS. Deviations of J_1-integral values gained from both methods are within 5.7 percent.

In all further investigations the J_1 integral values given in Table 4 will be used.

8. FIELD QUANTITIES

The dominant singularity solution for a cracked plate in a power law hardening material has been given independently by Hutchinson [21] and Rice and Rosengren [22] for both mode I and mode II stress distributions. The solutions which are known as the HRR singular field were generalized by the solution for the mixed-mode stress distributions presented by Shih [27]. For the small-scale yielding case, the region around the crack tip can be divided, (according to the nature of singular material behavior), into three distinct areas [59] :

- the far tip field
- the near tip field and
- the intermediate zone.

Figure 15 identifies these areas.

8.1 THE FAR TIP FIELD

At distances large compared to the plastic zone size the stress and strain distribution is dominated by the $1/\sqrt{r}$ singularity from the linear elastic solution for the stress and displacement fields. A measure of the strength of the singularity is the path independent J-integral which can be related to the stress intensity factors K_I and K_{II} according to equation (2.2). A convenient definition which characterizes the relative strength of K_I and K_{II} in the far tip field was introduced by Shih [27] as :

$$M^e = \frac{2}{\pi} \tan^{-1}_{r \to 0} [\, \lim \frac{\sigma_{\theta\theta}}{\sigma_{r\theta}} \,] = \frac{2}{\pi} \tan^{-1} [\, \frac{K_I}{K_{II}} \,] \qquad (8.1)$$

M^e is referred to as the far tip field mixity parameter which ranges from 0 to 1 with $M^e=1$

for pure mode I and $M^e = 0$ for pure mode II.

8.2 THE NEAR TIP FIELD

For a strain hardening material which can be described by a power law, i.e. the Ramberg- Osgood relation, the stress-strain relation based on the deformation theory of plasticity is given as :

$$\epsilon_{ij} = \frac{1+\upsilon}{E} s_{ij} + \frac{1+2\upsilon}{3E} \sigma_{kk}\delta_{ij} + \frac{3}{2}\alpha\, \epsilon_y \left(\frac{\sigma}{\sigma_y}\right)^{n-1} \frac{s_{ij}}{\sigma_y} \qquad (8.2)$$

where σ_y is the yield stress,

s_{ij} is the deviatoric stress tensor given in equation (4.1),

σ is the effective stress given in equation (4.3),

ϵ_y is the yield strain,

υ is Poisson's ratio,

E is Young's modulus,

α is a material constant and

n is the hardening coefficient.

Large plastic strains can be expected in the near field so that (with negligible elastic strains) equation (8.2) becomes :

$$\epsilon_{ij} = \frac{3}{2}\alpha\, \epsilon_y \left(\frac{\sigma}{\sigma_y}\right)^{n-1} \frac{s_{ij}}{\sigma_y} \qquad (8.3)$$

It can be assumed that the only singularity contained in this region is associated with the crack tip. For a circular path of radius r, where $r_0 < r < D$, enclosing the crack tip (see Figure 15), the J-integral (according to equation (7.11)) remains path independent.

To ensure the path independence of the J-integral value the integrand must exhibit a 1/r singularity. Since the integrand is essentially a product of stress- and strain-like components, this product leads to a function (f) which is only dependent on θ multiplied by a 1/r term (assuming the material behavior satisfies equation (8.3)) :

$$\sigma_{ij}\,\epsilon_{ij} \longrightarrow \frac{f(\theta)}{r} \qquad (8.4)$$

Hutchinson [21] has shown this to be the case for power law hardening materials if the stresses and strains are given in polar coordinates. For a power hardening law satisfying equation (8.3), equation (8.4) implies that the following relations hold :

$$\begin{aligned} \sigma_{ij} &= C\, r^{-\frac{1}{n+1}}\, \tilde{\sigma}_{ij}(\theta) \\ \epsilon_{ij} &= C\, r^{-\frac{n}{n+1}}\, \tilde{\epsilon}_{ij}(\theta) \\ u_i &= C\, r^{\frac{1}{n+1}}\, \tilde{u}_i(\theta) \end{aligned} \qquad (8.5)$$

where σ_{ij}, ϵ_{ij} and u_i are stress, strain and displacement functions in polar representation where i and j are radial and angular components and

C is a material dependent constant term.

Different from the asymptotic solution for linear-elastic material behavior, therefore, the singular fields in the elastic-plastic range are dependent on the hardening characteristic of the material.

Rice and Rosengren [22] and Hutchinson [21] solved equation (8.5) for the stress, strain and displacement functions by introducing an Airy stress function. A partial differential equation governing the stress function can be derived from the compatibility equation which can be reduced to a fourth order nonlinear differential equation and solved by a higher order finite difference scheme. A more detailed discussion of the procedure can be found in [59].

The constant term C can be determined by taking advantage of the path independence of the J-integral. Substitution of equations (8.5) into the definition of the J-integral (equation (7.1)) leads to the determination of the constant C as :

$$C = \left(\frac{J}{\alpha\, \epsilon_y \sigma_y\, I_n}\right)^{\frac{1}{n+1}} \tag{8.6}$$

where α is a material constant ,

ϵ_y is the yield strain,

σ_y is the yield stress,

n is the hardening exponent and

I_n is a constant given by :

$$I_n = \int_{-\pi}^{\pi} \left\{ \frac{n}{n+1} \tilde{\sigma}_{\theta} \cos\theta - \left[\sin\theta \left(\tilde{\sigma}_{rr} \left(\tilde{u}_{\theta} - \frac{\partial \tilde{u}_r}{\partial\theta} \right) - \tilde{\sigma}_{r\theta} \left(\tilde{u}_r + \frac{\partial \tilde{u}_{\theta}}{\partial\theta} \right) \right) + \frac{1}{n+1} \left(\tilde{\sigma}_{rr} \tilde{u}_r + \tilde{\sigma}_{r\theta} \tilde{u}_{\theta} \right) \cos\theta \right] \right\} d\theta$$

These equations (which were originally formulated for pure mode I) can be extended for the case of mixed modes. Due to the path independence of the J_1-integral (regardless of mixed-mode contributions), all near tip field quantities remain under the control of the J_1-integral value.

In the same manner as the elastic mixity parameter (M^e in equation (8.1)) the plastic mixity factor M^P identifies the relative composition of mode I and mode II directly ahead of the tip according to :

$$M^{pl} = \frac{2}{\pi}\tan^{-1}\left[\lim_{r\to 0}\frac{\sigma_{\theta\theta}(r,\ \theta=0)}{\sigma_{r\theta}(r,\ \theta=0)}\right] = \frac{2}{\pi}\tan^{-1}\left|\frac{\tilde{\sigma}_{\theta\theta}(\theta=0,\ M^{pl})}{\sigma_{r\theta}(\theta=0,\ M^{pl})}\right| \qquad (8.7)$$

From equations (8.5 to 8.7) the formulas defining stress, strains and displacements in the near field of a crack under mixed-mode conditions can now be given as :

$$\begin{aligned}
\sigma_{ij} &= \left(\frac{J}{\alpha\epsilon_y\sigma_y I_n r}\right)^{\frac{1}{n+1}}\tilde{\sigma}_{ij}(\theta)\\
\epsilon_{ij} &= \left(\frac{J}{\alpha\epsilon_y\sigma_y I_n r}\right)^{\frac{n}{n+1}}\tilde{\epsilon}_{ij}(\theta) \qquad (8.8)\\
u_i &= \left(\frac{J}{\alpha\epsilon_y\sigma_y I_n}\right)^{\frac{n}{n+1}} r^{\frac{1}{n+1}}\ \tilde{u}_i(\theta)
\end{aligned}$$

The stress and displacement fields are therefore characterized by a $1/r^{(1/(n+1)}$ singularity whereas the strain field assumes a $1/r^{(n/(n+1)}$ singularity. In reality such large stress components cannot exist since geometry changes modify several aspects of the tip field and therefore limit the stress concentration at the tip (as indicated in the blunting analysis of McMeeking [60,61]).

8.3 THE INTERMEDIATE ZONE

Combination of the HRR field and the far field characterizes the stress and strain distribution and magnitude of the intermediate zone. Whereas its outer border is defined as the transition from the elastic to the plastic zone, its border to the HRR field can not be distinguished clearly. In general it can be assumed that the powers characterizing the field singularity of the intermediate zone show a smooth transition into the characteristic powers of the HRR field. No analytical solution has been found yet to connect near tip field and far tip field quantities [27,59].

9. DISCUSSION OF THE FIELD VARIABLES

Stresses and the strain energy densities around the crack tip of the investigated plane strain specimen were studied with respect to their singular behavior under varying mixed-mode conditions. All data were taken from the finite element analysis output.

9.1 THE STRESS FIELDS

Figure 16 shows the plot of the effective stress versus the distance ahead of the crack tip along the line $\theta = 0°$ for all mixed-modes cases considered. Four important features characterize the material response under the influence of mixed modes :

i) The effective stress increases sharply for higher mode II contributions under comparable loads. This tendency is also observable if the effective stresses around the crack tip is considered. Figure 17 shows the effective von Mises stress along a circular path having a radius of $r = 0.4$ mm away from the crack tip.

i i) For three cases of low mode II contributions there is a distinct transition zone between the elastic and the elastic-plastic zones. Both zones are separated by the yield stress of $\sigma_y = 265$ MPa.

i i i) The elastic-plastic zone shows in its outer region an increasing influence of the intermediate zone. Plastic strains which are of the order of their elastic counterparts result in a combination of the HRR field and the far field.

iv) At distances very close to the crack, i.e. less than 0.5 mm, the singularity governing the effective stress behavior is weaker than the singularity characterizing the elastic material behavior and can therefore be attributed to the HRR field. In Figure 18, using full logarithmic axes, the nature of occurring singularities are shown. For distances close to the crack tip, the equivalent stresses of all mixed modes are distinguished by parallel lines before the smooth transition into the intermediate zone which show particularly weak singular behavior. For four cases of strong mode I contribution the elastic singularity is sharply separated from the elastic-plastic zone.

Figure 19 shows the y -component of the stress tensor versus the distance from the crack along a line $\theta = 0°$ for all mixed-modes cases considered. Increasing mode II contribution results in a steady decrease in the values of the stress component in y-direction which approach zero for the case of pure mode II. For distances less than approximately 0.2 mm away from the crack tip significant scatter in the y-component of the stresses for mixed modes of high mode II contribution can be observed. It is assumed that this stems from the influence of the badly distorted crack tip which is exposed to an increased rotation as mode II contributions grow. Since stresses are a second order quantity, (that means they are calculated from displacement derivatives obtained from the finite element solution) this effect may be amplified.

The powers of the singularities can easily be determined if the stress is assumed to follow the form :

$$\sigma_\theta = C\, r^{\Upsilon}\, \sigma_\theta \qquad (9.1)$$

In full logarithmic notation of equation (9.1) the parameter Υ indicates the slope according to :

$$\log(\sigma_\theta) = \Upsilon \log(r) + \log(C\, \sigma_\theta) \qquad (9.2)$$

The extraction of the exponent Υ has been performed using a least square approximation for all mixed-modes cases considered. Table 5 lists these powers for distances from the crack which contain the characteristic singularity. Compared to a predicted value of the power of $\Upsilon = -1/7$ for the employed material, it can be seen that for increasing mode II contributions this value is approached. It reaches the predicted value of $\Upsilon = -0.1428$ almost exactly in the case of pure mode II. For overwhelming contributions of mode I the HRR solution characterizing power was not reached even for closest distances to the crack tip. This is mainly caused by the distinct crack-tip blunting which results in a decrease in the effective stress and weakens their singular behavior. The elastic singularity which could be determined for four cases showed excellent agreement with the predicted value of $\Upsilon = -0.5$.

9.2 STRESS AND STRAIN DISTRIBUTION, PLASTIC ZONE SIZE AND CRACK BLUNTING

Contour plots of the effective von Mises stress in the vicinity of the crack tip allow a good qualitative assessment of the body response under the influence of a crack under mixed-mode loading.

Figures 20 to 26 display the contours of the effective stress in a zone of 1 mm radius around the crack tip for a selection of mixed-modes cases (which are identified on each plot). The typical symmetric butterfly shape of the stress contours in the case of mode I incline and assume asymmetric shapes through stages of mixed modes with increasing mode II contributions until the contours show the typical compact and symmetric mode II pattern.

The increasing concentration of the von Mises stresses around the crack tip is significant for higher mode II contributions. While for overwhelming mode I contributions elastic regions can be still observed, the zone considered is entirely plastic in the range of higher mode II values.

The shapes and magnitudes of the effective stresses and their variations between 1 mm and 10 mm radii for mixed modes and 2 mm to 20 mm radii for pure mode II around the crack tip are shown in Figures 27 to 33. Here the influence of mode II contributions results in higher effective stresses and, consequently, in larger plastic zone sizes.

The outermost contours of the equivalent plastic strains represent a good measures of the plastic zone size. Figures 34 to 37 are contour plots of effective plastic strains for selected mixed-mode cases in a circular region of 1 mm radius around the crack tip. The increasing gradient of plastic strains around the crack tip is evident. Figures 38 to 43 show the effective plastic strains in the region of 1 to 10 mm around the crack tip for all mixed modes and the region 2 to 20 mm for the case of pure mode II.

Figures 44 to 48 show the deformed mesh for a selection of mixed-modes cases in a region of 1 mm radius around the tip. The displacements are magnified by a factor of two. In the case of pure mode I, a parabolic shaped crack blunting can be observed. In chapter 6.1 it was pointed out that the employed crack tip elements can only approximate the strain assymptote. For increasing influence of mode II it can be seen that the crack-tip opening decreases with increasing mode II contribution and the crack tip tends to rotate in a clockwise direction, which reaches its extremum in the case of pure mode II. In the case of high mode II values, the extreme hydrostatic state of stress around the tip cannot be relieved by crack-tip blunting (as in cases with overwhelming mode I contributions) where finite strains create a relatively smooth crack tip.

Figures 49 to 52 depict only the upper and lower element layers around the crack tip in deformed and undeformed states (with a magnification factor of 10) for selected cases of mixed-mode loading. The influence of the rotation of the crack tip and the deviation from the center line of the undeformed crack is distinct for cases of high mode II values.

Figures 53 to 56 show deformed versus undeformed meshes of the outer region between 1 and 10 mm radii around the crack.

9.3 THE STRAIN ENERGY DENSITY

The strain energy density criterion, according to Sih [31,32], has not only been capable of predicting fracture under brittle material behavior, but also fracture in the elastic-plastic regime.

The strain energy density, using the notation of Sih, is given as :

$$\left(\frac{dW}{dV}\right) = \int_0^{\epsilon_{ij}} \sigma_{ij} \, d\epsilon_{ij} \qquad (9.3)$$

where ϵ_{ij} is the strain tensor and

σ_{ij} is the stress tensor.

The fact that excessive change in shape can be associated with yielding while excessive change in volume can be associated with fracture lead to the formulation of the strain energy density criterion for elastic plastic material behavior. It is postulated, [31,32], that maximum yielding occurs when the strain energy density reaches its maximum value $(dW/dV)_{max}$ whereas fracture initiation is associated with minimum strain energy density $(dW/dV)_{min}$. Chow and Xu [31] investigated the extension of the modification of the strain energy criterion in the elastic-plastic regime for the case of mixed-mode loading. It was observed that the strain energy density criterion led to incorrect predictions of the angle of fracture initiation since two local minima can be observed for some mixed-mode cases.

Figure 57 shows the variation of the strain energy density versus the angle θ along a circle of radius r=0.4 mm around the crack for selected cases of mixed-mode loading. The minimum strain energy density is located at angles from 180° for pure mode I to 90° for pure mode II. This contradicts experimental evidence [68-70]. Therefore the assumption of the crack growth direction was restated by Sih [71] that the direction of maximum value of $(dW/dV)_{min}$ governs the onset of crack growth. These values range between $\theta = 0°$ for mode I to $\theta = -90°$ for the case of of pure mode II and are given in Table 6 for all cases of mixed-mode loading considered.

In contrast to the maximum values of the strain energy density, which increase sharply for growing mode II contribution due to higher stress and strain components around the crack, the maximum values of $(dW/dV)_{min}$ remain for all cases remarkably constant.

Very good agreement between the location of $(dW/dV)_{max}$ and the maximum yield can be found by comparing the the angular position of the highest effective stress in Figure 17 and Figures 20 to 26 with the predicted values by the strain energy density criterion.

The singular behavior of the strain energy density versus the distances ahead of the crack along the line $\theta = 0°$ is depicted in Figure 58 in full logarithmic representation. In equation (8.5) it has been assumed that the strain energy density is governed by a 1/r singualrity inside the HRR field. It is evident that low contributions of mode II values result in weaker singularities in the strain energy density as the intermediate zone is approached. Determination of the powers of the singularities which are given in Table 7 demonstrate that the determined powers are in excellent agreement with the predicted value even for intermediate cases of mixed-mode loading. Cases distinguished by low mode II contribution show clearly the weak singular behavior inside the intermediate zone. As the crack tip is approached, it can be seen that the singular behavior of these cases converges towards 1/r.

This observation reinforces the correctness of the assumption in equation (8.5) that the HRR field solution is valid if the strain energy density exposes a 1/r singularity inside the plastic zone around a crack.

10. RESOLVING THE STRESS FUNCTIONS FROM FINITE ELEMENT RESULTS

The stress functions can be resolved from near tip field stress and displacement components obtained from the finite element results. All parameters required for 65 equally spaced nodes along a circular path of radius r = 0.4 mm around a crack were read from the ABAQUS data output file. Figure 18 shows that the selected radius is still within the dominant crack-tip singular field for all mixed-modes cases. Paths closer to the crack tip showed significant scatter in the values of σ_{rr} and $\sigma_{\theta\theta}$ components.

Determination of the stress function results in solving the three equations given in equation (8.8), where the components of σ_{ij} and u_i are given in polar coordinates :

$$\tilde{\sigma}_{ij} = \left(\frac{J}{\alpha \epsilon_y \sigma_y I_n r} \right)^{-\frac{1}{n+1}} \sigma_{ij}$$

$$\tilde{u}_i = \left(\frac{J}{\alpha \epsilon_y \sigma_y I_n} \right)^{-\frac{n}{n+1}} r^{-\frac{1}{n+1}} u_i \tag{10.1}$$

$$I_n = \int_{-\pi}^{\pi} \left\{ \frac{n}{n+1} \tilde{\sigma}_e \cos\theta - \left[\sin\theta \left(\tilde{\sigma}_{rr} \left(\tilde{u}_\theta - \frac{\partial \tilde{u}_r}{\partial \theta} \right) - \tilde{\sigma}_{r\theta} \left(\tilde{u}_r + \frac{\partial \tilde{u}_\theta}{\partial \theta} \right) \right) + \frac{1}{n+1} \left(\tilde{\sigma}_{rr} \tilde{u}_r + \tilde{\sigma}_{r\theta} \tilde{u}_\theta \right) \cos\theta \right] \right\} d\theta$$

The equivalent stress σ_e for the case of negligible elasticity in the case of plane strain is given as :

$$\tilde{\sigma}_e = \sqrt{3 \left(\tilde{\sigma}_{rr} - \tilde{\sigma}_{\theta\theta} \right) + \tilde{\sigma}_{r\theta}} \tag{10.2}$$

Due to the dependence of I_n on values of σ_{ij} , u_i and its angular derivatives (along a circular path taken from $-\pi$ to π), the solution of this system of equations can only be accomplished iteratively. In the present case, use of the interval halving method was made which showed rapid convergence for all cases considered. Figure 59 explains the principle of the interval halving method.

For an initial estimate of I_n the stress and displacement functions are calculated according to equation (10.1). The derivatives of the nodal displacements with respect to θ are obtained using a sixth order finite difference formula and the integration is performed using Simpson's second order integration rule. For incrementally increasing values of I_n, both stress and displacement components and derivatives are calculated and substituted into equation (10.2) to gain a new value of I_n. The calculated value of I_n approaches the assumed value of I_n and finally surpasses it. Since this can be expressed as the difference (F) between the assumed value I_{na} and the calculated value I_{nc}

$$F = I_{na} - I_{nc}, \tag{10.3}$$

a change of sign in (F) is expected between two incremental values of I_{na}. The following interval halving procedure narrows the interval where the change in sign has occurred down to a specified residual. A numerically accurate value for I_n can therefore be obtained.

Figures 60 to 69 show the stress functions σ_{rr}, $\sigma_{\theta\theta}$, $\sigma_{r\theta}$ and the effective stress function σ_e which are normalized by setting the maximum value of the θ -variation of the effective stress to unity.

For all cases considered, the components $\sigma_{\theta\theta}$ and $\sigma_{r\theta}$ show the expected value of zero on the crack surfaces, that is, for angles of $\theta = \pm \pi$. In contrast to pure mode I in the linear elastic case, σ_{rr} assumes positive values on either side of the crack flank. On opposite surfaces of the crack σ_{rr} is positive for both pure mode I and a mixed-mode case distinguished by the stress intensity ratio of $K_I/K_{II} = 2222/178$. This observation contradicts Shih's statement [27] that " for any deviation of mode I, the minus sign holds in:

$$\sigma_{rr}(\theta=\pi) = -\sigma_{rr}(\theta=-\pi) \tag{10.4}$$

for $0 \leq M^P < \pi$."

Also, the equivalence of the magnitudes of radial stress components on the surfaces of the crack at equal distance from the crack could not be shown except for the symmetic cases of both pure mode I and mode II. This can also be seen from the magnitude of the effective von Mises stresses on the crack surfaces in Figures 20 to 26. Since the effective stress contains σ_{rr} as the only component different from zero, their contours had to match up at the crack flanks. Even though the observation of equal radial stresses on crack surfaces by Rice and Budiansky [71] seems plausible, no reason for this mismatch could be found. This phenomenon could also be observed in other studies on mixed-mode fracture [27,72,73].

From equation (8.7) the mixity parameter M^{P} can be resolved from the stress components $\sigma_{\theta\theta}$ and $\sigma_{r\theta}$ of the finite element results. Some scatter in the ratios of $\sigma_{\theta\theta}$ over $\sigma_{r\theta}$ for distances of less than 0.5 mm from the crack tip was observed and, therefore, a least square approximation was employed through all datapoints for distances ranging from 0.08 to 1 mm from the crack tip.

Figure 70 shows the ratios of $\sigma_{\theta\theta}$ over $\sigma_{r\theta}$ of same integration points along the crack and their corresponding least square approximations for three mixed-mode cases. The constant character of the curves is evident.

The relationship between the calculated values of the mixity parameter M^{P} and the constant I_n given in equation (8.6) is shown in Figure 71. The results compare well with those generated by Shih [27] for the hardening powers of $n = 5$ and $n = 13$.

11. CONCLUSIONS AND RECOMMENDATIONS FOR FURTHER RESEARCH

In the present study, local crack-tip quantities were investigated for general mixed-mode crack problems under the condition of plane strain. In order to become independent of a specific specimen geometry, the local crack-tip region was modeled as a disk with the crack tip at its center. Displacements on the boundary of the local crack region were calculated from assumed combinations of stress intensity factors for mode I and mode II.

The strain energy density criterion, according to Sih, was applied as a fracture criterion. This provides a concise relationship between a given strain energy density factor and the stress intensity factors, K_I and K_{II}. For ten comparable cases of loading (which span the range from pure mode I to pure mode II) the body response for elastic-plastic material behavior was calculated using the finite element package ABAQUS. The eight node plane strain isoparametric elements employed were degenerated into triangular shaped elements around the crack tip to produce a 1/r singularity in strains. The material data of the stainless steel A304 was used in the finite element calculation.

The path independent J_1-integral (which is a governing parameter of the amplitude of the crack-tip singularities of the stress and strain fields) was calculated according to the method of virtual crack-tip extension that is available in ABAQUS. The direct integration method was applied for four cases of mixed-mode loading, which had to be subdivided into separate consecutive steps to reach convergence. For these cases the virtual crack extension method could not be applied by ABAQUS. The J_1-integral value was calculated using the direct integration method along nine circular paths whose radii from the crack tip spanned between 0.6 and 8.3 mm. Generally, very good path independence was observed which indicated the correctness of the obtained values and justified for their further use. Good agreement between the J_1-integral values obtained by both methods was observed when both were calculated. Deviations between the results obtained by both methods were within 5.7 percent for all cases considered.

J_2-integral values, which have attained limited usage in the field of fracture mechanics, were also evaluated. Less path independence especially for cases of more balanced mode I and mode II contributions was observed due to larger numerical errors in the evaluation of the displacements which was caused by higher displacement gradients in the y -direction.

The characteristic singular behavior of stresses and strains within the HRR field, the intermediate zone, and the far field was best expressed by the dependence of the effective von Mises stress on the distance from the crack tip, along the line $\theta = 0°$. Extraction of the powers characterizing the singular behavior of stresses and strains indicated the dependence of the size of the HRR field on increasing mode II contributions. In the case of pure mode I, the characteristic exponent of -1/7 (for the given material) in the effective von Mises stress was never reached due to the distinct influence of crack-tip blunting. Extreme hydrostatic stresses in the vicinity of the crack tip are reduced by finite strains and the stress-free crack-tip surfaces. For higher mode II contributions, the crack width decreased significantly to an almost sharp crack in the case of pure mode II. Larger plastic zone sizes and less crack-tip blunting result, therefore, in a distinct HRR-field of increasing size which was observed to be valid for a distance of approximately 25 J/σ_y in the case of pure mode II. Accordingly, the effective stress increased sharply for higher mode II contributions.

The strain energy density was investigated to determine its applicability as a fracture criterion for elastic-plastic material behavior under mixed-mode loading. It was stated by Sih [29] that the maximum yield occurs where the strain energy reaches its maximum which could be verified in this study. The modified formulation of the condition that crack extension occurs under the angle where the minimum of the strain energy density shows a maximum seems to be promising. For increasing mode II values the direction of crack growth initiation could be shown to move from 0° to -90° relative to the crack plane. This is comparable to the results of the linear elastic solution.

An emphasis of the present study was the numerical extraction of the stress functions from the finite element solution, for a given material with a hardening factor of six. The stress functions obtained compared reasonably well with those obtained by Shih. Theoretical considerations suggest radial stresses of equal magnitude for equal distances from the crack tip on either crack surface. This would imply that the radial stress function (which is the only component different from zero on the crack surface) has the same magnitude at either side of the crack surface. This could only be shown for the symmetric mode I case and the skew-symmetric mode II case. In all other cases of mixed-mode loading a deviation in the magnitude of the radial stress component on either side of the crack could be observed. The effective von Mises stress (which is only dependent on the radial stress along the surfaces of the crack) showed this mismatch also. For any amount of mode II contribution, the predicted change in sign of the radial stress acting on opposite crack surfaces was not verified by the finite element results. One case investigated, where the specimen was subjected to a load resulting in stress concentration factors of $K_I = 2222$ and $K_{II} = 178\ N\sqrt{mm^3}$, showed positive radial stresses on either side of the crack surface. The finite element calculations indicated that the sign of σ_{rr} on the crack surface jumps suddenly from positive to negative values for a more intermediate mixed-mode combination.

The investigation of the observed discrepancy between the behavior of theoretical radial stresses along the crack surface and the finite element solution was not studied in this thesis. An important extension of this work should include research on this phenomenon.

An extension of this study should include investigations of the local crack-tip quantities of a suggested mixed-mode specimen. The mixed-mode fracture specimen (due to Richard [34]) has been shown to simulate very well arbitrary mixed modes ranging from pure mode I to pure mode II and should be given consideration. Both numerical and experimental studies are necessary to further investigate two interesting concepts of fracture criteria which predict both the onset of crack growth and the direction of crack extension for ductile materials under mixed-mode loading :

i) The strain energy density criterion according to Sih

The modified formulation of the predicted angle of fracture initiation appears to be promising in the finite element results but needs further experimental confirmation. Further investigation of crack growth initiation in relation to its associated strain energy density , especially in the range of high mode II values seems necessary.

ii) The T-criterion according to Theocaris

This criterion (which has been extended very recently for mixed-mode loadings under ductile material behavior) incorporates the HRR field solution. Experiments with inclined cracks in a center cracked panel showed good agreement in the prediction of the angle of extension versus the crack and failure loads. Both finite element analysis and experimental investigations with a specimen which can reproduce all combinations of mode I and II may establish this criterion in the field of fracture mechanics.

REFERENCES

[1] Inglis, C. E., " Stresses in a Plate Due to the Presence of Cracks and Sharp Corners," Transition of the Royal Institute of Naval Architects, 60, pp. 219, (1913).

[2] Griffith,A. A., " The Phenomena of Rupture and Flow in Solids," Philosophical Transactions of the Royal Society of London, Ser. A221, p. 163,(1921).

[3] Griffith,A. A., " The Theory of Rupture," Proceedings of the First International Congress for Applied Mechanics," Delft, p. 55, (1924).

[4] Irwin, G. R., " Fracture Dynamics," Fracture of Metals, American Society For Metals, Cleveland, pp. 147-166, (1948).

[5] Orowan, E., " Fracture and Strength of Solids," Report on Progress in Physics,XII, p. 195, (1948).

[6] Irwin, G. R., " Handbuch der Physik," Vol. 79, Springer Verlag Berlin, pp. A49-A53, (1958).

[7] Westergaard, H. M., " Bearing Presssures and Cracks," Transactions of the ASME, Journal of Applied Mechanics, Vol. 66, pp. A49-A53,(1939).

[8] Irwin, G. R., Kies, J. A., Smith, H. L., " Fracture Strengths Relative to Onset and Arrest of Crack Propagation," Proceedings of the American Society For Testing and Materials, 58, pp 640-657, (1958).

[9] Wells, A. A., " Application of Fracture Mechanics at and Beyond General Yielding," British Welding Journal, 10, pp. 640-657, (1958).

[10] Dugdale, D. S., " Yielding of Steel Sheets Containing Slits," Journal of the Mechanics and Physics of Solids, 8. pp. 100-108, (1960).

[11] Eshelby, J. R., " The Continuum Theory of Lattice Defects," Solid State Physics, Vol. III, Academic Press, (1956).

[12] Cherepanov, G. L., " Cracks in Solids," International Journal of Solids and Structures, 5, pp. 863-871, (1969).

[13] Rice, J. R., " A Path Independent Integral and the Approximate Analysis of Strain Concentration by Notches and Cracks," Journal of Applied Mechanics, 35, pp. 379-386, (1968).

[14] Begley, J. A., Landes, J. D., " The Effect of Specimen Geometry on J_{IC}," Fracture Toughness, ASTM STP 514, American Society for Testing and Materials,

Philadelphia, pp. 24-29, (1972).

[15] Kishimoto, K., Aoki, S., Sakata, M., " On the Path Independent Integral J," Engineering Fracture Mechanics, 13, pp. 841-850, (1983).

[16] Blackburn, W. S., " Contour Integration Around Crack Tips for Combined Mixed Mode Load and Strain Controlled Loading of an Elastic Plastic Material," International Journal of Fracture, 32, 93-104, (1986).

[17] Miyamoto, H., Kateyama, K., Kikuchi, M. Machida, K., " The J_{ext}-Integral Based on the Concept of Effective Energy Release Rate," Elastic Plastic Fracture: Second Symposium, Vol. I - Inelastic Crack Analysis, ASTM STP 803, American Society for Testing and Materials, pp. I-116 - I-129, (1983).

[18] Ewing, P. D., Williams, J. G., " The Fracture of Spherical Shells under Pressure and Circular Tubes with Angled Cracks in Tension," International Journal of Fracture, 10, pp. 537-577, (1974).

[19] Atluri, S. N., " Energetic Approaches and Path-Independent Integrals in Fracture Mechanics," in Computational Methods in the Mechanics of Fracture, S. N. Atluri, ed., Elsevier Science Publishers, B.V., pp, 122-165, (1986).

[20] Atluri, S. N., Kobayashi, A. S., " Elastic Plastic Fracture (Quasi-Static)," in Computational Methods in the Mechanics of Fracture, S. N. Atluri, ed., Elsevier Science Publishers, B.V., pp. 56-83, (1986).

[21] Hutchinson, J. W., " Singular Behavior at the End of a Tensile Crack in a Power Hardening Material," Journal of the Mechanics and Physics and Solids, Volume 16, pp. 13-31, (1968).

[22] Rice, J. R., Rosengren, G. F., " Plane Strain Deformation near a Crack-Tip in a Power Law Hardening Material," Journal of the Mechanics and Physics of Solids, Volume 16, pp. 2-30, (1968).

[23] Shih, C. F., German, M. D., " Requirements for a One Parameter Characterization of Crack-Tip Fields by the HRR-Singularity," International Journal of Fracture, Vol. 17, No. 1, pp. 27-43, (1981).

[24] Shih, C.F., " Relationship between the J-integral and the Crack Opening Displacement for Stationary and Extending Cracks," Journal of the Mechanics and Physics of Solids, Vol. 29, pp. 304-326, (1981).

[25] Needleman, A., Tvergaard, V., " Crack Tip Stress and Strain Deformation Fields in a Solid with a Vertex on its Yield Surface," Elastic Plastic Fracture: Second Symposium, Vol. I - Inelastic Crack Analysis, ASTM STP 803, American Society for Testing and Materials, pp. I-80 - I-115, (1983).

[26] Yagawa, G., Tatsuhiko, A., Yoshio, A., " Crack Analysis of Power Hardening Materials Using a Penalty Function and Superposition Method," Fracture Mechanics Twelfth Conference, ASTM STP 700, American Society of Testing and Materials, pp. 439-452, (1980).

[27] Shih, C. F., " Elastic Plastic Analysis of Combined Mode Crack Problems," Ph.D. Thesis, Harvard University, (1973).

[28] Shih, C. F., " Small Scale Yielding Analysis of Mixed Mode Plane Strain Crack Problems," Fracture Analysis, ASTM STP 560, American Society for Testing and Materials, pp. 187-210, (1974).

[29] Sih, G. C., " Methods of Analysis and Solution of Crack Problems," in Mechanics of Fracture, ed. G. C. Sih, Noordhoff International Publishing, Leyden, (1973).

[30] Sih, G. C., Madenci, E., " Fracture Initiation under Gross Yielding : Strain Energy Criterion," Engineering Fracture Mechanics, Vol. 18, No. 3, pp. 667-677, (1983).

[31] Chow, C. L., Xu, J., " Mixed Mode Ductile Fracture Using the Strain Energy Density Criterion," International Journal of Fracture, 28, pp. 17-28, (1985).

[32] Theocaris, P. S., " Affinities Between Criteria Based on Components of Stresses and Energy Density," International Journal of Fracture, 32, pp, 51-57, (1987).

[33] Theocaris, P. S., Adrianaopoulos, N. P., " The T-Criterion Applied to Ductile Fracture," International Journal of Fracture, 20, R125-R130, (1982).

[34] Richard, H. A., " Examination of Brittle Fracture Criteria for Overlapping Mode I and Mode II Loading Applied to Cracks," AFMMS-Conference, Freiburg, (1983).

[35] Awaji, H., Sato, S., " Combined Mode Fracture Toughness Measurement by the Disk Test," Journal of Engineering Materials and Technology, Vol. 100, pp. 175-182, (1978).

[36] Mushkelishvili, N. I., " Some Basic Problems of Mathematical Theory of Elasticity," Noordhoff International Publishing, Leyden, (1953).

[37] Williams, M. L., " On the Stress Distribution at the Base of a Stationary Crack," Journal of Applied Mecahnics, Vol. 24, pp. 109-114, (1957).

[38] Sih, G. C., " Stress Distribution Near Internal Crack Tips for Longitudial Shear Cracks," Journal of Applied Mechanics, 32, pp. 51-58, (1965).

[39] Eftis, J., Subromonian, N., Liebowitz, H., " Crack Border Stress and Displacement Equations Revisited," Engineering Fracture Mechanics, Vol. 9, pp. 189-210, (1977).

[40] Eftis, J., " Load Biaxiality and Fracture : a Two-Sided History of Complementing Errors," Engineering Fracture Mechanics, Vol. 26, No. 4, (1987).

[41] Theocaris, P. S. Michopoulos, J. G., " A Closed Form Solution of a Slant Crack Under Biaxial Loading," Engineering Fracture Mechanics, Vol. 26, No. 4, (1987).

[42] Irwin, G. R., Fracture Mechanics, Structural Mechanics, Eds. J. N. Goodier and N. J. Hoff, Pergamon Press, Oxford, (1960).

[43] Hussain, M. A., Pu, S. L., Underwood, J., " Strain Energy Release Rate for a Crack Under Combined Mode I an d Mode II," Fracture Analysis, ASTM STP 560, American Society for Testing and Materials, pp. 2-28, (1974).

[44] DiLeonardo, G., " Fracture Toughness Characterization of Materials Under Mixed Mode Loading," International Journal of Fracture, Vol. 15, No. 6, pp.537-552, (1979).

[45] Nuismer, R. J., " An Energy Release Rate Criterion for Mixed Mode Fracture," International Journal of Fracture, 11, pp. 245-250, (1975).

[46] Yehia, N. A., " Automatic Tracing of Crack Growth via Finite Elements," Dissertation, Rensselaer Polytechnic Institute, (1985).

[47] Melin, S., " Fracture from a Straight Crack Subjected to Mixed Mode Loading," International Journal of Fracture 32, pp. 257-263, (1987).

[48] Zienkiewicz, O. C., " The Finite Element Method, " McGraw Hill, Ltd., (1977).

[49] Chakrabarty, J. , " Theory of Plasticity," McGraw Hill, Inc., (1987).

[50] Henshell, R. D., Shaw, K. G., " Crack Tip Elements are Unnecessary," International Journal for Numerical Methods in Engineering, Vol. 10, No.1, pp. 25-37, (1976).

[51] Barsoum, R. S., " On the Use of Isoparametric Finite Elements in Linear Fracture Mechanics," International Journal for Numerical Methods in Engineering, Vol. 10, No.1, pp. 25-37, (1976).

[52] Shin, C. F., deLorenzi, " On the Use of 2D Isoparametric Elements for Calculations in the Fully Plastic Range," International Journal of Fracture 13, pp. 507-511,(1980).

the Fully Plastic Range," International Journal of Fracture 13, pp. 507-511,(1980).

[53] Lamain, L. G., " Numerical Analysis in LEFM," in Elastic Plastic Fracture Mechanics, Proceedings of the 4th Advanced Seminar on Fracture Mechanics, Joint Research Centre, Ispra, Italy, ed. L. H. Larsson, D. Reidel Publ. Company, (1985).

[54] Wellman, G. W., Rolfe, S. T., Dodds, R. H., " Three Dimensional Elastic Plastic Fracture Mechanics of Three Point Specimen," Fracture Mechanics : Sixteenth Symposium, ASTM STP 868, M. F. Kanninen and A. T. Hopper, Eds., American Society for Testing and Materials, Philadelphia, pp. 214-237, (1985).

[55] ASTM A304, Alloy Steel Bars Subject to End-quench Hardenability Requirements; Steel Bars, Forgings, Bearings, Chains, Springs, American Society of Testing and Materials, Philadelphia, pp. 164-213, (1981).

[56] Newman, J. C., Jr., " An Evaluation of Fracture Analysis Methods," Elastic Plastic Fracture Mechanics Technology, ASTM STP 896, J. C. Newman, Jr. and F. J. Loss, Eds., American Society for Testing and Materials, Philadelphia, pp. 5-96, (1985).

[57] ABAQUS Version 4/5/175, Hibbit, Karlsson and Sorenson, Inc., User's Manual, Theory, Example Problems, (1985).

[58] Knowles, J. K., Sternberg, E., " On a Class of Conservation Laws in Linearized and Finite Elastostatics," Archive for Rational Mechanics and Analysis, 44, pp. 187-211, (1972).

[59] Kanninen, M. F., Popelar, C. H., Advanced Fracture Mechanics, Oxford University Press, (1985).

[60] McMeeking, R. M., " Finite Deformation Analysis of Crack Tip Opening in Elastic Plastic Materials and Implications for Fracture," Journal of the Mechanics and Physics of Solids, Vol. 25, pp. 357-381, (1977).

[61] McMeeking, R. M., " Path Dependence of the J-Integral and the Role of J as a Parameter Characterizing the Near Tip Field," Flaw Growth and Fracture, ASTM STP 631, American Society for Testing and Materials, pp. 28-41, (1977).

[62] Hellen, T. K., Blackburn, W. S., Jackson, A. D., " An Integral Associated with the State of a Crack-Tip in a Non-Elastic Material," International of Journal Fracture pp. 183-200, (1977).

[63] Blackburn, W. S., " Contour Integration Around Crack Tips for Combined Mixed Mode

[64] Begley, J. A., Landes, J. D., Wilson, W. K., " An Estimation Model for the Application of the J-Integral," Fracture Analysis, ASTM STP 560, American Society for Testing and Materials, pp. 155-169, (1974).

[65] Baker, A., " The J-Concept : Theoretical Basis and its Use in EPFM," in Elastic Plastic Fracture Mechanics, Proceedings of the 4th Advanced Seminar on Fracture Mechanics, Joint Research Centre, Ispra, Italy, ed. L. H. Larsson, D. Reidel Publ. Company, (1985).

[66] Nagtegaal, J. C., " Finite Element Analysis of Fracture Mechanics Problems," MARC Analysis Research Corporation, Palo Alto, California.

[67] Parks, D. M., " A Stiffness Derivative Finite Element Technique for Determination of Elastic Crack Tip Stress Intensity Factors," International Journal of Fracture, 10, pp. 487-502, (1974).

[68] Pook, L. P.," The Effect of Crack Angle in Fracture Mechanics," Engineering Fracture Mechanics, Vol. 3, No. 3, pp. 205-218, (1971).

[69] Liu, A. F., " Crack Growth and Failure of Aluminium Plates Under In-plane Shear," presented at the AIAA 11th Aerospace Sciences Meeting, Washington, D.C., (1973).

[70] Shah, R. C., " Fracture Under Combined Modes in 4340 Steel," Fracture Analysis ASTM STP 560, American Society for Testing and Materials, pp. 29-52, (1974).

[71] Budiansky, B., Rice, J. R., " Conservation Laws and Energy Release Rates," Journal of Applied Mechanics, Transactions of the ASME, pp. 201-203, (1973).

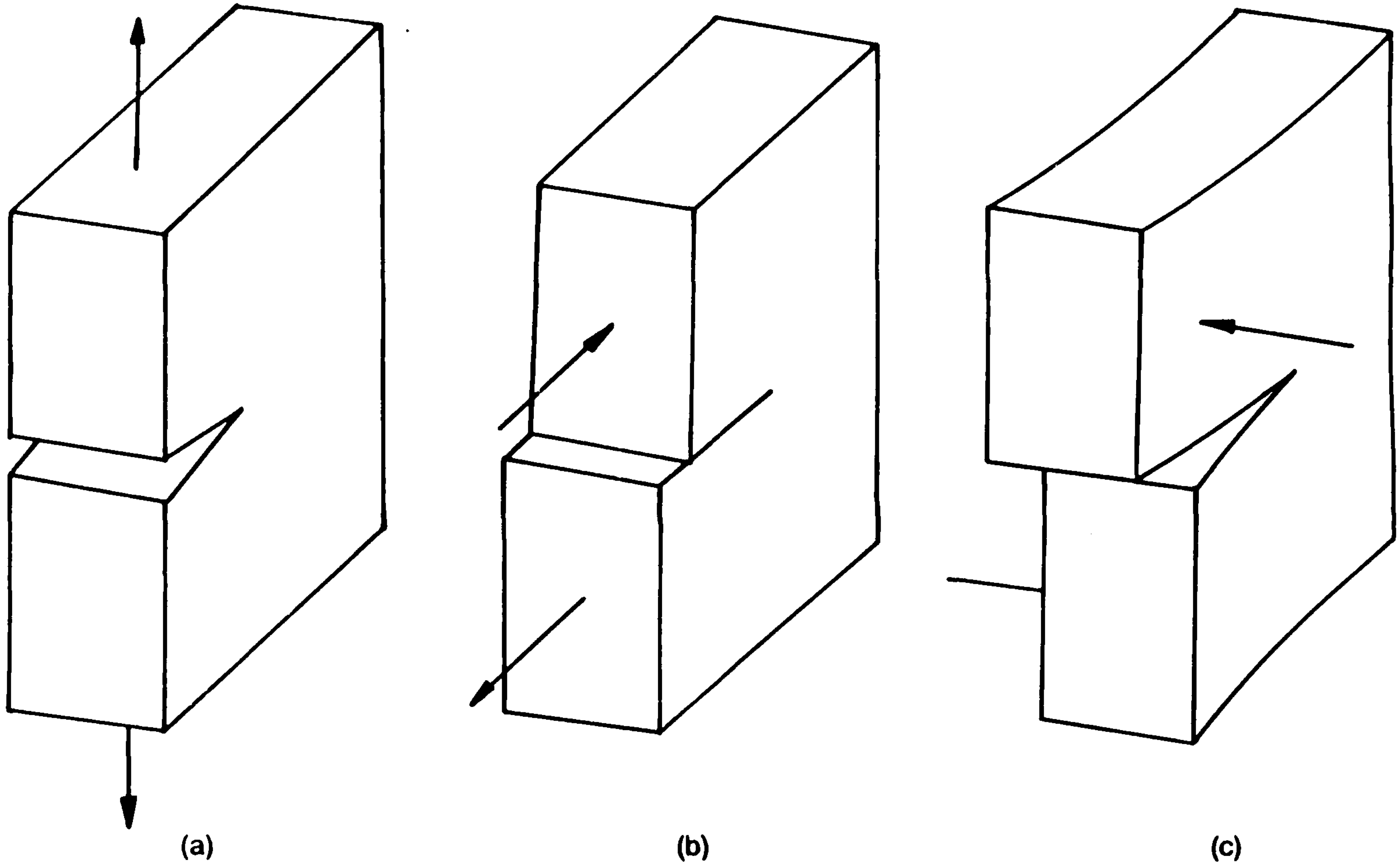

Figure 1 : Definition of the three modes of fracture :

(a) opening mode, (mode I),
(b) sliding mode, (mode II) and
(c) tearing mode, (mode III).

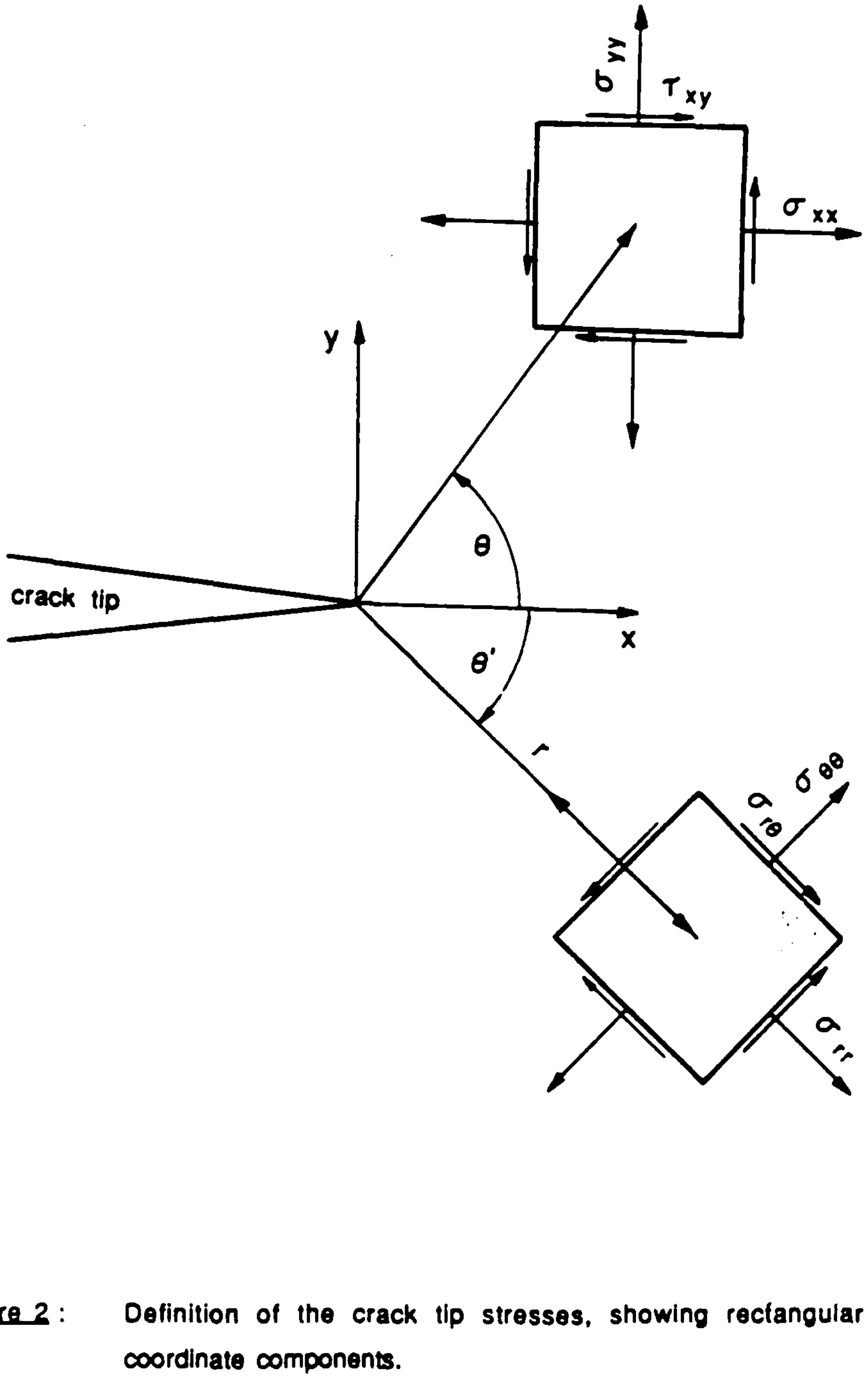
σ yy
τ xy
σ xx
y
θ
crack tip
x
θ'
r
σ θθ
σ rθ
σ rr

Figure 2 : Definition of the crack tip stresses, showing rectangular and polar coordinate components.

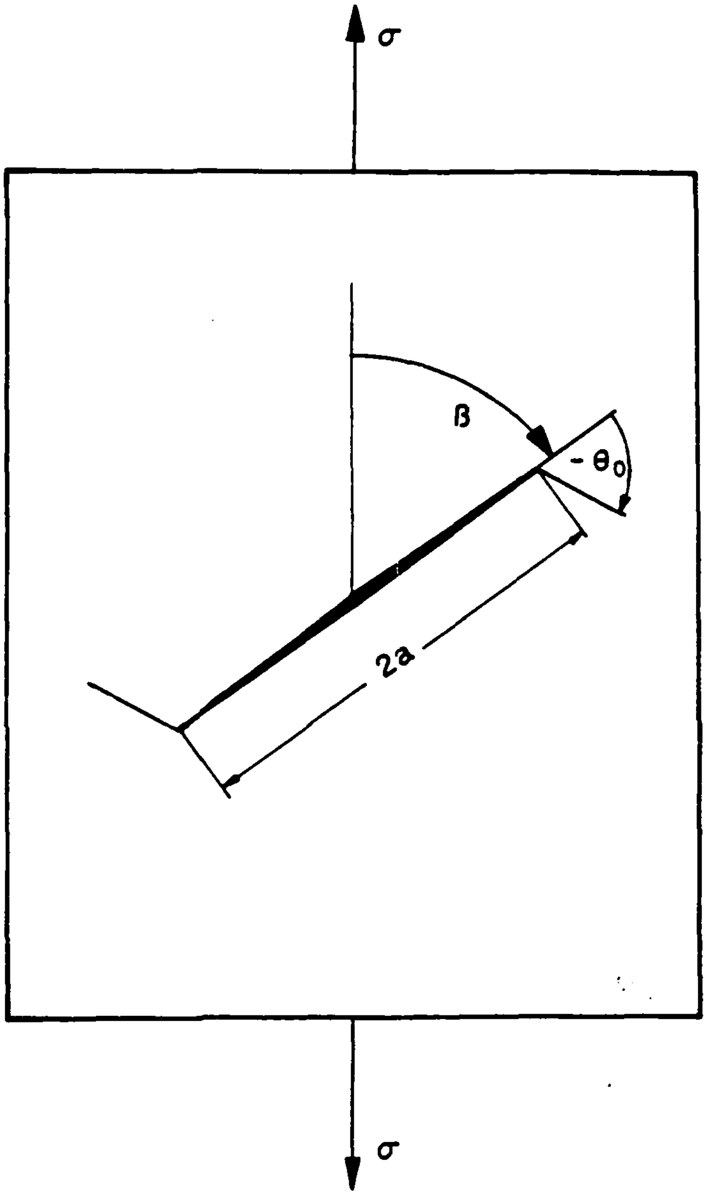

Figure 3 : Definition of crack angle and fracture angle in the center cracked panel with slanted crack under uniaxial tensile stress.

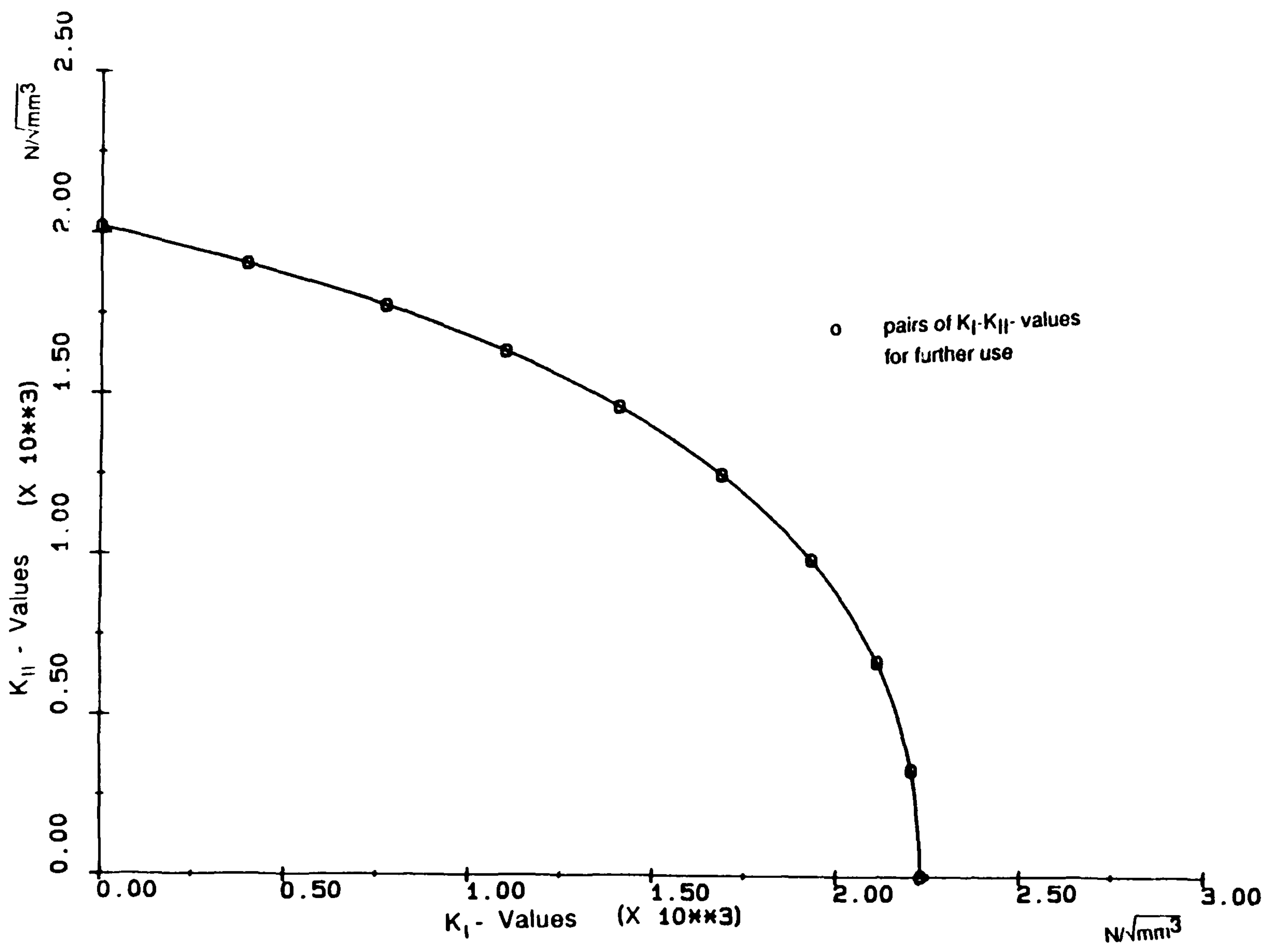

Figure 4 : K_I- K_{II} curve according to the fracture criterion due to Sih [29].

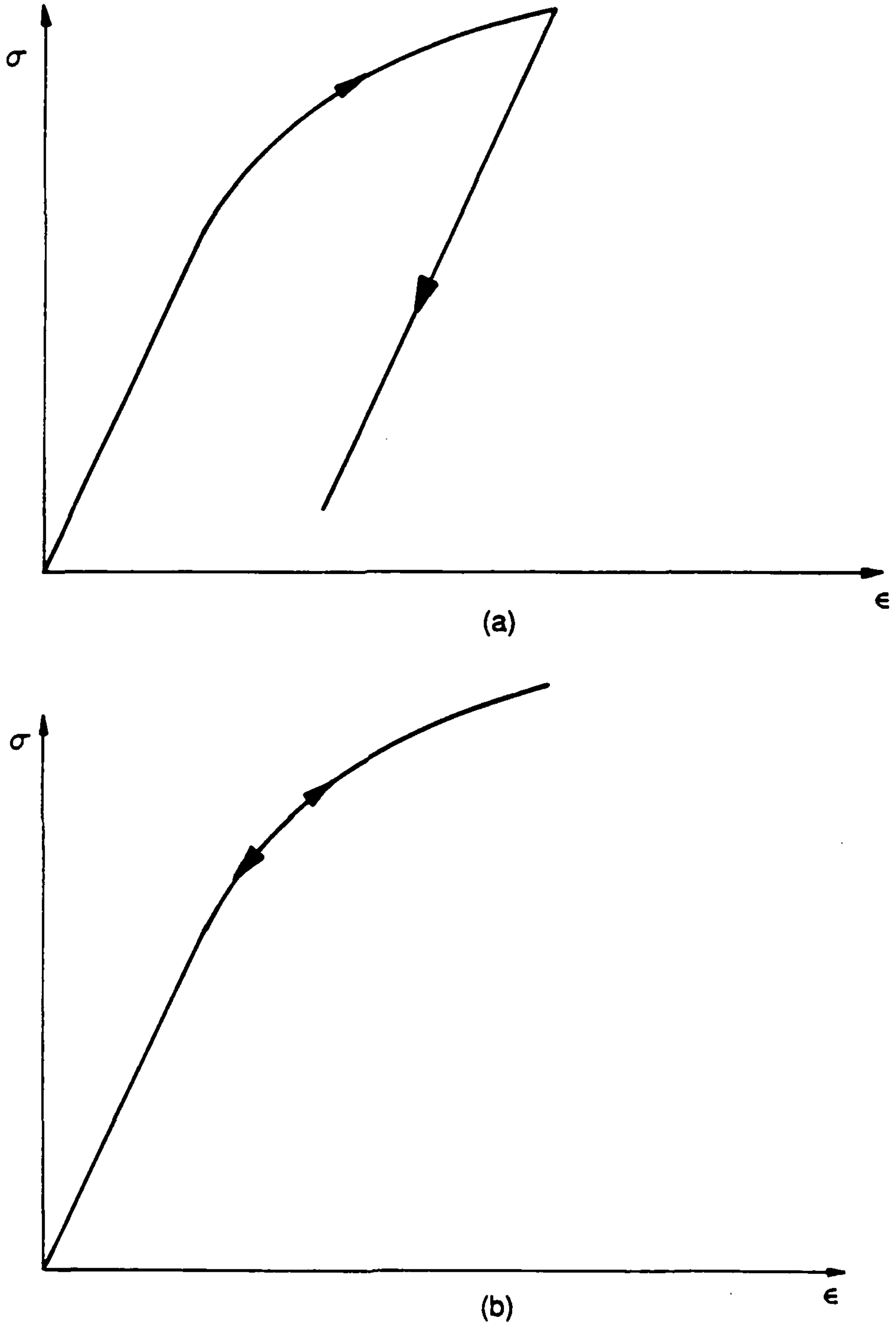

(a)

(b)

Figure 5 : Idealized constitutive material behavior :

(a) incrementally elastic-plastic material conforming to incremental theory of plasticity,

(b) incrementally elastic-plastic material conforming to deformation theory of plasticity.

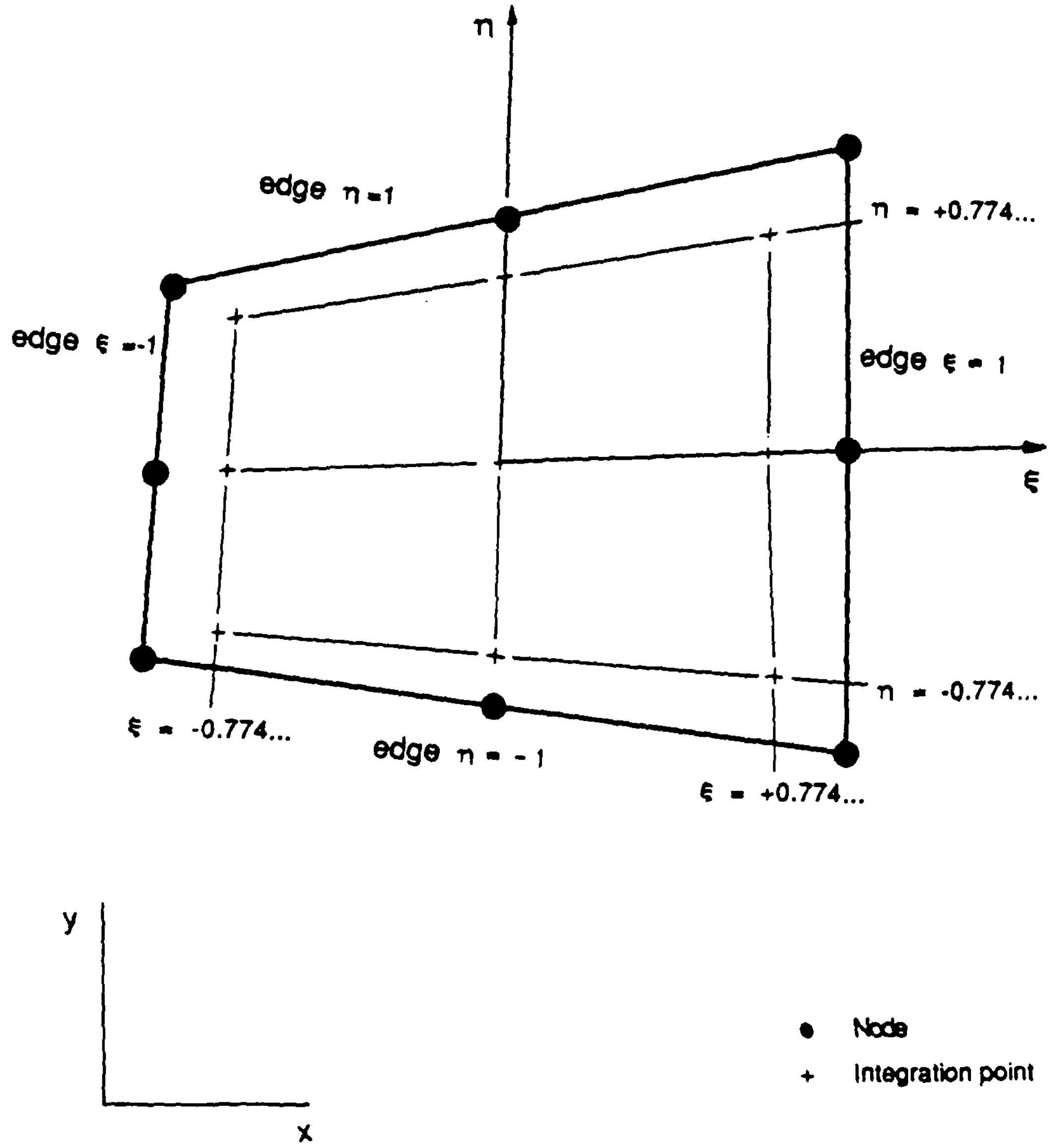
η
edge η =1
η = +0.774...
edge ξ =-1
edge ξ = 1
ξ
η = -0.774...
ξ = -0.774...
edge η = - 1
ξ = +0.774...
y
x
● Node
+ Integration point

Figure 6 : Mapping of the eight-node prabolic element from spacial coordinates (x, y) to local coordiantes (ξ, η).

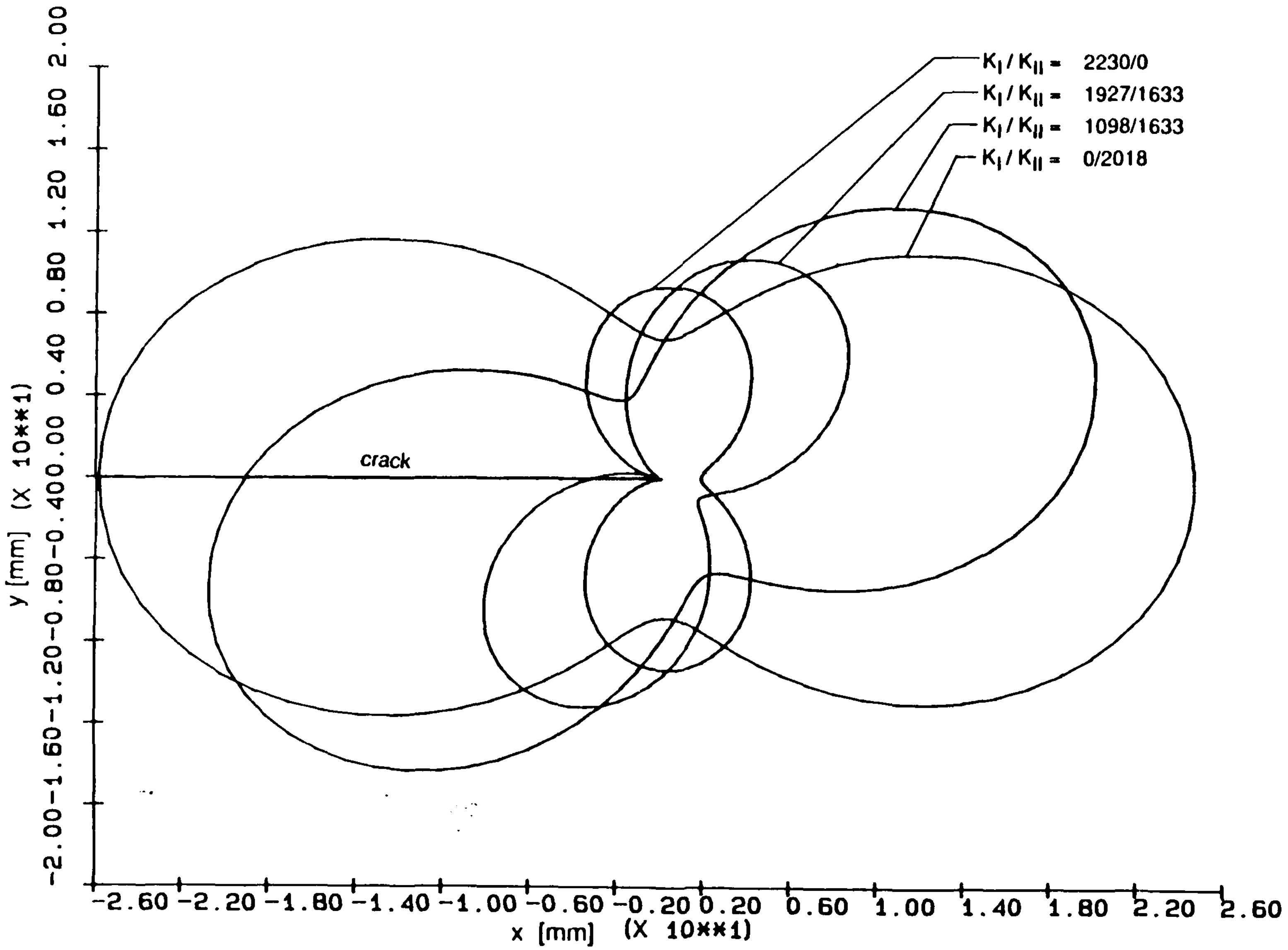

Figure 7 : Contour plots of the von Mises yield stress for selected mixed-mode cases.

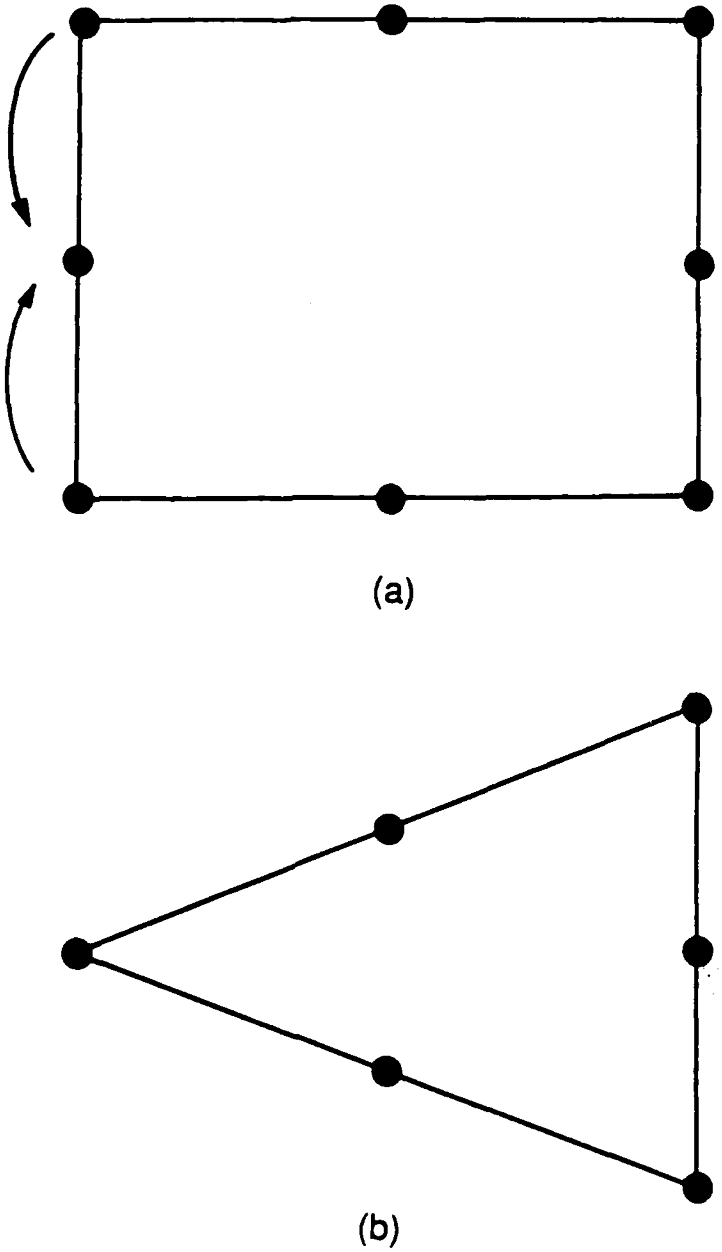

Figure 8 : Generation of the eight-node collapsed element :

(a) rectangular eight-node element,

(b) degenerated triangular eight-node element.

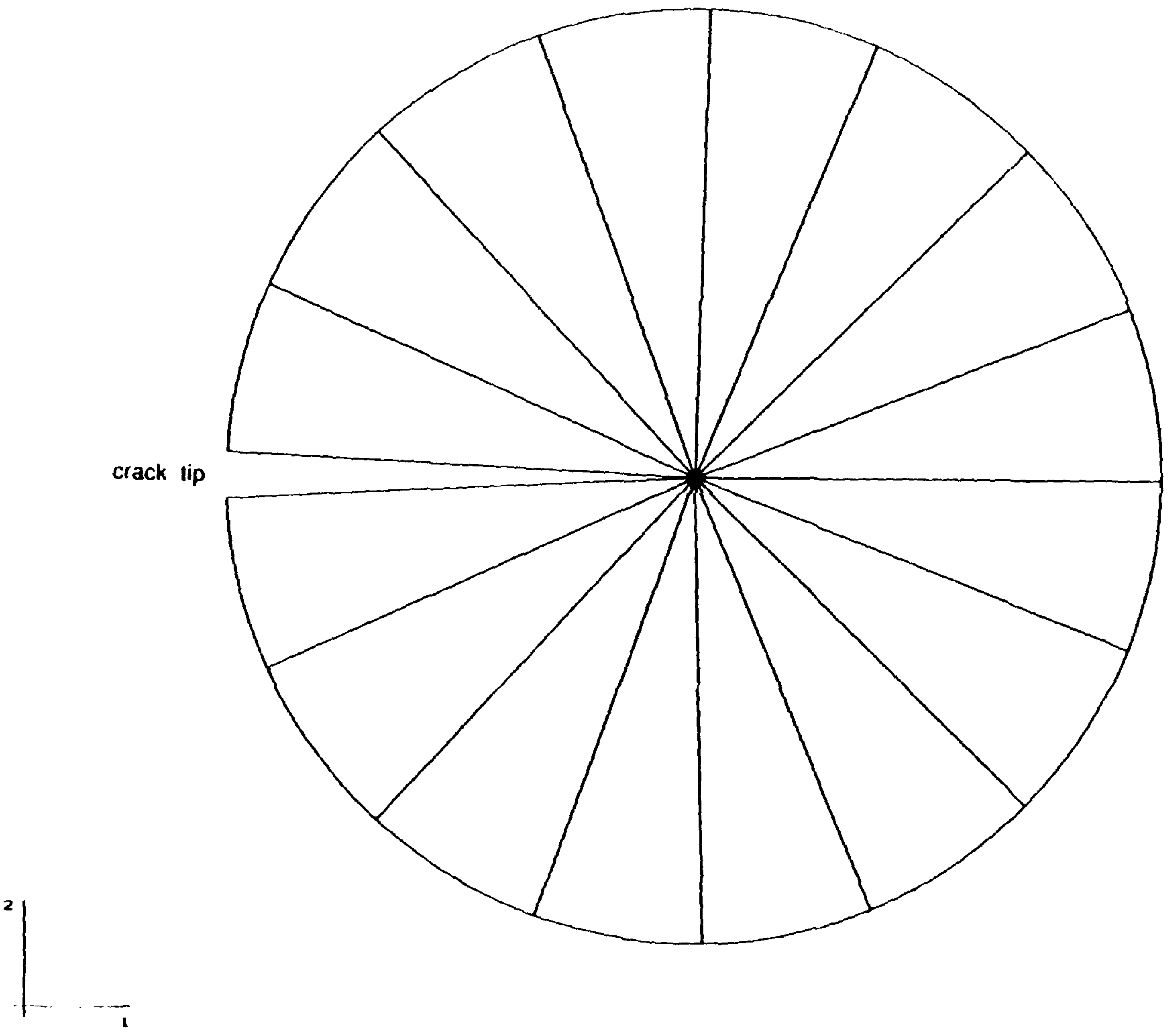
crack tip
2
1

Figure 9 : Configuration of the degenerated crack tip elements.

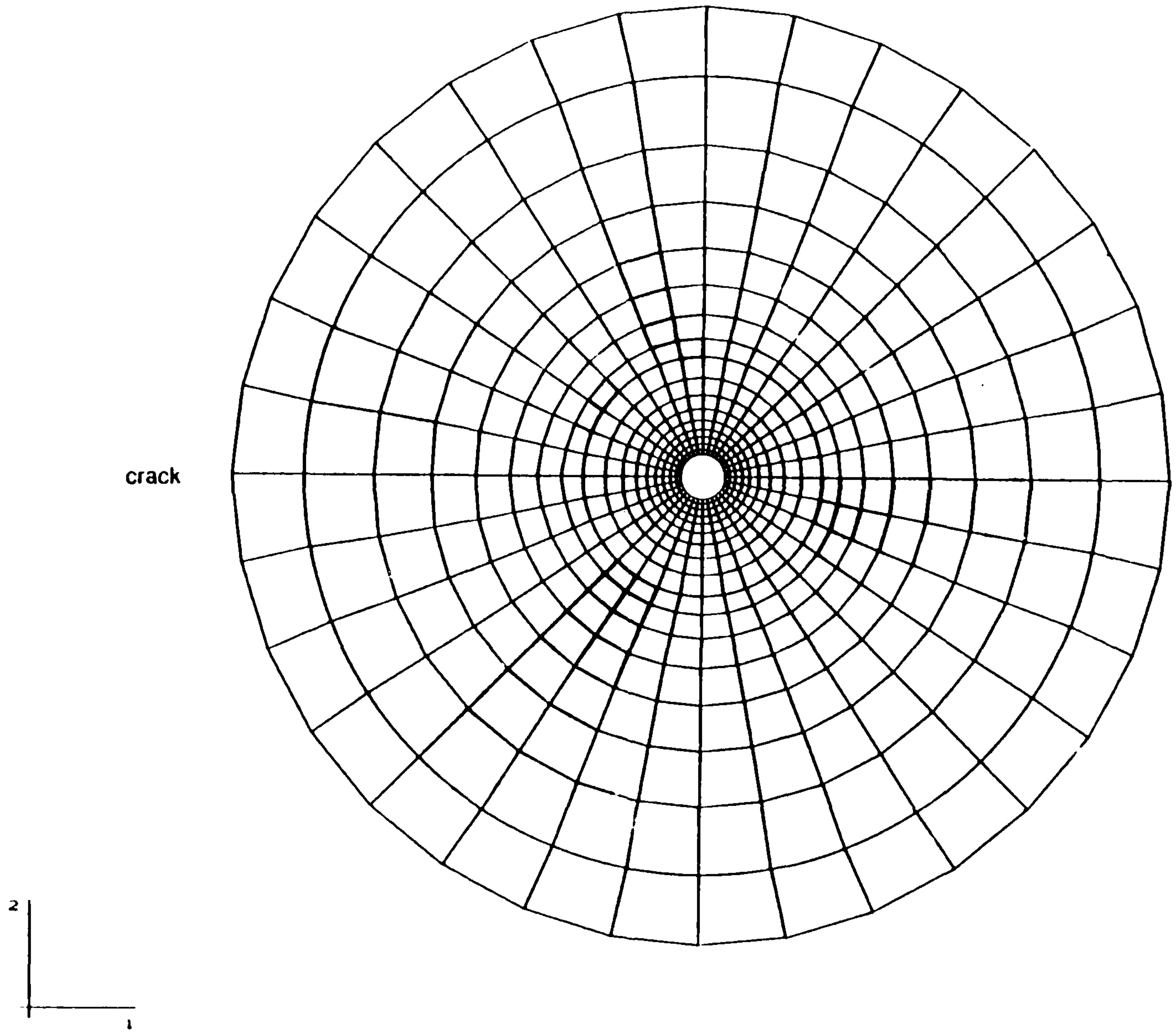

Figure 10 : Main fan of the finite element model of the specimen, inner radius : 1mm, outer radius : 10 mm.

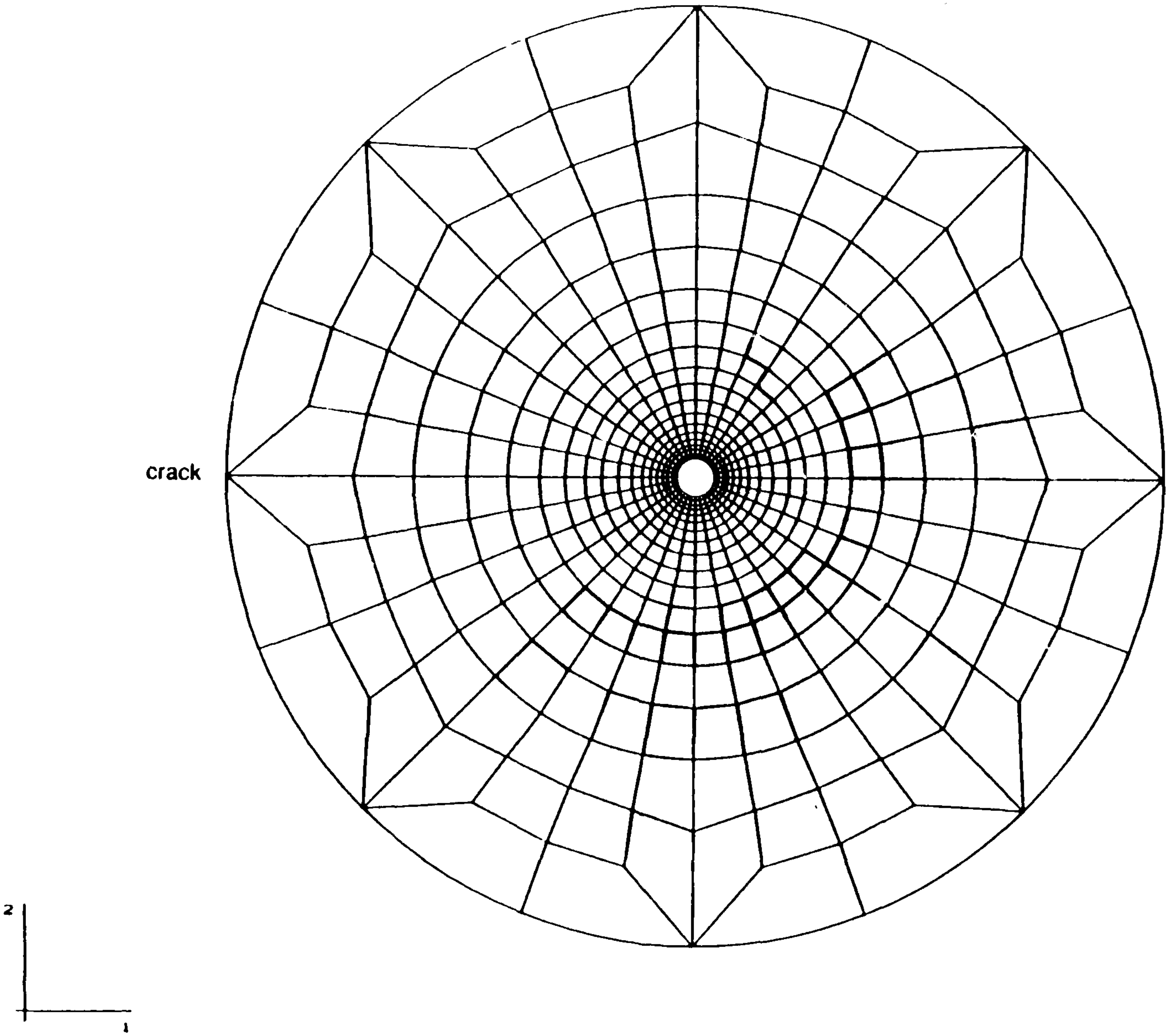

Figure 11 : Boundary of the finite element mesh of the specimen, inner radius : 5mm, outer radius : 100 mm.

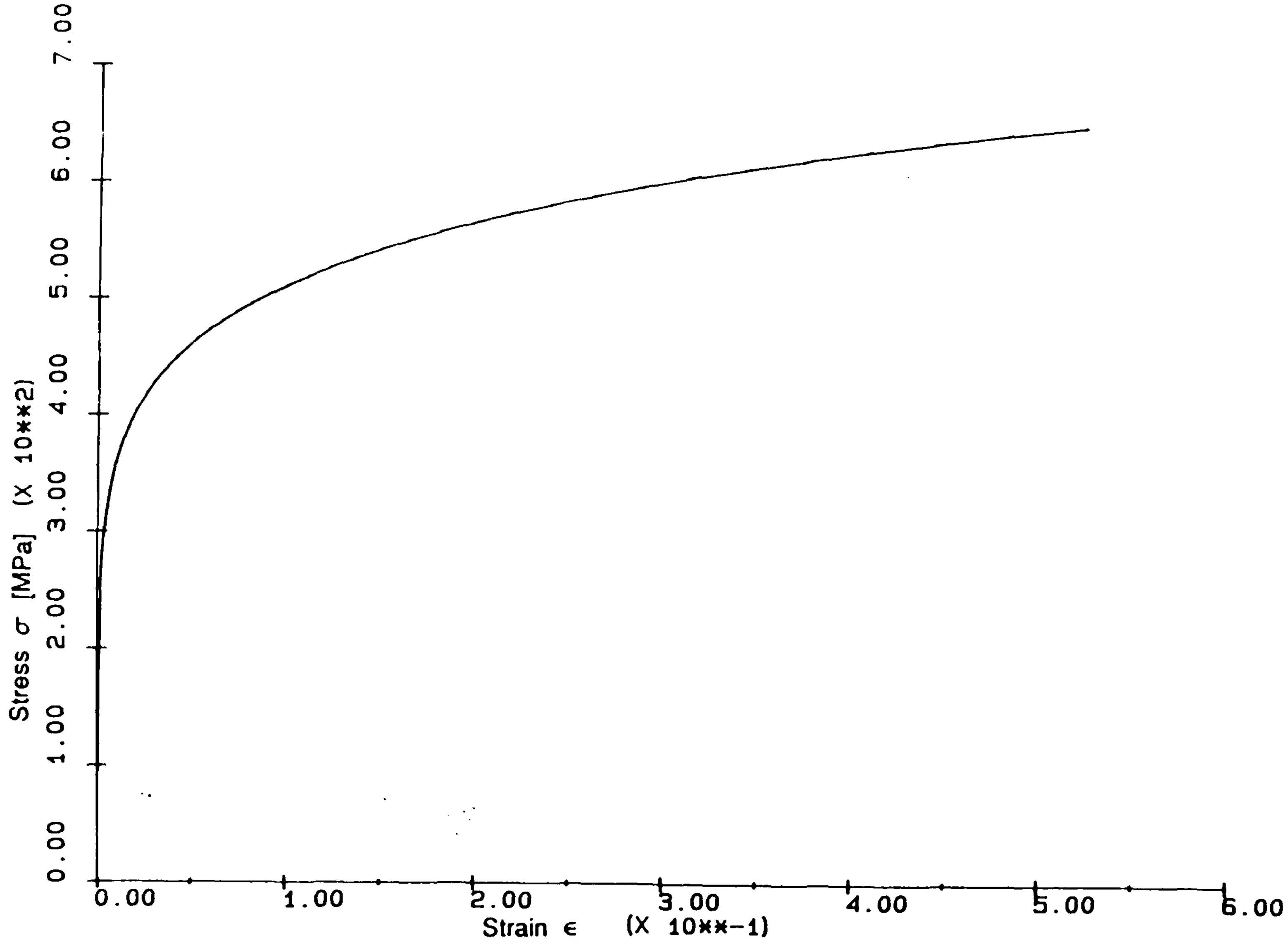

Figure 12 : Stress - strain curve of the steel A304.

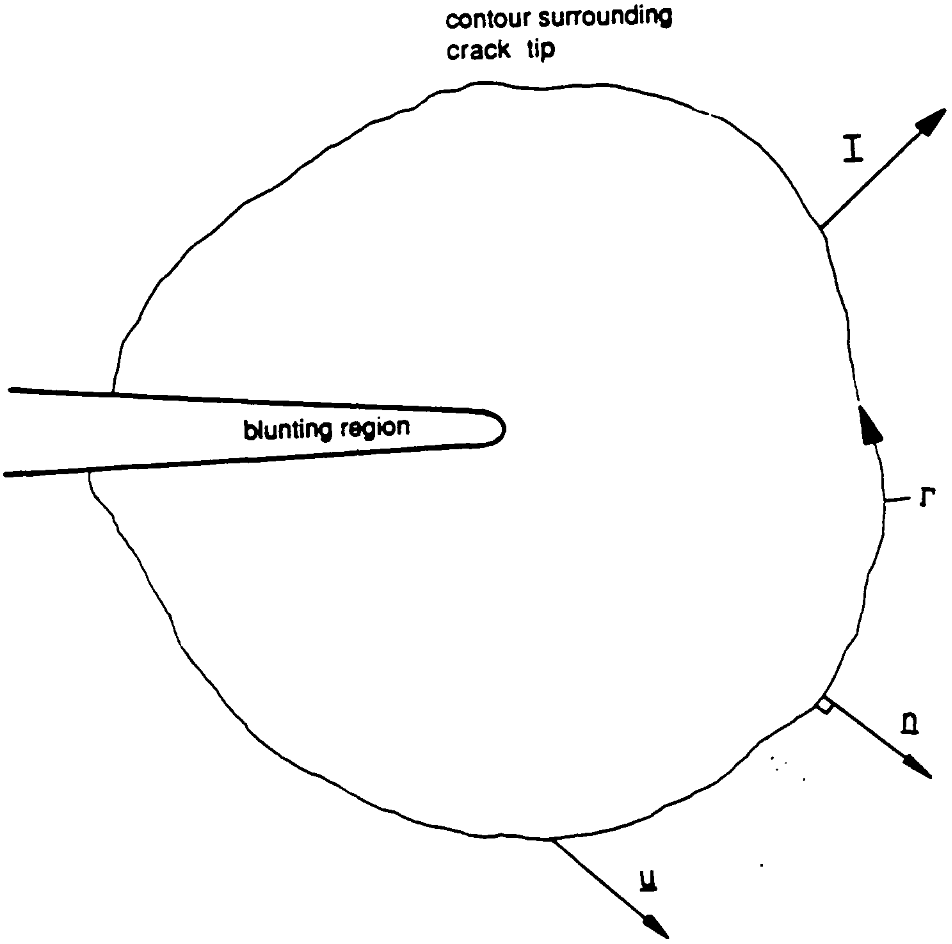
contour surrounding
crack tip
T
blunting region
Γ
n
u

Figure 13 : A contour Γ around the crack tip and parameters defining the J-integral.

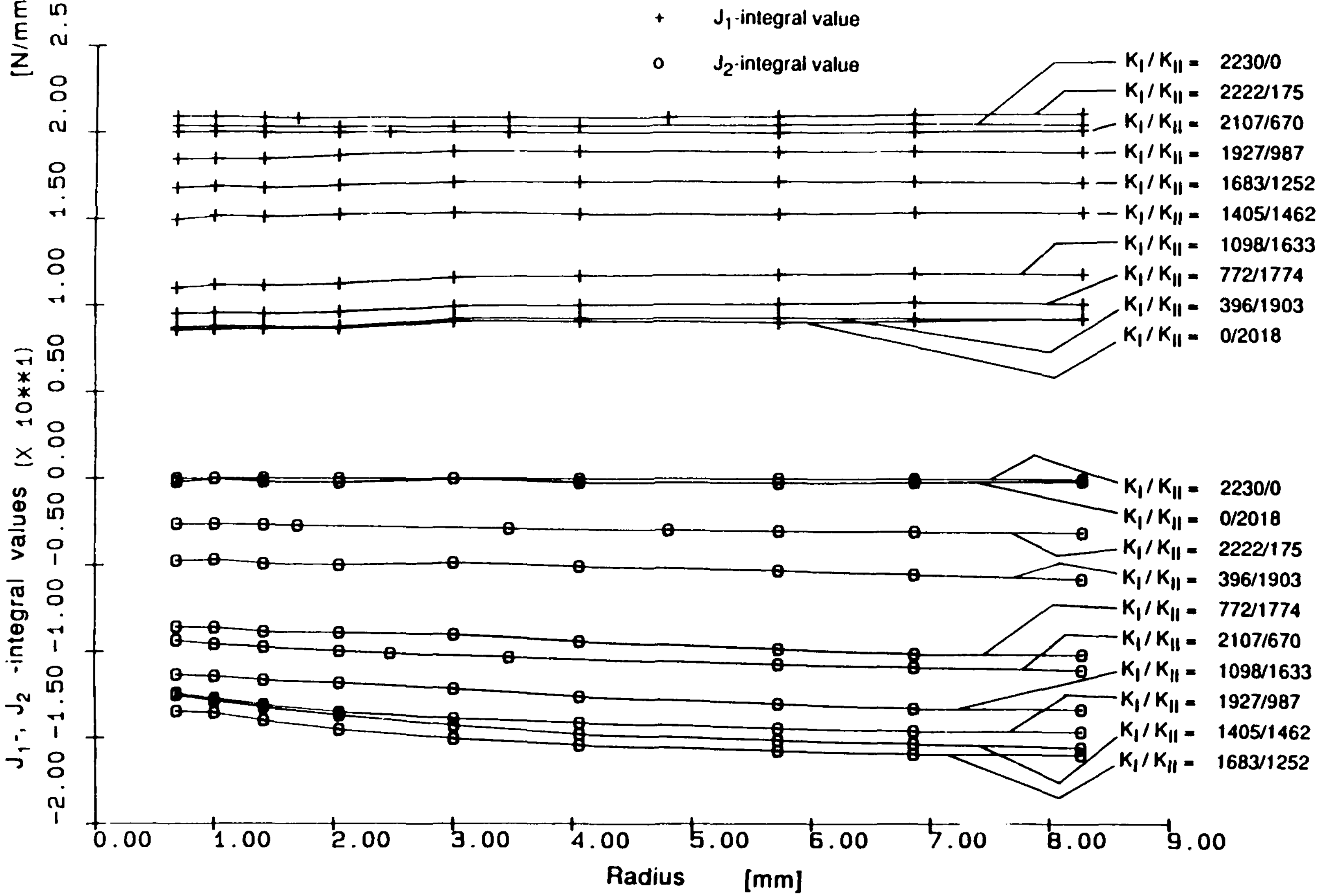

Figure 14 : J$_1$- and J$_2$ -integral values for all mixed-mode cases considered.

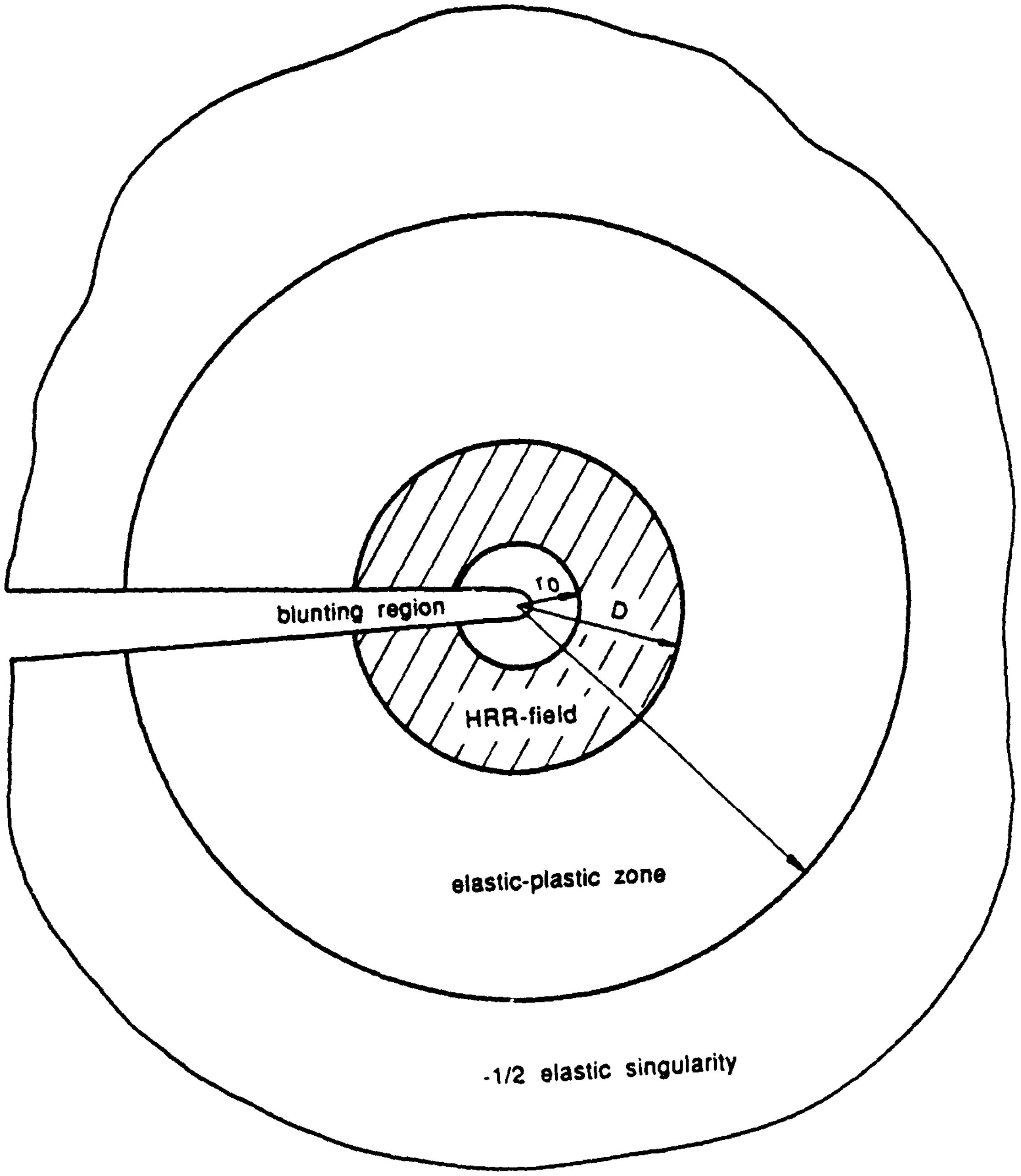
blunting region
r_0
D
HRR-field
elastic-plastic zone
-1/2 elastic singularity

Figure 15 : Illustration of the crack tip region under small scale yielding condition.

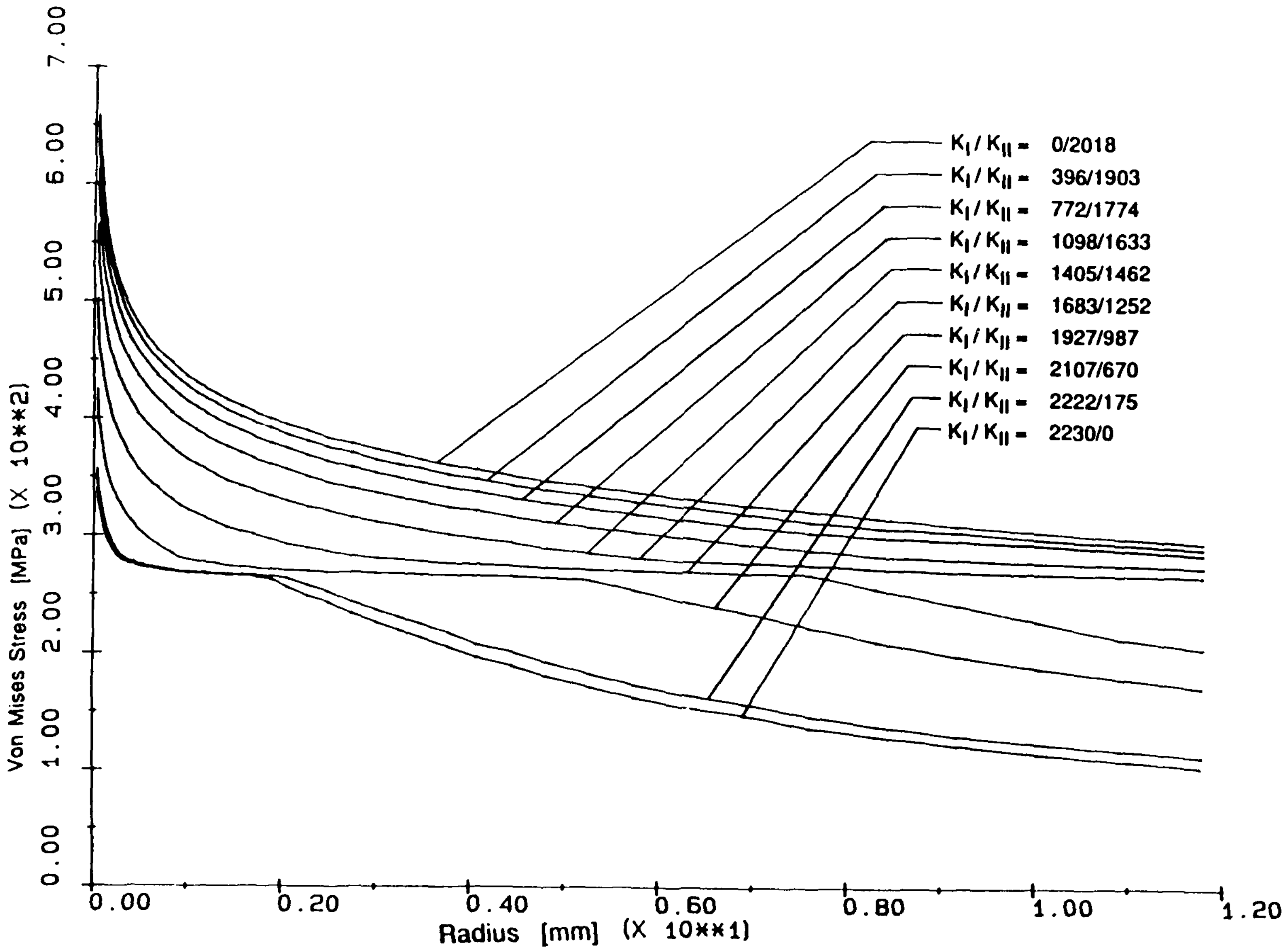

Figure 16 : Effective von Mises stresses along line θ = 0° for all mixed-mode cases considered.

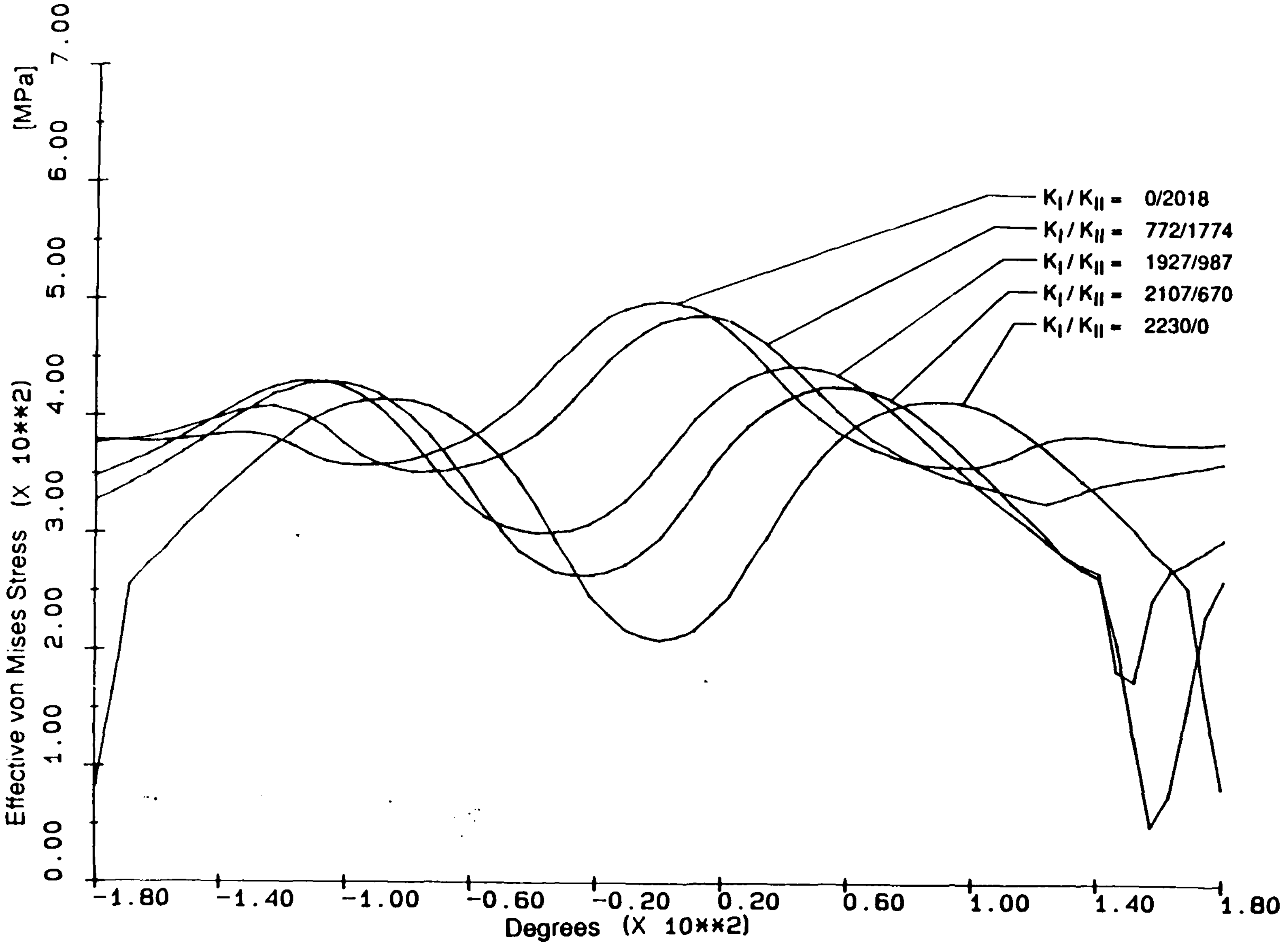

Figure 17 : Effective von Mises stresses around crack tip. Radius r = 0.4 mm for selected mixed-mode cases.

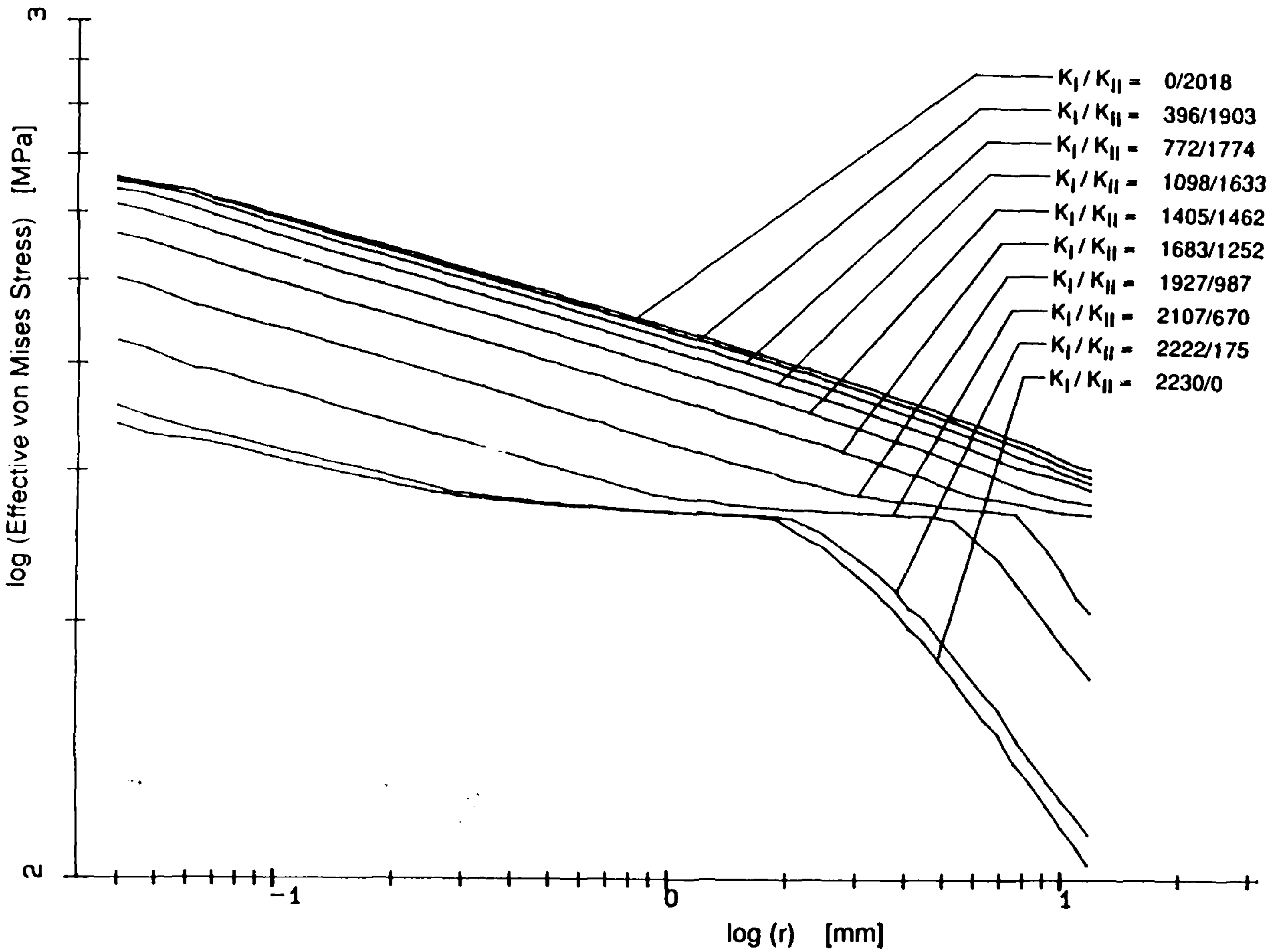

Figure 18 : Full logarithmic representation of effective von Mises stresses along line $\theta = 0°$ for all of mixed-mode cases considered.

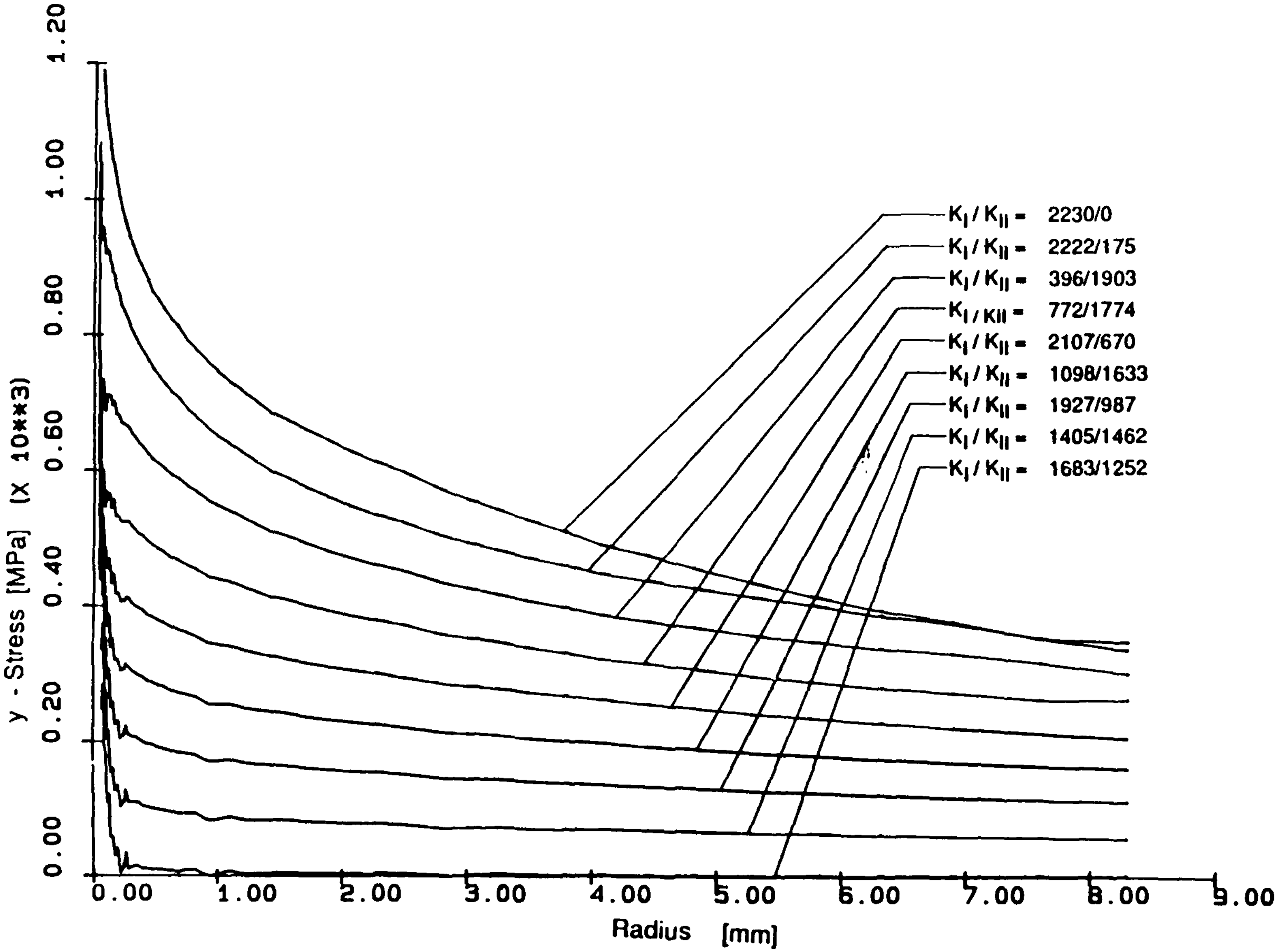

Figure 19 : σ_y- stresses along line θ = 0° for selected mixed-mode cases.

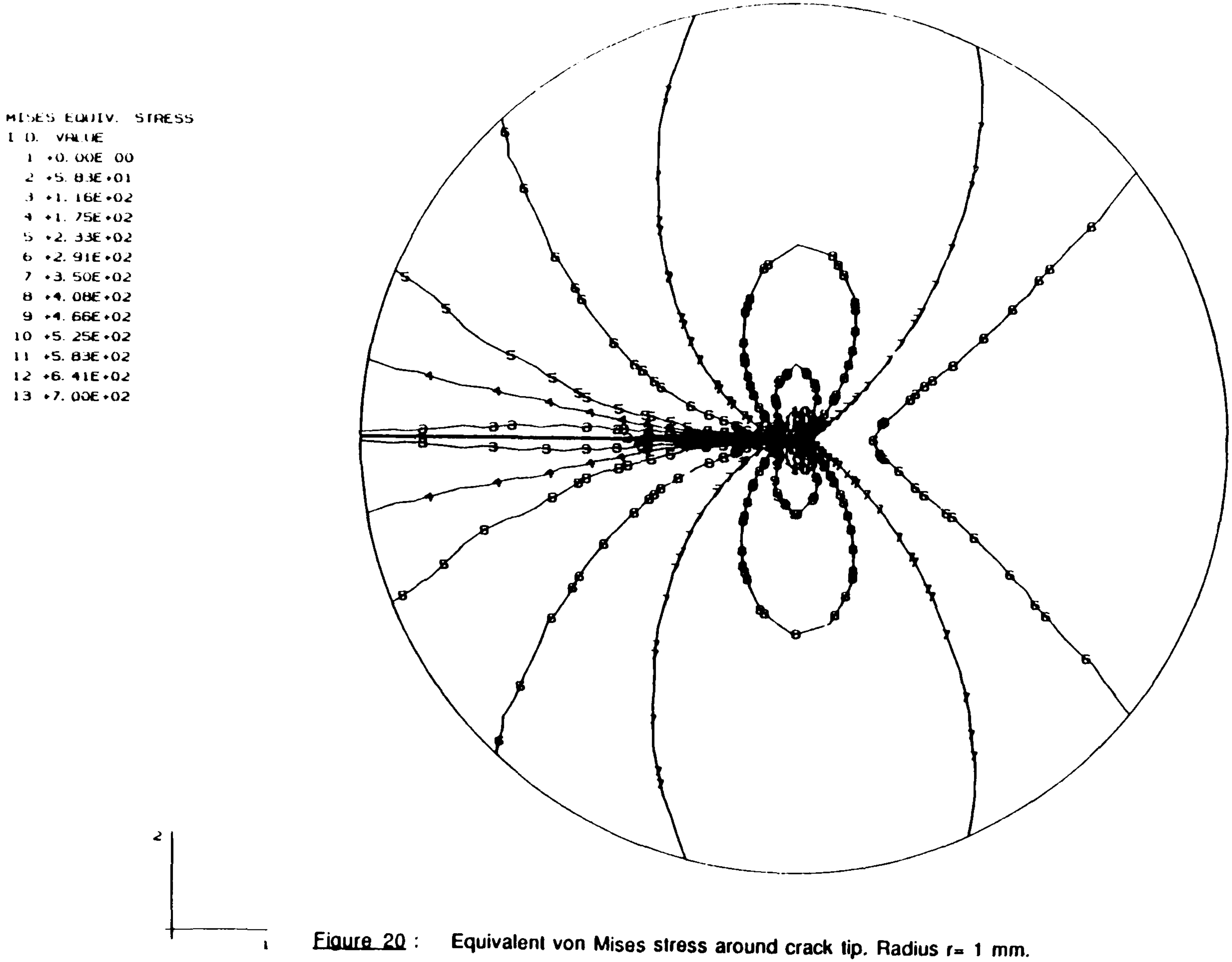

Figure 20 : Equivalent von Mises stress around crack tip. Radius $r = 1$ mm.
Stress intensity factor ratio : $K_I/K_{II} = 2230/0$.

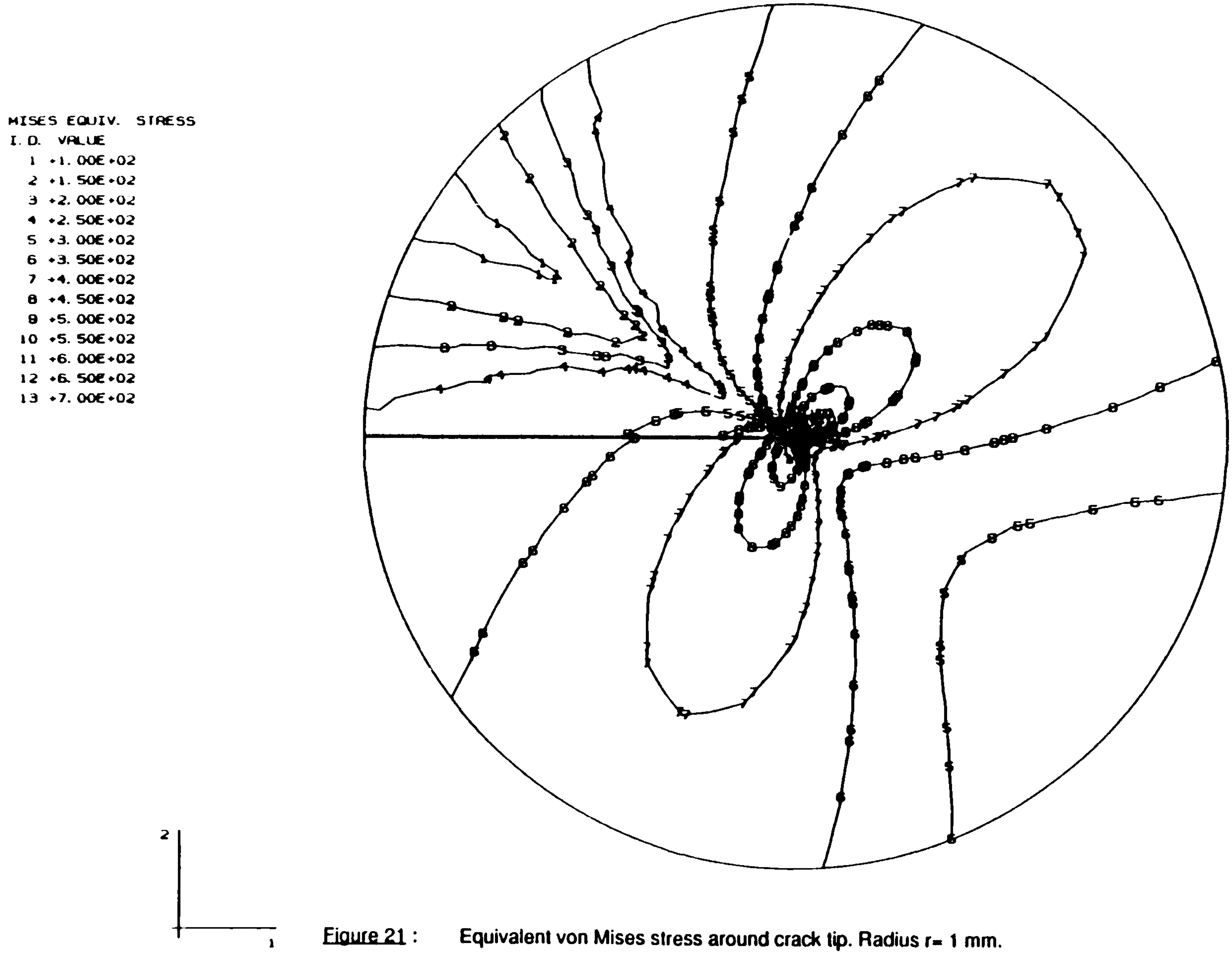

Figure 21 : Equivalent von Mises stress around crack tip. Radius r= 1 mm.

Stress intensity factor ratio : K_I/K_{II} = 1927/987.

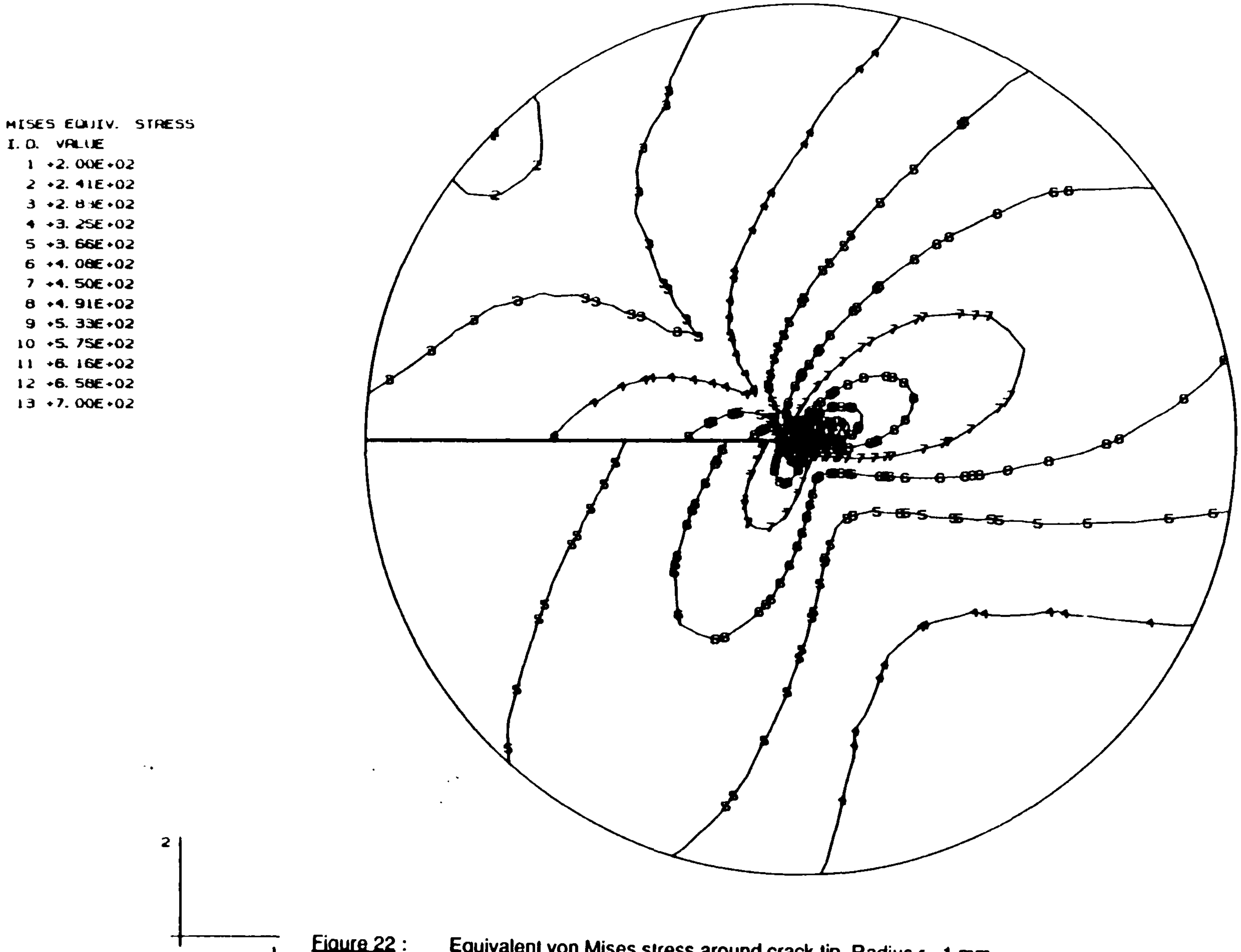

Figure 22 : Equivalent von Mises stress around crack tip. Radius r= 1 mm.

Stress intensity factor ratio : K_I/K_{II} = 1683/1252.

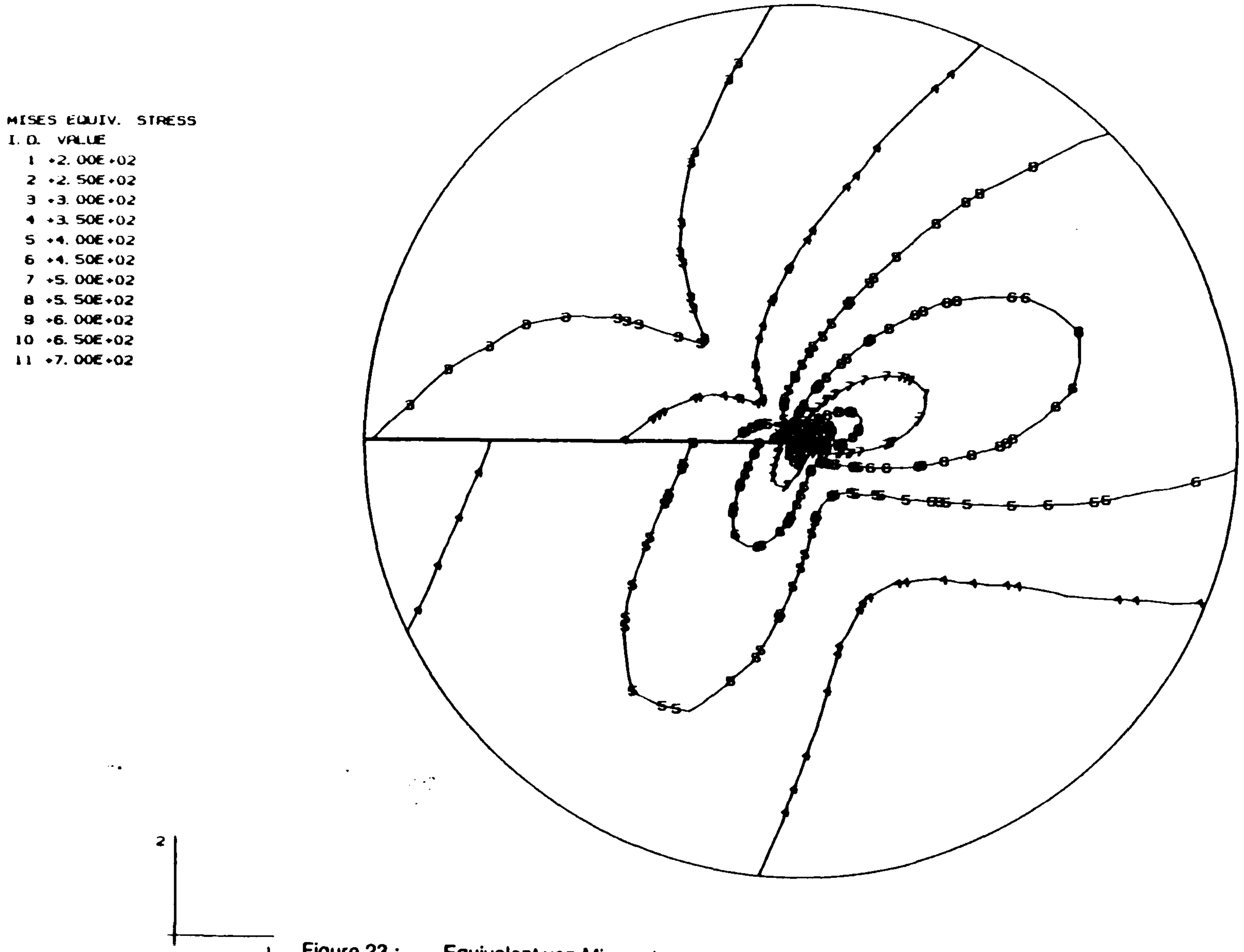

Figure 23 : Equivalent von Mises stress around crack tip. Radius r= 1 mm.

Stress intensity factor ratio : K_I/K_{II} = 1405/1462.

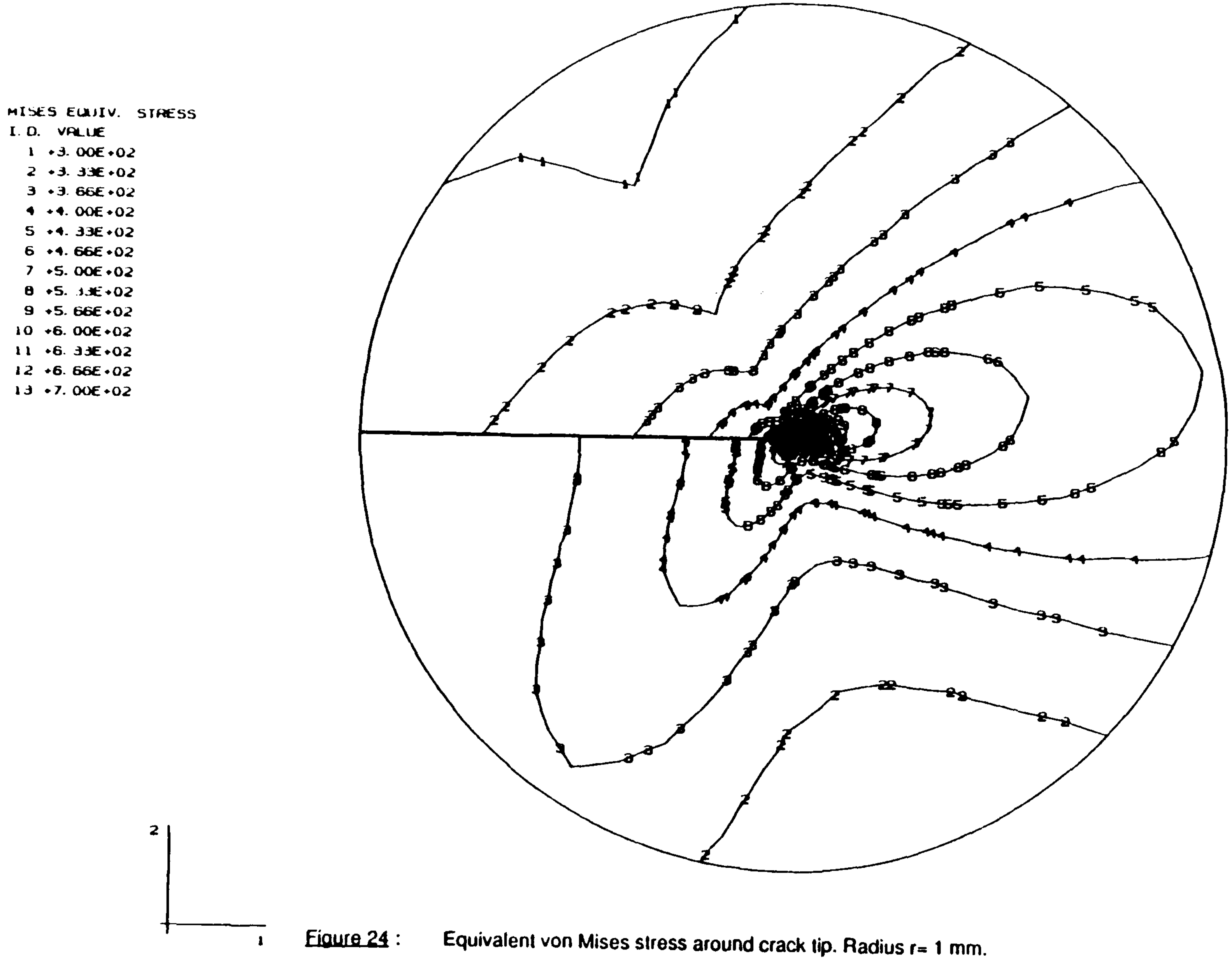

Figure 24 : Equivalent von Mises stress around crack tip. Radius r= 1 mm.

Stress intensity factor ratio : K_I/K_{II} = 772/1774.

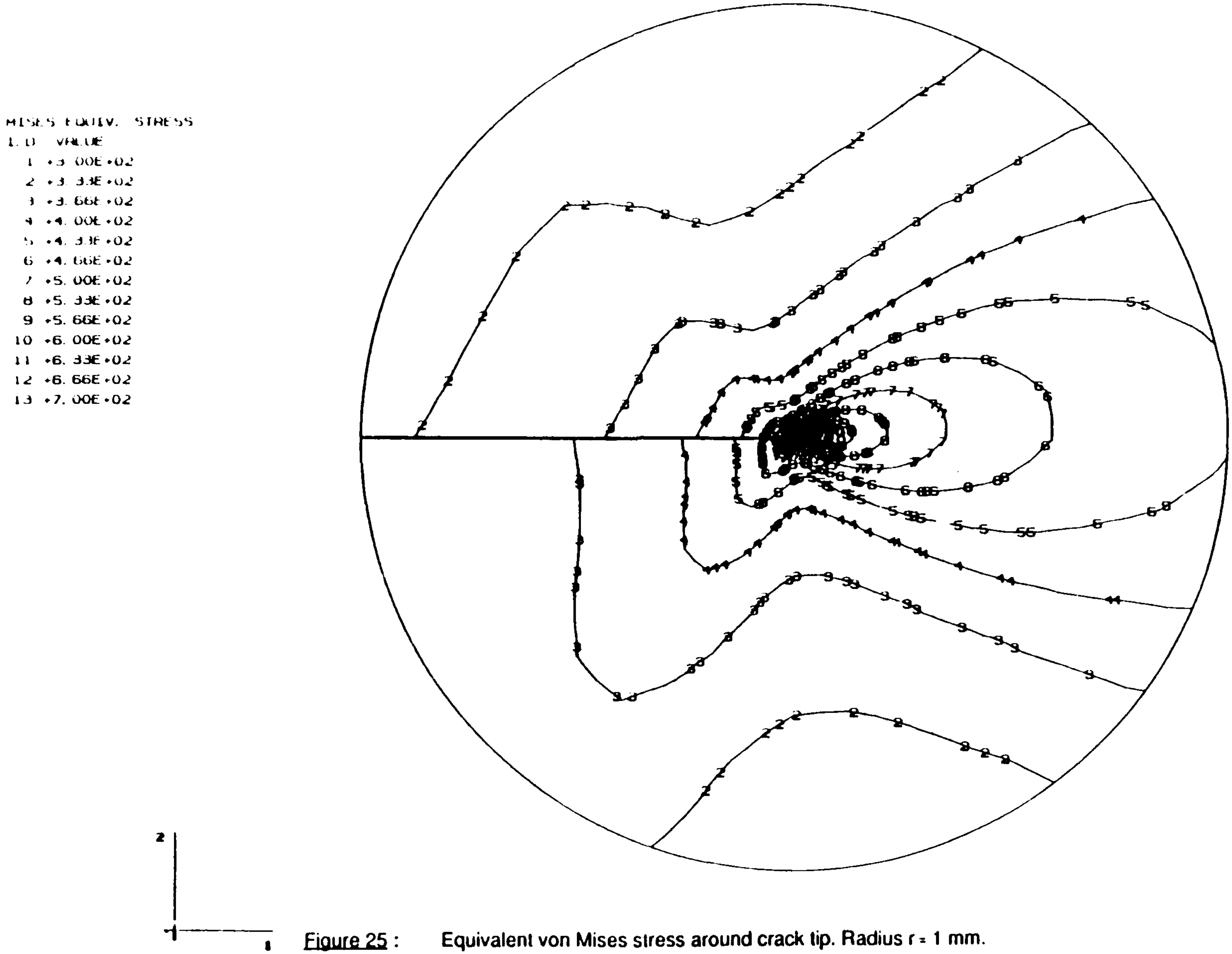

Figure 25 : Equivalent von Mises stress around crack tip. Radius r = 1 mm.

Stress intensity factor ratio : $K_I/K_{II} = 396/1903$.

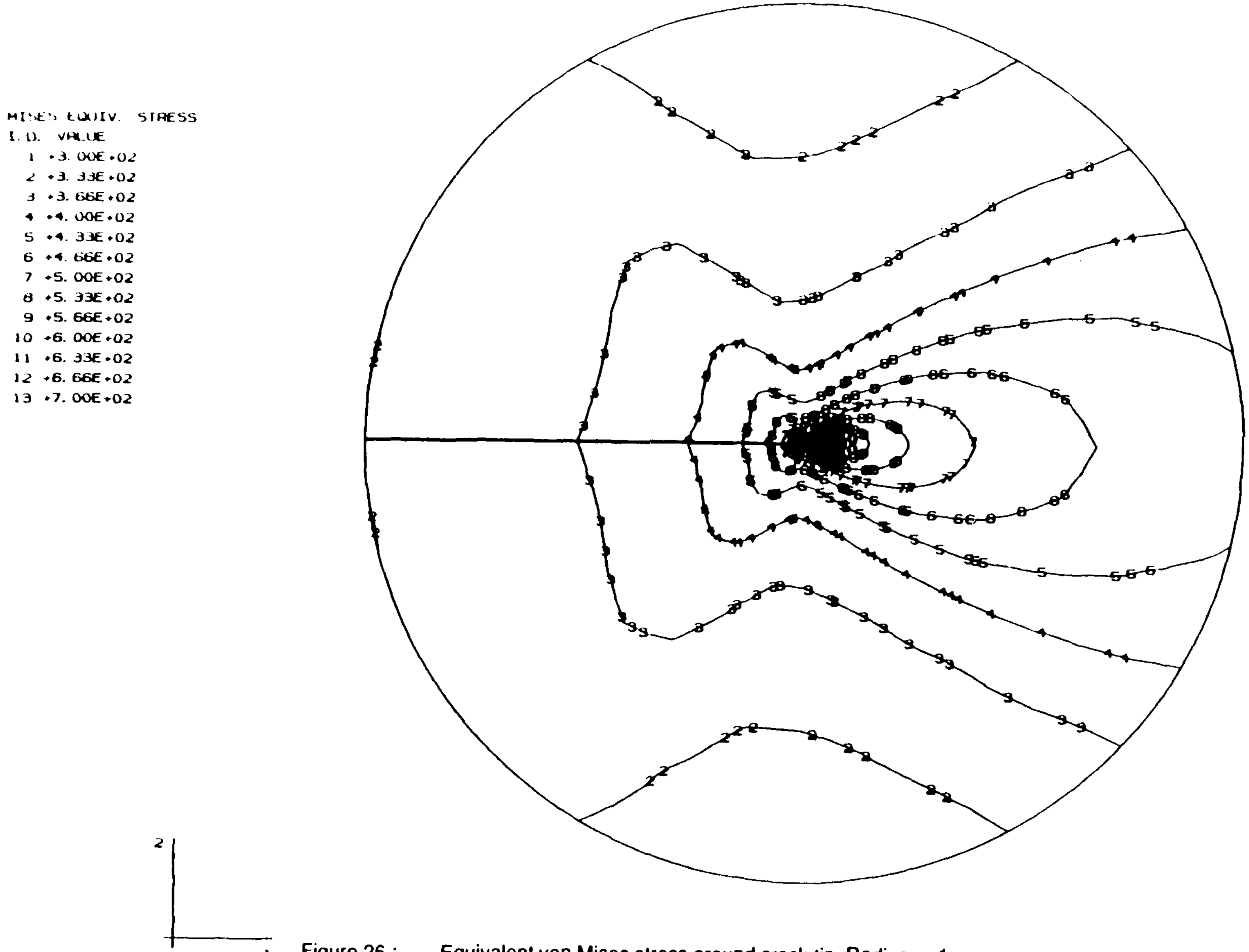

Figure 26 : Equivalent von Mises stress around crack tip. Radius r= 1 mm.

Stress intensity factor ratio : K_I/K_{II} = 0/2018.

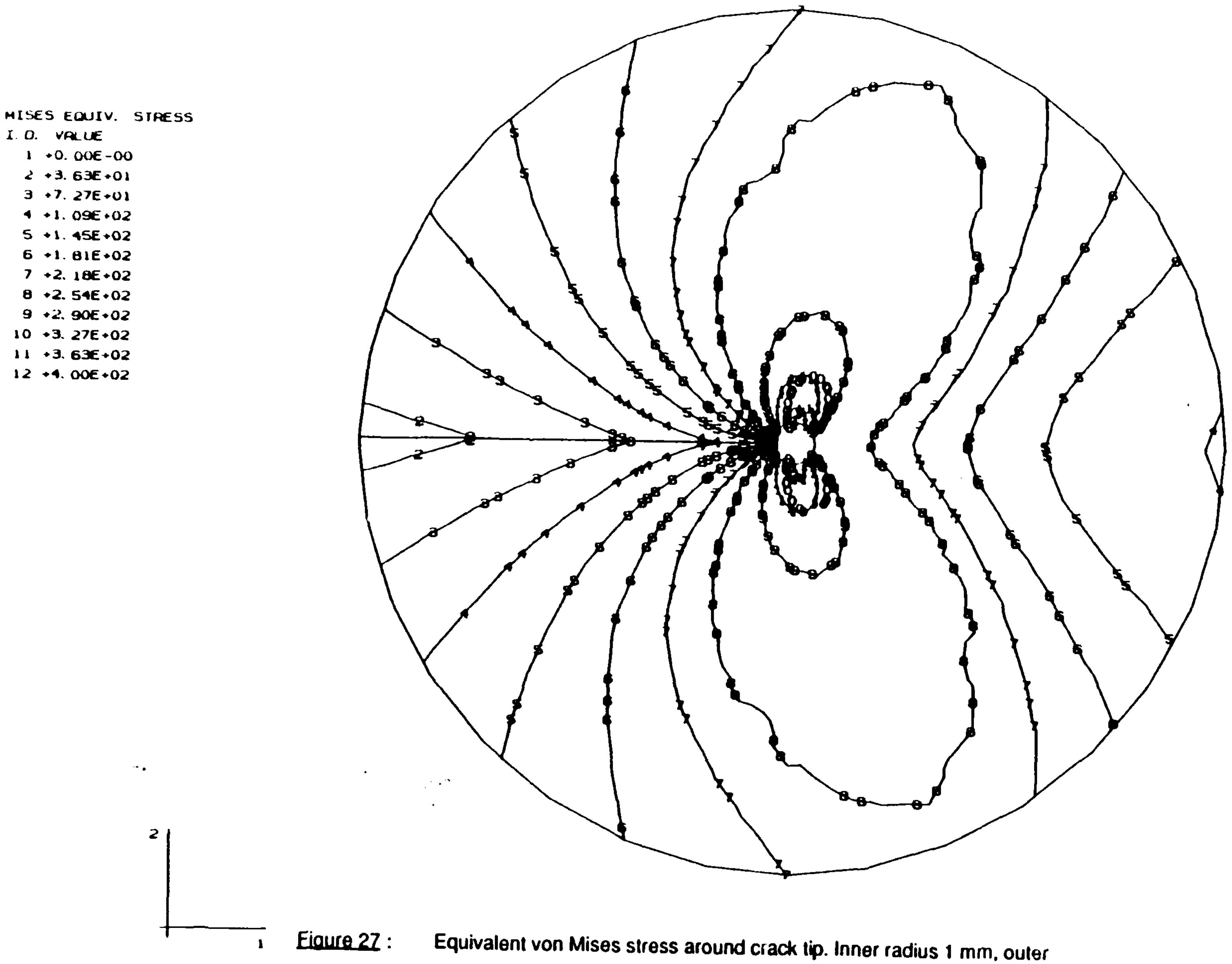

Figure 27 : Equivalent von Mises stress around crack tip. Inner radius 1 mm, outer radius 10 mm.

Stress intensity factor ratio : K_I/K_{II} = 2230/0.

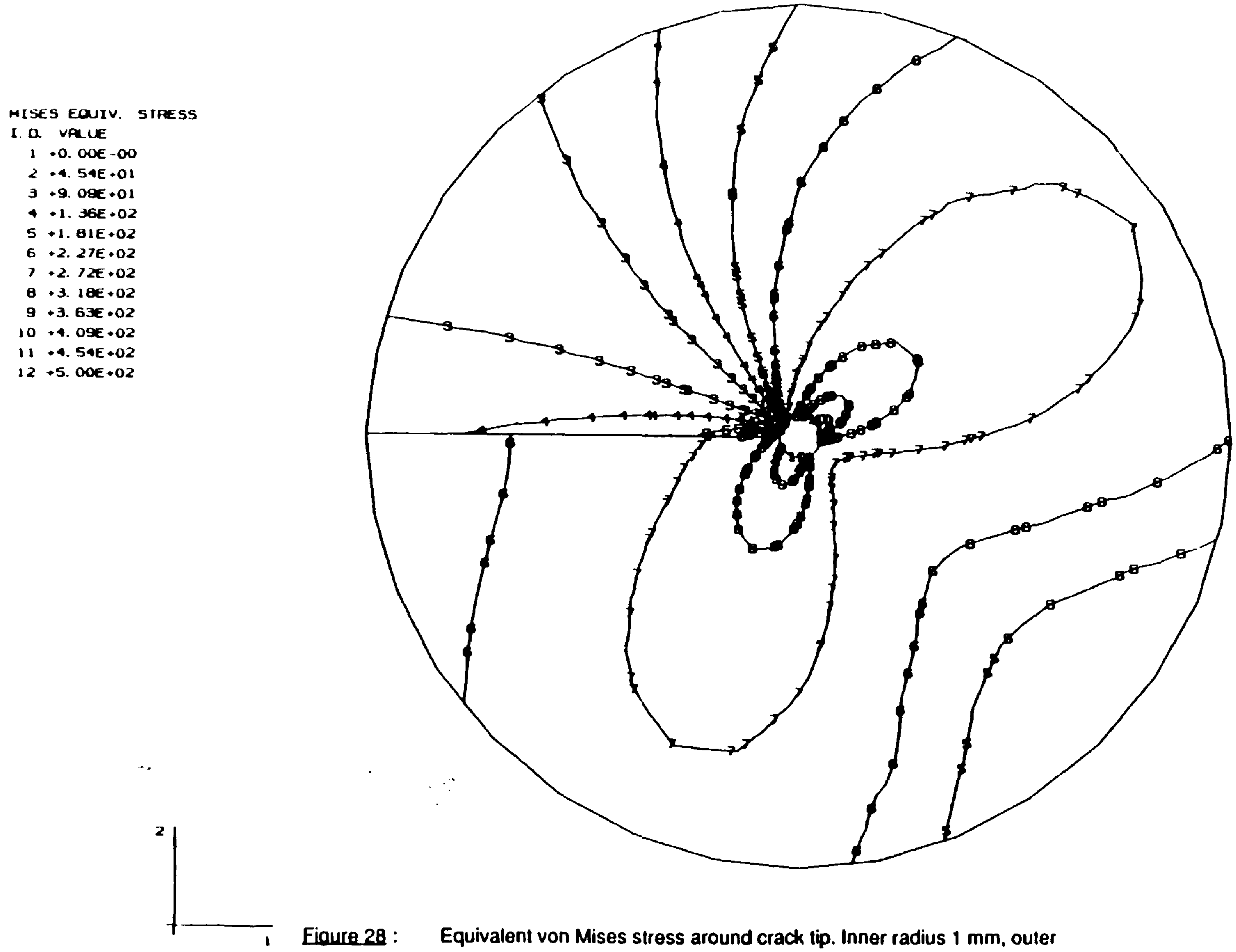

Figure 28 : Equivalent von Mises stress around crack tip. Inner radius 1 mm, outer radius 10 mm.

Stress intensity factor ratio : K_I/K_{II} = 1927/987.

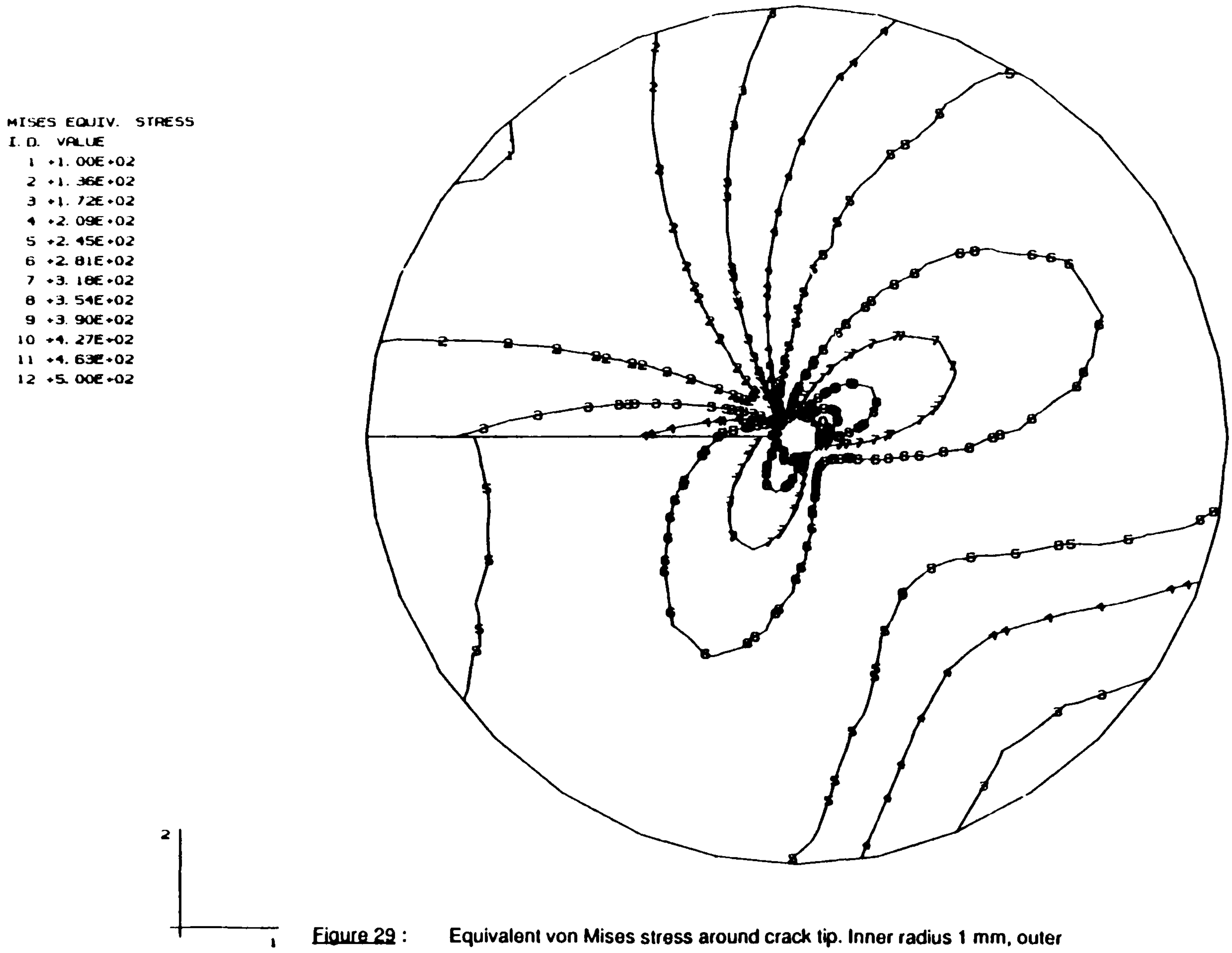

Figure 29 : Equivalent von Mises stress around crack tip. Inner radius 1 mm, outer radius 10 mm.

Stress intensity factor ratio : K_I/K_{II} = 1683/1252.

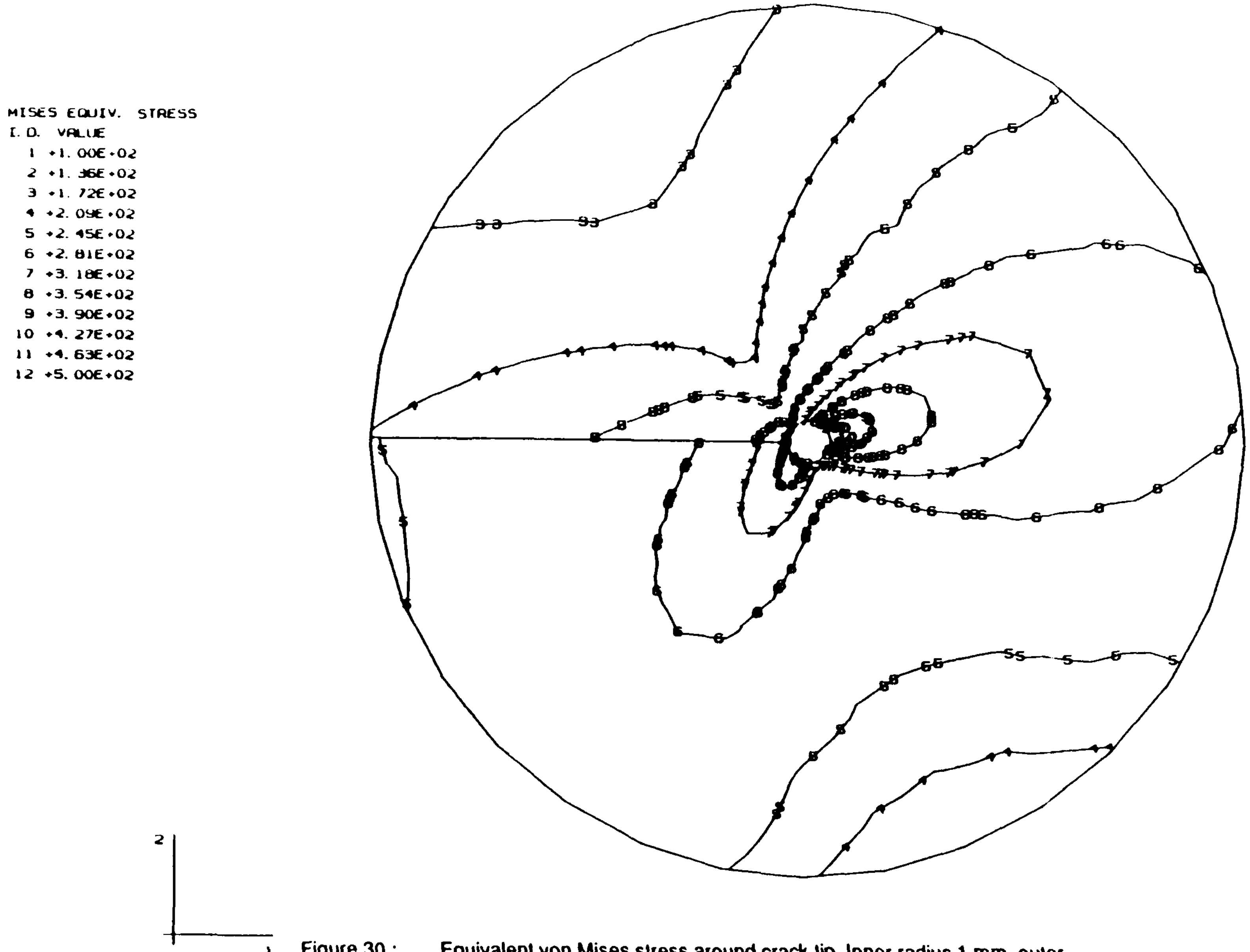

Figure 30 : Equivalent von Mises stress around crack tip. Inner radius 1 mm, outer radius 10 mm.

Stress intensity factor ratio : K_I/K_{II} = 1098/1633.

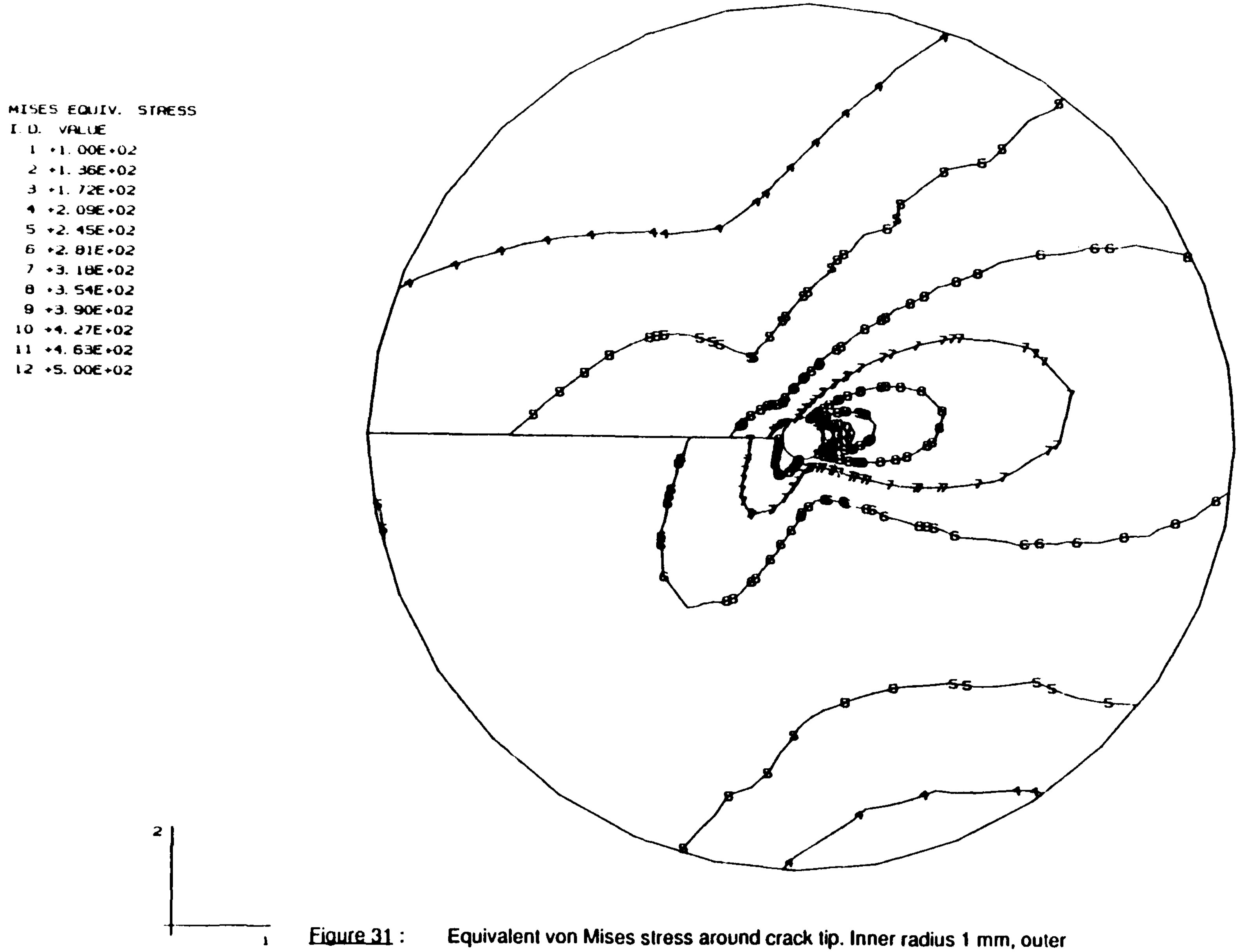

Figure 31 : Equivalent von Mises stress around crack tip. Inner radius 1 mm, outer radius 10 mm.

Stress intensity factor ratio : K_I/K_{II} = 772/1774.

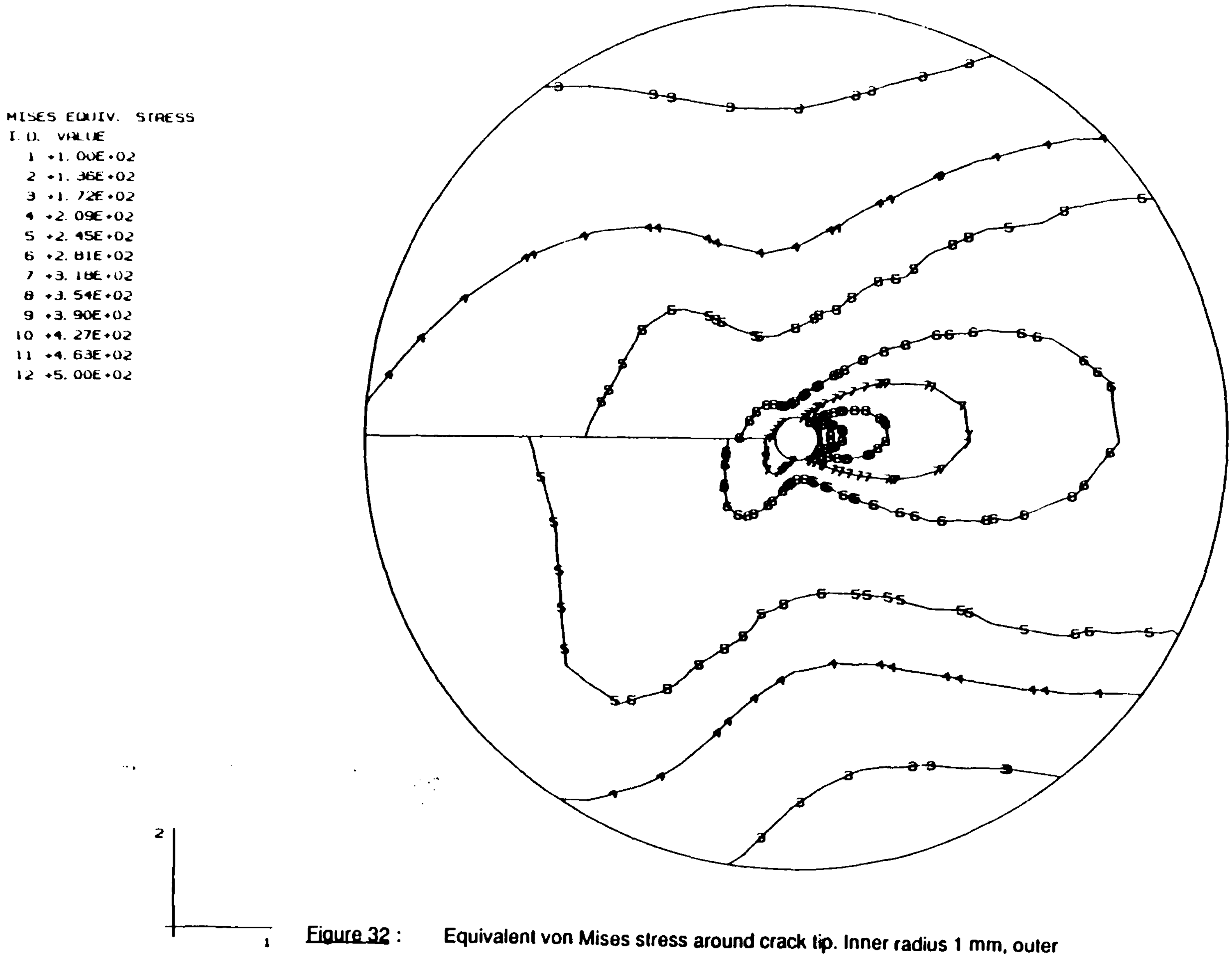

Figure 32 : Equivalent von Mises stress around crack tip. Inner radius 1 mm, outer radius 20 mm.

Stress intensity factor ratio : K_I/K_{II} = 396/1903.

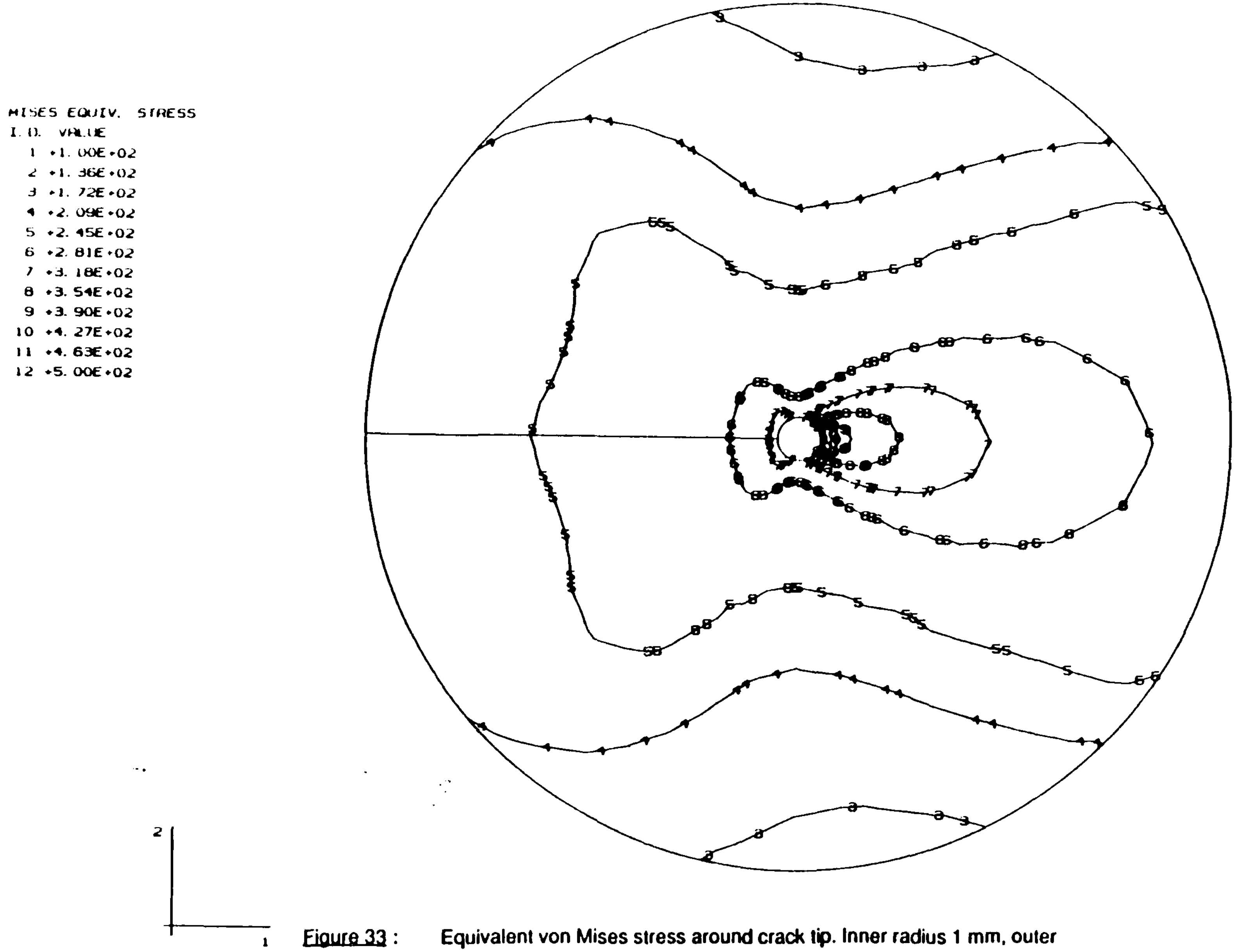

Figure 33 : Equivalent von Mises stress around crack tip. Inner radius 1 mm, outer radius 20 mm.

Stress intensity factor ratio : K_I/K_{II} = 0/2018.

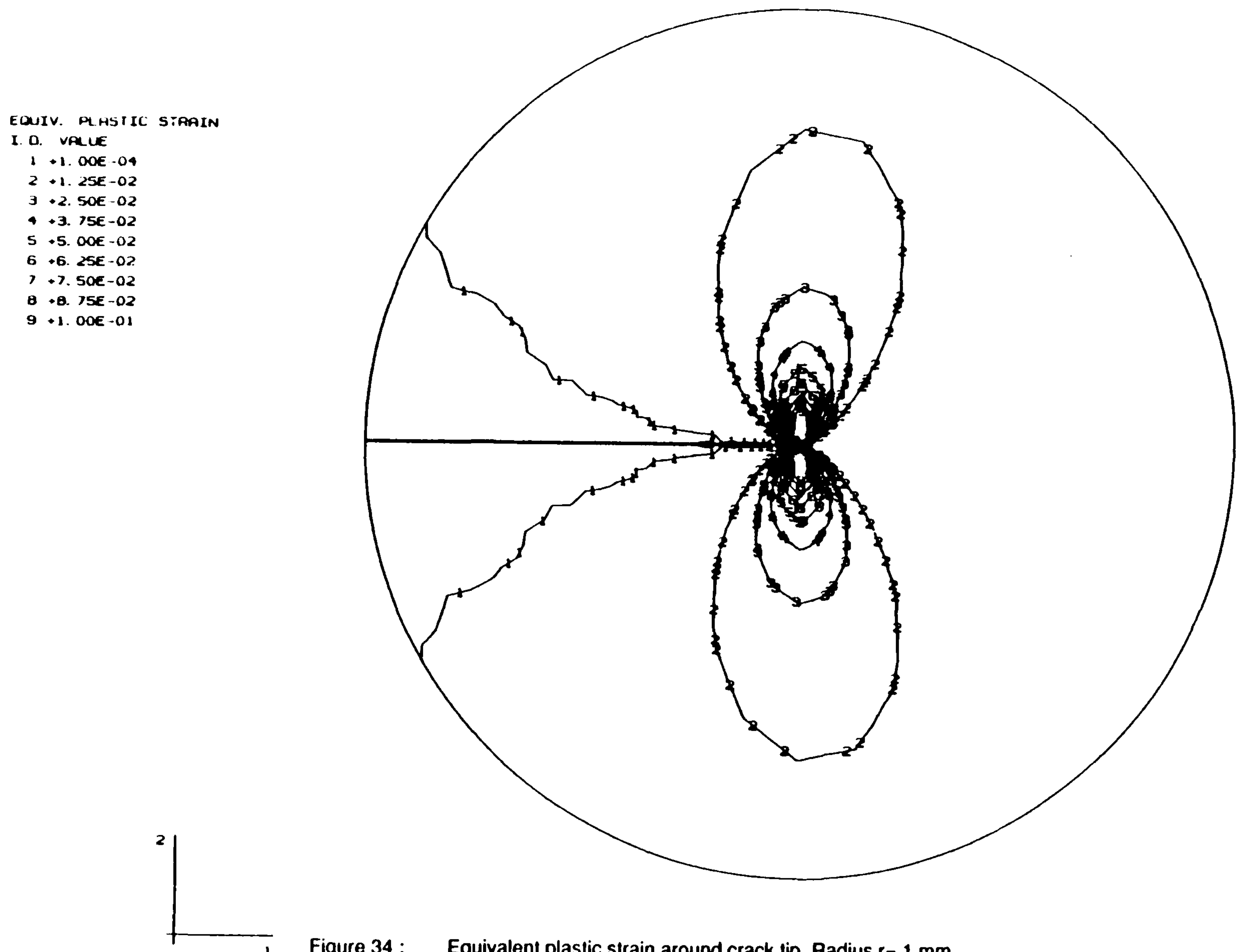

Figure 34 : Equivalent plastic strain around crack tip. Radius r= 1 mm.

Stress intensity factor ratio : K_I/K_{II} = 2230/0.

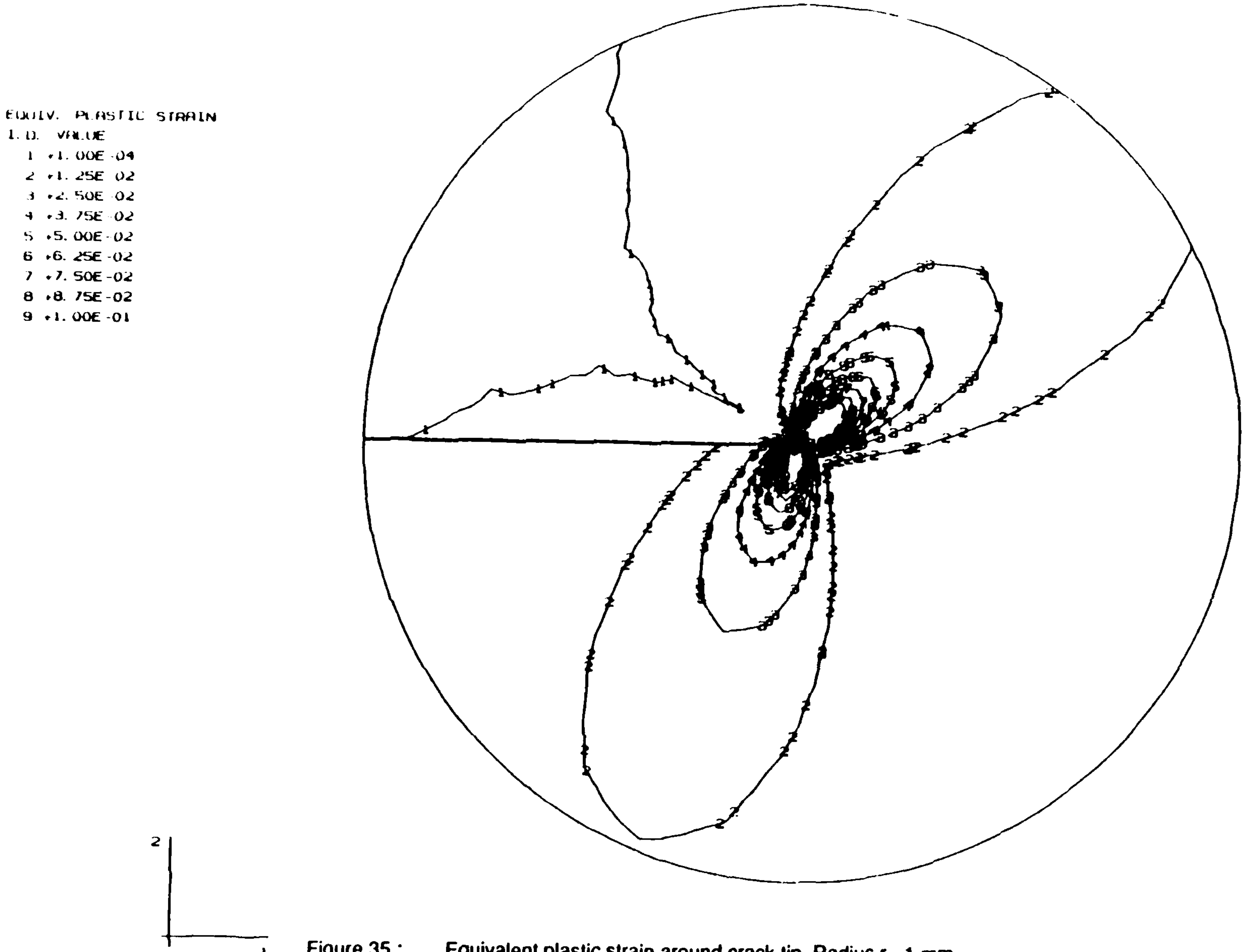

Figure 35 : Equivalent plastic strain around crack tip. Radius r= 1 mm.

Stress intensity factor ratio : K_I/K_{II} = 1927/987.

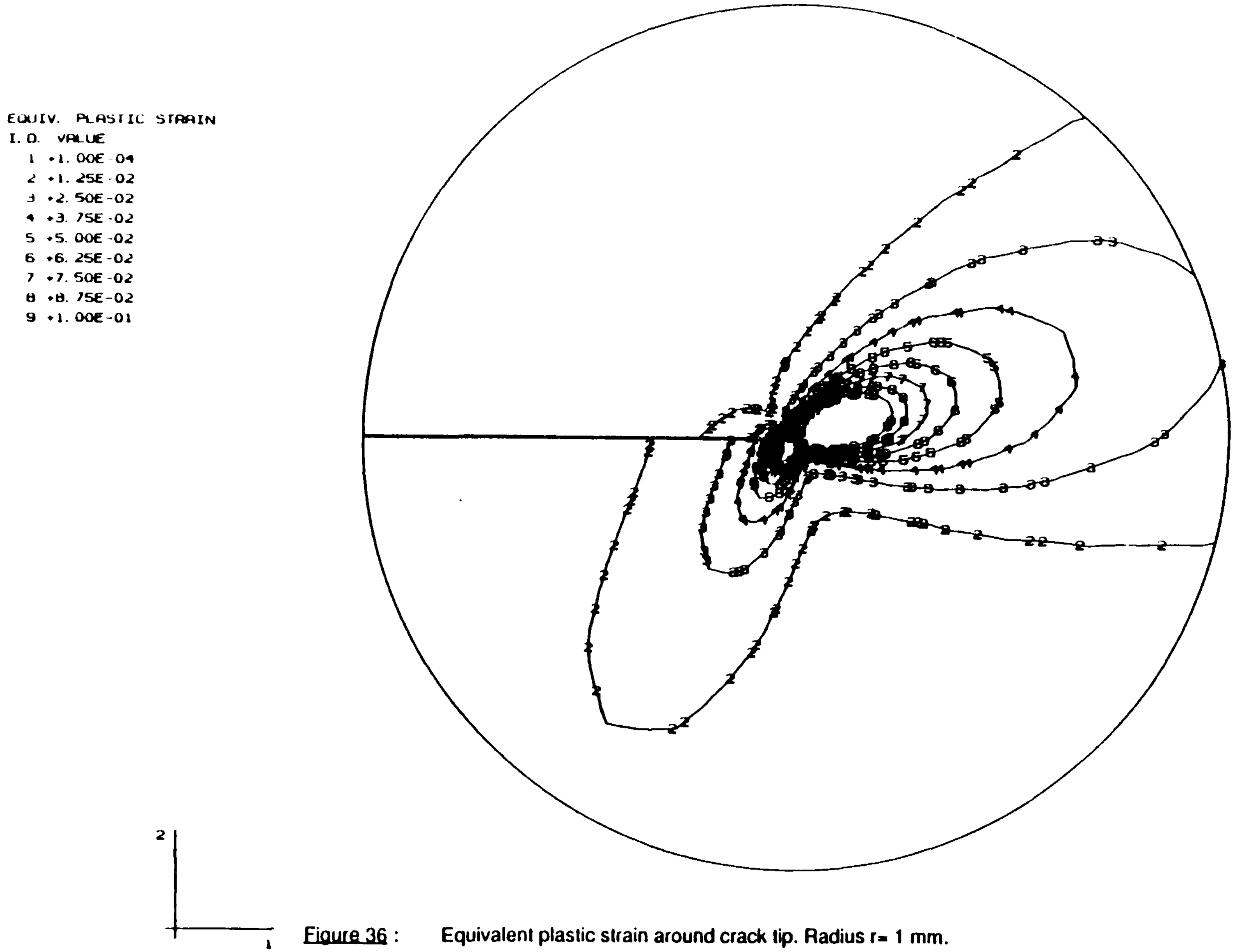

Figure 36 : Equivalent plastic strain around crack tip. Radius r= 1 mm.

Stress intensity factor ratio : K_I/K_{II} = 1098/1633.

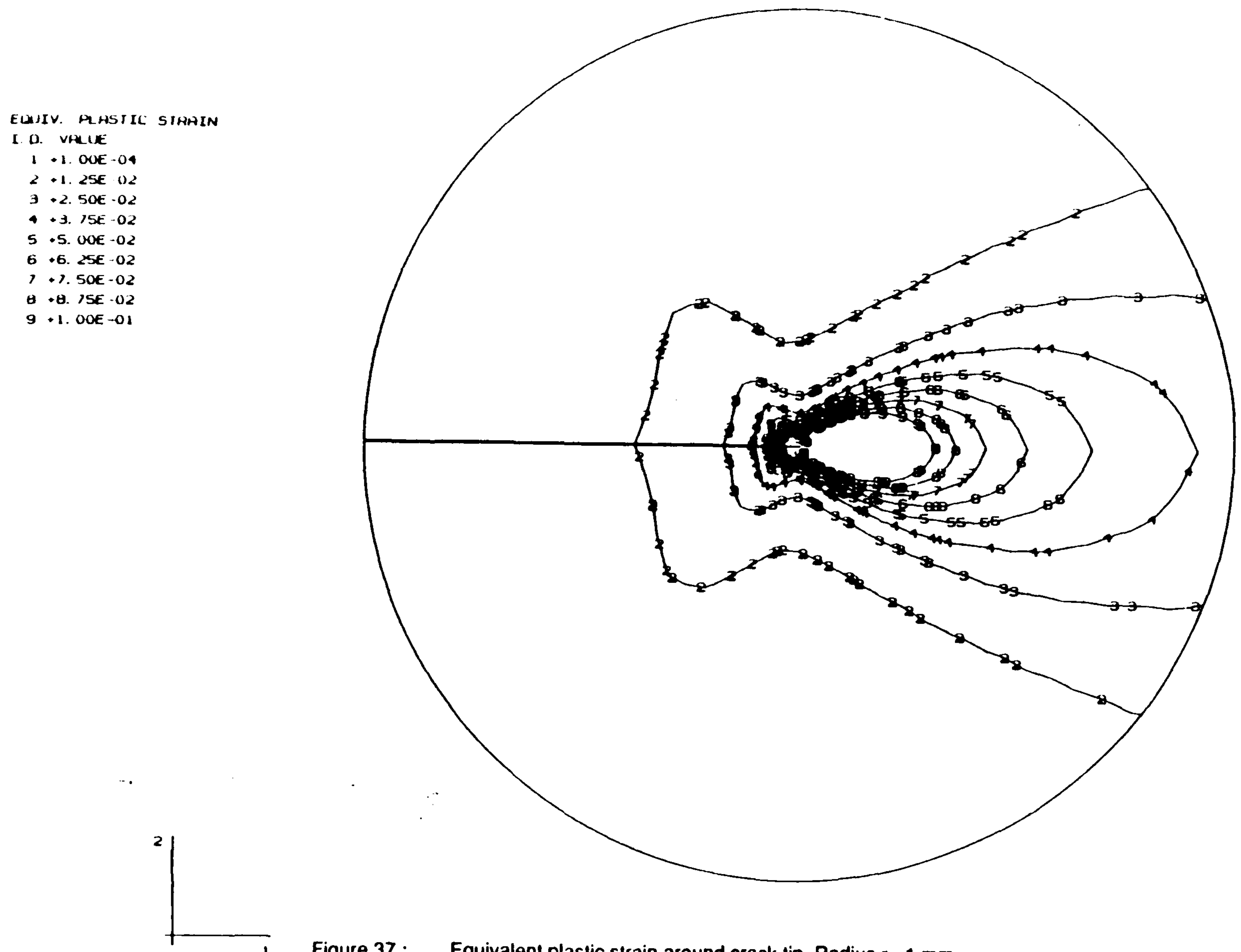

Figure 37 : Equivalent plastic strain around crack tip. Radius r= 1 mm.

Stress intensity factor ratio : K_I/K_{II} = 0/2018.

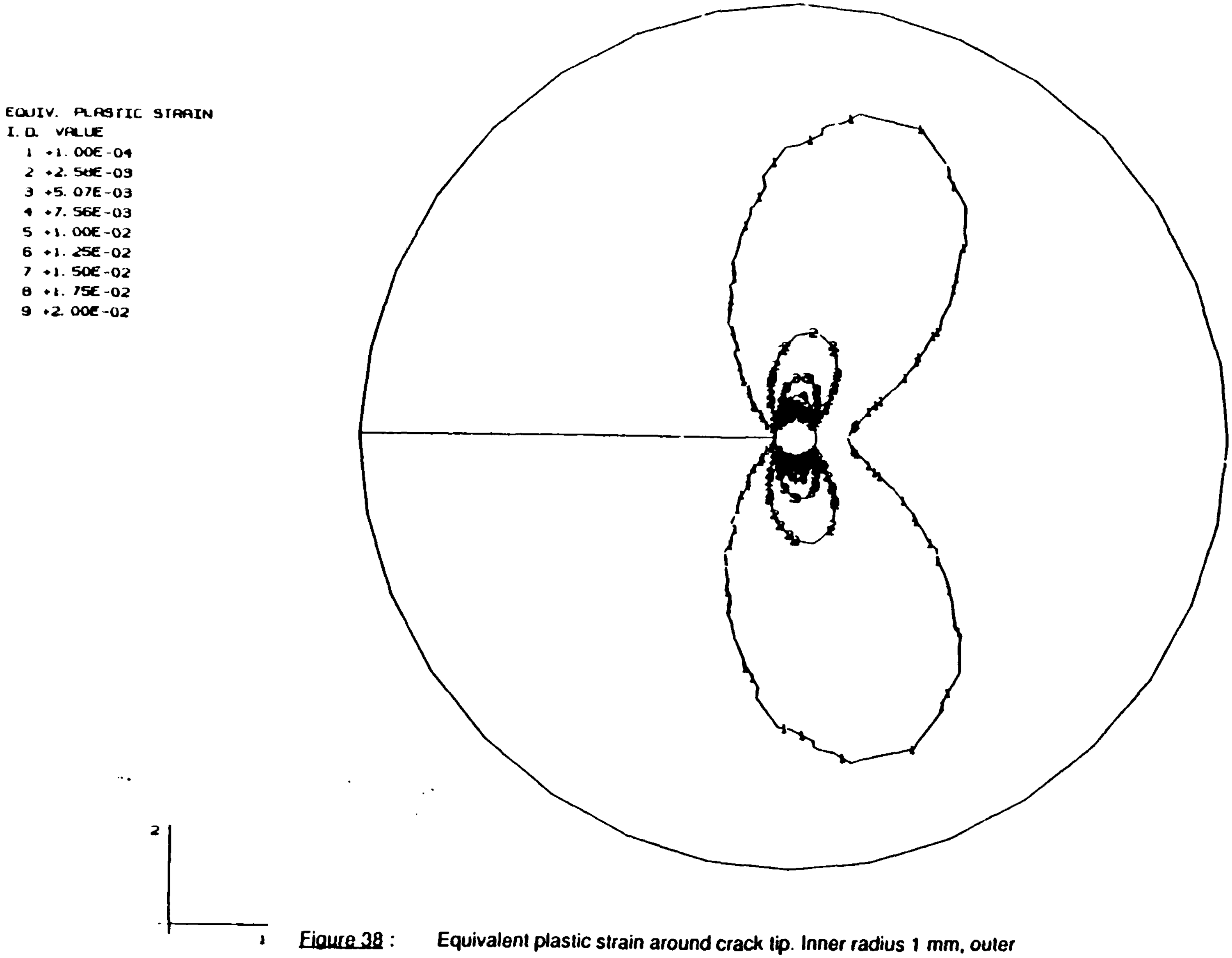

Figure 38 : Equivalent plastic strain around crack tip. Inner radius 1 mm, outer radius 10 mm. Stress intensity factor ratio : K_I/K_{II} = 2230/0.

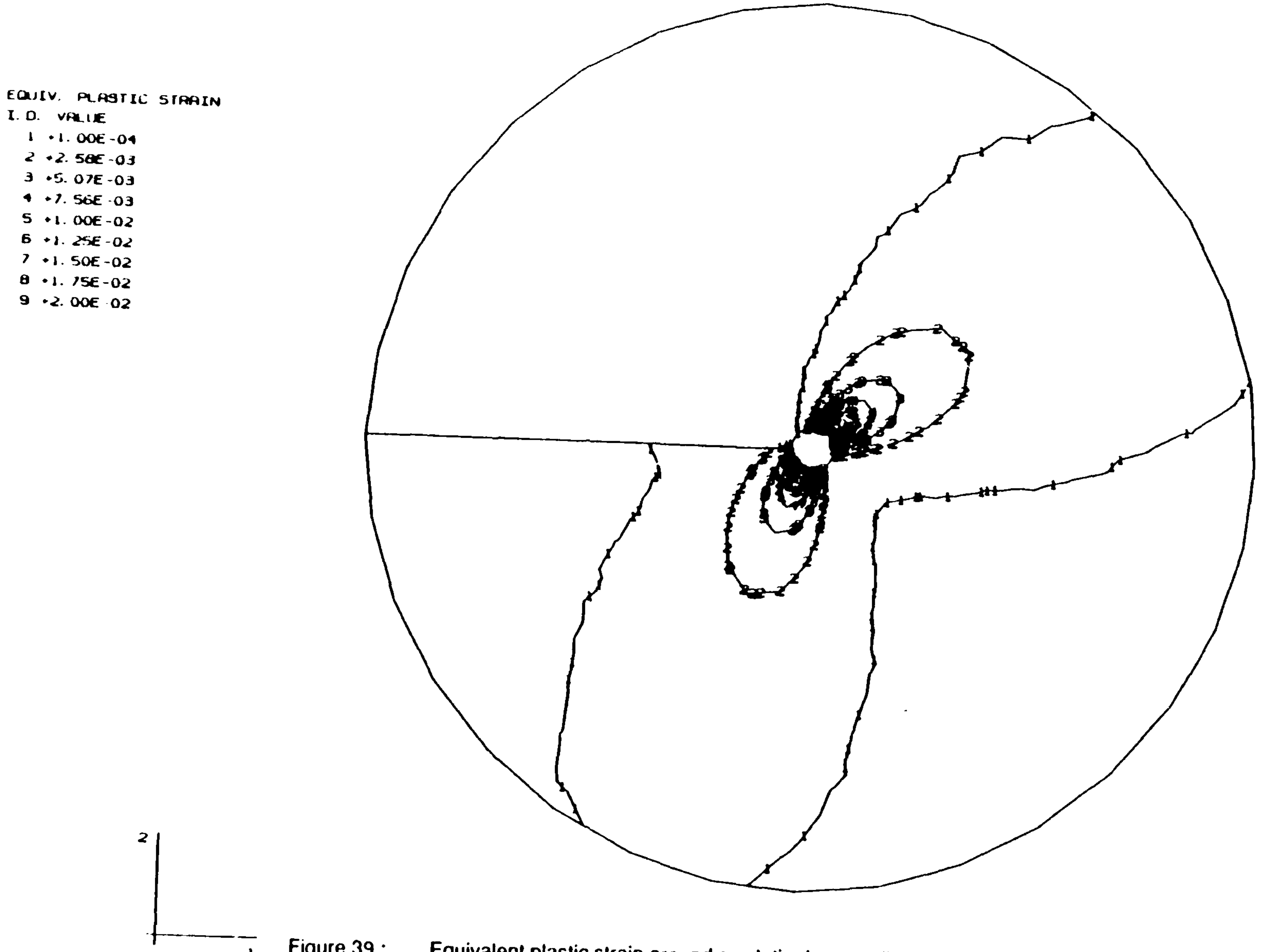

Figure 39 : Equivalent plastic strain around crack tip. Inner radius 1 mm, outer radius 10 mm. Stress intensity factor ratio : K_I/K_{II} = 1927/987.

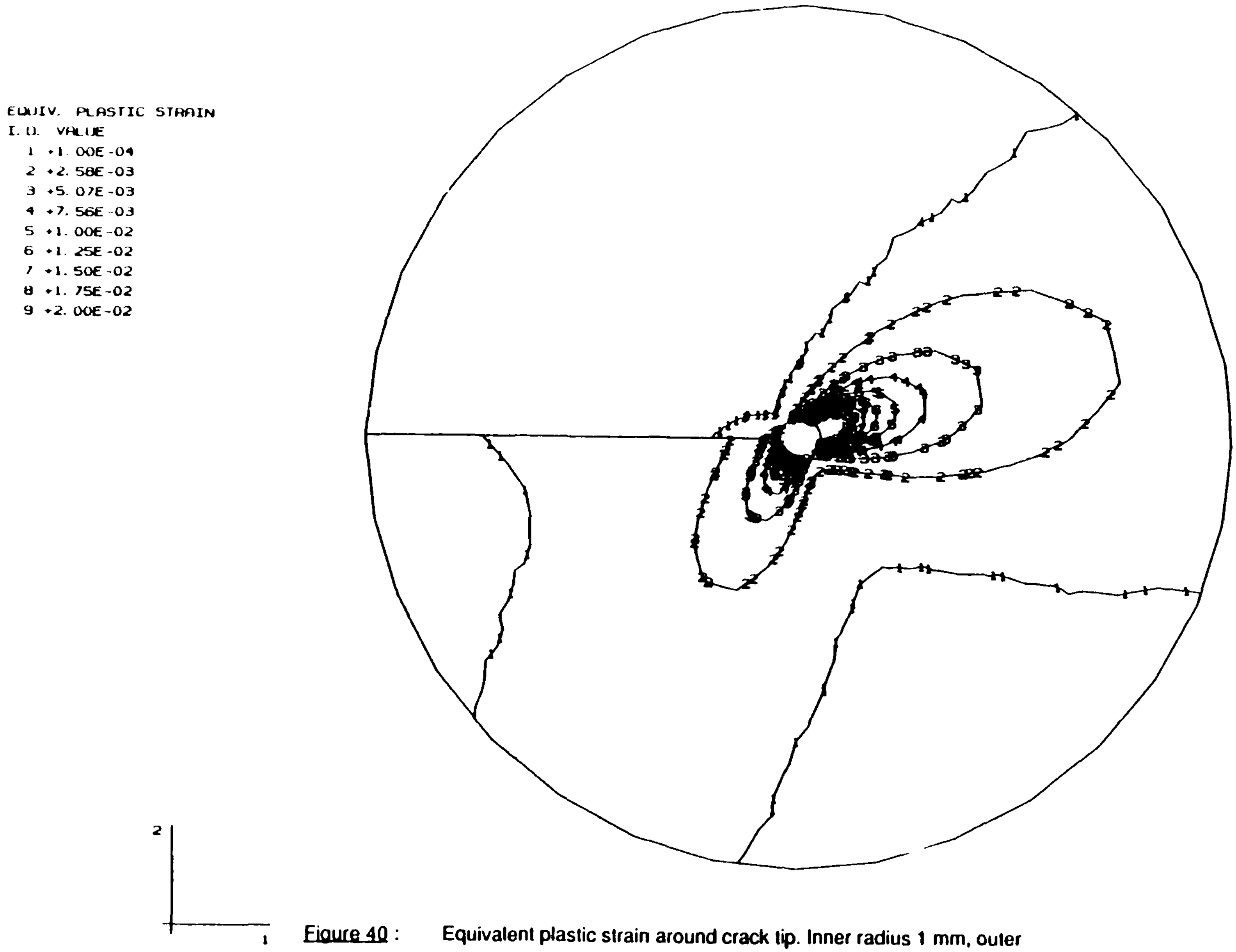

Figure 40 : Equivalent plastic strain around crack tip. Inner radius 1 mm, outer radius 10 mm. Stress intensity factor ratio : K_I/K_{II} = 1405/1462.

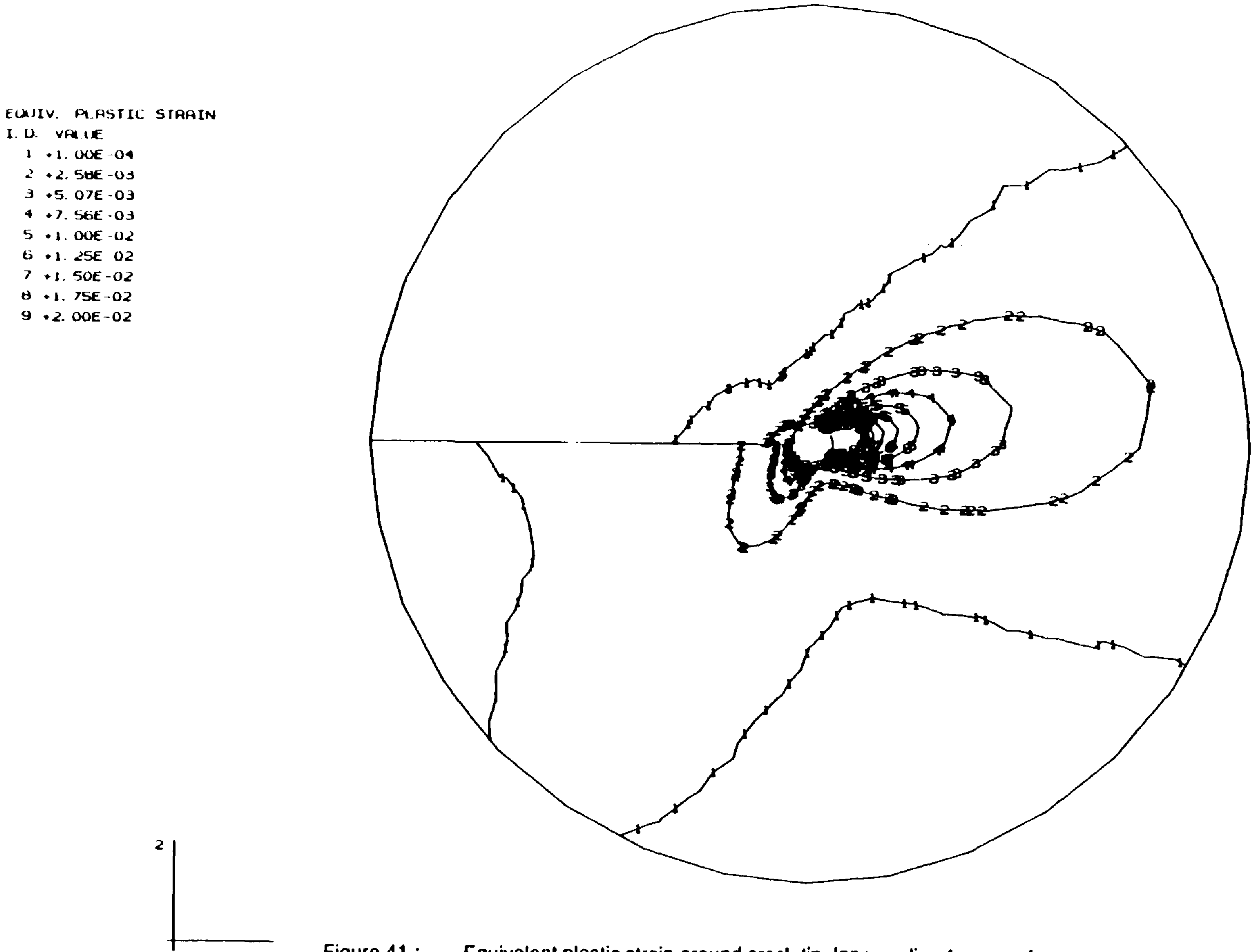

Figure 41 : Equivalent plastic strain around crack tip. Inner radius 1 mm, outer radius 10 mm. Stress intensity factor ratio : K_I/K_{II} = 772/1774.

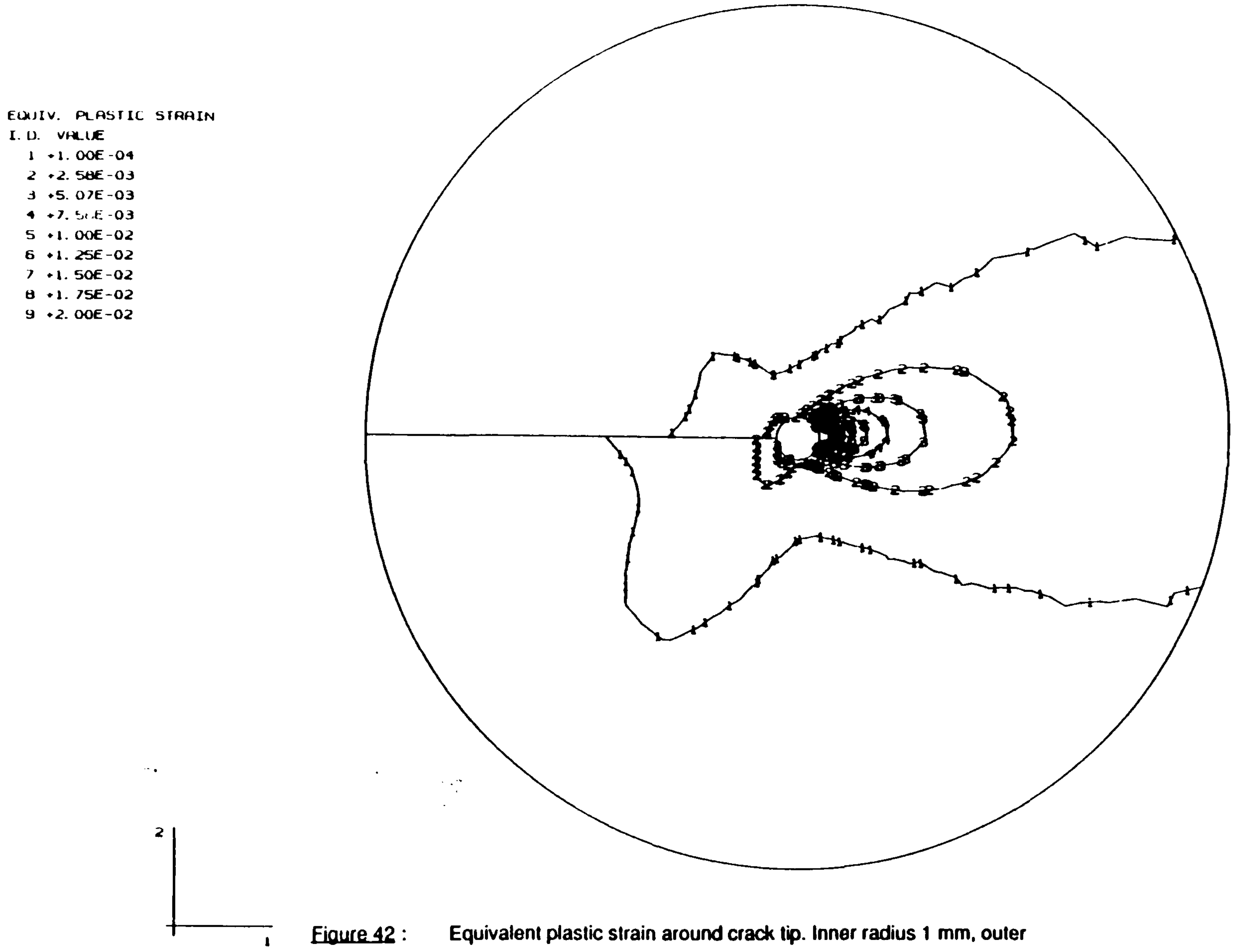

Figure 42 : Equivalent plastic strain around crack tip. Inner radius 1 mm, outer radius 20 mm. Stress intensity factor ratio : K_I/K_{II} = 396/1903.

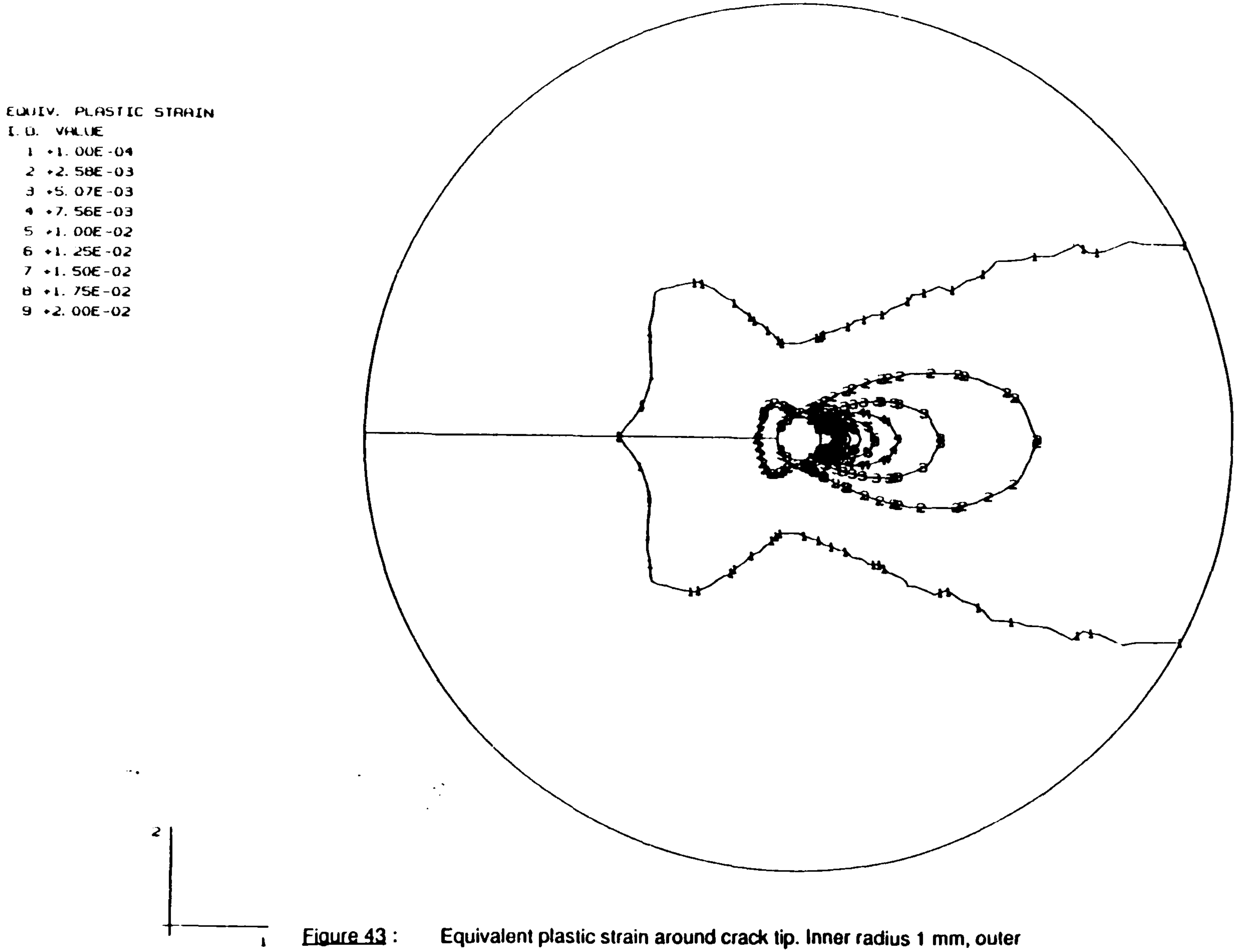

Figure 43 : Equivalent plastic strain around crack tip. Inner radius 1 mm, outer radius 20 mm. Stress intensity factor ratio : K_I/K_{II} = 0/2018.

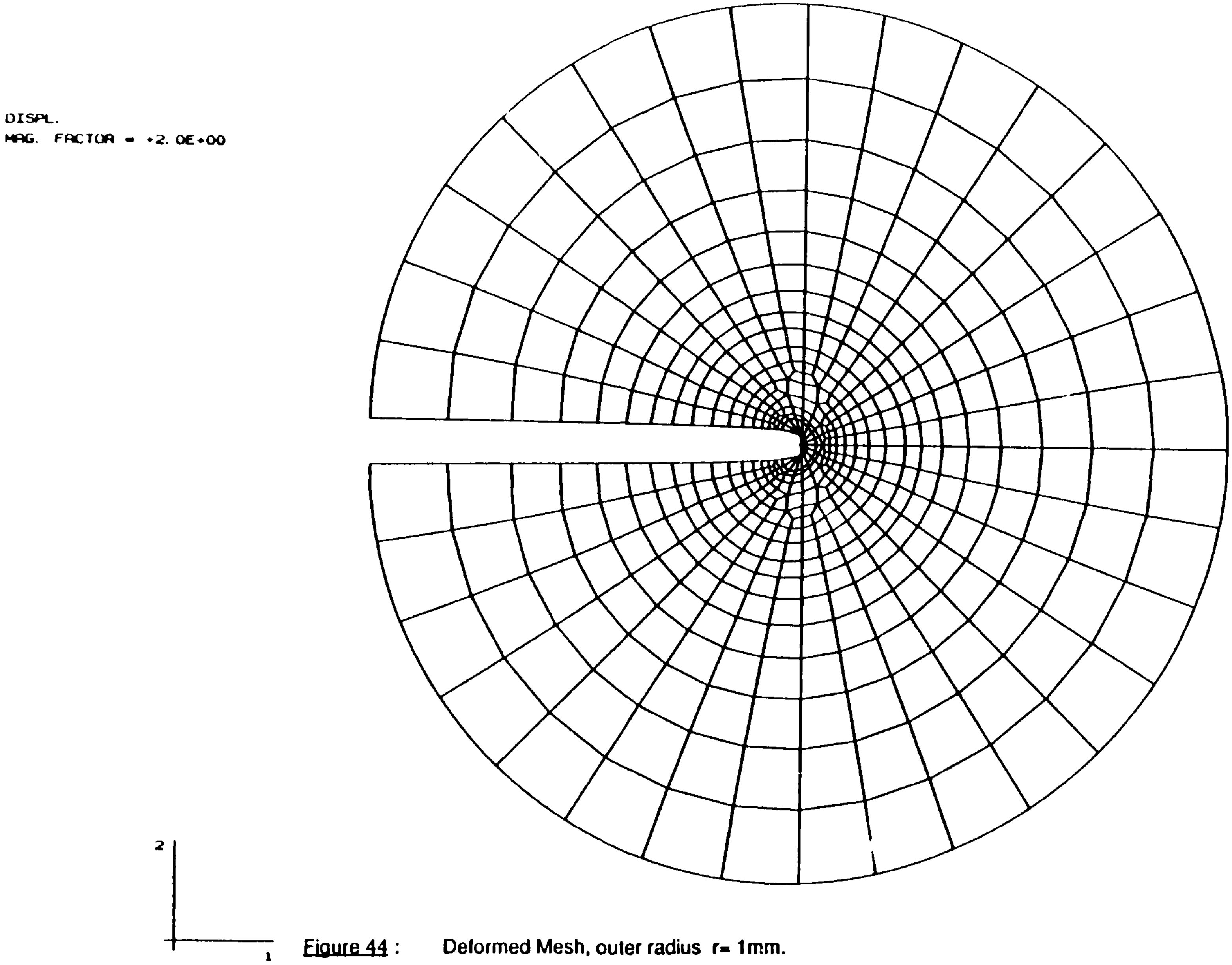
DISPL.
MAG. FACTOR = +2.0E+00
2
1

Figure 44 : Deformed Mesh, outer radius r= 1mm.

Stress intensity factor ratio : K_I/K_{II} = 2230/0.

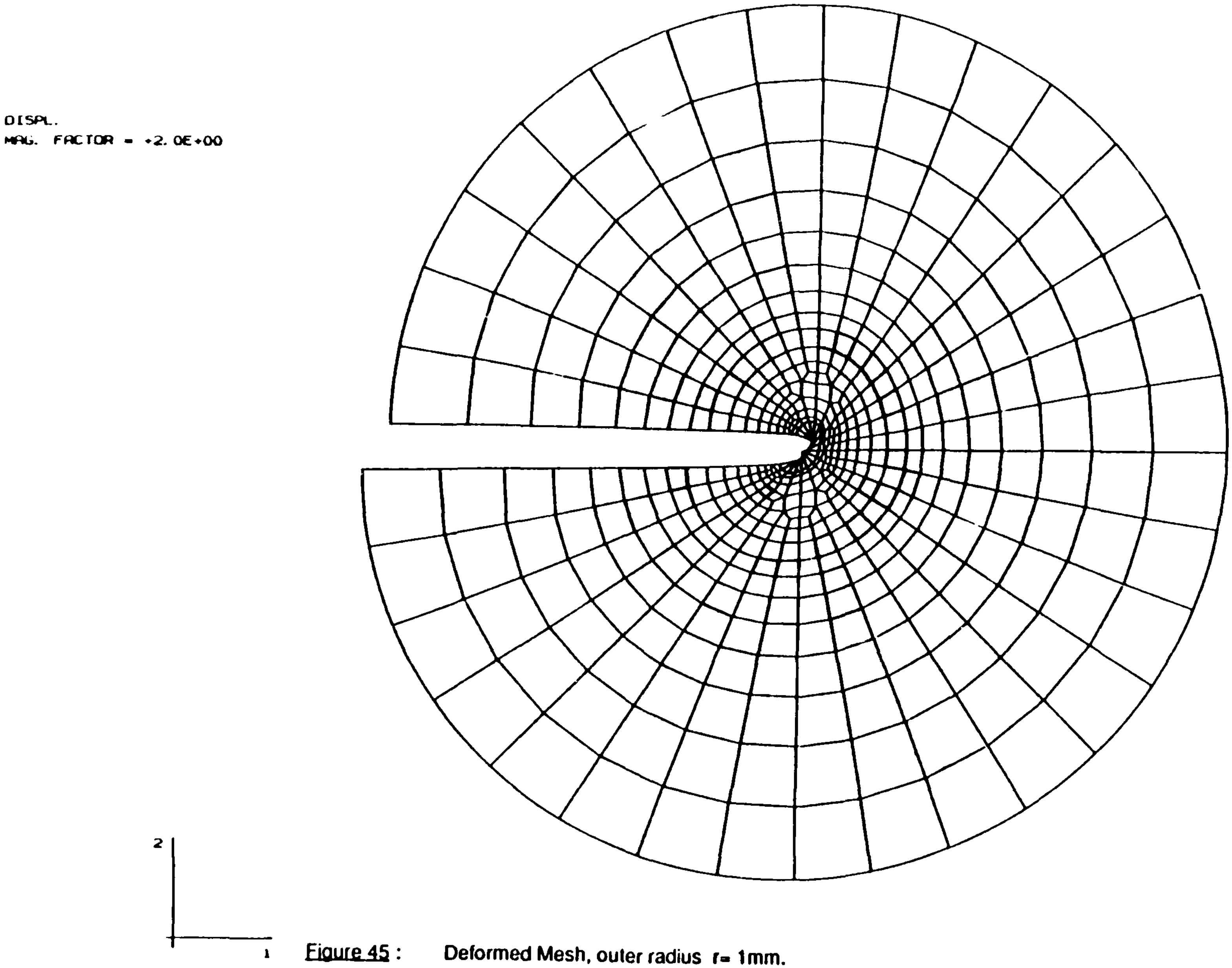
DISPL.
MAG. FACTOR = +2.0E+00
2
1

Figure 45 : Deformed Mesh, outer radius r= 1mm.

Stress intensity factor ratio : K_I/K_{II} = 1927/987.

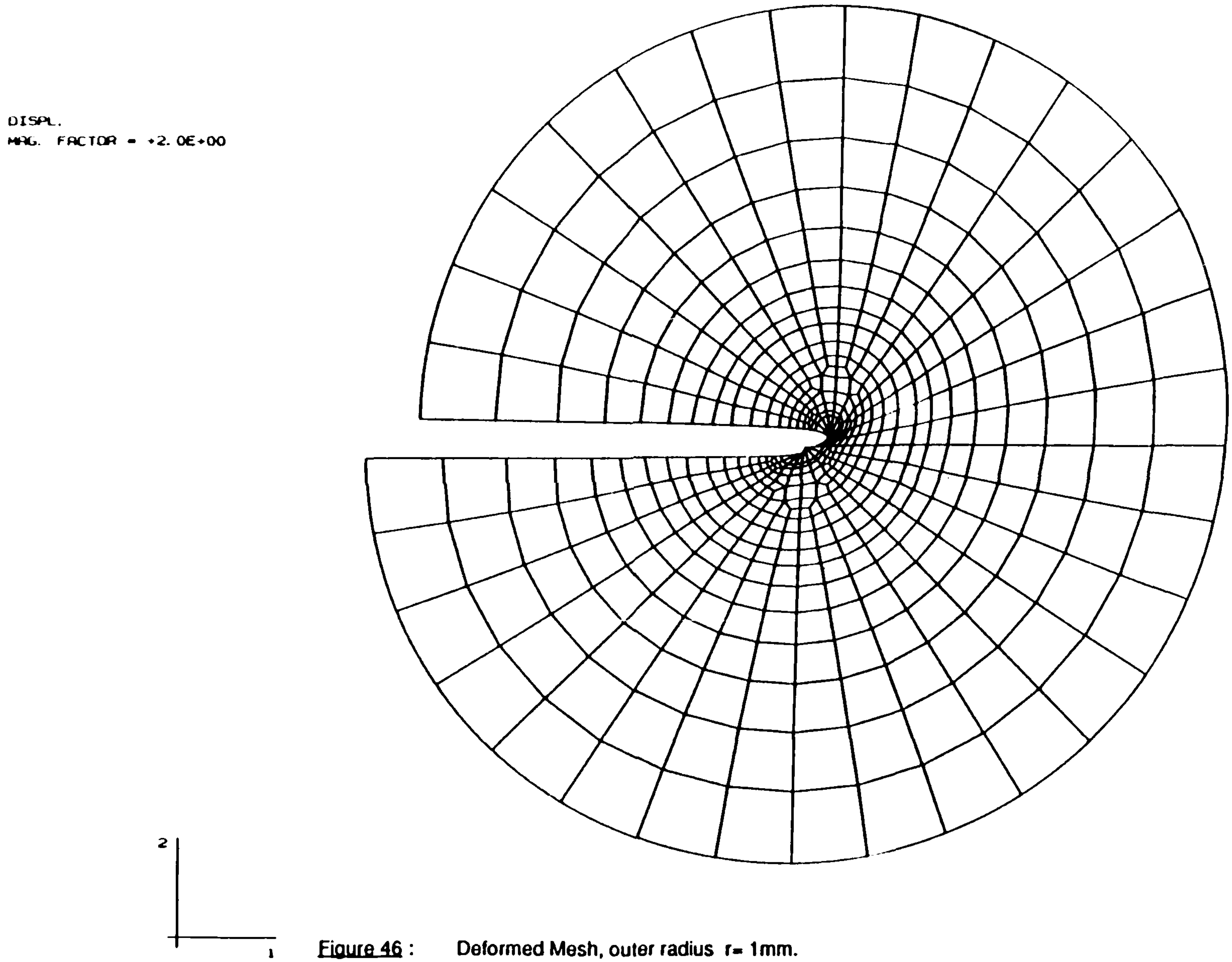
DISPL.
MAG. FACTOR = +2.0E+00
2
1

Figure 46 : Deformed Mesh, outer radius $r = 1$mm.

Stress intensity factor ratio : $K_I/K_{II} = 1405/1462$.

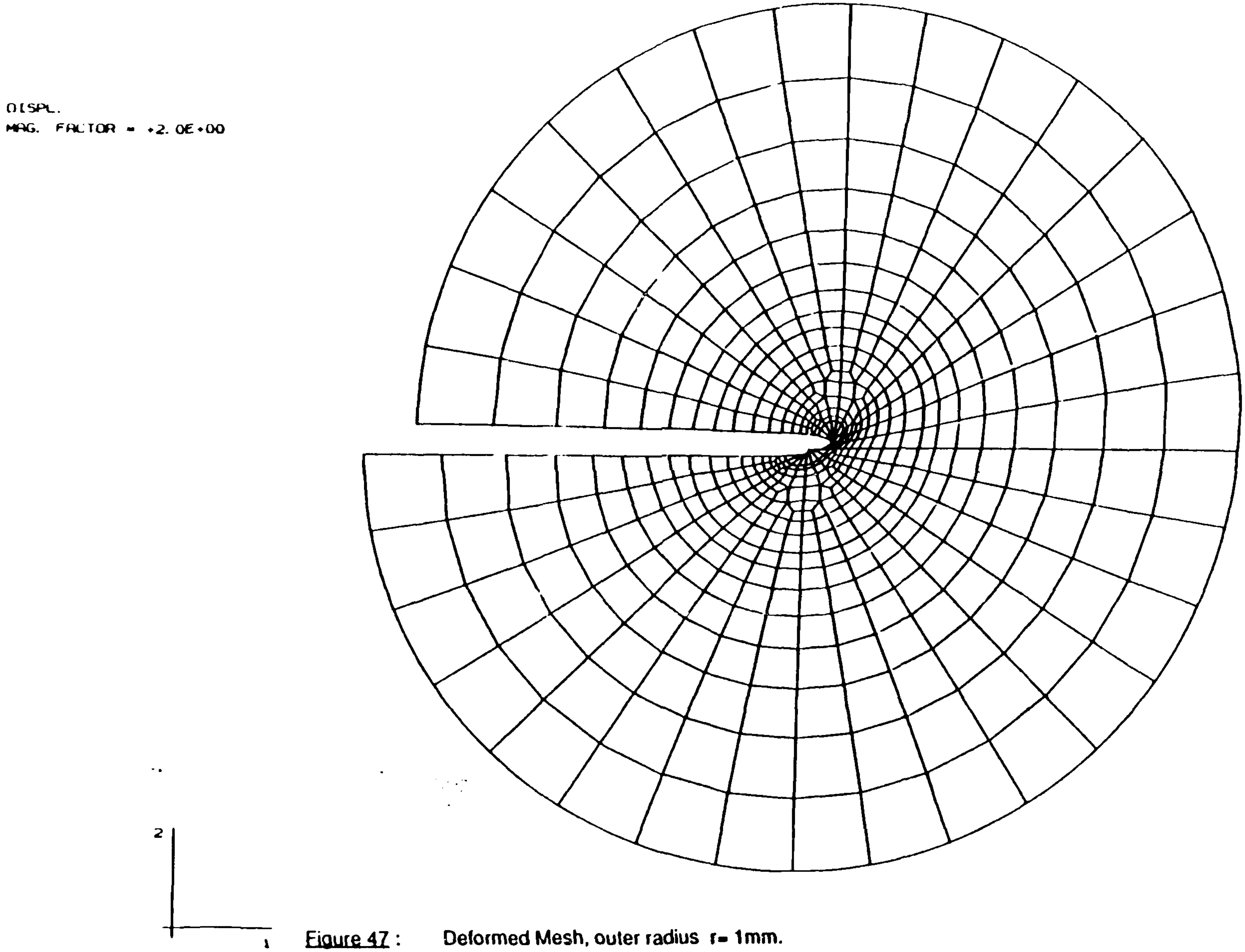
DISPL.
MAG. FACTOR = +2.0E+00
2
1

Figure 47 : Deformed Mesh, outer radius r= 1mm.

Stress intensity factor ratio : K_I/K_{II} = 1098/1633.

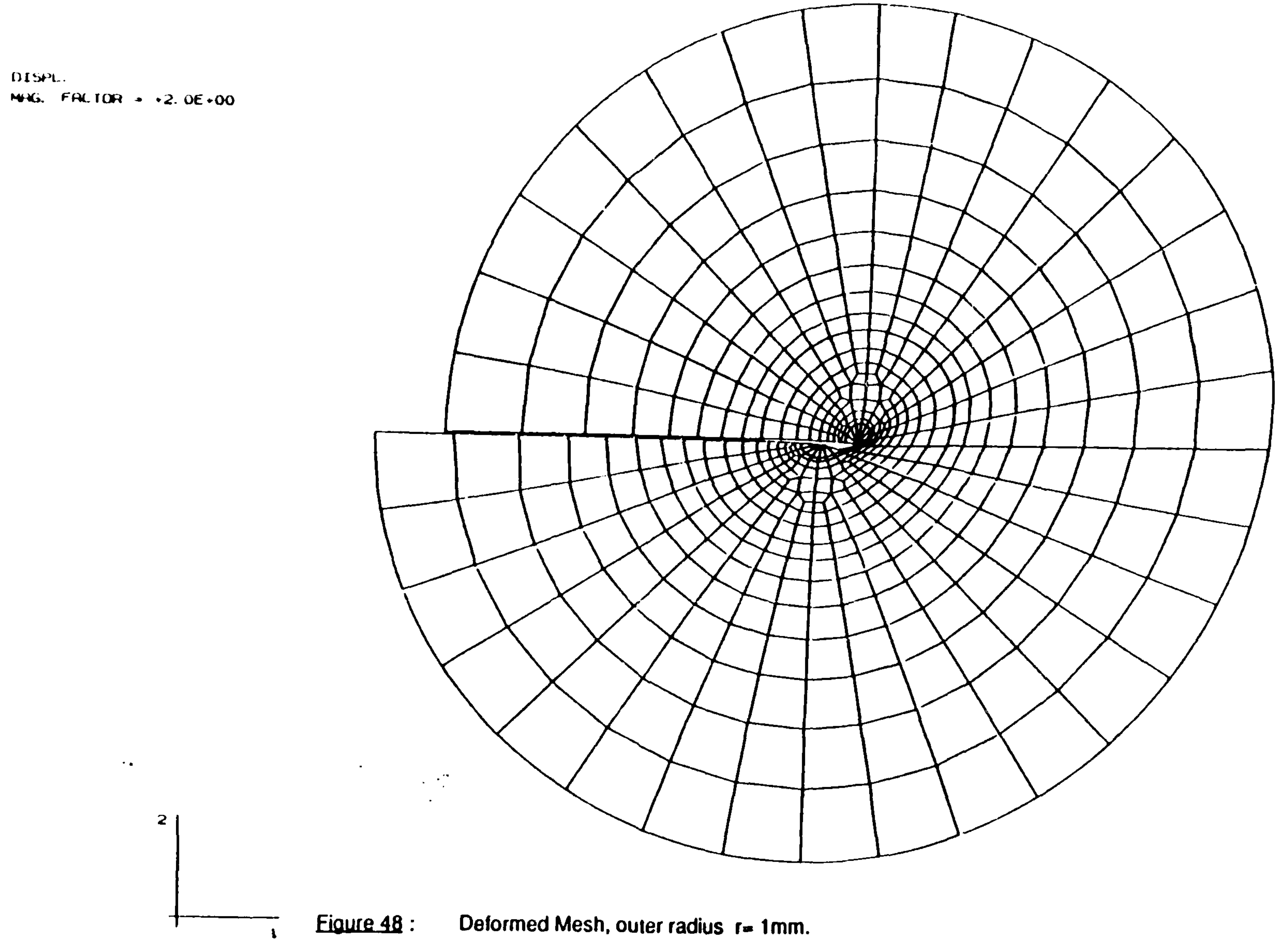
DISPL.
MAG. FACTOR = +2.0E+00
2
1

Figure 48 : Deformed Mesh, outer radius r= 1mm.

Stress intensity factor ratio : K_I/K_{II} = 0/2018.

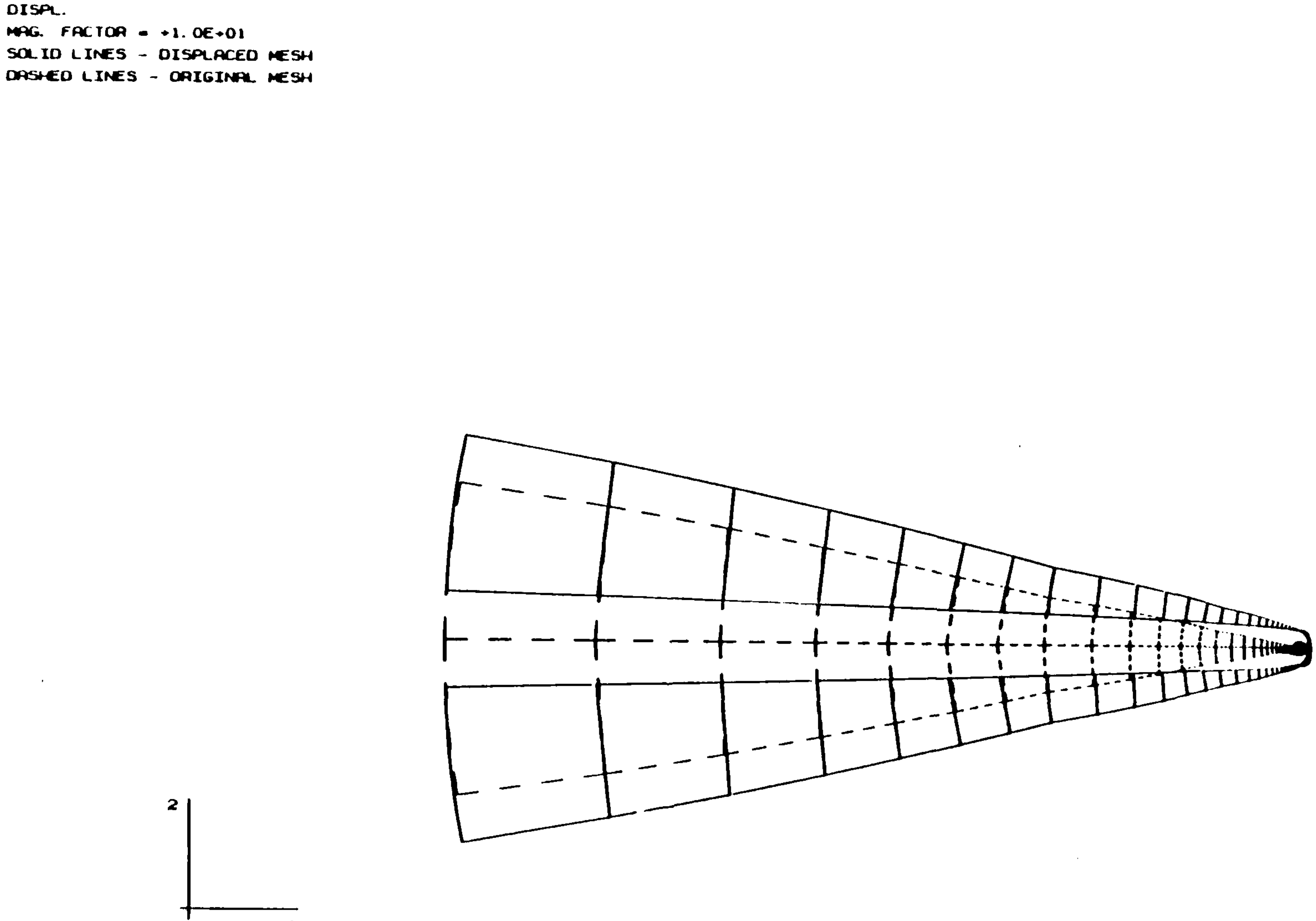
DISPL.
MAG. FACTOR = +1.0E+01
SOLID LINES - DISPLACED MESH
DASHED LINES - ORIGINAL MESH
2
1

Figure 49 : Crack deformation. Plotted crack length 10 mm.

Stress intensity factor ratio : K_I/K_{II} = 2230/0.

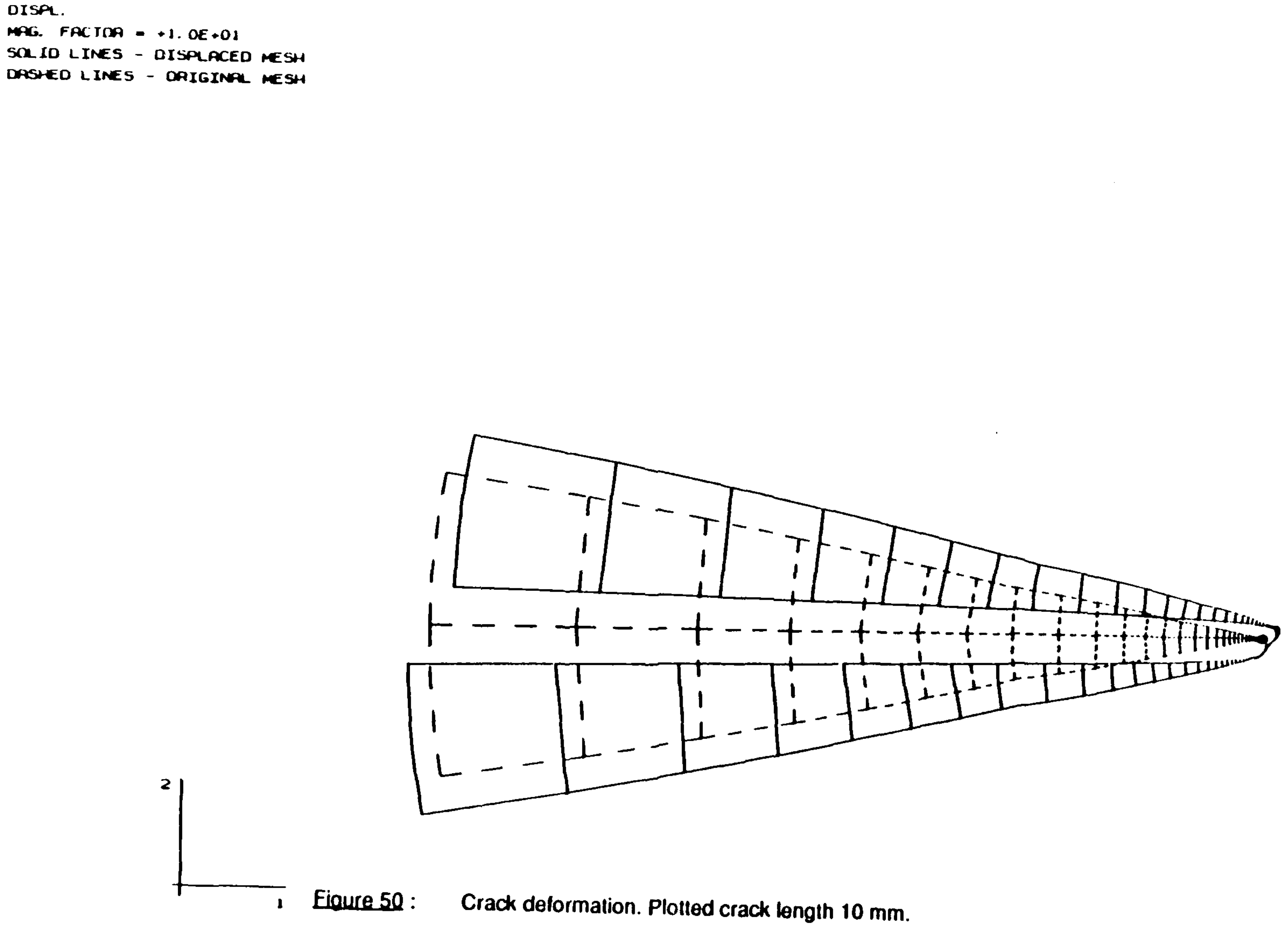
DISPL.
MAG. FACTOR = +1.0E+01
SOLID LINES - DISPLACED MESH
DASHED LINES - ORIGINAL MESH
2
1

Figure 50 : Crack deformation. Plotted crack length 10 mm.

Stress intensity factor ratio : K_I/K_{II} = 1927/987.

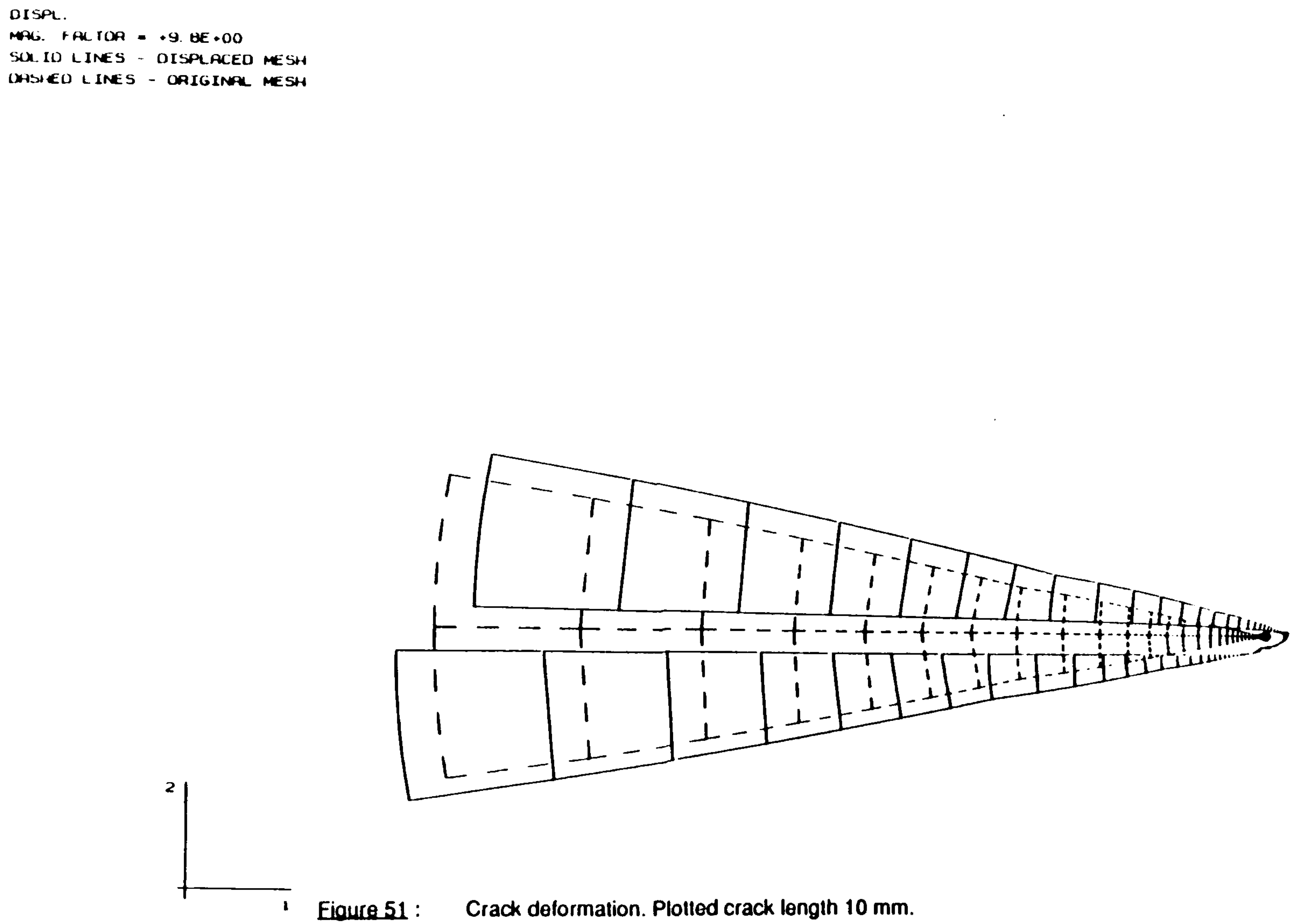
DISPL.
MAG. FACTOR = +9.8E+00
SOLID LINES - DISPLACED MESH
DASHED LINES - ORIGINAL MESH
2
1

Figure 51 : Crack deformation. Plotted crack length 10 mm.

Stress intensity factor ratio : K_I/K_{II} = 1098/1633.

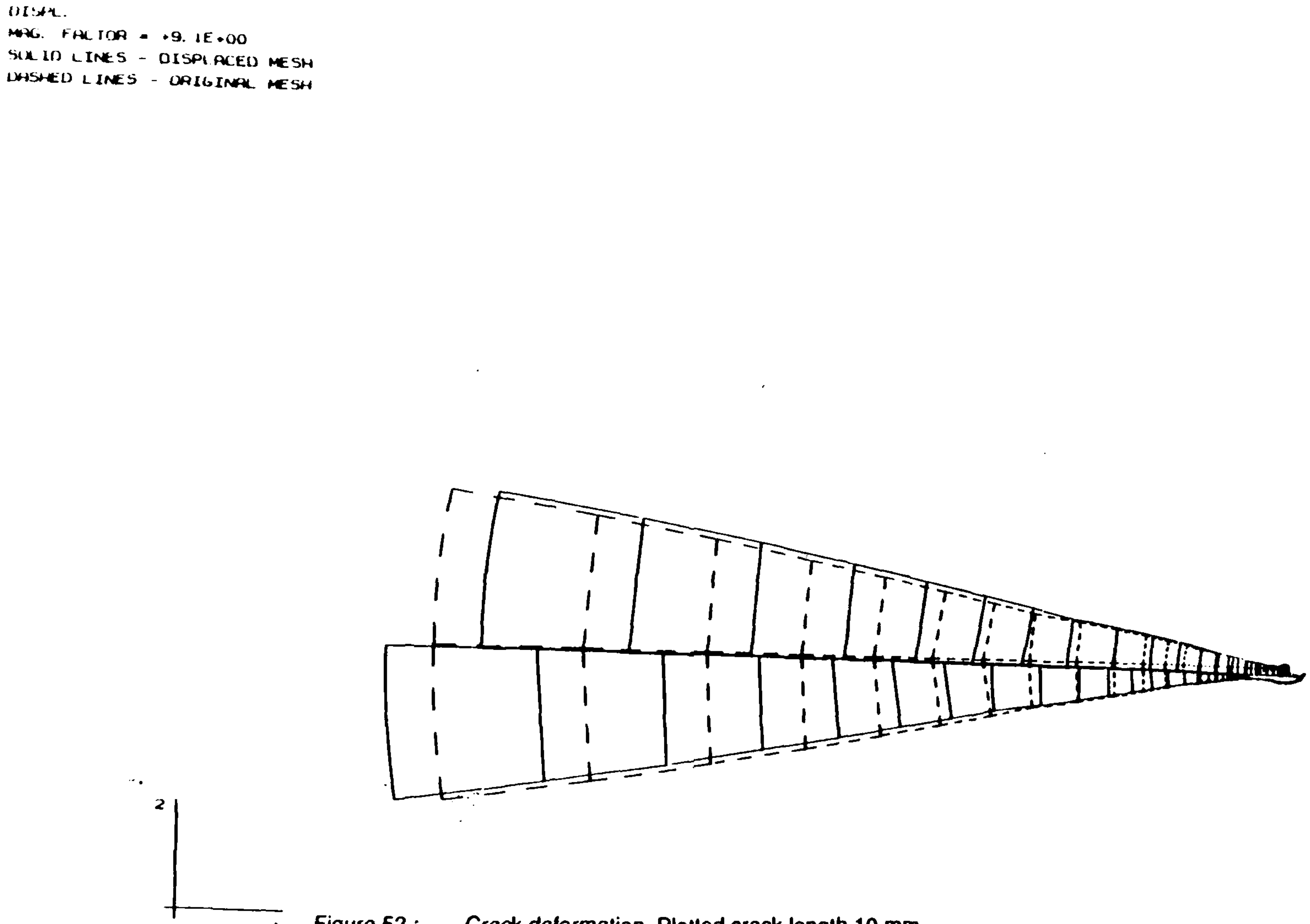
DISPL.
MAG. FACTOR = +9.1E+00
SOLID LINES - DISPLACED MESH
DASHED LINES - ORIGINAL MESH
2
1

Figure 52 : Crack deformation. Plotted crack length 10 mm.

Stress intensity factor ratio : K_I/K_{II} = 0/2018.

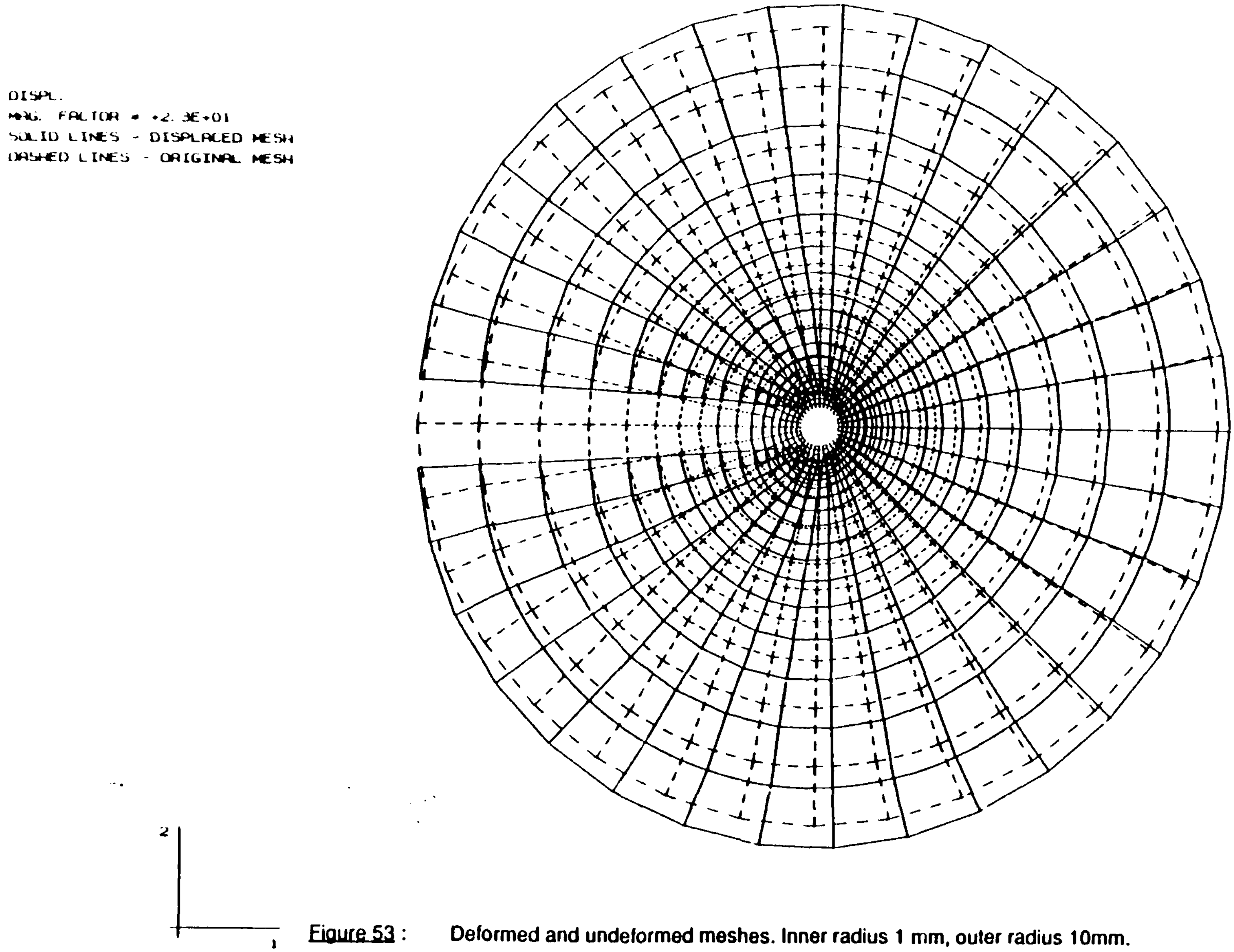
DISPL.
MAG. FACTOR = +2.3E+01
SOLID LINES - DISPLACED MESH
DASHED LINES - ORIGINAL MESH
2
1

Figure 53 : Deformed and undeformed meshes. Inner radius 1 mm, outer radius 10mm. Stress intensity factor ratio : $K_I/K_{II} = 2230/0$.

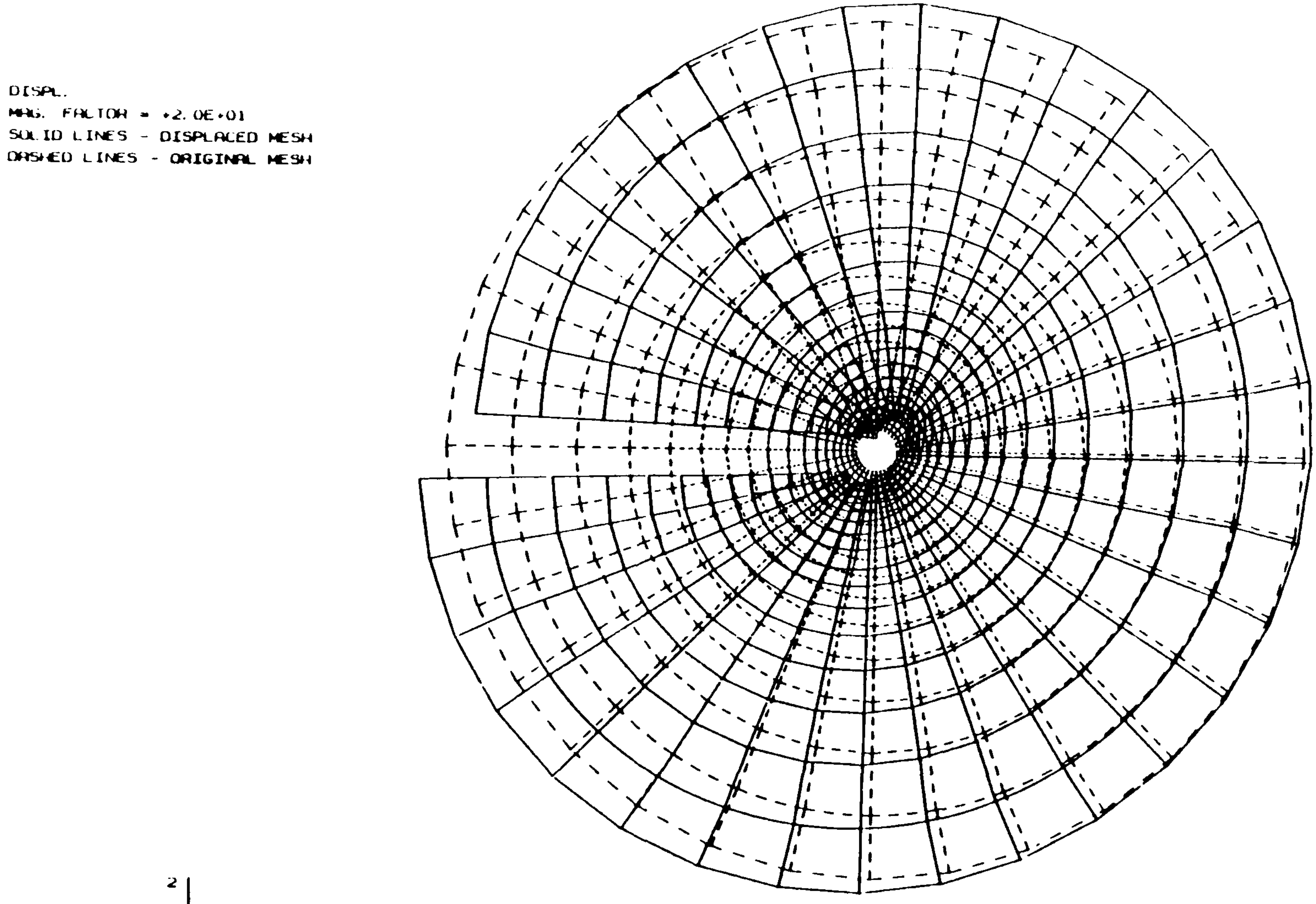
DISPL.
MAG. FACTOR = +2.0E+01
SOLID LINES - DISPLACED MESH
DASHED LINES - ORIGINAL MESH
2
1

Figure 54 : Deformed and undeformed meshes. Inner radius 1 mm, outer radius 10mm.
Stress intensity factor ratio : K_I/K_{II} = 1683/1252.

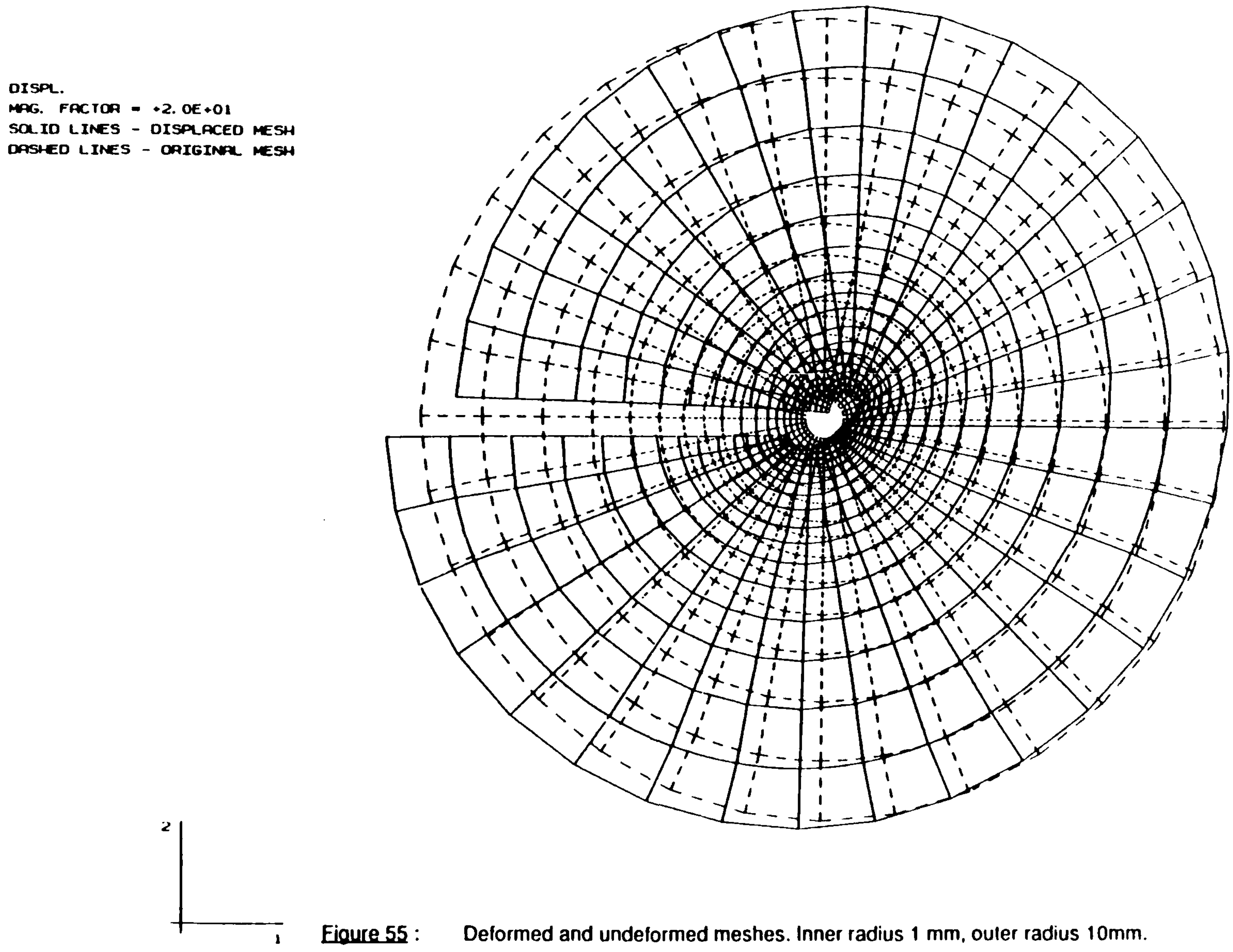
DISPL.
MAG. FACTOR = +2.0E+01
SOLID LINES - DISPLACED MESH
DASHED LINES - ORIGINAL MESH
2
1

Figure 55 : Deformed and undeformed meshes. Inner radius 1 mm, outer radius 10mm.

Stress intensity factor ratio : K_I/K_{II} = 1098/1633.

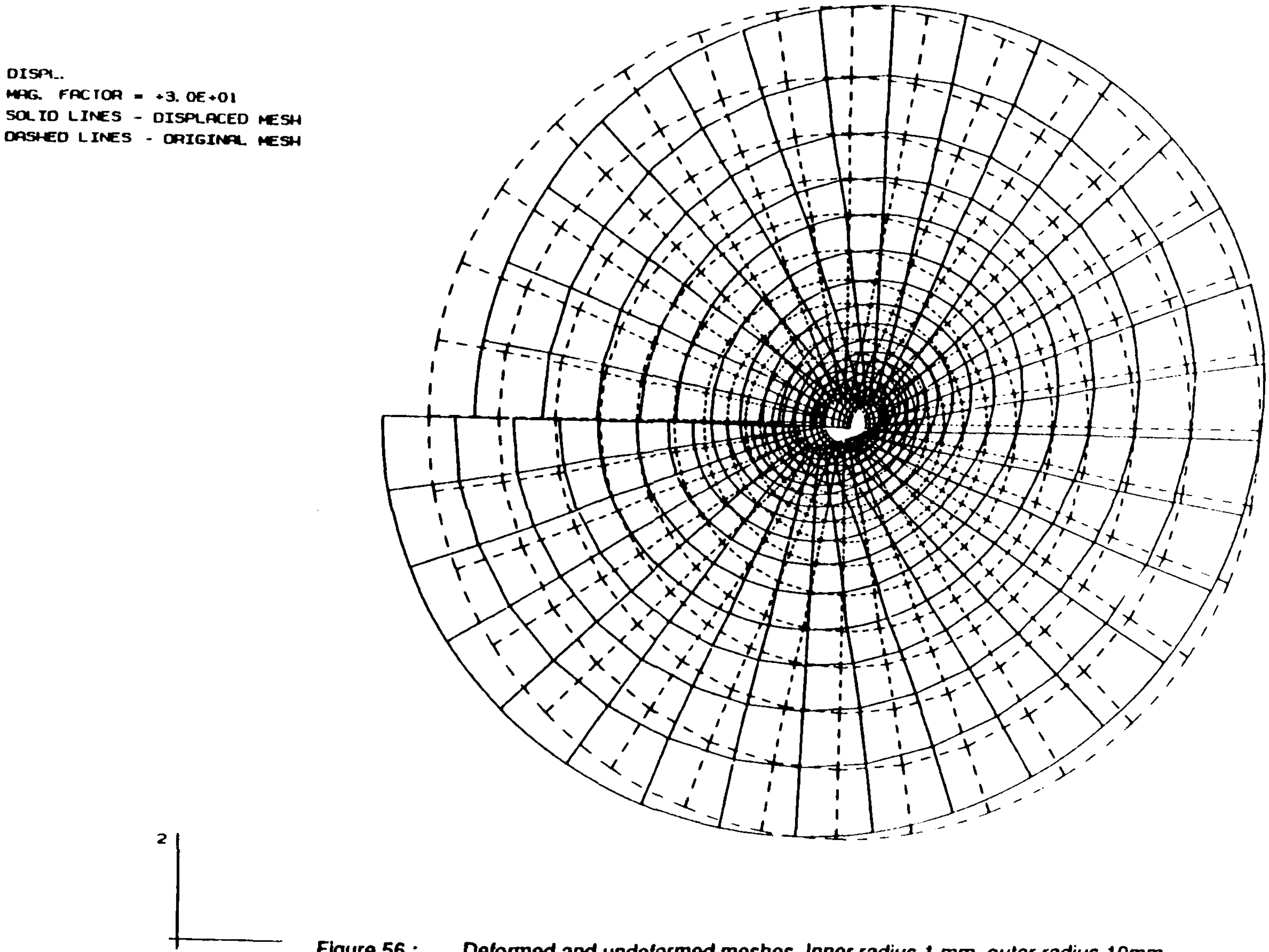
DISPL.
MAG. FACTOR = +3.0E+01
SOLID LINES - DISPLACED MESH
DASHED LINES - ORIGINAL MESH
2
1

Figure 56 : Deformed and undeformed meshes. Inner radius 1 mm, outer radius 10mm. Stress intensity factor ratio : K_I/K_{II} = 0/2018.

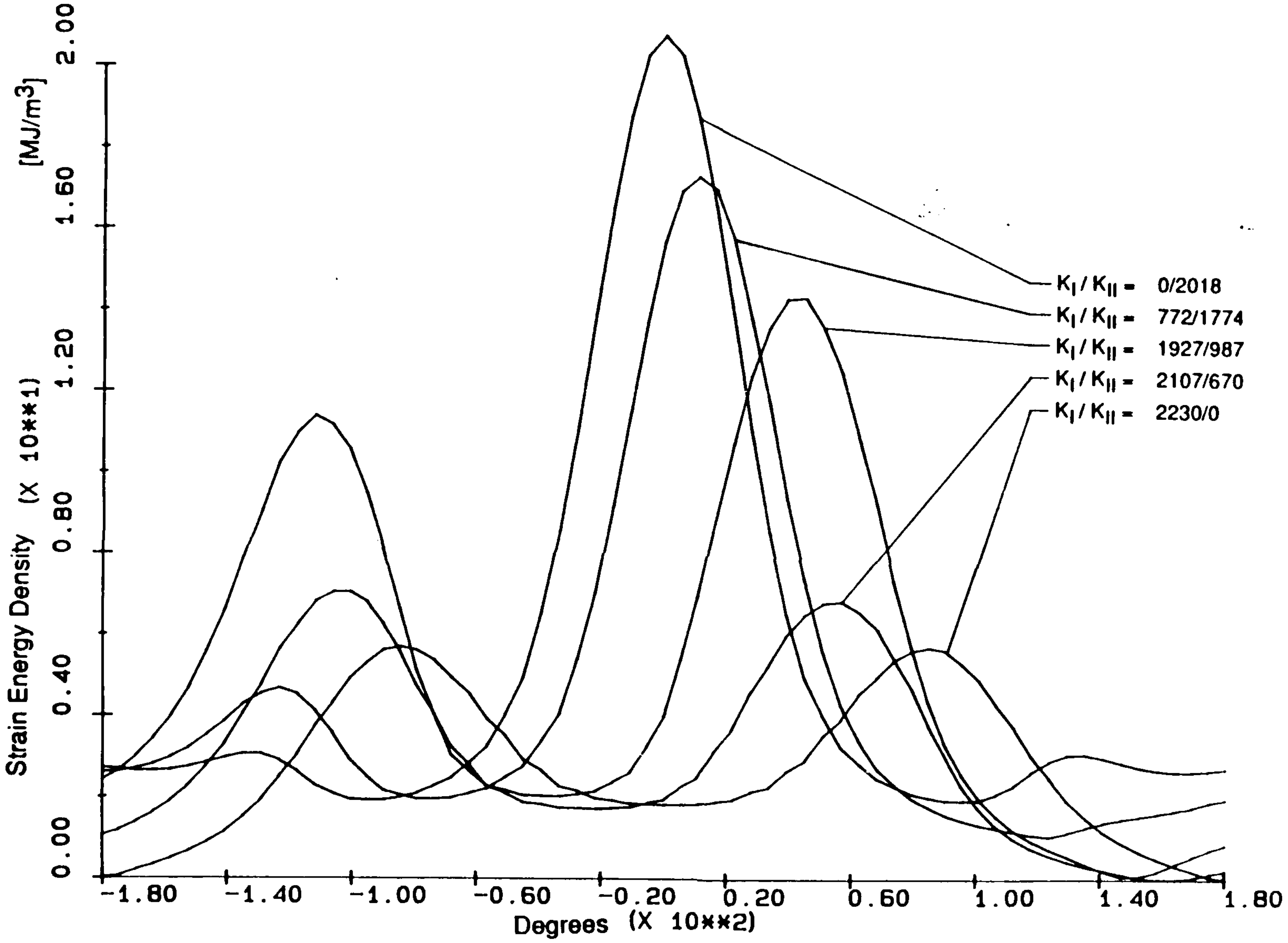

Figure 57 : Strain energy density along a circular path of radius r=0.4 mm around the crack tip for selected cases of mixed-mode loading.

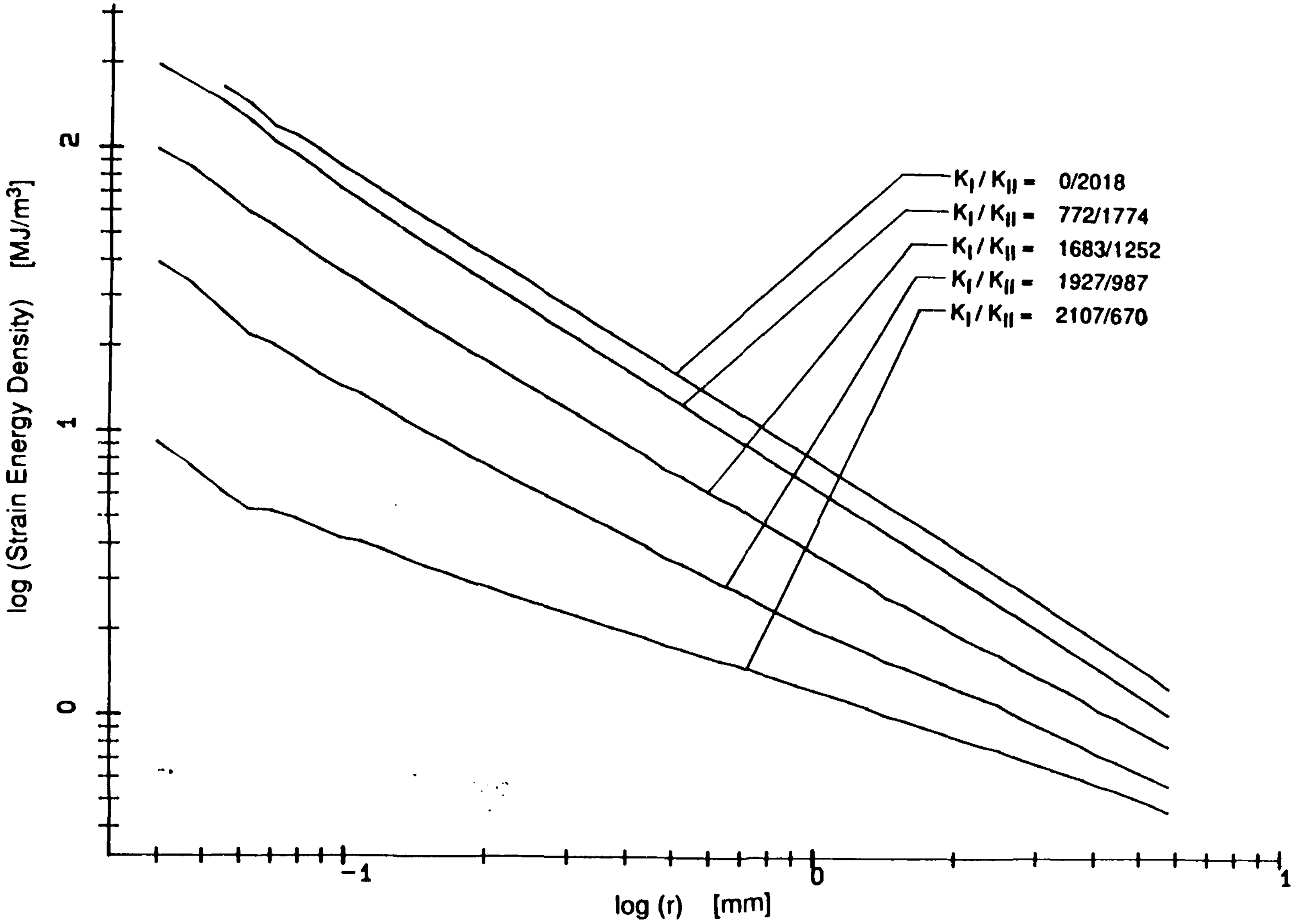

Figure 58 : Full logarithmic representation of the strain energy density along the line $\theta = 0°$ for selected mixed-mode cases.

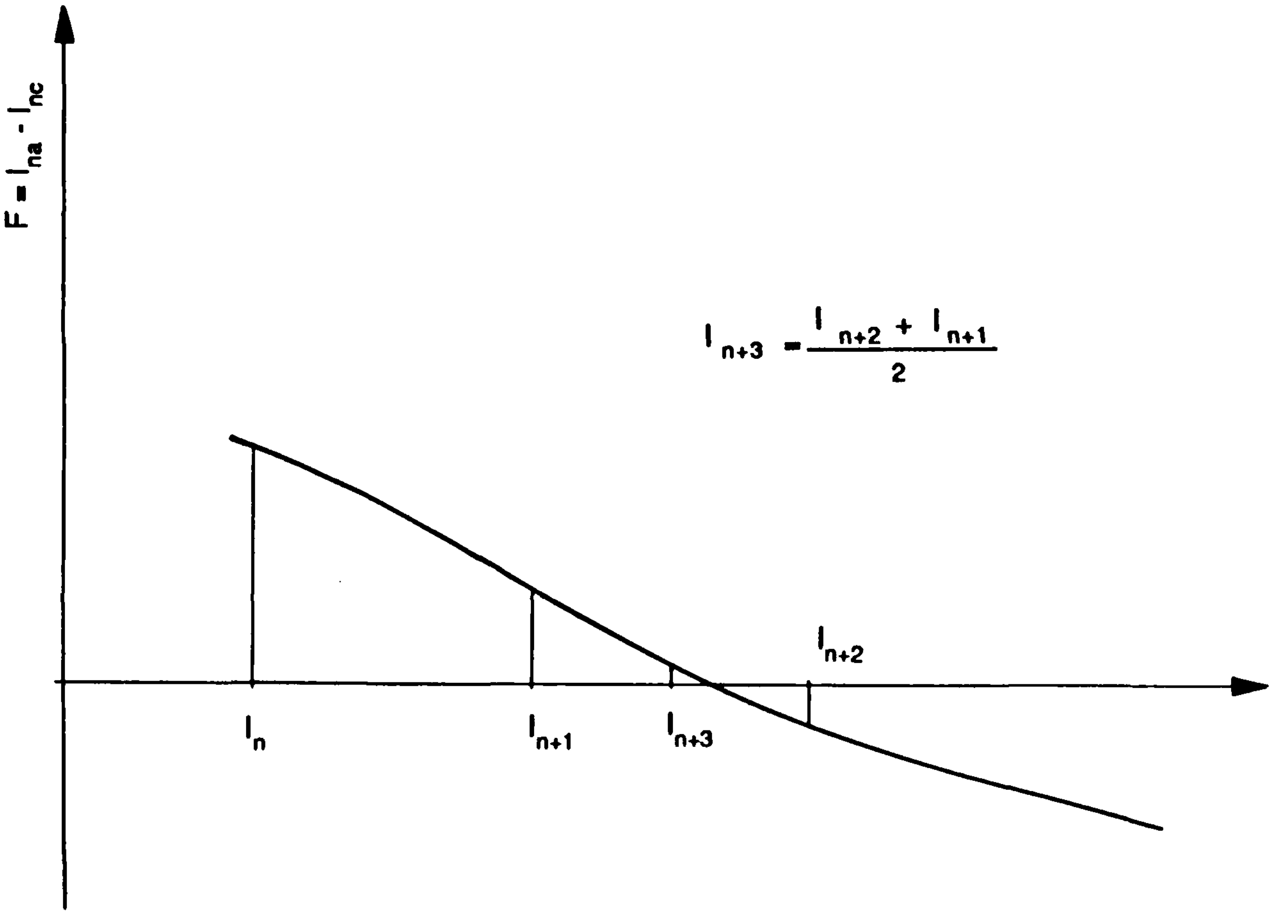
$F = I_{na} - I_{nc}$
$I_{n+3} = \frac{I_{n+2} + I_{n+1}}{2}$
I_{n+2}
I_n
I_{n+1}
I_{n+3}

Figure 59 : Graphical illustration of the interval halfing method.

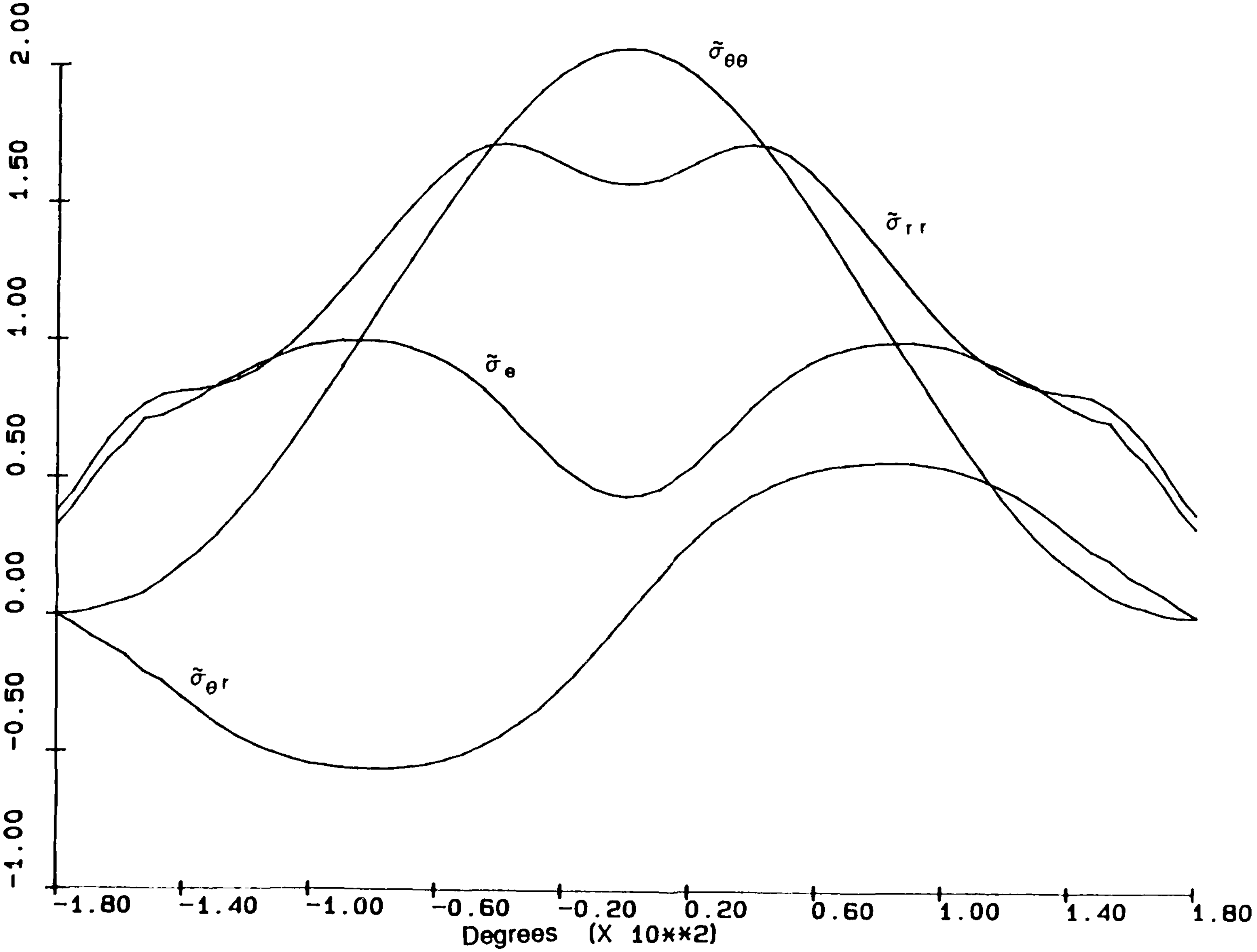

Figure 60 : Angular variation of the stress functions $\tilde{\sigma}_{rr}$,$\tilde{\sigma}_{\theta\theta}$,$\tilde{\sigma}_{e}$ and $\tilde{\sigma}_{r\theta}$.

Stress intensity factor ratio : K_I/K_{II} = 2230/0.

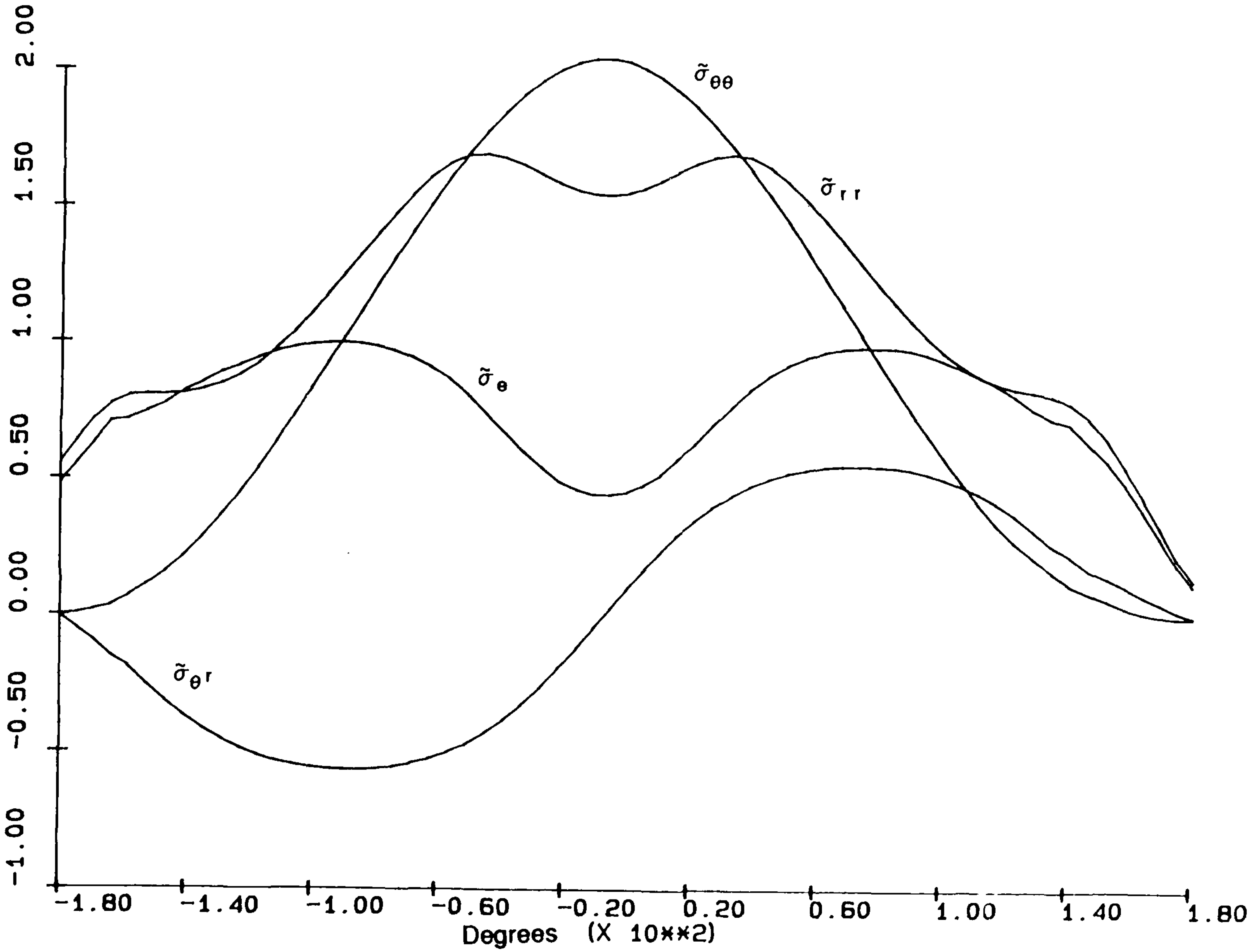

Figure 61 : Angular variation of the stress functions $\tilde{\sigma}_{rr}$, $\tilde{\sigma}_{\theta\theta}$, $\tilde{\sigma}_{\theta}$ and $\tilde{\sigma}_{r\theta}$.

Stress intensity factor ratio : $K_I/K_{II} = 2222/175$.

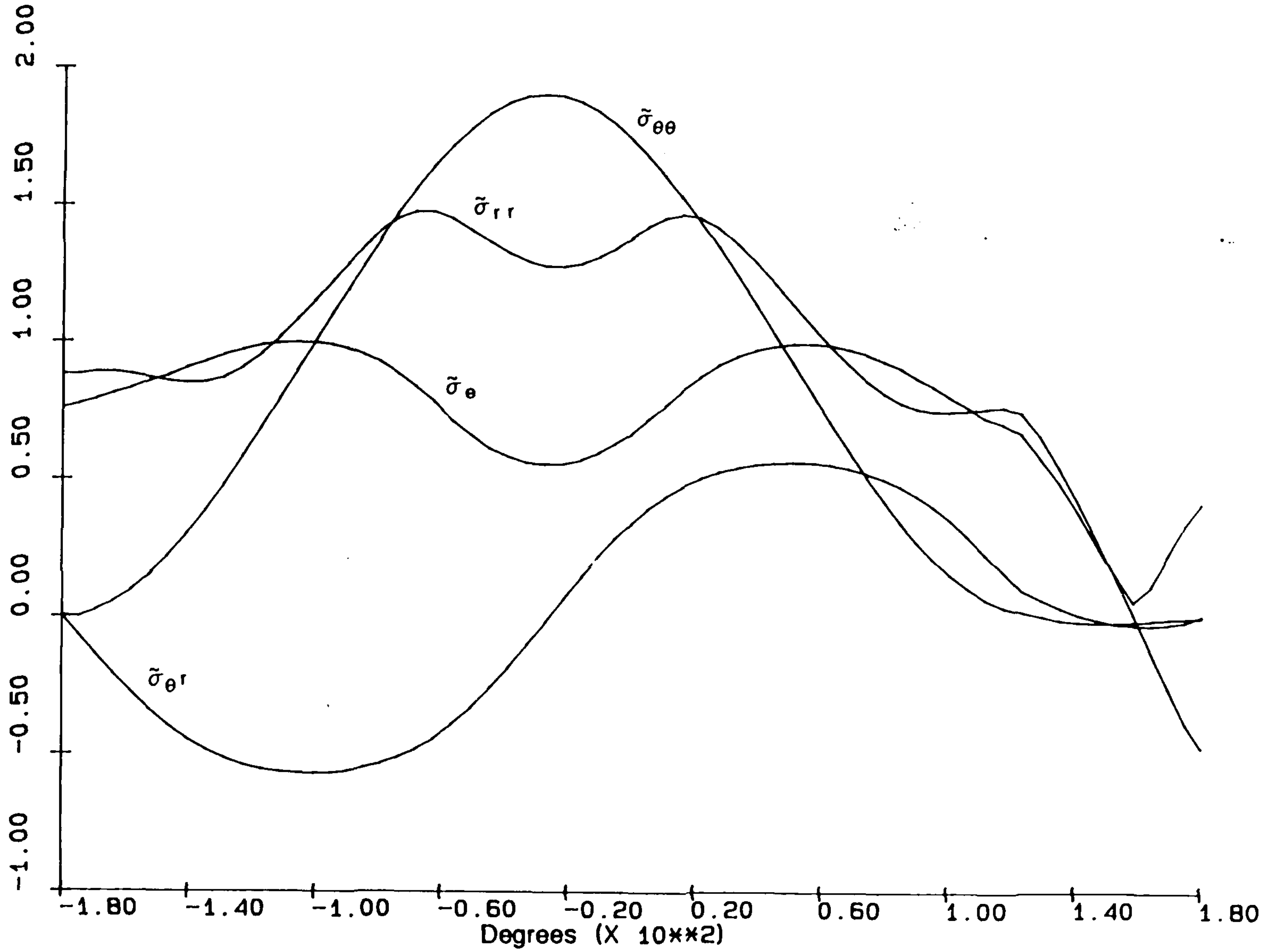

Figure 62 : Angular variation of the stress functions $\tilde{\sigma}_{rr}$,$\tilde{\sigma}_{\theta\theta}$,$\tilde{\sigma}_{e}$ and $\tilde{\sigma}_{r\theta}$.

Stress intensity factor ratio : K_I/K_{II} = 2107/670.

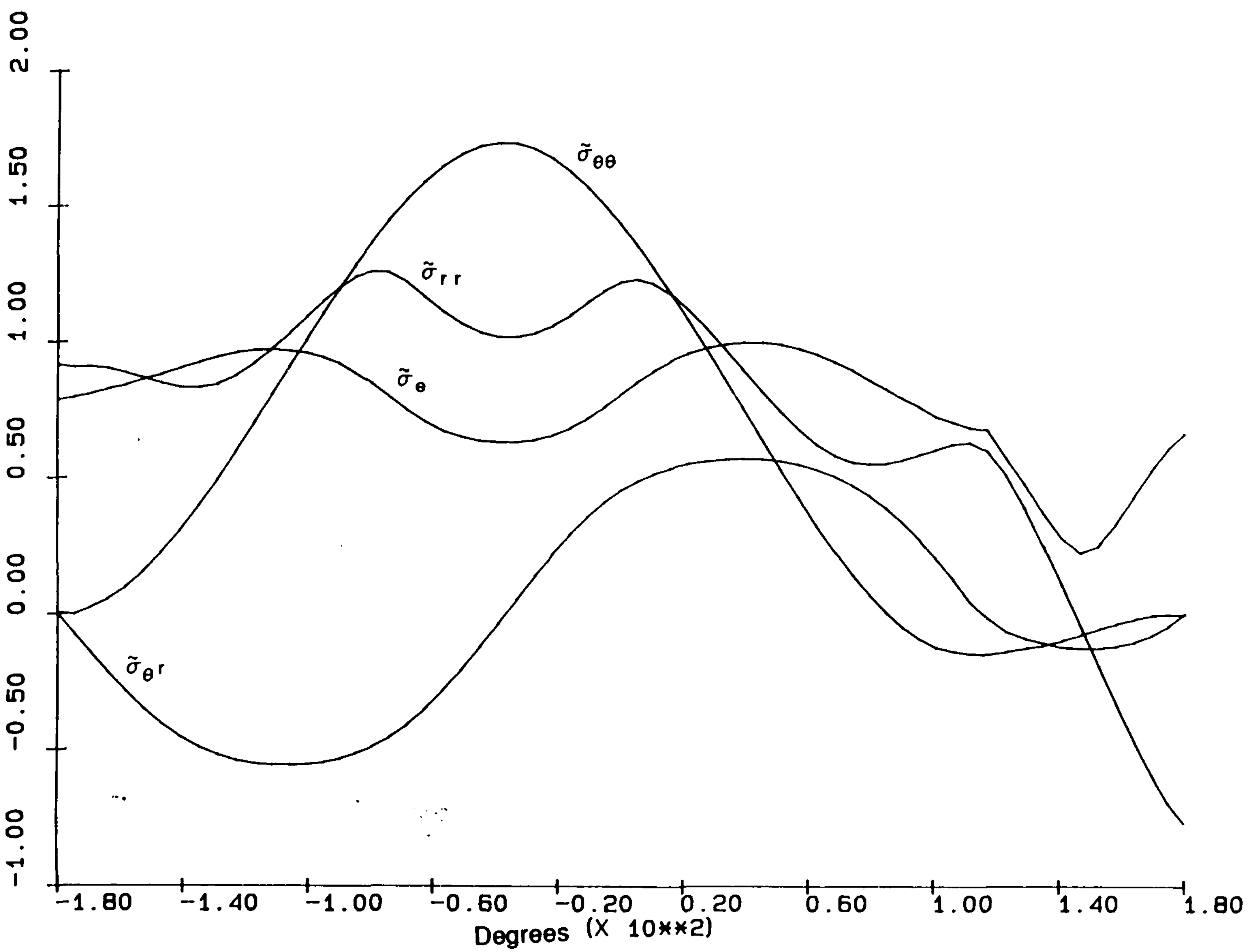

Figure 63 : Angular variation of the stress functions $\tilde{\sigma}_{rr}$,$\tilde{\sigma}_{\theta\theta}$,$\tilde{\sigma}_{e}$ and $\tilde{\sigma}_{r\theta}$.

Stress intensity factor ratio : K_I/K_{II} = 1927/987.

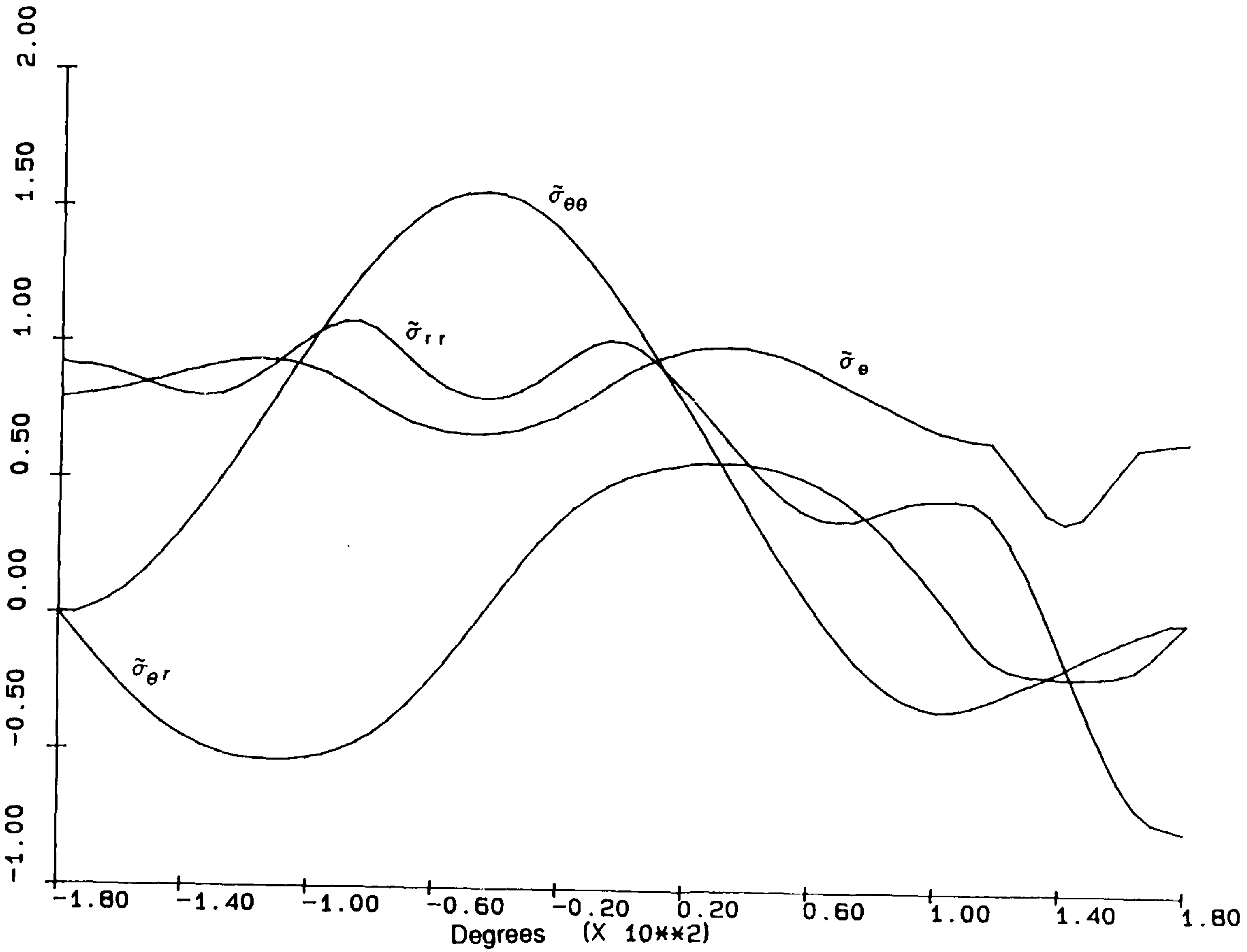

Figure 64 : Angular variation of the stress functions $\tilde{\sigma}_{rr}$,$\tilde{\sigma}_{\theta\theta}$,$\tilde{\sigma}_{e}$ and $\tilde{\sigma}_{r\theta}$.

Stress intensity factor ratio : K_I/K_{II} = 1683/1252.

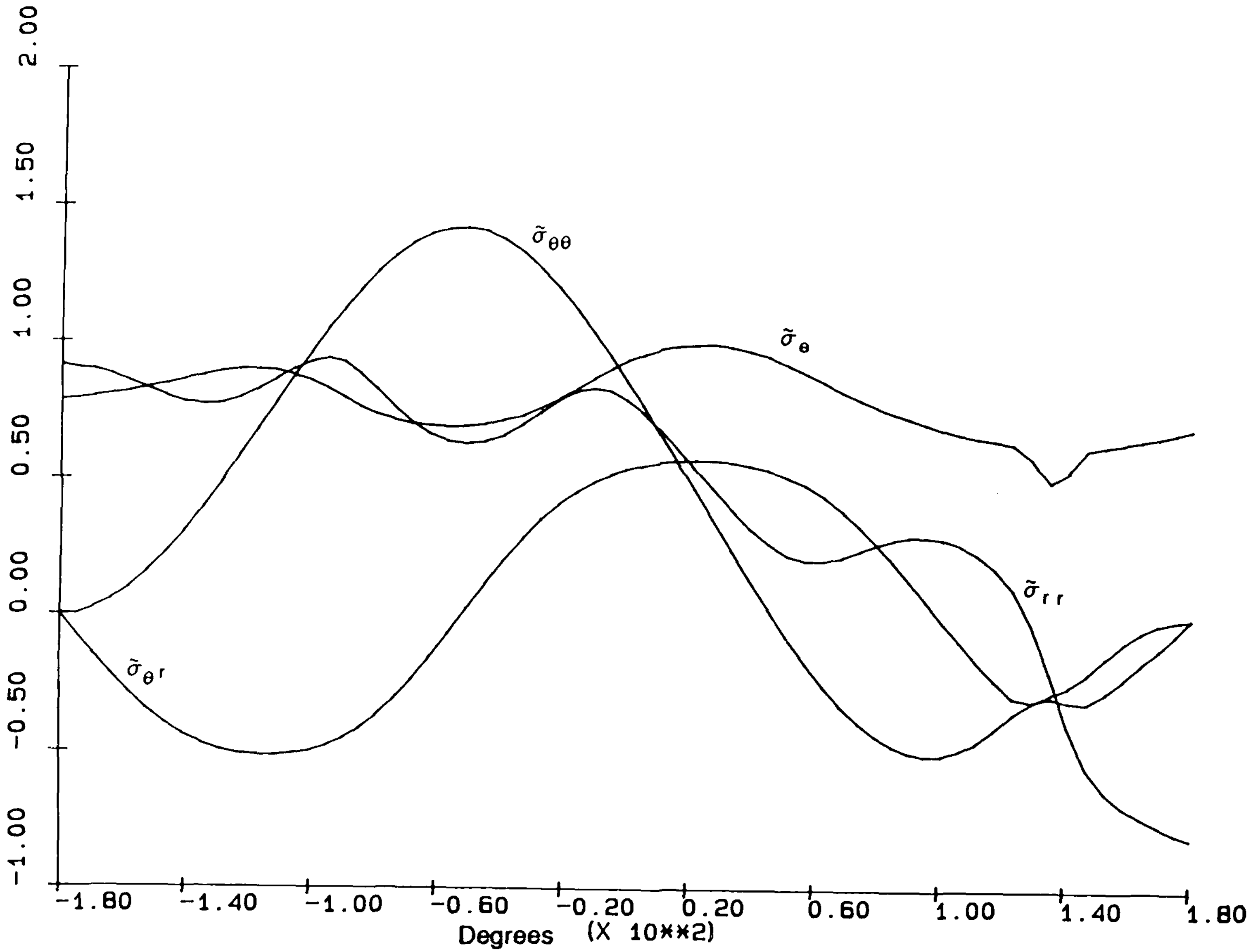

Figure 65 : Angular variation of the stress functions $\tilde{\sigma}_{rr}$, $\tilde{\sigma}_{\theta\theta}$, $\tilde{\sigma}_{\theta}$ and $\tilde{\sigma}_{r\theta}$.

Stress intensity factor ratio : K_I/K_{II} = 1405/1462.

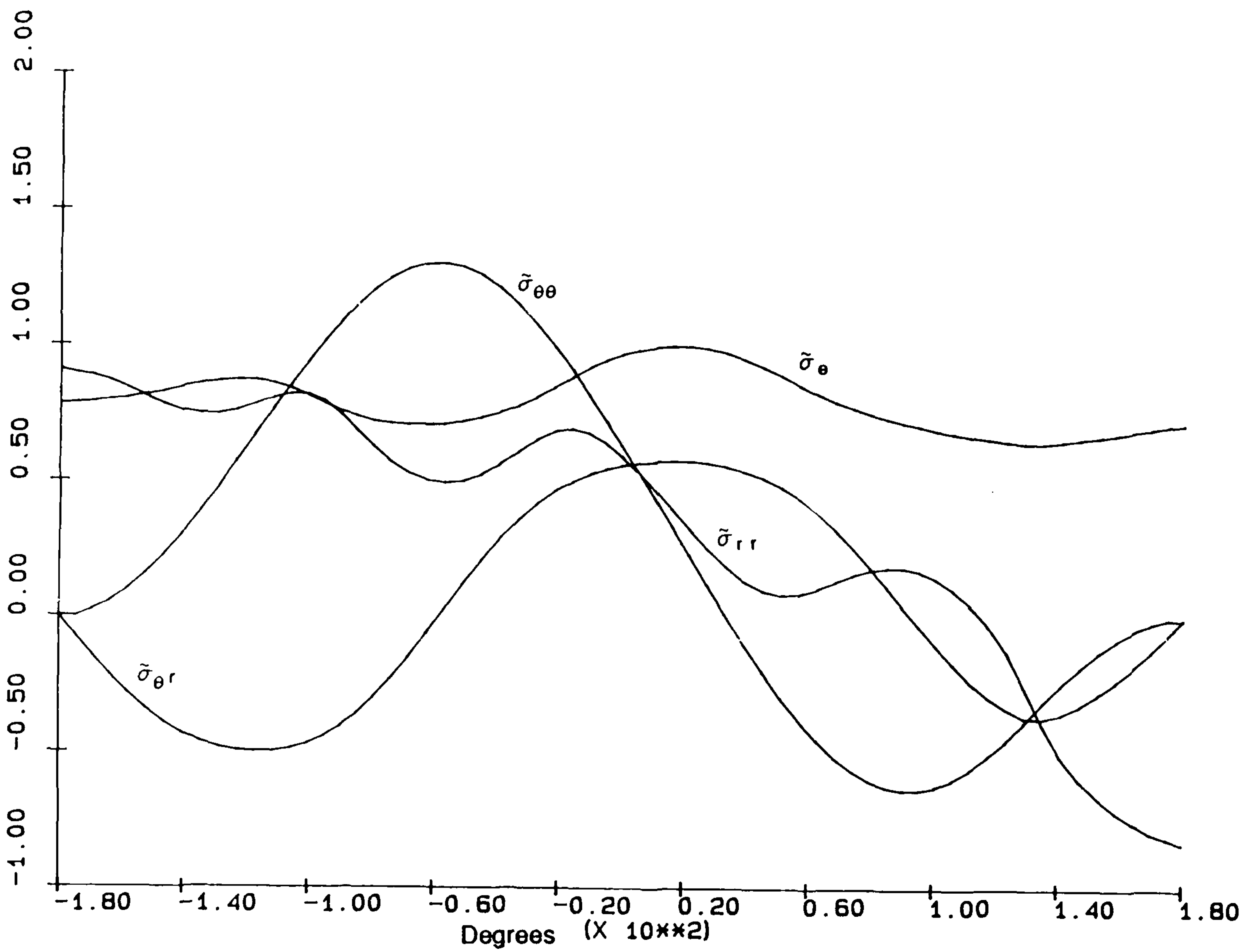

Figure 66 : Angular variation of the stress functions $\tilde{\sigma}_{rr}$, $\tilde{\sigma}_{\theta\theta}$, $\tilde{\sigma}_{e}$ and $\tilde{\sigma}_{r\theta}$.

Stress intensity factor ratio : K_I/K_{II} = 1098/1633.

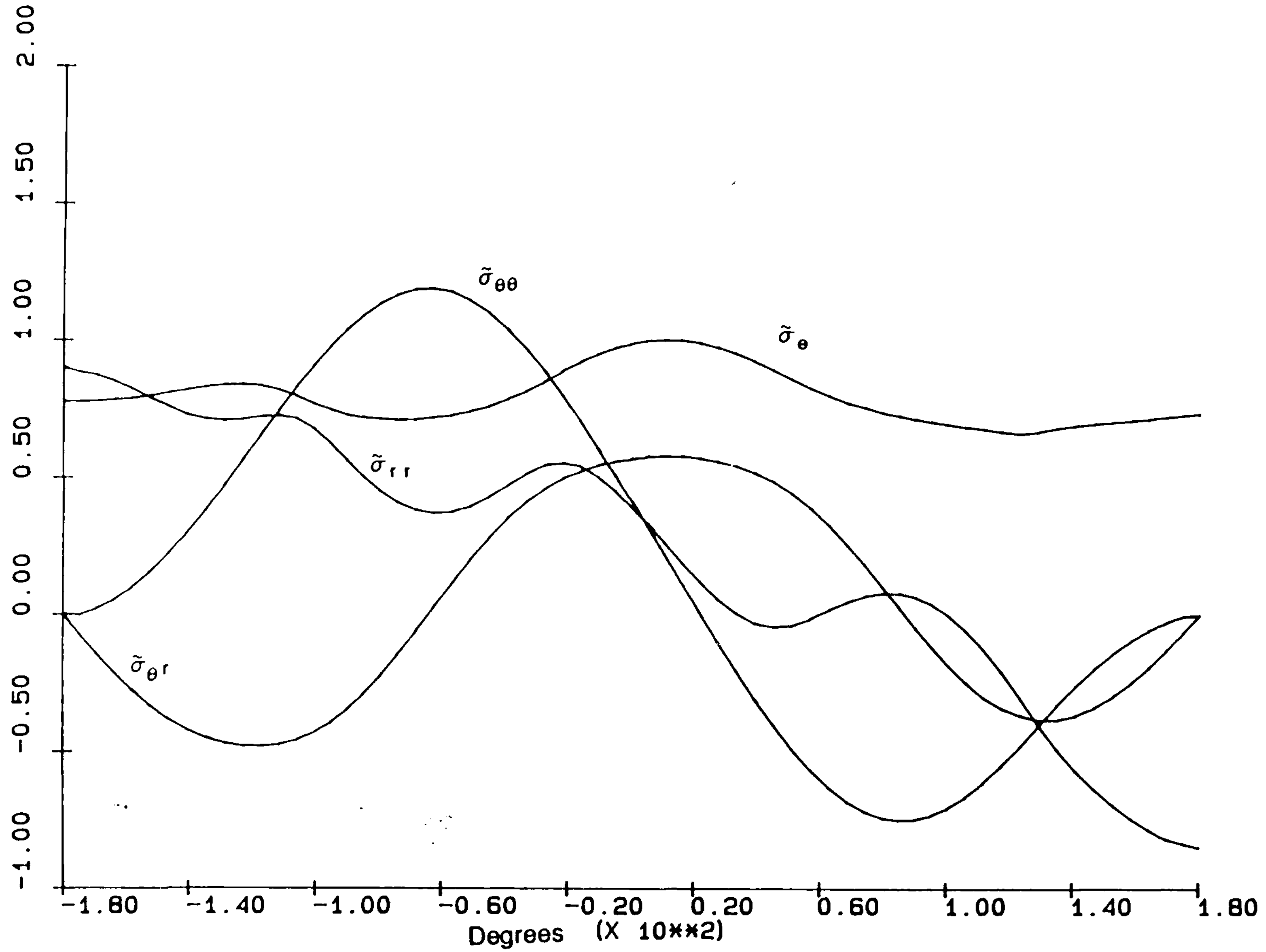

Figure 67 : Angular variation of the stress functions $\tilde{\sigma}_{rr}$, $\tilde{\sigma}_{\theta\theta}$, $\tilde{\sigma}_{e}$ and $\tilde{\sigma}_{r\theta}$.

Stress intensity factor ratio : K_I/K_{II} = 772/1774.

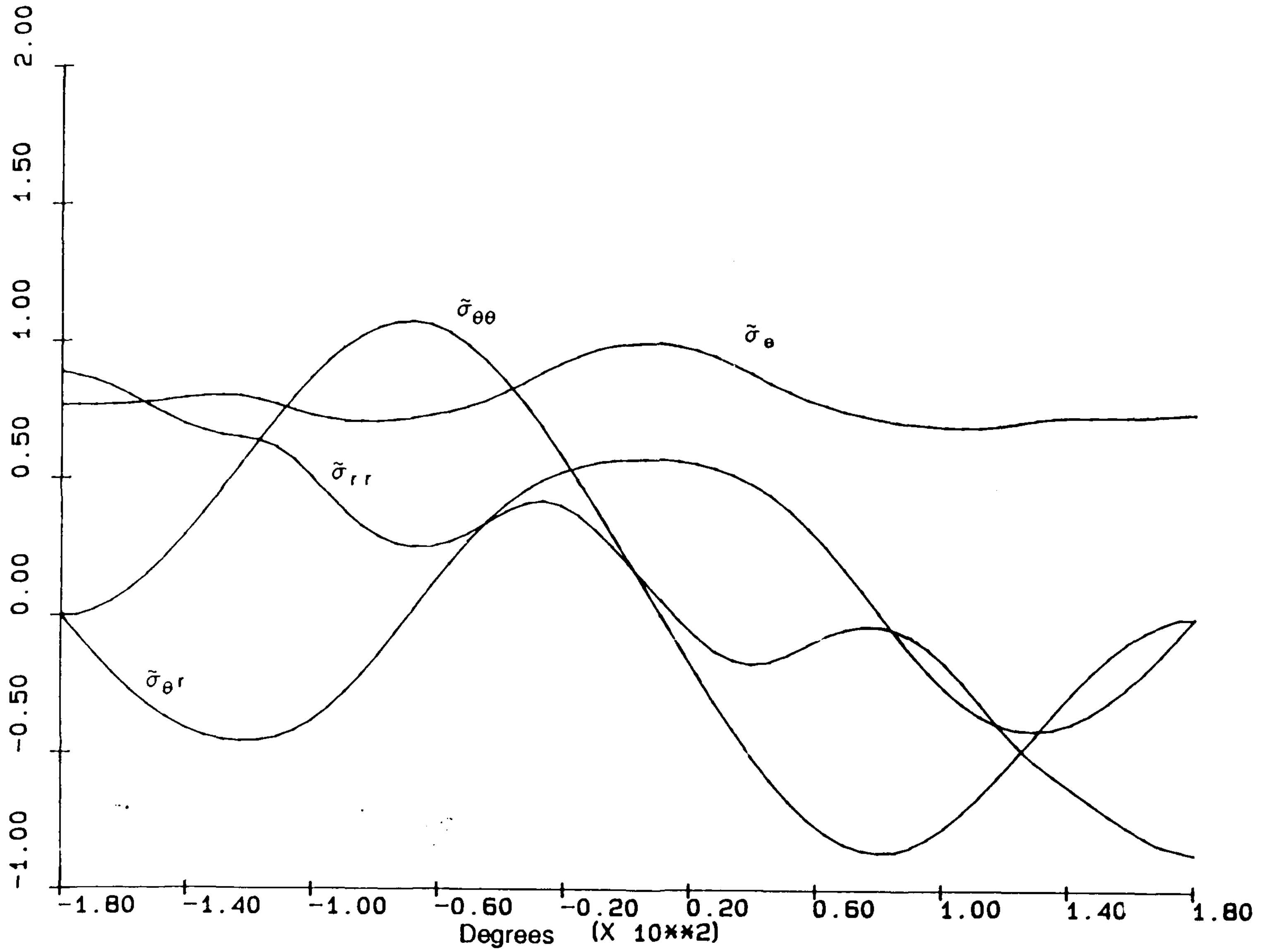

Figure 68 : Angular variation of the stress functions $\tilde{\sigma}_{rr}$, $\tilde{\sigma}_{\theta\theta}$, $\tilde{\sigma}_{\theta}$ and $\tilde{\sigma}_{r\theta}$.

Stress intensity factor ratio : K_I/K_{II} = 396/1903.

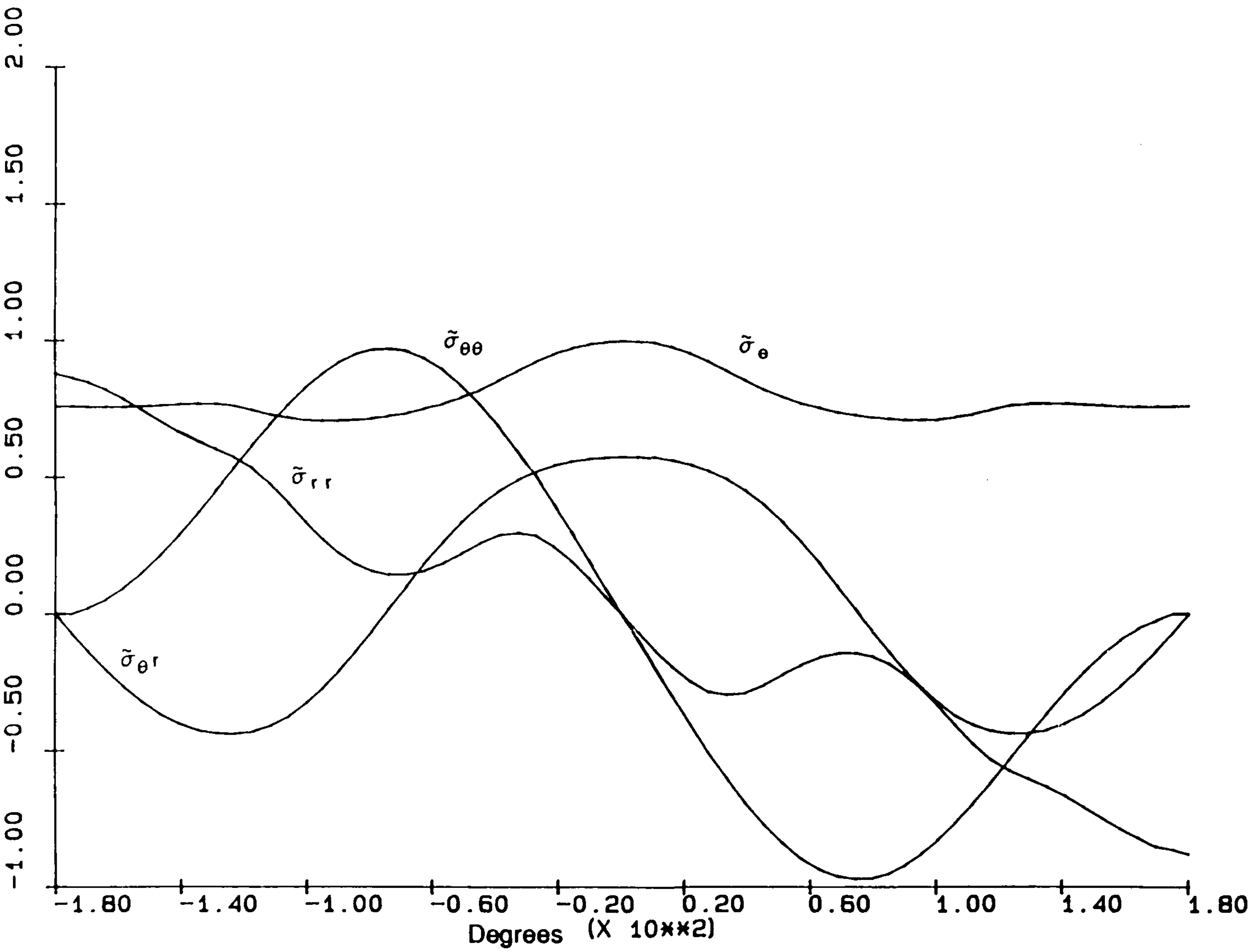

Figure 69 : Angular variation of the stress functions $\tilde{\sigma}_{rr}$, $\tilde{\sigma}_{\theta\theta}$, $\tilde{\sigma}_{e}$ and $\tilde{\sigma}_{r\theta}$.

Stress intensity factor ratio : K_I/K_{II} = 0/2018.

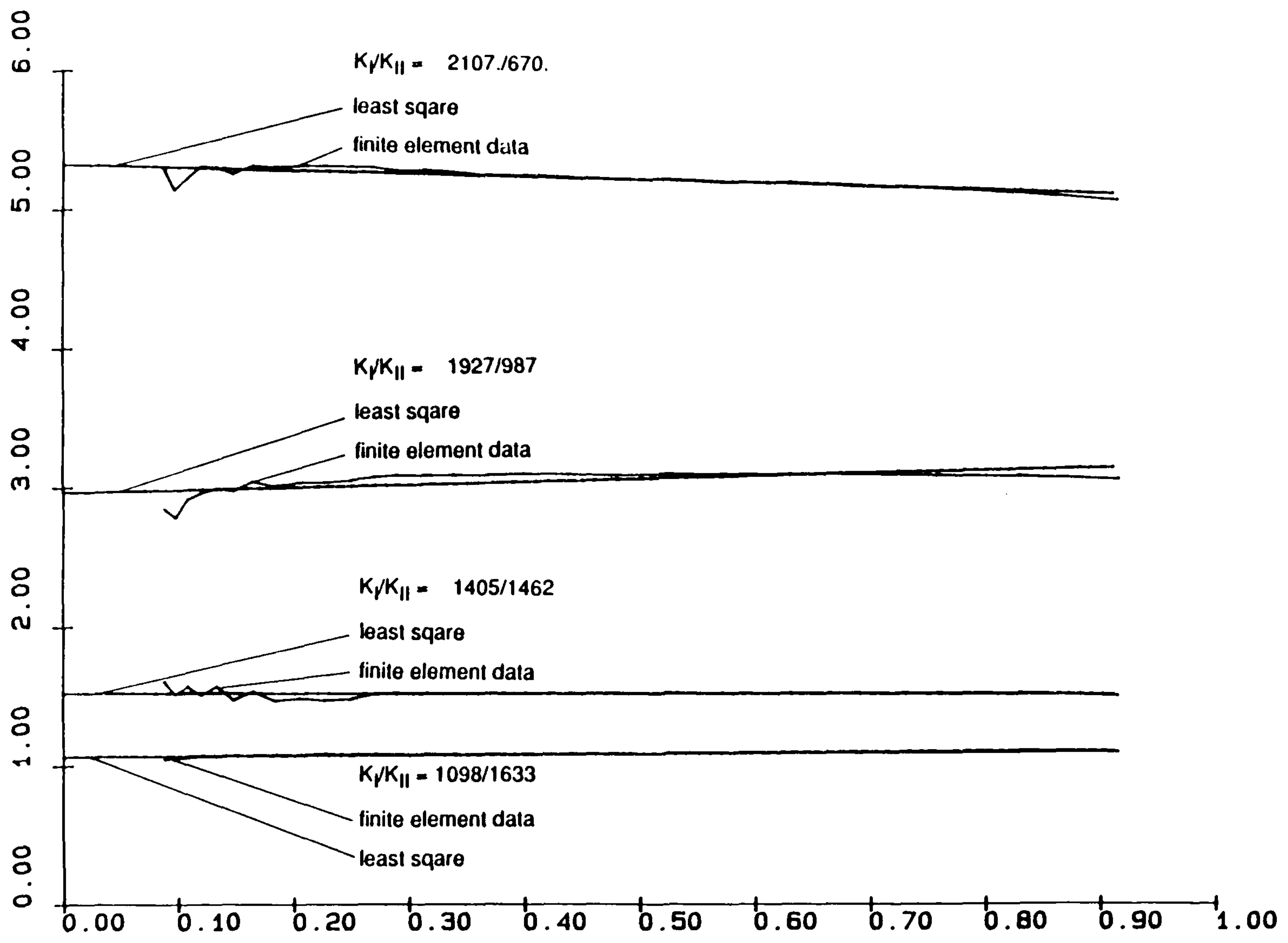

Figure 70 : Ratio of $\sigma_{\theta\theta}/\sigma_{r\theta}$ along the line θ =0° for selected mixed-mode cases.

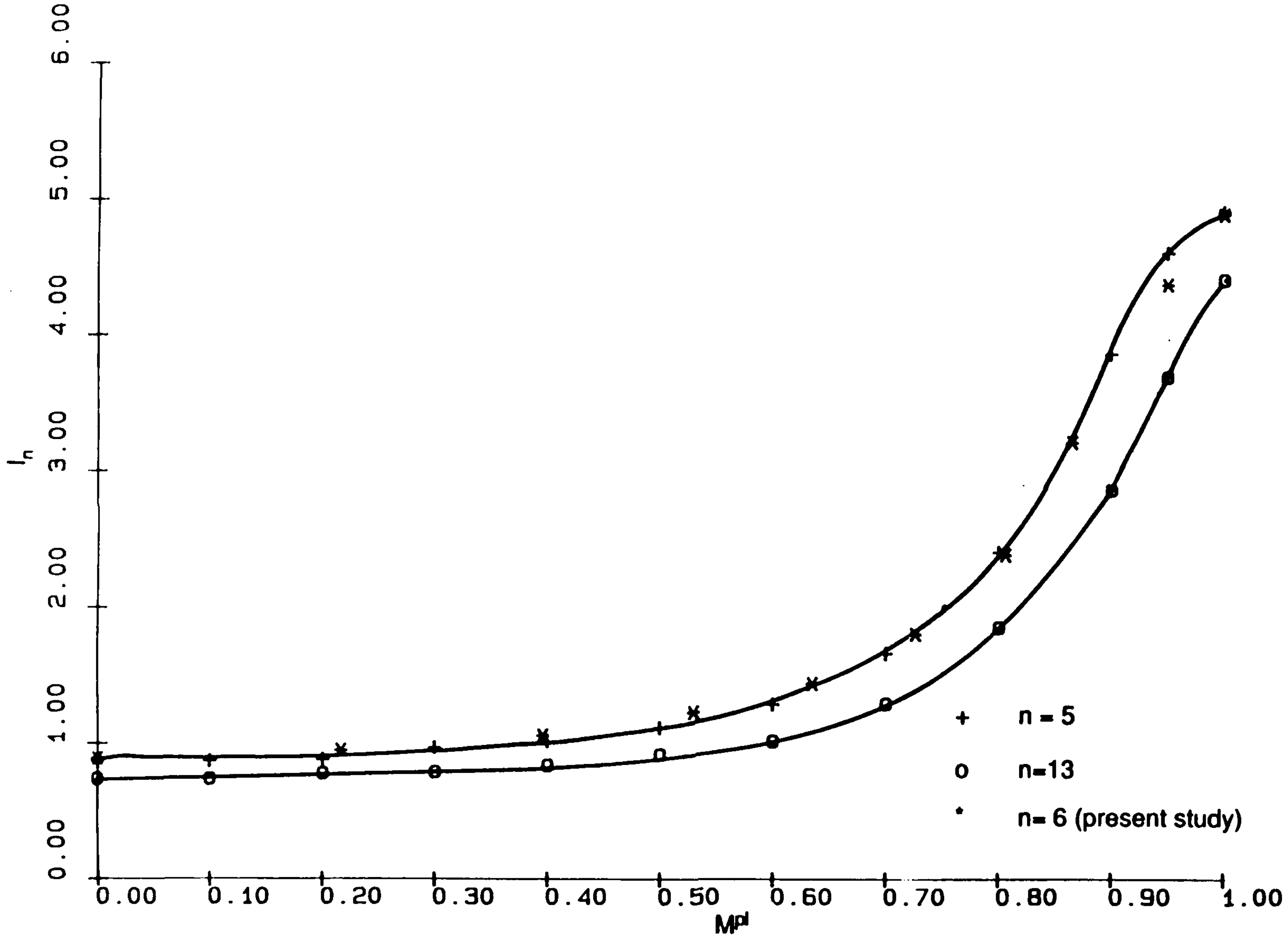

Figure 71 : I_n versus plastic mixity parameter M^{pl} for all cases of mixed modes considered. Comparison with the values of I_n obtained by Shih [27].

No.	K_I - Value [$N/\sqrt{mm^3}$]	K_{II} - Value [$N/\sqrt{mm^3}$]	Mixity Parameter (M^e)	
1	2230.0	0.	1.	pure mode I
2	2222.9	175.8	0.949	
3	2107.7	670.8	0.804	
4	1927.0	987.6	0.698	
5	1683.8	1252.0	0.584	
6	1405.6	1462.2	0.487	
7	1098.7	1633.8	0.377	
8	772.2	1774.5	0.261	
9	396.3	1903.8	0.130	
10	0.	2018.3	0.	pure mode II

Table 1 : K_I - K_{II} -values according to the fracture criterion by Sih. The elastic mixity parameter M^e is given by equation (8.1)

$$N_1 = \frac{1}{4} (1 - \xi) (1 - \eta) (-1 - \xi - \eta)$$

$$N_2 = \frac{1}{4} (1 + \xi) (1 - \eta) (-1 -+\xi - \eta)$$

$$N_3 = \frac{1}{4} (1 + \xi) (1 + \eta) (-1 + \xi + \eta)$$

$$N_4 = \frac{1}{4} (1 - \xi) (1 + \eta) (-1 - \xi + \eta)$$

$$N_5 = \frac{1}{2} (1 - \xi^2) (1 - \eta)$$

$$N_6 = \frac{1}{2} (1 + \xi) (1 - \eta^2)$$

$$N_7 = \frac{1}{2} (1 - \xi^2) (1 + \eta)$$

$$N_8 = \frac{1}{2} (1 - \xi) (1 - \eta^2)$$

Table 2 : Shape functions of the eight-node isoparametric finite element.

Chemical Composition in Weight Percent :

Element :	C	Mn	P	S	Cu	Si	Ni	Cr	Mo	Co	N
	0.03	1.62	0.034	0.015	0.31	0.43	10.04	18.3	0.31	0.15	0.07

Material Data :

Property :	Symbol	Unit	Value
Young's modulus	: E	MPa	203800.
Yield stress	: σ_y	MPa	265.
Maximal stress	: σ_{max}	MPa	640.
Poisson's ratio	: υ	-	0.3
Critical stress intensity factor	: K_{IC}	$N/\sqrt{mm^3}$	4300.
Critical J-integral value	: J_{1C}	N/mm	108.

Table 3 : Chemical composition and material data of the stainless steel A304.

No.	J-Integral Value (Vitual Crack Extension) [N/mm]	J-integral Value (Direct Integration) [N/mm]	Deviation %
1	20.49	20.50	0.05
2	20.97	21.17	0.95
3	-	20.21	-
4	-	18.94	-
5	-	17.19	-
6	-	15.46	-
7	11.57	11.88	2.61
8	9.94	10.22	2.74
9	9.28	9.87	5.77
10	9.19	9.73	5.55

Table 4 : Comparison of J-integral values obtained by the virtual crack extension method and the direct integration method.

Mixed Modes :

Number :	1	2	3	4	5	6	7	8	9	10
K_I :	2230.	2223.	2107.	1927.	1638.	1405.	1098.	772.	396.	0.
K_{II} :	0.	176.	671.	988.	1252.	1462.	1633.	1775.	1904.	2018.
HRR-Zone :										
inner radius :	0.08	0.08	0.08	0.08	0.1	0.1	0.1	0.1	0.2	0.2
outer radius :	0.12	0.12	0.3	1.	4.	6.	8.	8.	9.	9.
power :	-0.114	-0.119	-0.134	-0.134	-0.135	-0.140	-0.140	-0.141	-0.142	-0.143
Interm. Zone :										
inner radius :	0.15	0.15	0.9	2.	5.	8.	-	-	-	-
outer radius :	1.	1.	2.2	5.	10.	12.	-	-	-	-
power :	-0.0391	-0.041	-0.041	-0.060	-0.041	-0.053	-	-	-	-
Elastic Zone:										
inner radius :	2.	5.	6.	-	-	-	-	-	-	-
outer radius :	12.	12.	12.	-	-	-	-	-	-	-
power :	-0.51	-0.499	-0.50	-	-	-	-	-	-	-

Table 5 : Powers characterizing singular behavior of the effective von Mises stress along the line $\theta = 0°$ ahead of the crack tip. (All distances are given in mm)

Mixed Mode Cases :

No.	K_I [N/√mm^3]	K_{II} [N/√mm^3]	Predicted Fracture Angle	Magnitude of Strain Energy Density [MJ/m^3]
1	2230.	0.	0.	1.83
2	2222.9	175.8	-10.48	1.82
3	2107.7	670.8	-21.60	1.71
4	1927.0	987.6	-33.39	2.00
5	1638.8	1252.0	-45.00	2.22
6	1405.6	1462.2	-50.80	2.47
7	1098.7	1633.8	-68.03	1.89
8	772.2	1774.5	-79.15	1.95
9	396.3	1903.8	-84.56	1.82
10	0.	2018.3	-90.00	1.925

Table 6 : Fracture angle θ and corresponding strain energy density 0.4 mm from the crack tip for all mixed-mode cases considered.

Mixed Mode Cases :

No.	K_I	K_{II}	Range of Distance from Crack Tip Considered [mm]	Power of the Singularity	Correlation
	[N/√mm³]				
1	2230.0	0.	0.04 - 0.12	-0.622	-0.9999
2	2222.9	175.8	0.04 - 0.12	-0.699	-0.9996
3	2107.7	670.8	0.04 - 0.20	-0.880	-0.9994
4	1927.0	987.6	0.04 - 0.40	-0.943	-0.9997
5	1638.8	1252.0	0.04 - 0.80	-0.983	-0.9998
6	1405.6	1462.2	0.04 - 1.0	-1.030	-0.9999
7	1098.7	1633.8	0.04 - 1.0	-1.029	-0.9999
8	772.2	1774.5	0.04 - 1.0	-1.030	-0.9998
9	396.3	1903.8	0.04 - 1.0	-1.002	-0.9998
10	0.	2018.3	0.04 - 1.0	-1.000	-0.9999

Table 7 : Powers of the singularity of the strain energy density in the vicinity of the crack tip along the line $\theta=0°$ from least square approximation.

APPENDIX E: DUCTILE CRACK GROWTH SIMULATION - LOCAL DEFORMATION AND FIELD VARIABLE ANALYSIS

Ductile Crack Growth Simulation - Local Deformation and Field Variable Analysis

By

Kurt Kunze
Vordiplom September 1984, Universität Stuttgart

A Thesis submitted to

The Faculty of
The School of Engineering and Applied Science
of The George Washington University
in partial satisfaction of the requirements for the
degree of Master of Science in Engineering

December 1987

Thesis directed by
Erwin Thomas Moyer Jr., Ph.D.
Associate Professor of Engineering and Applied Science

ACKNOWLEDGMENTS

I would like to express my deep appreciation and thanks to my thesis advisor Professor E. Thomas Moyer Jr. for his technical guidance, support and patience during the development of this thesis. The numerous fruitful discussions with him helped me to develop an understanding for the fields of fracture mechanics and finite element methods.

This thesis research was carried out as part of the exchange program between The George Washington University and the Universität Stuttgart. I wish to express my gratitude to Professor Kussmaul, Professor Dietmann and Professor Liebowitz who are responsible for this program and made this project possible.

I would also like to thank the DAAD (German Academic Exchange Service) and the Studienstiftung des deutschen Volkes who also partly sponsored my study in the United States as well as this thesis research.

The research was carried out on an IBM 4341 provided to The George Washington University as part of the CAD - CAM initiative grant program from IBM. This grant also included the CAEDS system written by Structural Dynamics Research Corporation. Hibbitt, Karlsson and Sorensen made the use of the finite element system, ABAQUS, available to The George Washington University. I am indebted to all companies for providing the resources for this research work.

Finally, I am grateful to all those who made the successful completion of this thesis research possible.

ABSTRACT

In the present work, slow stable crack growth in a ductile material (A533B steel) is simulated numerically with a widely used state of the art commercial finite element code (ABAQUS). The finite element formulation uses the J_2 flow rule of incremental plasticity based on small deformation theory. An experimentally obtained load versus crack growth relation is employed as input and the finite element mesh models the upper half of a modified compact tension specimen. The material behavior is modeled with power law hardening (n = 10). Two meshes are used for the crack growth simulation: a coarse mesh with 1874 elements and 1946 nodes, and a fine mesh with 2914 elements and 3002 nodes. The finite element meshes consist of four - node bilinear plane strain isoparametric elements with eight degrees of freedom (type CPE4). Crack extension of eight millimeters for the coarse mesh and one millimeter for the fine mesh were simulated. The nodal release technique is used as a numerical crack growth simulation technique.

The evaluation of the results emphasizes two points: (i) to determine how well two crack growth criteria (J/CTOD and CTOA) characterize mode 1 crack extension under plane strain conditions and in what interval range they are applicable, and (ii) to examine the singular field variables at the onset of crack growth and associated with the quasi - static crack extension. The purpose of the second evaluation is to determine whether the singularity fields suggested by asymptotic methods exist independently from each other (whether a transition point between two different singularity fields can be identified) or whether a superposition of the singularity fields occurs ahead the stable advancing crack tip.

TABLE OF CONTENTS

ACKNOWLEDGMENTS

ABSTRACT

TABLE OF CONTENTS

LIST OF FIGURES

LIST OF TABLES

NOMENCLATURE

1. INTRODUCTION

2. NUMERICAL CRACK GROWTH SIMULATION TECHNIQUES

3. PREVIOUS INVESTIGATIONS OF NUMERICAL CRACK GROWTH SIMULATION

4. PROCEDURE OF THE PRESENT INVESTIGATION

5. FINITE ELEMENT MODELING
   - 5.1 MATERIAL
   - 5.2 MODEL DEFINITION
   - 5.3 FINITE ELEMENT MESH GENERATION
   - 5.3.1 MODEL CHECKING
   - 5.3.2 BANDWITH AND WAVEFRONT OPTIMIZATION

6. THE FINITE ELEMENT METHOD FOR STRUCTURAL ANALYSIS
   - 6.1 THE FINITE ELEMENT FORMULATION
   - 6.2 ELEMENT REPRESENTATION
   - 6.3 PROCEDURE FOR SOLVING THE FINITE ELEMENT FORMULATION
   - 6.4 COMPUTATIONAL PROCEDURE FOR THE PLASTICITY PROBLEM

7. INVESTIGATED CRITERIA FOR STABLE CRACK GROWTH
  7.1 J - INTEGRAL INTRODUCTION
  7.1.1 J - INTEGRAL DETERMINED BY THE VIRTUAL CRACK EXTENSION METHOD
  7.1.2 J - INTEGRAL AS CRITERION FOR STABLE CRACK GROWTH
  7.1.3 CALCULATION OF THE J - INTEGRAL
  7.1.4 DISCUSSION OF THE J - INTEGRAL AS CRITERION FOR STABLE CRACK GROWTH
  7.2 CRACK PROFILE GEOMETRY
  7.2.1 DEFINITION OF THE CRACK PROFILE PARAMETER
  7.2.2 DISCUSSION OF THE CRACK PROFILE PARAMETER
  7.2.3 CRACK TIP OPENING DISPLACEMENT (CTOD) - RESULTS
  7.2.4 CRACK TIP OPENING ANGLE (CTOA) - RESULTS
  7.3 RELATION BETWEEN J AND CTOD

8. INVESTIGATIONS OF THE FIELD VARIABLES FOR STABLE CRACK GROWTH
  8.1 THE FINITE ELEMENT RESULTS OF THE FIELD VARIABLES
  8.2 DISCUSSION OF THE FIELD VARIABLE RESULTS

9. CONCLUSIONS AND RECOMMENDATIONS FOR FUTURE INVESTIGATIONS

REFERENCES
FIGURES
TABLES

LIST OF FIGURES

Figure 1: The three local independent kinematic movements of the upper and lower surface with respect to each other.

Figure 2: Idealized constitutive material behavior.

Figure 3: Cottrell's model of cleavage fracture.

Figure 4: The schematic representation of a commonly used simple microscopic fracture criterion.

Figure 5: Local crack growth simulation in three dimensions.

Figure 6: Stiffness reduction accomplished with spring elements.

Figure 7: Load versus crack growth.

Figure 8: Step - wise crack growth simulation.

Figure 9: Stress - strain curve (A533B steel).

Figure 10: Dimensions of the employed Compact Tension specimen.

Figure 11a - 11b: Finite element modeling of the Compact Tension specimen (coarse mesh).

Figure 12a - 12c: Finite element modeling of the Compact Tension specimen (fine mesh).

Figure 13: Boundary conditions.

Figure 14: Eight d. o. f. bilinear element.

Figure 15: Mapping of the eight d. o. f. bilinear element from natural coordinates into xy - space.

Figure 16: Locations of the Gauss quadrature integration points within an eight d. o. f. bilinear isoparametric element.

Figure 17: Definition of the line of the J - integral around a notch.

Figure 18: Typical J - resistance curve.

Figure 19: Schematic of the fields surrounding a growing crack [34].

Figure 20: Evaluation line for the J - integral.

Figure 21: Verification paths for the path independence of the J - integral.

Figure 22: J - integral versus crack growth.

Figure 23: Load - line displacement versus crack growth.

Figure 24: "Tangent" - definition of the crack tip opening displacement.

Figure 25: Crack profile (coarse mesh, 0 - 1 mm crack growth).

Figure 26: Crack profile (coarse mesh, 1.25 - 3 mm crack growth).

Figure 27: Crack profile (coarse mesh, 4 - 8 mm crack growth).

Figure 28: Crack profile (fine mesh, 0 - 1 mm crack growth).

Figure 29a to 29q: Crack tip region shown for the advancing crack (coarse mesh, magnification factor 1).

Figure 30a to 30i: Crack tip region shown for the advancing crack (fine mesh, magnification factor 1).

Figure 31: Crack tip opening displacement versus crack growth (coarse mesh).

Figure 32: Crack tip opening displacement versus crack growth (fine mesh).

Figure 33: Crack tip opening angle versus crack growth (coarse mesh).

Figure 34: Schematic representation of the sensitivity of the CTOA dependent on the element size at the crack tip.

Figure 35: Crack tip opening angle versus crack growth (fine mesh).

Figure 36: "45°" definition of the crack opening displacement.

Figure 37: Dependence of d_n on n and σ_0/E for plane strain [18].

Figure 38: Prandtl slipline fields for a steadily growing crack.

Figure 39: Cartesian stress components at a crack tip.

Figure 40: Strain in y - direction along the line $\Theta = 0°$ for the advancing crack (fine mesh, 0 - 1 mm crack extension).

Figure 41: Strain in y - direction along the line $\Theta = 0^{\circ}$ for the advancing crack (coarse mesh, 0 - 1 mm crack extension).

Figure 42: Strain in y - direction along the line $\Theta = 0^{\circ}$ for the advancing crack (coarse mesh, 1.5 - 4 mm crack extension).

Figure 43: Strain in y - direction along the line $\Theta = 0^{\circ}$ for the advancing crack (coarse mesh, 5 - 8 mm crack extension).

Figure 44: Stress in y - direction along the line $\Theta = 0^{\circ}$ for the advancing crack (fine mesh, 0 - 1 mm crack extension).

Figure 45: Stress in y - direction along the line $\Theta = 0^{\circ}$ for the advancing crack (coarse mesh, 0 - 1 mm crack extension).

Figure 46: Stress in y - direction along the line $\Theta = 0^{\circ}$ for the advancing crack (coarse mesh, 1.5 - 4 mm crack extension).

Figure 47: Stress in y - direction along the line $\Theta = 0^{\circ}$ for the advancing crack (coarse mesh, 5 - 8 mm crack extension).

Figure 48: Von Mises equivalent stress along line $\Theta = 0^{\circ}$ for the advancing crack (coarse mesh, 0 - 1 mm crack extension).

Figure 49: Von Mises equivalent stress along line $\Theta = 0^{\circ}$ for the advancing crack (coarse mesh, 1.5 - 4 mm crack extension).

Figure 50: Von Mises equivalent stress along line $\Theta = 0^{\circ}$ for the advancing crack (coarse mesh, 5 - 8 mm crack extension).

Figure 51: Von Mises equivalent stress along line $\Theta = 0^{\circ}$ for the advancing crack (fine mesh, 0 - 1 mm crack extension).

Figure 52: Transition point position versus crack growth .

Figure 53: Log / log representation of the von Mises equivalent stress along line $\Theta = 0^{\circ}$ for the advancing crack (coarse mesh, 0 - 1 mm crack extension).

Figure 54: Log / log representation of the von Mises equivalent stress along line $\Theta = 0^{\circ}$ for the advancing crack (coarse mesh, 4 and 8 mm crack extension).

Figure 55: Elastic strain energy density along line $\Theta = 0^{\circ} - 180^{\circ}$ for the advancing crack (fine mesh, 0 - .75 mm crack extension).

Figure 56: Elastic strain energy density along line $\Theta = 0^\circ$ - 180° for the advancing crack (coarse mesh, 1 - 3 mm crack extension).

Figure 57: Elastic strain energy density along line $\Theta = 0^\circ$ - 180° for the advancing crack (coarse mesh, 4 - 8 mm crack extension).

Figure 58: Plastic strain energy density along line $\Theta = 0^\circ$ - 180° for the advancing crack (coarse mesh, 0 - 1 mm crack extension).

Figure 59: Plastic strain energy density along line $\Theta = 0^\circ$ - 180° for the advancing crack (coarse mesh, 1.5 - 4 mm crack extension).

Figure 60: Plastic strain energy density along line $\Theta = 0^\circ$ - 180° for the advancing crack (coarse mesh, 5 - 8 mm crack extension).

Figure 61a - 61m:Iso contours of the von Mises equivalent stress for the advancing crack (coarse mesh).

Figure 62: Behavior of the characteristic radius R_c of the strain intense region (sharply bordered region where the rate of energy dissipation is high).

LIST OF TABLES

Table 1: Relation between the external (applied) load and the crack growth (coarse mesh).

Table 2: Material composition of A533B steel [66] (in weight percent).

Table 3: Stress - strain properties of A533B steel.

Table 4: J - values for different paths.

Table 5: J - integral values over crack extension.

Table 6: Comparison of the results for the J - integral performed in this work with the work of Hoff [37].

NOMENCLATURE

$\underline{a}$	flow vector
$\underline{a}^e$	nodal displacement vector
A	scalar term in D_{ep}
$\underline{A}$	displacement - shape function polynomial matrix
a,b,c,d	length
$\underline{b}$	body force vector
$\underline{B}$	strain - displacement matrix
$\underline{D}$	elastic constitutive matrix
$\underline{D}_{ep}$	elastic - plastic constitutive matrix
$\underline{D}_{ep}^*$	$\underline{D}_{ep}$ known for a certain stress value
d_p	mean void initiation particle spacing
d_n	constant dependent on n and the state of stress
E	Young's modulus
$\underline{f}$	nodal force vector
$\underline{f}_p$	nodal force vector caused by surface traction
$\underline{f}_{pl}$	nodal force vector caused by load
$\underline{f}_{\epsilon a}$	nodal force vector caused by initial strains
$\underline{f}_{\sigma a}$	nodal force vector caused by initial stresses
F	yield criterion
g	material constant
G	strain energy release rate
h	element size
I_n	constant given in fig. 37
J	J - integral
$\underline{J}$	Jacobian matrix
J_W	part of J - integral caused by strain energy density

J_T	part of J - integral caused by surface traction
k	integer
k_n	constant
K	stress intensity factor
$\underline{K}^e$	element stiffness matrix
$\underline{K}^a$	assemblage stiffness matrix
l	length
m	material constant
n	strain hardening exponent
N	shape function
$\underline{N}$	shape function matrix
r	radius of polar coordinates
R	order of the nearly proportional loading zone
R_c	characteristic radius
s	safety factor
T	tearing modulus
$\underline{T}$	surface traction vector
t	thickness
$\underline{u}$	displacement vector
u,v	displacement in x,y direction
W	strain energy density
W_I	strain energy
W_E	external work
x,y	cartesian coordinates
α	material dependent constant
α_{ct}	crack tip opening angle
α_n	constant coefficient of assumed polynomial
α_s	constant

$\beta(\eta,\Theta)$	strain function
δ	crack tip opening displacement
δ_n	corrective factor
$\underline{\epsilon}$	strain
$\underline{\epsilon}_a$	initial strain
ϵ_o	yield strain
$\epsilon(\eta,\Theta)$	strain function
κ	hardening parameter
$\underline{\Psi}$	residual force
$\underline{\sigma}$	stress
$\underline{\sigma}_a$	initial stress
σ_o	yield stress
Γ	boundary where surface traction is applied
υ	Poisson's ratio
ξ,η	intrinsic coordinates

superscripts

T	transpose
e	element

1. INTRODUCTION

Under normal circumstances, a structural analysis assumes that the materials involved are ideal homogeneous flawless materials, (i.e. stresses and strains are uniformly distributed throughout a body). Inglis [1] first emphasized the significance of intense and localized concentrations of stresses around sharp notches. Neuber [2] resolved this observation of stress concentrations caused by notches by introducing stress concentration factors.

Griffith contributed pioneering work to this subject in the early 1920's [3,4]. He developed a continuum mechanics based formulation of the change in strain energy due to the presence of a crack in brittle elastic solid. Often this work is quoted as the starting point of fracture mechanics as an independent branch of mechanics. Sneddon [5] deduced expressions for the stress distribution in the neighborhood of a crack in an elastic solid from complex stress functions developed by Westergaard [6].

The next step in the development of the theory of fracture mechanics was made by Irwin in the 1950's. He observed that there are three independent local kinematic movements of the upper and lower crack surfaces with respect to each other (fig.1) [7].

1) Opening Mode or Mode 1
2) Sliding Mode or Mode 2
3) Tearing Mode or Mode 3

Essentially all stress systems in the near crack - tip region may be derived from these three modes of loading. Since the opening mode (or mode 1) represents the predominant stress situation in many practical cases, most of the research is done in this area. Building on the associated stress fields in the near crack - tip region of the three different crack movements, Irwin deduced the stress intensity factor (K) concept [8], where K describes the intensity of the elastic crack - tip stress field.

Previously Orowan recognized that for relatively ductile materials, the work done in plastic deformation is much larger then the energy required to form new crack surface [9]. From these observations Irwin defined a material property G which is the total energy released during crack extension [10]. In addition he demonstrated the equivalence of G and K for linear elastic material behavior. This property is the basis of brittle fracture mechanics today. Since the stress distribution characteristics around a crack are always the same, material properties can be found by testing suitable specimens. Such material properties like G_c (critical energy) or K_c (critical stress intensity factor), once found, can be compared with the G or K value of a body subjected to a certain load condition and the designed structure simply has to satisfy the following conditions

$$G < \frac{G_c}{s} \qquad \text{eq. 1.01}$$

$$K < \frac{K_c}{s} \qquad \text{eq. 1.02}$$

where s is the safety factor. Up to this point, linear elastic material behavior has been used as basic assumption to develop the theory. Therefore the discipline, using this principle, is called Linear Elastic Fracture Mechanics (LEFM).

Wells, in the early 1960's [11], introduced the concept of the crack opening displacement. This was the first example of a fracture concept developed beyond general yielding. Wells's work provided the basis for the semi empirical 'COD Design Curve' approach, used today (especially in the United Kingdom) for fracture under contained yielding conditions. Hutchinson [12] and Rice and Rosengren [13] derived (under the assumption of a power law hardening material in the nonlinear region of material behavior) solutions for the stresses and strains near a crack - tip using the deformation theory of plasticity. Rice subsequently [14] deduced an alternative (but equivalent) approach to the COD Design Curve. He introduced the J - integral, a path independent contour integral around the crack - tip. Although several path independent contour integrals have been advanced independently [15, 16, 17], for any fracture mechanics analysis where significant plasticity occurs, either the COD Design Curve or the J - integral is used. The approach essentially is the same as in linear elastic materials shown in eq. 1.01 and eq. 1.02, namely the designed structure has to satisfy the condition

$$J < \frac{J_c}{S} \qquad \text{eq. 1.03}$$

The discipline of fracture mechanics where elastic - plastic deformation must be taken into account is called Elastic Plastic Fracture Mechanics (EPFM). Due to the complexity of the problems in EPFM, progress in this discipline is not as advanced as in LEFM.

The Finite Element Method (FEM) is a numerical method which provides the opportunity to simulate elastic and plastic material behavior. By formulating different types of idealized constitutive behavior (not only nonlinear elastic corresponding to deformation theory of plasticity, but also incremental plastic corresponding to a flow theory of plasticity) (fig. 2), it is possible to characterize a fracture within a body under arbitrary load conditions. With this tool, bodies subjected to complex loading conditions (in elasticity as well as in plasticity) can be examined.

In fracture mechanics today, engineering calculations are not limited to the determination of the combination of the critical crack size - load conditions for fracture instability. In addition, calculations to determine the rate of progression of a crack are performed. There are several distinct types of crack growth:

- fatigue crack growth,
- creep crack growth,

- environmentally assisted crack growth, and
- stable crack growth.

Fatigue crack growth occurs in structures which are operating under alternating loads sufficiently severe to make fatigue resistance a primary design criterion. The approach for solving this problem is to relate the change in crack length with the number of applied load cycles. A widely used equation for this relation is the 'Paris Law' [18]

$$\frac{da}{dN} = g(\Delta K)^{m} \qquad \text{eq. 1.04}$$

where K_{max} is the upper load stress intensity factor,
K_{min} is the lower load stress intensity factor,
ΔK is $K_{max} - K_{min}$,
da is the crack length,
dN are the load cycles, and
g,m are material dependent constants.

One difficulty encountered is that an exact definition of the transition from initiation to propagation often is impossible.

Creep crack growth is a very important problem, particularly in the power generating industry and aircraft gas turbines. Metals show a creep behavior at temperatures greater than about thirty percent of their absolute melting temperatures. There are two competing mechanisms to describe the time dependent crack growth behavior. The first mechanism builds upon the blunting of the crack - tip. This phenomenon is observed experimentally and has been simulated numerically. Due to the crack - tip blunting, the stress field ahead of the crack relaxes and tends to retard crack growth. The other mechanism results in an accumulation of creep damage in the form of microcracks ahead the crack - tip. These microcracks join each other causing the crack to extend.

Environmentally assisted crack growth is an extremely complex problem and even experts in this field cannot always agree on the precise distinction between the different types of environmental cracking, characterized by corrosion, stress corrosion, and corrosion fatigue. Environmental effects on fatigue crack growth strongly depend on specific material - environment combinations, as well as on the frequency of the stress cycle, the wave form of the stress cycle and the temperature. In the case of high crack growth rates the environmental effects are often negligible.

In ductile materials (like A533B steel), slow stable crack growth is observed after the onset of crack growth due to extensive plastic deformation, although the structure may still remain in service. A fracture analysis based on the onset of crack growth, therefore, would lead to an overly conservative estimation and the structure would be prematurely removed from service. The problem to solve, is to determine what amount of stable crack growth is allowable prior to the onset of rapid crack propagation. Theoretical foundations for this subject are based on Elastic Plastic Fracture Mechanics (EPFM). Different approaches exist to solve this problem, but the major obstacle still is to find a fracture criterion which characterizes stable crack growth after crack initiation.

Parallel to the macro - description of fracture in structures, a micro - mechanism approach has been developed. The main disadvantage of this approach is the lack of experimental verification of proposed solutions. Nevertheless, much research has been performed in the past. In particular, the ability to relate micro - mechanisms of cleavage and ductile fracture to the fracture mechanics parameters such as K, J - integral, CTOD and CTOA seems to be the key for a successful application of this concept.

The micro - mechanism of fracture itself is divided into fast, uncontrollable crack extension and slow stable crack growth. Fast crack extension occurs below the cleavage transition temperature. This cleavage fracture is a brittle fracture but micro - plasticity is not excluded. Transgranular cleavage fracture occurs in structural steels of yield strengths generally less than 500 MPa, while intergranular cleavage occurs in higher strength alloy steels [19]. Zener [20] suggested that there is an array of dislocations at the initial stage of crack formation. As more dislocations enter this array they are squeezed together, producing a local stress concentration. This local stress concentration increases until a crack nucleus is generated. Stroh [21] presented an analysis of this approach. This analysis shows that cleavage fracture would not be predicted using this dislocation model. Since cleavage fracture is observed experimentally, the model proposed by Zener appears to be inadequate. Cottrell [23] suggested a mechanism which leads to easy nucleation in bcc metals. In this rather straightforward approach, two dislocations intersect on the cleavage plane and form a new dislocation. Equation 1.05 describes and fig. 3 shows this mechanism.

$$\frac{a}{2}\langle\bar{1}\bar{1}1\rangle_{(101)}+\frac{a}{2}\langle 111\rangle_{(\bar{1}01)}\rightarrow a\langle 001\rangle_{(001)} \qquad \text{eq. 1.05}$$

The new dislocation has a lower dislocation energy than the initial one, therefore, crack nucleation will be easy and crack extension is explainable by connecting different crack nuclei.

Above the fibrous/cleavage transition temperature materials behave in a fully ductile manner. This transition temperature for A533B steel is about room temperature. After reaching the transition temperature the crack advances by the coalescence of voids. These voids contain inclusions of second - phase as well as nonmetallic particles [24]. For the initiation of ductile fracture, a simple criterion commonly used is [25 to 27]

$$\delta_{ic} \sim (0.5 \text{ to } 2)\, d_p \qquad \text{eq. 1.06}$$

where δ_{ic} is the critical crack opening displacement and

d_p is the mean void initiation particle spacing.

Figure 4 shows this microscopic fracture criterion schematically. Unlike cleavage cracks, this ductile material behavior is based on cracks which are too blunt to be able to propagate in an uncontrollable, fast way. Local microscopic criteria for void growth ahead of the crack - tip have been proposed by Green and Knott [29] and Rice and Sorensen [30].

In the present work a macroscopic crack growth study is performed. Using an elastic - plastic (small strain) finite element analysis, a crack in a compact tension specimen is extended quasi statically under plane strain conditions. The material employed is the bainitic pressure vessel grade steel A533B and a power hardening law is used to represent the stress - strain relationship. The von Mises equivalent stress is used as a yield criterion. The macroscopic fracture criteria (J /CTOD and CTOA) are examined as to their usefulness to model slow stable crack growth.

An extended evaluation has been made into the field variables in the vicinity of a crack - tip. In particular the changing nature of the field variables for a growing crack is examined closely, from the onset of crack growth to eight millimeters of crack extension.

2. NUMERICAL CRACK GROWTH SIMULATION TECHNIQUES

A literature survey has shown that three different finite element methods are commonly used to simulate crack growth:

1) Node shifting,
2) Stiffness reduction,
3) Nodal release.

Node shifting is used particularly to simulate small amounts of crack growth, namely less than one element size. With this method crack blunting can be simulated very accurately by using higher order elements. If larger amounts of crack growth are needed, it is possible to combine node shifting with nodal release. An interesting application is the simulation of local three dimensional crack growth (fig. 5). Neither the nodal release nor the stiffness reduction methods can perform this simulation successfully.

Stiffness reduction conceptually is the same as nodal release, only the release algorithm is different. To accomplish stiffness reduction, spring or a combination of spring/gap elements are used (fig. 6). The stiffness in the y - direction is given by the spring constant of the spring elements. Crack growth is obtained by reducing the spring constant of the crack - tip element.

The nodal release method is probably the most widely used crack growth simulation technique. The crack is extended by releasing the crack - tip node. At the same time a reaction force is applied to the released node and then incrementally decreased to zero. The amount of crack growth, therefore, is restricted to the element size per step. Lamain [31] stated that only minor differences are observed, whether the reaction force is applied proportionally or nonproportionally. During the releasing process, the external force can be changed or held constant. It is possible to use higher order elements for this method, but care must be taken so that crack face overlapping due to the reaction force cannot occur.

3. PREVIOUS INVESTIGATIONS OF NUMERICAL CRACK GROWTH SIMULATION

One of the first numerical crack growth simulations was performed by Anderson [32] in 1972, in which he introduced the nodal release technique. For the case of plane stress and under the assumption of a constant crack - tip opening angle as the crack growth criteria, he released the crack - tip node and applied a reaction force to this node to maintain the initial zero displacement condition. Then he decreased the reaction force in five equal steps, keeping the external force constant. Although the assumption of a constant CTOA was quite arbitrary (and incorrect for the first few millimeters of crack growth), this work can be considered as the beginning of numerically stable crack growth simulation.

Sorensen [33] performed crack growth simulations for plane strain using Anderson's nodal release technique. He modeled crack extension for constant external loads between equidistant nodal points. He discussed different possible fracture criteria and applied "a critical opening at a small characteristic material distance from the crack - tip" as a criterion for stable crack growth.

In the 1970's, Shih et. al. performed extensive experimental and numerical research to find valid crack growth criteria [34]. He used the node shifting technique for the numerical approach. His basic results showed that the slope of the J resistance curve for A533B steel was constant for crack extension of approximately six percent of the remaining ligament. Furthermore he stated that the "COD - based criteria appears to be valid for larger amounts of crack growth". The tearing modulus proposed by Paris et. al. [35] based on J (tearing modulus: $T_J = (E/\sigma_0^2)(dJ/da)$) was constant only for a short range of crack growth. An alternative approach, the tearing modulus based on COD (tearing modulus: $T_\delta = (E/\sigma_0^2)(d\delta/da)$) was considered to be an "attractive alternative".

Saka et. al. [36], recognizing the weakness of the tearing modulus concept, introduced in 1983 a new tearing modulus $T_W = (1/R_c)\ (E/\sigma_o{}^2)(dW_p/da)$. The parameter T_W is a dimensionless representation of dW_p/da, the incremental plastic work done in a "circular region of characteristic radius R_c" at the growing crack - tip, where T_W is directly related to the amplitude of the singularity field. Saka determined R_c experimentally to be 0.28 millimeter for A533B steel and performed a numerical crack growth simulation. The input for the finite element analysis was an experimental load line displacement versus crack growth curve. Saka compared T_W with T_J and T_δ and concluded that T_W is definitely superior.

Hoff [37] modeled crack growth with spring and gap elements. Motivated by results from Shih, he used the J - integral for only the first four millimeters of crack growth. This number was explicitly given by Kanninen [18] as the limit for J controlled crack growth for A533B steel. For further crack extension Hoff used a constant CTOA value, verified by experimental data obtained from Shih [34].

4. PROCEDURE OF THE PRESENT INVESTIGATION

Although much research has been performed in the numerical simulation of stable crack growth, up to now an overall criterion that describes the quasi - static extension of a crack in ductile materials has not be found. The tearing modulus concepts (T_J, T_δ) suffer serious limitations, i.e., they show a constant behavior only for a short range of crack growth. The same appears to be true for the new tearing modulus parameter, T_W, introduced by Saka [36]. In his paper he performed a crack growth simulation controlled by this parameter up to 1.8 millimeter crack extension. His analysis, unfortunately excluded the prediction of the initiation of crack growth. In addition, his results showed a deviation of about 20 percent for T_W in this crack growth interval, which cannot be viewed as an improvement of over existing crack growth criteria.

The present work emphasizes two points: (i) to determine how well two crack growth criteria (J/CTOD and CTOA) characterize the crack extension in mode 1 under plane strain conditions and in what interval range they are applicable, and (ii) to examine the singular field variables for crack growth initiation and subsequent quasi - static crack extension, since the author believes that any successful crack criterion must be closely related to the field variables. As input for the finite element analysis, only an experimentally obtained load versus crack growth curve is used.

The stable crack growth is simulated by using the nodal release technique. The load versus crack growth curve (fig. 7) is linearly discretized in a such way that, when the load attains a certain value, the corresponding crack growth is modeled by releasing a corresponding number of nodes. The node release is accomplished by replacing the restrained degree of freedom of the crack - tip node by a reaction force, which is then gradually reduced to zero. After releasing the current crack - tip node the load again is increased until the requirement is satisfied for releasing the next node. The relation used between the applied load and the crack growth for the performed calculations is listed in table 1.

Since one could argue that crack growth has been observed to exhibit jumping (pop - in crack growth) behavior and that the simulation, therefore, essentially is linearizing the whole process, a second approach has been performed. Here the node is released at a constant load and the load is increased with the node restrained in the y - direction. This stepwise or jumping simulation is shown in fig. 8. The main disadvantage of the latter simulation technique is the required increase in CPU time, which is nearly doubled in comparison to the first approach.

The crack tip opening displacement for both simulations are compared for 2.25 millimeters of crack growth. The maximum deviation occurred for the y displacement at the last node that was released and was always less than three percent. For these reasons the stepwise approach was not pursued.

5. FINITE ELEMENT MODELING

5.1 MATERIAL

The material used for stable crack growth simulation is the bainitic pressure vessel grade A533B steel. This steel is representative of ductile materials and is widely used in pressure vessel applications. The material composition and the stress - strain properties are shown in table 2 and table 3. Ramberg and Osgood proposed the following constitutive law for simulating such material behavior

$$\frac{\epsilon}{\epsilon_0} = \frac{\sigma}{\sigma_0} + \alpha \left(\frac{\sigma}{\sigma_0}\right)^n \qquad \text{eq. 5.01}$$

where α and n are material dependent constants, and

σ_0, ϵ_0 are the yield stress and strain.

Since in the crack - tip region the elastic strains are negligible in comparison to the plastic strains, a simplification of eq. 5.01 yields

$$\frac{\epsilon}{\epsilon_0} = \alpha \left(\frac{\sigma}{\sigma_0}\right)^n \qquad \text{eq. 5.02}$$

which is a pure power law representation of the stress - strain curve. Using $\alpha = 1$ and $n = 10$ the material has been modeled with

$$\frac{\epsilon}{\epsilon_0} = \frac{\sigma}{\sigma_0} \qquad \text{eq. 5.03}$$

up to the yielding point and

$$\frac{\epsilon}{\epsilon_0} = \left(\frac{\sigma}{\sigma_0}\right)^n \qquad \text{eq. 5.04}$$

beyond yield.

As input for the finite element program, the stress - strain curve has to be represented in a multilinear discretized form. This has been achieved in 16 discretizations and the actual input stress - strain relation is shown in fig. 9.

5.2 MODEL DEFINITION

A compact tension specimen is chosen to simulate mode 1 stable crack growth. This specimen is chosen since it is a standard type of fracture specimen that has been investigated independently by Shih et al [34] and Hoff [37] and approximates plane strain conditions. The dimensions of the employed model are shown in fig. 10.

Two models are used for the crack growth simulation: one coarse mesh and one fine mesh. The coarse mesh (shown in fig. 11a and 11b) has 1874 elements and 1946 nodes. The element size in the region of crack growth is 0.25 millimeter. The fine mesh shown in fig. 12a to 12c has 2914 elements and 3002 nodes. Here the element size in the crack growth region is five times smaller than in the coarse mesh (0.05 mm). In the case of the coarse mesh, 32 nodes are released which is equivalent to eight millimeters crack growth. For the fine mesh 21 nodes are released to simulate one millimeter crack growth. For simplicity, the fine mesh model is created without loading holes, however, previous work indicates that the load is transfered to the crack - tip region reasonably well [38,39]. The boundary conditions are shown in fig. 13. To avoid rigid body motion the node ,*q* , is restrained in x and y - direction. All other restrained nodes are restricted from moving only in the y - direction.

5.3 FINITE ELEMENT MESH GENERATION

An important aspect of FEM analysis is the generation of the mesh. The two meshes used for the finite element analysis, are created with the software package CAEDS - Graphics on an IBM 5080 terminal. CAEDS (Computer Aided Engineering Design System) is a product of SDRC (Structural Dynamics Research Corporation) employed on a IBM 4341. The strength of this software package is its flexibility in finite element modeling and finite element solving. Since CAEDS has a direct interface with CADAM and CATIA (two engineering graphic design systems), it is possible to enter part geometry directly from either of those systems - entirely bypassing manual entry of data. After doing that, one can interactively add the load and boundary conditions and submit the job to the integrated finite element solver. The disadvantage of CAEDS is the restriction of its solver to linear finite element analysis. Other problems encountered on CAEDS are the limitation of the number of nodes and elements for a successful analysis and the lack of the support of certain element types (like plane strain elements) by the finite element solver. For these reasons, only the mesh creations were performed with CAEDS. One of the major challenges was to put most of the elements in the vicinity of the growing crack. This has been accomplished by using the Free - Mesh - Generator of CAEDS. This mesh generator automatically creates finite elements via the Triquamesh algorithm.

5.3.1 MODEL CHECKING

After a finite element mesh has been created, the necessary mesh checking often is a time consuming process. CAEDS provides a very powerful series of tools (the Model Checking Tools), for simplifying the model checking process. The model checking tools available in CAEDS are:

- free edge checking,
- coincident node checking,
- interior element angle checking,
- distorted element checking.

With this checking series, not only are modeling errors (which would make a finite element analysis impossible) identified, but the elements are also checked to determine, whether some modeling rules (aspect ratio, element angles) are violated. A violation of these modeling rules may introduce erroneous results.

5.3.2 BANDWITH AND WAVEFRONT OPTIMIZATION

In order to obtain improvements in the finite element solution process, CAEDS offers the ability to optimize the bandwith and wavefront of the finite element mesh. By working with free mesh generation, it is not possible to number the nodes in an optimum way. The resulting bandwith and wavefront of the final mesh thus becomes unacceptably large for meshes having 2000 - 3000 nodes. CAEDS uses the Gibbs - Poole - Stockmeyer algorithm to optimize either the bandwith or wavefront size by renumbering the nodes. It is possible to emphasize the optimization either for the bandwith or for the wavefront profile. After using this optimization tool for the two meshes created, the estimated CPU time reduction for performing the finite element analysis was 97 percent. Without this optimization a finite element analysis would not have been possible.

After the generation and optimization of the two meshes on CAEDS, the geometry and the connectivity of the elements were transferred by a special FORTRAN subroutine to the finite element program ABAQUS [40] for solution. This is necessary since the CAEDS finite element solver does not support plane strain elements (the state of stress within a compact tension specimen of this size is assumed to be plane strain) and lacks the ability to solve nonlinear elastic or plastic problems.

6. THE FINITE ELEMENT METHOD FOR STRUCTURAL ANALYSIS

Although a considerable amount of work has been performed to develop analytical methods for solving problems of elasticity [41, 42, 43] and plasticity [44, 45, 46], these methods are usable only for certain problems and analysis cases. In structures of arbitrary shape subjected to arbitrary load conditions, analytical methods often fail. In engineering practice, most problems are too complicated be solved analytically. For these cases, the finite element method is a very powerful computational tool for solving continuum mechanics and structural analysis problems with accuracy acceptable to engineers.

A complete introduction to the finite element method is far beyond the scope of this thesis and, therefore, only a brief overview is given. The interested reader is referred to the book of Zienkiewicz [47] which gives an excellent and complete introduction to the different approaches in finite element analysis.

The basic idea behind the finite element method is to divide a body into small subvolumes or (in two dimensions) a surface into small subregions. These subvolumes or subregions are called elements and are interconnected at nodal points along their boundaries. In the field of solid materials, this method is used to find the stresses and displacements of the structure being analyzed.

In the displacement approach to the finite element method (FEM), the displacements of the nodal points are the basic unknown parameters. To approximate the displacement field within each element, a set of functions is chosen. These displacement functions are called ' shape - functions'. The shape - functions depend largely upon the number of nodes associated to each element and the degrees of freedom. As a basic requirement they must include all possible rigid body displacements as well as all appropriate strain states.

If these functions, in addition, satisfy inter - element compatibility (which means that the highest derivative in the strain displacement relation must be finite) the displacement field will minimize the potential energy of the system. Then, the finite element solution represents an upper bound on total potential, and the solution will converge to the true solution as the mesh size is decreased. Inter - element compatibility may be violated to produce reasonable results, but an upper bound on the total potential is no longer guaranteed.

The strain within an element can be determined in terms of the nodal displacements. As a final step, the constitutive properties of the material will define the state of stress throughout the element and on its boundaries.

6.1 THE FINITE ELEMENT FORMULATION

When a body subjected to external forces is in equilibrium, the principle of virtual work is given by

$$\delta W_I = \delta W_E \qquad \text{eq. 6.01}$$

where δW_I is the total strain energy

and δW_E is the external work.

Use of the principle of virtual displacements gives

$$\delta W_I = \int_V \delta \underline{\epsilon}^T \underline{\sigma} \, dV \qquad \text{eq. 6.02}$$

and

$$\delta W_E = \int_V \delta \underline{u}^T \underline{b} \, dV + \int_\Gamma \delta \underline{u}^T \underline{T} \, d\Gamma + \sum_{p=1}^{k} \delta \underline{u}^T \underline{f}_p \qquad \text{eq. 6.03}$$

where $\delta \underline{\epsilon}$ is the strain vector associated with virtual strains,

$\underline{\sigma}$ is the stress vector,

$\underline{b}$ is the body forces,

V is the volume,

Γ	is the boundary where surface tractions are applied,
$\underline{f}_p$	is the load,
$\delta\underline{u}$	is the virtual displacement vector, and
$\underline{T}$	is the surface traction vector.

Substituting eq. 6.02 and eq. 6.03 into eq. 6.01 yields

$$\int_V \delta\underline{\epsilon}^T \underline{\sigma}\, dV - \left\{ \int_V \delta\underline{u}^T\underline{b}\, dV + \int_\Gamma \delta\underline{u}^T\underline{T} d\Gamma + \sum_{p=1}^{k} \delta\underline{u}^T\underline{f}_p \right\} = 0 \quad . \qquad \text{eq. 6.04}$$

In a finite element representation for solid materials the displacements, strains and their virtual counterparts can be expressed in the following form

$$\underline{u} = \underline{N}\, \underline{a}_i^e, \qquad \delta\underline{u} = \underline{N}\, \delta\underline{a}_i^e \qquad \text{eqs. 6.05a,6.05b}$$

$$\underline{\epsilon} = \underline{B}\, \underline{a}_i^e, \qquad \delta\underline{\epsilon} = \underline{B}\, \delta\underline{a}_i^e \qquad \text{eqs. 6.06a,6.06b}$$

or in a convenient discretized form for finite element applications

$$\underline{u} = \Sigma\, \underline{N}_i\, \underline{a}_i^e, \qquad \delta\underline{u} = \Sigma\, \underline{N}_i\, \delta\underline{a}_i^e \qquad \text{eqs. 6.07a,6.07b}$$

$$\underline{\epsilon} = \Sigma\, \underline{B}_i\, \underline{a}_i^e, \qquad \delta\underline{\epsilon} = \Sigma\, \underline{B}_i\, \delta\underline{a}_i^e \qquad \text{eqs. 6.08a,6.08b}$$

where	i	is the i th node,
	$\underline{a}_i^e$, $\delta\underline{a}_i^e$	are nodal displacements and their virtual counterparts,
	$\underline{N}_i$	is the global shape function for node i, and
	$\underline{B}_i$	is the global strain - displacement matrix.

The nature of $\underline{N}_i$ and $\underline{B}_i$ is explained in more detail in chapter 6.2. Using the principle of virtual displacement and substituting eq. 6.05b and eq. 606b into eq. 6.04 gives

$$\delta\underline{a}^{e,T} \left\{ \int_V \underline{B}^T\underline{\sigma}\, dV - \int_V \underline{N}^T\underline{b}\, dV - \int_\Gamma \underline{N}^T\underline{T} d\Gamma - \sum_{p=1}^{k} \underline{N}^T\underline{f}_p \right\} = 0 \qquad \text{eq. 6.09}$$

where the transposes of the virtual strains and displacements are

$$\delta\epsilon^T = \delta a^{e,T} B^T \qquad \text{eq. 6.10}$$

$$\delta u^T = \delta a^{e,T} N^T \qquad \text{eq. 6.11}$$

In addition the stress strain relation is defined as

$$\sigma = D(\epsilon - \epsilon_a) + \sigma_a \qquad \text{eq. 6.12}$$

where ϵ_a are the initial strains,

σ_a are the initial stresses, and

D is the constitutive matrix.

In the case of plane strain for linear elastic materials; D can be written as

$$D = \frac{E}{(1-2\upsilon)(1+\upsilon)} \begin{bmatrix} 1-\upsilon & \upsilon & 0 \\ \upsilon & 1-\upsilon & 0 \\ 0 & 0 & \frac{1-2\upsilon}{2} \end{bmatrix} \qquad \text{eq. 6.13}$$

where E is the Young's modulus, and

υ is the Poisson's ratio.

For elasto - plastic materials D is no longer a matrix containing only elastic constants. Basically two new factors must be introduced:

1) a yield criterion (F), and
2) a hardening parameter (κ).

After incorporating F and κ into eq. 6.13 it can be shown [48] that the constitutive matrix, $\underline{D}$, for elastic - plastic conditions is

$$\underline{D}_{ep} = \underline{D} - \frac{(\underline{D}\,\underline{a})(\underline{D}\,\underline{a})^{T}}{A + (\underline{D}\,\underline{a})^{T}\,\underline{a}} \qquad \text{eq. 6.14}$$

where	$\underline{a}$	represents the flow vector (a partial differentiation of the yield criterion with respect to the stresses)
and	A	is a scalar term, obtained as the local slope of the uniaxial stress/ plastic strain curve.

Thus, by use of eq. 6.14, eq. 6.13 can be rewritten

$$\underline{\sigma} = \underline{D}_{ep}\,(\underline{\epsilon} - \underline{\epsilon}_a) + \underline{\sigma} \qquad \text{eq. 6.15}$$

for elasto - plastic conditions. Substituting eq. 6.15 into 6.09 yields

$$\delta \underline{a}^{e,T}\left\{\left(\int_V \underline{B}^T \underline{D}_{ep} \underline{B}\, dV\right)\underline{a}^e - \int_V \underline{B}^T \underline{D}_{ep} \underline{\epsilon}_a\, dV + \int_V \underline{B}^T \underline{\sigma}_a\, dV - \int_V \underline{N}^T \underline{b}\, dV \right.$$

$$\left. - \int_{\Gamma} \underline{N}^T \underline{T}\, d\Gamma - \sum_{p=1}^{k} \underline{N}^T \underline{f}_p \right\} = 0 \,. \qquad \text{eq. 6.16}$$

Since $\delta \underline{a}^{e,T}$ is quite arbitrary and not necessarily zero, the term in the brackets must be zero to satisfy eq. 6.16, or

$$\left(\int_V \underline{B}^T \underline{D}_{ep} \underline{B}\, dV\right) a^e = \underline{f}_{\epsilon a} - \underline{f}_{\sigma a} + \underline{f}_b + \underline{f}_T + \underline{f}_{pl} \qquad \text{eq. 6.17}$$

where

$$\underline{f}_{\epsilon a} = \int_V \underline{B}^T \underline{D}_{ep} \underline{\epsilon}_a\, dV \qquad \text{eq. 6.18}$$

$$\underline{f}_{\sigma a} = \int_V \underline{B}^T \underline{\sigma}_a \, dV \qquad \text{eq. 6.19}$$

$$\underline{f}_b = \int_V \underline{N}^T \underline{b} \, dV \qquad \text{eq.6.20}$$

$$\underline{f}_T = \int_\Gamma \underline{N}^T \underline{T} \, d\Gamma \qquad \text{eq. 6.21}$$

$$\underline{f}_{pl} = \sum_{p=1}^{k} \underline{N}^T \underline{f}_p \, . \qquad \text{eq. 6.22}$$

Defining

$$\underline{f}^e = \underline{f}_{\epsilon a} - \underline{f}_{\sigma a} + \underline{f}_b + \underline{f}_T + \underline{f}_{pl} \qquad \text{eq. 6.23}$$

and

$$\underline{K}^e = \int_V \underline{B}^T \underline{D}_{ep} \underline{B} \, dV \qquad \text{eq. 6.24}$$

allows eq. 6.17 to be written as

$$\underline{K}^e \, \underline{a}^e = \underline{f}^e, \qquad \text{eq. 6.25}$$

where $\underline{K}^e$ is the stiffness matrix,
$\underline{a}^e$ are the nodal displacements,
$\underline{f}^e$ are the nodal forces.

Equation 6.25 can be viewed as the final representation of the finite element formulation for a solid material.

6.2 ELEMENT REPRESENTATION

In ABAQUS, elements of the type CPE4 (4 node bilinear plane strain isoparametric elements) were chosen for the model. This eight degrees of freedom (d.o.f.) element (two d.o.f. for each node) has the assumed displacement field [49]

$$\underline{u} = \begin{Bmatrix} u \\ v \end{Bmatrix} = \begin{bmatrix} 1 & x & y & xy & 0 & 0 & 0 & 0 \\ 0 & 0 & 0 & 0 & 1 & x & y & xy \end{bmatrix} \begin{Bmatrix} \alpha_1 \\ \alpha_2 \\ \alpha_3 \\ \vdots \\ \alpha_8 \end{Bmatrix} \qquad \text{eq 6.26}$$

or

$$u = \alpha_1 + \alpha_2 x + \alpha_3 y + \alpha_4 xy \qquad \text{eq. 6.27}$$

$$v = \alpha_5 + \alpha_6 x + \alpha_7 y + \alpha_8 xy \qquad \text{eq. 6.28}$$

where u is displacement in x - direction, and
v is displacement in y - direction

or in a more succinct form

$$\underline{u} = \underline{A}\,\underline{\alpha}_n \qquad \text{eq. 6.29}$$

where $\underline{\alpha}_n$ are the constant coefficients of the assumed polynomial.

The displacement field also can be written in the form

$$\underline{u} = \underline{N}\,\underline{a}^e \qquad \text{eq. 6.30}$$

where $\underline{N}$ are the shape functions, and
$\underline{a}^e$ are the nodal displacements.

The desired shape functions can be found directly from Lagrange's interpolation formula, which leads to

$$\begin{Bmatrix} u \\ v \end{Bmatrix} = \begin{bmatrix} N_1 & 0 & N_2 & 0 & N_3 & 0 & N_4 & 0 \\ 0 & N_1 & 0 & N_2 & 0 & N_3 & 0 & N_4 \end{bmatrix} \begin{Bmatrix} u_1 \\ v_1 \\ u_2 \\ v_2 \\ \vdots \\ u_4 \\ v_4 \end{Bmatrix} \qquad \text{eq. 6.31}$$

Inserting the coordinates of the nodes gives the following shape functions for the rectangular CPE4 element

$$N_1 = \frac{1}{4\,b\,c}\,(b - x)\,(c - y) \qquad \text{eq. 6.32}$$

$$N_2 = \frac{1}{4\,b\,c}\,(b + x)\,(c - y) \qquad \text{eq. 6.33}$$

$$N_3 = \frac{1}{4\,b\,c}\,(b + x)\,(c + y) \qquad \text{eq. 6.34}$$

$$N_4 = \frac{1}{4\,b\,c}\,(b - x)\,(c + y) \qquad \text{eq. 6.35}$$

where fig. 14 identifies the parameters used .

The shape functions connect the nodal displacements with the displacement field. Similarly the strain displacement matrix $\underline{B}$ connects the nodal displacements with the strain field. In the case of plane elasticity $\underline{B}$ can be written as

$$\underline{B} = \begin{bmatrix} \frac{\partial}{\partial x} & 0 \\ 0 & \frac{\partial}{\partial y} \\ \frac{\partial}{\partial y} & \frac{\partial}{\partial x} \end{bmatrix} \underline{N} \qquad \text{eq. 6.36}$$

Incorporating eqs. 6.32 - 6.35 into eq. 6.36 gives

$$\underline{B} = \frac{1}{4\,b\,c} \begin{bmatrix} -(c-y) & 0 & \text{etc.} \\ 0 & -(b-x) & \text{etc.} \\ -(b-x) & -(c-y) & \text{etc..} \end{bmatrix} \qquad \text{eq. 6.37}$$

Use of eqs. 6.32 to 6.36 permits the stiffness matrix to be evaluated as

$$\underline{K}^e = \int_{-c}^{c}\int_{-b}^{b} \underline{B}^T \underline{D}_{ep} \underline{B}\ t\ dx\,dy \qquad \text{eq. 6.38}$$

To evaluate arbitrary quadrilateral CPE4 elements, an intrinsic coordinate system defined for each element has to be introduced. In fig. 15 a linear element is shown with such a natural coordinate system. Axes ξ and η pass through the mid - points of opposite sides and the edges are defined by $\xi = \pm 1$ and $\eta = \pm 1$ regardless of how the element is oriented in the global coordinate system x,y. As a result of this definition node 1 has the intrinsic coordinates $\xi = \eta = -1$, node 2 $\xi = 1$ and $\eta = -1$ etc..

Using the discretized form of the displacements and strains eqs. 6.07 to 6.08, allows the individual shape functions to be written as

$$N_1 = \frac{1}{4}(1-\xi)(1-\eta) \qquad \text{eq. 6.39}$$

$$N_2 = \frac{1}{4}(1+\xi)(1-\eta) \qquad \text{eq. 6.40}$$

$$N_3 = \frac{1}{4}(1+\xi)(1+\eta) \qquad \text{eq. 6.41}$$

$$N_4 = \frac{1}{4}(1-\xi)(1+\eta) \qquad \text{eq. 6.42}$$

In general, u is parallel to the x- axis and v is parallel to the y - axis, but they are not necessarily parallel to ξ or η.

6.3 PROCEDURE FOR SOLVING THE FINITE ELEMENT FORMULATION

The evaluation of the formulated finite element problem is done by substituting eqs. 6.07b and 6.08b into eq. 6.09. Neglecting loads as well as initial strains and stresses permits eq. 6.16 to be rewritten in the form

$$\sum \delta \underline{a}_i^{e,T} \left\{ \int_V \underline{B}_i^T \underline{\sigma}\, dV - \int_V \underline{N}_i^T \underline{b}\, dV - \int_\Gamma \underline{N}_i^T \underline{T}\, d\Gamma \right\} = 0 . \qquad \text{eq. 6.43}$$

Then the element representation developed in chapter 6.2 is used to evaluate all contributions to eq. 6.43 separately for each element. The displacements for each element can be obtained from eq. 6.07a as

$$\underline{u}^e = \sum \underline{N}_i^e \underline{a}_i^e . \qquad \text{eq.6.44}$$

For an isoparametric element, the x and y coordinates within an element can be evaluated as

$$\begin{Bmatrix} x^e \\ y^e \end{Bmatrix} = \sum_{i=1}^{k} \begin{bmatrix} N_i^e & 0 \\ 0 & N_i^e \end{bmatrix} \begin{Bmatrix} x_i^e \\ y_i^e \end{Bmatrix} . \qquad \text{eq. 6.45}$$

Then the Jacobian matrix may be evaluated as

$$\underline{J}^e = \begin{bmatrix} \frac{\partial x}{\partial \xi} & \frac{\partial y}{\partial \xi} \\ \frac{\partial x}{\partial \eta} & \frac{\partial y}{\partial \eta} \end{bmatrix} = \begin{bmatrix} \sum_{i=1}^{k} \frac{\partial N_i^e}{\partial \xi} x_i^e & \sum_{i=1}^{k} \frac{\partial N_i^e}{\partial \xi} y_i^e \\ \sum_{i=1}^{k} \frac{\partial N_i^e}{\partial \eta} x_i^e & \sum_{i=1}^{k} \frac{\partial N_i^e}{\partial \eta} y_i^e \end{bmatrix} \qquad \text{eq. 6.46}$$

The volume of each element is given as

$$dV^e = t \operatorname{Det} \underline{J}^e \, d\xi \, d\eta \qquad \text{eq. 6.47}$$

Following the same approach as for the displacements, the strain displacement relationships for each element can be written

$$\underline{\epsilon}^e = \Sigma\, \underline{B}_i^e\, \underline{a}_i^e\,, \qquad \text{eq. 6.48}$$

in the case of plane strain

$$\underline{B}_i^e = \begin{bmatrix} \left(\frac{\partial N_i}{\partial x}\right)^e & 0 \\ 0 & \left(\frac{\partial N_i}{\partial y}\right)^e \\ \left(\frac{\partial N_i}{\partial y}\right)^e & \left(\frac{\partial N_i}{\partial x}\right)^e \end{bmatrix} \qquad \text{eq. 6.49}$$

and thickness,*t*, is chosen as unity. The chain rule may be used to evaluate

$$\frac{\partial N_i^e}{\partial x} = \frac{\partial N_i^e}{\partial \xi}\frac{\partial \xi}{\partial x} + \frac{\partial N_i^e}{\partial \eta}\frac{\partial \eta}{\partial x} \qquad \text{eq. 6.50}$$

and

$$\frac{\partial N_i^e}{\partial y} = \frac{\partial N_i^e}{\partial \xi}\frac{\partial \xi}{\partial y} + \frac{\partial N_i^e}{\partial \eta}\frac{\partial \eta}{\partial y}\,. \qquad \text{eq. 6.51}$$

The derivatives $(\partial\xi/\partial x)$,$(\partial\eta/\partial x)$, etc. can be obtained from the inverse of the Jacobian matrix, and the stress - strain relationship for each element can be written as

$$\underline{\sigma}^e = \underline{D}_{ep}^e\, \underline{\epsilon}^e = \underline{D}_{ep}^e\, \Sigma\, \underline{B}_j^e\, \underline{a}_j^e. \qquad \text{eq.6.52}$$

Substituting eq. 6.52 into the first term in the brackets of eq. 6.43, again neglecting loads and initial strains and stresses, gives as the contribution from element e to the right side of eq. 6.25

$$\Sigma \, \underline{K}_{ij}^{e} \, \underline{a}_{j}^{e} = \int_{V} \underline{B}_{i}^{e,T} \, \underline{D}_{ep}^{e} \left(\sum_{j=1}^{k} \underline{B}_{j}^{e} \, \underline{a}_{j}^{e} \right) dV \qquad \text{eq. 6.53}$$

where $\underline{K}_{ij}^{e}$ is the submatrix of the element stiffness matrix $\underline{K}^{e}$. The contribution of element e to the body force term $\underline{f}_{b}$ is

$$\underline{f}_{b,i}^{e} = \int_{V} \underline{N}_{i}^{e,T} \, \underline{b}^{e} \, dV \qquad \text{eq. 6.54}$$

and the surface traction term is

$$\underline{f}_{T,i}^{e} = \int_{\Gamma} \underline{N}_{i}^{e,T} \, \underline{T}^{e} \, d\Gamma . \qquad \text{eq. 6.55}$$

The actual integrations were evaluated numerically in the intrinsic coordinate system. The most used widely method (as in ABAQUS), is the Gauss quadrature method. The submatrix $\underline{K}_{ij}^{e}$ has the form

$$\underline{K}_{ij}^{e} = \int_{-1}^{1}\int_{-1}^{1} \underline{B}_{i}^{e,T} \underline{D}_{ep}^{e} \, \underline{B}_{j}^{e} \, \text{Det} \, \underline{J}^{e} \, d\xi \, d\eta . \qquad \text{eq. 6.56}$$

The nodal forces at node i caused by the body forces and surface tractions are

$$\underline{f}^{e} = \underline{f}_{bi}^{e} + \underline{f}_{Ti}^{e} \qquad \text{eq.6.57}$$

with

$$\underline{f}_{b,i}^{e} = \int_{-1}^{1}\int_{-1}^{1} \underline{N}_{i}^{e,T} \, \underline{b}^{e} \, \text{Det} \, \underline{J}^{e} \, d\xi \, d\eta \qquad \text{eq. 6.58}$$

and

$$\underline{f}_{T,i}^{e} = \int_{-1}^{1}\int_{-1}^{1} \underline{N}_{i}^{e,T} \, \underline{T}^{e} \, \text{Det} \, \underline{J}^{e} \, d\xi \, d\eta . \qquad \text{eq. 6.59}$$

The strains and stresses are thus not determined at the nodal points but at the so called 'integration points'. In the CPE4 elements these integration points are marked in fig. 16. The Gauss - Legendre method locates the integration points in a way that the greatest accuracy is achieved for a given number of them.

6.4 COMPUTATIONAL PROCEDURE FOR THE PLASTICITY PROBLEM

Since large deformations occur during the finite element simulation of the stably growing crack, a short introduction is given about the solution procedure in elastic - plastic finite element analysis. The form of the stiffness matrix given in eq. 6.24 suggests that a straightforward solution of the finite element formulation may be possible. This indeed is true for the elastic case where an explicit relationship of the form of eq. 6.12 (with $\underline{\sigma} = \underline{\sigma}(\epsilon)$ for nonlinear elasticity) is available. On the contrary, such an explicit relationship is no longer available for the complex nature of plasticity.

The approach employed to solve the plasticity problem utilizes the fact that the matrix $\underline{D}_{ep}$ (eq. 6.14) is known for a certain stress value and loading direction, and the stresses can be integrated as shown in eq. 6.60 from

$$d\underline{\sigma} = \underline{D}_{ep}^{*}\, d\underline{\epsilon} \qquad \text{eq. 6.60}$$

where $\underline{D}_{ep}^{*}$ is known for a certain stress value and loading direction.

A solution for eq. 6.60 can be obtained with incremental mathematical procedures. During the iteration process of the elasto - plastic analysis, the equilibrium equation (eq. 6.01) cannot be exactly satisfied, thus a system of residual forces $\underline{\Psi}$ will exist such that

$$\underline{\Psi} = \int_V \underline{B}^T \underline{\sigma}\, dV - \left(\underline{f} + \int_V \underline{N}^T \underline{b}\, dV\right) \neq 0 \qquad \text{eq. 6.61}$$

where $\underline{b}$ is the body force vector, and

$\underline{f}$ the external force vector.

Substituting the incremental forms of eq. 6.06 and 6.60 into 6.61 for an increment of load gives

$$\underline{\Delta\Psi} = \underline{K}^{a}\underline{\Delta u} - \left(\underline{\Delta f} + \int_{V} \underline{N}^{T}\underline{\Delta b}\,dV\right) \neq 0 \qquad \text{eq. 6.62}$$

where $\underline{K}^{a}$ is defined as the element stiffness matrix (eq. 6.23). With the help of incremental displacements $\underline{\Delta u}$, an iterative correction of

$$\delta\underline{u}^{k} = [\underline{K}^{a,k}]^{-1}\ \underline{\Delta\psi}^{k} \qquad \text{eq. 6.63}$$

is calculated using the Newton - Raphson method where

$\delta\underline{u}^{k}$ is used as a corrective factor.

After a prescribed number of iterations, the improved displacement is determined by

$$\Delta\underline{u}^{k+1} = \Delta\underline{u}^{k} + \delta\underline{u}^{k} \qquad \text{eq. 6.65}$$

$\Delta\underline{u}^{k+1}$ now is resubstituted into eq. 6.62 and the residual force is calculated. In ABAQUS the maximum residual force is chosen by the user with the parameter PTOL/MTOL. If the calculated residual force is too high, the whole iteration process must be repeated. The disadvantage of this procedure is that the stiffness matrix $\underline{K}^{a}$ must be calculated during each iteration. Therefore this method is usually avoided in large finite element codes. An alternative numerical procedure is the modified Newton Raphson method, where the stiffness matrix is only occasionally recalculated. The initial stiffness method is such a modified Newton Raphson method, where, for the the whole iteration process, the initial elastic stiffness matrix is used.

7. INVESTIGATED CRITERIA FOR STABLE CRACK GROWTH

7.1 J - INTEGRAL INTRODUCTION

The J - integral, which is equal to the strain energy release rate (for elastic materials), was first introduced by Rice [14] in 1968. Under the assumption of a linear or nonlinear elastic material free of body forces and subjected to two dimensional deformation fields (i.e., plane strain or plane stress), the closed line integral, J, around a notch parallel to the x - axis is path independent (see Fig. 17). The J - integral is defined by

$$J = \int_{\Gamma} \left(W dy - T_i \frac{\partial u_i}{\partial x} ds \right) \qquad \text{eq. 7.01}$$

where

$$W = W(x,y) = W(\epsilon) = \int_0^{\epsilon} \sigma_{ij} d\epsilon_{ij} \qquad \text{eq. 7.02}$$

is the strain energy density (equivalent to the area under the nonlinear stress - strain curve). Also

$$\epsilon = (\epsilon_{ij}) \qquad \text{eq. 7.03}$$

is the infinitesimal strain tensor,

$$T_i = \sigma_{ij} n_j \qquad \text{eq. 7.04}$$

is the traction vector defined according to the outward normal along Γ,

u_i is the displacement vector, and

ds is an element of arc length along Γ.

The proof of the path independence of J is given in [14] for a notch with a finite radius r. However, an application of this integration formulation is also possible for sharp cracks, if an arbitrary small curve Γ around the crack - tip is assumed, which reduces to zero in the limit. The crack - tip, therefore, can be interpreted as a singularity of the deformation field. McMeeking [50] determined the value of J near crack - tip and found out that the evaluation of J in the vicinity of the crack - tip is not accurate. A practical limit on the size of the J - integral contour for the mode 1 compact tension specimen has been pointed out by Hoff [37]. He suggests that J should not be calculated along contours closer than 5δ from the crack - tip, where δ is the crack tip opening displacement.

For elastic - plastic calculations in the region of small - scale yielding, the J - integral now is used extensively in fracture mechanics, instead of the stress - intensity factor K, which is only valid for linear elastic calculations. In the elastic case the J - integral is equal to the elastic potential energy release rate, G. By using the principle of virtual work, it is possible to derive the relation

$$G = \alpha_s \frac{K^2}{E} \qquad \text{eq. 7.05}$$

where

$\alpha_s = 1$	for plane stress,
$\alpha_s = (1 - \upsilon^2)$	for plane strain,
E	is the Young's modulus,
υ	is the Poisson's ratio,

and therefore (with $J = G$ in the linear elastic case)

$$J = \alpha_s \frac{K^2}{E} . \qquad \text{eq. 7.06}$$

7.1.1 J - INTEGRAL DETERMINED BY THE VIRTUAL CRACK EXTENSION METHOD

A second method to evaluate the J - integral is the 'Virtual Crack Extension' method, first introduced by Parks [51] for the linear elastic case and later extended to non - linear material behavior [52]. Since this method can be implemented very easily in FEM codes, most commercial codes like ABAQUS and MARC use this technique. The technique is based on moving nodes a small distance around the crack - tip by and estimating the energy change. Since the potential energy does not change much with a slightly different crack - tip configuration, this method works very well. Problems are encountered, however, when using collapsed elements. In this case only one of the several existing crack - tip nodes is fixed. The displaced crack configuration is so different from the original one that the result for the J - integral would be completely incorrect. This can be avoided by using two rings of elements at some distance away but enclosing the crack - tip [31].

7.1.2 J - INTEGRAL AS CRITERION FOR STABLE CRACK - GROWTH

As discussed earlier, the J - integral is valid (i.e., the J - integral is path independent) only for elastic materials subjected to two dimensional deformation fields.

Goldman and Hutchinson [53] showed that the J - integral formulation may be extended even to elastic - plastic materials for cases of monotonically increasing load (no unloading). This implies that J is strictly valid for analyzing only stationary cracks, since one of the characteristics of crack growth is elastic unloading and non - proportional plastic deformation near the crack - tip. Nevertheless, the J - integral is also used to analyze crack growth for small amounts of crack extension [18, 34, 37], primarily because of the lack of other reliable crack growth criteria.

Hutchinson and Paris [54] have examined the necessary conditions for J controlled crack growth and concluded that the most important consideration for using J as a crack growth criterion is that nearly proportional plastic deformation occurs. In this case, the deformation theory of plasticity and the incremental flow theory yield nearly identical results. Figure 18 shows a typical J - resistance curve for an intermediate strength steel under plane strain conditions. The dominant strain field as derived in the deformation theory is

$$\epsilon_{ij} = k_n \left(\frac{J}{r}\right)^{\frac{n}{n+1}} \tilde{\epsilon}_{ij}(\Theta) \qquad \text{eq. 7.07}$$

where	k_n	is a constant,
	r, Θ	are planar - polar coordinates centered at the crack - tip
and	ϵ_{ij}	is a function which depends on n, the strain hardening index, and whether plane stress or plane strain is involved.

In Fig. 19 the crack - tip conditions are schematically shown. Elastic unloading occurs only in the direct vicinity of the crack extension zone (Δa). However, it is difficult to define the size of the zone where the loading is nonproportional. Kanninen [18] suggests that this zone size is of the order of ,*l*, which is shown in Fig. 18. It should be clear by inspection that one condition for J controlled crack growth is that

$$\Delta a << R. \qquad \text{eq. 7.08}$$

For mode 1 the crack is assumed to advance by an amount da in the x - direction. The resulting increment in the strain field is

$$d\epsilon_{ij} = k_n \frac{n}{n+1} \left(\frac{J}{r}\right)^{\frac{n}{n+1}} \frac{dJ}{J} \tilde{\epsilon}_{ij}(\Theta) - k_n J^{\frac{n}{n+1}} da \frac{\partial}{\partial x} \left(r^{-\frac{n}{n+1}} \tilde{\epsilon}_{ij}(\Theta) \right) \qquad \text{eq. 7.09}$$

For a coordinate system attached to the crack tip using

$$\frac{\partial}{\partial x} = \cos\theta \frac{\partial}{\partial r} - \frac{\sin\theta}{r} \frac{\partial}{\partial \theta}, \qquad \text{eq. 7.10}$$

eq. 7.09 becomes

$$d\epsilon_{ij} = k_n \left(\frac{J}{r}\right)^{\frac{n}{n+1}} \left[\frac{n}{n+1} \frac{dJ}{J} \tilde{\epsilon}_{ij}(\theta) + \frac{da}{r} \tilde{\beta}_{ij}(\theta) \right], \qquad \text{eq. 7.11}$$

where

$$\tilde{\beta}_{ij}(\theta) = \frac{n}{n+1} \cos\theta \, \tilde{\epsilon}_{ij}(\theta) + \sin\theta \frac{\partial}{\partial\theta} \tilde{\epsilon}_{ij}(\theta). \qquad \text{eq. 7.12}$$

Inspection of eq. 7.11 shows that the first term corresponds to a proportional loading (for $dJ > 0$) and therefore $d\epsilon_{ij} \propto \tilde{\epsilon}_{ij}$. The second term, however, is nonproportional. It is easy to see that the second term in the bracket is of the same order of magnitude as the first term. Therefore, J controlled crack growth should be valid if the proportional loading term is much larger than the nonproportional loading term, or

$$\frac{dJ}{J} \gg \frac{da}{r}. \qquad \text{eq.7.13}$$

By definition

$$\frac{1}{l} = \frac{dJ}{da} \frac{1}{J} \qquad \text{eq.7.14}$$

where l again can be viewed as the initial crack growth associated with the doubling of J above J_c, fig. 18 [18].

If

$$l \ll R \qquad \text{eq. 7.15}$$

then there exists an annular region

$$l \ll r \ll R \qquad \text{eq. 7.16}$$

in which the plastic loading is predominantly proportional and the singularity field (ie. Eqs. 7.07 and 7.11) is dominant.

By introducing a nondimensional parameter defined by

$$\omega = \frac{b}{J}\,\frac{dJ}{da}, \qquad \text{eq.7.17}$$

it is possible to formulate a condition for J controlled growth in a fully yielded specimen. Here b is the uncracked ligament and R will be a fraction of b. Thus, finally, $\omega \gg 1$ can be stated as requirement for J controlled growth.

7.1.3 CALCULATION OF THE J - INTEGRAL

The integration of the J - integral in the CT specimen is performed along a rectangular path which is divided into six sections. Due to the symmetry of the plate and loading only the upper half of the integral is evaluated and the result is then multiplied by 2. The integration paths are shown in fig. 20. By use of eq. 7.01, the J - integral can be separated into two parts

$$J = J_W - J_T \ , \qquad \text{eq. 7.18}$$

where

$$J_W = \int_{\Gamma} W dy \qquad \text{eq. 7.19}$$

and

$$J_T = \int_{\Gamma} \left(\sigma_{xx} n_x \frac{\partial u_x}{\partial x} + \sigma_{xy} n_y \frac{\partial u_x}{\partial x} + \sigma_{yx} n_x \frac{\partial u_y}{\partial x} + \sigma_{yy} n_y \frac{\partial u_y}{\partial x} \right) ds \qquad \text{eq. 7.20}$$

Equations 7.19 and 7.20 are applied on each path (using the direction of the normal vector), which leads to

Path 1

$$J_1 = J_{W_1} - J_{T_1} = \int_a^b W_1 dy - \int_a^b \left(\sigma_{xx} \frac{\partial u_x}{\partial x} + \sigma_{yx} \frac{\partial u_y}{\partial x} \right) dy \qquad \text{eq. 7.21}$$

Path 2

$$J_2 = J_{W_2} - J_{T_2} = 0 - \int_b^c \left(\sigma_{xy} \frac{\partial u_x}{\partial x} + \sigma_{yy} \frac{\partial u_y}{\partial x} \right) dx \qquad \text{eq. 7.22}$$

Path 3

$$J_3 = J_{W_3} - J_{T_3} = \int_c^d W_3 dy - \int_c^d \left(- \sigma_{xx} \frac{\partial u_x}{\partial x} - \sigma_{yx} \frac{\partial u_y}{\partial x} \right) dy \qquad \text{eq. 7.23}$$

Summing up Eqs. 7.21 to 7.23

$$J = 2 \left\{ \int_a^b W_1 dy - \int_a^b \left(\sigma_{xx} \frac{\partial u_x}{\partial x} + \sigma_{yx} \frac{\partial u_y}{\partial x} \right) dy - \int_b^c \left(\sigma_{xy} \frac{\partial u_x}{\partial x} + \sigma_{yy} \frac{\partial u_y}{\partial x} \right) dx \right.$$

$$\text{eq. 7.24}$$

$$\left. + \int_c^d W_3 dy + \int_c^d \left(\sigma_{xx} \frac{\partial u_x}{\partial x} + \sigma_{yx} \frac{\partial u_y}{\partial x} \right) dy \right\}$$

yields the final integration formula.

The actual integration of J was done numerically using the average values of the stresses, strains and strain energies from the integration points of the participating elements. Second and fourth order finite difference operators were used for evaluating $\partial u_y/\partial x$.

To verify the path independence, the J - integral was calculated for 4 paths (see Fig. 21). The J - integral values of the 4 paths differ by 8.2% which can be viewed as the deviation from the path independence of J using this numerical approach (Table 4). For the extension of the crack the J - integral is calculated on path 2 (Table 5). Figure 22 shows the J - integral plotted against the crack growth. During the first millimeter of crack growth J exhibits an unexpected behavior. For the first 0.5 millimeter of crack growth the J value is increasing less than for the next 0.5 millimeter. After 1 millimeter of crack extension the J versus Δa curve shows the expected behavior. For the first 2.5 millimeters of crack growth the J value increases nearly linearly; beyond that point the slope is decreasing. An interesting point is that the load line - displacement versus crack growth (Δa) curve shows a similar behavior (fig. 23). By using a linear least square interpolation for the first 2.5 millimeters of crack growth, a slope of 393.1 MPa is obtained. The initial value of J was 89.878 N/mm at a load of 5300N.

Table 6 shows the results of the finite element analysis compared with the results from Hoff [37]. Hoff's J versus Δa curve (which actually was his input for the first four millimeters crack growth) reproduces the experimental data almost exactly. The reason why the initial J values differ so much is easy explained. Hoff's load versus Δa curve (as a result of his calculation) is significantly higher than the experimentally obtained curve. This however, was the input of the calculation performed in this paper. Therefore, his load at crack initiation was also higher (~ 7000N) which explains the higher value of the initial J - integral. The slopes of the J versus Δa curves agree very well with Hoff's prediction.

Using eq. 7.17 to determine whether J controlled crack growth is reasonable leads to

$$\omega = \frac{b}{J}\,\frac{dJ}{da} = 375$$

in comparison to ~ 150 obtained by Hoff. The difference between these results is mainly caused by the different J - values at crack initiation. Kanninen [18] pointed out that the question of what is the smallest value of ω for which J controlled crack growth is assured remains unanswered.

7.1.4 DISCUSSION OF THE J - INTEGRAL AS A CRITERION FOR STABLE CRACK GROWTH

Although extensive research has been done to support the use of the J - integral as a crack growth criterion for small amounts of crack growth, the validity of such work is still doubtful. The ω - value (which should be considered as the overall crack growth criteria) obtained in this research, differs significantly from those reported in [18]. A lower bound for ω is not known. In addition, the strain hardening exponent n and the state of stress has a large influence on eq. 7.17. The calculation performed in this work and its comparison to other results showed that the slope ($\Delta J/\Delta a$) is most reliable for the use as a crack growth criteria for smaller amounts ($\Delta a < 0.036b$) of crack growth.

7.2 CRACK PROFILE GEOMETRY

Many authors have employed fracture criteria based on the crack opening profile geometry. Examples include the COD (Crack Opening Displacement), CTOD (Crack Tip Opening Displacement) and CTOA (Crack Tip Opening Angle). Unfortunately, the critical values of these parameters are highly sensitive to their precise definition. There is no universal agreement on appropriate definitions for COD, CTOD, or CTOA. In fact, Schwalbe noted that, at a recent conference, no less than seven different definitions of CTOD were presented [55]. The main objective of using crack profile geometry parameters is to describe the conditions at the crack - tip, or to find characteristic parameters which describe the crack - tip condition from the beginning of crack initiation until failure, including stable as well as unstable crack growth.

7.2.1 DEFINITION OF THE CRACK - PROFILE PARAMETERS

Two different crack profile parameters are studied in this work:

α) δ_t - the 'tangent' definition of the crack opening displacement.

Actually the deformed far field crack front is (in this case) extrapolated linearly to the original crack - tip (fig. 24). This definition is often used with FEM calculations when the crack - tip is not modeled accurately enough to show that the crack tip opening angle at crack initiation is π radians. A necessary condition for the use of δ_t as crack tip opening displacement is that the deformed far field crack front be a straight line. In this analysis this requirement is satisfied for the fine as well as for the coarse mesh.

β) α_{ct} - defined as the crack tip opening angle (CTOA). A commonly used representation of α_{ct} is

$$\alpha_{ct} = \tan^{-1} \frac{2\,(v_{ct+1})}{h} \qquad \text{eq. 7.25}$$

v_{ct} is the y - displacement of the first node beyond the crack - tip, and h is the element size.

Since the crack growth is simulated with uniform step size, the determination of α_{ct} from this definition can be quite accurate.

7.2.2 DISCUSSION OF THE CRACK PROFILE PARAMETER

The deformed crack profiles for the coarse as well as for the fine mesh are shown in fig. 25 to 28. For better display, the vertical scale is amplified in the figures. The actual profiles are given for both meshes in fig. 29a to 29q and fig. 30a to 30h. The fine mesh predicts a blunter crack opening profile than the coarse mesh, which is more consistent with experimental observations.

7.2.3 CRACK TIP OPENING DISPLACEMENT (CTOD) - RESULTS

The CTOD versus crack growth (Δa) diagram for the coarse mesh is shown in fig. 31. Since the J - integral and the CTOD are similar concepts, both the J - Δa and the CTOD - Δa curves have the same shape. The slope of the CTOD - Δa curve increases for the the first millimeter of crack extension, although not to the same extent as the J - Δa curve. This behavior is confirmed by fig. 32 which shows the CTOD - Δa curve from the fine mesh for the first millimeter crack extension. After 1 millimeter of crack extension the slope of the CTOD versus Δa curve begins to decrease. The results demonstrate that the CTOD versus Δa curve is approximately linear for crack extension up to 2.5 millimeters. After 2.5 millimeters of crack growth, however, no linearity is apparent.

7.2.4 CRACK TIP OPENING ANGLE (CTOA) - RESULTS

The problem of establishing a standard definition for the CTOA has been examined by various authors [33, 56]. Rice [57, 58] obtained for stable crack growth (non - hardening materials) a displacement distribution proportional to ln(1/r). Applying this distribution leads to the conclusion that the crack tip opening angle is not defined for $r = 0$ since $d\delta/dr \rightarrow \infty$ as $r \rightarrow 0$, a result that has been observed experimentally [18,36].

The CTOA - Δa curve calculated for the coarse mesh is shown in fig. 33. For the first two millimeters of crack growth, the CTOA - Δa curve shows a completely unstable behavior. It should be clear that eq. 7.25 and the given element size *h* can not simulate the CTOA very close to the crack - tip. This definition should be considered as a secant approximation. This is especially true for high strain hardening exponents ($n = 10$ in our case). In fig. 34 an attempt is made to show the sensitivity of the CTOA definition to the onset of crack growth. It can be seen that the angles are smaller when larger elements are used. However, the inconsistency in these results was the primary reason for developing the fine mesh (the first CTOA was approximately 0.4 radians in comparison to a theoretical value of π radians). The results of the fine mesh (fig. 35) show an initial value of one radian at the beginning of the crack growth (which agrees with the experimentally observed crack blunting much better than the coarse mesh). After the rapid decrease of the CTOA - Δa curve for the first node release (0.05 mm step width), however, the fine mesh shows the same trend as the coarse.

Hoff [37] also observed an unstable behavior in the CTOA - Δa curve. He stated as reasons the ambiguous definition of α as well as mesh refinement errors due to his node release technique with gap and spring elements. This is not true for the calculation presented in this thesis, since the step - width was constant during node release. An explanation for the present instability could be that CTOA is not well defined when r approaches zero. More research is needed to get further information about the nature of the CTOA for $r \rightarrow 0$.

A constant CTOA ~ 0.23 radians is achieved after six millimeters of crack extension, which is in excellent agreement of the experimental value of 0.22 radians [37].

7.3 RELATION BETWEEN J AND CTOD

Shih [59] developed a relationship between the CTOD and the J - integral for a static crack that exploits the dominance of the HRR - singularity in the crack - tip region. He obtained

$$\delta_{45} = d_n \frac{J}{\sigma_o} \qquad \text{eq. 7.26}$$

where δ_{45} is the crack tip opening displacement defined in fig. 36, and

d_n is a constant.

The constant d_n depends mainly on the state of stress and on the strain hardening coefficient n. Although he used a different definition for the crack tip opening displacement, a comparison of the results with the results obtained in the fine mesh calculation is possible. The constant d_n was evaluated from fig. 37 which shows the dependence of d_n from n and σ_o/ E for plane strain.

Use of this diagram as illustrated gives $d_n = 0.5$. The calculation for J at crack initiation yields 102.53 N/mm in comparison to 88.44 N/mm by direct evaluation of J with the line integral. Since it can be expected that the 45 degree definition of δ Shih used in deriving eq. 7.28 would lead to a slightly lower value of δ, the results can be viewed as in good agreement.

8. INVESTIGATIONS OF THE FIELD VARIABLES FOR STABLE CRACK GROWTH

One approach to representing the singular field in the vicinity of the crack - tip is to describe it in terms of the strain singularity. For stationary cracks Rice and Rosengren [13] and Hutchinson [12] developed solutions for the near crack - tip fields using the deformation theory of plasticity and a power hardening law. The stresses, strains and displacements are of the form

$$\sigma_{ij} = \sigma_0 \left(\frac{J}{\alpha \epsilon_0 \sigma_0 I_n r} \right)^{\frac{1}{n+1}} \tilde{\sigma}_{ij}(\Theta, n) \qquad \text{eq. 8.01}$$

$$\epsilon_{ij} = \alpha \epsilon_0 \left(\frac{J}{\alpha \epsilon_0 \sigma_0 I_n r} \right)^{\frac{n}{n+1}} \tilde{\epsilon}_{ij}(\Theta, n) \qquad \text{eq.8.02}$$

$$u_i = \alpha \epsilon_0 r \left(\frac{J}{\alpha \epsilon_0 \sigma_0 I_n r} \right)^{\frac{n}{n+1}} \tilde{u}_i(\Theta, n) \qquad \text{eq. 8.03}$$

where σ_{ij}, ϵ_{ij} and u_{ij} are functions of Θ and n,

α is the coefficient of the Ramberg Osgood material description,

I_n a constant given in [18],

σ_0, ϵ_0 are the yield stress / strain.

A stably growing crack in a ductile material causes large deformations in front of and elastic unloading behind the crack - tip. Cracks opened by tensile mode 1 loadings are of particular interest since most fracture failures occur under mode 1 conditions. Unfortunately, the mathematical problems are so complex that no general analytical solutions are available.

The characteristics of the elastic - perfectly plastic strain singularity of plane strain stable crack growth has been investigated by Rice [57,58], Rice and Sorensen [30] and Cherepanov [60]. In these analyses, the Prandtl slip line theory (a technique where the stresses are determined by interpreting a slip line diagram according to prescribed rules) was used to investigate the nature of the elastic - plastic strain singularity in the centered fan sector moving with a growing crack. The Prandtl field results for a stationary crack have been modified by introducing an elastic unloading sector for the advancing crack. It has been found that this sector is approximately between $\Theta_1 = 115°$ and $\Theta_2 = 163°$ [61]. This sector is shown in fig. 38.

For a stationary crack, the elastic - perfectly plastic asymptotic strain singularity is proportional to (1/r) [12,13]. The results of the investigations for plane strain stable crack growth suggest that the nature of this singularity changes to a weaker ln(1/r) proportionality [59]. The reason for this could be that the crack is extending into material which has already been deformed plastically so that complete refocusing of the strain field ahead of the crack - tip is prevented [33].

Drugan et al. [62] constructed an exact solution for the plane strain near - tip stress field of an advancing crack for nonhardening materials by specializing Rice's more general formula. Sham [63] performed a finite element study to verify this solution and his results agreed very well with Drugan's analytical predictions.

In a more general investigation of stress - strain fields for stably growing cracks, Amazigo and Hutchinson [64] examined a linear strain hardening material. Using J_2 flow theory of plasticity, they identified a loading and an unloading zone near the crack - tip. Nevertheless, they did not include a sector of reverse plasticity (fig. 38 sector C) in the wake of the advancing crack found as a result of Drugan's solution. In deriving their results, Amazigo and Hutchinson followed a procedure similar to the HRR singularity approach. A nonlinear stress rate function has been generated to represent the stress - strain fields and the order of the elastic unloading zone has been determined dependent on the slope of the linearly simulated plastic part of the stress - strain relation.

8.1 THE FINITE ELEMENT RESULTS OF THE FIELD VARIABLES

As mentioned above, there is no exact solution available to describe the field variables of a stably growing crack for the general case of a power law hardening material. In the discussion of the field quantities from the present finite element solution, the emphasis is placed on the transition between the different parameter fields displayed by the curves. The definition of the representation of the curves are given in fig. 39. It is clear that for pure mode 1 loading the line $\Theta = 0°$ best shows the phenomena described above and thus the various quantities are shown along this line.

The strong HRR field strain singularity for the stationary crack is quite evident on the y - direction strain curve along the line $\Theta = 0°$ of the fine mesh (fig. 40). It is self evident that the coarse mesh is not able to simulate this, nearly 1/r singularity for the stationary crack. As the crack grows larger and larger the predominance of the HRR field near the crack - tip decreases. Nevertheless, the characteristics of the y - direction strain curves change very slowly (fig. 41 to 43). Only after five millimeters of crack extension is the strain field singularity observed to be significantly weaker than at the onset of crack growth (fig. 43). One possible explanation for this strain curve behavior could be the smoothing effect of the elastic strain component for the first increment of crack extension.

The y - direction stresses relative to the crack - tip along the line $\Theta = 0°$ exhibit little change for the first millimeter of crack growth, for the fine as well as the coarse mesh (fig. 44 to 47). This is not very surprising since the known theories assume only slightly different singularities for the near - tip field of the advancing crack and the stationary crack. For larger amount of crack extension the singularity tends to become stronger. The points marked in fig. 45 could be interpreted as the transition between an intermediate zone, where the plastic strain is comparable in magnitude with the elastic strain and the K field. The transition between the intermediate zone and the HRR field is not resolvable. For a crack extension of more than one millimeter the influence of the K field is diminished and the transition points are no longer identifiable.

The von Mises stress for the line $\Theta = 0°$ clearly reveals the transition between the intermediate zone and the K field for both meshes (fig. 48 to 51). The transition points, which were hardly detectable for the stress in y - direction (fig. 45), are now very evident. Since the applied external load increases as the crack advances, the transition points change toward larger r values. The crack growth versus transition point position is depicted in fig. 52. At the beginning of crack extension the transition points change very rapidly, while the change decreases as the crack grows larger. For the growing crack, a resolution of the crack - tip singularity from the HRR field; as well as the HRR field from the intermediate zone is not possible even with the fine mesh (fig. 51). For closer examination, a log/log representation of the von Mises curve is plotted in fig. 53 and 54. Indeed, the changes in slope circled in fig. 53 could be interpreted as the transition between the HRR field and the intermediate zone.

The elastic strain energy density (W_{el}) is shown for the early stages of crack extension in fig. 55 for the fine mesh along the line $\Theta = 0°$ & 180° (negative values of r represent $\Theta = 180°$). After the onset of crack growth, the elastic strain energy density is seen to decrease dramatically. For the next steps, the magnitude of W_{el} was nearly constant, although the applied external load increased significantly during crack extension. This behavior characterizes in an excellent way the ductile material behavior, namely, if the the load were to be held constant instead of being increased, the crack would arrest. Due to the strong gradient of W_{el} for the first step, this behavior could not be resolved with the coarse mesh. Figures 56 and 57 depict the W_{el} characteristics for subsequent crack extension with the coarse mesh, and show that the magnitude of the maximum value of W_{el} decreases for the growing crack. The maximum values of W_{el} plotted in fig. 55 to 57 should only be interpreted qualitatively due to the numerical inaccuracy associated with the elements located directly at the crack - tip.

The plastic strain energy density (W_{pl}) for the advancing crack is plotted for the line $\Theta = 0°$ & 180° in fig. 58 to 60. The curves show that the maximum value of W_{pl} is located behind the crack - tip. It is more important, however, that the energy dissipation is sharply bordered and, for larger amounts of crack growth, is nearly constant over a certain length that is extending with the advancing crack, a result which could possibly be employed in a local crack characterization. As already discussed in chapter 2, Saka [35] performed detailed research into the feasibility of the plastic dissipation as a local crack growth criterion. He stated that the intense region of the plastic dissipation is circular with its origin at the tip. In addition, he determined the characteristic radius of this circle to be 0.28 millimeter for approximately two millimeters of crack extension. In contrast, the results of the present analysis indicate that the intense region of W_{pl} is located behind the crack - tip. The radius of this intense region (assumed to have a circular shape) has been determined to be approximately one millimeter for two millimeters crack extension and is clearly a function of the crack extension.

For the estimation of the plastic zone size, the von Mises stress is illustrated for the advancing crack in fig. 61a to 61m. In the present analyses the yield stress is 382 MPa. At the onset of crack extension the plastic zone exhibits the typical butterfly shape, and, as the crack grows, the plastic zone becomes more characterized by a bending behavior towards the uncracked ligament. After 0.25 millimeter of crack growth, plastic hinging occurs at the end of the uncracked ligament due to the moment caused by the applied external load. At step 4 ($\Delta a = 0.75$ mm, $P = 7650$ N) the plastic zone of the crack joins the plastic hinging region. With increasing crack growth, the crack - tip moves from the middle of the highest von Mises stress contour to its left border and it seems that for further crack growth the crack - tip would restrain the highest von Mises stress contour. One interesting region of the compact tension specimen is right in front of the crack - tip. In this region the magnitude of the von Mises stress is decreasing towards the line $\Theta = 0°$. A reasonable explanation for this could be the superposition of the stress parallel to the external load with the stress due to the resulting moment.

8.2 DISCUSSION OF THE FIELD VARIABLE RESULTS

The theory of stable crack growth in ductile materials suggests that the region ahead a crack - tip should be divided into four regions:

1) The crack - tip singularity for advancing cracks,
2) the HRR field,
3) an intermediate zone where the plastic strain is comparable in magnitude with the elastic strain, and
3) the K field.

In the present finite element study, only the transitions between the HRR field - intermediate zone and intermediate zone - K field could be identified. Neither the fine nor the coarse meshes are able to resolve the crack - tip singularity of the advancing crack from the HRR field. Although one could argue that the finite element formulation is smoothing the results and, therefore, such a separation may not be observable with this method, the nature of the obtained stress curves clearly suggest that the crack - tip singularity is superposed onto the HRR field rather than appearing separately.

9. CONCLUSIONS AND RECOMMENDATIONS FOR FUTURE RESEARCH

In the present work, slow stable crack growth in ductile material has been simulated numerically with a widely used commercial finite element code (ABAQUS). An experimentally obtained load versus crack growth relation was used as input and J/CTOD and CTOA crack growth criteria in ductile fracture mechanics were investigated. In addition the field parameters ahead of the tip of the growing crack were investigated.

Existing theories about the asymptotic fields ahead of a crack - tip for an advancing crack indicate that there should exist four regions. The results of the finite element analysis show the near crack - tip field of the advancing crack and the HRR field characterizing the stationary crack are superposed on each other and do not appear independently. The only transitions which are resolvable are the transitions between the HRR field - intermediate zone (the zone where the plastic strain is comparable in magnitude with the elastic strain) and the intermediate zone - K field. The strain field tends to a significantly weaker singularity as the crack grows larger, whereas the stress field remains nearly unchanged even for large amounts of crack growth. In addition, the plastic dissipation energy field attains its maximum value behind the crack - tip and, for larger amounts of crack growth, the plastic energy dissipation possesses a nearly constant value over a certain fixed distance.

The results of the finite element analyses performed in this work show that the J - integral / CTOD concepts do not appear promising as crack growth criteria. This is not very surprising since the J - integral concept is strictly valid only for stationary cracks, although the slope of the J resistance curve ($\Delta J/\Delta a$) does appear to be useful as a crack growth controlling parameter for limited amount of crack growth ($\Delta a < 0.036b$). This indeed, is a very important result because other crack growth criteria available are not able to simulate this region of crack growth very well. One of these criteria is the crack tip opening angle (CTOA), in which a constant CTOA is achieved after six millimeters of crack extension. Evaluation of the finite element results for the advancing crack indicate that the use of the CTOA, as a crack growth criteria, is not very accurate for small amounts of crack extension. In addition, any definition of the CTOA fails for r approaching the limit $r \rightarrow 0$. Obviously there exists a gap between the region where the J - integral is path independent (and the slope of the J - resistance curve characterizes the crack growth) and the region where the CTOA is constant and therefore applicable as a crack growth criterion. For this reason, a combination of ($\Delta J / \Delta a$) and the CTOA as the crack growth criteria proposed by Kanninen and Popelar [18] and recently applied by Hoff [37] is at best, an approximation where the extent of the error remains to be determined. To make numerical crack growth simulation techniques applicable for practical problems future research should be focused on three points:

1) The amount of crack growth for which the J - integral is nearly path independent needs to be known for a much wider range of materials and geometries. The ω approach of Hutchinson and Paris does not seem promising. In addition, Kanninen [18] pointed out that the question of determining the smallest value of ω to assure J controlled crack growth remains unanswered.

2) An unambiguous definition of the CTOA needs to be established, and the amount of crack growth when the CTOA begins to be constant needs to be better understood. Since the CTOA appears to be material dependent [33], more experimental research needs to be done to answer these questions.

3) An additional crack growth criterion needs to be developed for the region between J - and CTOA controlled crack growth. This new criterion could even replace one or both of the crack growth criteria mentioned above. Two new energy based crack growth criteria may be able to satisfy the requirement(s) mentioned above:

(i) the plastic dissipation energy criteria introduced by Saka [36]. The idea behind this criterion is that the plastic dissipation energy determined in an intense strain region with a characteristic radius R_c and written in a dimensionless representation causes crack growth when a critical value is exceeded. As discussed earlier, the results given in Ref. [36] differ from the analysis presented in this work. Nevertheless fig. 62 shows how the characteristic radius R_c for the strain intense region could be defined from the point of view of this work. An interesting fact is that for larger amounts of crack growth the characteristic diameter ($2R_c$) appears to be approximately of the order of the crack extension Δa.

(ii) the strain energy density criterion proposed by Sih [65]. The basic hypothesis behind this criterion is that the maximum yielding is assumed to coincide with maximum strain energy density and the fracture initiation with minimum strain energy density. Failure occurs now if either the maximum strain energy density or the minimum strain energy density exceed a critical value. Since the strain energy density is easy to measure (area under the stress/strain curve) this new approach looks promising.

REFERENCES

[1] C.E. Inglis, Trans. Roy. Inst. Naval Architects 60, 219, (1913).

[2] H. Neuber, "Theory of Notch Stresses", Edwards, Michigan, (1946). "Kerbspannungslehre. Grundlagen fuer genaue Spannungsrechnung". Springer Verlag, Berlin,(1937).

[3] A. A. Griffith, Phil. Trans. Roy. Soc. London, Ser. A221,163,(1921).

[4] A. A. Griffith, In Proceedings of the 1st International Congress for Applied Mechanics, Delft, p.55. (1924).

[5] I. N. Sneddon, "The Distribution of Stress in the Neighborhood of a Crack in an Elastic Solid", Proceedings of the Royal Society, A, Vol. 187, pp229 - 238, (1946).

[6] H. M. Westergaard, "Bearing Pressure and Cracks", Transactions of the AMSE, Journal of Applied Mechanics, Vol. 66, pp. A49 - A53, (1939).

[7] G. R. Irwin, J. Appl. Mechanics, 24, 361, (1957).

[8] G. R. Irwin, "Handbuch der Physik", Vol. 79, Springer-Verlag, Berlin, pp. 551 - 590, (1958).

[9] E. Orowan, "Energy Criteria of Fracture", Welding Research Supplement, Vol. 20, p. 1575, (1955).

[10] G. R. Irwin, " Relation of stresses near a crack to the crack extension force", Proc. 9th Int'l Congress of Applied Mech., Uni. of Brussels, Vol. VIII, Chap. XII, pp. 245 - 251, (1957).

[11] A. A. Wells, "Application of Fracture Mechanics at Beyond General Yielding", British Welding Journal, 10, pp. 563 - 570, (1963).

[12] J. W. Hutchinson, "Singular Behavior at the End of a Tensile Crack in a Hardening Material", Journal of the Mechanics and Physics of Solids, 16, pp. 13 - 31, (1968).

[13] J. R. Rice and G. F. Rosengren, "Plane Strain Deformation Near a Crack Tip in a Power-Law Hardening Material", Journal of the Mechanics and Physics of Solids, 35, pp. 379 - 386, (1968).

[14] J. R. Rice, "A Path Independent Integral and the Approximate Analysis of Strain Concentrations by Notches and Cracks", Journal of Applied Mechanics, 35, pp. 379 - 386, (1968).

[15] J. L. Sanders, "On the Griffith-Irwin Fracture Theory", Journal of Applied Mechanics, 27, pp. 352 - 353, (1960).

[16] J. D. Eshelby, "Energy Relations on the Energy-Momentum Tensor in Continuum Mechanics", In Elastic Behavior of Solids, M.F. Kanninen et. al. (ed.), McGraw-Hill, New York, pp. 77 - 115, (1969).

[17] G, P. Cherepanov, " On Crack Propagation in Solids", International Journal of Solids and Structures, 5, pp. 863 - 871, (1969).

[18] M. F. Kanninen and C. H. Popelar, "Advanced Fracture Mechanics", Oxford Engineering Science Series, 15, (1985).

[19] J. F. Knott, "Microscopic Aspects of Crack Extension", In Advances in Elasto Plasic Fracture Mechanics, L. H. Larsson (ed.), Applied Science Publishers LTD, London, p. 21, (1979).

[20] C. Zener, "Micromechanism of Fracture", ASM 40, p. 3131, (1948).

[21] A. N. Stroh, "The Formation of Cracks as a Result of Plastic Flow", Proc. Roy. Soc. A 223, pp. 404 - 414, (1954).

[22] W. Dahl and D. Dormagen, "Micromechanisms of Crack Initiation and Crack Propagation", In Porceedings of the 4th Advanced Seminar on Fracture Mechanics, p203, (1983).

[23] A. H. Cottrell, "Theory of Brittle Fracture in Steel and Similar Materials", Trans. AIME 212, p. 192, (1958).

[24] J. F. Knott, " Micromechanisms of Fibrous Crack Extension in Engineering Alloys", Met.Sci. 14, p. 375, (1980).

[25] F. A. McClintock, In Physics of Strength and Plasticity, A.S.Argon (ed.), M.I.T. Press, Cambridge, Ma, p. 307, (1964).

[26] J. R. Rice and Tracey, Journal of the Mechanics and Physics of Solids, Vol. 17, p. 201, (1969).

[27] J. R. Rice and Johnson, In Inelastic Behavior of Solids, M.A.Kanninen et. al. (ed.), McGraw-Hill, New York, p.641, (1970).

[28] R. O. Richie, "Slow Crack Growth: Macroscopic and Microscopic Aspects", R.B.Tait and G.G.Garret (ed.), Pergamon Press Inc., New York, p. 100, (1984).

[29] G. Green and J. F. Knott, Journal of the Mechanics and Physics of Solids, Vol. 23, p.167, (1975).

[30] J. R. Rice and E. P. Sorensen, "Continuing Crack Tip Deformation and Fracture for Plane-Strain Crack Growth in Elastic-Plastic Solids", Journal of the Mechanics and Physics of Solids, Vol. 26, pp. 163 - 186, (1978).

[31] L. G. Lamain, "Numerical Analysis in EPFM", In Elastic-Plastic Fracture Mechanics, L.H.Larsson (ed.), D. Reidel Publishing Company, pp. 227 - 261, (1983).

[32] H. Anderson, "A Finite Element Representation of Stable Crack Growth", Journal of the Mechanics and Physics of Solids, Vol. 21, pp. 337 - 356, (1972).

[33] E. P. Sorenson, "A Numerical Investigation of Plane Strain Stable Yielding Condition", 17 ASTM STP 668, pp. 151 - 174, (1979).

[34] Shih, de Lorenzi and Andrews, "Studies on Crack at Initiation and Stable Crack Growth", ASTM STP 668, pp. 65 - 120, (1979).

[35] P. C. Paris et. al. "Theory of Instability of the Tearing Mode of Elastic-Plastic Crack Growth", ASTM STP 668, pp. 5 - 36, (1979).

[36] M. Saka et. al., "A Criterion Based on Crack Tip Energy Dissipation in Plane-Strain Crack Growth under Large Scale Yielding", ASTM STP 803, pp. I 130 - I 158, (1983).

[37] R. Hoff, "A new Finite Element Technique for Modeling Stable Crack Growth", Engineering Fracture Mechanics, Vol. 23, No. 1, pp. 105 - 118, (1986).

[38] P. D. Hilton and G. C. Sih, In Mechanics of Fracture, Noordhoff, Leyden, Netherlands, Vol. 1, pp. 426 - 476, (1973).

[39] J.C. Newman,Jr., "Stress Analysis of the Compact Tension Specimen Including the Effects of Pin Loading", Fracture Analysis, ASTM STP 560, pp105 - 121, (1974).

[40] ABAQUS Version 4/5/175, Hibbitt, Karlsson and Sorenson, Inc., (1985).

[41] N. I. Muskhelishvili, "Mathematical Theory of Elasticity", Noordhoff International Publishing, Leyden, (1977).

[42] I. S. Sokolnikoff, "Mathematical Theory of Elasticity", Robert E. Krieger Publishing Company, Florida, (1983).

[43] S. P. Timoshenko, "Theory of Elasticity", McGraw-Hill Book Company,(1970).

[44] P. Ludwik, "Elemente der Technologischen Mechanik", Springer Verlag, Berlin (1909).

[45] L. Prandtl, "Zeitschrift für angewandte Mathematik und Mechanik", Vol. 8, p.85, (1928).

[46] Bauschinger, Der Zivilingenieur, pp. 27 - 289, (1881).

[47] O. C. Zienkiewicz, "The Finite Element Method", McGraw-Hill, UK, 3rd edition, (1977).

[48] D. R. J. Owen and A. J. Fawkes, "Engineering Fracture Mechanics", Pineridge Press Ltd., Swansea, U.K., (1983).

[49] R. D. Cook, "Concepts and Applications of Finite Element Analysis", John Wiley and Sons, New York, (1981).

[50] R. M. McMeeking, "Path Dependence of the J-Intergral and the Role of J as a Parameter Characterizing the Near-Tip Field", ASTM STP 631, pp. 28 - 41, (1977).

[51] D. M. Parks, "A Stiffness-Derivative Finite Element Technique for Determination of Elastic Crack Tip Stress Intensity Factors", Int. J. of Frac., Vol. 10, pp. 487 - 502, (1974).

[52] D. M. Parks, "The Virtual Crack Extension Method for Non-Linear Material Behavior", Computer Methods in Mechanics and Engineering, Vol. 12. pp. 353 - 364, (1977).

[53] N. L. Goldman and J. W. Hutchinson, Int. J. Solids Structures, pp. 575 - 591, (1975).

[54] J. W. Hutchinson and P. C. Paris, "Stability Analysis of J-Controlled Crack Growth", In Elastic Plastic Fracture, ASTM STP 668, pp. 37 - 64, (1979).

[55] K. H. Schwalbe, "The Crack Tip Opening Displacement in Elastic - Plastic Fracture Mechanics", Springer-Verlag, Berlin, (1986).

[56] R. M. McMeeking, "Journal of the Mechanics and Physics of Solids", Vol. 25, pp. 357 - 381, (1977).

[57] J. R. Rice, In "Fracture: An Advanced Treatise", H. Liebowitz, (ed.) Vol. 2, Academic Press, New York, pp. 191 - 311, (1968).

[58] J. R. Rice, In "Mechanics and Mechanisms of Crack Growth", M. J. May (ed.), British Steel Corporation Physical Metallurgy Centre Publication, pp. 14 - 39, (1975).

[59] C. F. Shih, "Relationships between the J-Integral and the Crack Opening Displacement for Stationary and Extending Cracks", J. Mech. Phys. Solids, Vol. 29. No. 4. pp. 305 - 326, (1981).

[60] G. P. Cherepanov, "Mechanics of Brittle Fracture (in Russian), Nauka, Moscow, 1974, English translation, Eds. McGraw-Hill, New York, pp. 284 - 289, (1979).

[61] J. R. Rice, W. J. Dragan and T. L. Sham, "Elastic-Plastic Analysis of Growing Cracks", In ASTM STP 700, pp. 189 - 221, (1980).

[62] W. J. Dragan, J. R. Rice, and T. L. Sham, J. Mech. Phys. Solids, Vol. 30, p. 447, (1982) and erratum, Vol. 31, p.191, (1983).

[63] T. L. Sham, "A Finite-Element Study of the Asymptotic Near-Tip Fields for Model Plane-Strain Cracks Growing Stably", In Elastic - Plastic Fracture, ASTM STP 803, Vol. 1, pp. I 52 - I 79, (1981).

[64] J. C. Amazigo and J. W. Hutchinson, "Crack Tip Fields in Steady Crack-Growth with linear Strain-Hardening", J. Mech. Phys. Solids, Vol. 25, pp. 81 - 97, (1977).

[65] G. C. Sih and E. Madenci, "Fracture Initiation under Gross Yielding: Strain Energy Density Criterion", Engineering Fracture Mechanics, Vol. 18, No. 3, pp. 667 - 677, (1983).

[66] W. R. Andrews, "CTOD and J-Relationships for a Growing Crack", In The Crack Tip Opening Displacement in Elastic-Plastic Fracture Mechanics, K. H. Schwalbe (ed.), Springer-Verlag, Berlin, p. 191, (1985).

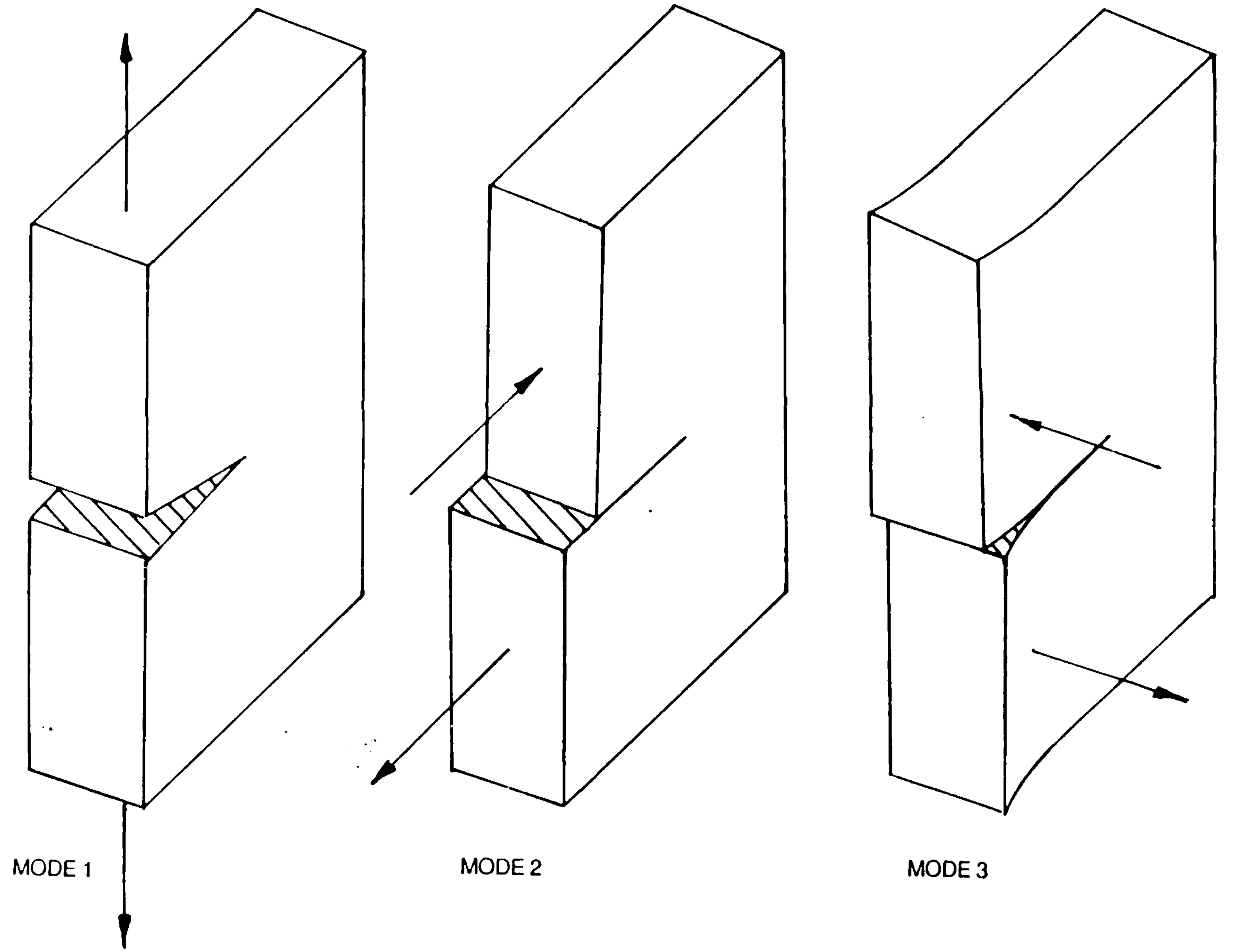
MODE 1
MODE 2
MODE 3

Figure 1: The three independent kinematic movements of the upper and lower surface with respect to each other.

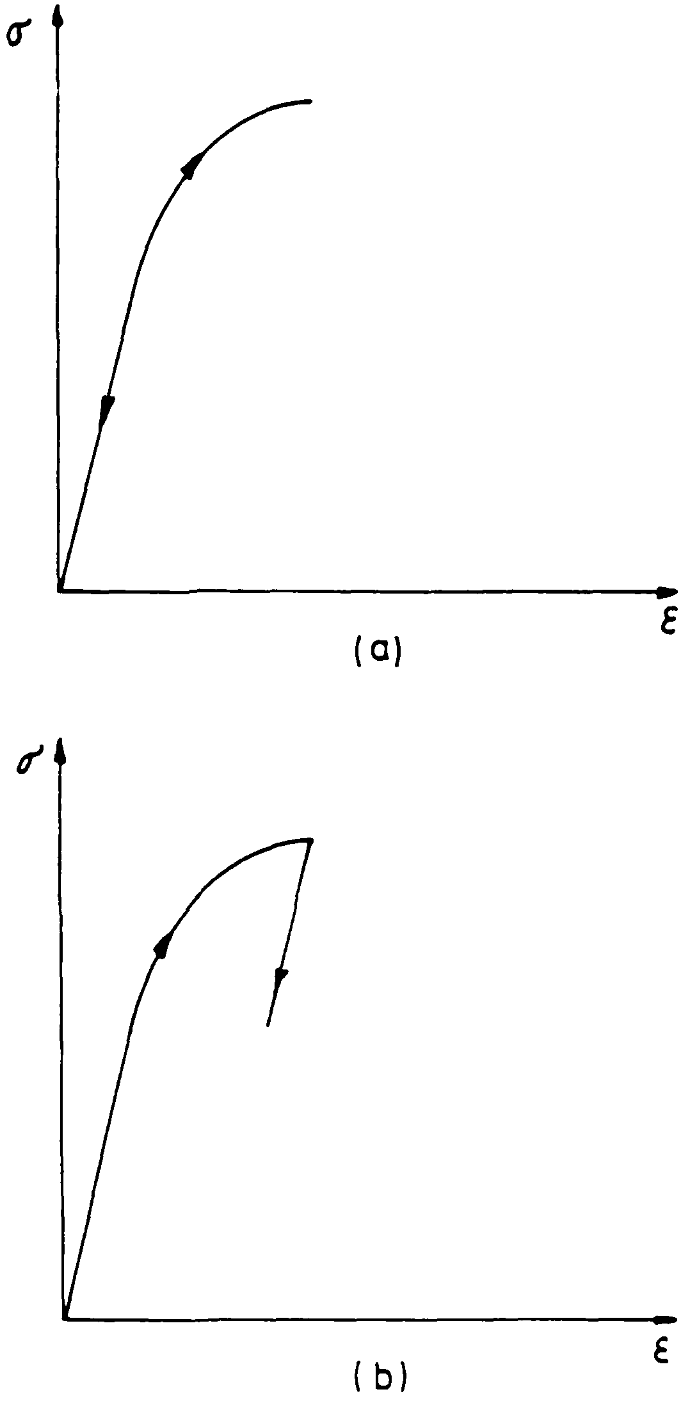

Figure 2: Idealized constitutive material behavior:

a) non - linear elastic conforming to deformation theory of plasticity,

b) incrementally - plastic conforming to flow theory of plasticity.

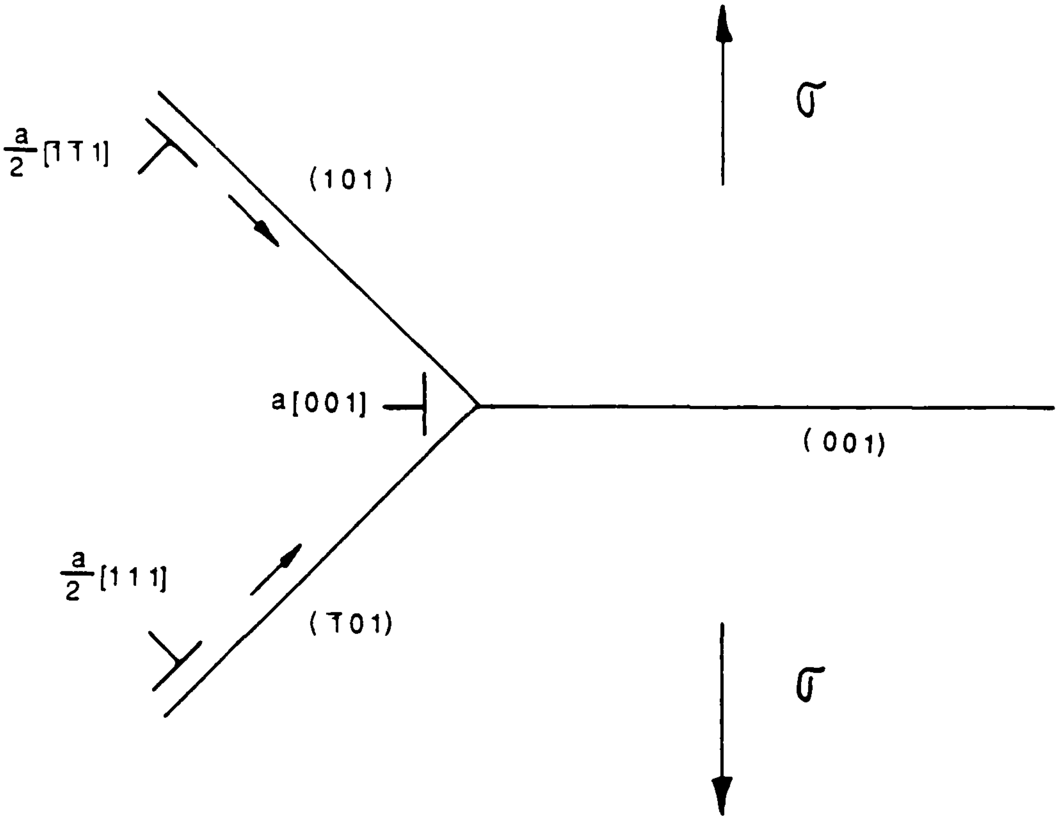
$\frac{a}{2}[1\bar{1}1]$
(101)
σ
a[001]
(001)
$\frac{a}{2}[111]$
$(\bar{1}01)$
σ

Figure 3: Cottrell's model of cleavage fracture (nucleation in bcc metals).

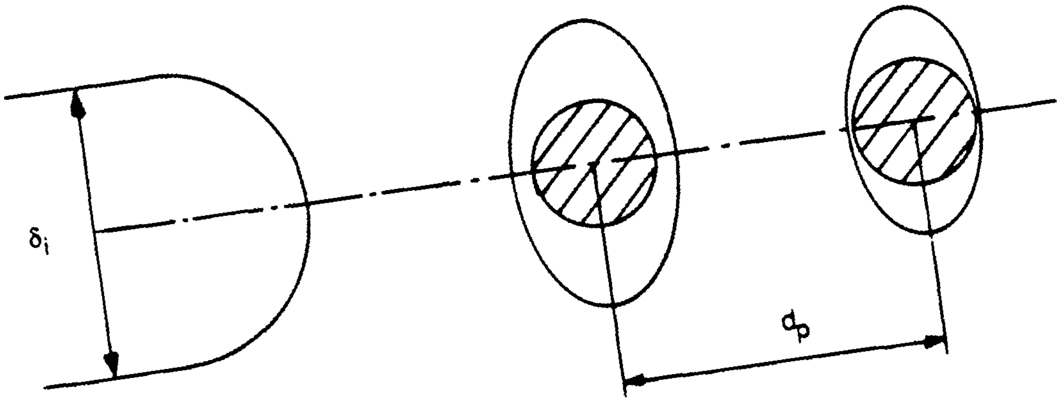

Figure 4: The schematic representation of a commonly used simple microscopic fracture criterion [28].

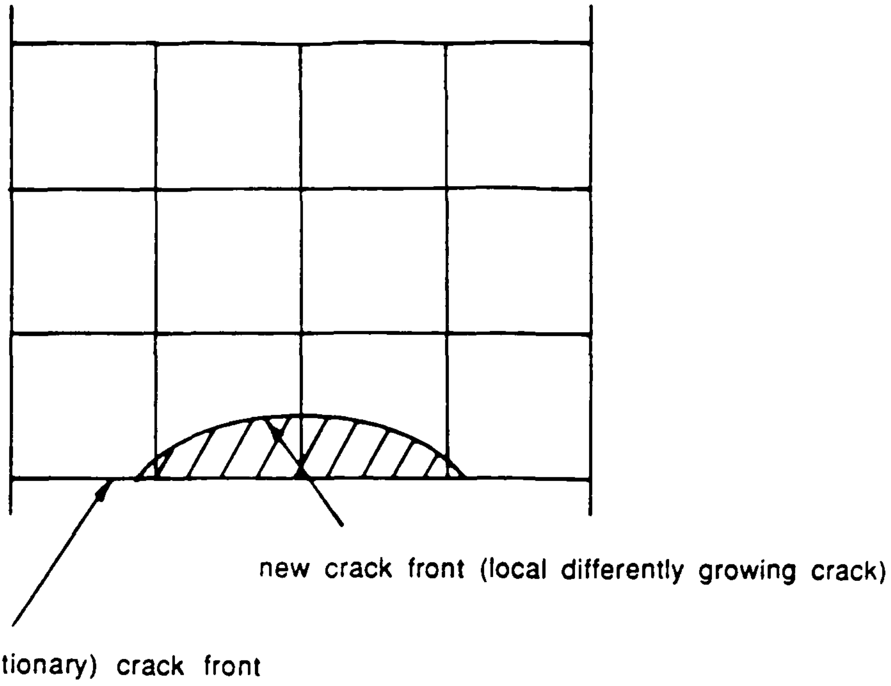
new crack front (local differently growing crack)
original (stationary) crack front

Figure 5: Local crack growth simulation in three dimensions.

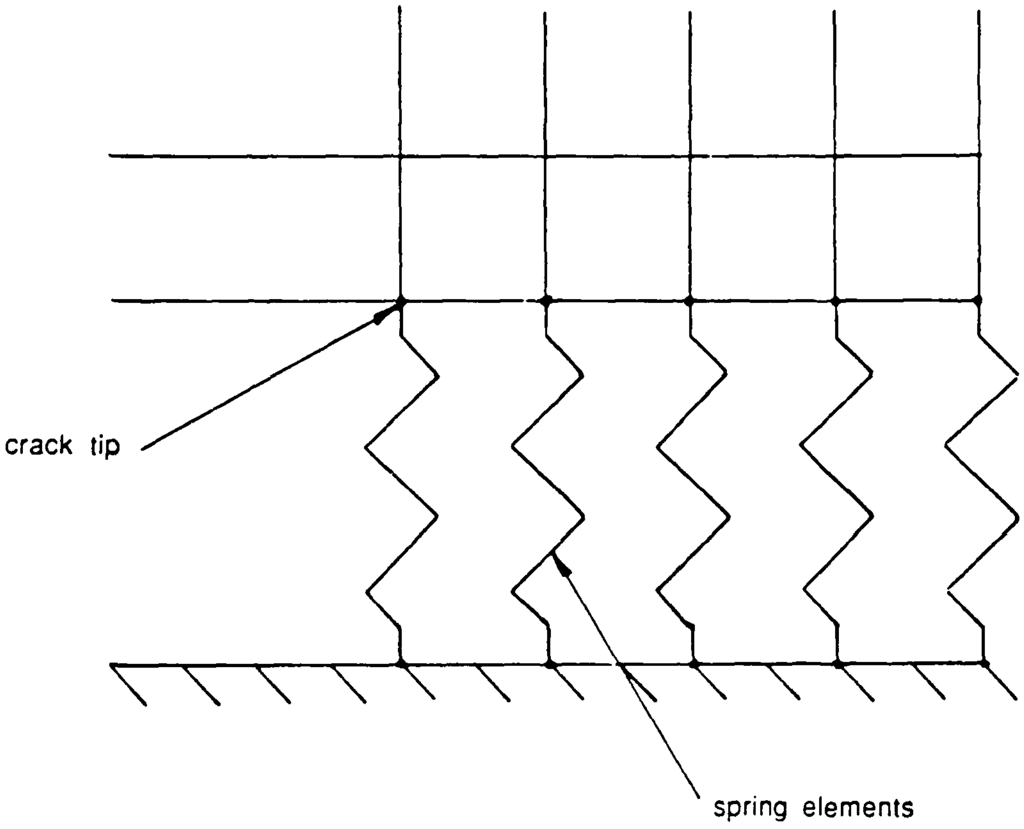
crack tip
spring elements

Figure 6: Stiffness reduction accomplished with spring elements.

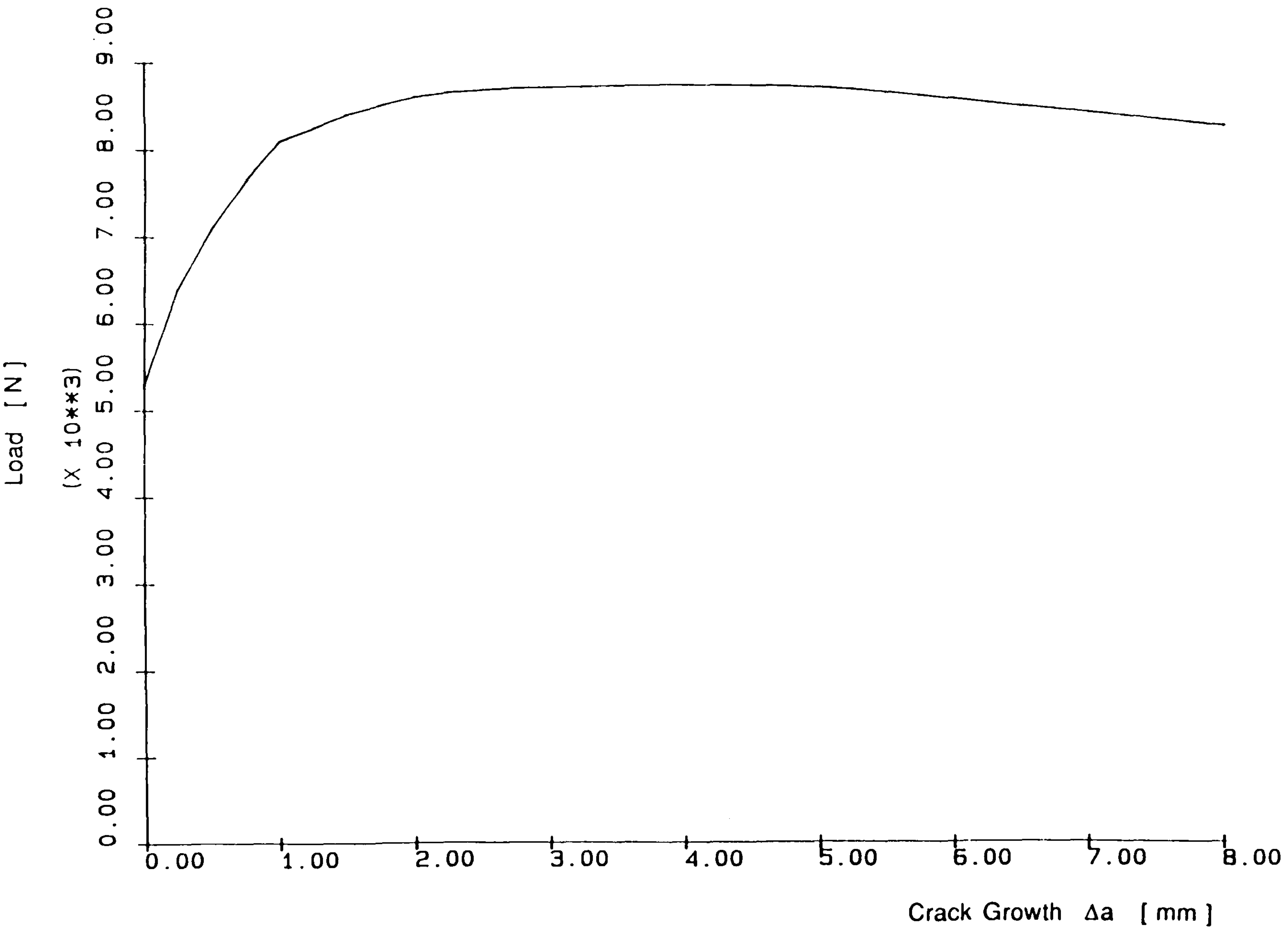

Figure 7: Load vs. crack growth.

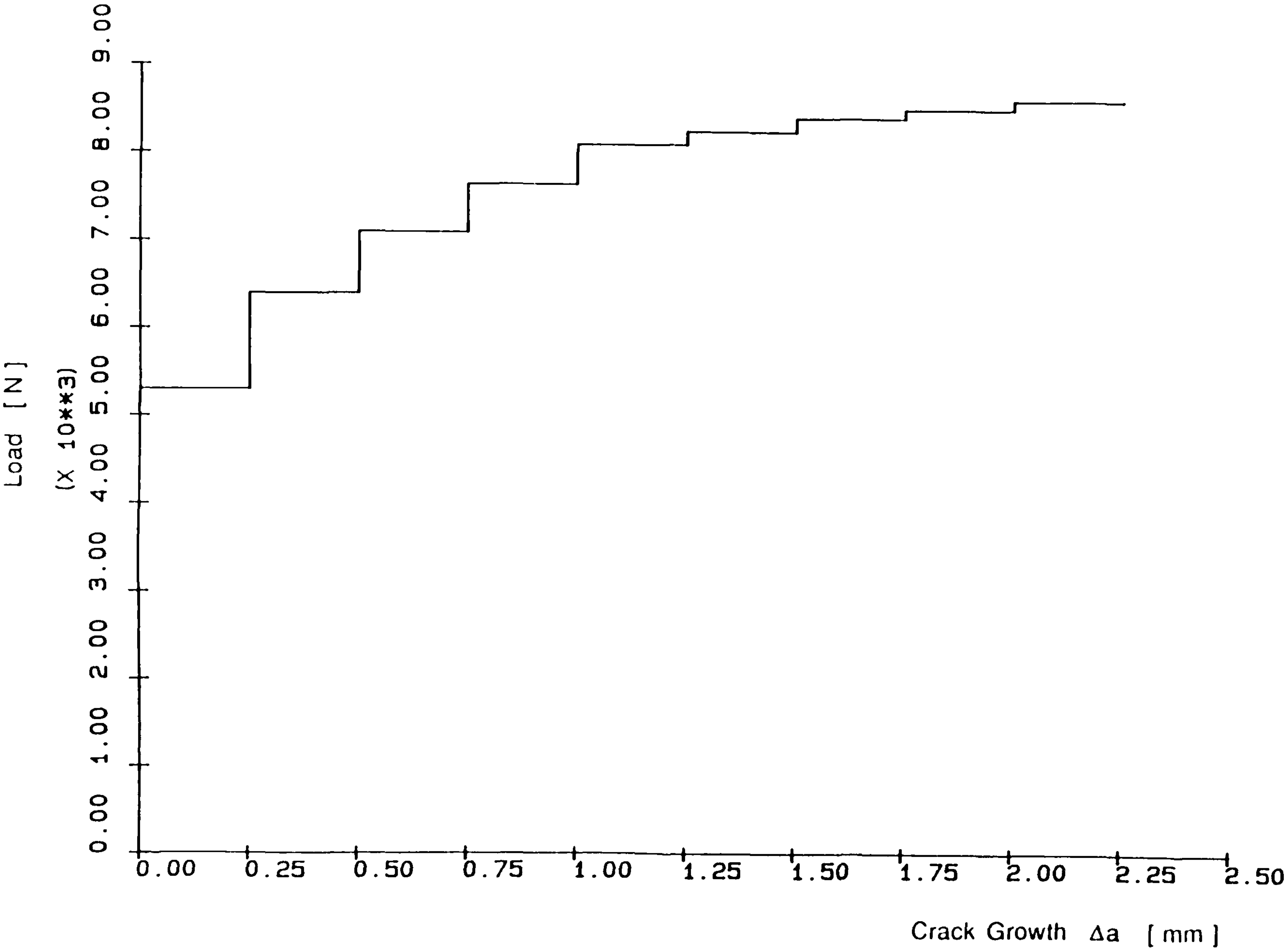

Figure 8. Pop in crack growth simulation.

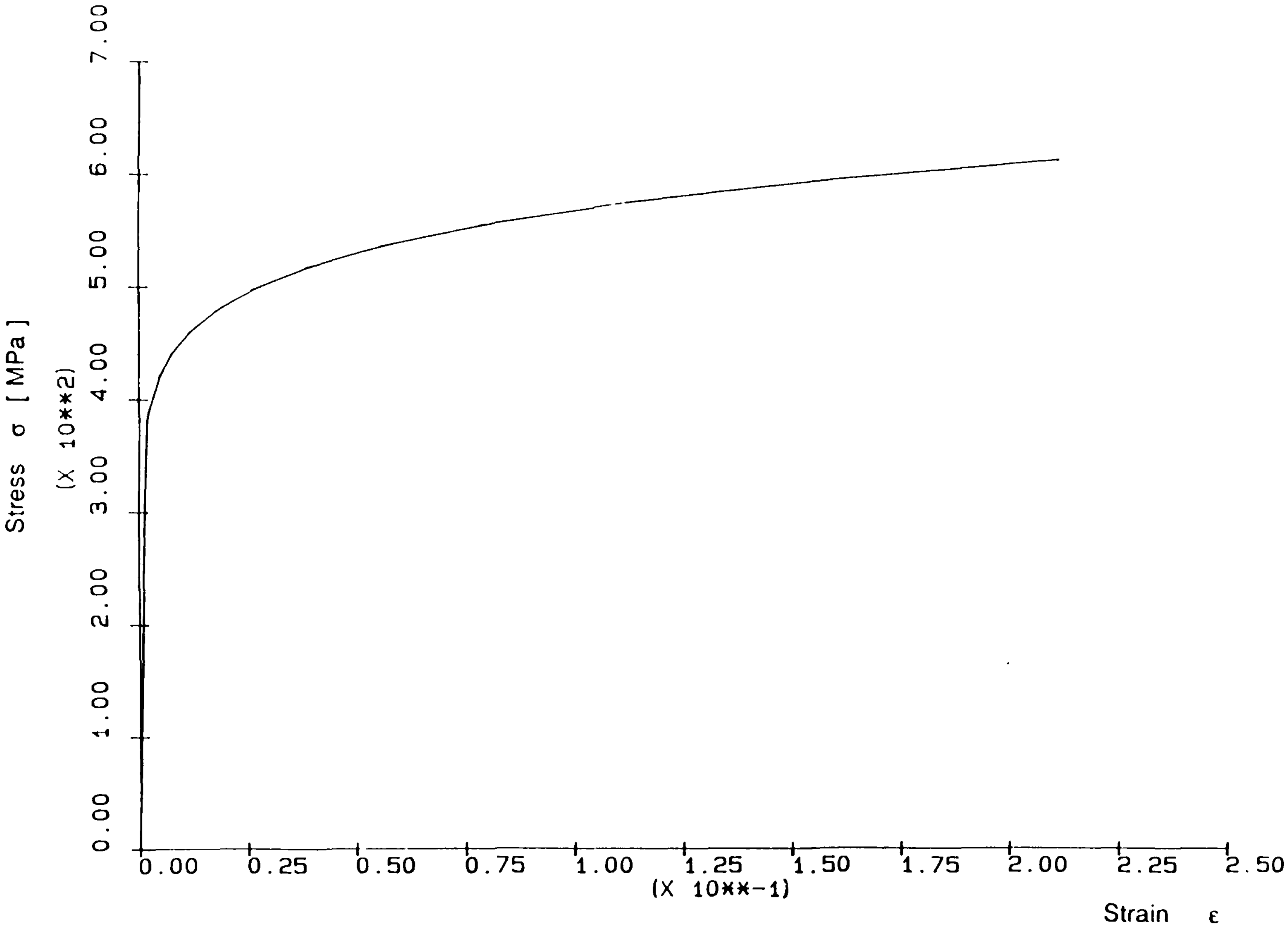

__Figure 9:__ Stress vs. strain (A533B steel)

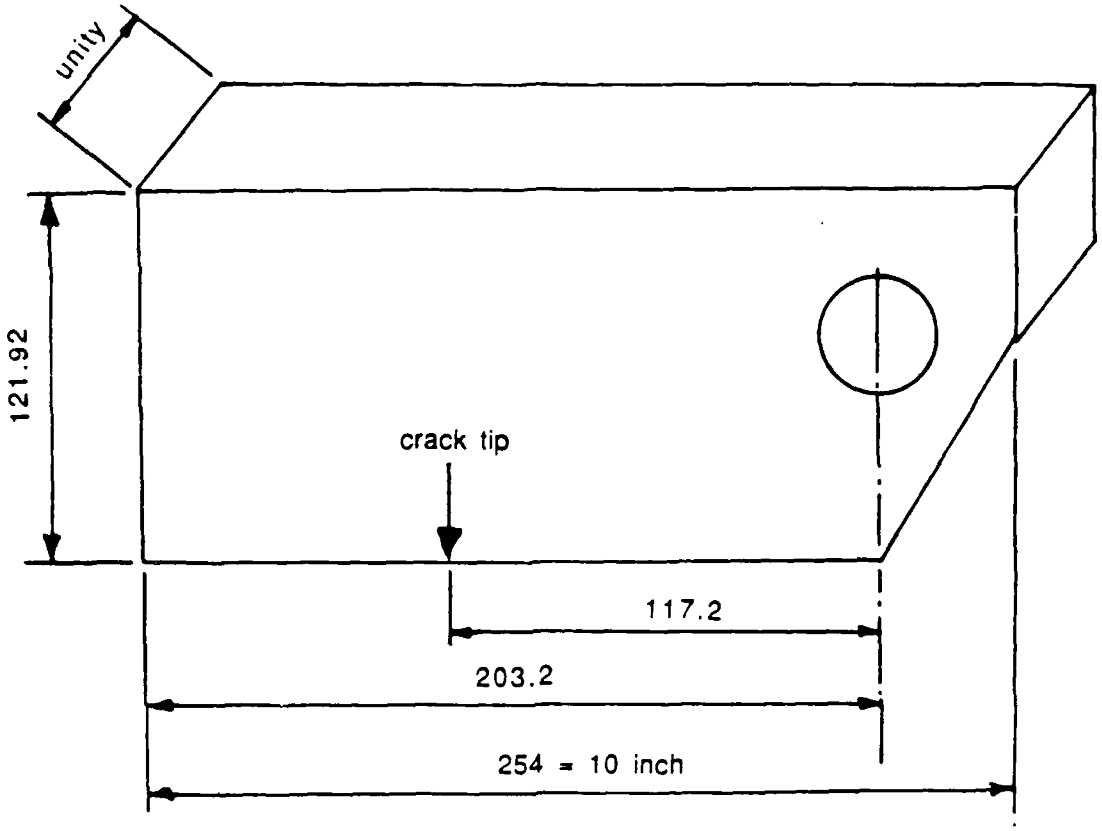
unity
121.92
crack tip
117.2
203.2
254 = 10 inch

Figure 10: Dimensions of the employed Compact Tension specimen (only one half of the specimen is shown, all quantities are given in millimeter).

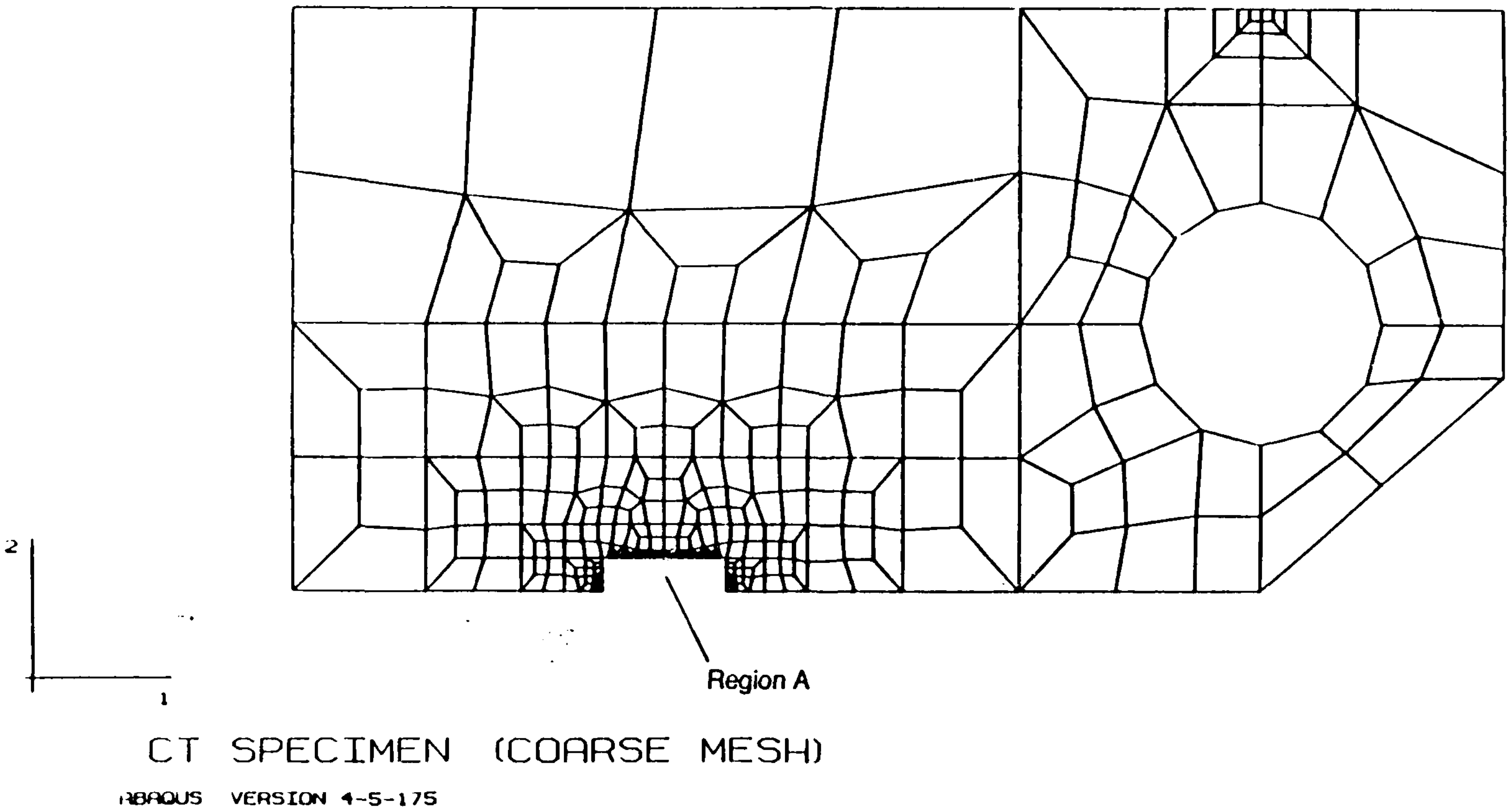
2
1
Region A
CT SPECIMEN (COARSE MESH)
ABAQUS VERSION 4-5-175

Figure 11a: Finite element modeling of the Compact Tension specimen (coarse mesh).

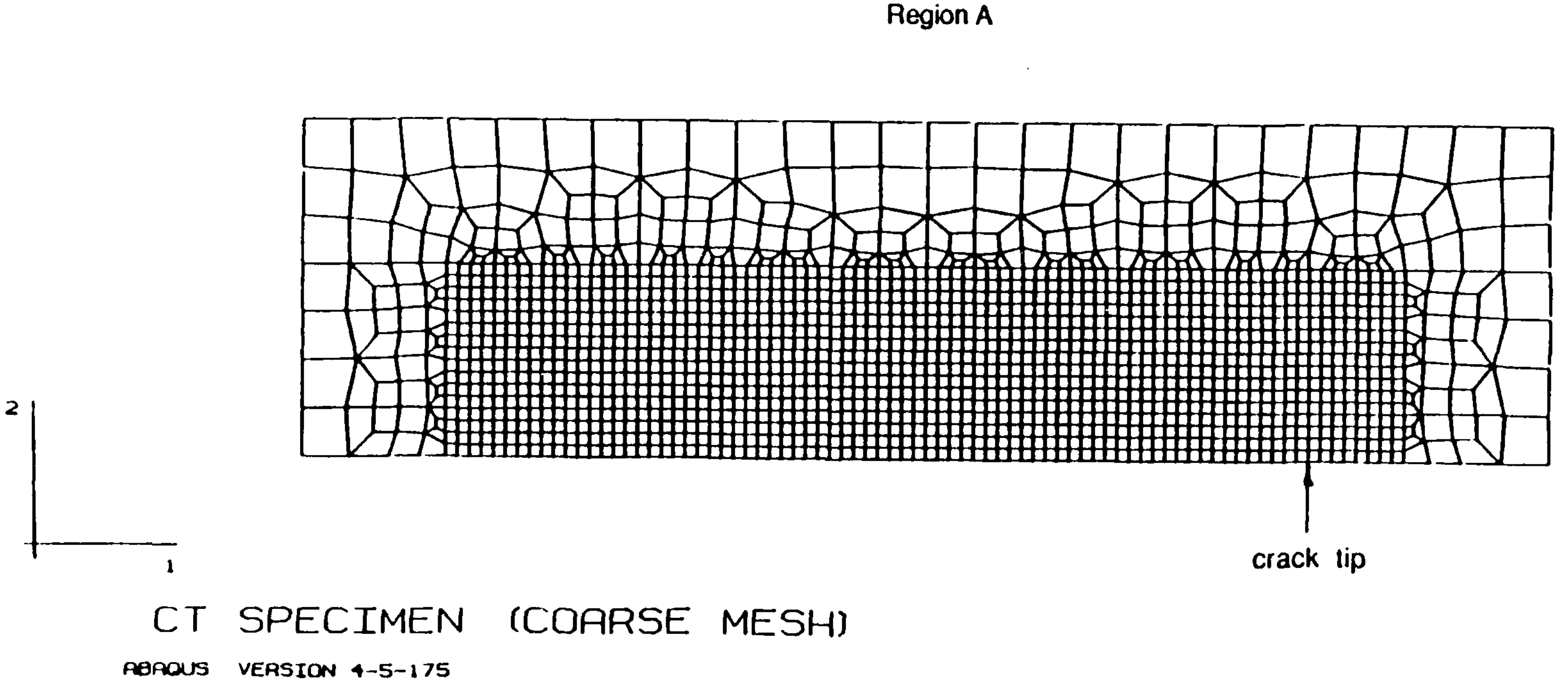
Region A
crack tip
2
1
CT SPECIMEN (COARSE MESH)
ABAQUS VERSION 4-5-175

Figure 11b: Finite element modeling of the Compact Tension specimen (coarse mesh).

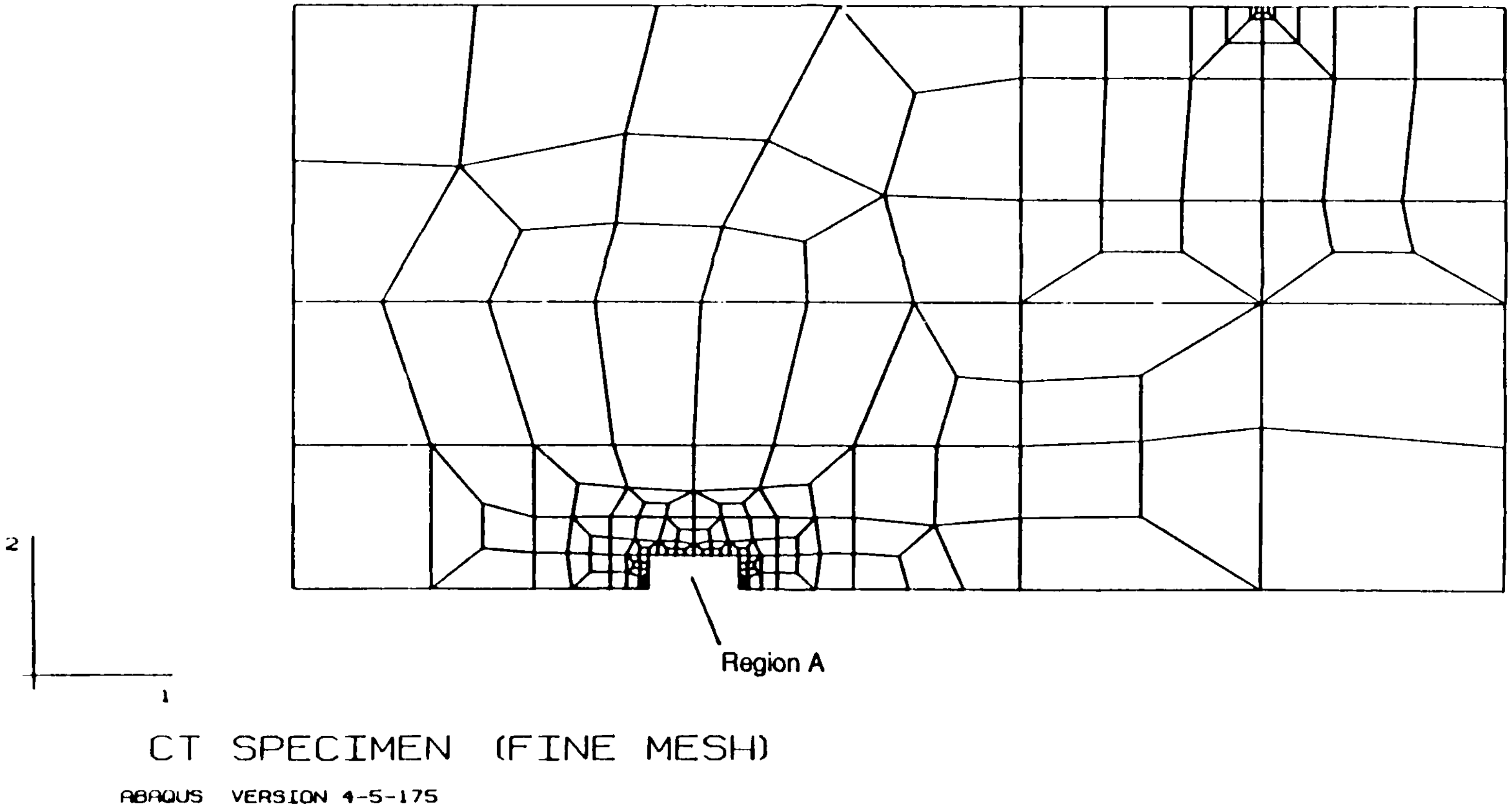
Region A
2
1
CT SPECIMEN (FINE MESH)
ABAQUS VERSION 4-5-175

Figure 12a: Finite element modeling of the Compact Tension specimen (fine mesh).

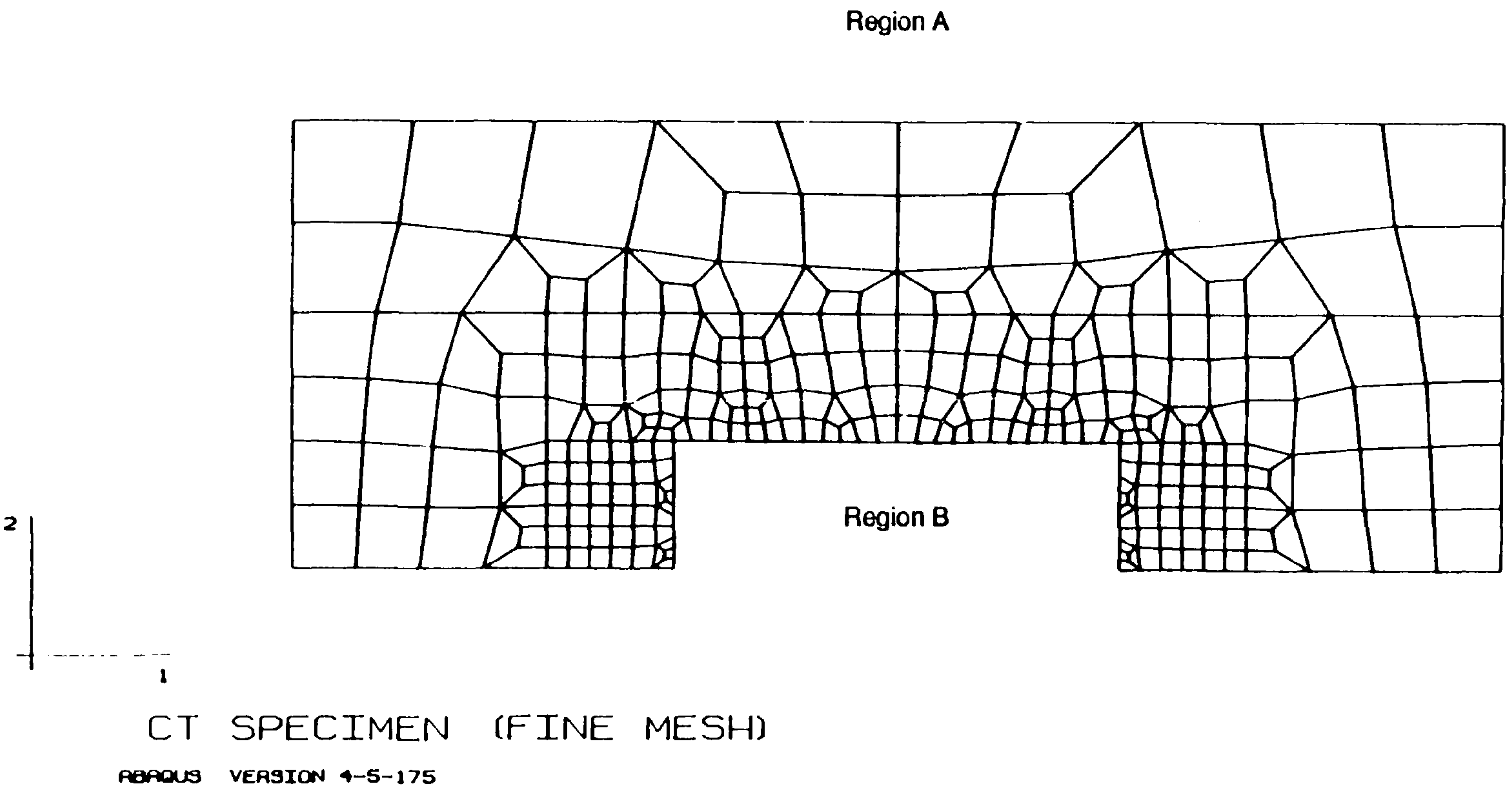
Region A
Region B
2
1
CT SPECIMEN (FINE MESH)
ABAQUS VERSION 4-5-175

Figure 12b. Finite element modeling of the Compact Tension specimen (fine mesh).

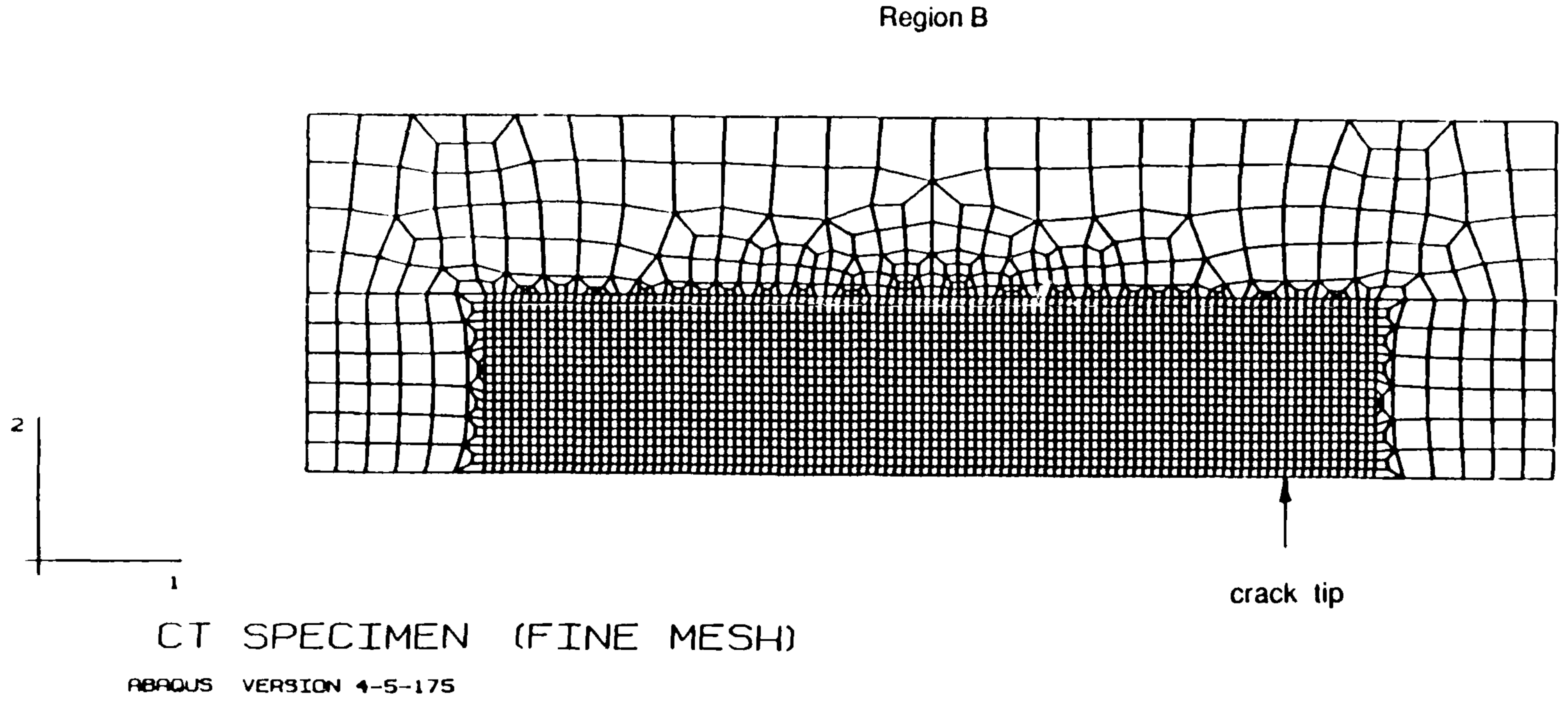
Region B
crack tip
2
1
CT SPECIMEN (FINE MESH)
ABAQUS VERSION 4-5-175

Figure 12c: Finite element modeling of the Compact Tension specimen (fine mesh).

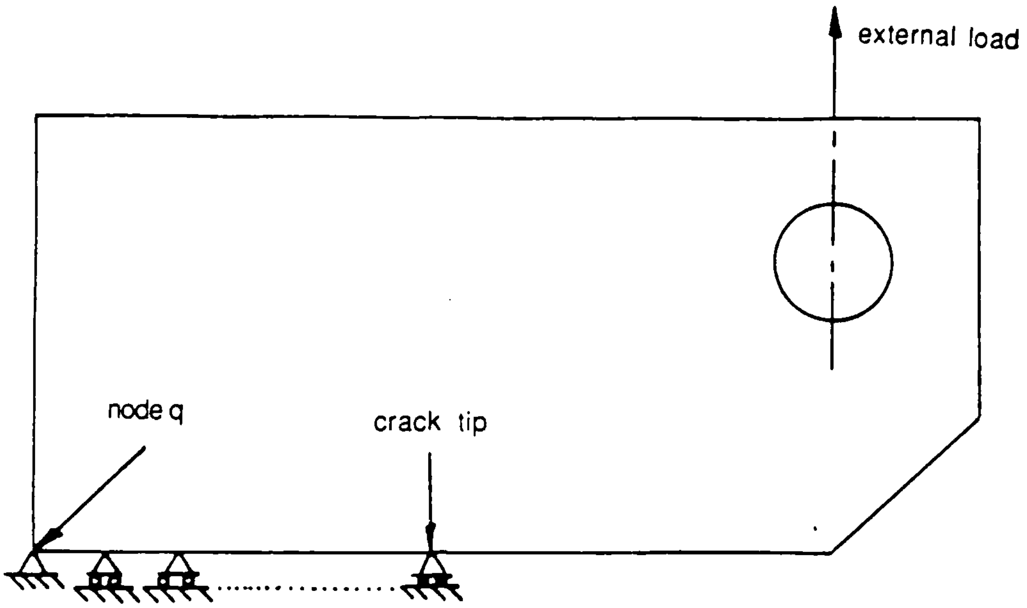
external load
node q
crack tip

Figure 13: Boundary conditions.

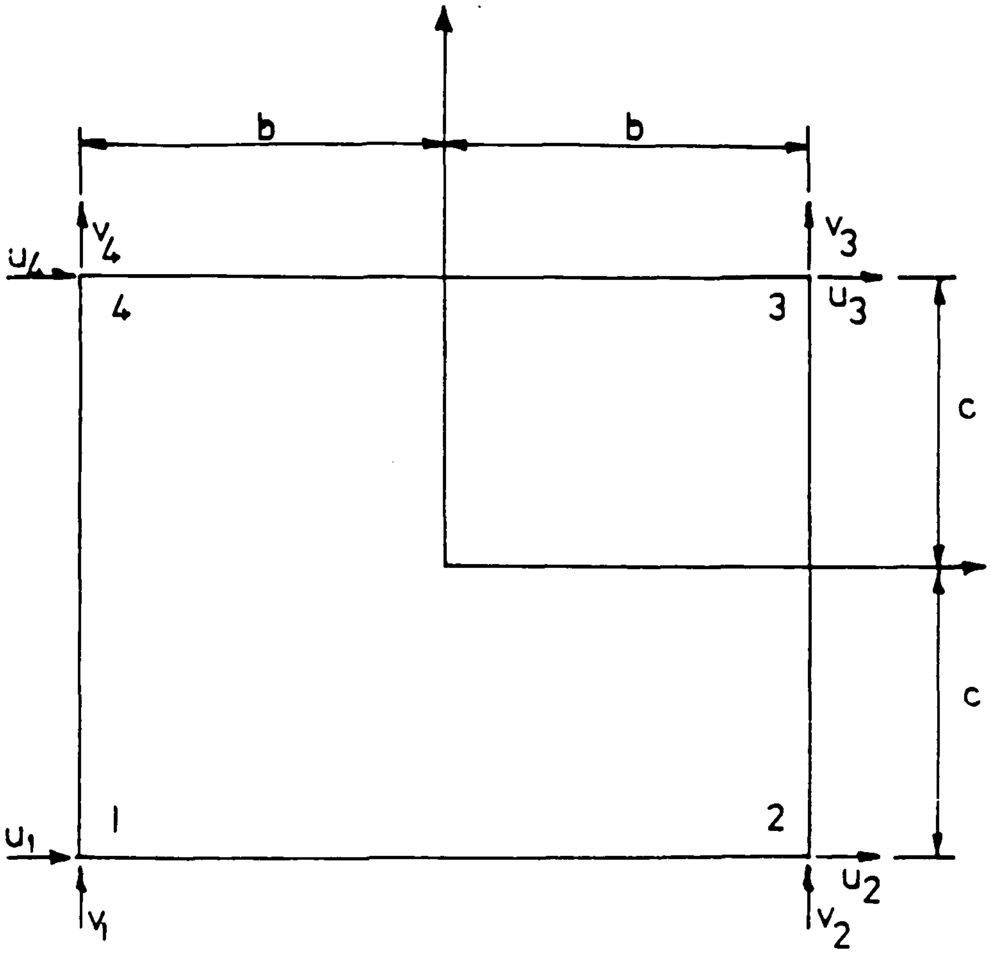
b
b
v4
v3
u4
u3
4
3
c
c
1
2
u1
u2
v1
v2

Figure 14: Eight d. o. f. bilinear element.

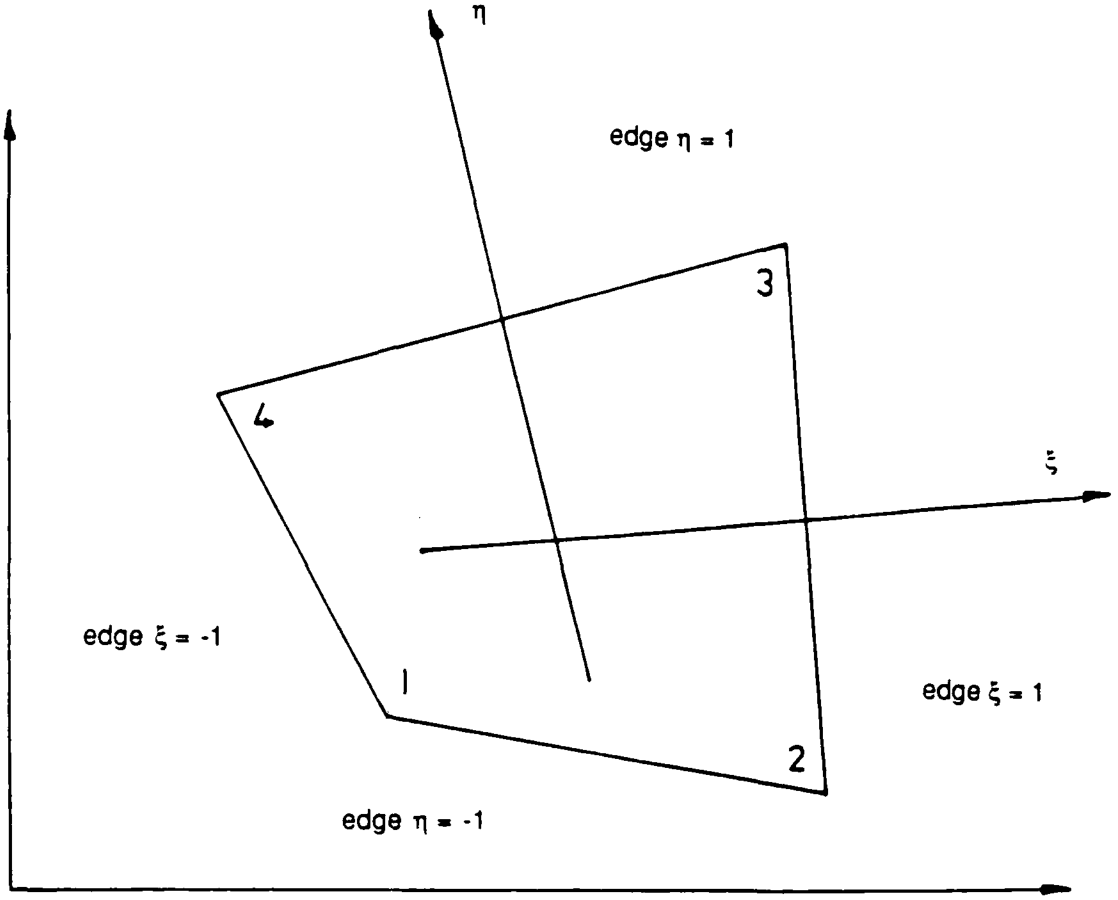
η
edge η = 1
3
4
ξ
edge ξ = -1
1
edge ξ = 1
2
edge η = -1

Figure 15: Mapping of the eight d. o. f. bilinear element from natural coordinates into xy - space.

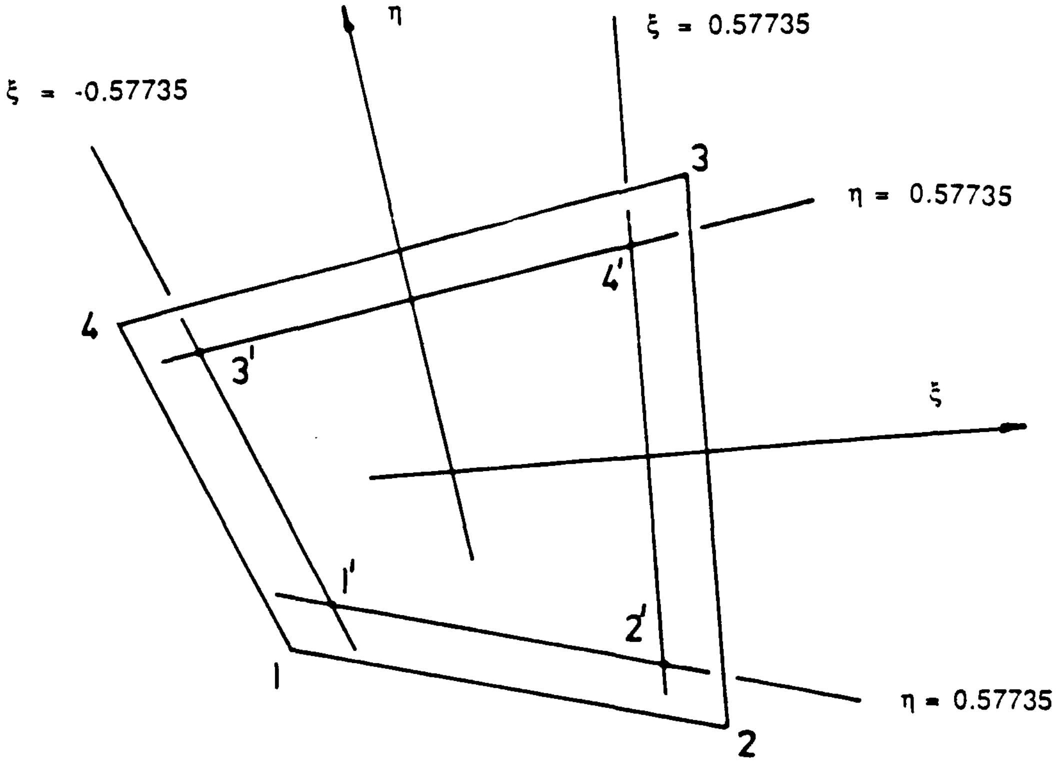
η
ξ = 0.57735
ξ = -0.57735
3
η = 0.57735
4'
4
3'
ξ
1'
2'
1
η = 0.57735
2

Figure 16: Locations of the Gauss quadrature integration points within an eight d. o. f. bilinear isoparametric element.

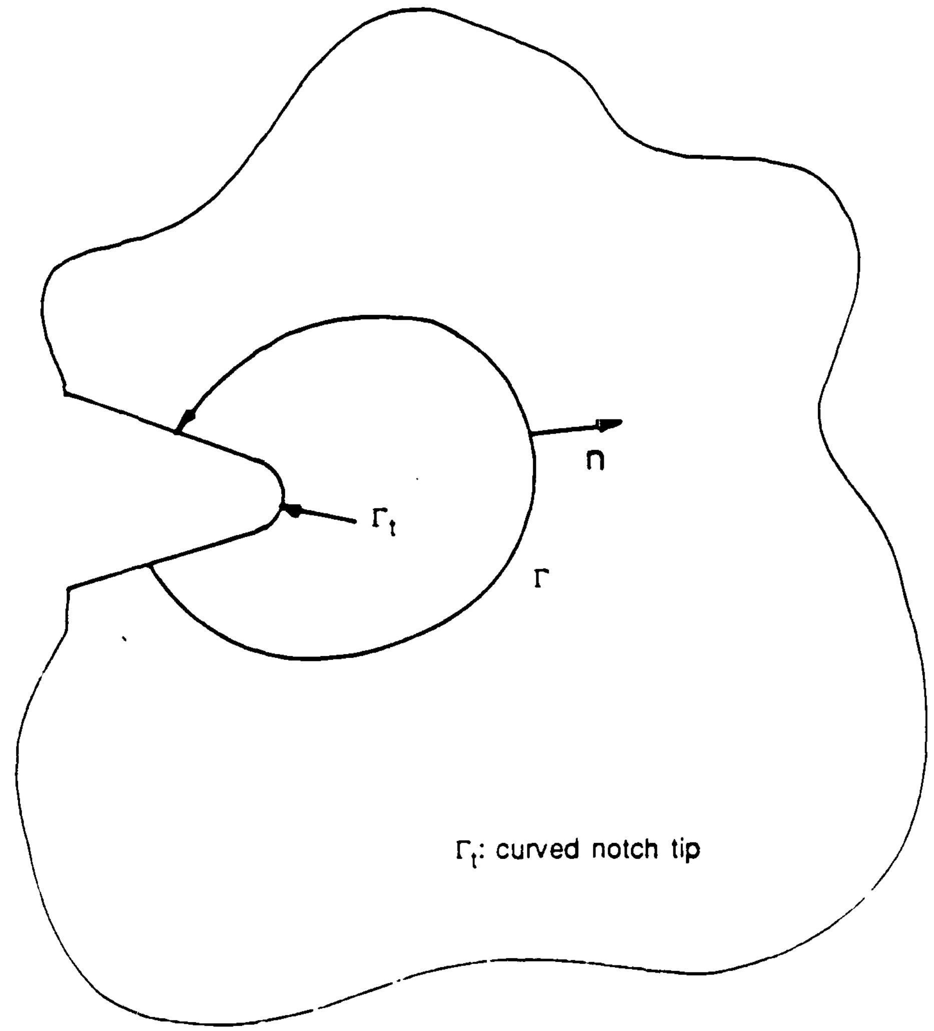

n
Γ_t
Γ
Γ_t: curved notch tip

Figure 17: Definition of the line of the J - integral around a notch.

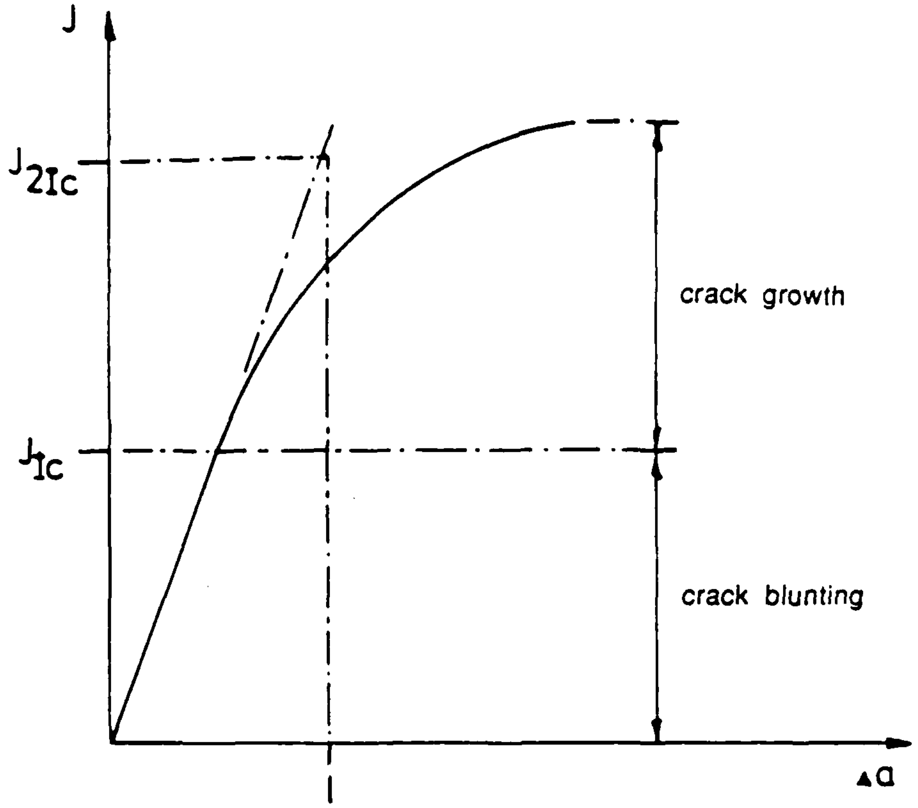

Figure 18: Typical J - resistance curve.

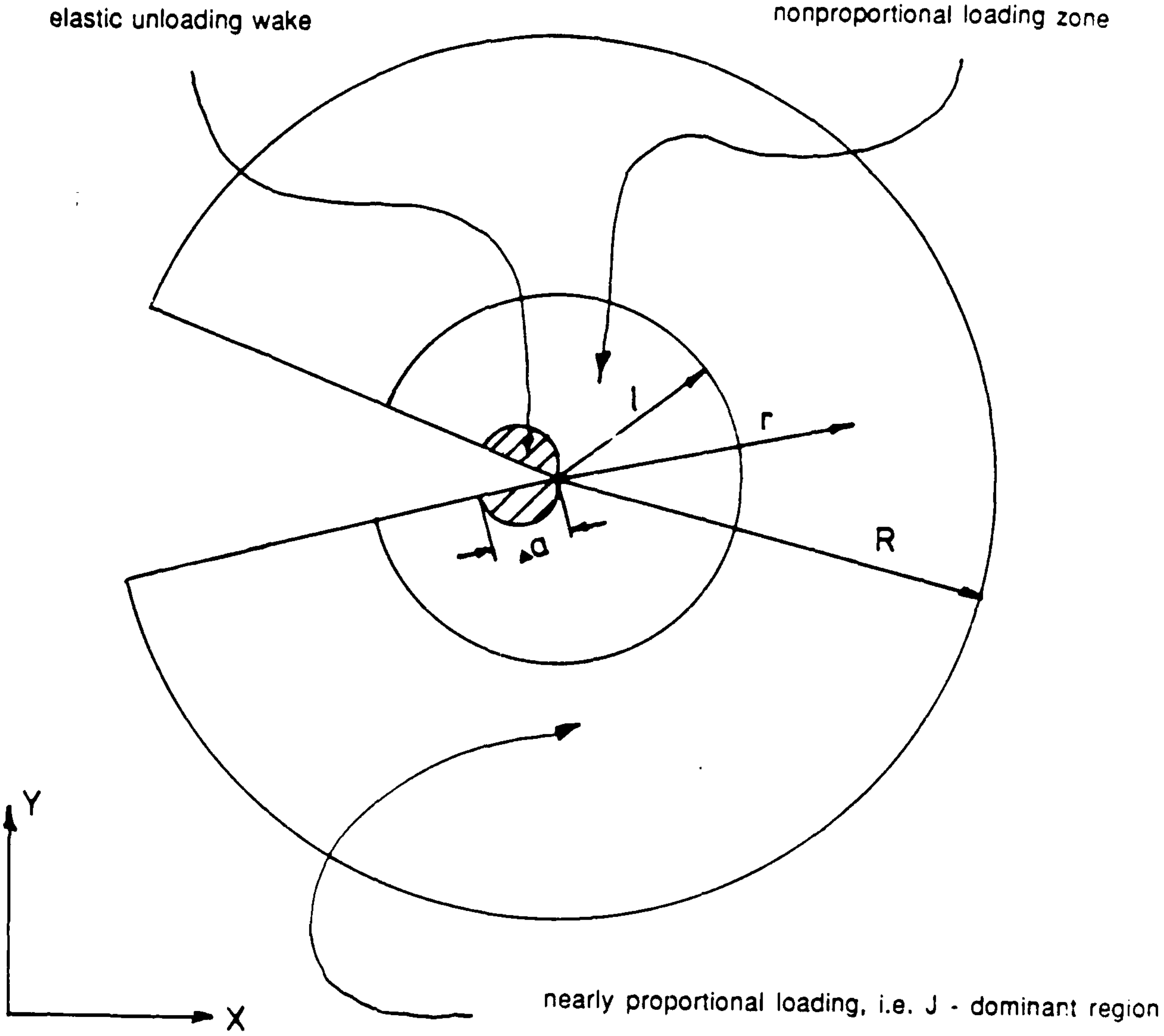
elastic unloading wake
nonproportional loading zone
l
r
R
Δa
Y
X
nearly proportional loading, i.e. J - dominant region

Figure 19: Schematic of the fields surrounding a growing crack [34].

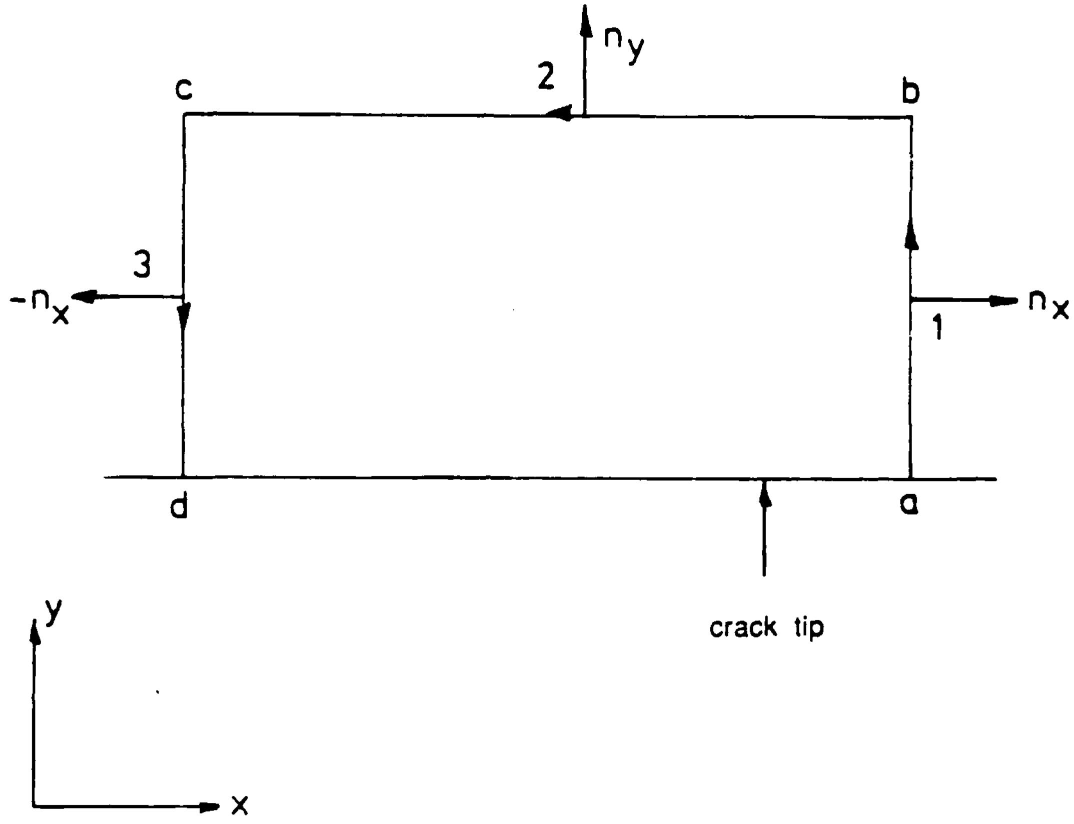
n_y
2
c
b
3
-n_x
n_x
1
d
a
y
crack tip
x

Figure 20: Evaluation line for the J - integral.

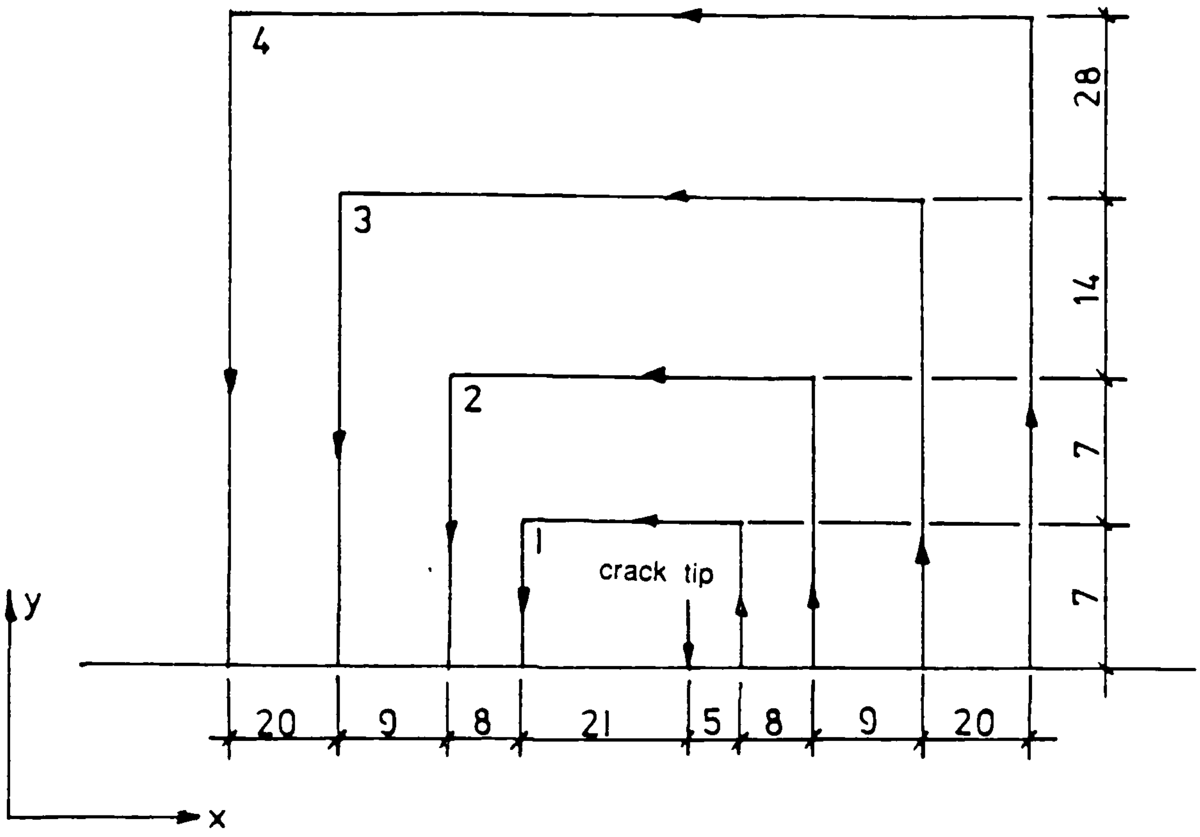
4
3
2
1
crack tip
y
x
20
9
8
21
5
8
9
20
28
14
7
7

Figure 21: Verification paths for the path independence of the J - integral.

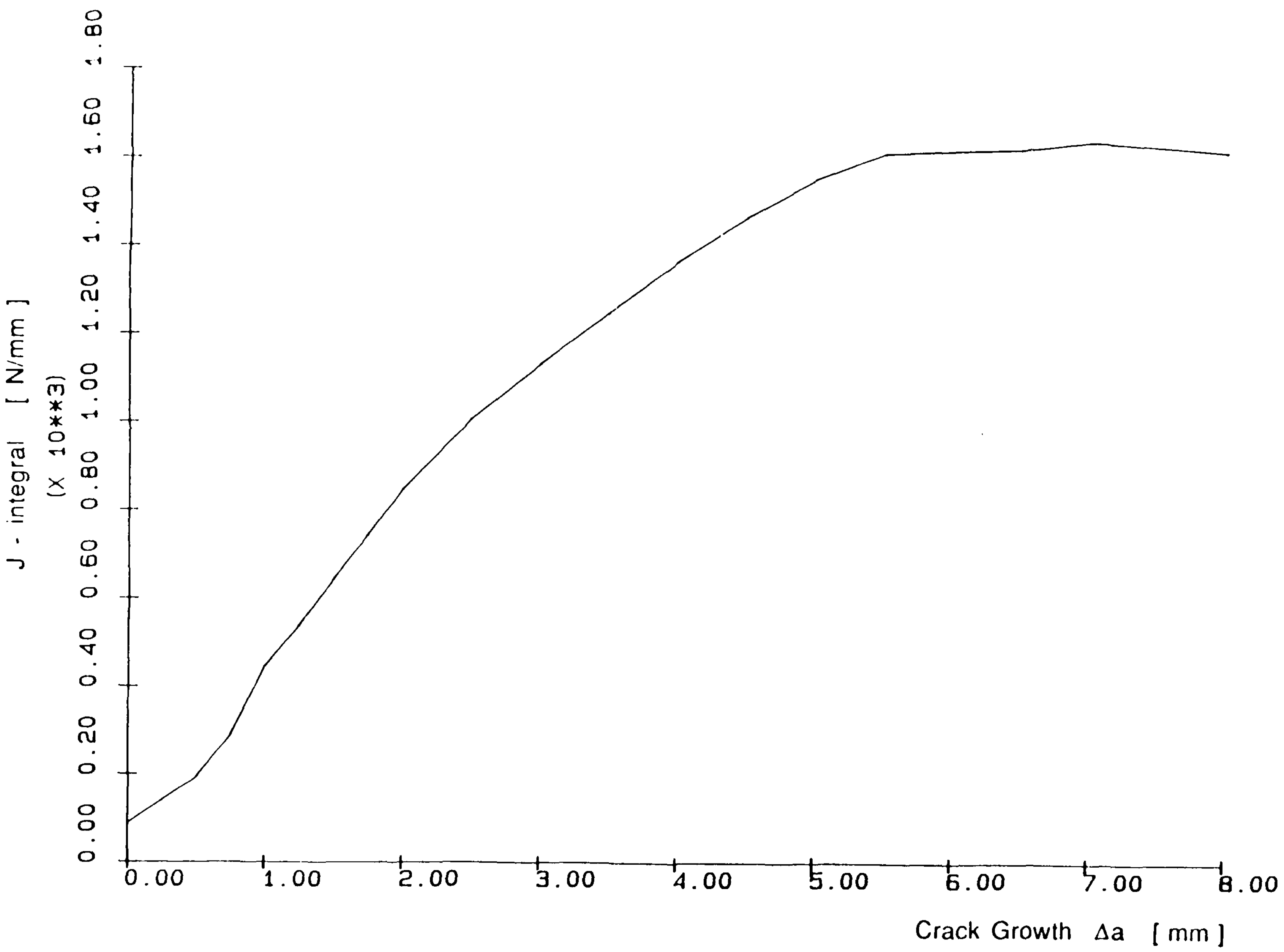

Figure 22: J - integral vs. crack growth.

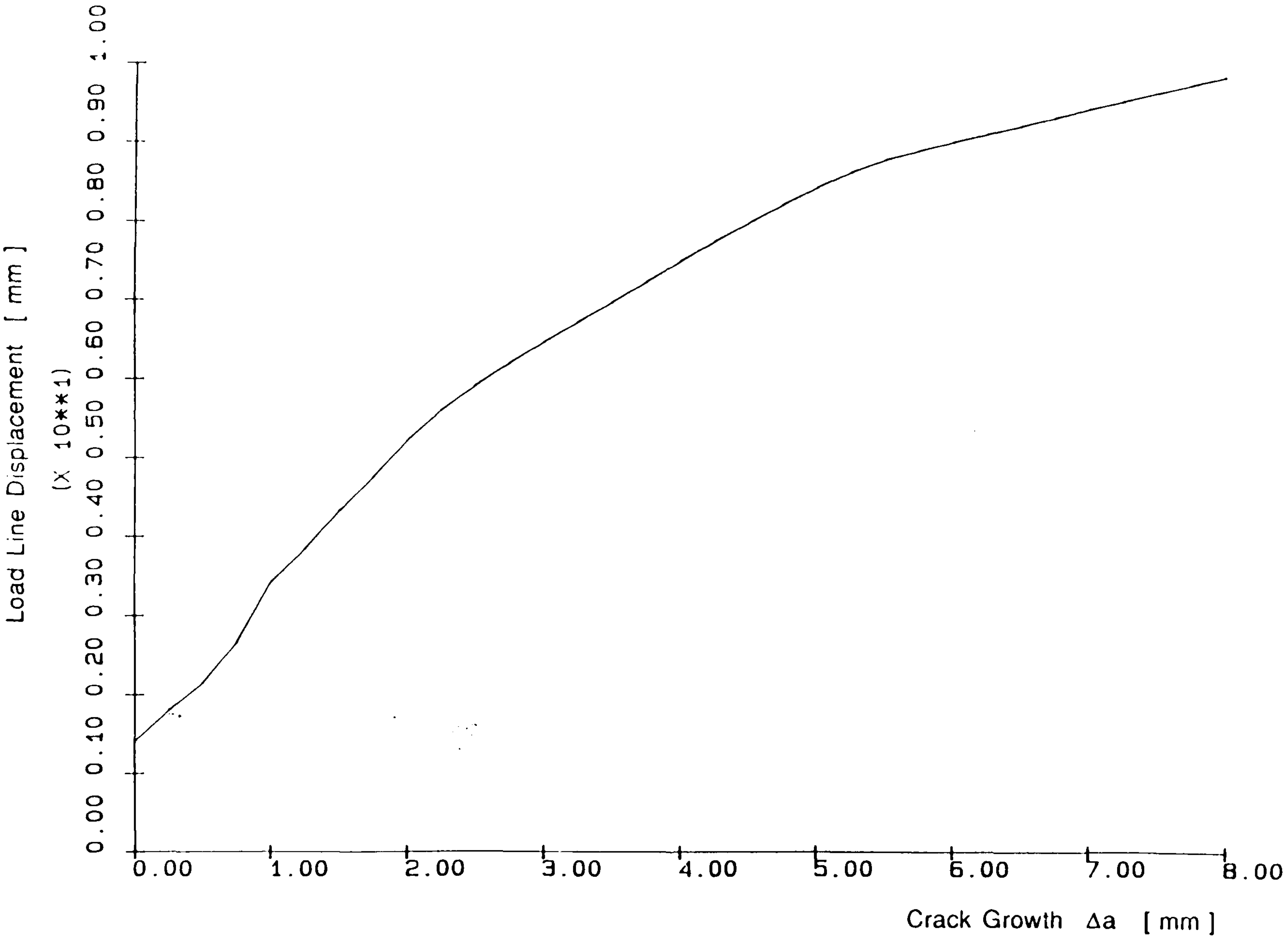

Figure 23: Load - line displacement vs. crack growth

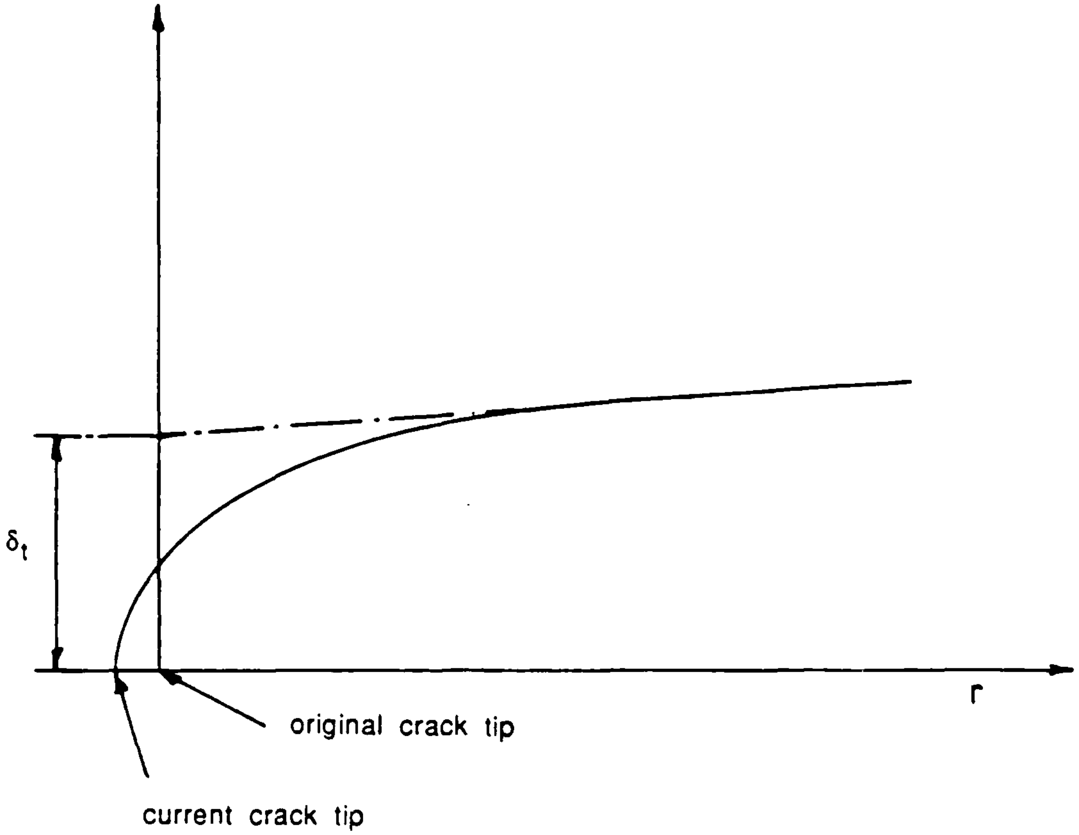
δ_t
r
original crack tip
current crack tip

Figure 24: "Tangent" - definition of the crack tip opening displacement.

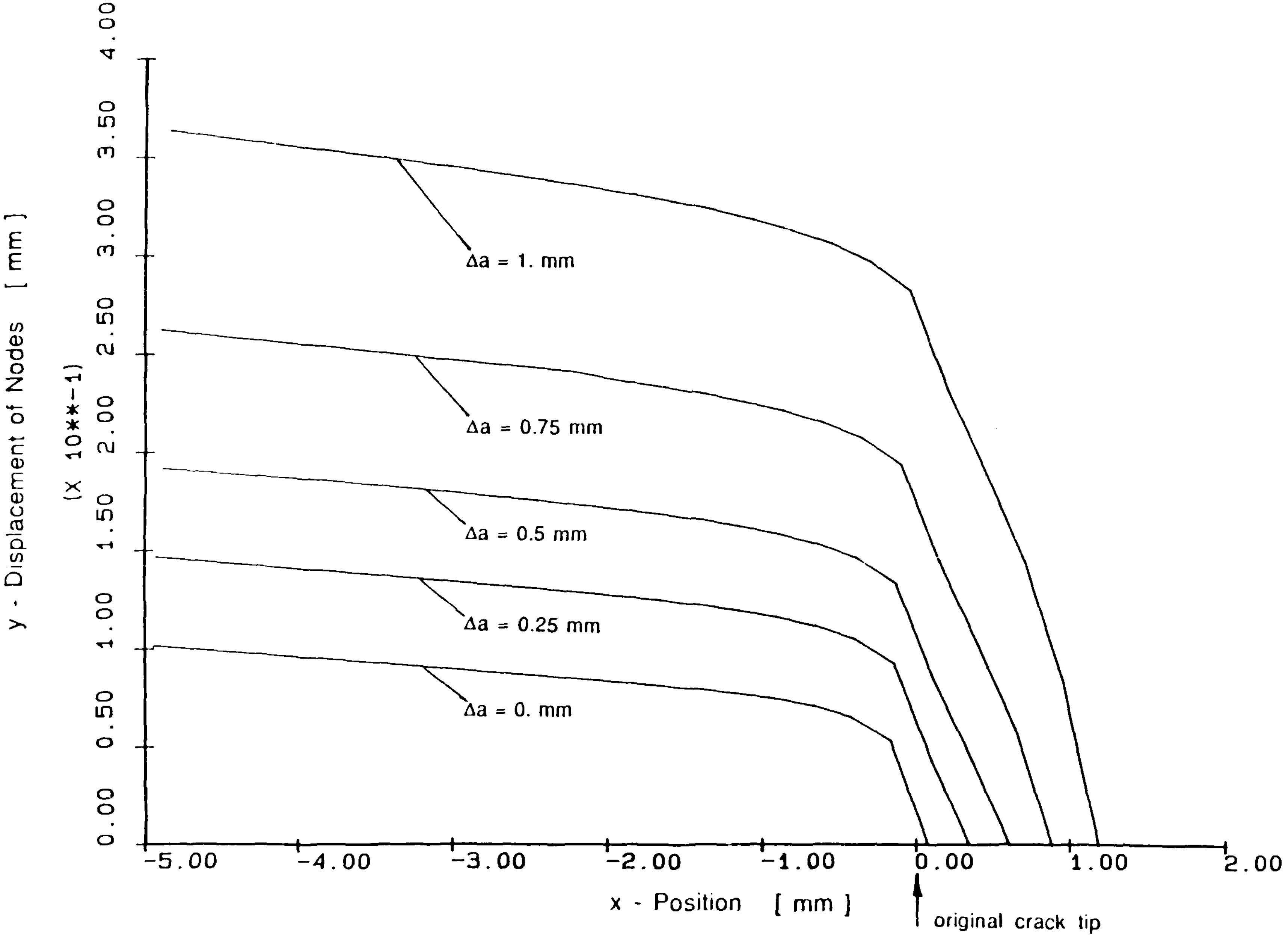

Figure 25: Crack profile (coarse mesh, 0 - 1 mm crack growth).

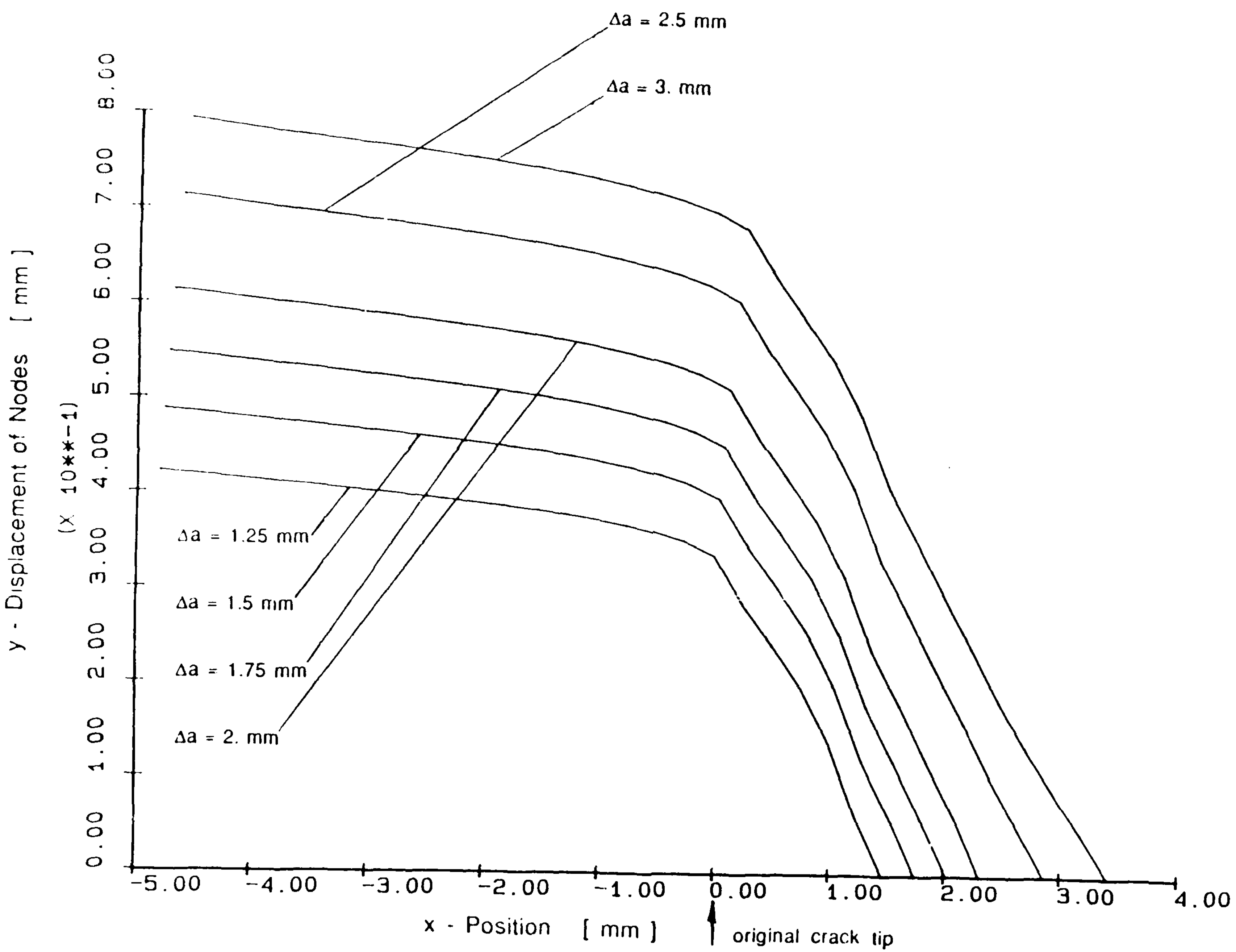

Figure 26. Crack profile (coarse mesh, 1.25 - 3 mm crack growth).

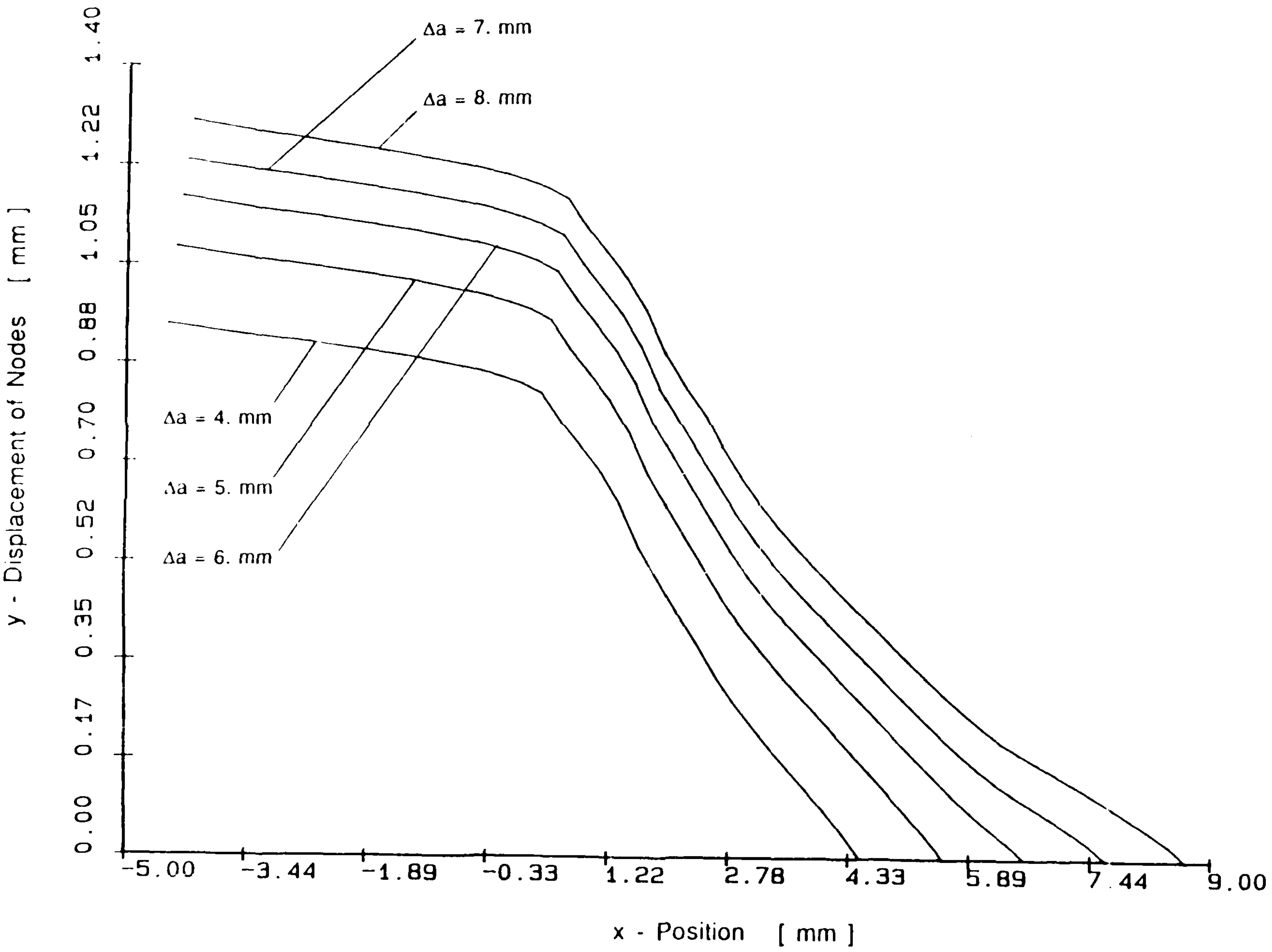

Figure 27. Crack profile (coarse mesh, 4 - 8 mm crack growth).

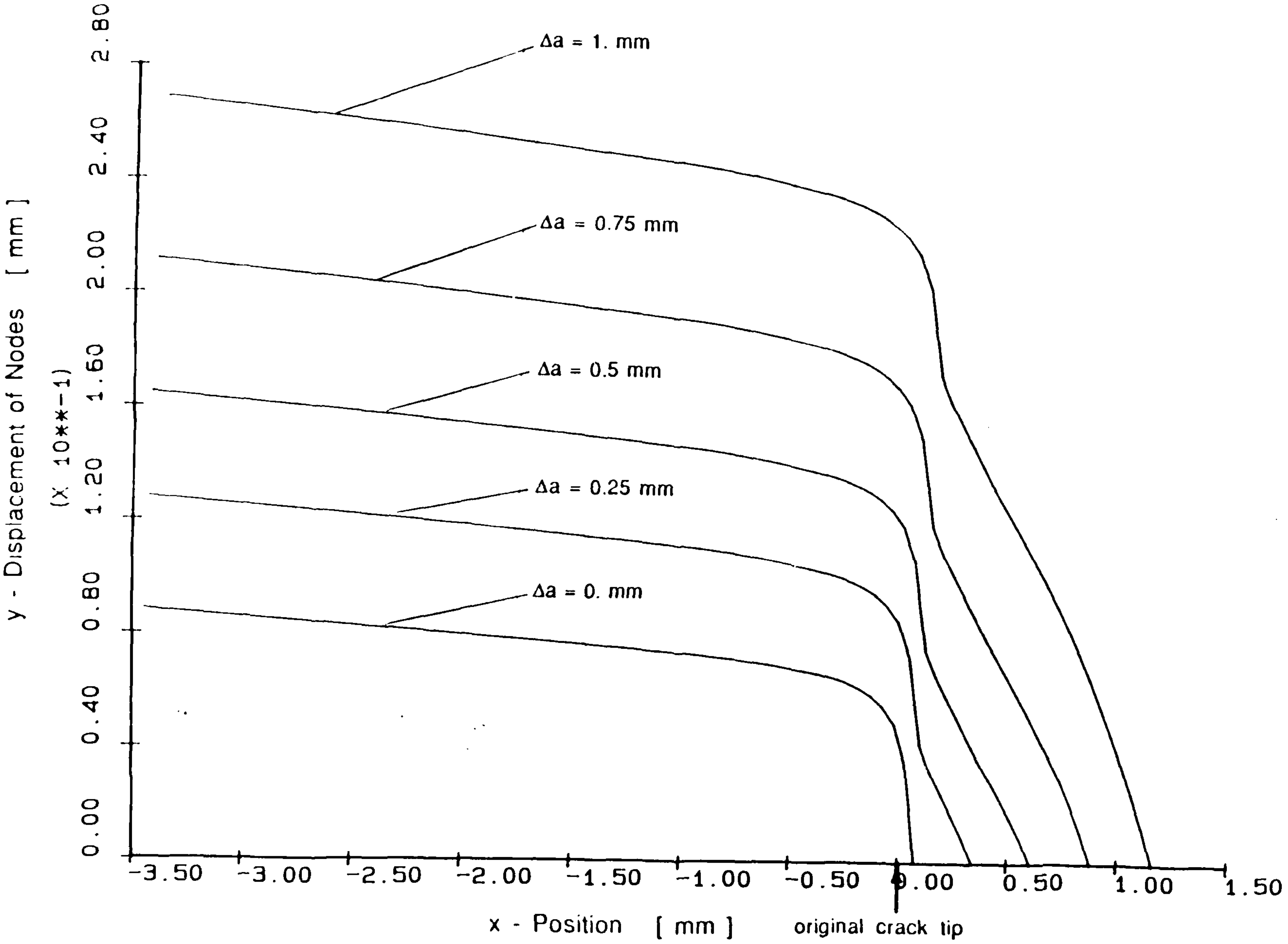

Figure 28: Crack profile (fine mesh, 0 - 1 mm crack growth).

Figure 29a: Crack tip region (coarse mesh).

- load 5300 N

- Δa 0. mm

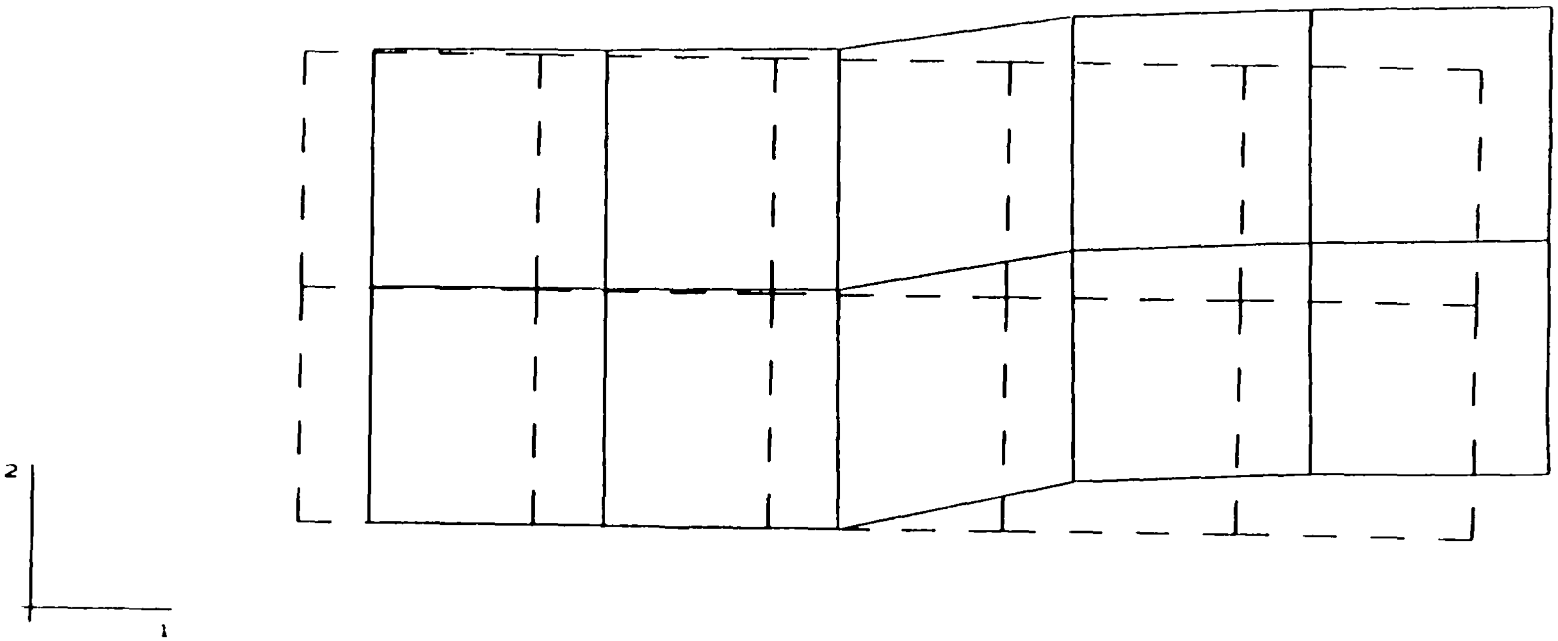
DISPL.
MAG. FACTOR = +1.0E+00
SOLID LINES - DISPLACED MESH
DASHED LINES - ORIGINAL MESH
2
1
CT - SPECIMEN
STEP 1 INCREMENT 1
ABAQUS VERSION 4-5-175

Figure 29b: Crack tip region (coarse mesh).

- load 6400 N

- Δa 0.25 mm

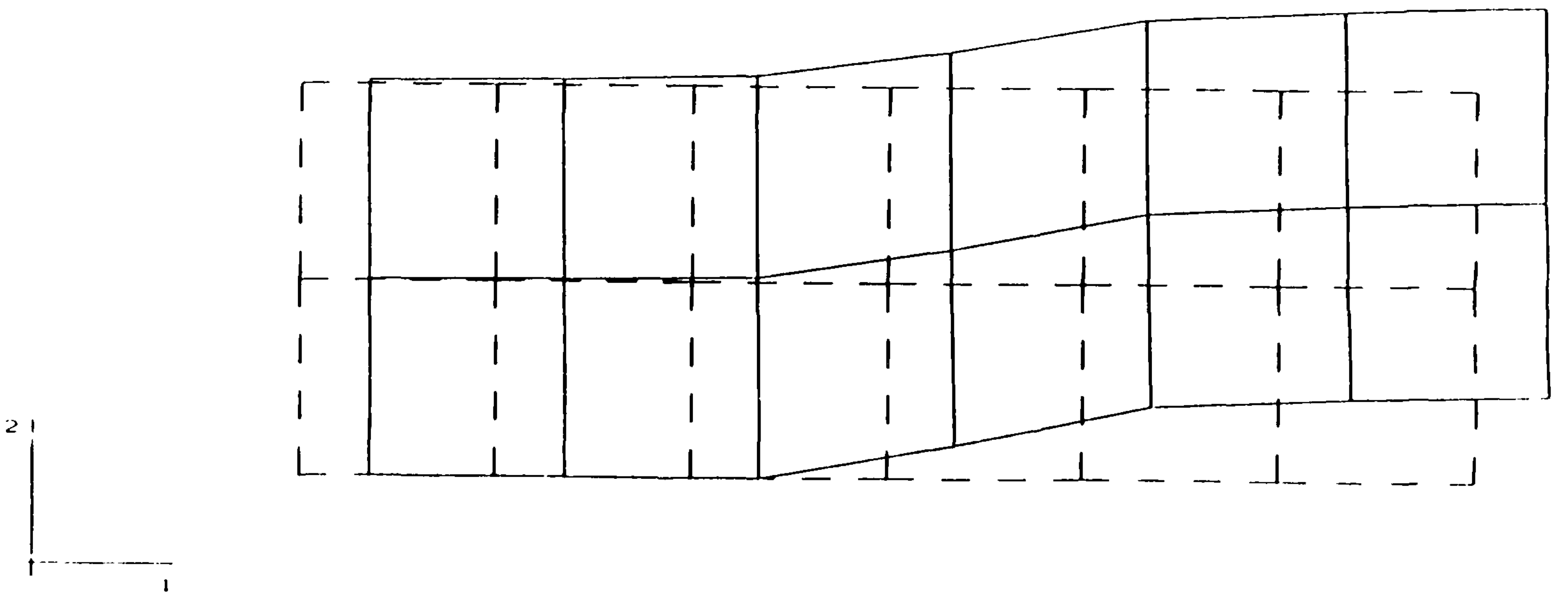
DISPL.
MAG. FACTOR = +1.0E+00
SOLID LINES - DISPLACED MESH
DASHED LINES - ORIGINAL MESH
2
1
CT - SPECIMEN
STEP 2 INCREMENT 1
ABAQUS VERSION 4-5-175

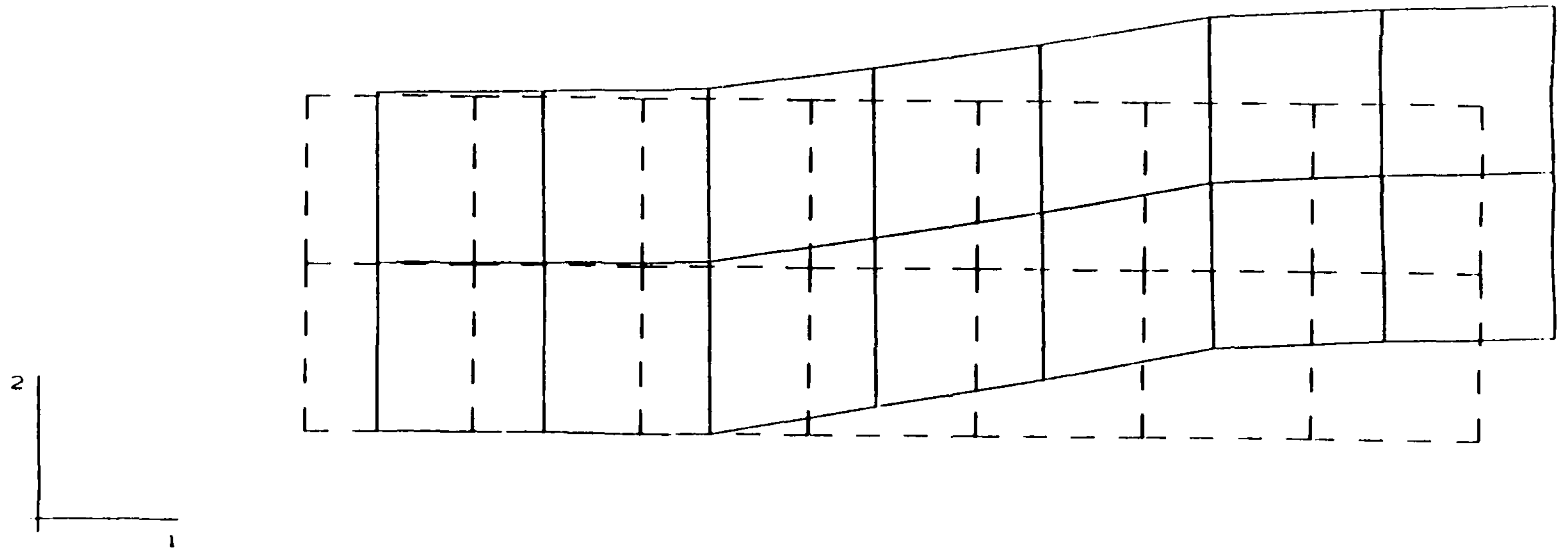
DISPL.
MAG. FACTOR = +1.0E+00
SOLID LINES - DISPLACED MESH
DASHED LINES - ORIGINAL MESH
2
1
CT - SPECIMEN
STEP 3 INCREMENT 1
ABAQUS VERSION 4-5-175

Figure 29c: Crack tip region (coarse mesh).

- load 7100 N
- Δa 0.5 mm

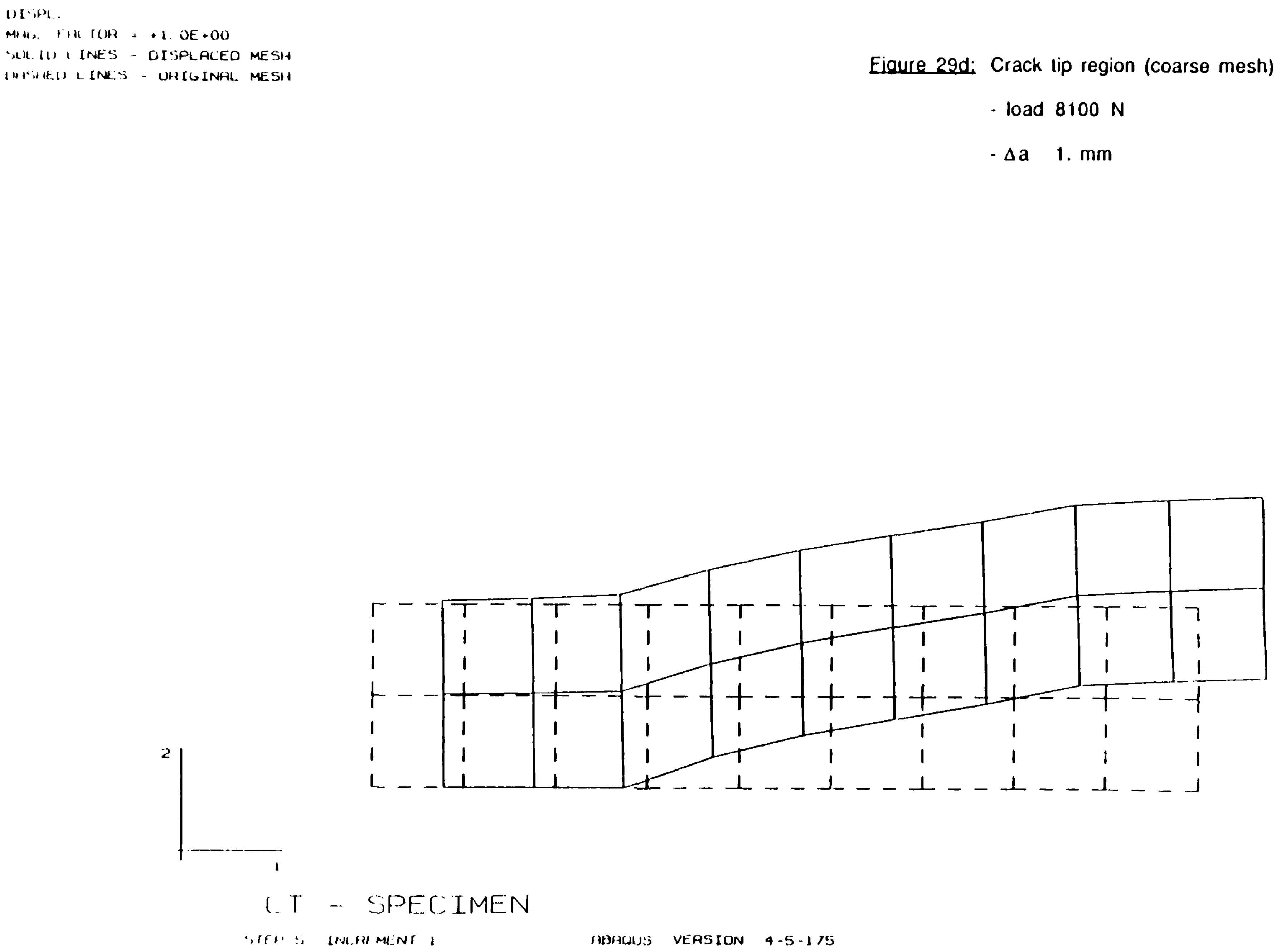
DISPL.
MAG. FACTOR = +1.0E+00
SOLID LINES - DISPLACED MESH
DASHED LINES - ORIGINAL MESH
2
1
CT - SPECIMEN
STEP 5 INCREMENT 1
ABAQUS VERSION 4-5-175

Figure 29d: Crack tip region (coarse mesh).

- load 8100 N

- Δa 1. mm

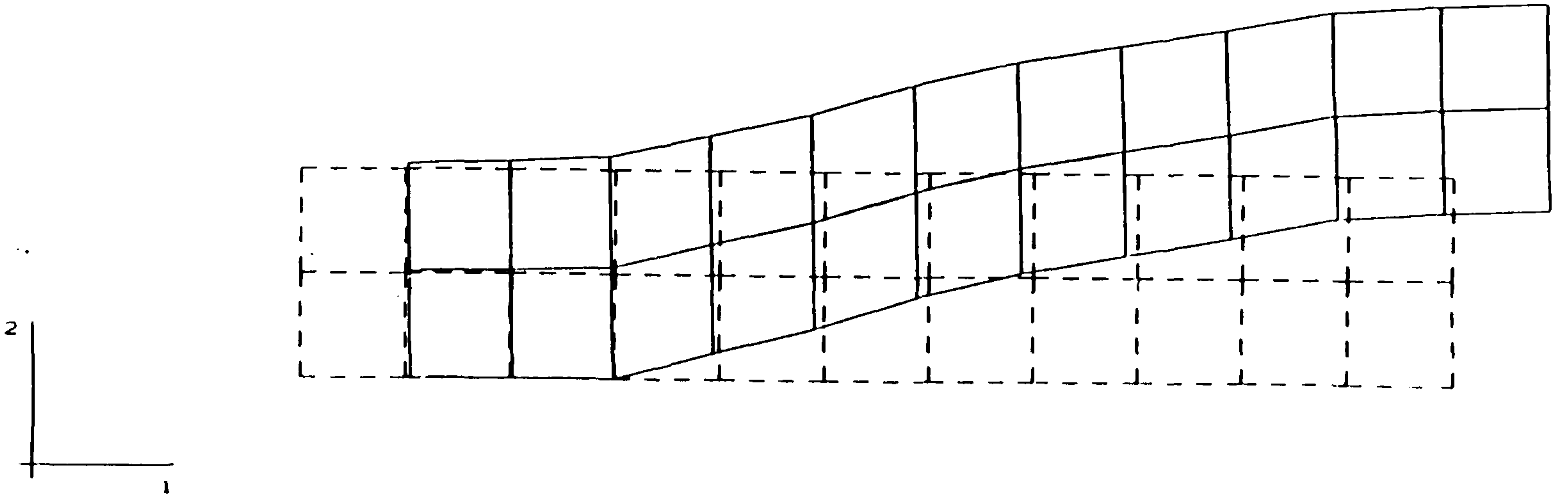
DISPL.
MAG. FACTOR = +1.0E+00
SOLID LINES - DISPLACED MESH
DASHED LINES - ORIGINAL MESH
2
1
CT - SPECIMEN
STEP 7 INCREMENT 1
ABAQUS VERSION 4-5-175

Figure 29e: Crack tip region (coarse mesh).

- load 8400 N
- Δa 1.5 mm

Figure 29f: Crack tip region (coarse mesh).

- load 8600 N

- Δa 2. mm

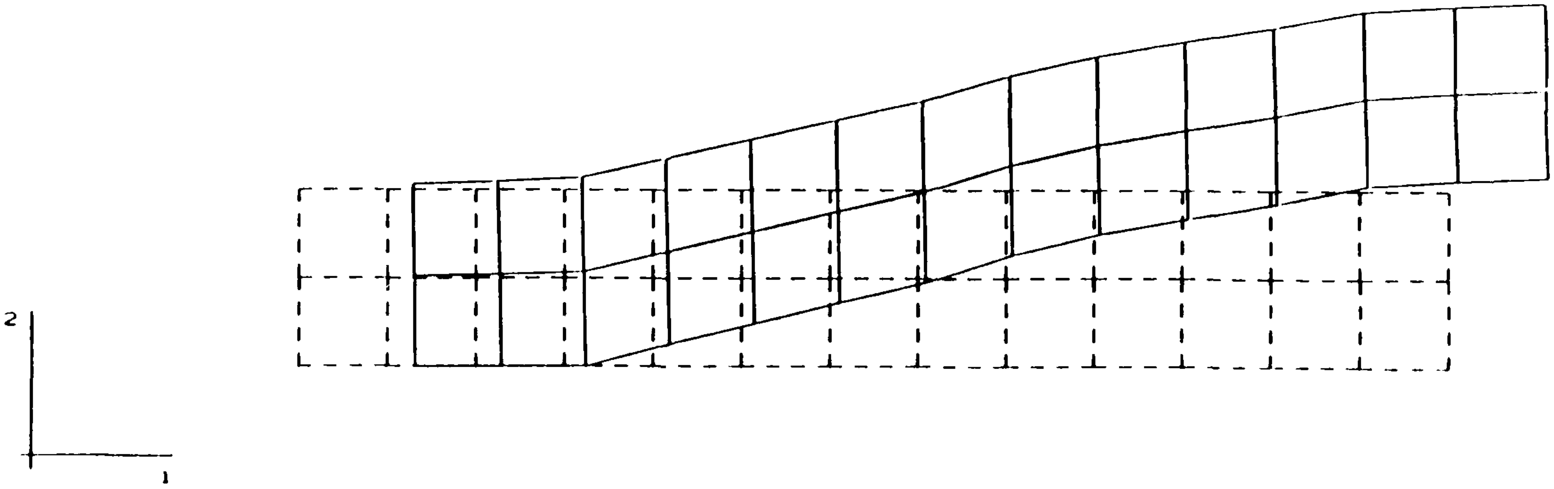
DISPL.
MAG. FACTOR = +1.0E+00
SOLID LINES - DISPLACED MESH
DASHED LINES - ORIGINAL MESH
2
1
CT - SPECIMEN
STEP 9 INCREMENT 1
ABAQUS VERSION 4-5-175

Figure 29a: Crack tip region (coarse mesh).

- load 8690 N
- Δa 2.5 mm

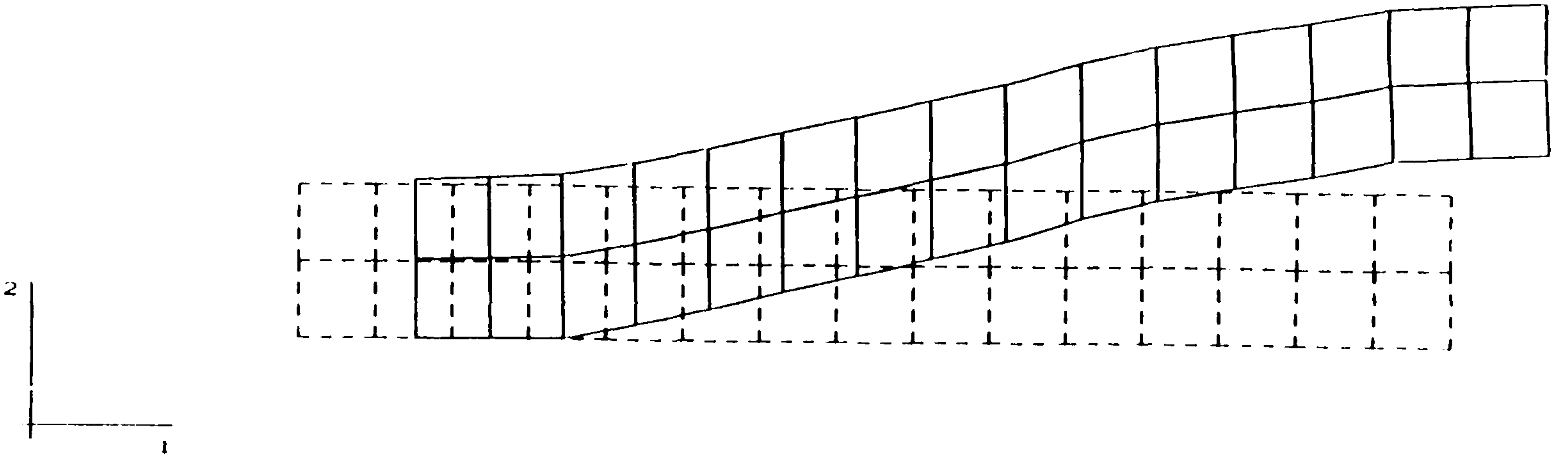
DISPL.
MAG. FACTOR = +1.0E+00
SOLID LINES - DISPLACED MESH
DASHED LINES - ORIGINAL MESH
2
1
CT - SPECIMEN
STEP 11 INCREMENT 1
ABAQUS VERSION 4-5-175

Figure 29h: Crack tip region (coarse mesh).

- load 8720 N
- Δa 3. mm

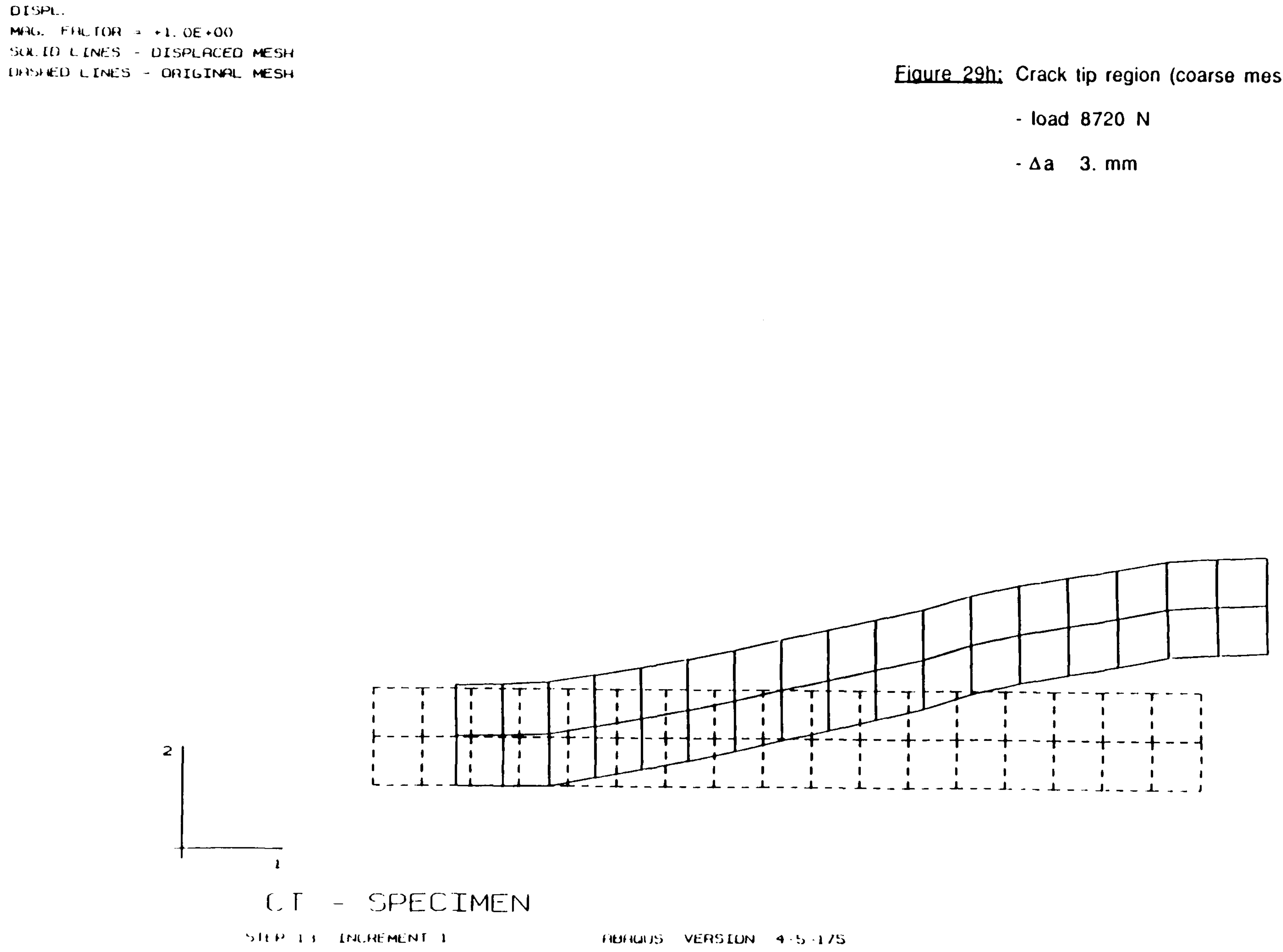
DISPL.
MAG. FACTOR = +1.0E+00
SOLID LINES - DISPLACED MESH
DASHED LINES - ORIGINAL MESH
2
1
CT - SPECIMEN
STEP 13 INCREMENT 1
ABAQUS VERSION 4-5-175

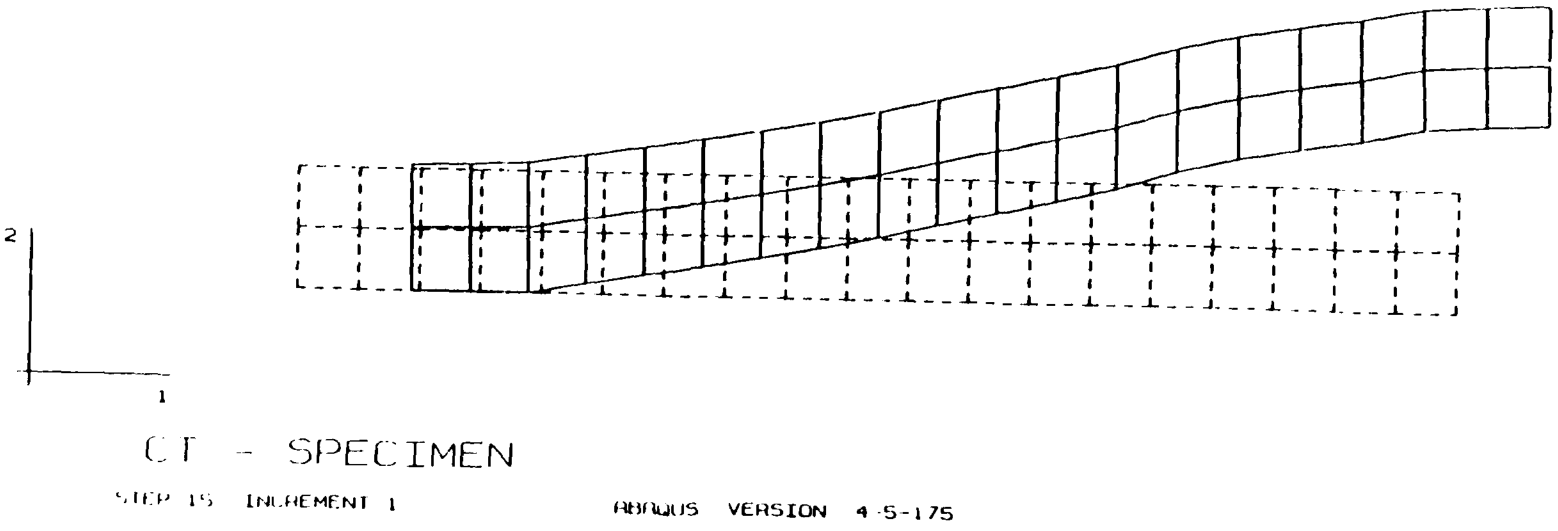
DISPL.
MAG. FACTOR = +1.0E+00
SOLID LINES - DISPLACED MESH
DASHED LINES - ORIGINAL MESH
2
1
CT - SPECIMEN
STEP 15 INCREMENT 1
ABAQUS VERSION 4-5-175

Figure 29i: Crack tip region (coarse mesh).

- load 8729 N

- Δa 3.5 mm

DISPL.
MAG. FACTOR = +1.0E+00
SOLID LINES - DISPLACED MESH
DASHED LINES - ORIGINAL MESH

Figure 29i: Crack tip region (coarse mesh).

- load 8734 N
- Δa 4. mm

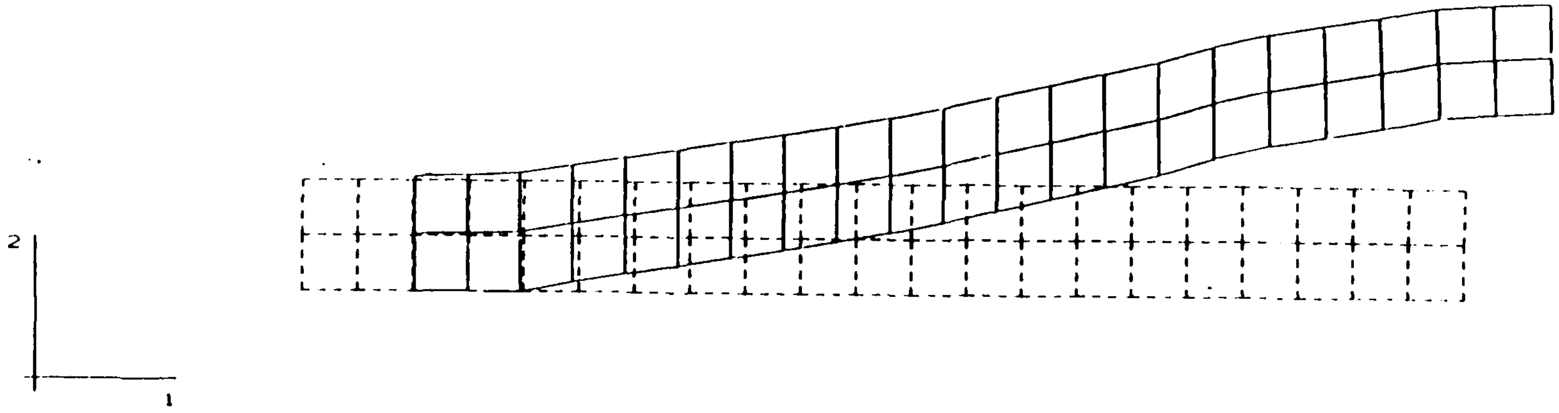

CT - SPECIMEN

STEP 17 INCREMENT 1 ABAQUS VERSION 4-5-175

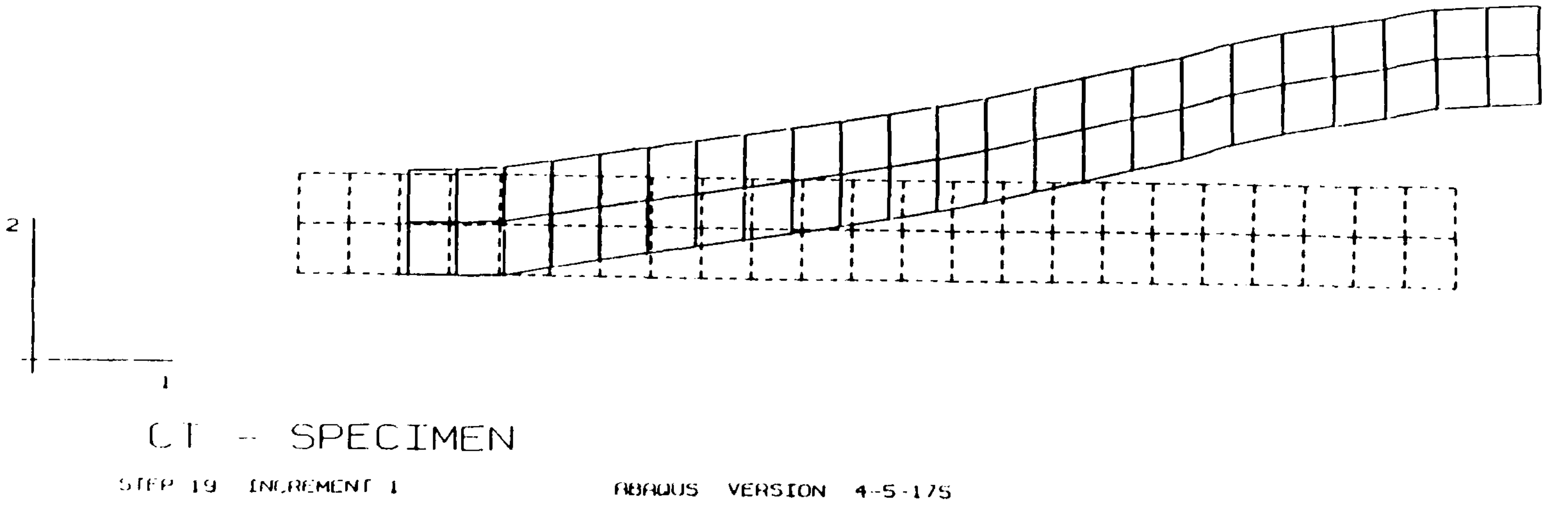
DISPL.
MAG. FACTOR = +1.0E+00
SOLID LINES - DISPLACED MESH
DASHED LINES - ORIGINAL MESH
2
1
CT - SPECIMEN
STEP 19 INCREMENT 1
ABAQUS VERSION 4-5-175

Figure 29k: Crack tip region (coarse mesh).

- load 8725 N
- Δa 4.5 mm

DISPL.
MAG. FACTOR = +1.0E+00
SOLID LINES - DISPLACED MESH
DASHED LINES - ORIGINAL MESH

Figure 291: Crack tip region (coarse mesh).

- load 8700 N
- Δa 5. mm

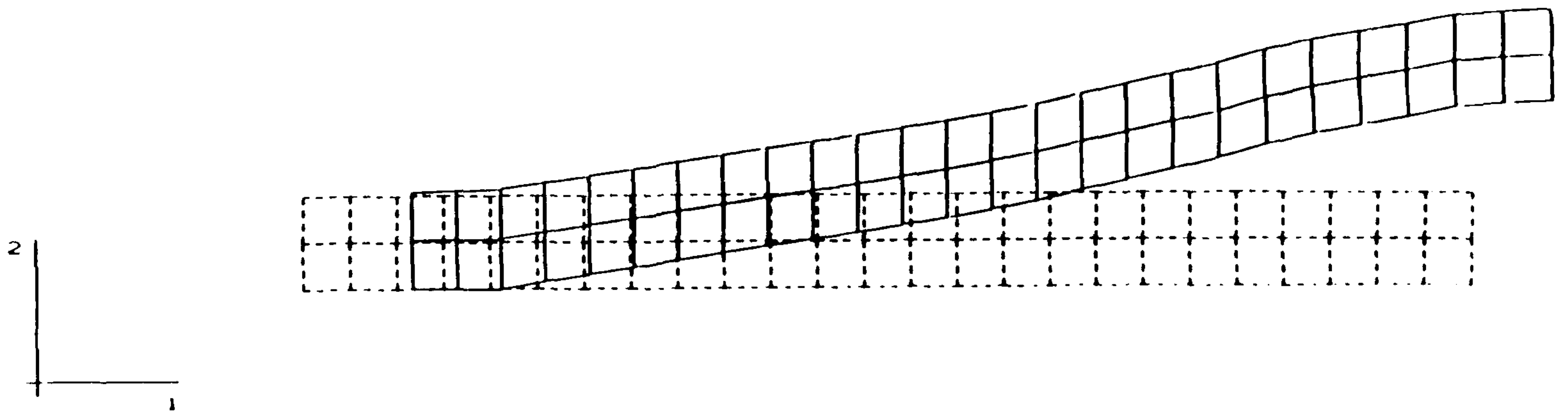

CT - SPECIMEN

STEP 21 INCREMENT 1 ABAQUS VERSION 4-5-175

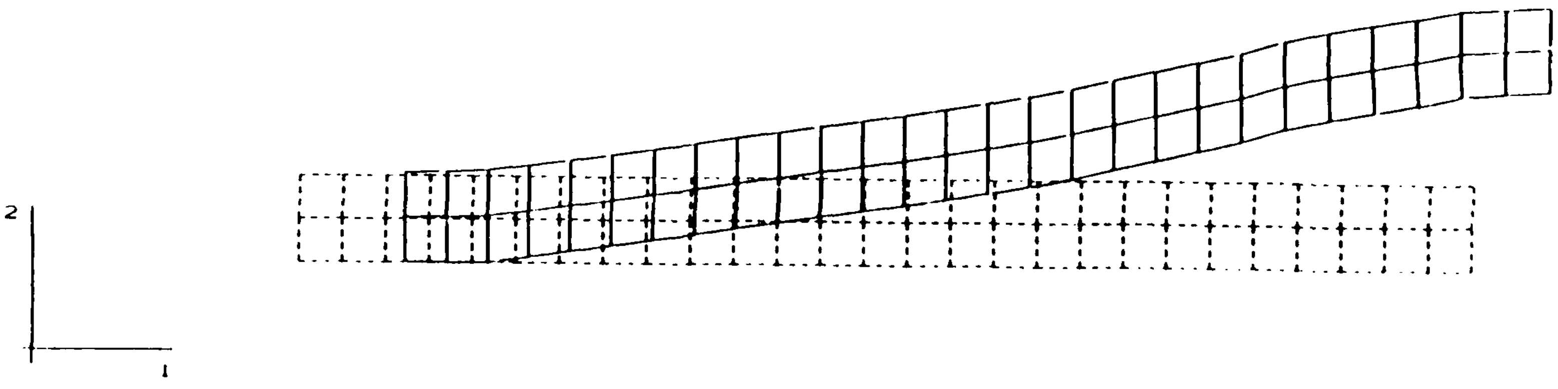
DISPL.
MAG. FACTOR = +1.0E+00
SOLID LINES - DISPLACED MESH
DASHED LINES - ORIGINAL MESH
2
1
CT - SPECIMEN
STEP 21 INCREMENT 1
ABAQUS VERSION 4-5-175

Figure 29m: Crack tip region (coarse mesh).

- load 8650 N

- Δa 5.5 mm

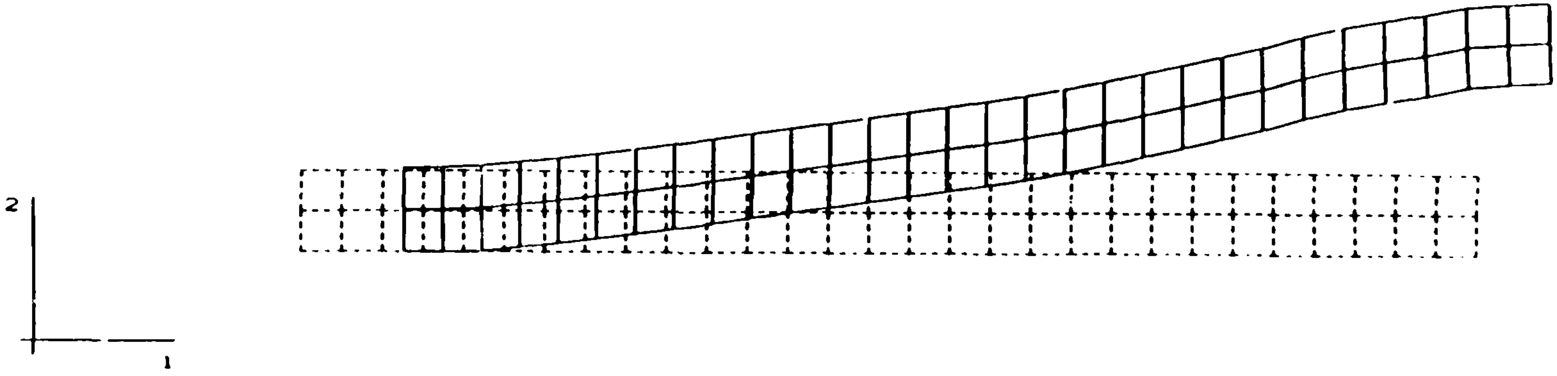

DISPL.
MAG. FACTOR = +1.0E+00
SOLID LINES - DISPLACED MESH
DASHED LINES - ORIGINAL MESH
2
1
CT - SPECIMEN
STEP 25 INCREMENT 1
ABAQUS VERSION 4-5-175

Figure 29n: Crack tip region (coarse mesh).

- load 8570 N

- Δa 6. mm

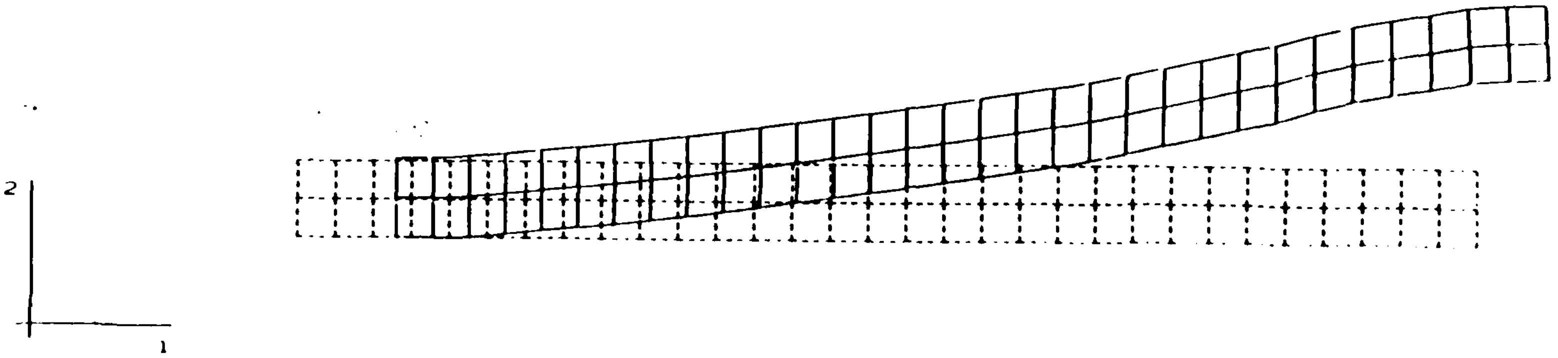
DISPL.
MAG. FACTOR = +1.0E+00
SOLID LINES - DISPLACED MESH
DASHED LINES - ORIGINAL MESH
2
1
CT - SPECIMEN
STEP 27 INCREMENT 1
ABAQUS VERSION 4-5-175

Figure 29o: Crack tip region (coarse mesh).

- load 8490 N
- Δa 6.5 mm

Figure 29p: Crack tip region (coarse mesh).

- load 8410 N
- Δa   7. mm

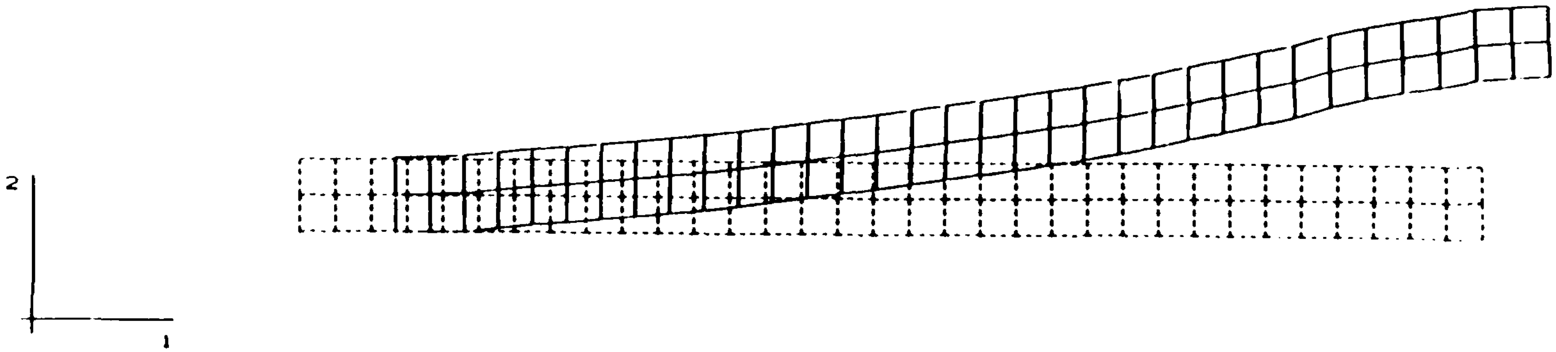
DISPL.
MAG. FACTOR = +1.0E+00
SOLID LINES - DISPLACED MESH
DASHED LINES - ORIGINAL MESH
2
1
CT - SPECIMEN
STEP 29 INCREMENT 1
ABAQUS VERSION 4-5-175

Figure 29q: Crack tip region (coarse mesh).

- load 8250 N
- Δa 8. mm

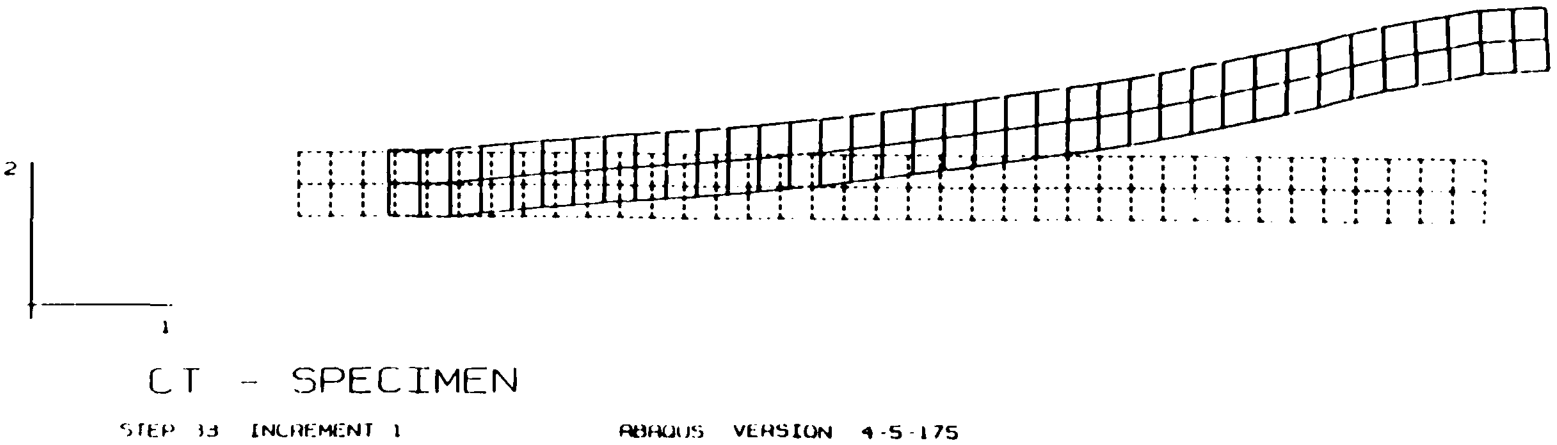
DISPL.
MAG. FACTOR = +1.0E+00
SOLID LINES - DISPLACED MESH
DASHED LINES - ORIGINAL MESH
2
1
CT - SPECIMEN
STEP 33 INCREMENT 1
ABAQUS VERSION 4-5-175

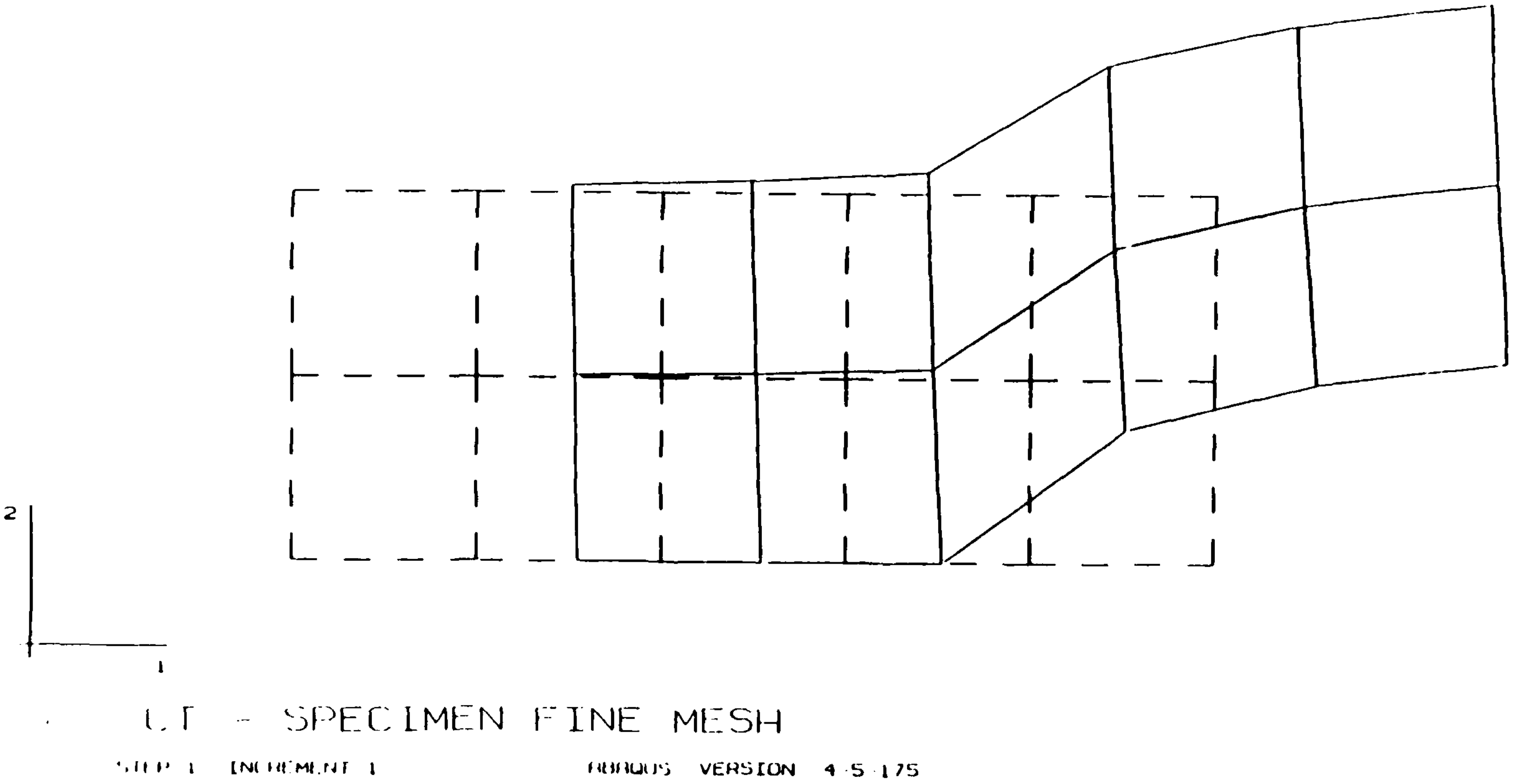
DISPL.
MAG. FACTOR = +1.0E+00
SOLID LINES - DISPLACED MESH
DASHED LINES - ORIGINAL MESH
2
1
CT - SPECIMEN FINE MESH
STEP 1 INCREMENT 1
ABAQUS VERSION 4-5-175

Figure 30a: Crack tip region (fine mesh).

- *load* 5300 N

- Δa 0. mm

Figure 30b: Crack tip region (fine mesh).

- load 5520 N
- Δa 0.05 mm

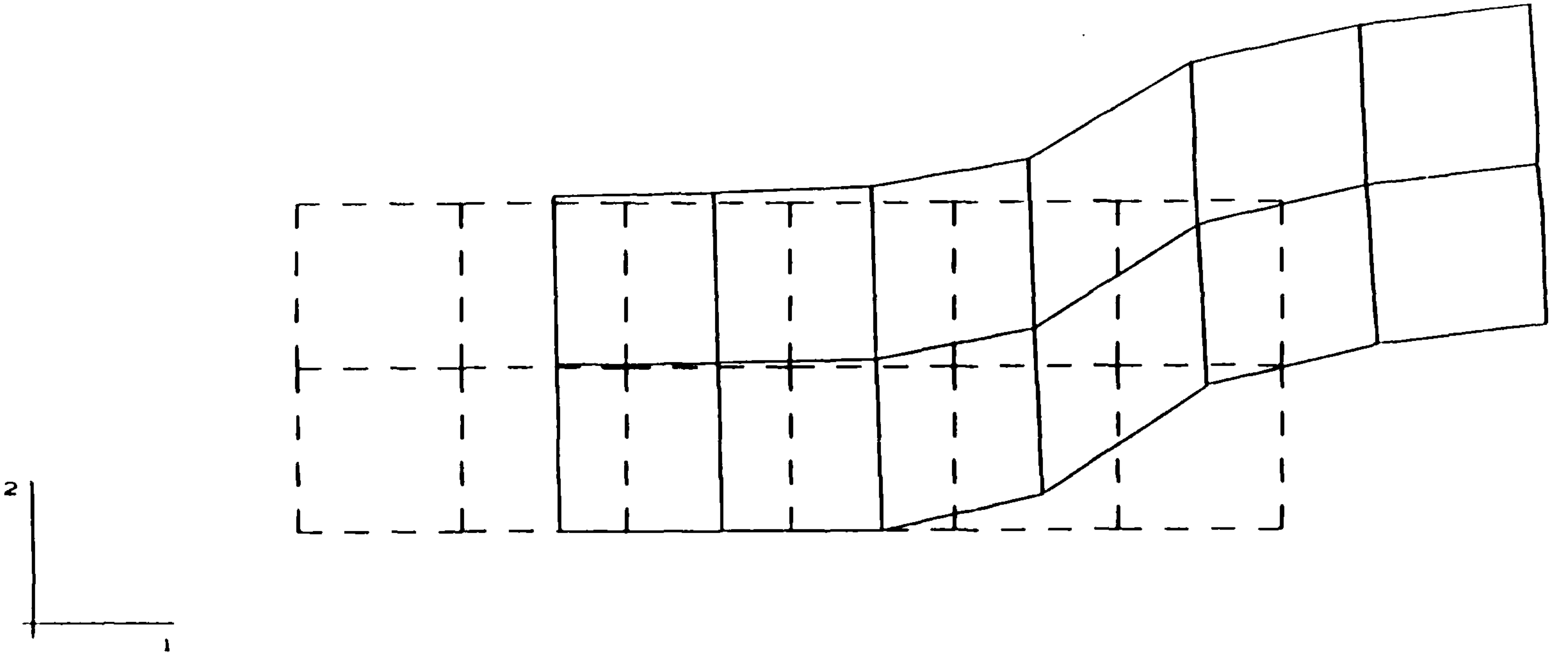
DISPL.
MAG. FACTOR = +1.0E+00
SOLID LINES - DISPLACED MESH
DASHED LINES - ORIGINAL MESH
2
1
CT - SPECIMEN FINE MESH
STEP 2 INCREMENT 1
ABAQUS VERSION 4-5-175

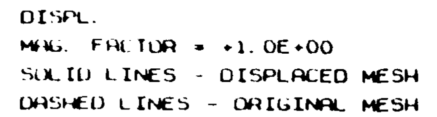
DISPL.
MAG. FACTOR = +1.0E+00
SOLID LINES - DISPLACED MESH
DASHED LINES - ORIGINAL MESH

Figure 30c: Crack tip region (fine mesh).

- load 5720 N
- Δa 0.1 mm

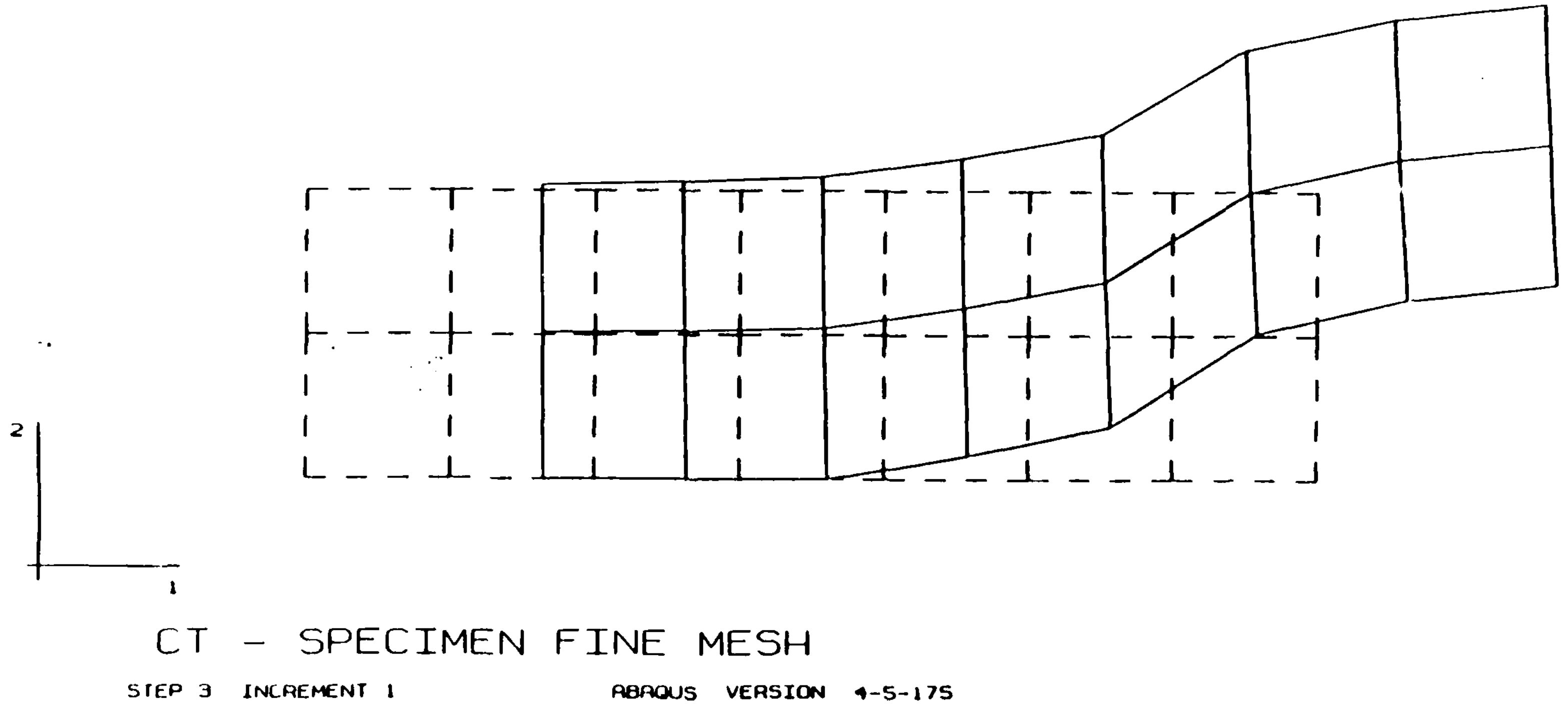
2
1
CT - SPECIMEN FINE MESH
STEP 3 INCREMENT 1
ABAQUS VERSION 4-5-175

Figure 30d: Crack tip region (fine mesh).

- load 5960 N
- Δa 0.15 mm

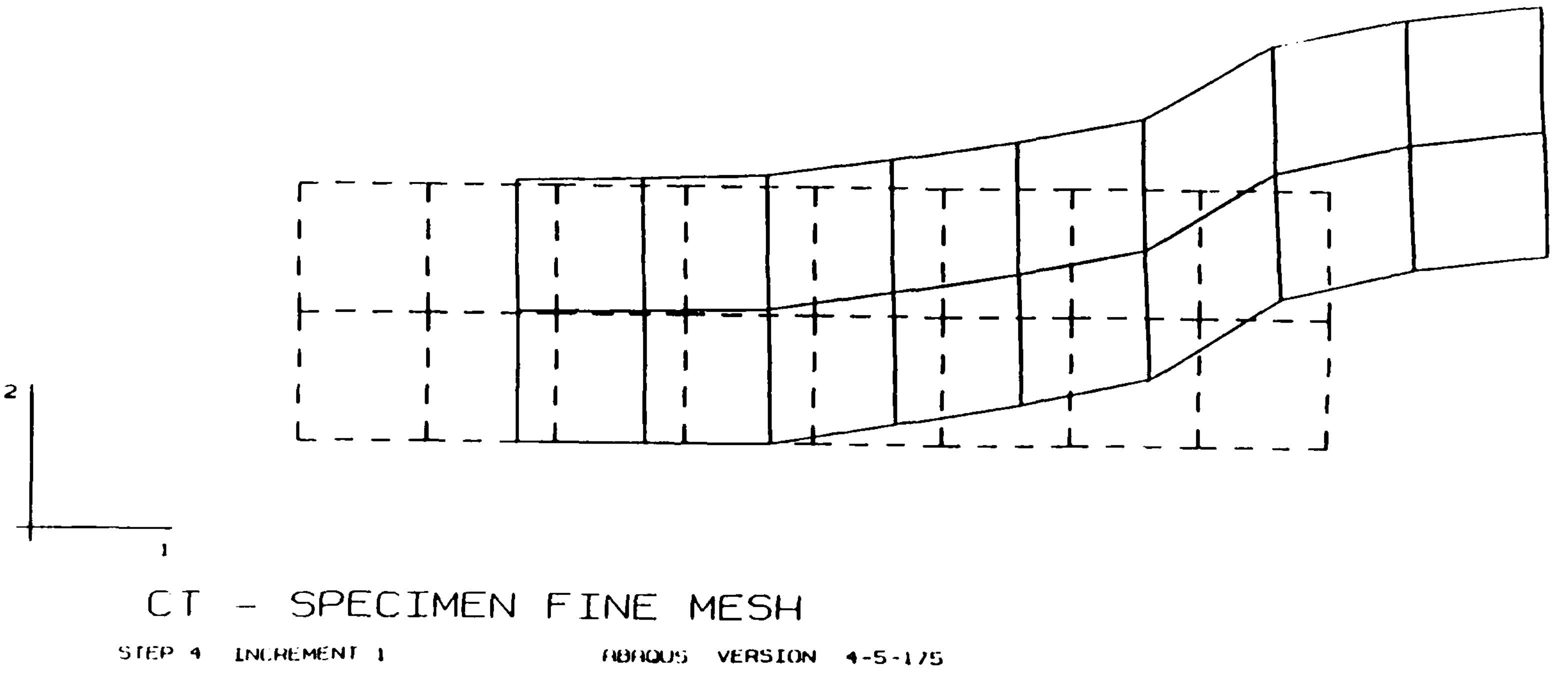
DISPL.
MAG. FACTOR = +1.0E+00
SOLID LINES - DISPLACED MESH
DASHED LINES - ORIGINAL MESH
2
1
CT - SPECIMEN FINE MESH
STEP 4 INCREMENT 1
ABAQUS VERSION 4-5-175

Figure 30e: Crack tip region (fine mesh).

- load 6180 N
- Δa 0.2 mm

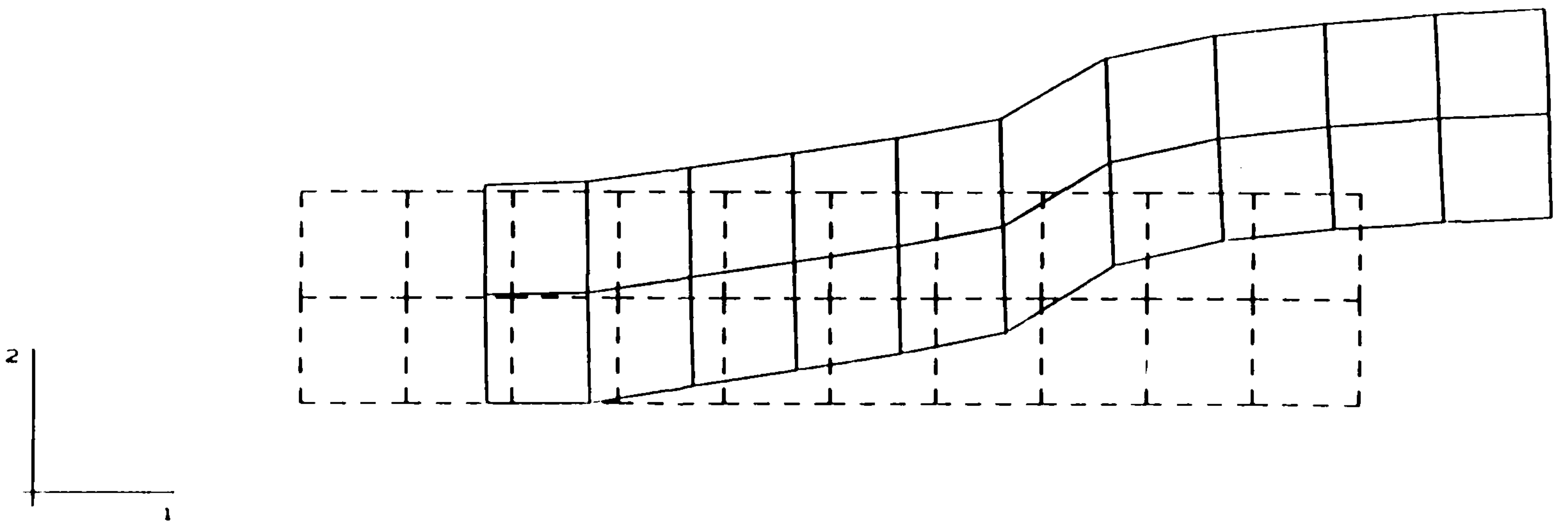
DISPL.
MAG. FACTOR = +1.0E+00
SOLID LINES - DISPLACED MESH
DASHED LINES - ORIGINAL MESH
2
1
CT - SPECIMEN FINE MESH
STEP 5 INCREMENT 1
ABAQUS VERSION 4-5-175

Figure 30f: Crack tip region (fine mesh).

- load 6400 N
- Δa 0.25 mm

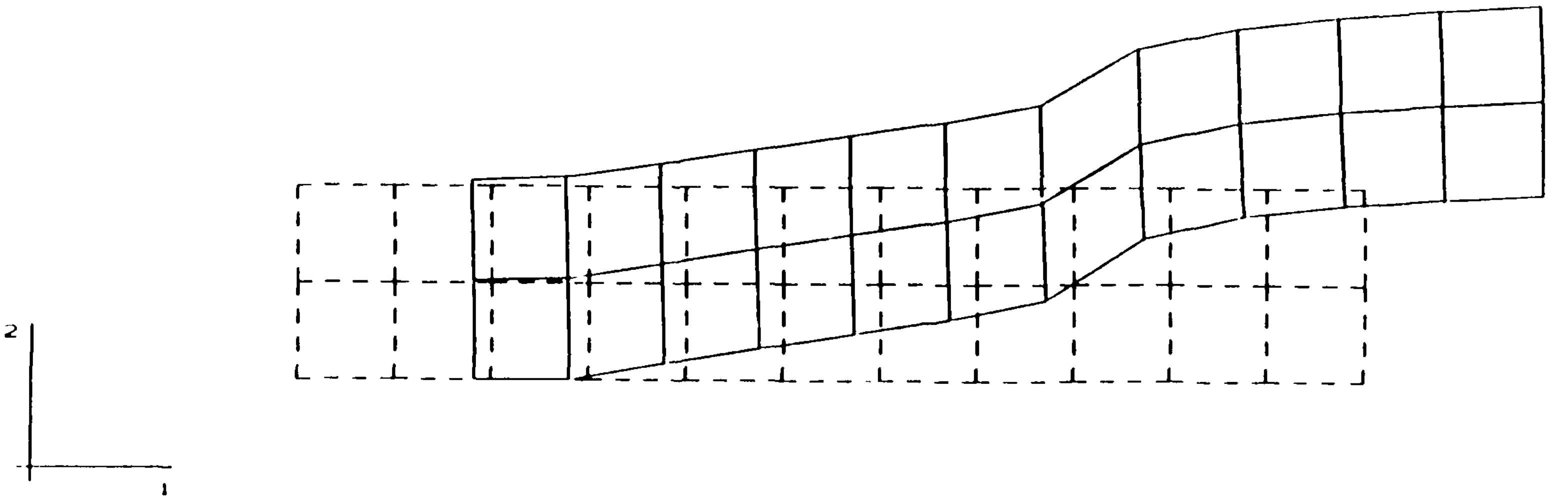
DISPL.
MAG. FACTOR = +1.0E+00
SOLID LINES - DISPLACED MESH
DASHED LINES - ORIGINAL MESH
2
1
CT - SPECZMEN FINE MESH
STEP 6 INCREMENT 1
ABAQUS VERSION 4-5-175

Figure 30g: Crack tip region (fine mesh).

- load 7100 N

- Δa 0.5 mm

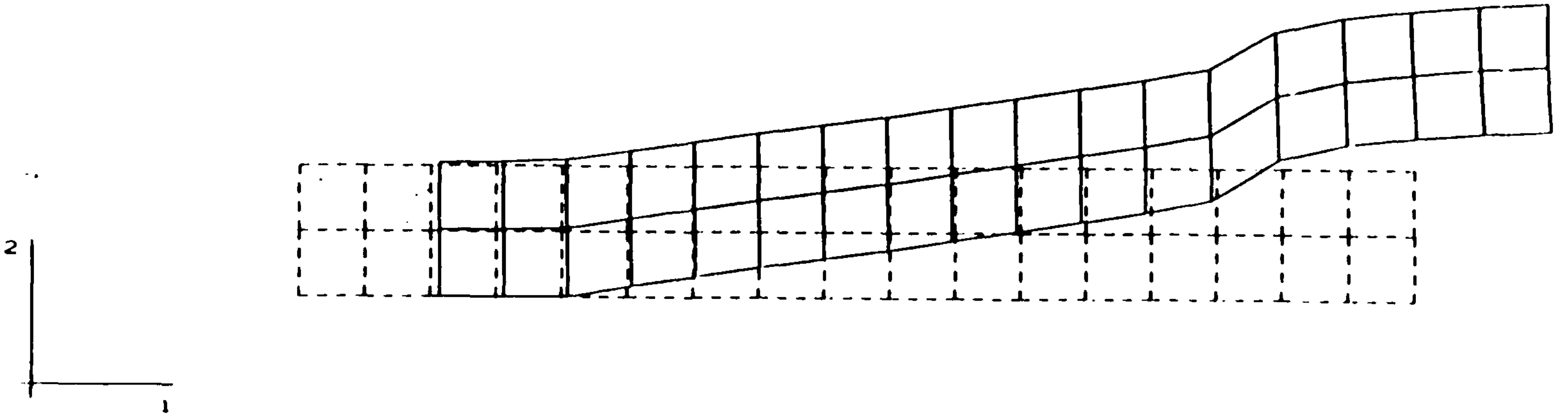
DISPL.
MAG. FACTOR = +1.0E+00
SOLID LINES - DISPLACED MESH
DASHED LINES - ORIGINAL MESH
2
1
CT - SPECIMEN FINE MESH
STEP 11 INCREMENT 1
ABAQUS VERSION 4-5-175

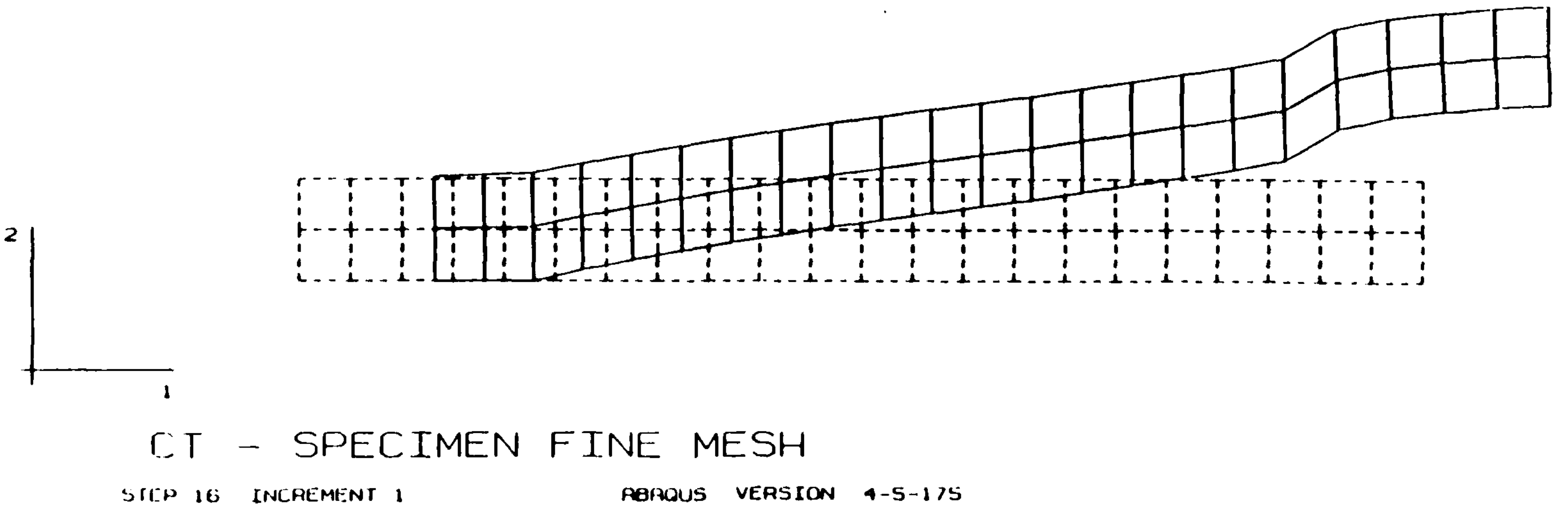
DISPL.
MAG. FACTOR = +1.0E+00
SOLID LINES - DISPLACED MESH
DASHED LINES - ORIGINAL MESH
2
1
CT - SPECIMEN FINE MESH
STEP 16 INCREMENT 1
ABAQUS VERSION 4-5-175

Figure 30h: Crack tip region (fine mesh).

- load 7650 N
- Δa 0.75 mm

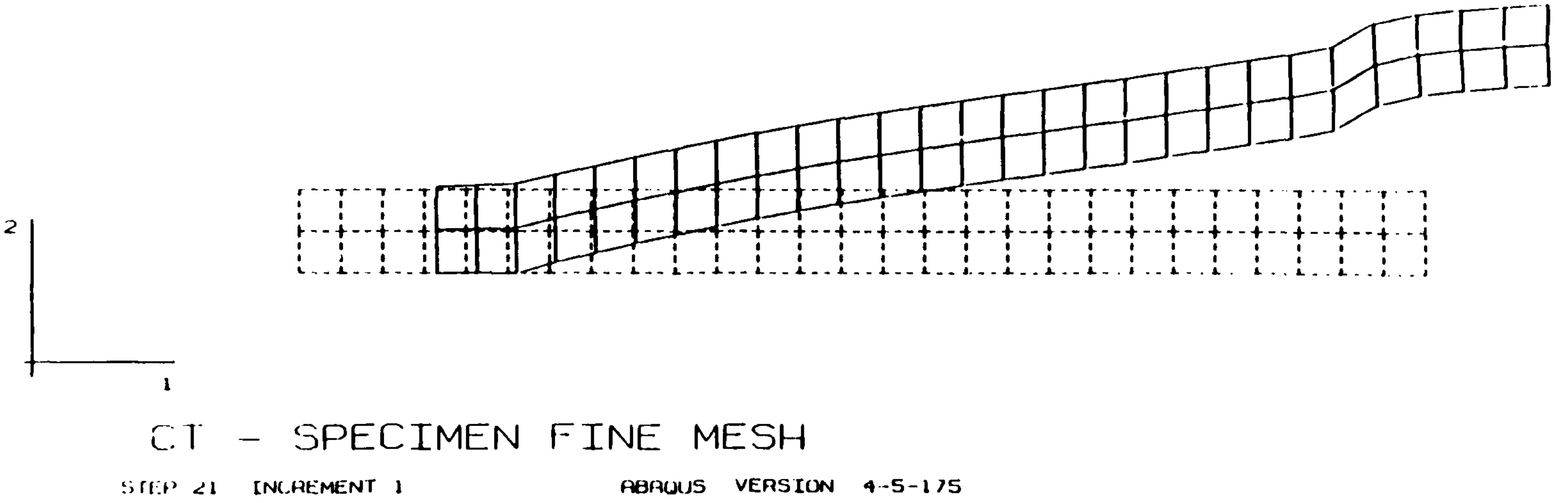
DISPL.
MAG. FACTOR = +1.0E+00
SOLID LINES - DISPLACED MESH
DASHED LINES - ORIGINAL MESH
2
1
CT - SPECIMEN FINE MESH
STEP 21 INCREMENT 1
ABAQUS VERSION 4-5-175

Figure 30i: Crack tip region (fine mesh).

- load 8100 N

- Δa 1. mm

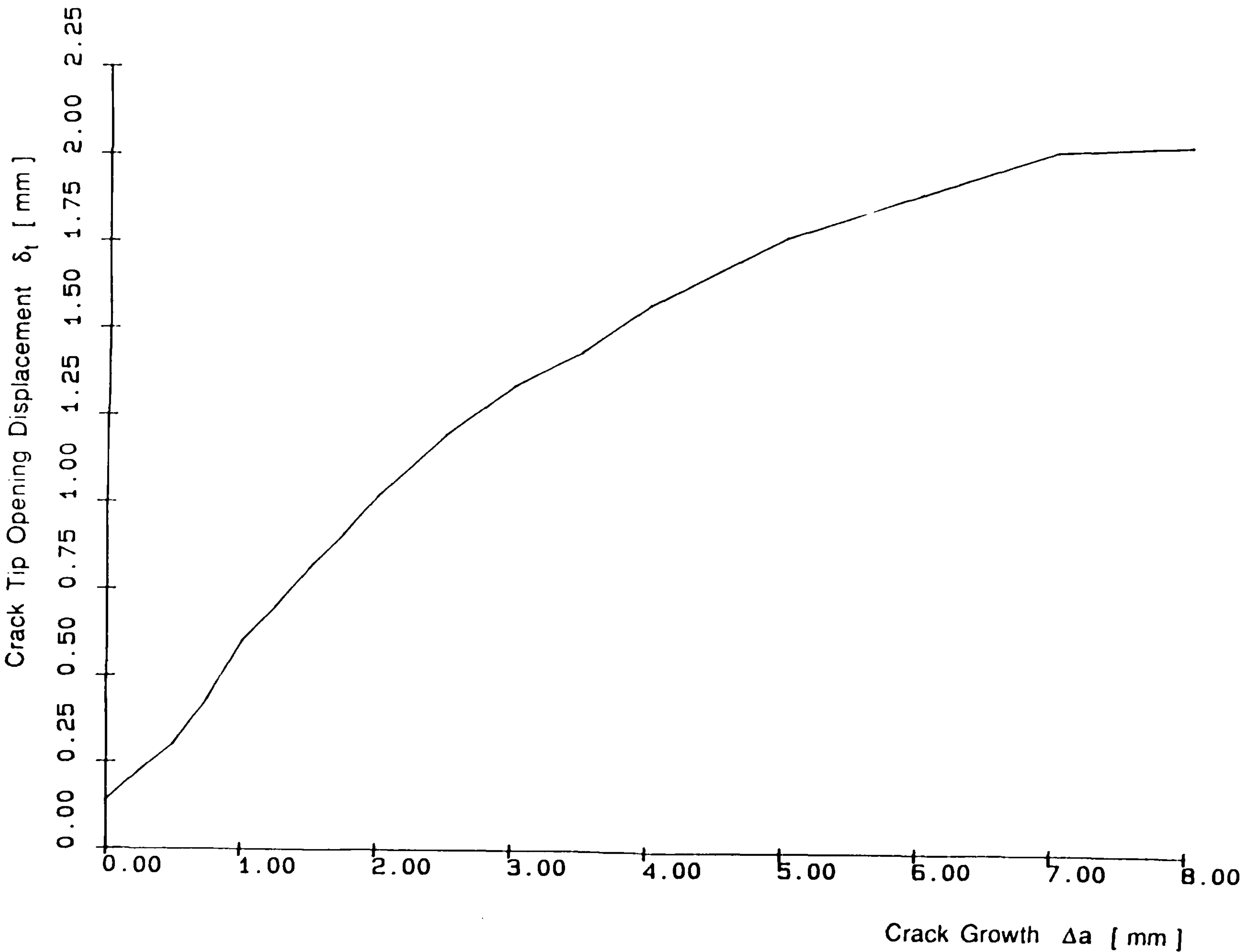

Figure 31. Crack tip opening displacement vs. crack growth (coarse mesh).

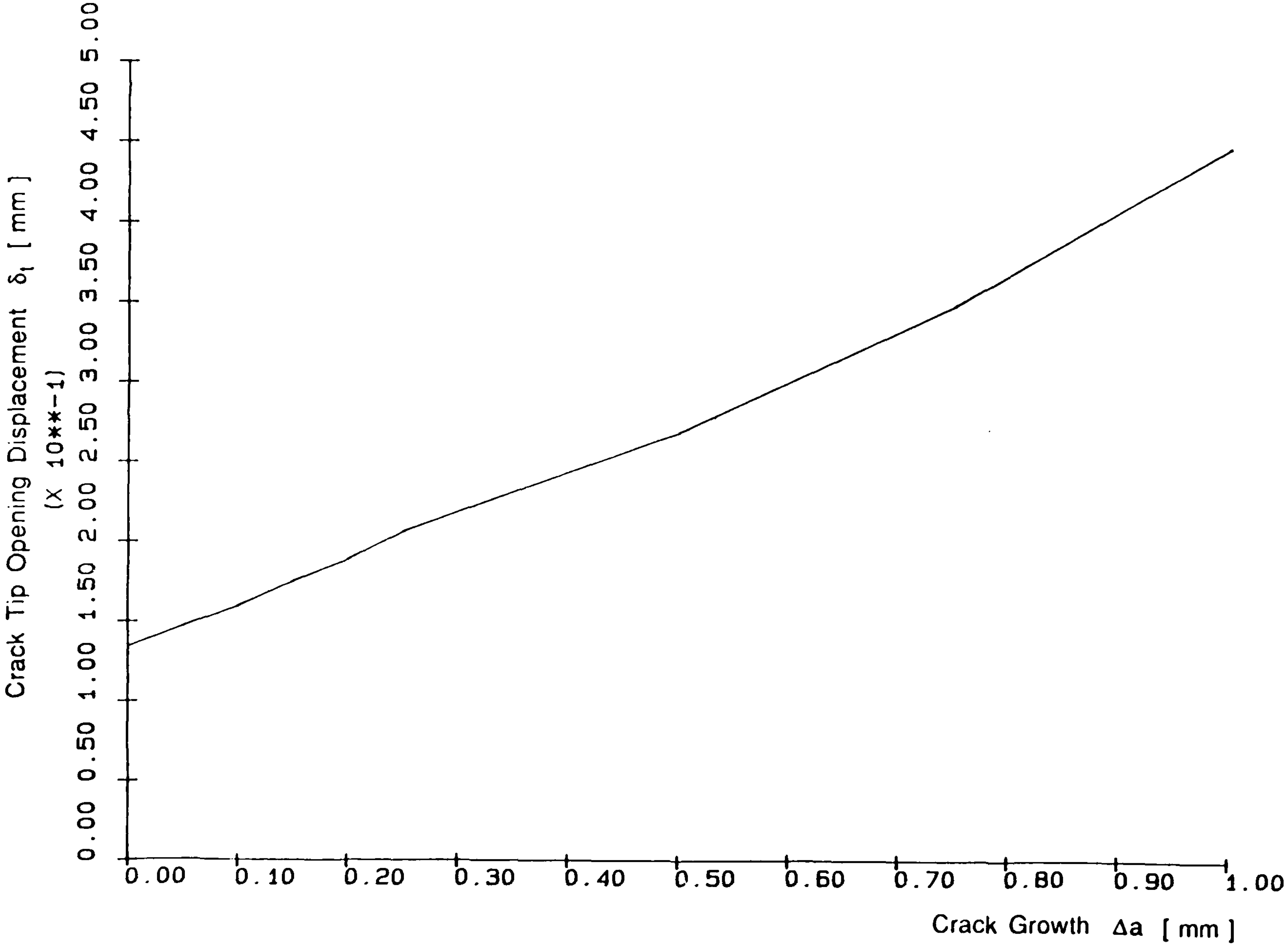

Figure 32: Crack tip opening displacement vs. crack growth (line mesh).

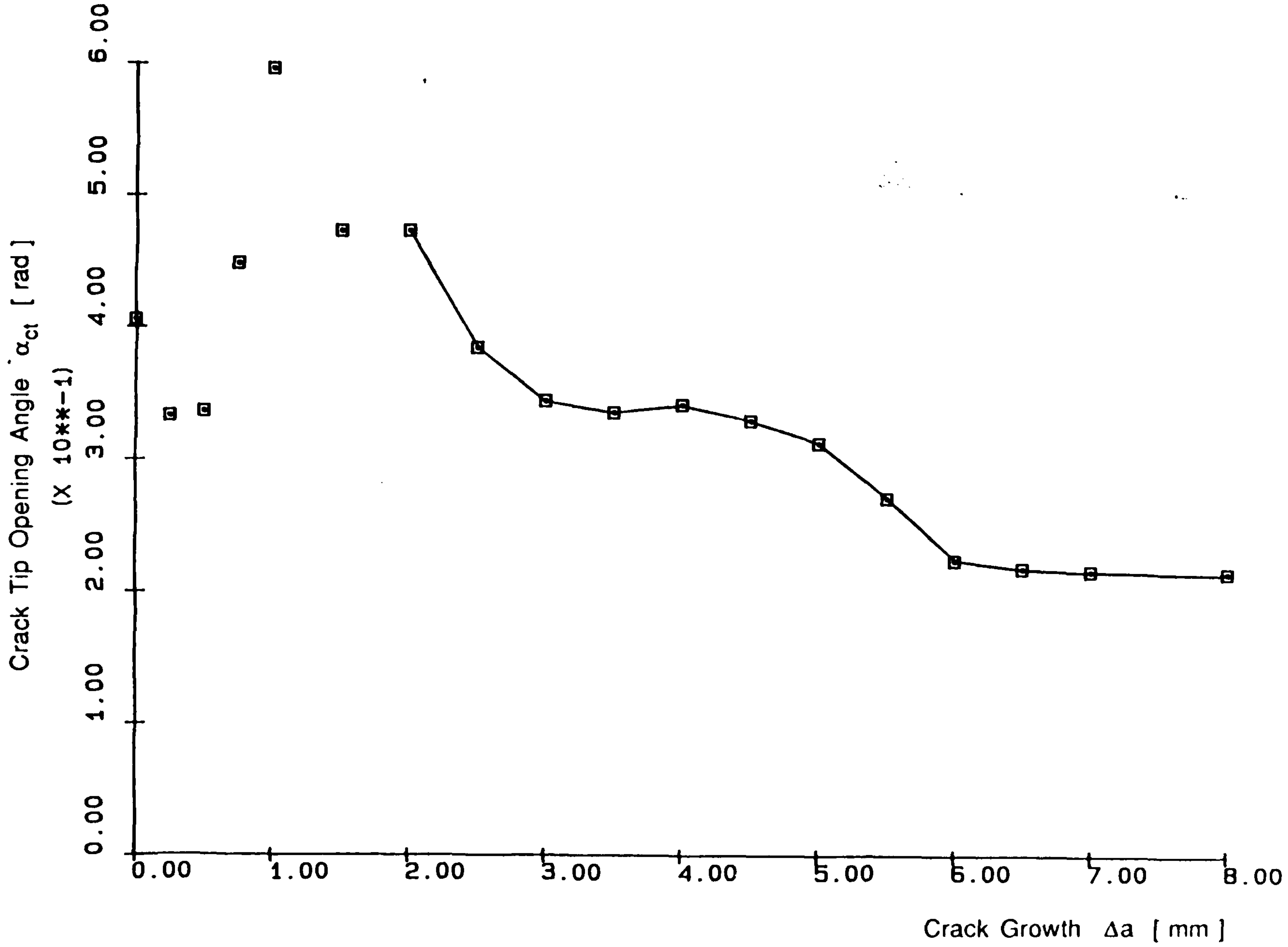

Figure 33: Crack tip opening angle vs. crack growth (coarse mesh).

In the performed calculation the fine mesh has five times smaller elements in the vicinity of the crack tip than the coarse mesh.

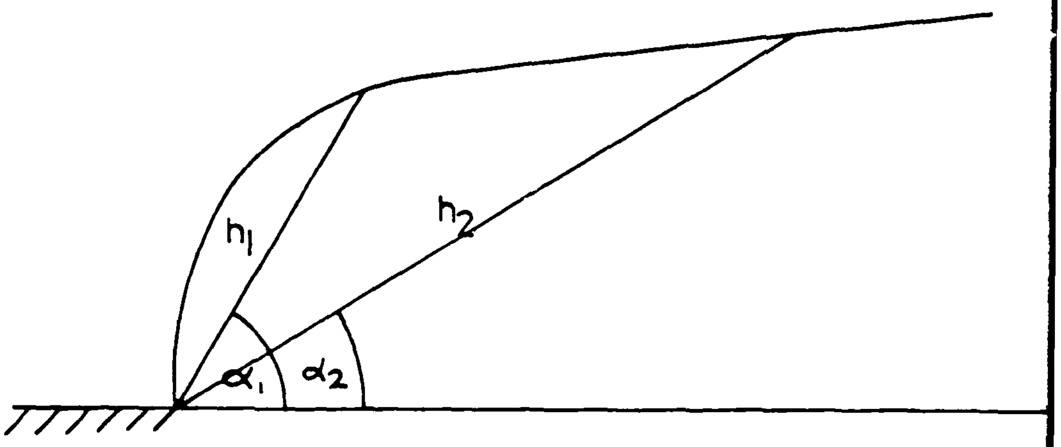

$h_2 = 2\,h_1$ $\alpha_1 > \alpha_2$

Figure 34: Schematic representation of the sensitivity of the CTOA dependent on the element size.

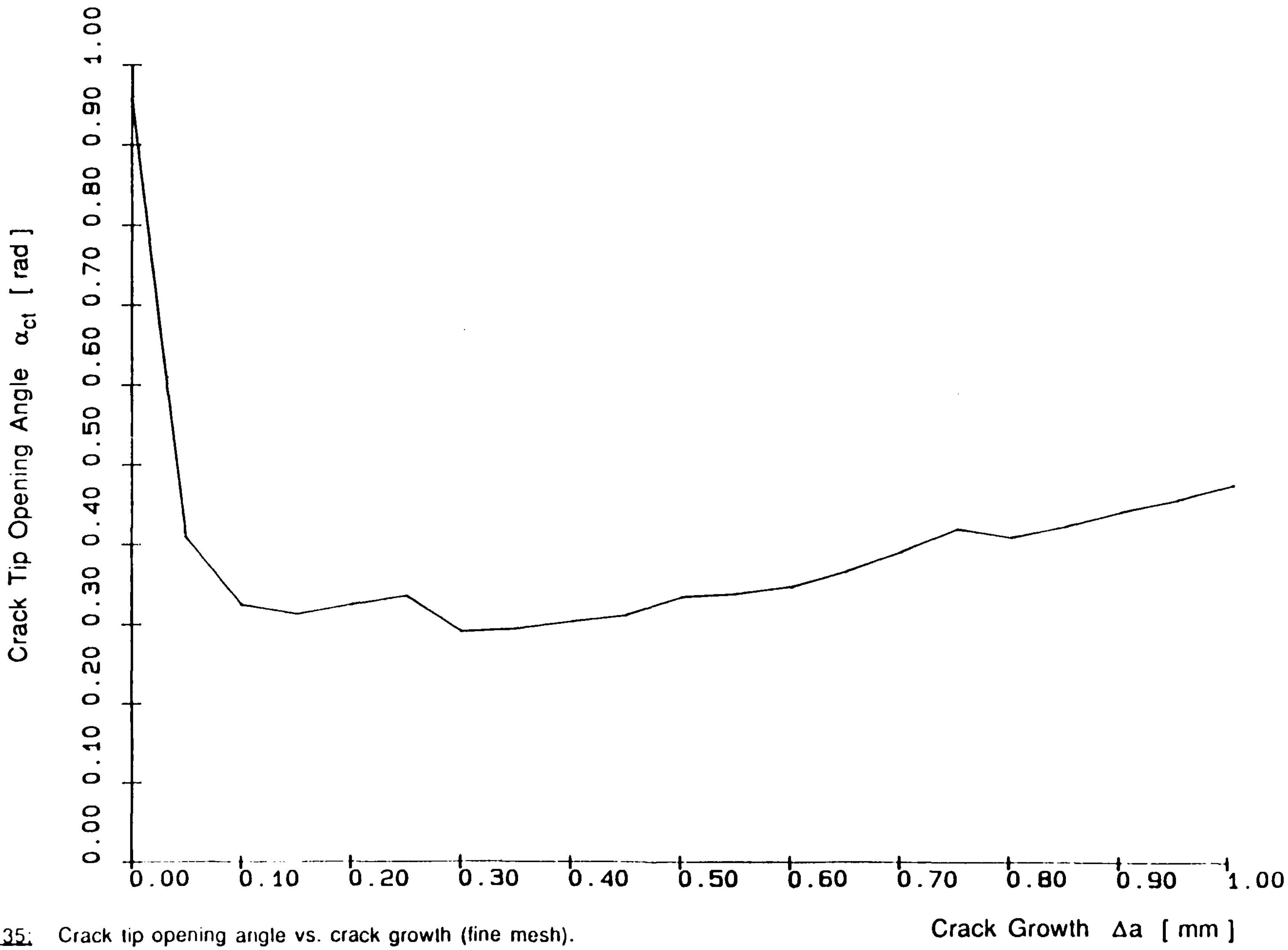

Figure 35: Crack tip opening angle vs. crack growth (fine mesh).

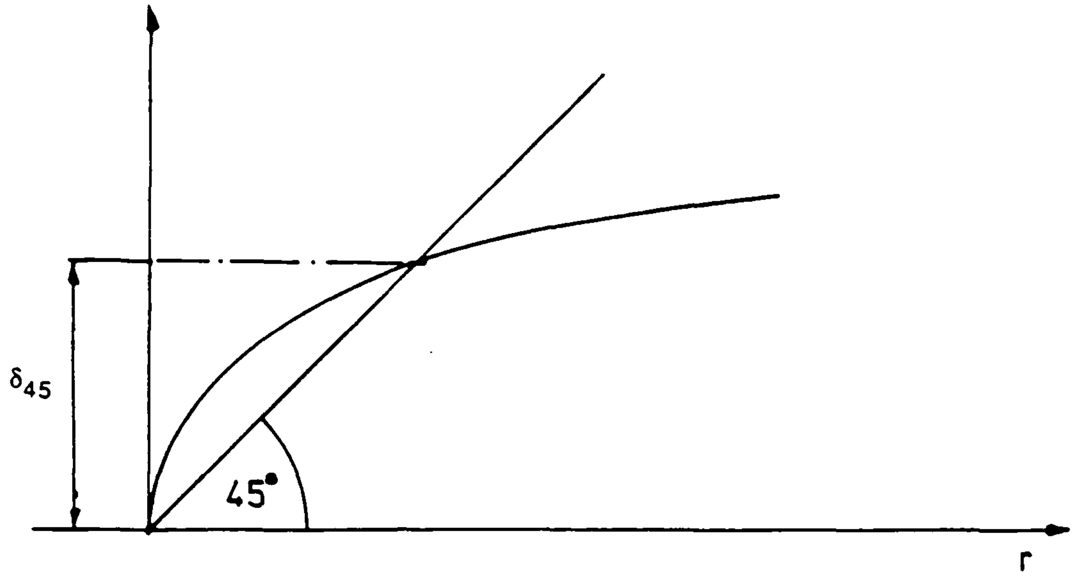
δ_{45}
45°
r

Figure 36: "45°" definition of the crack opening displacement.

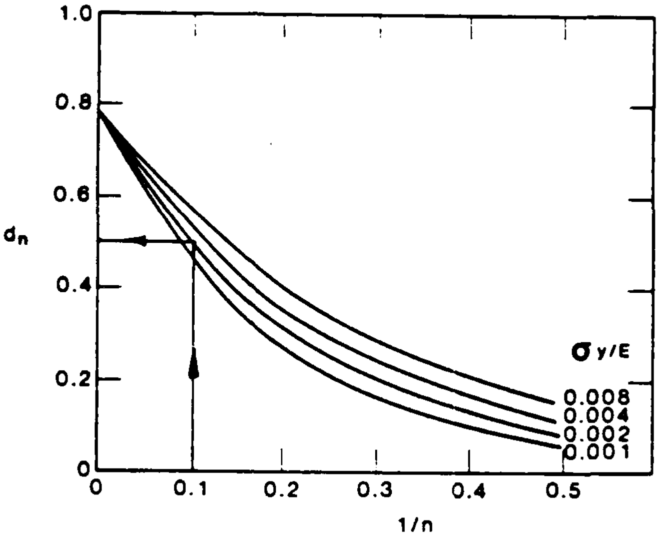

Figure 37: Dependence of d_n on n and σ_o/E for plane strain [18].

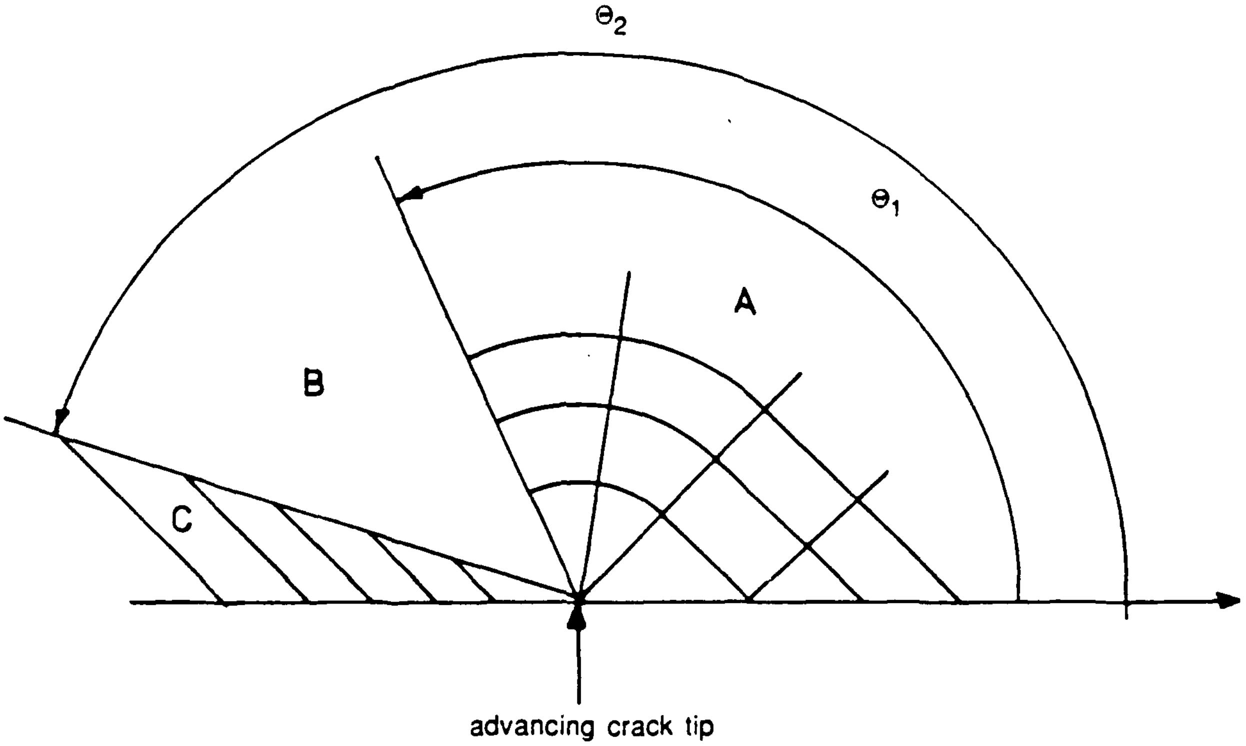
Θ_2
Θ_1
A
B
C
advancing crack tip

Zone B: Elastic unloading.

Zone C: Reverse plasticity.

Figure 38: Prandtl slip - line fields for steadily growing crack (in x - direction).

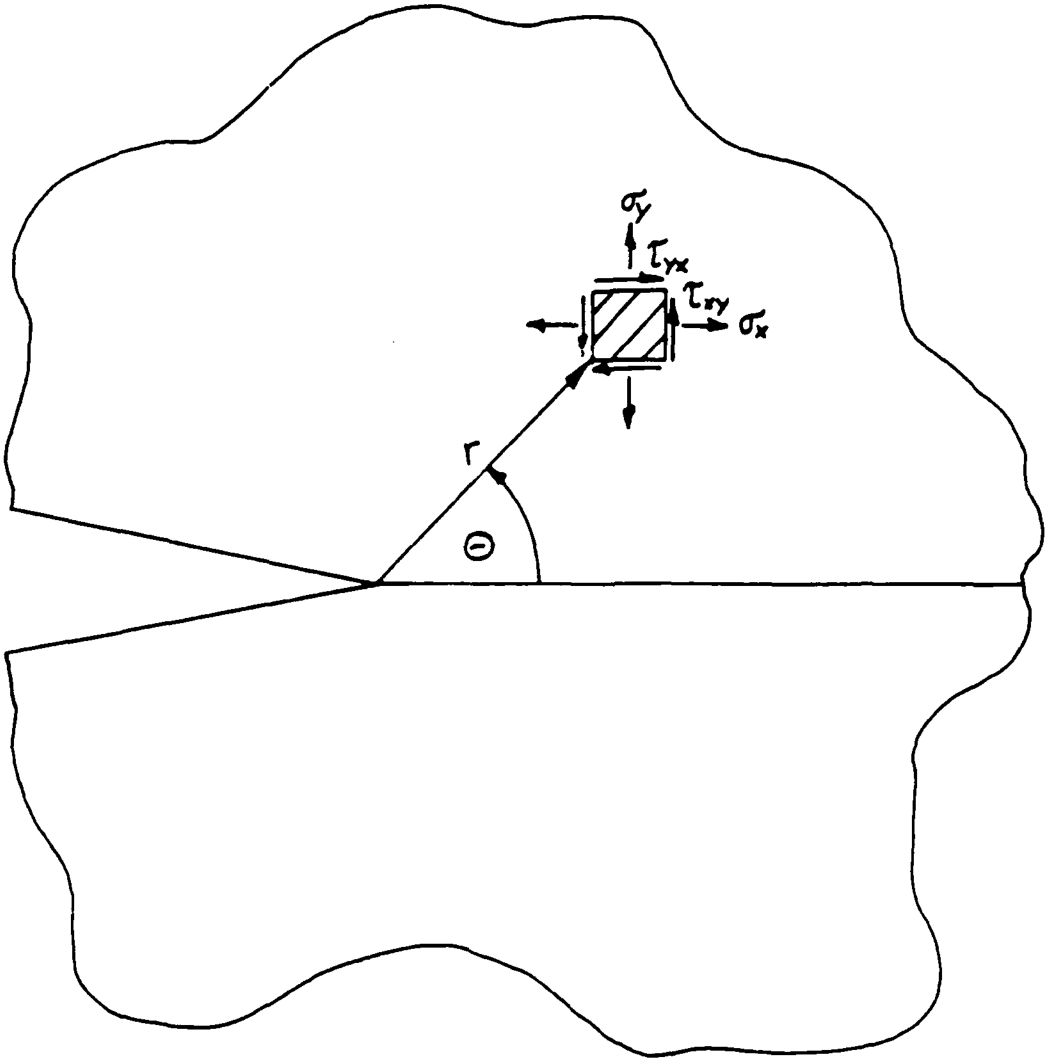
σ_y
τ_{yx}
τ_{xy}
σ_x
r
Θ

Figure 39: Cartesian stress components at the crack tip.

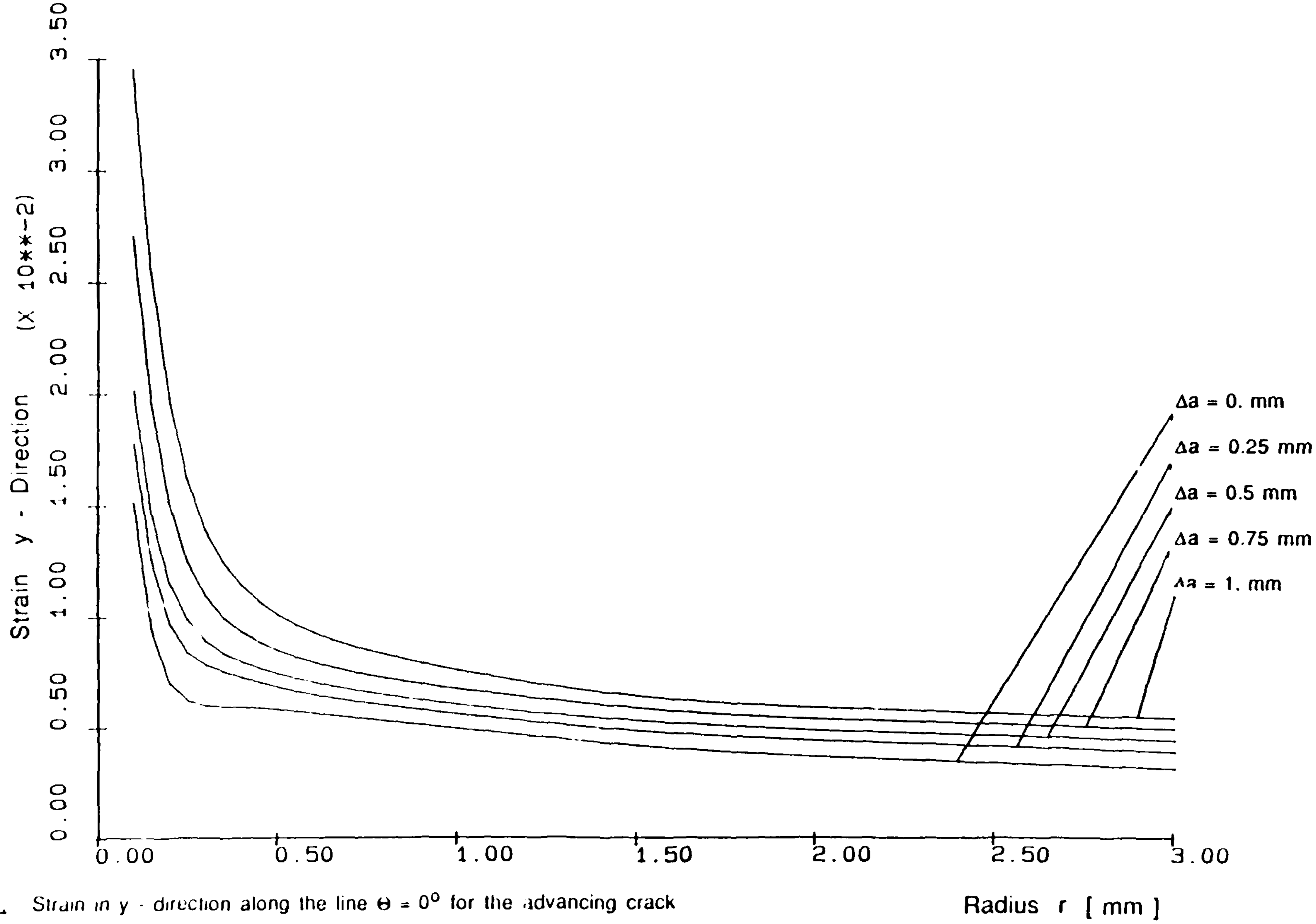

Figure 40. Strain in y - direction along the line Θ = 0° for the advancing crack

ne mesh).

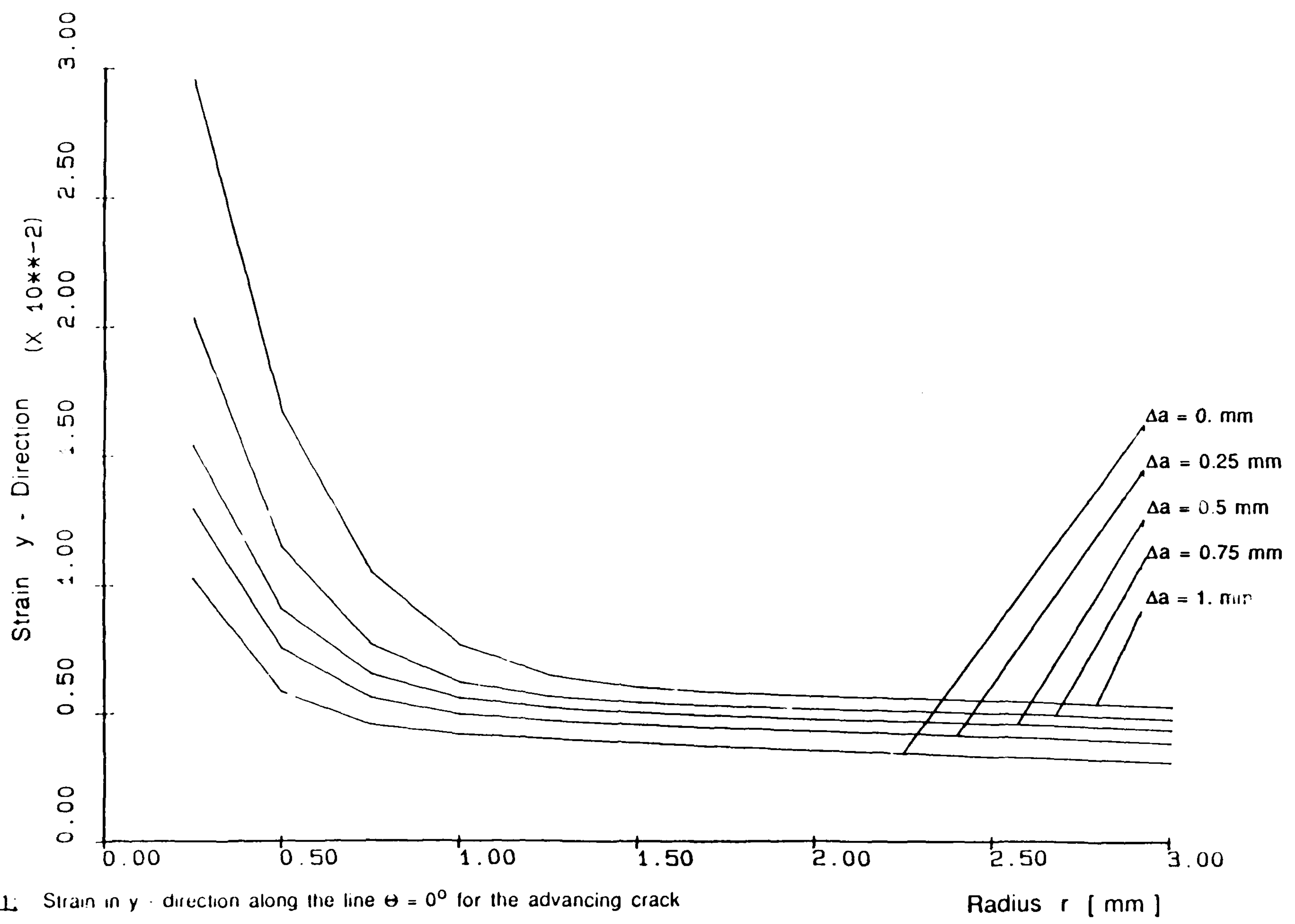

Figure 41: Strain in y - direction along the line $\Theta = 0^{\circ}$ for the advancing crack

coarse mesh).

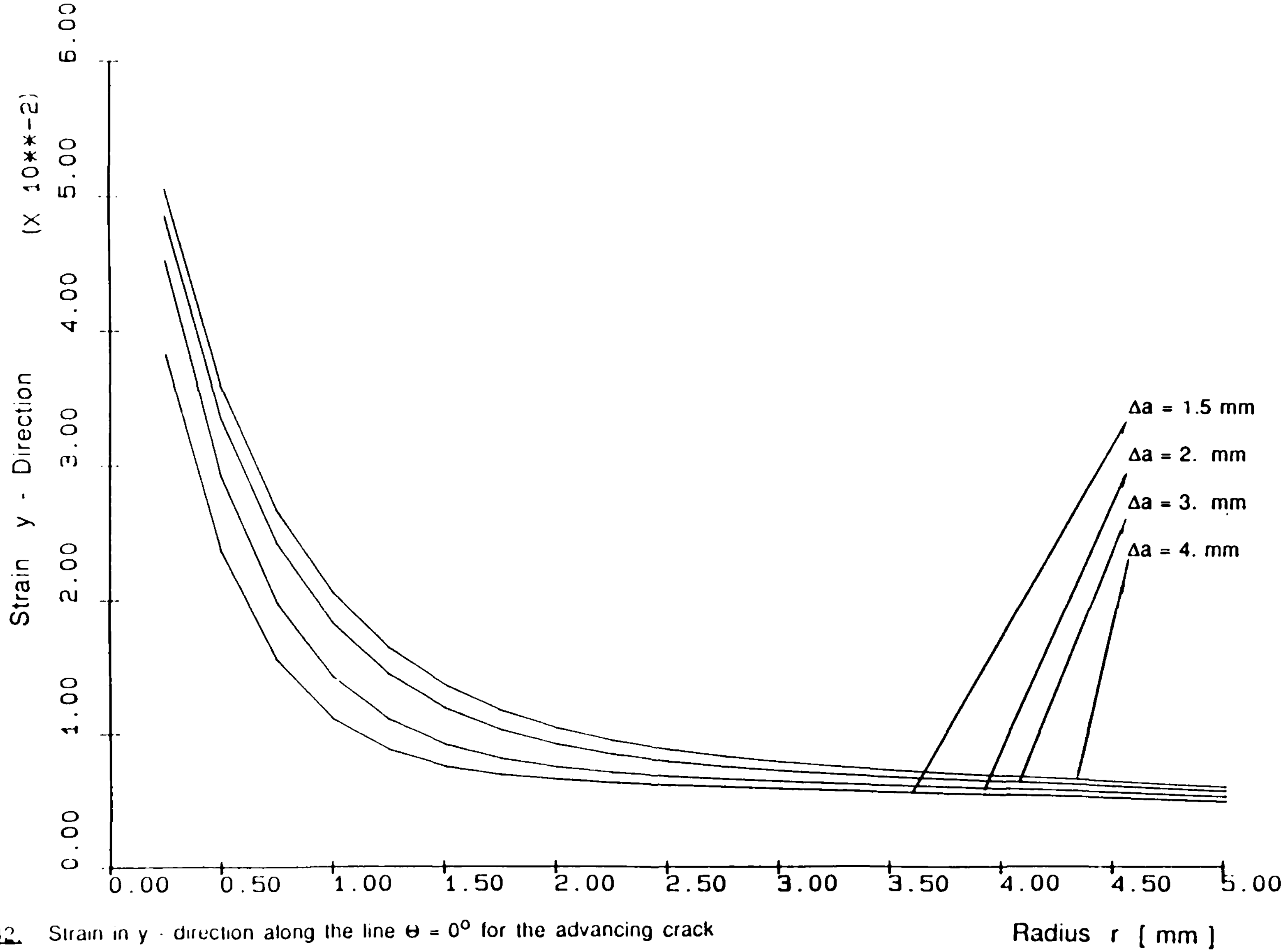

Figure 42. Strain in y - direction along the line Θ = 0° for the advancing crack

oarse mesh).

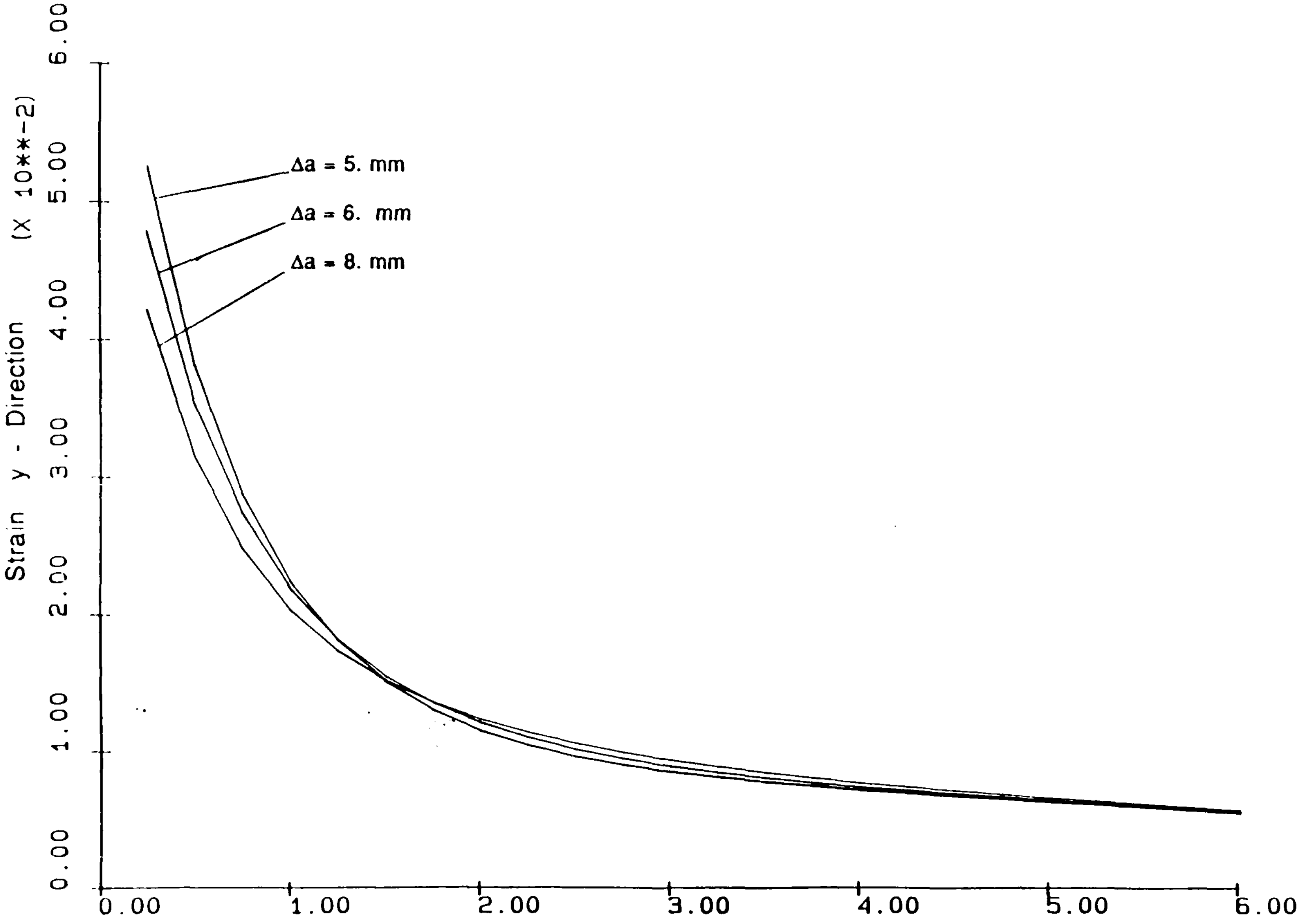

Figure 43: Strain in y - direction along the line $\Theta = 0^o$ for the advancing crack coarse mesh).

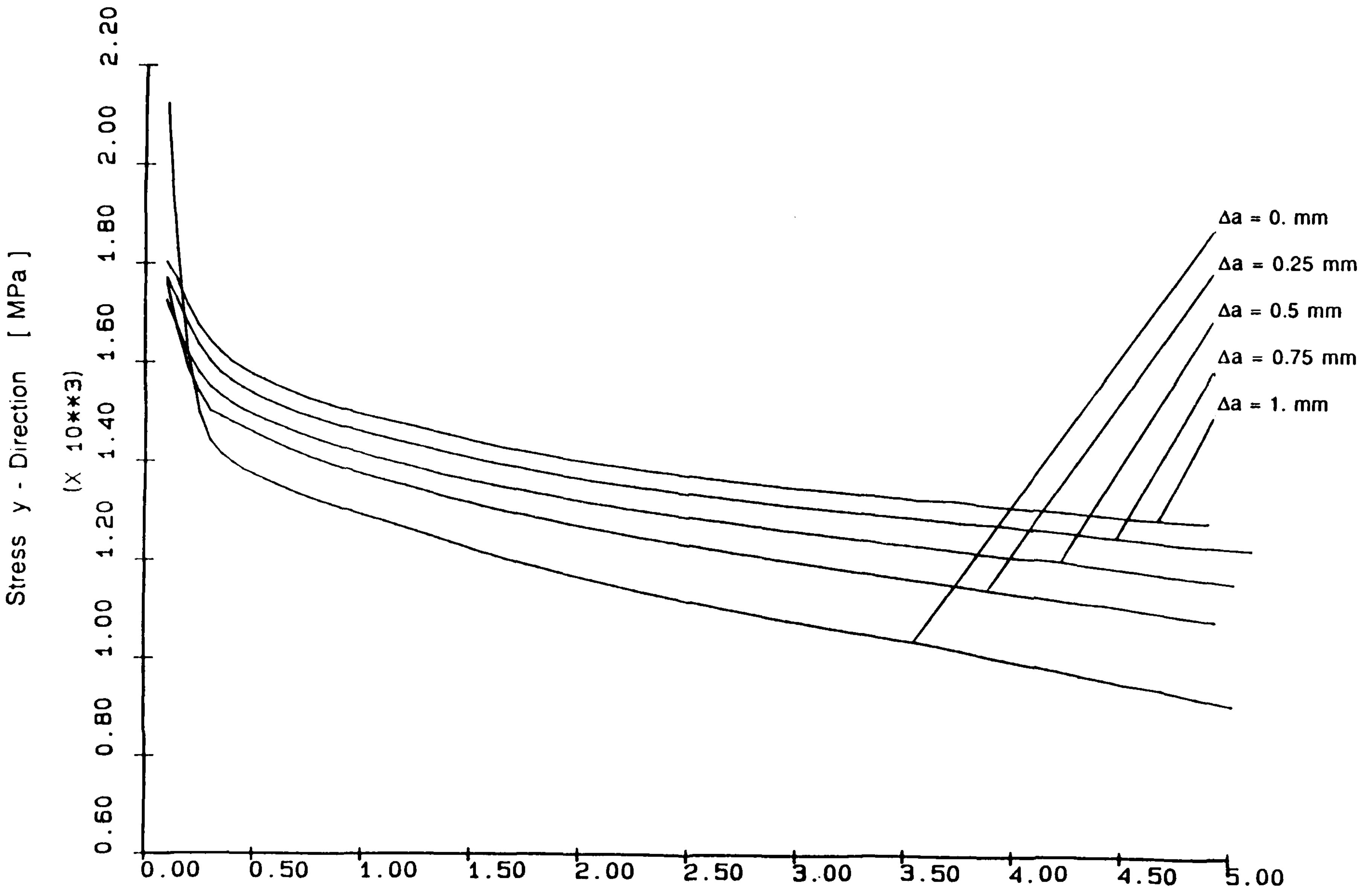

Figure 44: Stress in y - direction along the line $\Theta = 0^o$ for the advancing crack

ne mesh).

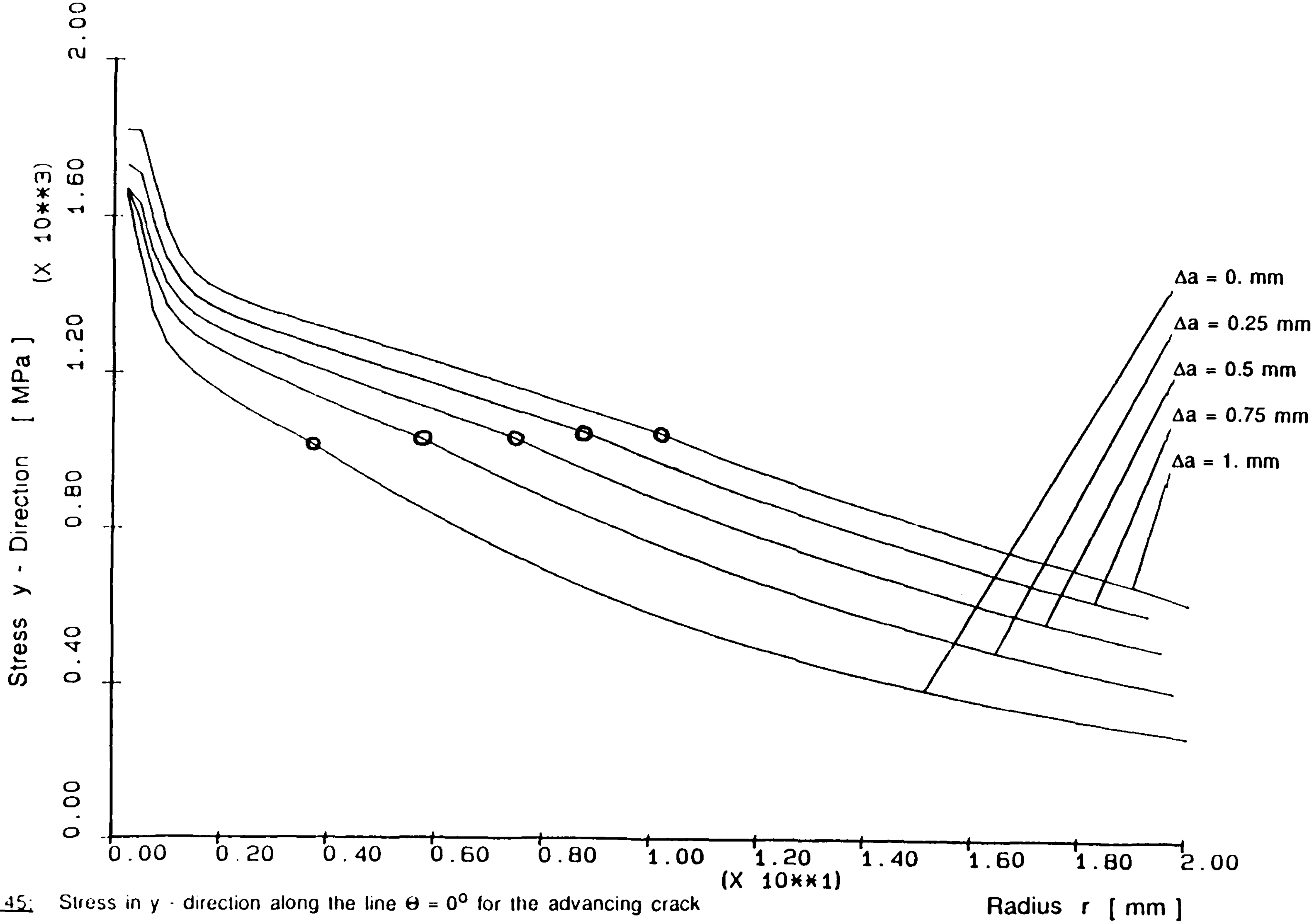

Figure 45: Stress in y - direction along the line $\Theta = 0^\circ$ for the advancing crack

oarse mesh).

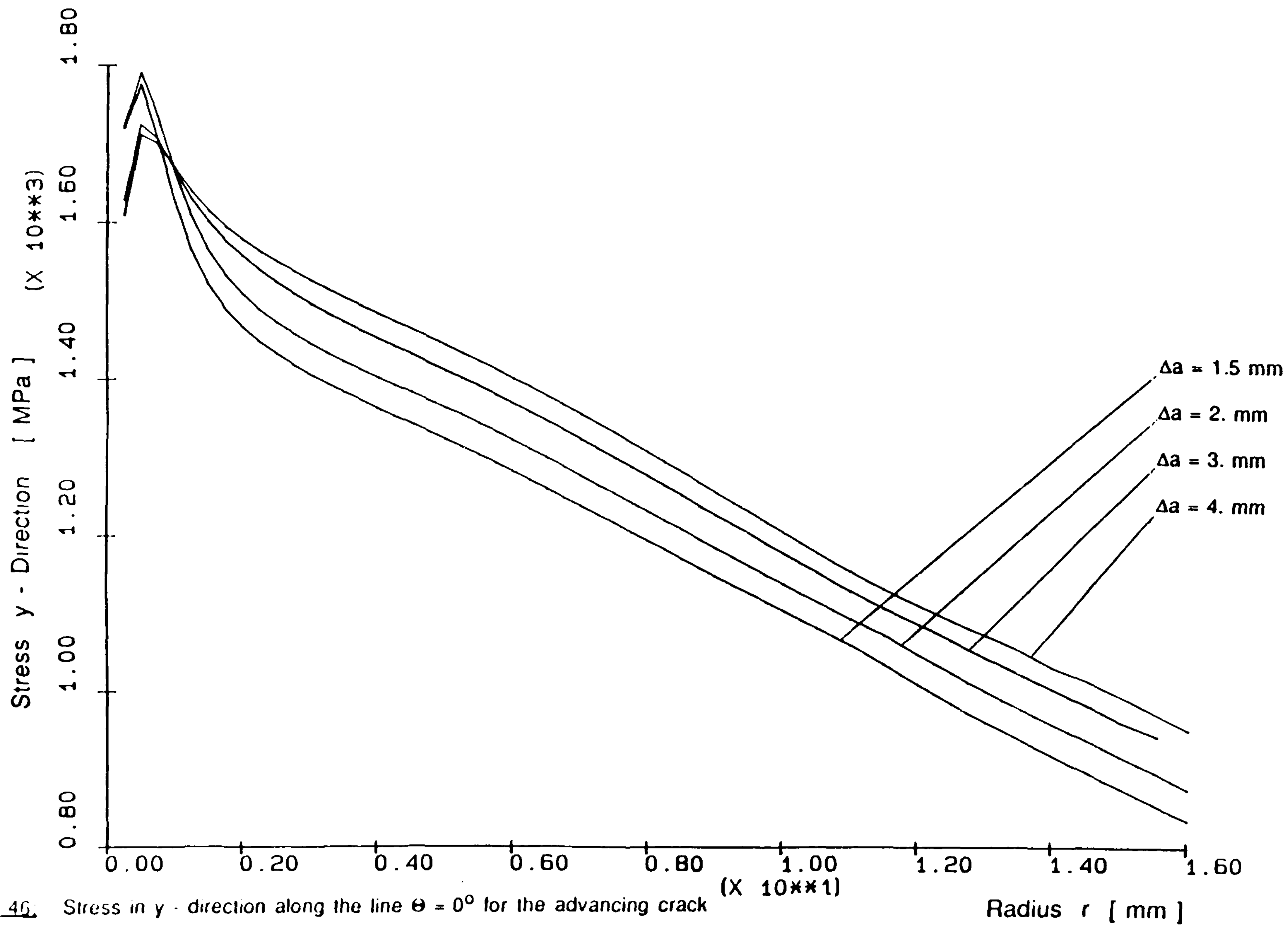

Figure 46: Stress in y - direction along the line $\Theta = 0^{o}$ for the advancing crack (coarse mesh).

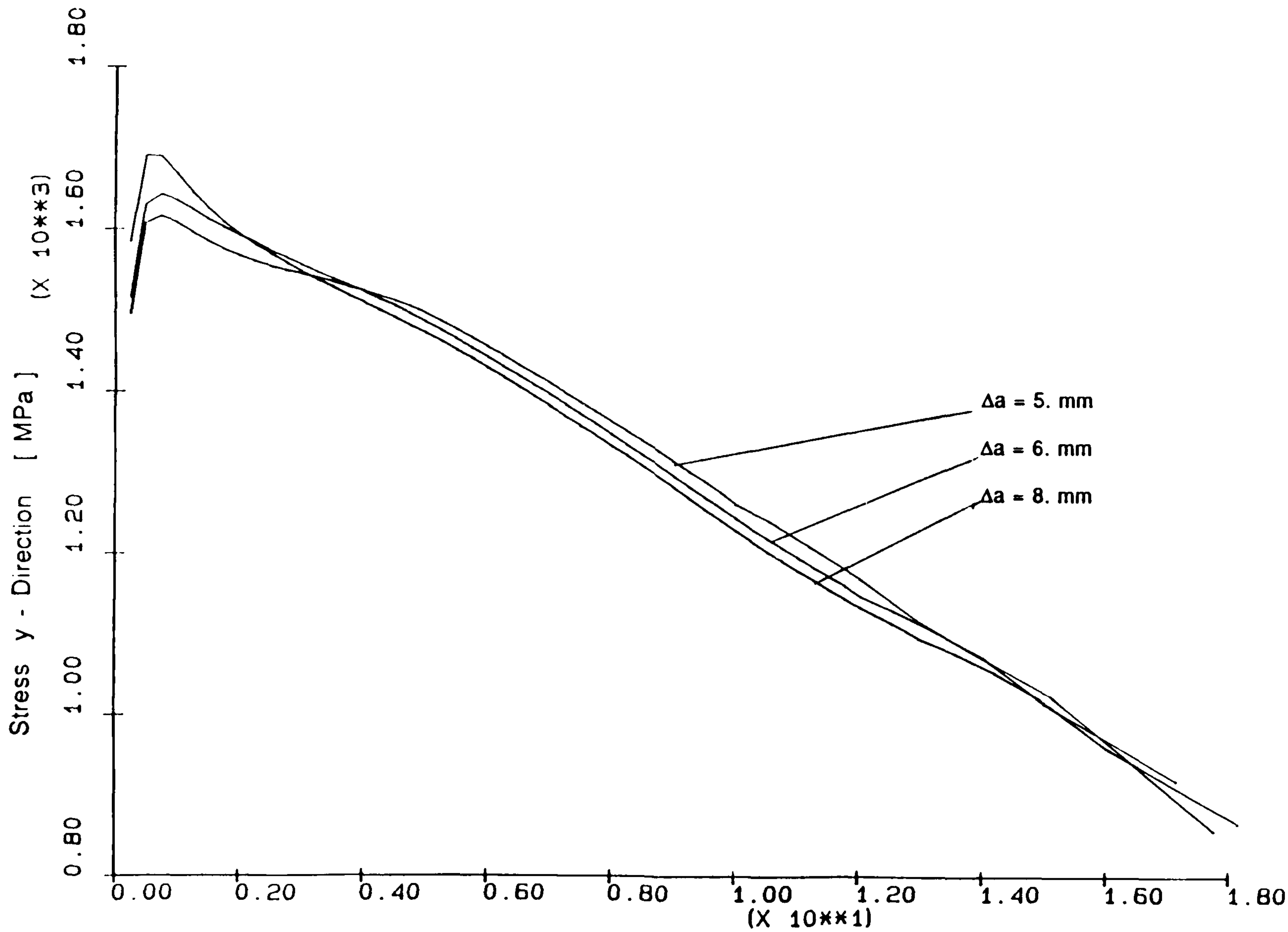

Figure 47: Stress in y - direction along the line $\Theta = 0^{\circ}$ for the advancing crack (coarse mesh).

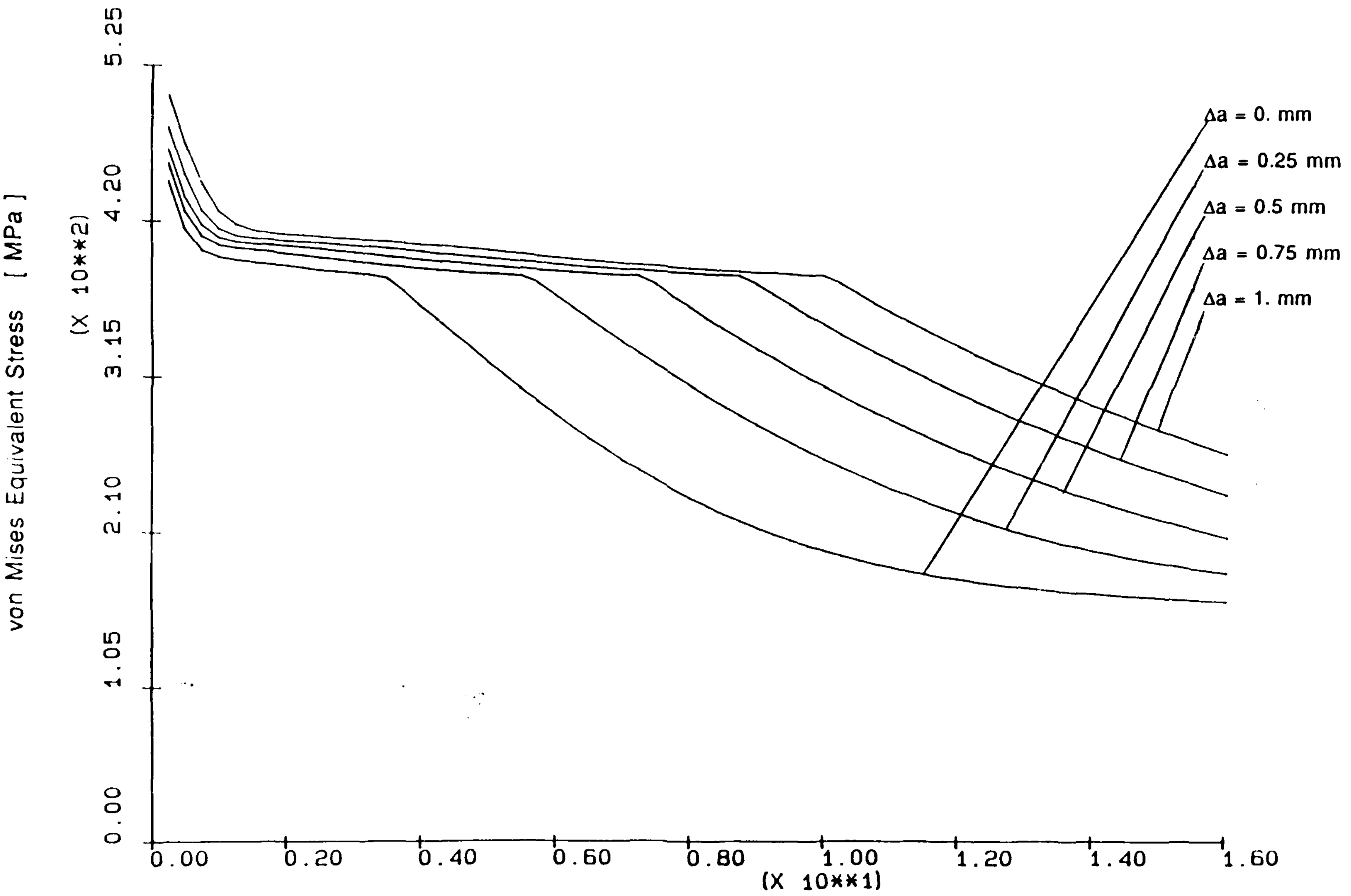

Figure 48: Von Mises equivalent stress along line $\Theta = 0^{\circ}$ for the advancing crack (coarse mesh).

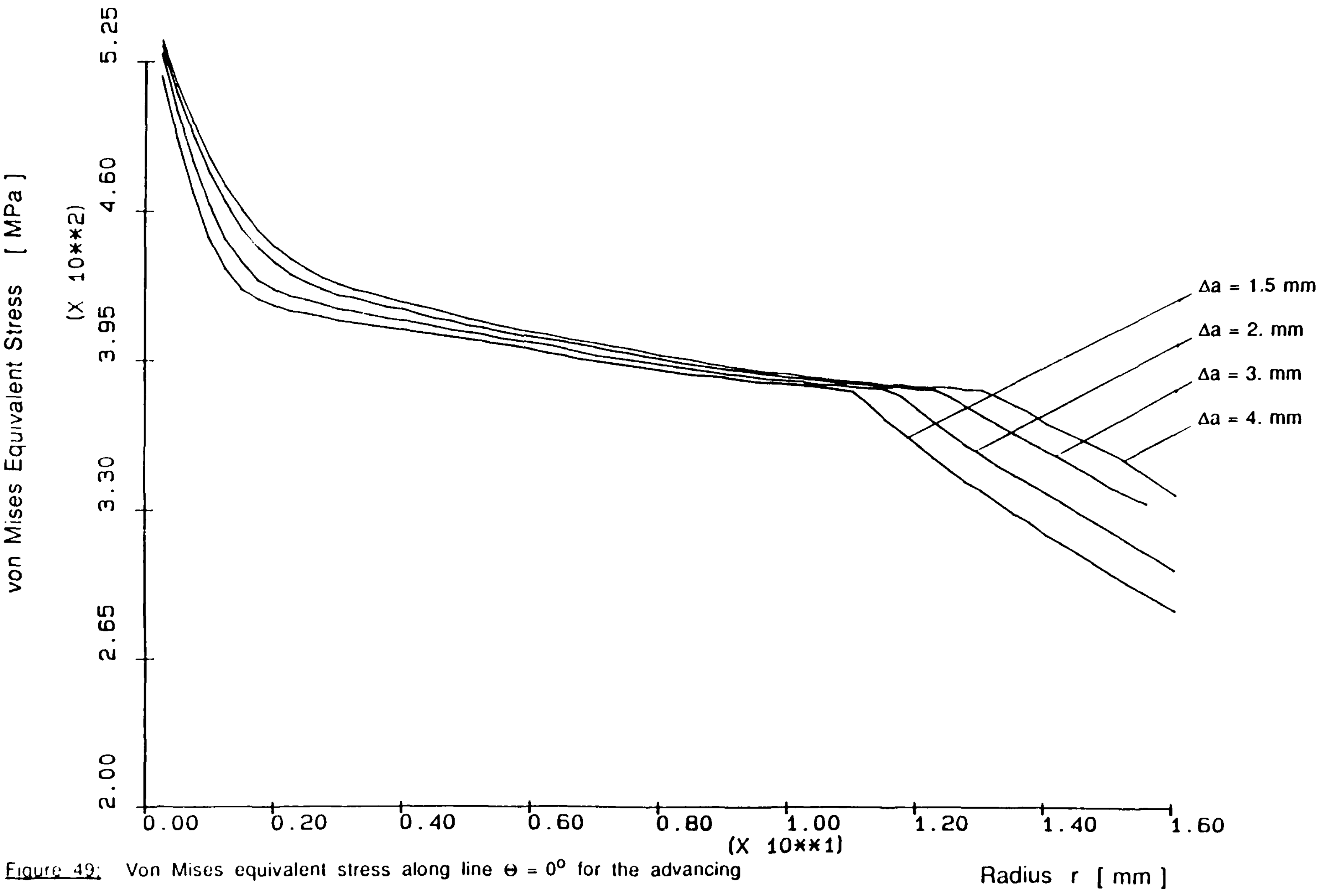

Figure 49: Von Mises equivalent stress along line $\Theta = 0^{o}$ for the advancing crack (coarse mesh).

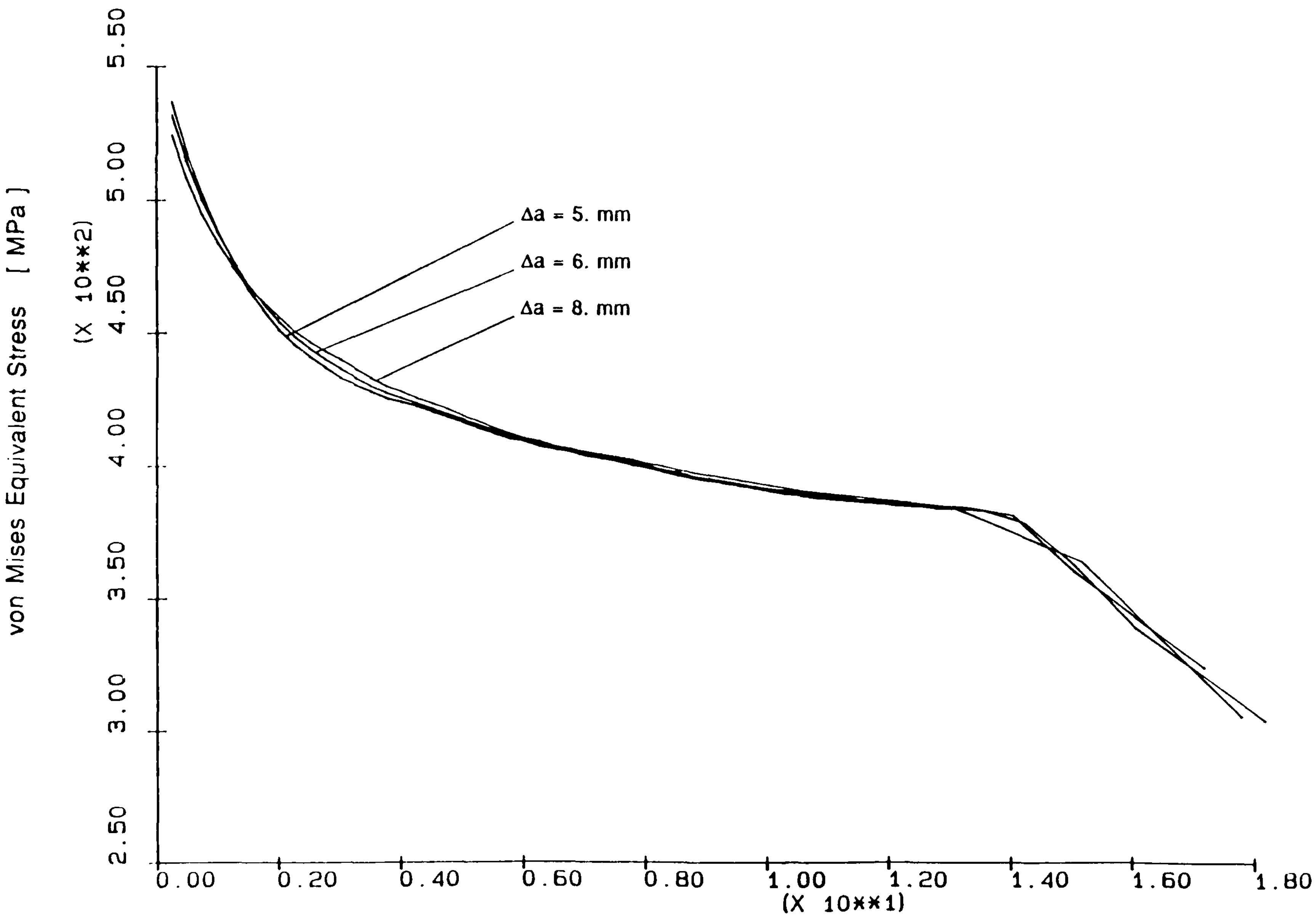

Figure 50: Von Mises equivalent stress along line $\Theta = 0^{o}$ for the advancing crack (coarse mesh).

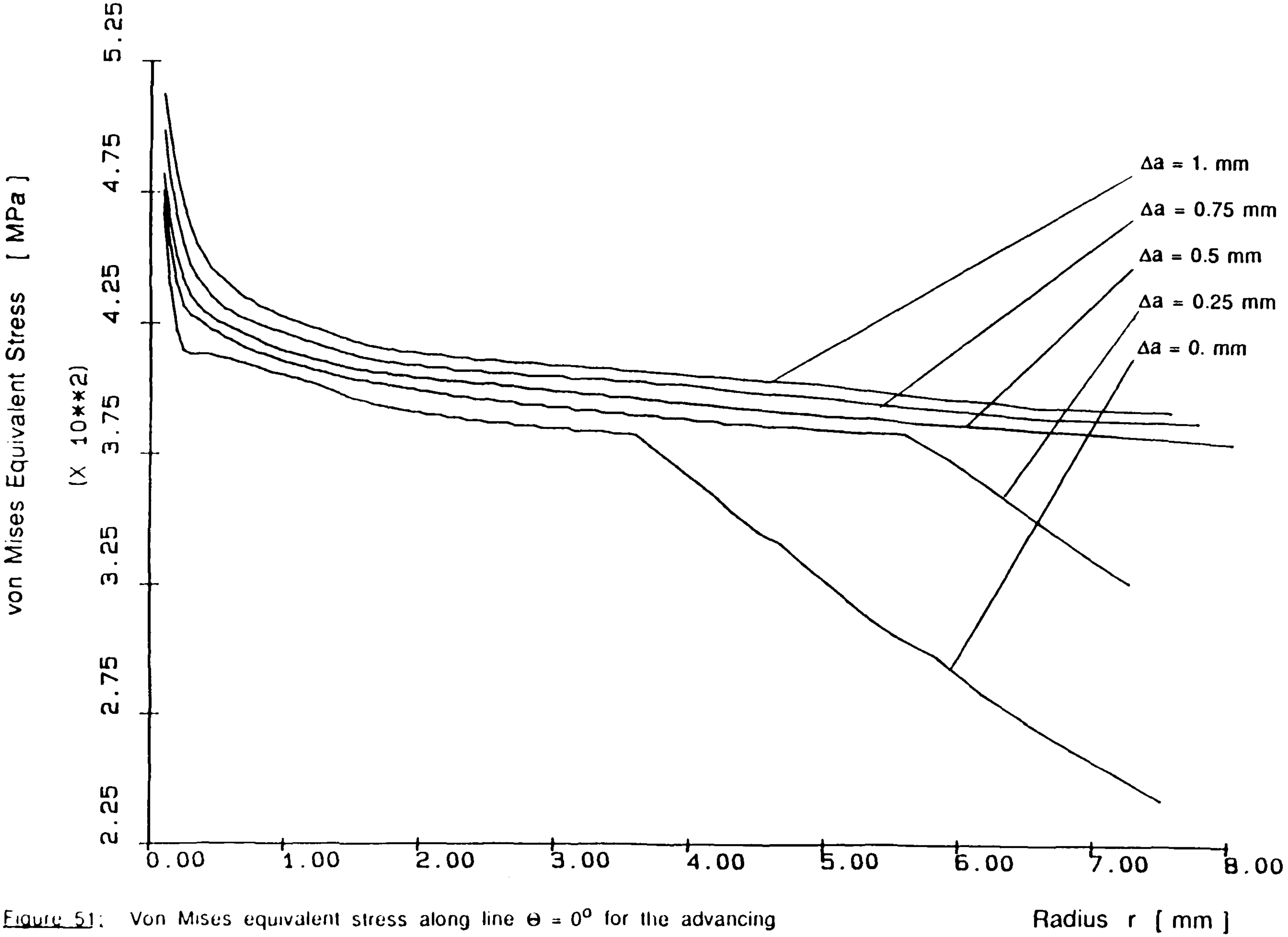

Figure 51: Von Mises equivalent stress along line $\Theta = 0^{o}$ for the advancing crack (line mesh).

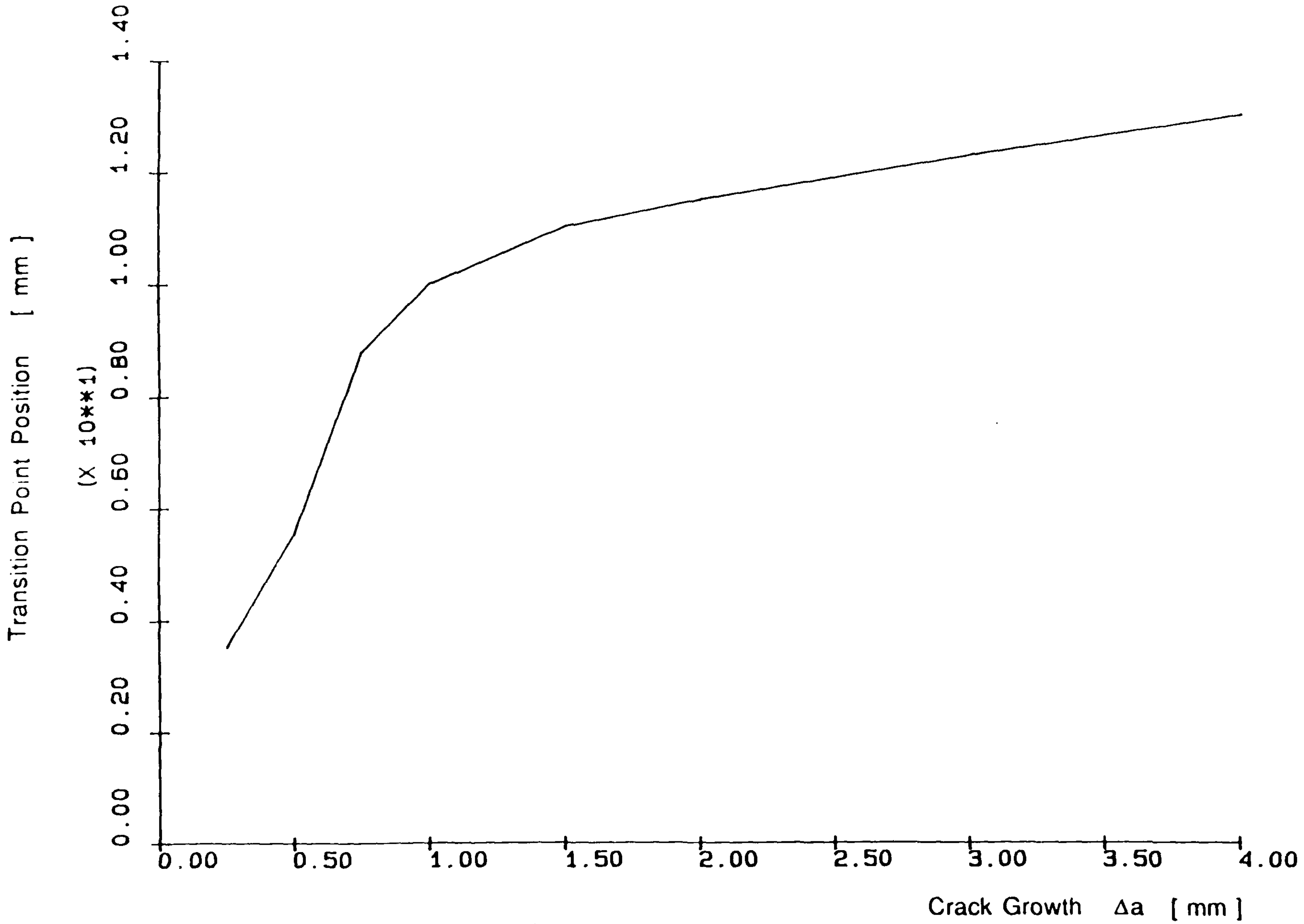

Figure 52: Transition point position vs. crack growth.

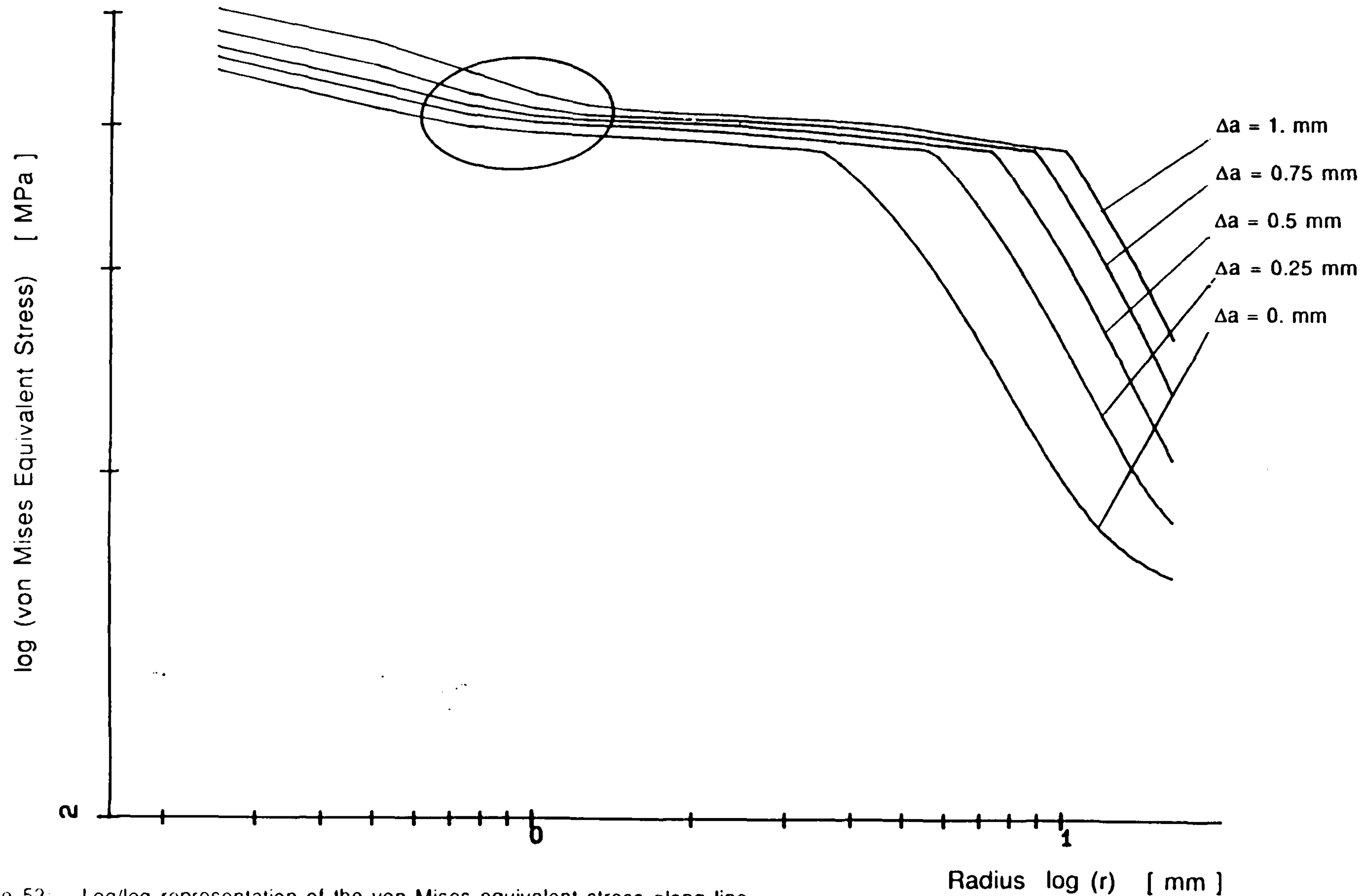

Figure 53: Log/log representation of the von Mises equivalent stress along line $\theta = 0^{o}$ for the advancing crack (coarse mesh).

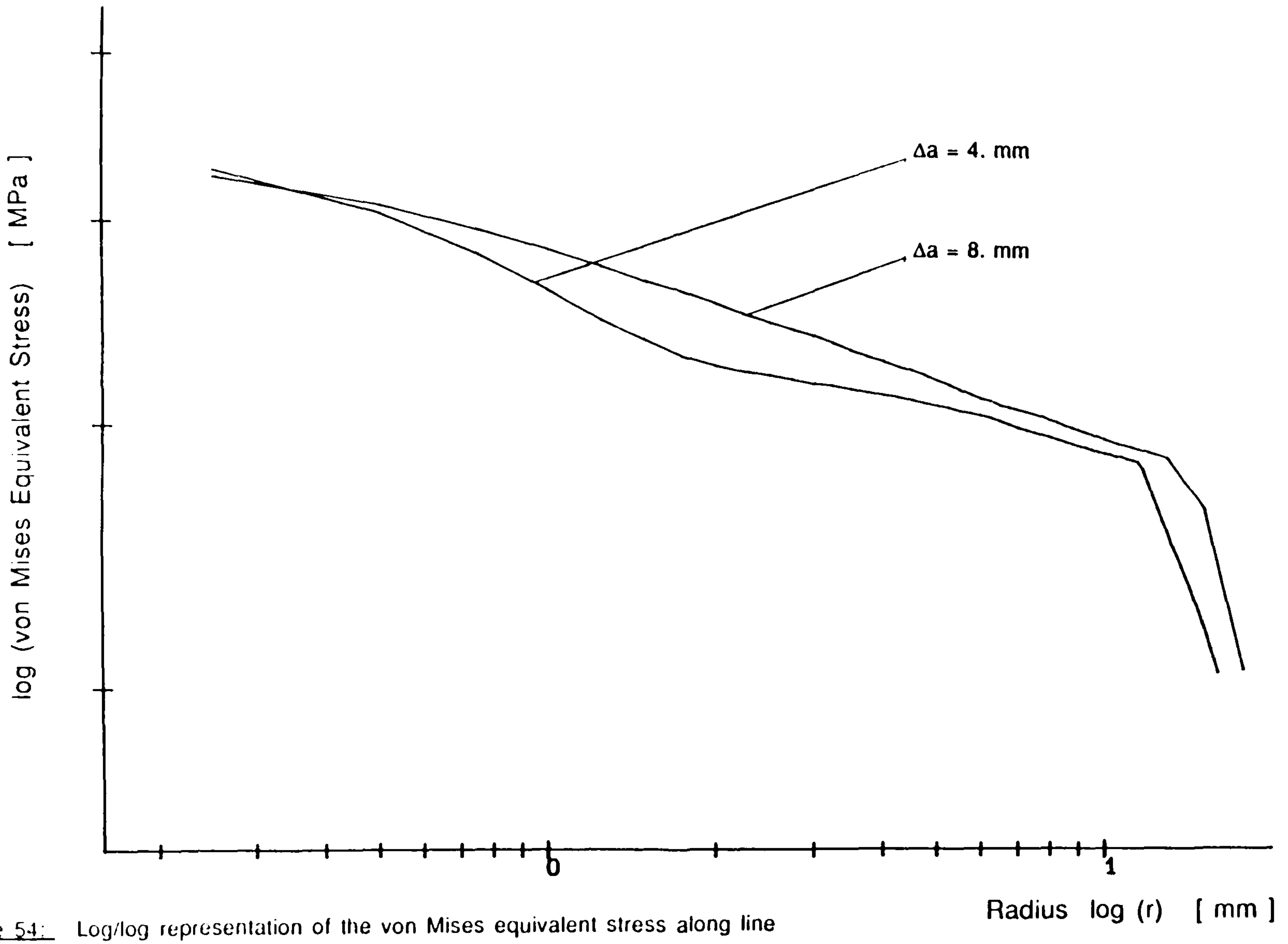

Figure 54: Log/log representation of the von Mises equivalent stress along line $\Theta = 0^o$ for the advancing crack (coarse mesh).

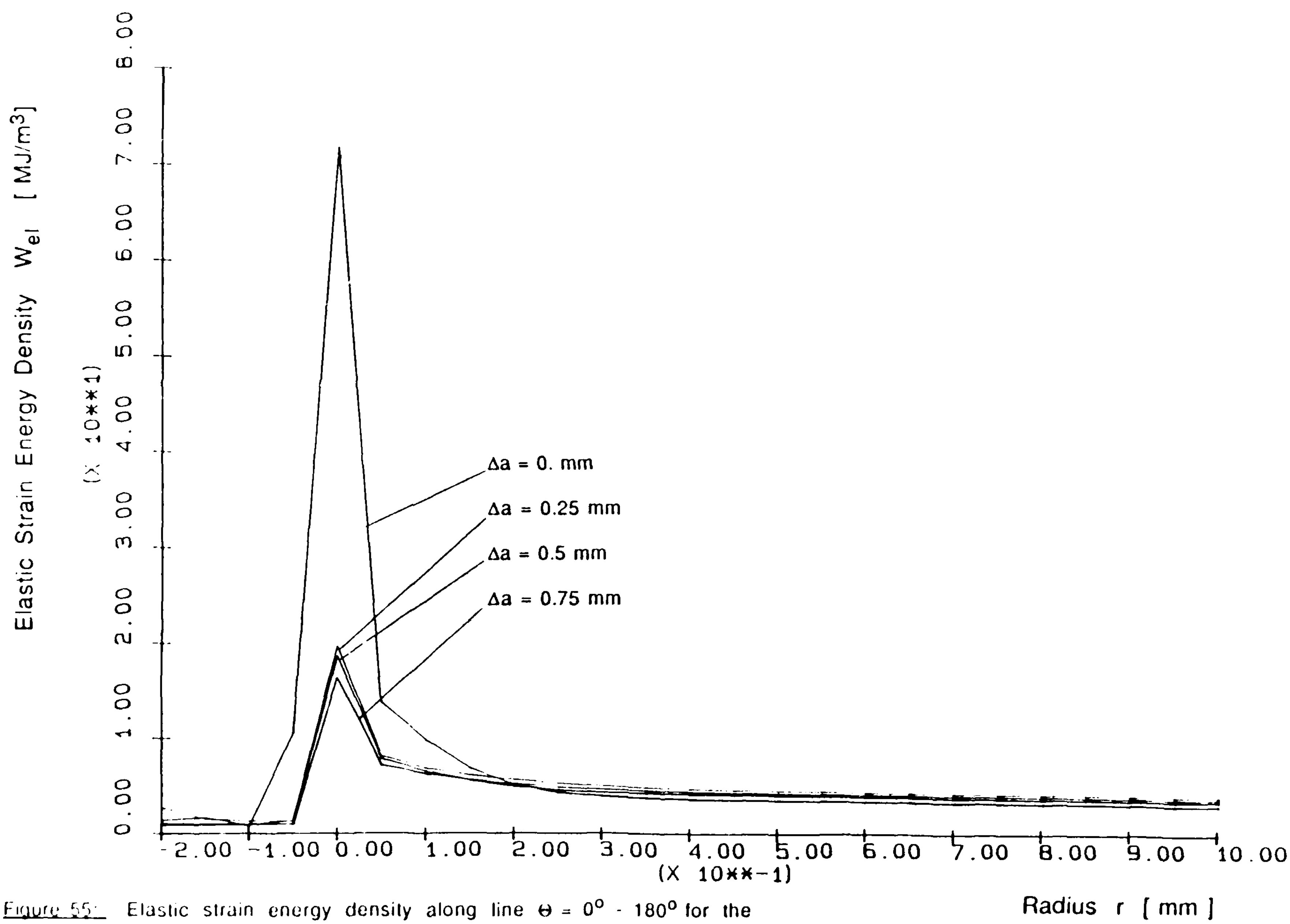

Figure 55: Elastic strain energy density along line $\Theta = 0^{\circ} - 180^{\circ}$ for the advancing crack (fine mesh).

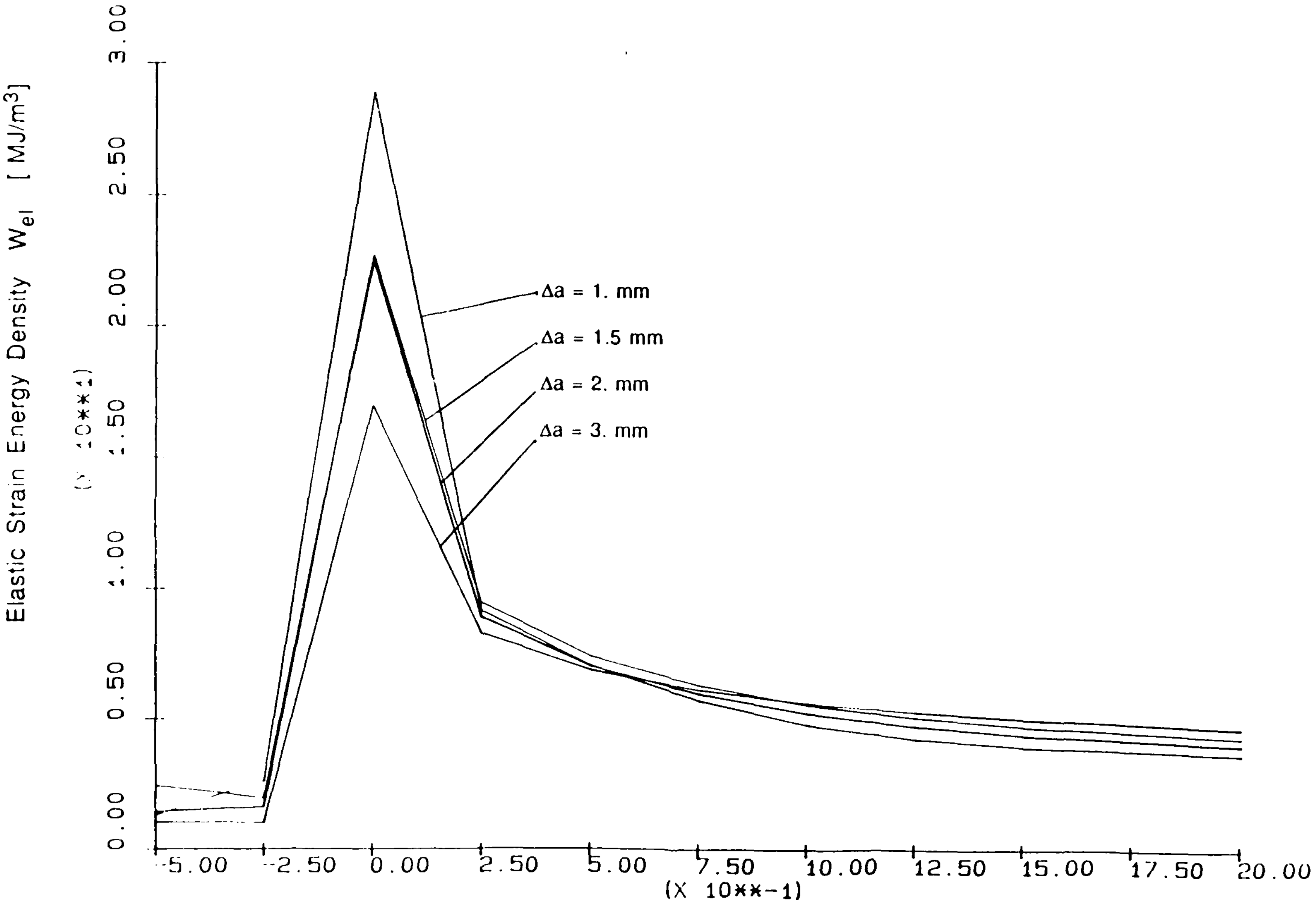

Figure 56 Elastic strain energy density along line Θ = 0° - 180° for the advancing crack (coarse mesh).

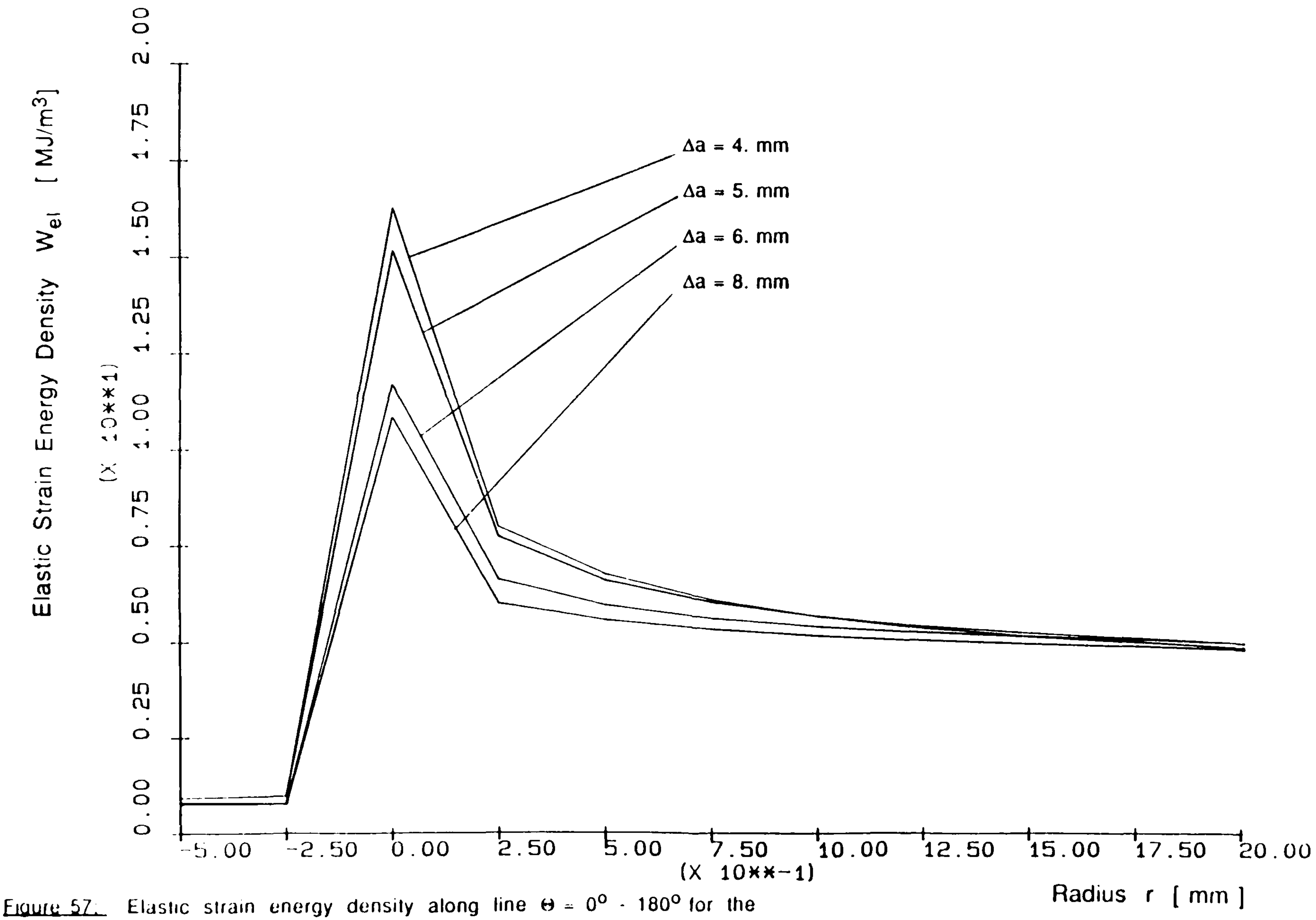

Figure 57: Elastic strain energy density along line $\Theta = 0^{\circ} - 180^{\circ}$ for the advancing crack (coarse mesh).

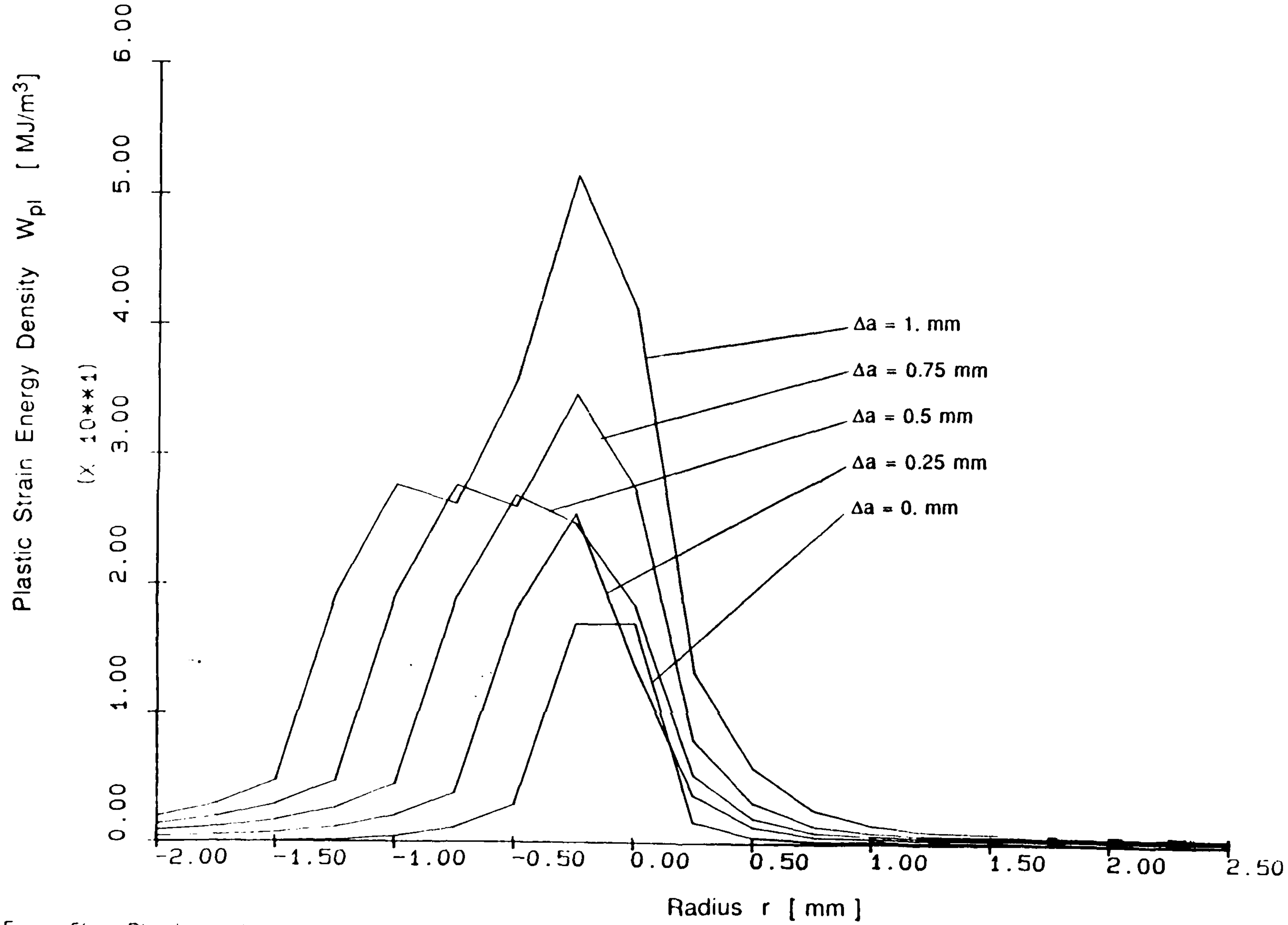

Figure 58 Plastic strain energy density along line $\Theta = 0^\circ$ - 18 or the

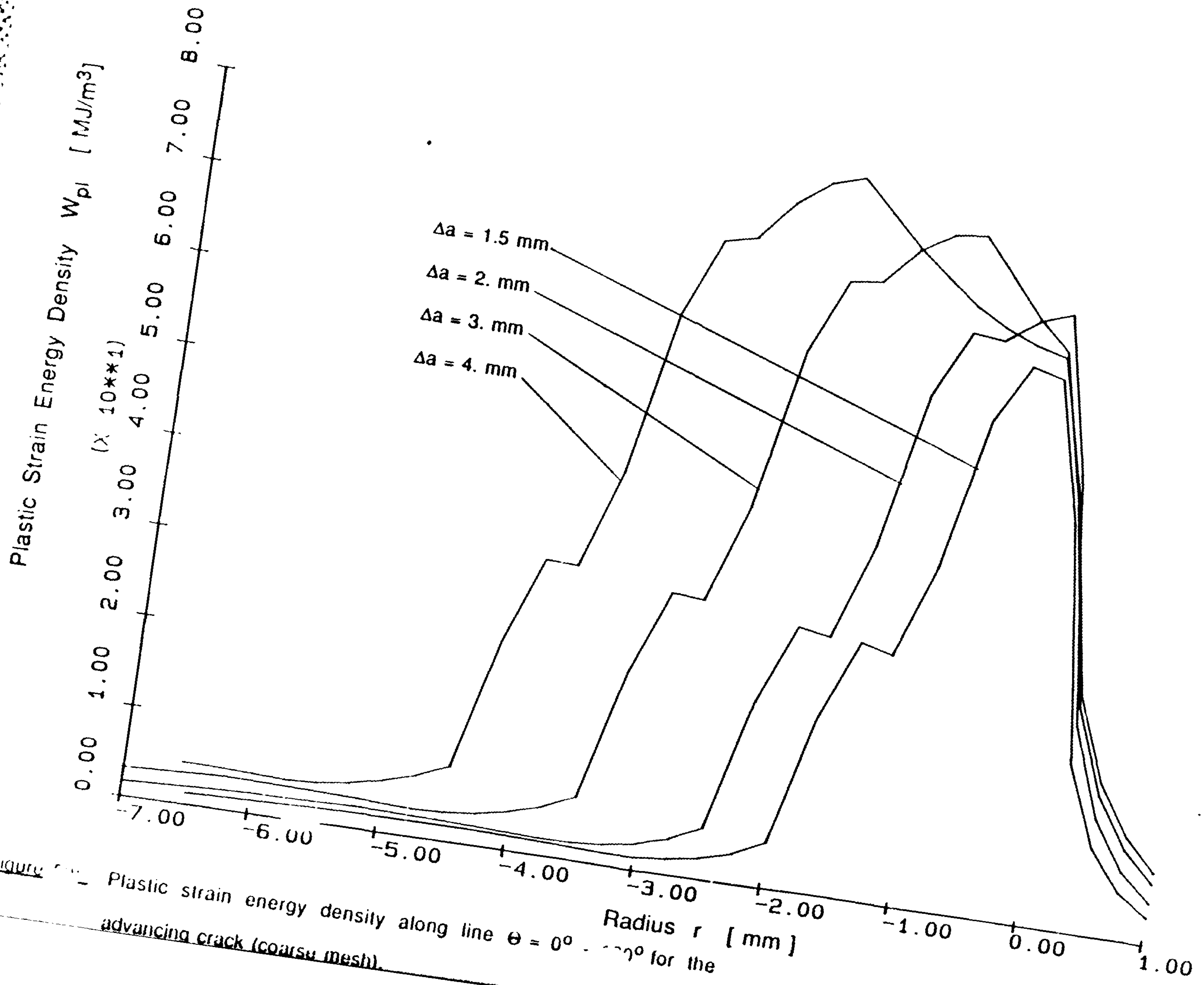

Figure [illegible] Plastic strain energy density along line $\Theta = 0^{\circ}$ - [illegible] for the advancing crack (coarse mesh).

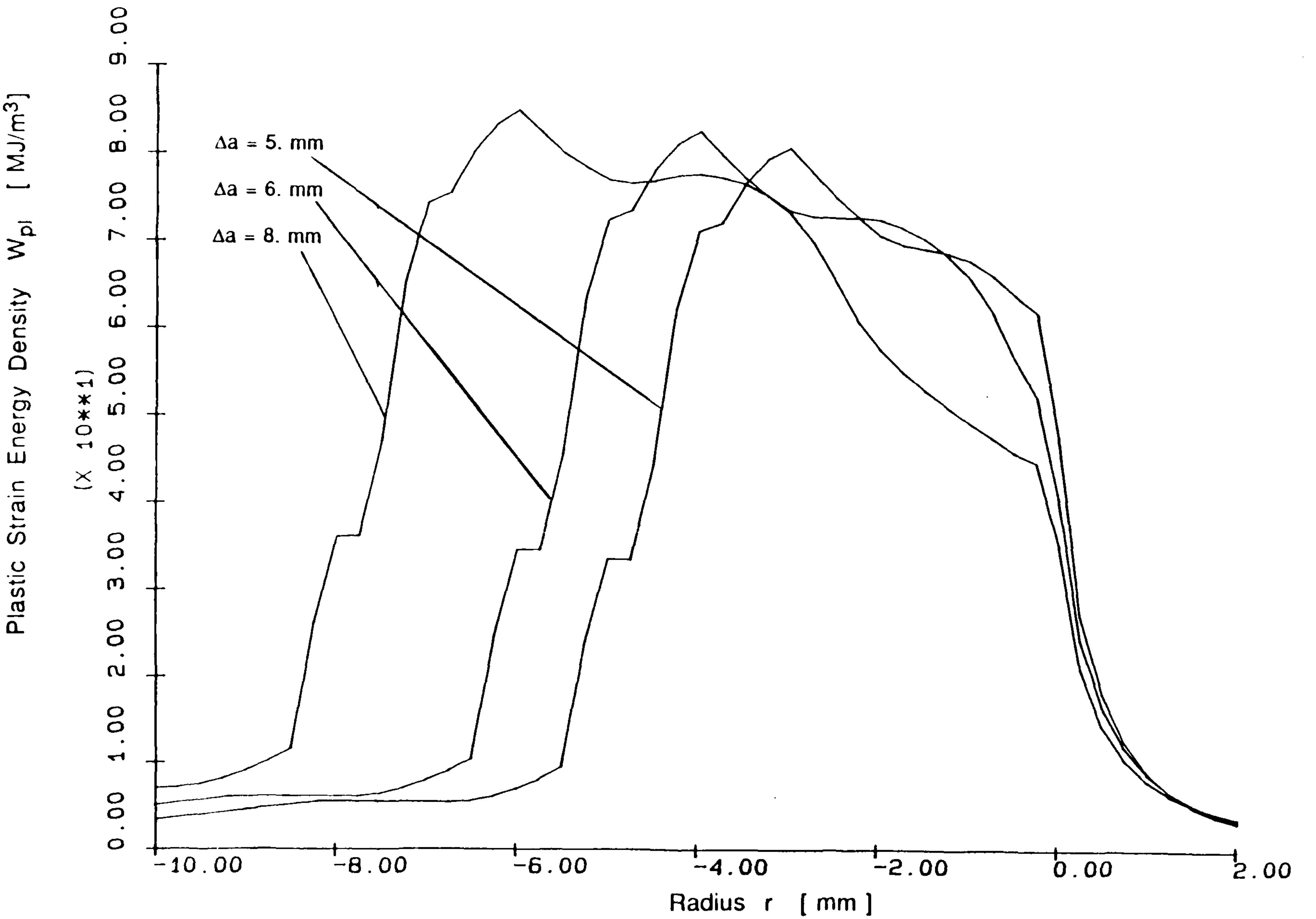

Figure 60 Plastic strain energy density along line $\Theta = 0^o - 180^o$ for the

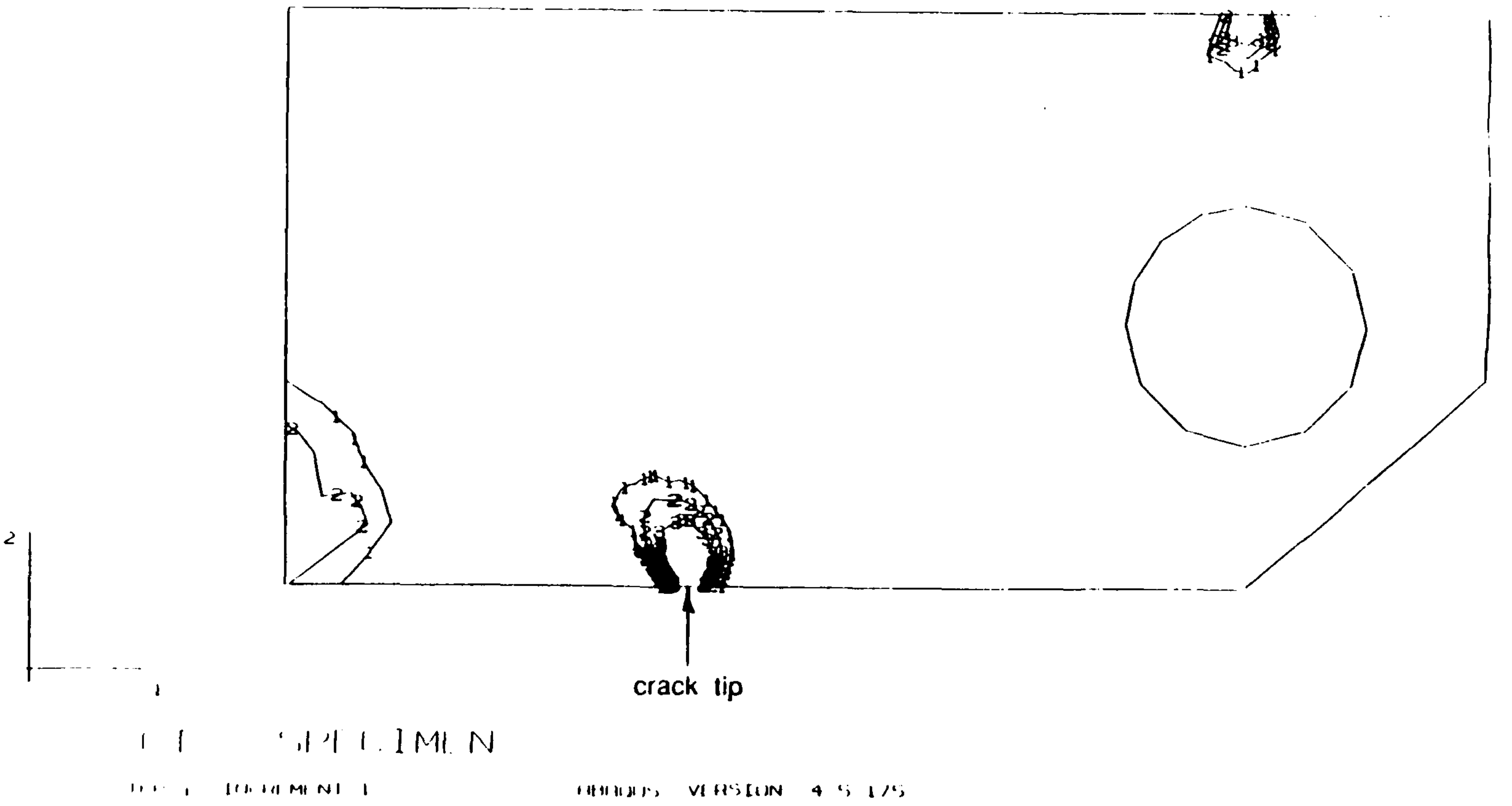
MISES EQUIV. STRESS
I.D. VALUE
1 +2.83E+02
2 +3.[illegible]E+02
3 +3.83E+02
crack tip
2
1
CT SPECIMEN
STEP 1 INCREMENT 1
ABAQUS VERSION 4 5 175

Figure 61a: Iso contours of the von Mises stress (coarse mesh).

- load 5300 N

- Δa 0. mm

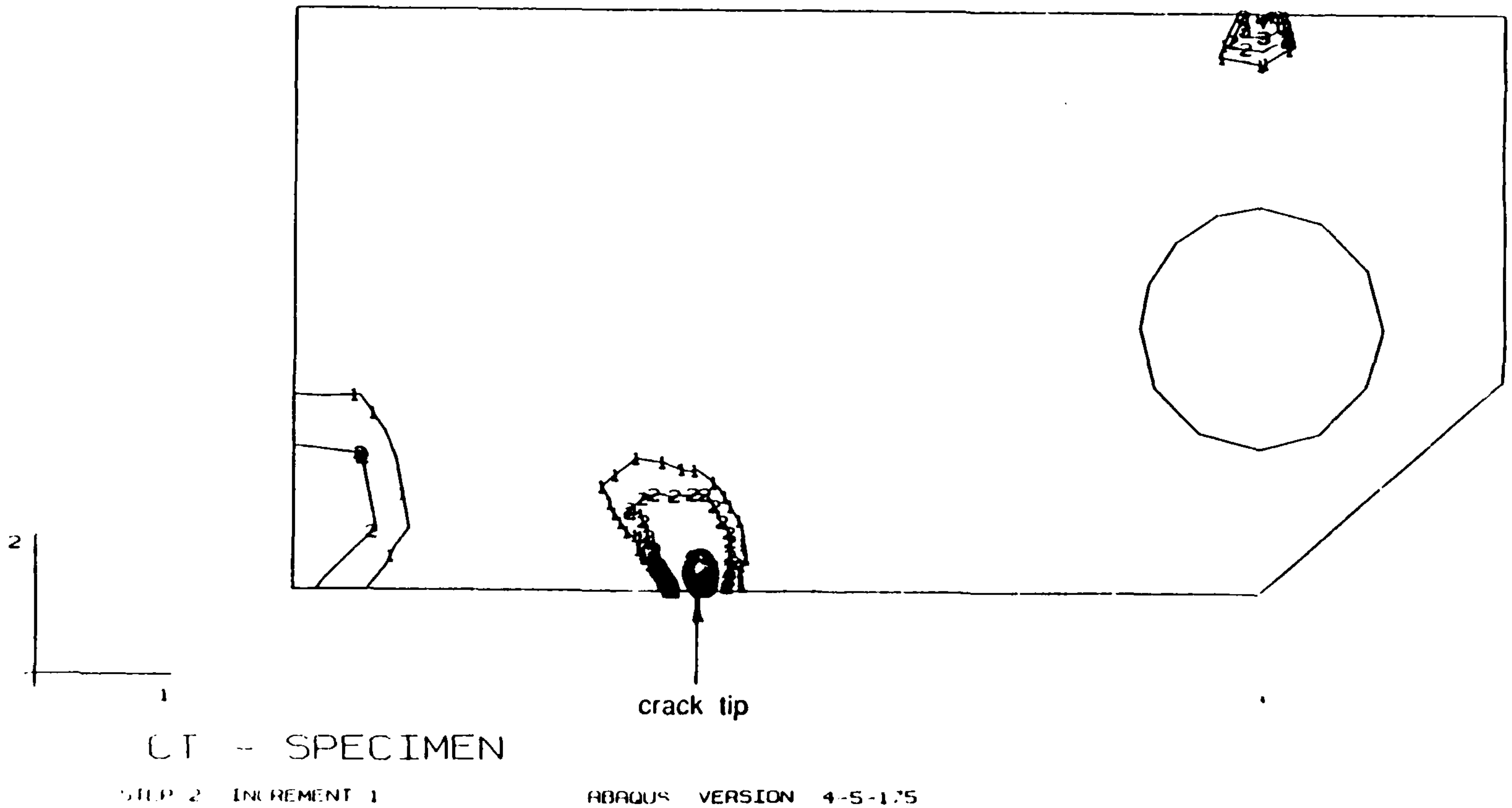
MISES EQUIV. STRESS
I. D. VALUE
1 +3. 32E+02
2 +3. 82E+02
3 +4. 32E+02
4 +4. 82E+02
2
1
crack tip
CT - SPECIMEN
STEP 2 INCREMENT 1
ABAQUS VERSION 4-5-175

Figure 61b: Iso contours of the von Mises stress (coarse mesh).

- load 6400 N
- Δa 0.25 mm

Figure 61c: Iso contours of the von Mises stress (coarse mesh).

- load 7100 N

- Δa 0.5 mm

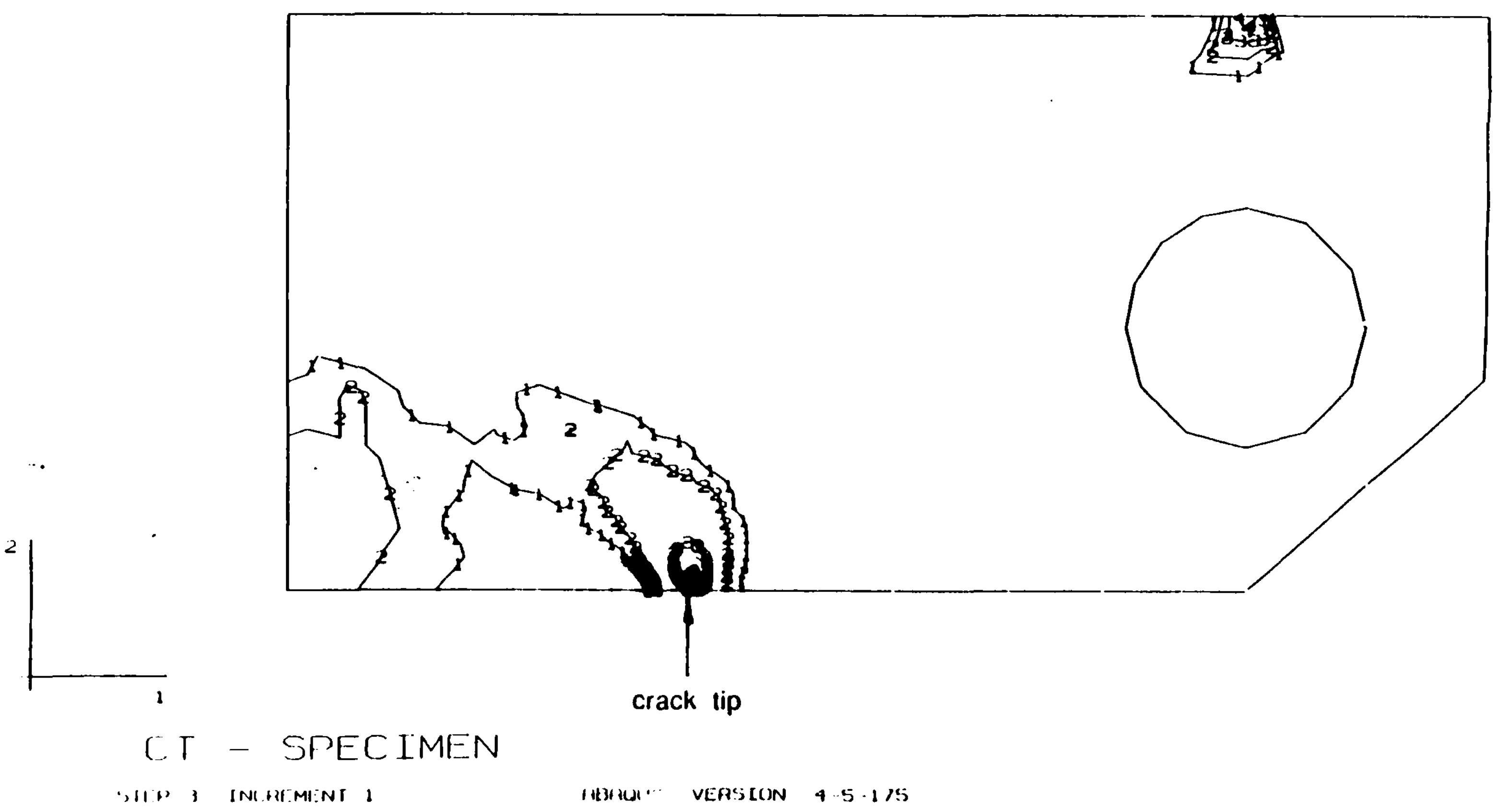
MISES EQUIV. STRESS
I.D. VALUE
1 +3.32E+02
2 +3.82E+02
3 +4.32E+02
4 +4.82E+02
1
2
3
crack tip
2
1
CT - SPECIMEN
STEP 3 INCREMENT 1
ABAQUS VERSION 4-5-175

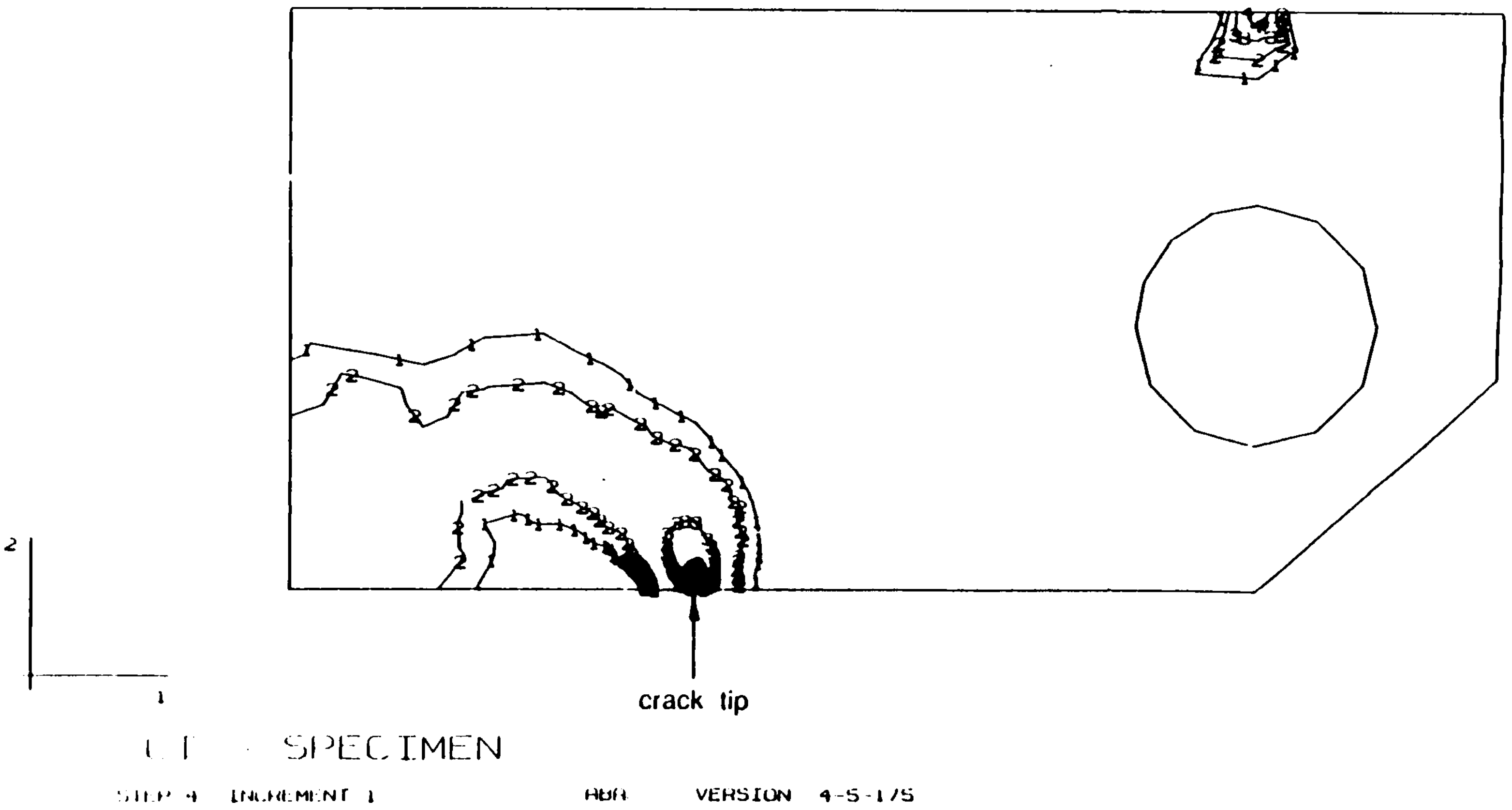

Figure 61d: Iso contours of the von Mises stress (coarse mesh).

- load 7650 N

- Δa 0.75 mm

Figure 61e: Iso contours of the von Mises stress (coarse mesh).

- load 8100 N

- Δa 1. mm

MISES EQUIV. STRESS
I. D. VALUE
1 +3. 32E+02
2 +3. 82E+02
3 +4. 32E+02
4 +4. 82E+02

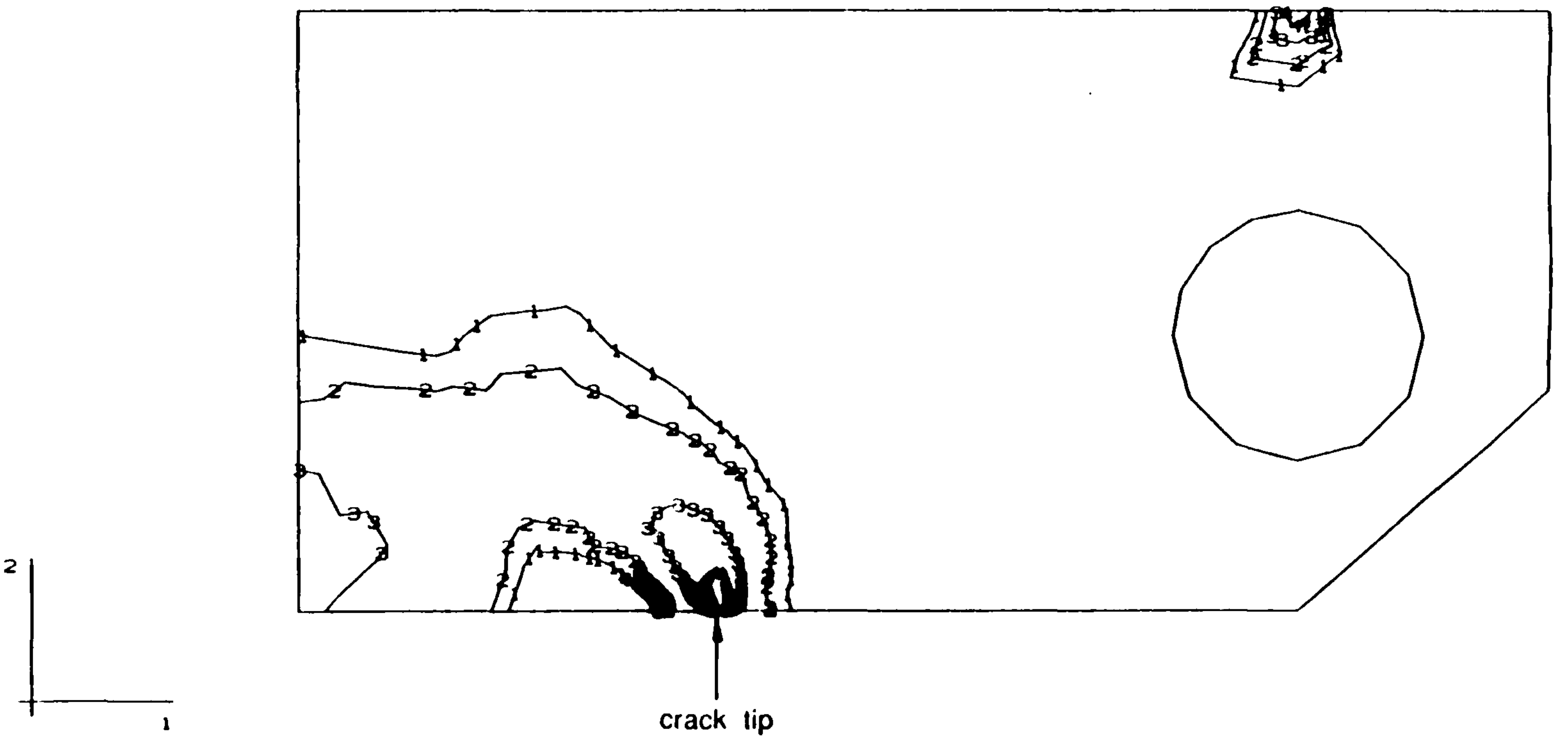

CT - SPECIMEN

STEP 5 INCREMENT 1 ABAQ' VERSION 4-5-175

Figure 61f: Iso contours of the von Mises stress (coarse mesh).

- load 8400 N

- Δa 1.5 mm

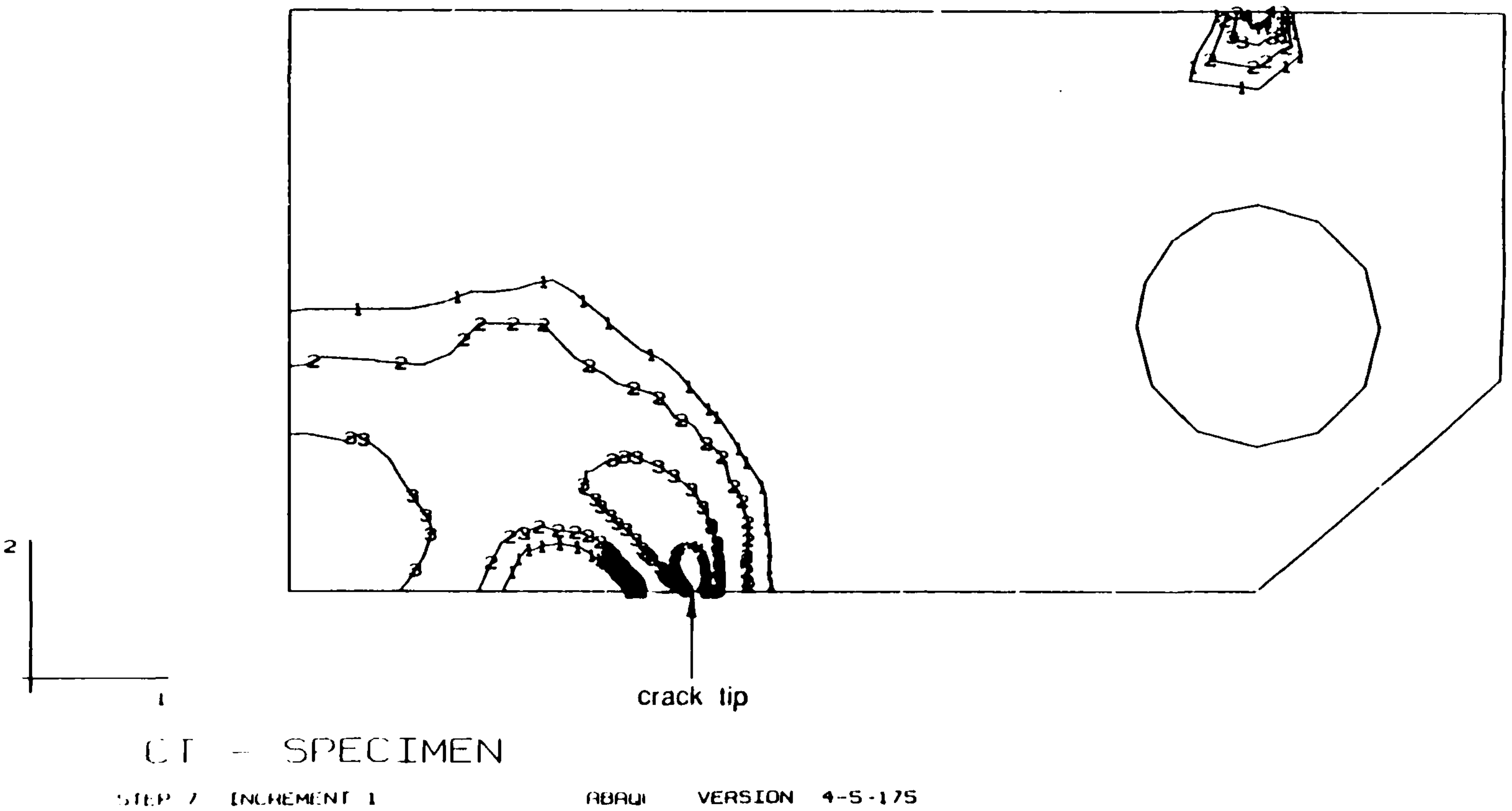

Figure 61a: Iso contours of the von Mises stress (coarse mesh).

- load 8600 N

- Δa 2. mm

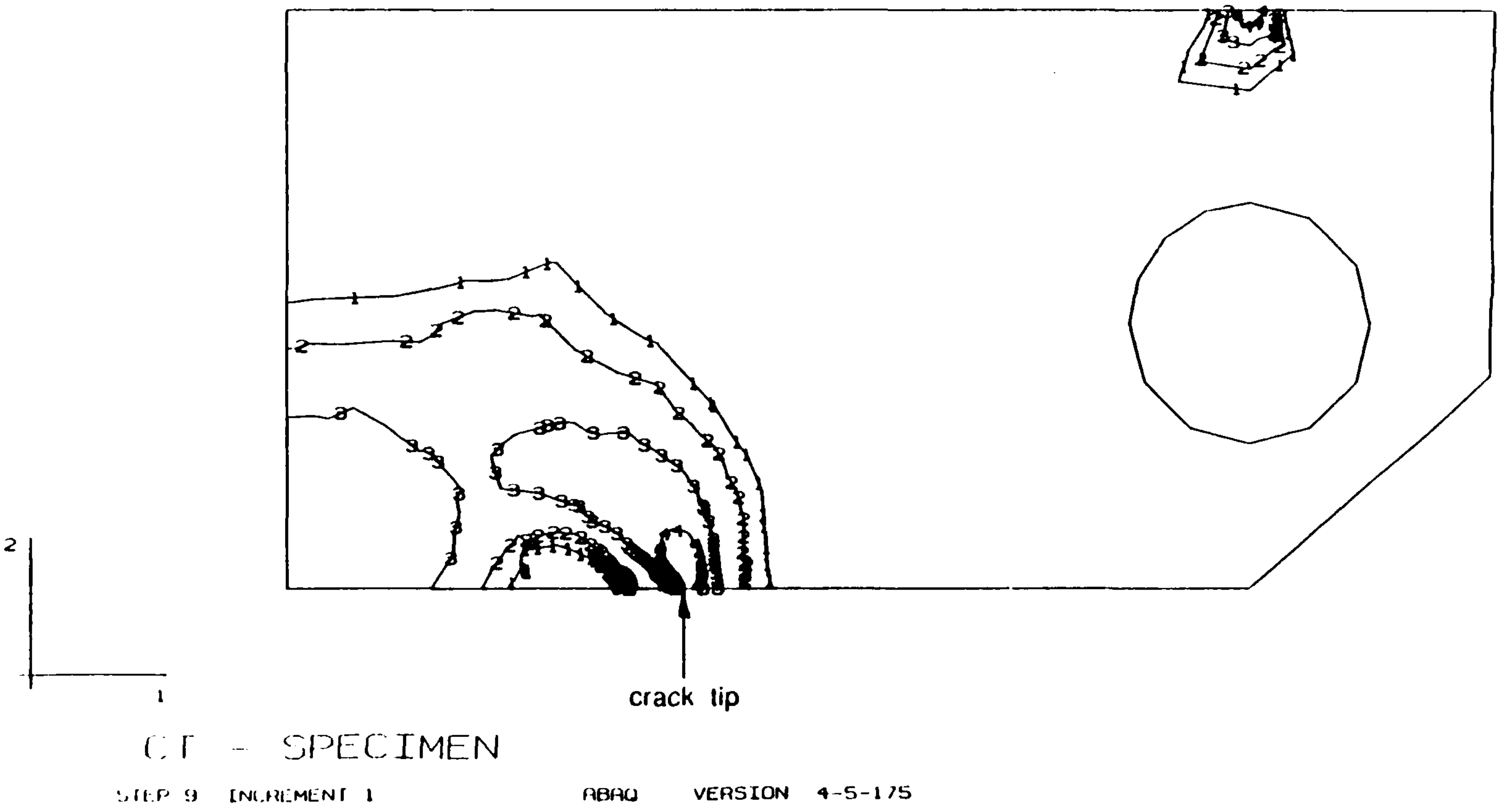

Figure 61h: Iso contours of the von Mises stress (coarse mesh).

- load 8690 N
- Δa 2.5 mm

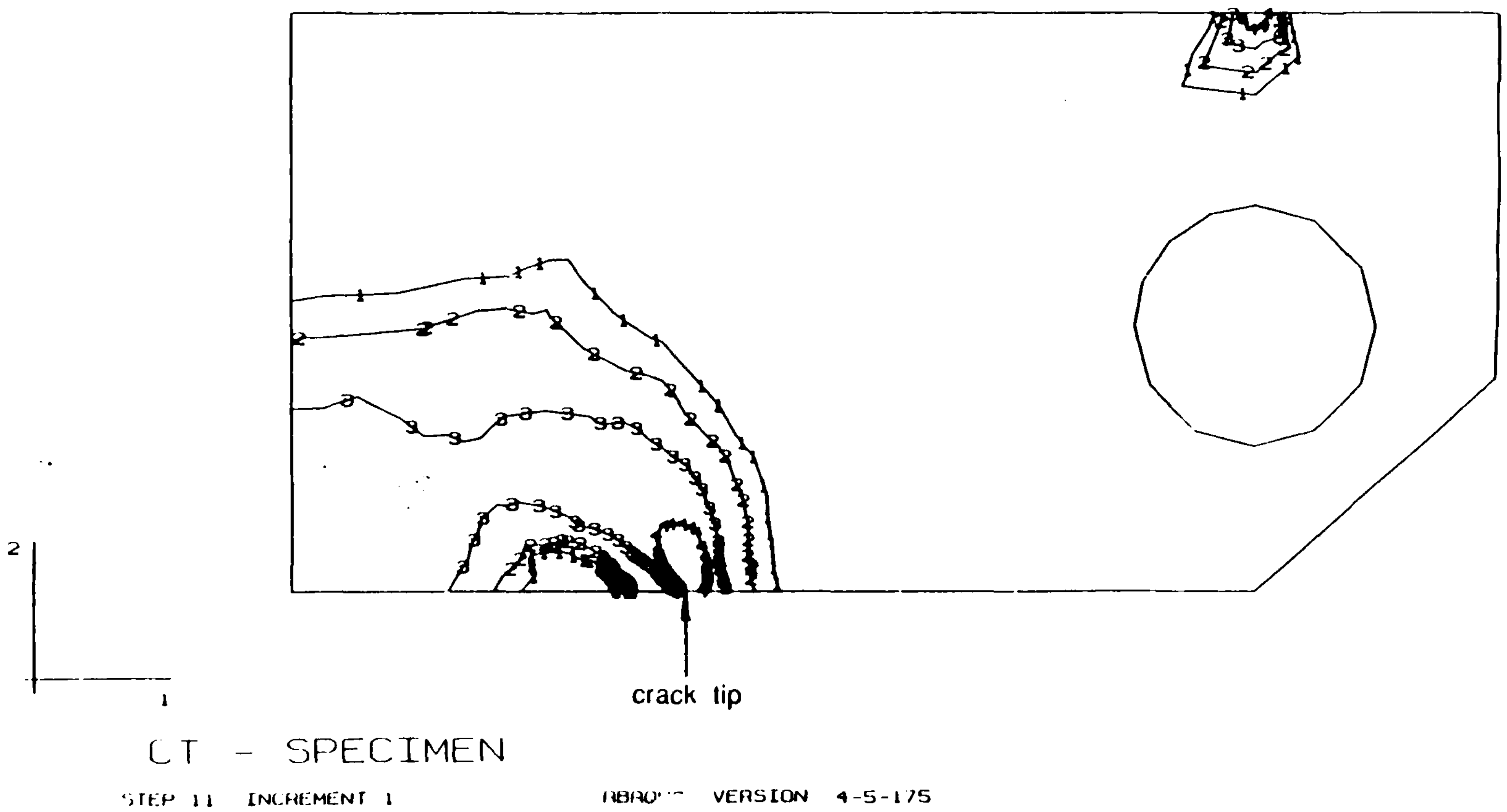

Figure 61i: Iso contours of the von Mises stress (coarse mesh).

- load 8720 N

- Δa 3. mm

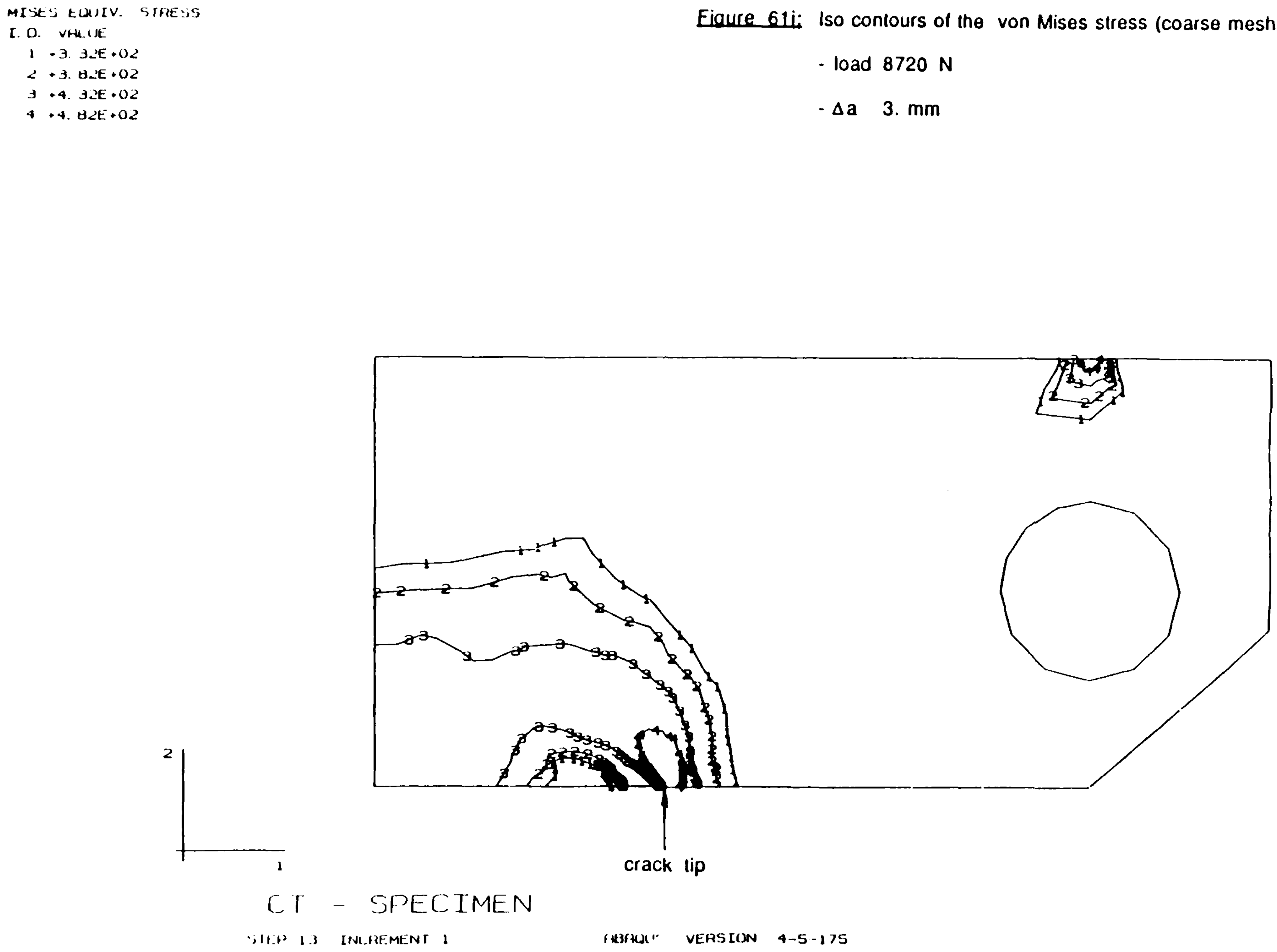

Figure 61j: Iso contours of the von Mises stress (coarse mesh).

- load 8734 N

- Δa 4. mm

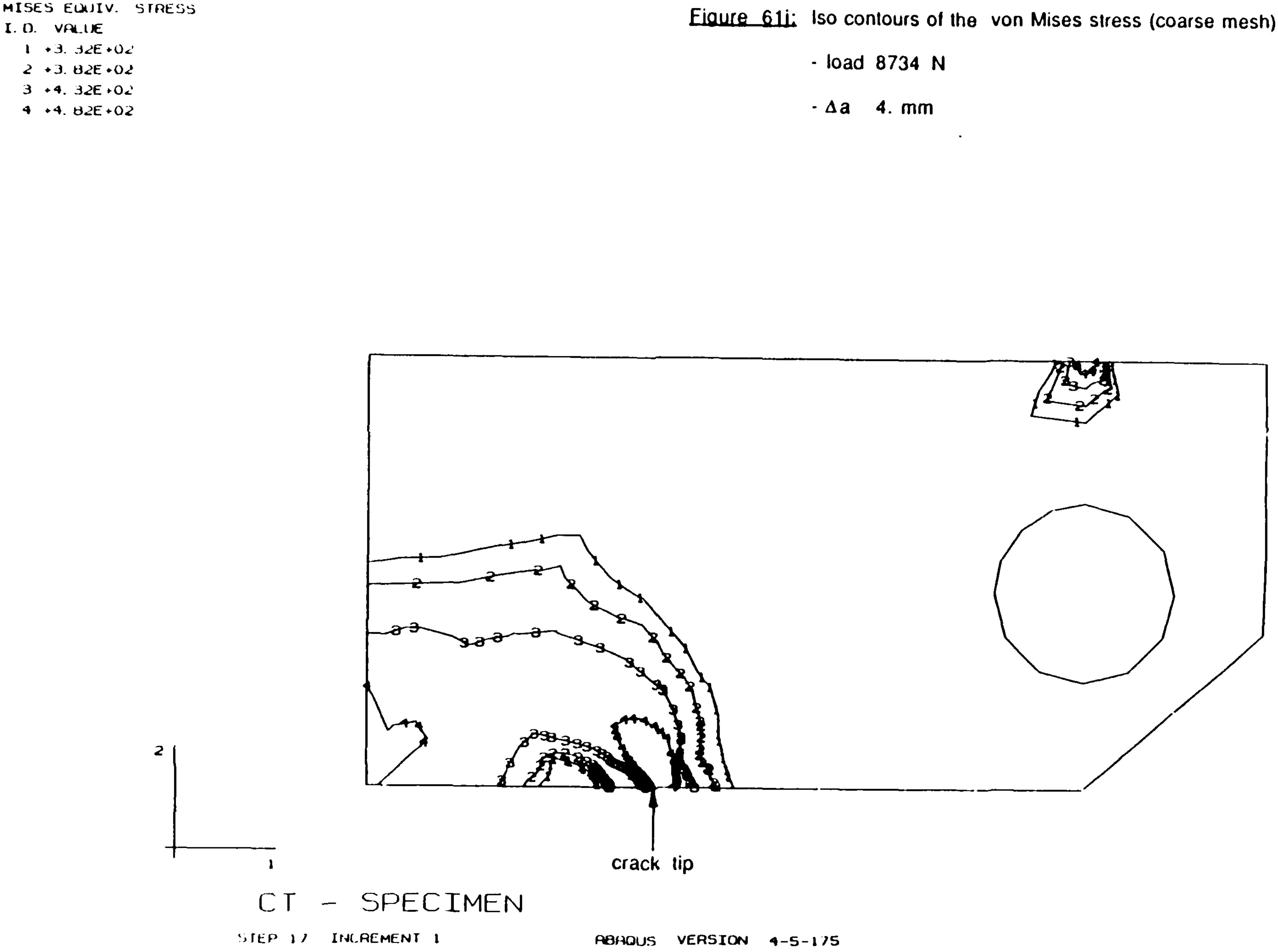

Figure 61k: Iso contours of the von Mises stress (coarse mesh).

- load 8700 N

- Δa 5. mm

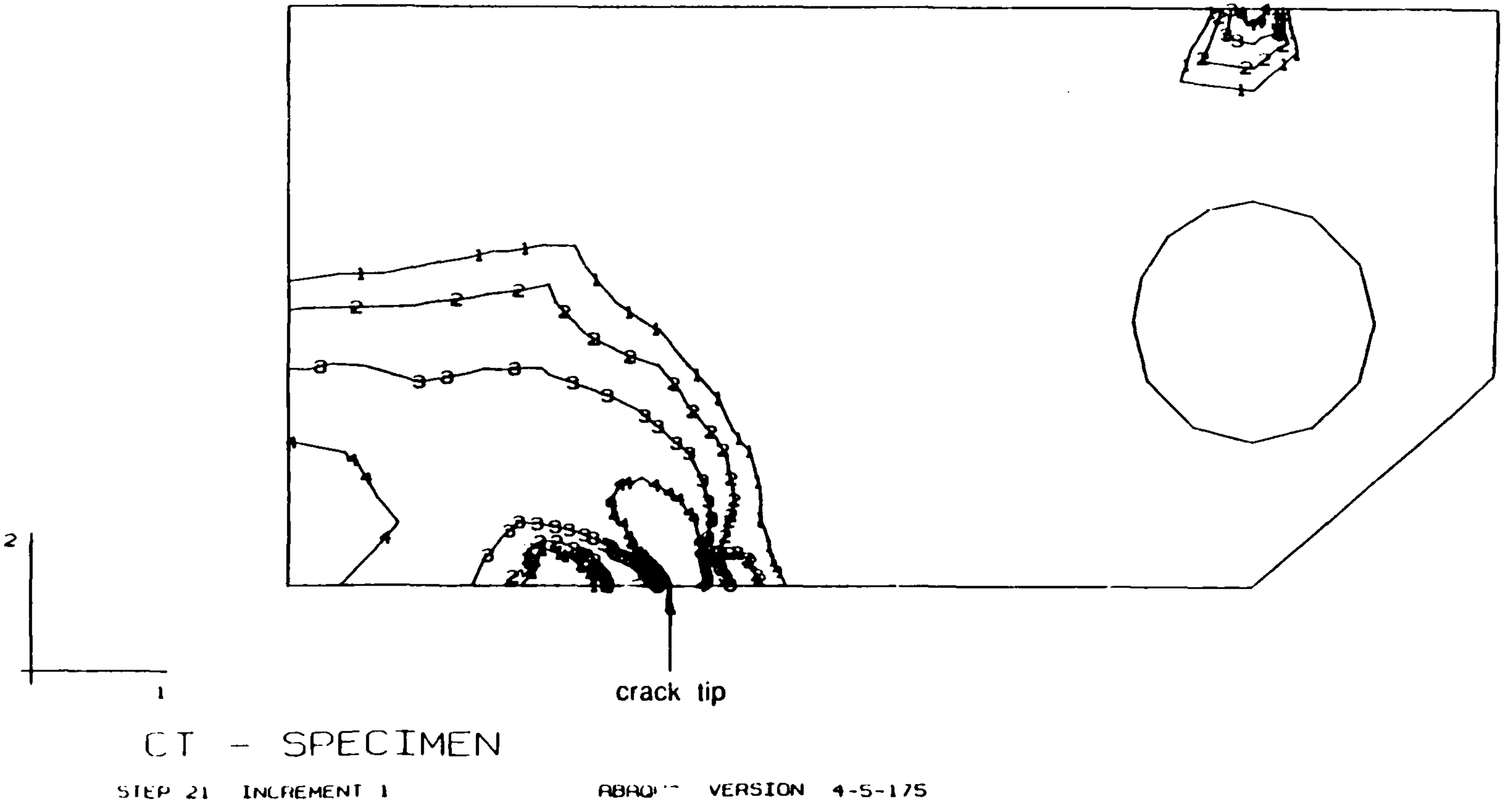
MISES EQUIV. STRESS
I. D. VALUE
1 +3. 32E+02
2 +3. 82E+02
3 +4. 32E+02
4 +4. 82E+02
1
2
3
4
2
1
crack tip
CT - SPECIMEN
STEP 21 INCREMENT 1
ABAQ'' VERSION 4-5-175

Figure 611: Iso contours of the von Mises stress (coarse mesh).

- load 8570 N

- Δa 6. mm

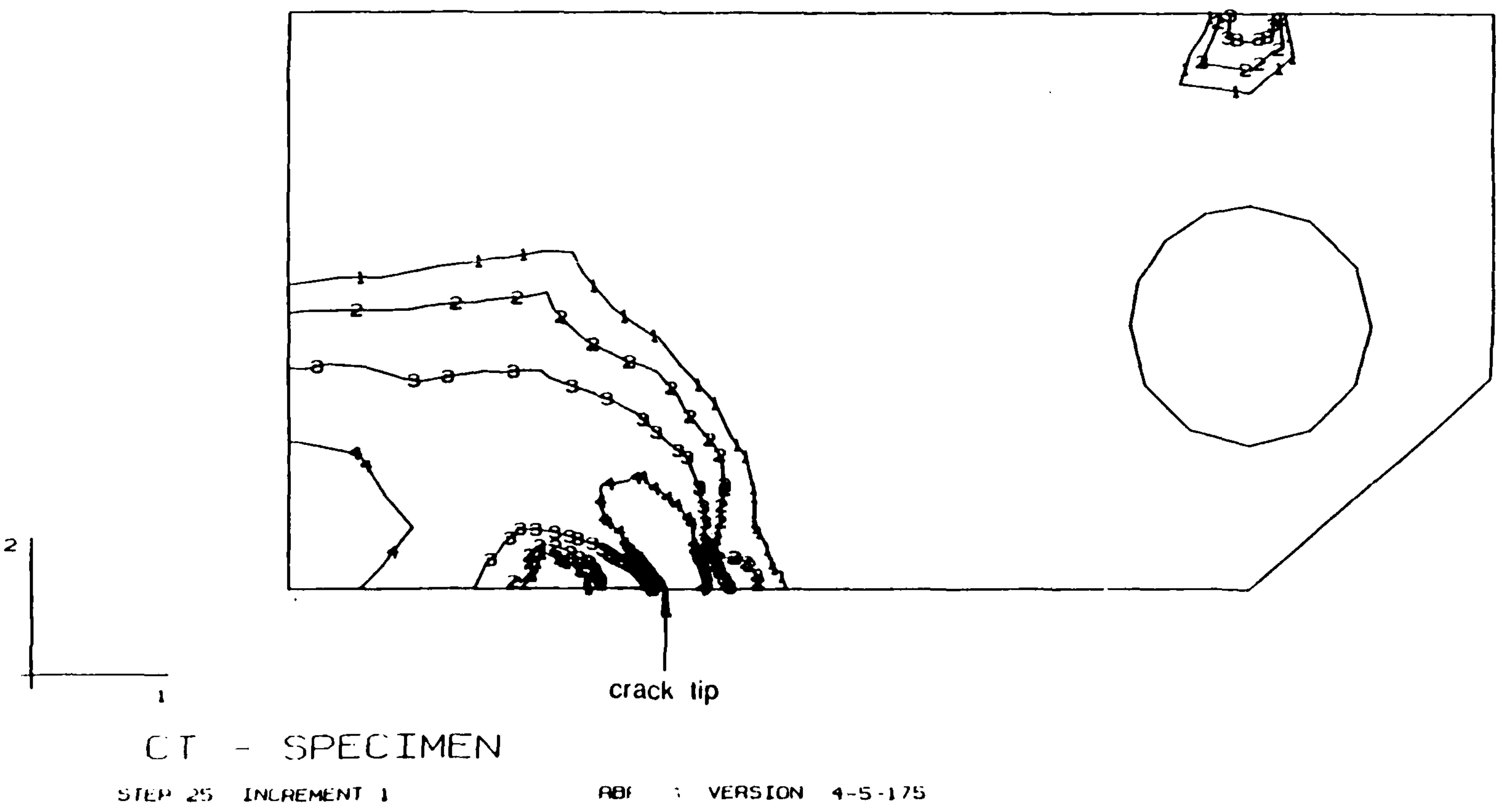

Figure 61m: Iso contours of the von Mises stress (coarse mesh).

- load 8250 N

- Δa 8. mm

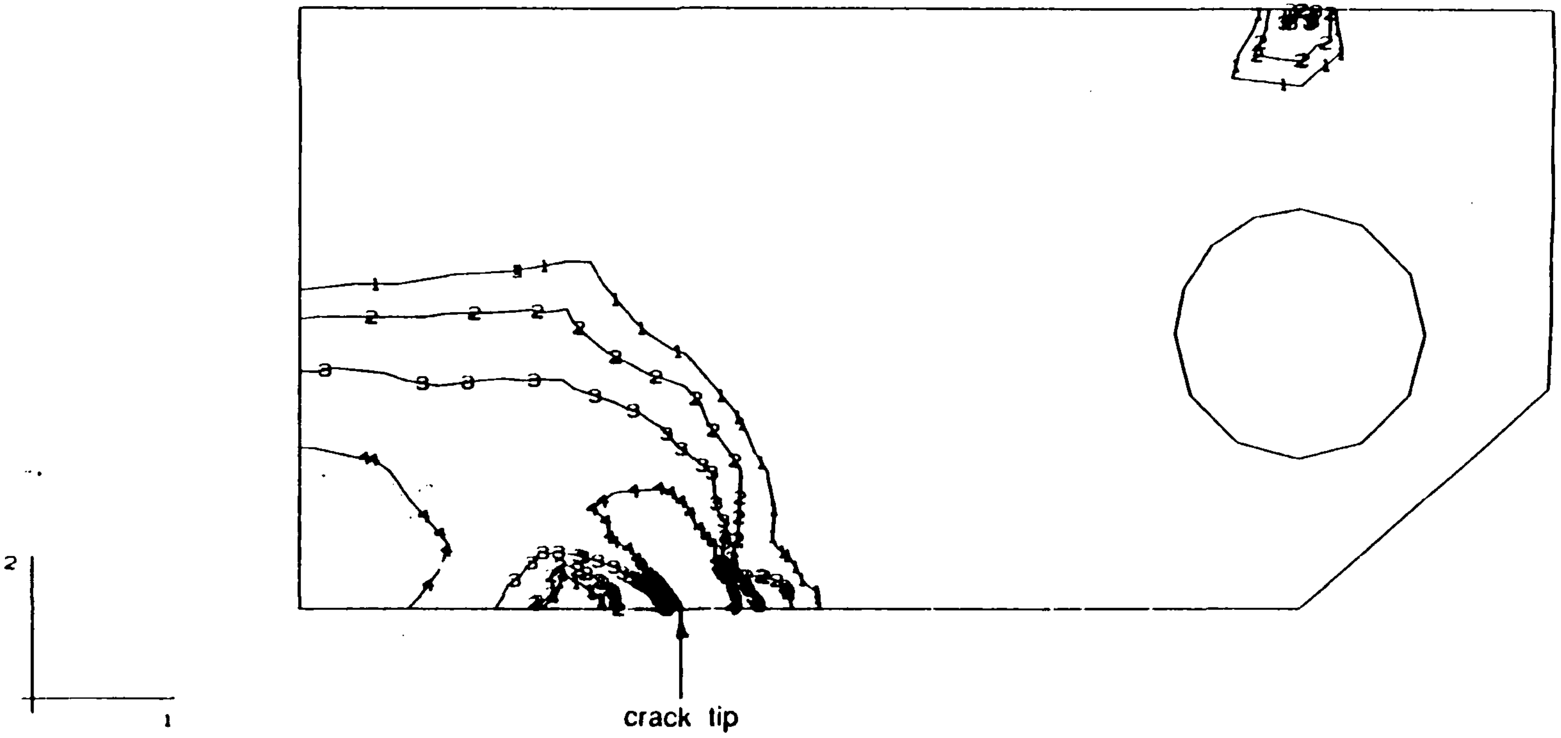
MISES EQUIV. STRESS
I. D. VALUE
1 +3. 32E+02
2 +3. 82E+02
3 +4. 32E+02
4 +4. 82E+02
1
2
3
4
2
1
crack tip
CT - SPECIMEN
STEP 33 INCREMENT 1
ABAC VERSION 4-5-175

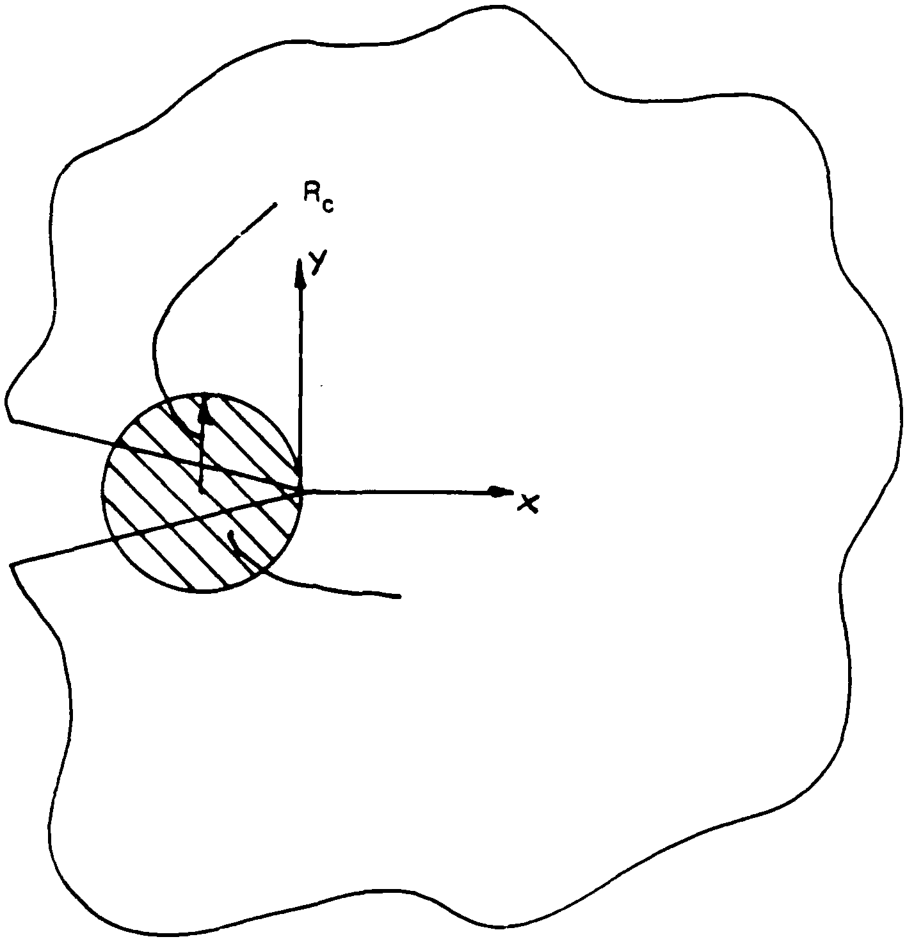

For larger amounts of crack growth: $2\,R_c \approx \Delta a$

Figure 62: Behavior of the characteristic radius R_c of the strain intense region (sharply bordered region where the rate of energy dissipation is high).

Table 1: Relation between the external (applied) load and the crack growth (coarse mesh).

coarse mesh		fine mesh	
F [N]	Δa [mm]	F[N]	Δa [mm]
5300	0	5300	0
6400	.25	5520	.05
7100	.5	5720	.1
7650	.75	5960	.15
8100	1.	6180	.2
8250	1.25	6400	.25
8400	1.5	6540	.3
8500	1.75	6680	.35
8600	2.	6820	.4
8660	2.25	6960	.45
8690	2.5	7100	.5
8710	2.75	7210	.55
8720	3.	7320	.6
8725	3.25	7430	.65
8729	3.5	7540	.7
8732	3.75	7650	.75
8734	4.	7740	.8
8732	4.25	7830	.85
8725	4.5	7920	.9
8715	4.75	8010	.95
8700	5.	8100	1.
8680	5.25		
8650	5.5		
8610	5.75		
8570	6.		
8530	6.25		
8490	6.5		
8450	6.75		
8410	7.		
8370	7.25		
8330	7.5		
8290	7.75		
8250	8.		

Table 2: Material composition of A533B steel [66] (in weight percent).

C	Mn	P	S	Si	Ni	Mo
0.2	1.22	0.01	0.016	0.15	0.65	0.54

Table 3: Stress - strain properties of A533B steel.

σ_0	ϵ_0	n	E	α
382.866 MPa	0.001933	10	197620 MPa	1

Table 4: J - integral values for different paths.

J - integral value	Path
89.88 N/mm	1
88.44 N/mm	2
82.57 N/mm	3
82.48 N/mm	4

Table 5: J - integral over crack growth.

J - integral	Δa
88.437	0
141.117	.25
193.161	.5
287.161	.75
444.633	1.
536.557	1.25
644.079	1.5
742.951	1.75
847.117	2.
1008.026	2.5
1133.745	3.
1251.212	3.5
1366.434	4.
1469.011	4.5
1554.629	5.
1614.482	5.5
1620.146	6.
1624.624	6.5
1642.07	7.
1618.571	8.

Table 6: Comparison of the results for the J - integral performed in this work with the work of Hoff [37].

	J at the onset of crack extension.	slope of the J - Δa curve for the first 2,5 mm crack extension.
this work	89.878 N/mm	393.1 MPa ,using least square curve fitting
Hoff	200 N/mm	360 MPa